WL-TR-93-3104

PROCEEDINGS OF DAMPING '93

VOL 2 OF 3

AD-A274 227

B.L. PORTIS, COMPILER

CSA ENGINEERING, INC.
2850 W. BAYSHORE ROAD
PALO ALTO, CALIFORNIA 94303-3843

JUNE 1993

INTERIM REPORT FOR 02/01/93-02/28/93

DTIC
ELECTE
DEC 23 1993
S
A

APPROVED FOR PUBLIC RELEASE; DISTRIBUTION IS UNLIMITED.

WRIGHT LABORATORY

FLIGHT DYNAMICS DIRECTORATE
WRIGHT LABORATORY
AIR FORCE MATERIEL COMMAND
WRIGHT PATTERSON AFB OH 45433-7562

93 12 23 006

93-31149

NOTICE

WHEN GOVERNMENT DRAWINGS, SPECIFICATIONS, OR OTHER DATA ARE USED FOR ANY PURPOSE OTHER THAN IN CONNECTION WITH A DEFINITELY GOVERNMENT-RELATED PROCUREMENT, THE UNITED STATES GOVERNMENT INCURS NO RESPONSIBILITY OR ANY OBLIGATION WHATSOEVER. THE FACT THAT THE GOVERNMENT MAY HAVE FORMULATED OR IN ANY WAY SUPPLIED THE SAID DRAWINGS, SPECIFICATIONS, OR OTHER DATA, IS NOT TO BE REGARDED BY IMPLICATION, OR OTHERWISE IN ANY OTHER PERSON OR CORPORATION; OR AS CONVEYING ANY RIGHTS OR PERMISSION TO MANUFACTURE, USE, OR SELL ANY PATENTED INVENTION THAT MAY IN ANY WAY BE RELATED THERETO.

THIS TECHNICAL REPORT HAS BEEN REVIEWED AND IS APPROVED FOR PUBLICATION.

Paul D. Lindquist
Aerospace Engineer
Acoustics and Sonic Fatigue

Ralph M. Shimovetz
Section Leader
Acoustics and Sonic Fatigue

John Ach, Acting Chief
Aerospace Engineer
Acoustics and Sonic Fatigue

REPORT DOCUMENTATION PAGE

Form Approved
OMB No. 0704-0188

1. AGENCY USE ONLY (Leave blank)	2. REPORT DATE	3. REPORT TYPE AND DATES COVERED
	JUN 1993	FINAL FEB 93 – FEB 93

4. TITLE AND SUBTITLE

PROCEEDINGS OF DAMPING '93
VOLUME 2 OF 3

5. FUNDING NUMBERS

C   F33615-89-C-3201
PE   63215C
PR   L502
TA   00
WU   20

6. AUTHOR(S)

BONNIE L. PORTIS, COMPILER

7. PERFORMING ORGANIZATION NAME(S) AND ADDRESS(ES)

CSA ENGINEERING, INC.
2850 W. BAYSHORE RD.
PALO ALTO, CA 94303-3843

8. PERFORMING ORGANIZATION REPORT NUMBER

9. SPONSORING/MONITORING AGENCY NAME(S) AND ADDRESS(ES)

WL/FIBGC (CAPT JOHN R. MACKAMAN)
FLIGHT DYNAMICS DIRECTORATE
WRIGHT LABORATORY
AIR FORCE MATERIEL COMMAND
WRIGHT-PATTERSON AFB OH 45433-7006

10. SPONSORING/MONITORING AGENCY REPORT NUMBER

WL-TR-93-3104

11. SUPPLEMENTARY NOTES

12a. DISTRIBUTION/AVAILABILITY STATEMENT

APPROVED FOR PUBLIC RELEASE; DISTRIBUTION UNLIMITED

12b. DISTRIBUTION CODE

13. ABSTRACT (Maximum 200 words)

PRESENTED ARE INDIVIDUAL PAPERS OF DAMPING '93, HELD 24-26 FEBRUARY 1993 IN SAN FRANSISCO. THE SUBJECTS INCLUDED: PASSIVE DAMPING CONCEPTS; PASSIVE DAMPING ANALYSIS AND DESIGN TECHNIQUES; OPTIMIZATION; DAMPED CONTROL/STRUCTURF INTERACTION; VISCOELASTIC MATERIAL TESTING AND CHARACTERIZATION; HIGHLY DAMPEL MATERIALS; VIBRATION SUPPRESSION TECHNIQUES; DAMPING IDENTIFICATION AND DYNAW TESTING; APPLICATIONS TO AIRCRAFT; SPACE STRUCTURES; MARINE STRUCTURES; AND COMMERCIAL PRODUCTS; DEFENSE APPLICATIONS; AND PAYOFFS OF VIBRATION SUPPRESSION.

14. SUBJECT TERMS

VIBRATION DAMPING, PASSIVE DAMPING
CONTROL/STRUCTURES INTERACTION

15. NUMBER OF PAGES

423

16. PRICE CODE

17. SECURITY CLASSIFICATION OF REPORT	18. SECURITY CLASSIFICATION OF THIS PAGE	19. SECURITY CLASSIFICATION OF ABSTRACT	20. LIMITATION OF ABSTRACT
UNCLASSIFIED	UNCLASSIFIED	UNCLASSIFIED	UL

Workshop Administration

Director
Dr. Lynn C. Rogers
Oak Ridge National Lab

Technical Chairman
Dr. Conor D. Johnson
CSA Engineering, Inc.

Administrative Chairman
Bonnie L. Portis
CSA Engineering, Inc.

Session Chairmen

Dr. Mohan Aswani, *Aerospace Corporation*
Mr. Eric M. Austin, *CSA Engineering, Inc.*
Mr. L. Porter Davis, *Honeywell, Inc.*
Mr. William Driscoll, *3M*
Mr. Robert Dunning, *Lockheed*
Dr. John P. Henderson, *Materials and Vibration Engineering*
Dr. Darel E. Hodgson, *E*Sorb Systems*
Dr. Robert Holman, *Hughes Aircraft Company*
Mr. J. Warren Hoskins, *Lockheed Missiles and Space Company*
Dr. Roy Ikegami, *Boeing Aerospace and Electronics*
Dr. Conor D. Johnson, *CSA Engineering, Inc.*
Dr. James Kelly, *EERC, University of California at Berkeley*
Dr. Edward Kerwin, *Bolt, Beranek and Newman, Inc.*
Dr. John Kirby, *McDonnell Douglas Aerospace Company*
Mr. Robert Krumme, *CMS, Inc.*
Lt. Col. Steve Lamberson, *AFWL/ARDI*
Capt. Vincent J. Levraea, *Wright Laboratory, Flight Dynamics Directorate*
Mr. Salvatore Liguore, *McDonnell Douglas Aerospace Company*
Mr. Paul Lindquist, *Wright Laboratory, Flight Dynamics Directorate*
Capt. John R. Mackaman, *Wright Laboratory, Flight Dynamics Directorate*
Mr. Rory Ninneman, *Phillips Laboratory*
Mr. Ted Nye, *TRW Space and Technology Group*
Mr. Jerome Pearson, *Wright Laboratory, Flight Dynamics Directorate*
Mr. Ken Qassim, *Phillips Laboratory*
Dr. Mohan Rao, *Michigan Technological University*
Mr. Stanley Sattinger, *Westinghouse Science and Technology Center*

iii

Dr. Daniel Segalman, *Sandia National Labs*

Dr. Jaak Soovere, *Lockheed Aeronautical*

Capt. Daniel Stech, *United States Air Force Academy*

Mr. Ralph Tate, *Loral Vought Systems*

Dr. John Tracy, *McDonnell Douglas Aerospace Company*

Dr. Ben Wada, *Jet Propulsion Laboratory*

Ms. Catherine Wong, *Naval Surface Warfare Center*

Mr. Michael Zeigler, *Wright Laboratory, Flight Dynamics Directorate*

FOREWORD

This publication includes individual papers of **Damping '93** held February 24-26, 1993, San Francisco, California. The Conference was sponsored by the Air Force Wright Laboratory, Flight Dynamics Directorate, Wright-Patterson Air Force Base, Ohio.

TABLE OF CONTENTS

*Not available for publication   vi

TABLE OF CONTENTS (continued)

*Not available for publication   vii

TABLE OF CONTENTS (continued)

*Not available for publication   viii

TABLE OF CONTENTS (continued)

TABLE OF CONTENTS (continued)

*Not available for publication   x

TABLE OF CONTENTS (continued)

*Not available for publication   xi

TABLE OF CONTENTS (continued)

Paper No.

*Not available for publication

TABLE OF CONTENTS (continued)

*Not available for publication

TABLE OF CONTENTS (continued)

*Not available for publication   xiv

TABLE OF CONTENTS (continued)

The following is a list of authors and their addresses who where unable to submit their papers for publication in the Damping '93 Proceedings.

Dr. John W. Lincoln
USAF/ASC/ENFS
Area B, Building 125
2335 Seventh Street, Suite 6
Wright-Patterson AFB, OH 454433-7809
telephone: (513) 255-2576
fax: (513) 476-4546

John Molnar
GE Astro Space
P.O. Box 800
MS NP 1A
Princeton, NJ 94303-0800
telephone: (609) 951-7804
fax: (609) 951-7911

Eric M. Austin
CSA Engineering, Inc.
2850 West Bayshore Road
Palo Alto, CA 94303-3843
telephone: (415) 494-7351
fax: (415) 494-8749

Wing Kam Liu
Northwestern University
Department of Mechanical Engineering
Evanston, IL 60208-3111
telephone: (708) 491-7094
fax: (708) 491-3915

Antonio M. Claret
Escola de Minas / UFOP
Pc Tiradentes No. 20
CEP 35400-000 Ouro Preto, MG
Brasil
telephone: (031) 551-1139
fax: (031) 551-1689

Dr. Lynn C. Rogers
Oak Ridge National Lab
USAF/WL/FIBG (Center for Passive Damping)
Area B, Building 24C, Room 220
2145 Fifth Street, Suite 2
Wright-Patterson AFB< OH 45433-7006
telephone: (513) 255-6622 extension 252
fax: (513) 255-6684

John Andriulli
Oak Ridge National Lab
K-25, Site/K-1225, MS-7294
P.O. Box 2003
Oak Ridge, TN 37831-7294
telephone: (615) 576-0424
fax: (615) 574-8481

Dr. M. Groper
Western Michigan University
College of Engineering and Applied Sciences
Department of Mechanical and Aeronautical Engineering
Kalamazoo, MI 49008-5065
telephone: (616) 387-3380
fax: (616) 387-4024

Salvatore L. Liguore
McDonnell Douglas Aerospace
P.O. Box 516
St. Louis, MO 63166-0516
telephone: (314) 232-3109
fax: (314) 777-1171

Capt. Vincent Levraea
WL/FIBG, Wright Laboratory
2145 Fifth Street, Suite 2
Wright-Patterson AFB, OH 45433-70'k.
telephone: (513) 255-5229 extension 452
fax: (513) 255-6685

Col. Ronald Bagley
WL/FIB, Wright Laboratory
Wright-Patterson AFB, OH 45433-7006
telephone: (513) 255-5200 extension 457
fax: (513) 255-6684

Dr. Shian-Ing Chen
China Steel Corporation
Lin Hai Industrial District
P.O. Box 47-29
Hsiao Kang, Kaohsiung
81233 Taiwan, Republic of China
telephone: 07-802-1111 extension 3353
fax: 07-802-2511

Dr. W. M. Patten
The University of Oklahoma
School of Aerospace and Mechanical Engineering
865 Asp Avenue, Room 212
Norman, OK 73019-0601
telephone: (405) 325-5011
fax: (405) 325-1088

Ilja D. Tsukernikov
Head of Vibroacoustics Sector
123308 Moscow, Marshal Zhukov Avenue, 1
Russia
telephone: (095) 195-6974
fax: (095) 195-1043

Boris A. Seliverstov
Chief of Laboratory
123308 Moscow, Marshal Zhukov Avenue, 1
Russia
telephone: (095) 195-6974
fax: (095) 195-1043

H. A. Ahmadi
Malaysian Rubber Producer's Research Association
Brickendonbury
Hertford SG13 8NL, England
telephone: (0992) 584-966
fax: (0992) 554-837

Dr. S. O. Oyadiji
University of Manchester
Engineering Department
Simon Building
Manshester M13 9PL, United Kingdom
telephone: (44) 61-275-4444
fax: (44) 61-275-3844

<div style="border:1px solid black; padding:20px; text-align:center;">

Performance/Sizing Tradeoffs
in Active and Passive Launch Isolation

</div>

Damping '93

February 24-26, 1993
Hotel Nikko
San Francisco, CA

PERFORMANCE/SIZING TRADEOFFS IN ACTIVE AND PASSIVE LAUNCH ISOLATION

David C. Cunningham
Honeywell Inc.
Satellite Systems Operation
Glendale, AZ 85308-9650

ABSTRACT

Active and passive systems for spacecraft launch isolation are compared in terms of performance and size. Performance is characterized by the peak acceleration provided to the isolated payload, and includes the component due to the quasistatic acceleration transient (due to ignition and burnout, as well as random vibration). Size is characterized by the peak-to-peak stroke during launch, and again contains both a quasistatic acceleration and a random component.

INTRODUCTION

Both active (magnetic) and passive (viscous) isolators are finding increasing application in spacecraft because of the need to provide high pointing stability and quiescent vibration to sensitive experiments. The use of these mechanisms for launch isolation, however, has been very limited, even though the launch environment typically determines the size of all structural elements in the device being launched (e.g., bearings, housings, circuit boards, etc).

To better understand the tradeoffs involved between performance and sizing of both active and passive isolators for launch, the study reported in this paper was performed.

PROBLEM DESCRIPTION

As an example of an application that would benefit from launch isolation, a current-production momentum wheel program is used. In this program, the wheel is isolated at approximately 15 Hz to reduce the transmission of emitted vibration from the wheel into the spacecraft under operational (in-orbit) conditions. The isolator designed for this program is *not* required to operate during launch; in fact, it includes stops that are designed to limit travel during launch. The wheel weighs approximately 194 lb and is launched on a Titan IV.

In reviewing launch vibration data for Titan IV, two effects are apparent: a random vibration and a quasistatic acceleration profile. The quasistatic acceleration is bounded by a constant 3.5g having a step turn-on and turn-off as shown in Fig. 1a. As will be discussed later in this paper, the sharp turn-off is of importance in determining the total stroke of the isolator. Random vibration is modeled by the acceleration Power Spectral Density (PSD) shown in Fig. 1b. This is the design or qualification level for which the isolation system must show positive load margins.
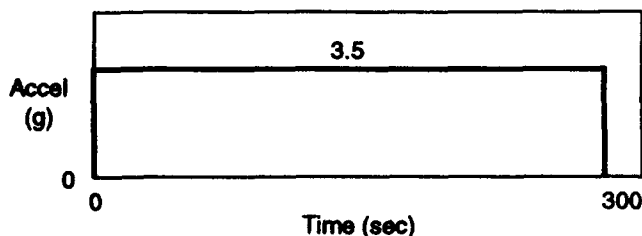
Fig. 1a Quasi-static Acceleration
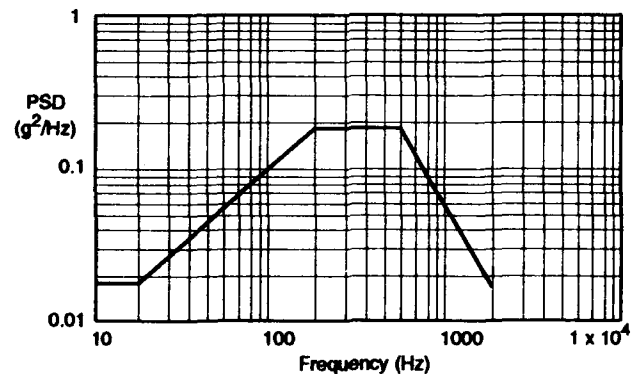
Fig. 1b Base Acceleration PSD

The following sections of this report evaluate performance and sizing of different isolator designs for this launch environment. Depending on the form of isolation considered, each isolator can be described by two or more design parameters (in addition to the suspended mass, which is considered fixed). For example, the simplest isolator is characterized by a parallel stiffness and damping constant. We parameterize each of the isolators to make the study as general as possible. The parameter that is varied is the open-loop crossover frequency, because it has the most direct effect on both performance and size. In this context, performance is taken as the peak acceleration of the isolated payload in g's, and sizing is taken as the peak-to-peak stroke of the isolator. The other parameter(s) in the isolator is generally associated with its peaking and/or roll-off characteristics; these were not parameterized, but were fixed at what seemed to be reasonable values for the application.

PASSIVE SECOND-ORDER ISOLATOR

The simplest isolator design consists of a parallel spring and damper as shown in Fig. 2. This is the form of isolation currently used on the Titan IV momentum wheel program, which is taken as the example for this study, with the exception that the production isolator includes stops that limit the travel (and isolation) during launch.

A block diagram of the isolator is shown in Fig. 3. Note that the mechanical impedance consists of a normalizing gain factor and a lead term. Although not necessary for the purposes of this paper, it is a simple matter to relate the open-loop design parameters α and ωco to the hardware parameters K and C:

$$K = M \cdot \omega co^2 \tag{1}$$

$$C = M \cdot \omega co / \alpha \tag{2}$$
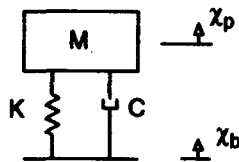
Fig. 2 Passive Second-order Isolator Schematic
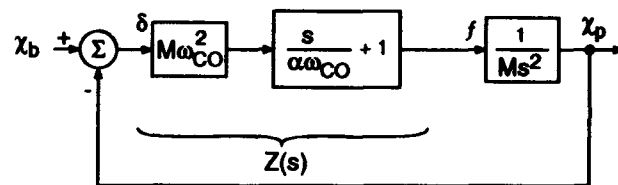
Fig. 3 Passive Second-order Isolator Block Diagram

Typically, C is relatively small in this type of isolator, causing the zero at $\alpha\omega co$ to be well above the crossover frequency ωco. Fig. 4 shows a Bode diagram of the open-loop system. We fix α to be 5.5 for this isolator, which provides a Q of about 6, which is typical for this type of design. The crossover frequency ωco is then varied to see the effect on the isolation transfer function, the payload acceleration, and the relative stroke across the isolator itself.

Letting Z(s) denote the complex mechanical impedance, GI(s) the isolation transfer function (payload acceleration over base acceleration), and GΔ the stroke transfer function (relative displacement between the payload and base divided by the base acceleration):

$$Z(s) = (M \cdot \omega co^2) \cdot \left(\frac{s}{\alpha \cdot \omega co} + 1 \right) \tag{3}$$

$$GI(s) = \frac{Z(s)}{M \cdot s^2 + Z(s)} \tag{4}$$

$$G\Delta(s) = \frac{386 \cdot M}{M \cdot s^2 + Z(s)} \tag{5}$$
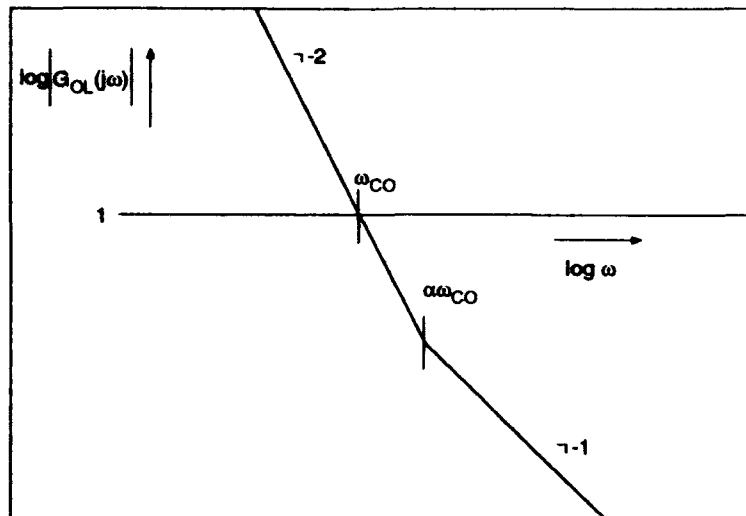
Fig. 4 Open-loop Bode Diagram of Passive Second-order Isolator

The response to the random vibration component is obtained in the frequency domain. The payload PSD is simply the base PSD times the magnitude squared of GI(s), and the peak value is obtained by taking the square root of the integral of the PSD and multiplying by 3. Similarly, the stroke response is obtained by multiplying the base PSD by the magnitude square of GΔ(s), integrating across the frequency range, taking the square root, and multiplying by 6 to get the peak-to-peak value.

To obtain the transient response of the system to the step acceleration of 3.5g, a simple time domain simulation is made. The peak acceleration is noted as well as the peak-to-peak stroke.

Finally, the random and transient response accelerations and strokes are added to obtain the worst-case values; this is shown in Table 1 below. As would be expected, the payload acceleration increases as the bandwidth (which is proportional to the crossover frequency) increases, and the stroke decreases. However, the peak acceleration due to the launch transient is nearly independent of the bandwidth.

Table 1 Passive Second-order Isolator Performance

Performance	Crossover Frequency (Hz)		
	13.0	16.0	20.0
Payload Acceleration due to PSD (g's pk)	4.51	5.17	5.88
Stroke due to PSD (in. pk-pk)	0.514	0.388	0.282
Payload Acceleration due to 3.5g step (g's pk)	6.24	6.23	6.19
Stroke due to 3.5g step (in. pk-pk)	0.519	0.357	0.225
Total Payload Acceleration (g's pk)	10.75	11.40	12.07
Total Stroke (in. pk-pk)	1.033	0.745	0.507

PASSIVE (OR ACTIVE) THIRD-ORDER ISOLATOR

Fig. 5 shows the mechanical schematic of an isolator that includes a series spring. This (or any other) passive isolator could also be implemented actively. A block diagram of the dynamics is shown in Fig. 6. Again, the open-loop impedance parameters ω_{co} and α can be related to the mechanical model parameters KA, KB, and CA:

$$KA = M \cdot \omega_{co}^2/\alpha \tag{6}$$

$$KB = KA \cdot (\alpha^2 - 1) \tag{7}$$

$$CA = KB/(\alpha \cdot \omega_{co}) \tag{8}$$

Fig. 7 is a Bode plot of the open-loop gain of this system. It should be noted from Fig. 7 that the isolator parameters have been selected in a particular way to cause the lead and lag frequencies to be equally spaced below and above the crossover frequency. By making the geometric mean of the lead and lag frequencies equal to the crossover frequency, the phase margin of the system is maximum, and the damping (for a given lead/lag separation) will also be maximized. We refer to this type of isolator as *tuned* because there is an optimum value (given by Eq. (8)) for the damping constant CA that maximizes the damping.
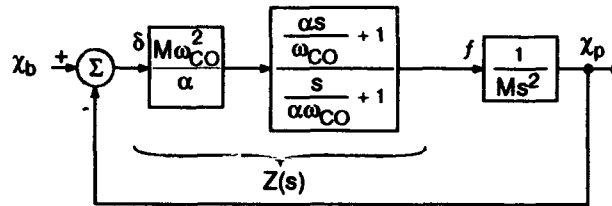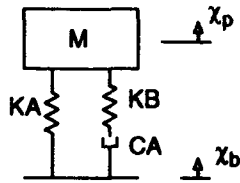
Fig.5 Third-order Isolator Schematic

Fig. 6 Third-order Isolator Block Diagram
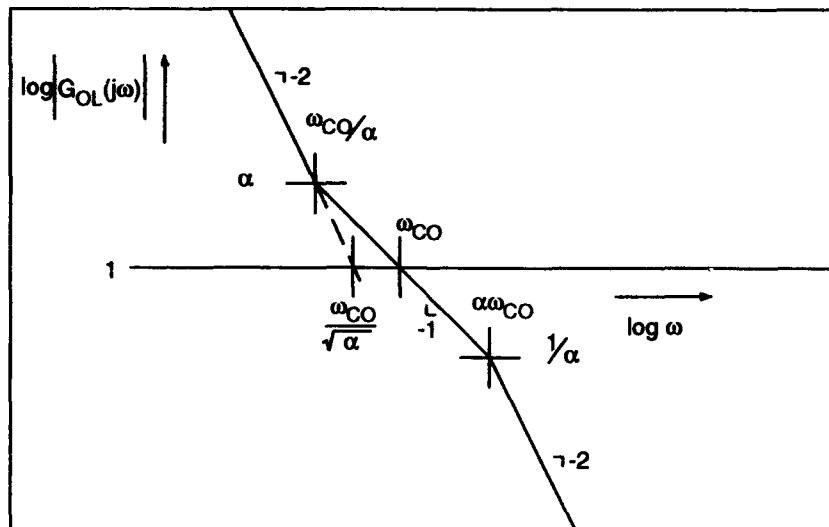
Fig. 7 Open-loop Bode Diagram of Third-order Isolator

To illustrate the effect of varying the separation ratio (α^2) on the isolation transfer function, the crossover frequency was held constant at 20 Hz, and the plots shown in Fig. 8 were generated. It should be remembered that these are third-order-system responses, and the peaking is due not only to the complex pole pair, but also to a real zero below the natural frequency. When the system is properly *tuned*, the three poles all have the same natural frequency; two are complex conjugates and the third is real.

The isolation transfer characteristics shown in Fig. 8 may be compared with the isolation characteristic of a second-order isolator such as discussed in the previous section. For a system of the same natural frequency and peaking (Q), the third-order system provides greater isolation at high frequencies.
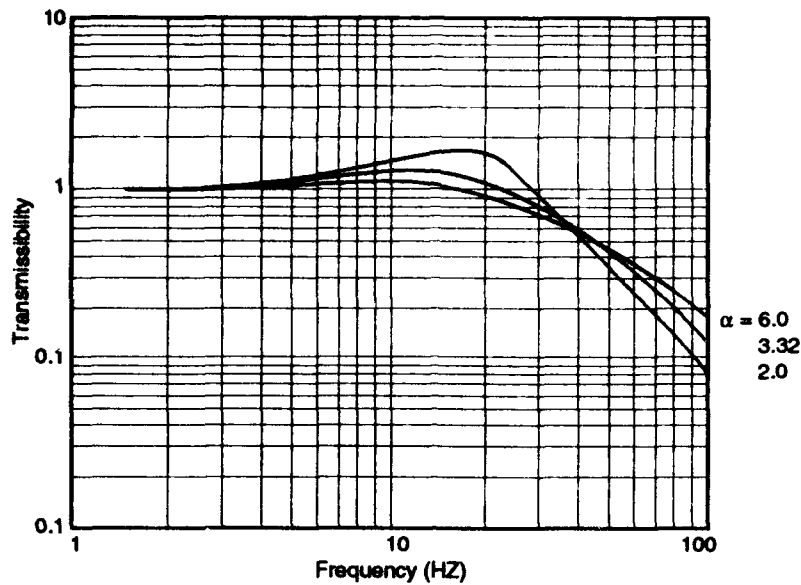
Fig. 8 Third-order Isolation Transfer Characteristics

A typical value for α was selected to be 3.32, and the accelerations and strokes resulting from the random vibration PSD and 3.5g step transient were computed using the same procedure as outlined in the previous section. Results are listed in Table 2.

Table 2 Third-order (Tuned) Isolator Performance

Performance	Crossover Frequency (Hz)				
	13.0	16.0	20.0	24.0	29.0
Total Payload Acceleration (g's pk)	6.63	6.97	7.45	7.95	8.58
Total Stroke (in. pk-pk)	1.110	0.762	0.511	0.371	0.268

ACTIVE ISOLATOR WITH INTEGRATION (FOURTH ORDER)

The passive second- and third-order isolators have a static stroke proportional to the steady-state acceleration, which is significant. For example, the 20 Hz third-order isolator stroke of 0.511 in. includes a static deflection of 0.284 in. A potential advantage in an active system is the capability to include a free integrator that would drive this steady-state stroke to zero. This is shown in the schematic of Fig. 9, the block diagram in Fig. 10, and the Bode plot of Fig. 11.
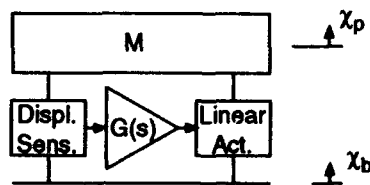
Fig. 9 Active Fourth-order Isolator Schematic
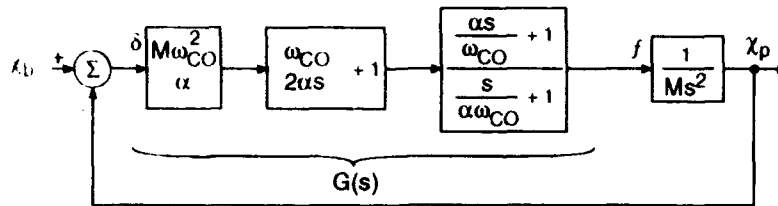
Fig. 10 Active Fourth-order Isolator Block Diagram
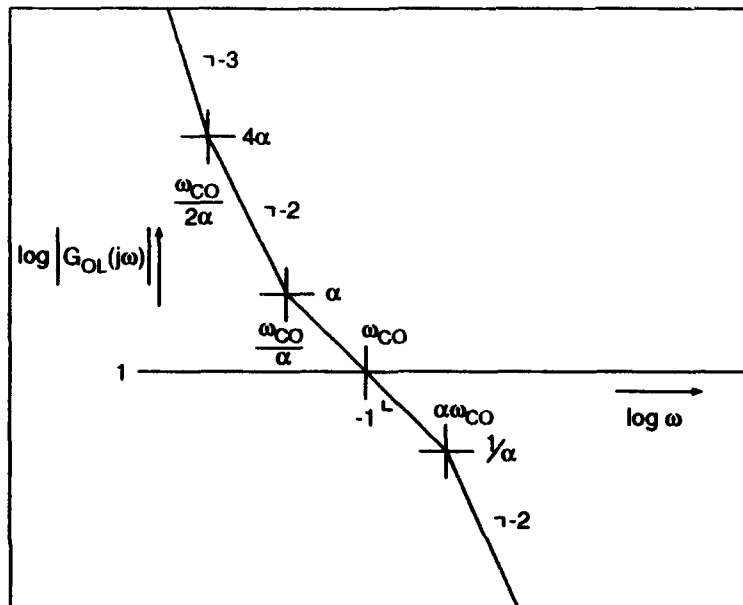
Fig. 11 Open-loop Bode Diagram of Active Fourth-order Isolator

In the region around the open-loop crossover, the active system is identical to the passive, third-order, tuned system described above; however, at low frequencies below $\omega co/(2 \cdot \alpha)$ the loop transfer function is dominated by the integral term.

This approach works fine until the launch acceleration is removed. At that time, the integrator has acquired an output that exactly balances the force due to the 3.5g steady-state acceleration. But when the 3.5g is suddenly removed, the integrator causes the payload to move *up*. This results in a transient response at the end of launch that is equal and opposite to the transient that occurred at the start of launch. The peak-to-peak stroke that sizes the actuator and position sensor thereby doubles, resulting in a net stroke increase over the passive system without the integrator.

Table 3 summarizes the accelerations and strokes.

Table 3 Performance of Active Isolator with Integrator (Fourth Order)

Performance	Crossover Frequency (Hz)			
	13.0	16.0	20.0	24.0
Total Payload Acceleration (g's pk)	7.27	7.64	8.15	8.68
Total Stroke (in. pk-pk)	1.151	0.805	0.544	0.396

ACTIVE ISOLATOR WITH HIGH-ORDER ROLLOFF (SIXTH ORDER)

Another potential advantage of an active system is its ability to provide high-order rolloff. For the same bandwidth isolator, the attenuation at high frequencies will be much greater. Assuming the stroke to be related to the low- and/or mid-frequency characteristics, this approach should provide better isolation at about the same stroke.

The schematic diagram of this isolator is the same as Fig. 9. The block diagram given in Fig. 12 shows that the compensation comprises a first-order zero followed by two identical second-order lags. The Bode diagram of Fig. 13 shows that the zero frequency is a factor of α below the crossover, and the lag breaks are at a factor of $\lambda \cdot \alpha$ above crossover. After some experimenting, α was selected to be 3 and λ was chosen to be 1.5. A damping ratio of $\zeta = 0.5$ is used on the quadratic terms. Note that no free integrator is used, for the reasons cited in the previous section.
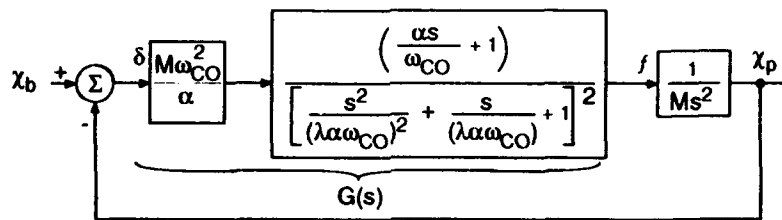
Fig. 12 Active Sixth-order Isolator Block Diagram
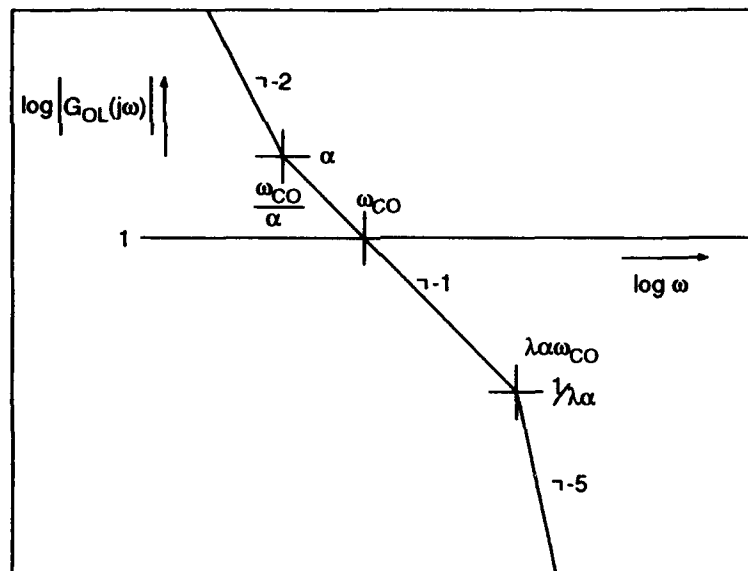
Fig. 13 Open-loop Bode Diagram of Active Sixth-order Isolator

Table 4 lists the results of varying the crossover frequency. Although the stroke is approximately the same as a third-order tuned system having the same crossover frequency, the peak acceleration is higher. This is predominantly due to the random component of vibration, not the 3.5g transient response. The high-order isolator provides a steep high-frequency rolloff, but it also has a broad transmissibility around resonance. Because the random vibration PSD increases with frequency in the range between 20 and 200 Hz, any tendency of the isolator to maintain transmissibility in this frequency range results in an increased payload acceleration. At frequencies above 100 Hz, the high-order isolation out-performs the passive tuned isolator, but this improvement is more than compensated for by the poorer isolation below 100 Hz.

Table 4 Performance of Active High-order Isolator (Sixth Order)

Performance	Crossover Frequency (Hz)			
	13.0	16.0	20.0	24.0
Total Payload Acceleration (g's pk)	8.38	9.02	9.90	10.82
Total Stroke (in. pk-pk)	1.041	0.719	0.485	0.355

ACTIVE ISOLATOR WITH INERTIAL SENSING (FIFTH ORDER)

The tuned third-order isolator described in the Passive (or Active) Third-order Isolator section can be augmented by an accelerometer feedback loop. The idea is to sense the payload inertial acceleration and force it towards zero over a selected frequency range, using an actuator such as shown in Fig. 14. Although the diagram in Fig. 14 shows the system as all active, it can also be implemented in a hybrid fashion, using a passive isolator to replace the displacement sensor and G(s) compensator.
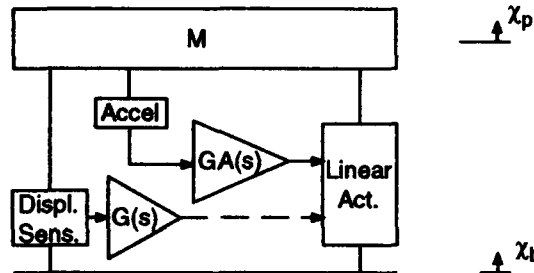
Fig. 14 Tuned Inertial Sensing Isolator Schematic

Fig. 15 shows the block diagram of the tuned inertial sensing isolator. The *outer loop* involving displacement δ is identical to the passive (or active) third-order isolator design, and the inner loop involving payload acceleration a_p is intended to provide a higher effective mass over the frequency range bounded by $\omega 1$ and $\omega 2$. If the accelerometer bandwidth was not limited on the low end by $\omega 1$, the static stroke of the isolator would increase under the 3.5g static load. The high frequency bandwidth $\omega 2$ is necessary to prevent excessive noise in the servo.
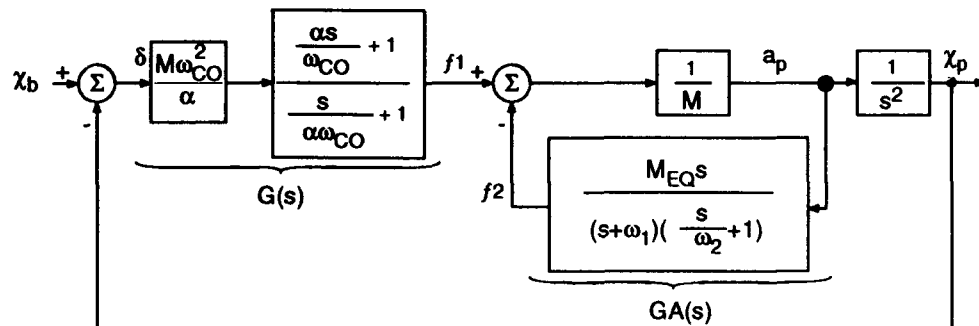
Fig. 15 Tuned Inertial Sensing Isolator Block Diagram

Fig. 16 shows the open-loop Bode plot. It should be noted that the frequencies $\omega1$ and $\omega2$ are the same as the lead and lag frequencies used in the displacement loop:

$$\omega1 = \omega co/\alpha \tag{9}$$

$$\omega2 = \alpha \cdot \omega co \tag{10}$$
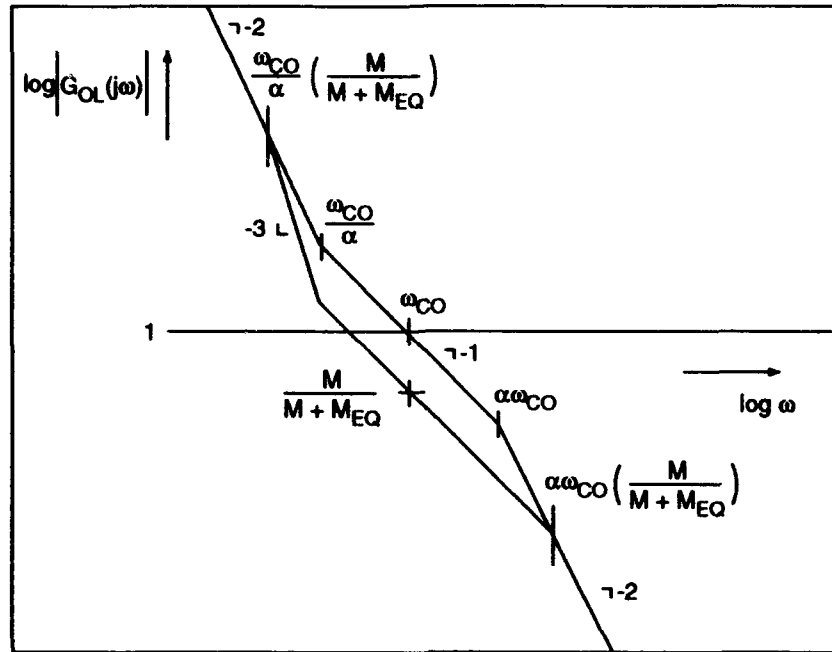
Fig. 16 Open-loop Bode Plot of Tuned Inertial Sensing Isolator

Two values were tried for the equivalent (augmented) mass: Meq = M and Meq = 2 · M. Results are listed in Table 5. Increasing the equivalent mass has the effect of increasing the stroke and slightly lowering the peak acceleration.

Table 5 Accelerometer Augmented Isolator Performance

Performance	Crossover Frequency (Hz) and Equivalent Mass		
	20.0 M	20.0 2 x M	24.0 2 x M
Total Payload Acceleration (g's pk)	6.81	6.67	6.94
Total Stroke (in. pk-pk)	0.649	0.830	0.610

SUMMARY

Peak acceleration is plotted against peak-to-peak stroke in Fig. 17 for each of the isolators studied. Performance is proportional to peak acceleration, and size is proportional to the peak-to-peak stroke for either active or passive isolators, therefore, the best design would be closest to the origin in Fig. 17.
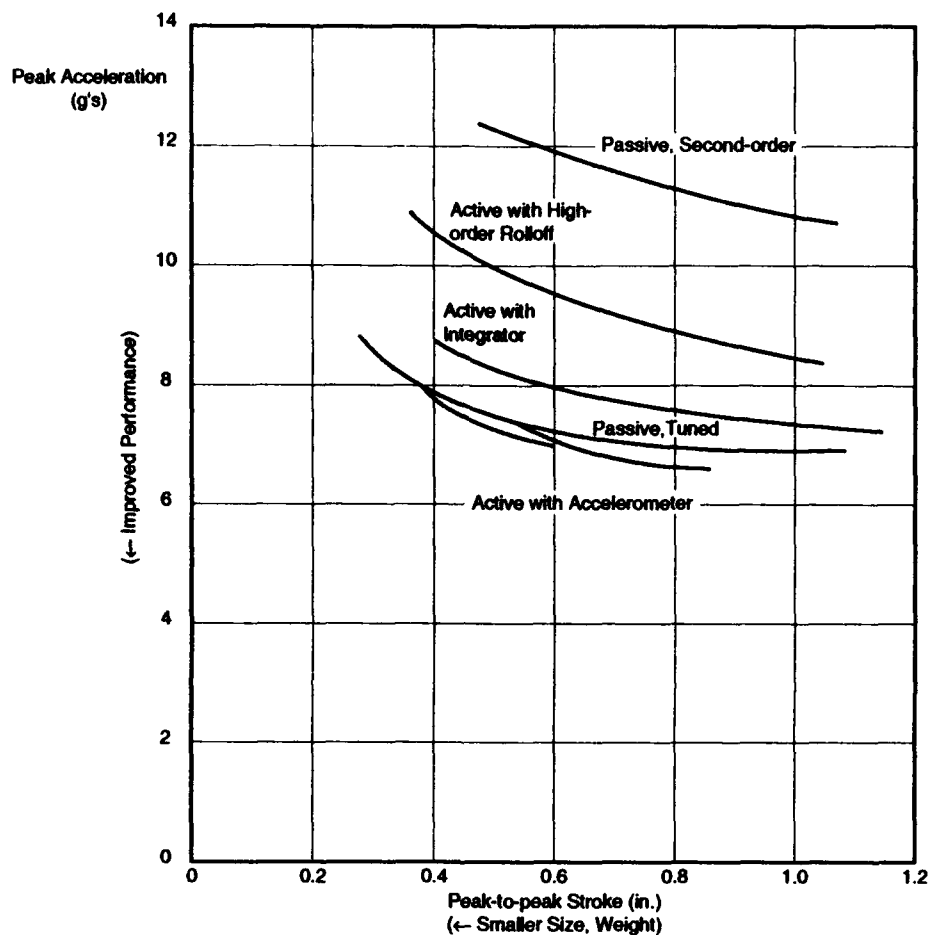
Fig. 17 Comparison of Launch Isolator Performance

Based on these results, it is concluded that:

(1) The tuned third-order passive isolator shows significant isolation improvement over the conventional second-order isolator.

(2) The use of a free integrator or higher-order rolloff (possible in an active isolator) does not result in net improvement in performance and/or sizing.

(3) Accelerometer augmentation of the tuned third-order isolator provides a small improvement.

It should be emphasized again, that these results are based on a specific launch vibration environment and may not be applicable to other applications.

A LAUNCH ISOLATION SYSTEM FOR THE SHUTTLE RESUPPLIED HUBBLE SPACE TELESCOPE SOLAR ARRAY

Porter Davis, Terry Allen, and John Vise
Honeywell Inc.
Satellite Systems Operation
Glendale, Arizona 85308-9650

ABSTRACT

A new shuttle-based payload launch isolation system, developed specifically to reduce launch and landing vibration for the Hubble Space Telescope replacement solar arrays, can be reconfigured to accommodate a wide variety of shuttle payloads, including small satellites. The six-axis system provides break frequencies of approximately 8 Hz in each of six axes for a 2240-lb payload. High values of viscous damping improve performance over systems with zero or very low damping. The system is made up of four sets of three isolator elements (or tripods) attached at four locations on the payload and twelve locations on the shuttle interface. The angles formed by this arrangement of elements enable the system to be configured or reconfigured to provide the performance needed in each axis, while the elements themselves remain identical. Minor changes to the design would enable the system to accommodate payloads of up to 4250 lb. Larger payloads could be accommodated by adding additional elements. The system could potentially be used as a satellite launch isolator; this would reduce the cost and weight of some satellites or their subsystems and enable others, which had been qualified for lower-vibration-level launch systems, to be launched by the shuttle. A large operating temperature range (-43 to +49 °C) avoids the need of costly active thermal control.

INTRODUCTION

Honeywell completed the Solar Array Carrier Isolator (SACI) program in August 1992 with the delivery of the system to Fairchild Space. The SACI is a subsystem of the Hubble Space Telescope's Solar Array Carrier being developed by Fairchild for NASA Goddard. Swales and Associates Inc., provided system analyses. NASA will use this system and the Shuttle to resupply new solar arrays to the Hubble Space Telescope. As of September 1992, the carrier was being assembled at the NASA facility by Fairchild.

The SACI is required to reduce launch and landing loads that would cause damage if the solar arrays were hard mounted to either the shuttle directly or the carrier. The original solar arrays were protected by virtue of the large mass and flexibility of the telescope. Analysis showed that isolating the carrier with undamped spring elements would adequately reduce the higher frequency response but would cause a problem at the resonance frequency. This fact demanded the development of the SACI system with its ability to provide high values of damping. An alternative to isolating the arrays would have been to redesign them. NASA judged this to be a higher-dollar cost alternative.

SYSTEM DESCRIPTION

The SACI is part of the solar array carrier, shown in Fig. 1. The SACI is composed of 12 elements arranged in four tripods. The tripods attach between the solar array support structure and a pallet assembly. A photograph of one tripod undergoing static load testing is shown in Fig. 2.

Each element is modeled as a classical two-parameter viscously damped system (Fig. 3). Tests confirmed that it was not necessary to model stiction or end play; this is because the launch or landing loads and displacements are large compared to seal friction or ball-joint end play. NASTRAN models of the complete structure were a part of the total analysis. Much of the design synthesis was conducted to determine the optimum amount of damping and the maximum stroke requirements.
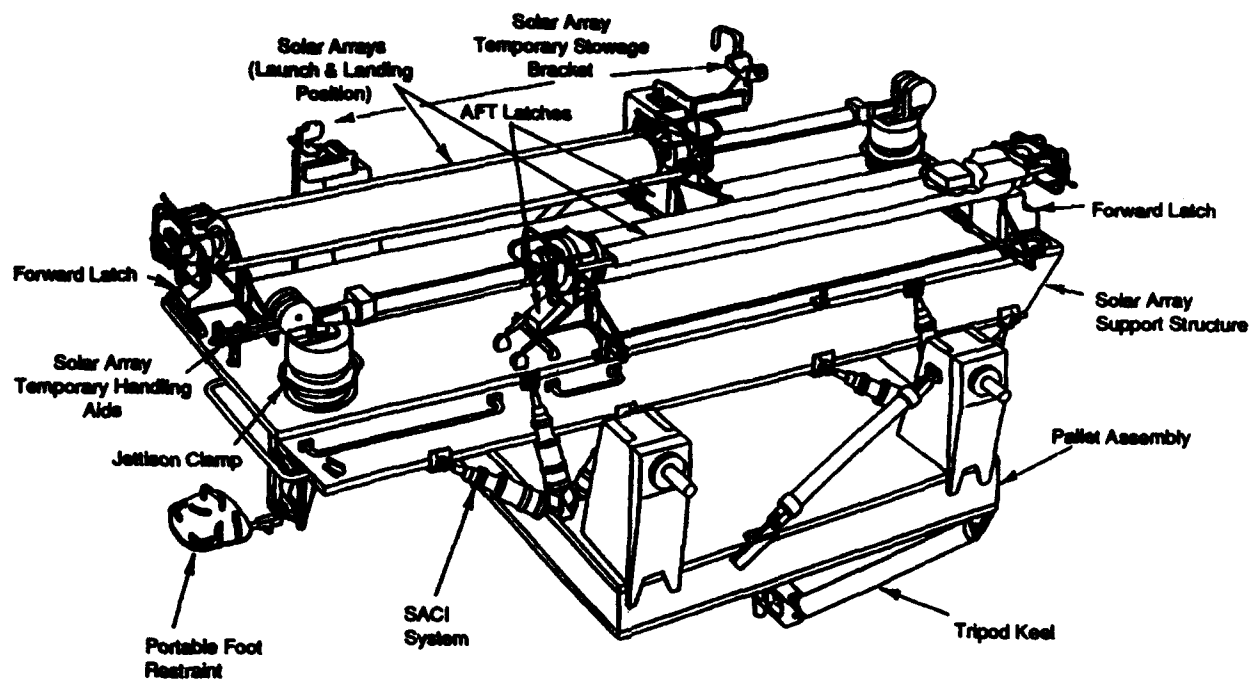
Fig. 1. Solar Array Carrier
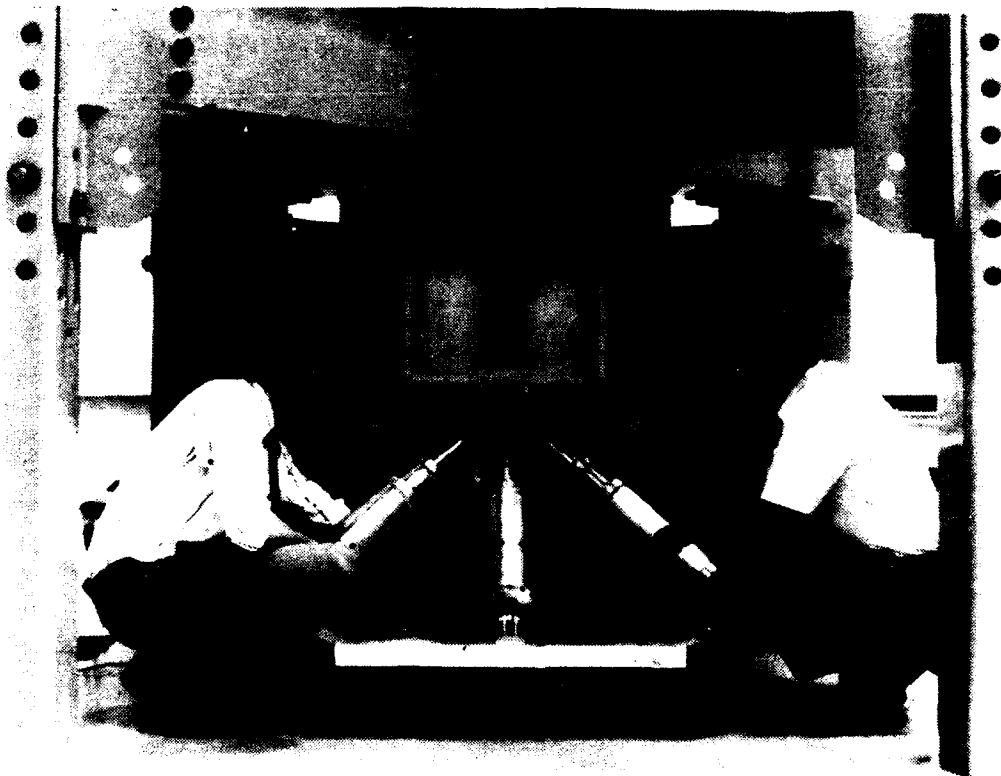
Fig. 2. SACI Tripod During Static Load Testing
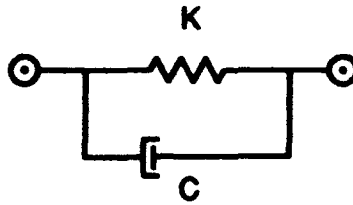
Fig. 3. Two-parameter Element Models

Significant consideration was given to an undamped isolation system as well as the damped SACI system. Fig. 4, Steady-state Transmissibility, draws a fundamental comparison between the unisolated system with a small amount of damping (2%) and the isolated system with a varying degree of damping. K_M is the modal stiffness of the structure when hard mounted.
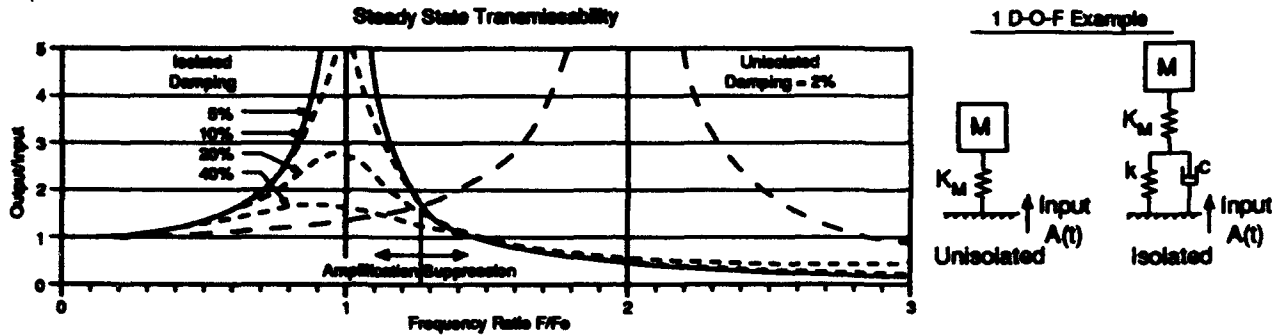
Fig. 4. Steady-state Transmissibility

Fig. 5 provides the acceleration response, due to landing in the worst-case axis, for three systems: an unisolated, an isolated and undamped, and an isolated and damped system. The latter is the analytical prediction for the SACI. Note that the isolated and undamped system reduces the higher frequency – but the damped SACI system provides better overall isolation.
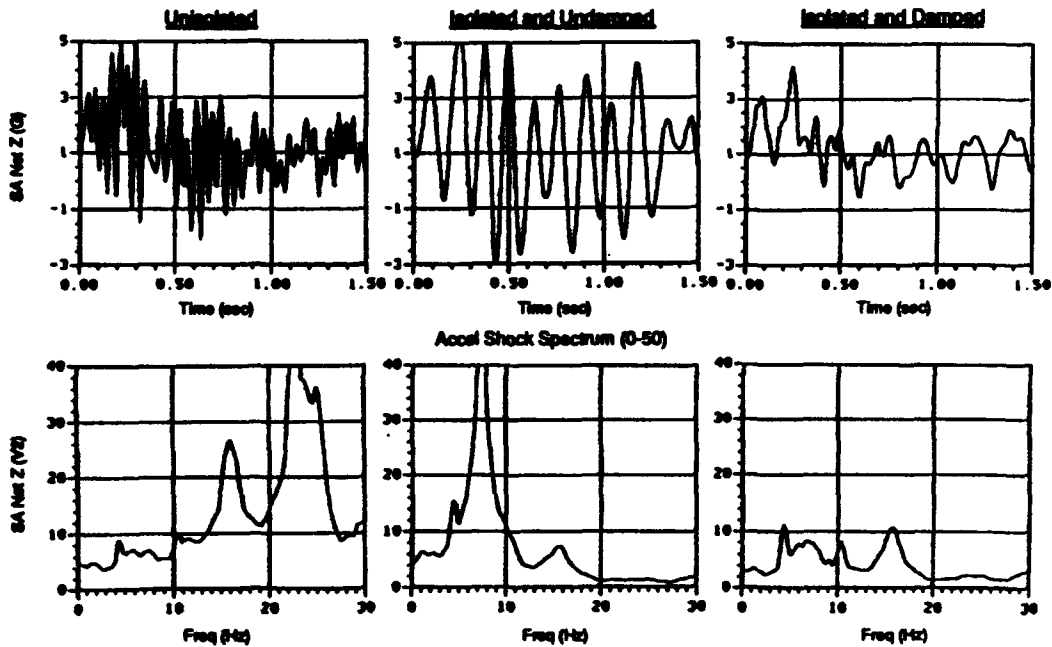
Fig. 5. Acceleration Response to Landing (Case LG-7443)

ELEMENT DESCRIPTION

The SACI element is shown partially disassembled in Fig. 6. A cross-sectional sketch is provided in Fig. 7. The element provides both damping and stiffness. Damping is provided by the motion of the piston within the damper cylinder. As motion occurs, fluid is forced from one side of the piston through a rather narrow annulus, formed by the piston and the cylinder, to the other side of the piston. This action shears the fluid, resulting in a force opposing the motion and directly proportional to the velocity. The isolation spring provides a force directly proportional to the displacement.
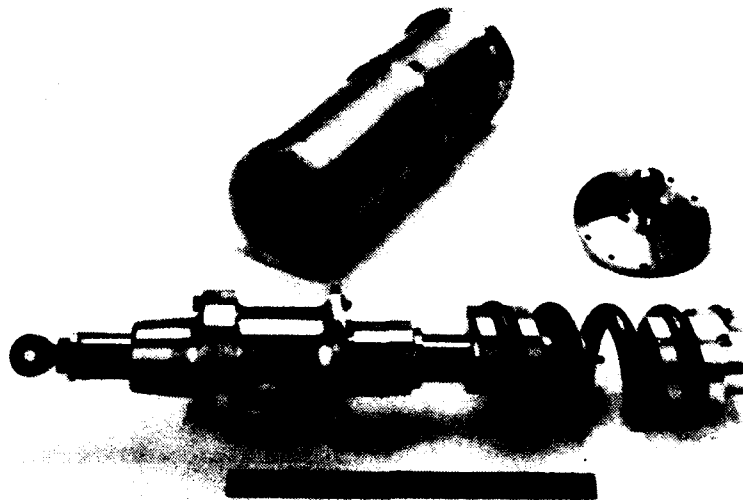
Fig. 6. Solar Array Carrier Isolator Element, Partially Disassembled
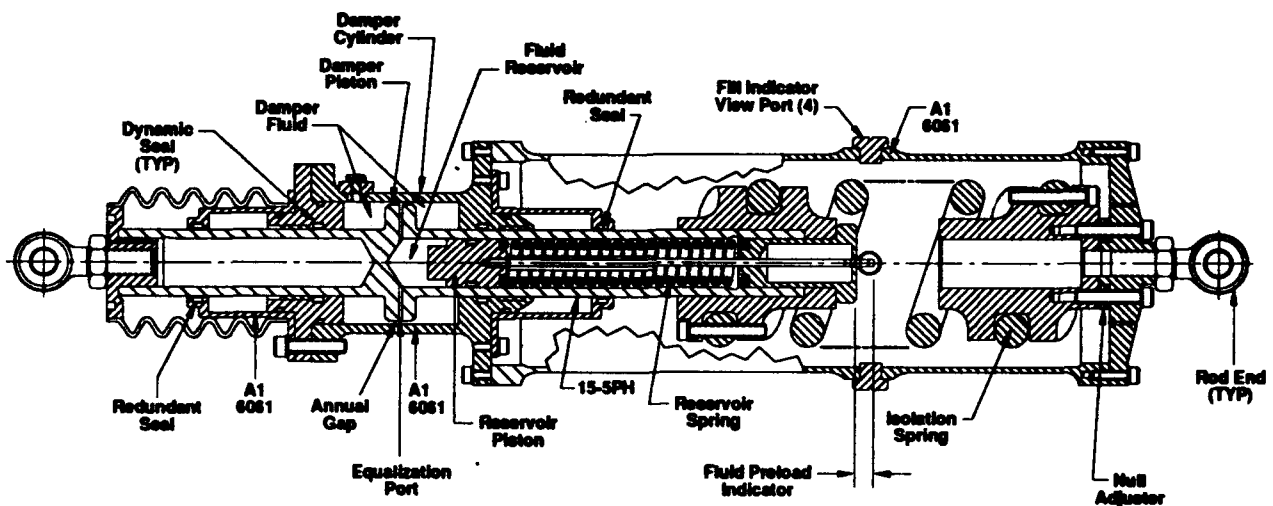
Fig. 7. Isolator Element Cross Section

The element is designed to meet a 20-year mission life with refurbishment allowed every 5 years. Within each 5-year segment is 4.3 years of ground storage, 0.7 years of Orbiter integration, and 1 shuttle mission. Slight leakage from the pressure chamber may occur during the life of the unit. The outer housing provides a redundant fluid seal to contain the fluid within the element to avoid any possibility of external contamination. A spring-loaded reservoir housed within the element's shaft provides reserve oil to make up for any loss. This reservoir also accommodates thermal expansion and contraction of the fluid. The spring preload ensures that the fluid will remain under positive pressure during launch and landing. This prevents voids from occurring within the fluid, which could result in high vibration levels similar to "water hammer."

The elements are filled with 500 centistoke, McGhan Nusil CV-7300, controlled-volatility silicone fluid designed for applications requiring low outgassing (Collected, Volatile, Condensable Mass [CVCM] 0.01%; Total Mass Loss [TML] 0.50%). The vapor pressure is estimated by the manufacturer to be less than 10^{-20} mm of mercury; and outgassing is an order of magnitude lower than typical lubricants used for space applications.

Titanium alloy is used for both the damper spring and the reservoir spring to provide both size and weight savings. Life tests performed by the spring manufacturer demonstrated full, reversing cycle lives greater than five times the performance specification requirement of 100,000 cycles.

Because SACI isolators develop high internal pressure during operation, the piston and cylinder assembly was classified as a fracture-critical pressure vessel. As a result, an extensive fracture mechanics analysis was performed to verify safe life and leak-before-burst per NASA requirements for manned (Shuttle) missions. In addition, fracture mechanics techniques were used to show that there was no danger of fracture at the rod ends of the isolator, which would create a free swinging condition that could damage adjacent structures.

The element was initially designed to operate over a temperature range of 10 to 30 °C. Later, to lower costs, NASA elected to eliminate temperature controls from the cargo pallet and require the elements to operate from -43 to 49 °C. An extensive study and test program confirmed the need to change seal materials and fits to avoid seal leaks at the extreme low-temperature limit. Acceptable values of stiction, long wear life, resistance to radiation, and outgassing requirements also had to be maintained. The result was the selection of fluorosilicone and ethylenepropylene elastomers and the elimination of fluorocarbon elastomers. A brief summary of the element specifications are presented in Table 1.

Table 1. Isolator Element Specification

Item	Description
Life	20 years*
Length	27 in.
Weight	22.5 lb
Stiffness	3750 lb/in.
Damping	
Ambient	32.7 lb-s/in.
Cold (-43 °C)	143.9 lb-s/in.
Resonant frequency	8 Hz axial
Resonant frequency	100 Hz lateral
Resonant Q, Ambient	2.4 axial
Deflection	±0.9 in.
Velocity, Test Rqmts	
Ambient	40.3 in./s
Cold (-43 °C)	15.0 in./s
Hot (+49 °C)	45.6 in./s
*With refurbishments allowed at 5-year intervals	

TESTING

Element performance testing was carried out by mounting one end of the isolator to a rigid mass, while the other end was vibrated axially. Acceleration was measured and a transmissibility plot was generated. Stiffness and damping were then calculated. The setup is shown in Fig. 8. The transmissibility at 27 °C for one of the isolators is shown in Fig. 9.
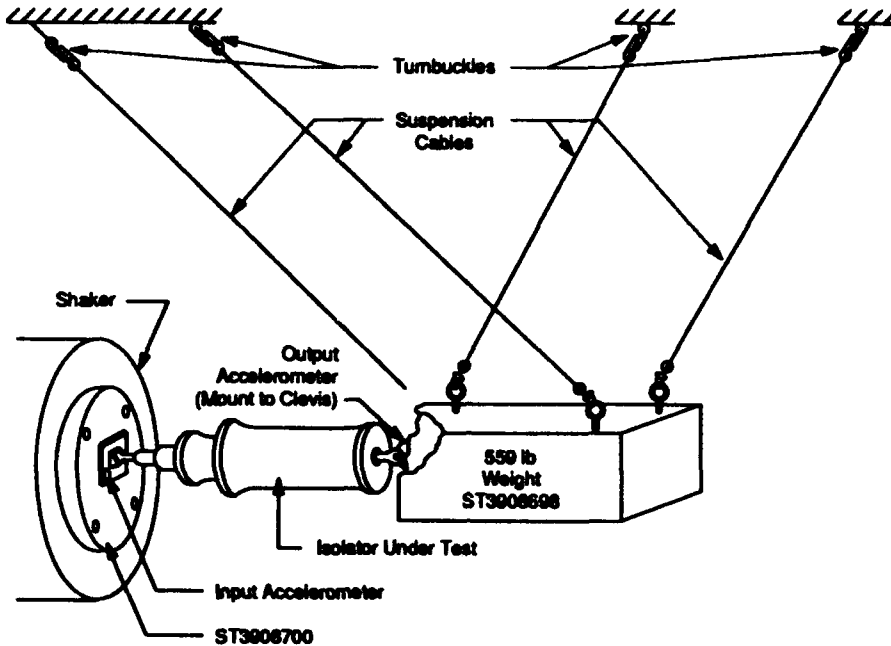
Fig. 8. Element Performance Test Setup
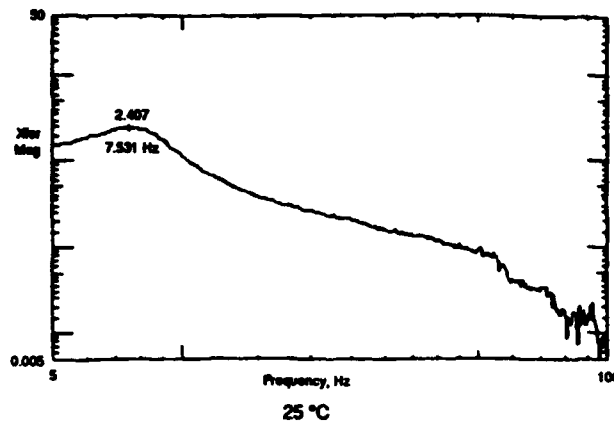
Fig. 9. Measured Transmissibility at 25 °C

Damping ratios of the elements ranged from 22% at 27 °C to 101% at -43 °C. With this element performance, system performance is predicted to exhibit the same damping values in certain axes and damping ratios as low as 11% and 50% for corresponding temperature conditions in other axes. Under these conditions, loads on the solar arrays will be reduced a minimum of 2 to 1 when compared to a hard mount. RMS launch vibration spectrums are expected to be reduced by at least 10 to 1.

Other tests required to qualify the elements included:

- Over pressure (1200 psi)
- Over velocity

- Breakaway friction
- Random vibration (lateral and axial)
- Thermal cycle
- Excursion extremes
- Lateral stiffness
- Spring life (100,000 full-stroke cycles)

ADAPTABILITY TO OTHER PAYLOADS

The SACI can be adapted to a large variety of payloads ranging in size, weight, shape, and isolation needs. This may be accomplished by making one or more of the following changes:

- Number of elements used and their orientation
- Element damping
- Element stiffness

Changing the number of elements, their points of attachment, or orientation can avoid the need to change the design of the elements themselves. Once the element impedance is known, system performance in a payload frame of reference is a simple matter of geometry and axis transformation. Reconfiguration of the elements that form the truss can provide the specific performance desired in each of the six spatial axes. The SACI uses 12 elements located in tripods at four separate locations. Four of the 12 elements provide redundancy. Without redundancy the system would be composed of four sets of bipods or eight total elements. Six is the minimum quantity that can be used to provide six-axis isolation; Honeywell developed such a system for a French satellite.[1]

The amount of damping can be changed simply by changing the viscosity of the damping fluid. Available viscosities range from 1 to 300,000 centistokes.

Stiffness of the element is a function of the size of the coiled spring (or isolation spring). Analyses were conducted to determine how large a spring could be used without changing any part of the design other than the spring itself and its holder. A summary of the results are shown in Fig. 10, which compares the capabilities of the current design to what is called a future maximum capability. Fig. 11 shows a cross section of the element with the enlarged spring diameter in phantom. Fig. 12 is a spring-design summary that shows that the new spring at full stroke endures the same maximum stress as the current design. The conclusion is that the stiffness capacity could be increased from 3,729 lb/in. to 7,994 lb/in. This would increase the maximum potential energy that could be absorbed (since stroke is not changed) from 1,510 to 3,238 in.-lb. Changing the spring stiffness within these limits provides a significant range of capability while avoiding the need for a risky requalification program.

Description	Solar Array		Future Maximum Capability
	(Current)	(Spec)	
Length	27 in.	Same	No change
Diameter	5.42 in.	Same	No change
Weight	23 lb	31 lb	31 lb
Spring stress	85 kpsi	85 (kps)	No change
Stroke	0.9	Same	0.9
Stiffness	3750 lb/in.	Same	7994 lb/in.
Damping coefficient	32.7 lb/s/in.	Same	69.7 lb/s/in.
Maximum velocity	32.2 in./s		No change
Temperature range	-35 to 49 °C	Same	No change
	20 to 30 °C	Same	No change
Static load capacity	3729 lb	3375	7195
Maximum payload weight	2200	2200	4245
First-mode frequency	8 Hz		No change
Piston area	3.93 in.^{2}	None	11.24 in.^{2}
Maximum damping pressure	473 psi	None	355 psi
Preload pressure	199 psi	None	100 psi

Fig. 10. SACI Capabilities Summary
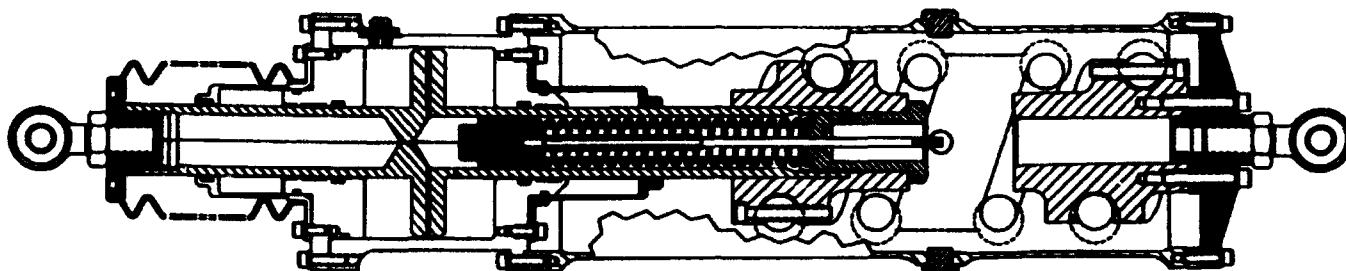
Fig. 11. SACI with Enlarged Spring

Design	N	D	DW	E	Wt/CIN	Y	L/D<4	Freq	Stress	K	F	Energy	L	WT	
1	2.2	3	0.75	5.6	0.18	0.9	2.01	530	85,347	3,730	3,358	1,510	6.20	1.88	SACI
2	2.4	3	0.8	5.6	0.18	0.9	2.17	519	85,411	4,425	3,982	1,792	6.51	2.04	
3	2.6	3	0.85	5.6	0.18	0.9	2.34	509	85,752	5,205	4,685	2,108	7.03	2.50	
4	2.4	3.2	0.895	5.6	0.18	0.9	2.24	510	85,531	5,711	5,140	2,313	7.17	2.73	
5	2.6	3.2	0.95	5.6	0.18	0.9	2.42	500	85,866	6,692	6,023	2,710	7.74	3.33	
6	2.8	3.2	1	5.6	0.18	0.9	2.59	488	85,825	7,629	6,866	3,090	8.29	3.98	
7	2.7	3.3	1.035	5.6	0.18	0.9	2.64	489	95,877	7,894	7,105	3,238	8.86	4.15	Enlarged SACI
8	2.7	3.3	1.11	5.6	0.18	0.9	2.72	529	96,163	10,952	9,857	4,435	8.98	4.87	
9	2.8	3.3	0.86	5.6	0.18	1.2	2.30	395	85,990	3,805	4,566	2,740	7.60	3.03	
10	2.8	3	0.895	5.6	0.18	0.9	2.51	497	85,644	5,941	5,347	2,406	7.52	2.99	
11	3.1	3	0.96	5.6	0.18	0.9	2.76	482	85,591	7,103	6,393	2,877	8.29	3.80	
12	2.7	3.3	1.1	5.6	0.18	0.9	2.70	524	94,877	10,562	9,506	4,278	8.91	4.78	

N – Number of turns
D – Coil diameter (in.)
DW – Wire diameter (in.)
E – Modulus of elasticity (lb/in.^{2})/1000000
WT/in.^{3} – density
Y – Stroke (in.)
SI – Spring index (D/DW)

KS – Shear-stress deflection factor
Stress – Combined shear and torsion
K – Stiffness (lb/in.)
L – Length (in.)
WT – weight (lb)
L/D – length/diameter

Freq – spring frequency (Hz)
F – force (lb)
WT – weight (lb)
Energy – Energy (in.-lb)

Fig. 12. Spring Design Alternatives

Fig. 13 provides an approximation of the interrelationship of break frequency, payload weight, spring stiffness, and the number of isolators. SACI, with the solar array carrier payload of 2240 lb, is marked on the plot. This plot can be used to provide a "ball park" figure for an end user with a different set of payload requirements. The plot assumes the isolator configuration remains the same as that described for the solar arrays. A more accurate analysis can be performed when a specific configuration is selected.
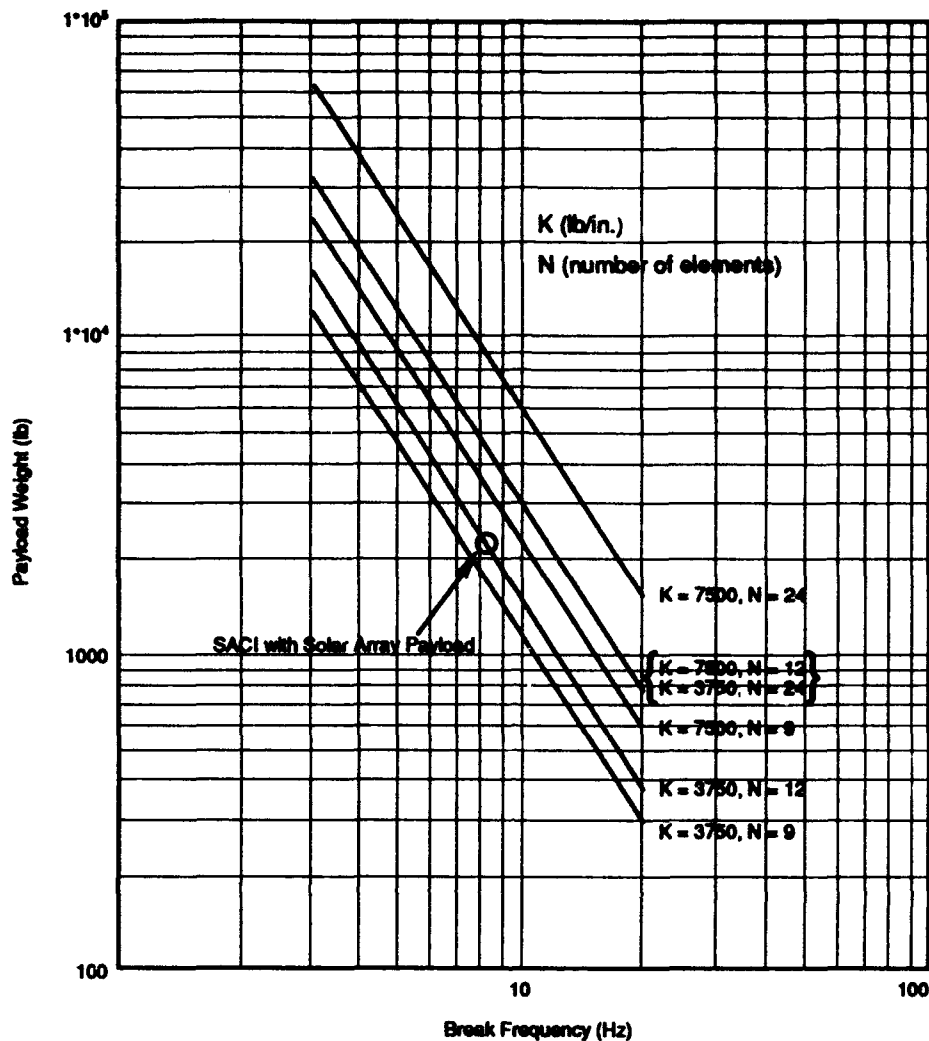
Fig. 13. Payload Weight vs Frequency, Spring Stiffness, and Number of Isolators

GROWING DEMAND FOR LAUNCH ISOLATION

Launch vibrations are a major cost factor in the development of payloads, not only in dollars, but in size, weight, power, reliability, and schedule. Launch vibrations dictate the design of almost all spacecraft, their subsystems, and components. The Hubble solar arrays are only one example. The reaction wheels on the Hubble Space Telescope, which use very large bearings simply to withstand launch, are another example. The Skynet satellite, launched on a Titan III in 1990, required a complete launch isolation system because of a sensitive antennae subsystem. Several other launch isolation systems have been employed in a variety of applications over the years, including a Shuttle-based system developed by NASA Marshall Space Flight Center (MSFC). These examples are evidence of the fundamental need for launch isolation systems. The demand should increase even more rapidly in the near term because of several new factors:

- The availability of qualified isolation systems such as the SACI
- Increased number of sensitive optical subsystems and payloads carried within new satellites that can be replaced in orbit
- The move to small satellites, which expose their components to vibration levels in the 18 to 40g category, up from the 9 to 16g levels for which most components and subsystems have been qualified
- The general awareness of the community to launch and operational dynamics issues brought on by the Strategic Defense Initiative, NASA, and the Air Force through their research into control structure interactions

CONCLUSIONS

1. Significant amounts of viscous or rate-proportional damping substantially improves an undamped isolation system.

2. RMS launch vibration spectrums are reduced by an order-of-magnitude with properly designed launch isolation systems.

3. Operation over large temperature range is possible without active thermal control.

4. A truss-like system enables analysis and reconfiguration of the system to accommodate a wide variety of payloads varying in size, weight, and isolation needs without costly element redesign and requalification.

5. Spring size can be doubled and damping can be changed _almost_ _without_ _limit_ to provide additional payload adaptability.

6. The SACI launch isolation system is the first adaptable system to be qualified for shuttle applications. The cost, risk reductions, and schedule savings advantages for sensitive payloads and small satellites should lead to repeated application of this system.

REFERENCES

[1] David Cunningham, Porter Davis, and Frank Schmitt, "A Multiaxis Isolation System for the French Earth Observation Satellite's Magnetic Bearing Reaction Wheel," Conference on Active Materials and Adaptive Structures, Nov. 1991

CREDITS

A NEW STRUCTURAL DESIGN CONCEPT FOR LAUNCH VEHICLE SHROUDS TO DECREASE PAYLOAD NOISE ENVIRONMENT

Jefferson F. Newton
Roy Ikegami
Paul D. Nedervelt

Boeing Defense & Space Group
Structures Technology
Seattle, WA

ABSTRACT

This paper describes the design, analysis, fabrication and testing of a structural design concept for launch vehicle shrouds which provides increased sound absorption and transmission loss while decreasing cost and weight. The design utilizes a synergism between very lightweight stiff, deep panels; carefully tailored constrained layer damping; and tuned cavity absorption using Helmholtz resonators. Analyses were performed to predict panel composite loss factors using modal strain energy methods. Tuned cavity absorber characteristics were analyzed and tested, and statistical energy analyses (SEA) were used to predict panel test results and noise reductions for full size shrouds. Shroud structure utilizing this concept was designed. Acoustic testing was performed to provide proof of concept. Structural test articles were built using fabrication methods developed to obtain realistic cost and weight data.

INTRODUCTION

The impetus behind this work was the need for a shroud structure that would decrease the noise and vibration environment for payloads on board large launch vehicles during lift-off. In the course of concept development, testing, and trade studies performed over the past three years, it has become evident that this structure also provides cost, weight, and stiffness benefits over current shroud designs and is a promising candidate for applications other than payload shrouds.

Initial noise and vibration reduction concepts were based upon application of earlier Boeing research on passive viscoelastic damping (PVD), performed on independent research and development [1], and the "Reliability for Satellite Equipment in Environmental Vibration (RELSAT)" contract performed by Boeing for Wright Laboratories Flight Dynamics Laboratory [2], to shrouds for future launch vehicles. It was clear from the outset that a new approach to acoustic protection would be necessary for the large boosters envisioned for future space programs. The reasons for this are that, as boosters become larger, the rocket exhaust noise not only increases in absolute magnitude, but it peaks at lower and lower frequencies. In fact, for boosters planned for the National Launch System (NLS) 1.5-Stage and Heavy Lift Launch Vehicle (HLLV), the noise spectrum at lift-off peaks

between 50 and 100 Hz. As shown in Figure 1, for the HLLV, fully two-thirds of the sound power lies below 100 ''z! Figure 2 illustrates that at these frequencies the noise suppression techniques presently relied upon are of little use. Such things as fiberglass blankets, foam, lead-loaded vinyl, etc., which are effective at higher frequencies, become almost totally ineffective below 100 Hz. This fact in conjunction with the low frequency peaking of the noise spectrum result in a "noise window" in the spectral region between 50 and 200 Hertz in which new noise suppression techniques must be developed.
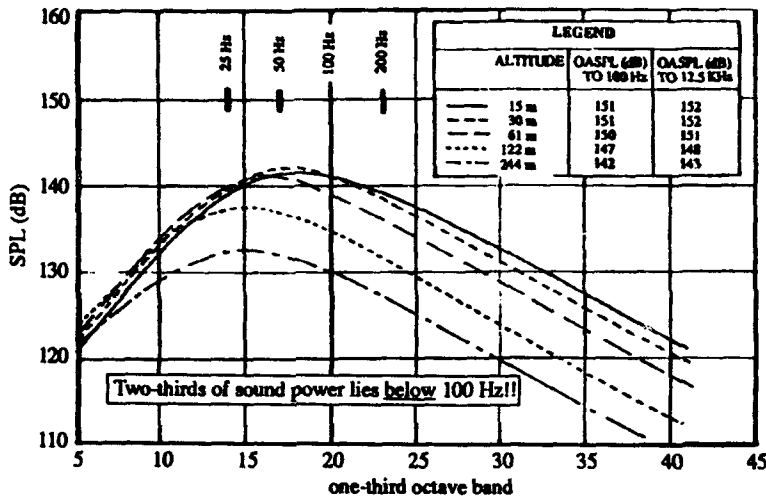
Figure 1. HLLV Shroud Exterior Noise at Lift-Off Peaks at Low Frequency
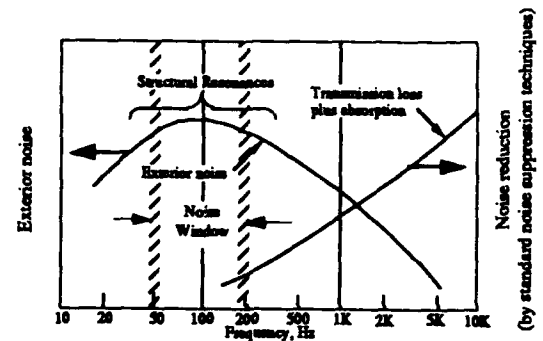
Figure 2. Launch Vehicle Noise Problem

The intention of this study was to investigate alternative approaches, preferably doing away with the fiber-glass acoustic blankets currently in use. The result is a new structural design concept called "Macrocore" which combines PVD (to enhance transmission loss) and tuned cavity resonators (to provide absorption in the noise window) into a very stiff, lightweight shroud structure. Testing, analysis, and trade studies conducted over the past three years have confirmed that this structure is superior acoustically to conventional shroud construction, especially at low frequencies. It is lighter in weight, lower in cost, and does away with the fiberglass blankets. In the following sections, the theory and design concept development, and the results of tests, analyses, and trade studies are described.

DISCUSSION

Theory

As mentioned above, the higher frequency region does not usually present a problem as regards exhaust jet noise within the payload shroud. Mass law transmission loss and the intrinsic absorption of nearly any structure used as a payload shroud will provide sufficient noise reduction above a few hundred Hertz. It is in the low frequency region that the problem occurs. For this reason, it was decided to look into the practicability of utilizing two basic concepts to provide the needed noise reduction (NR) at low frequencies: (1) PVD to increase transmission loss (TL), and (2) tuned cavity resonators to provide tailored absorption. We will discuss these two concepts separately, and then explain how they are combined in the Macrocore structure.

Passive Damping. Passive damping is effective in increasing TL in a panel above the critical frequency, f_c, which is defined as that frequency at which the panel bending wave velocity is equal to the velocity of sound in air. [3] The relationship between frequency, panel bending wave velocity, panel bending stiffness, and f_c is shown in Figure 3. Here it is seen that panel bending wave velocity,
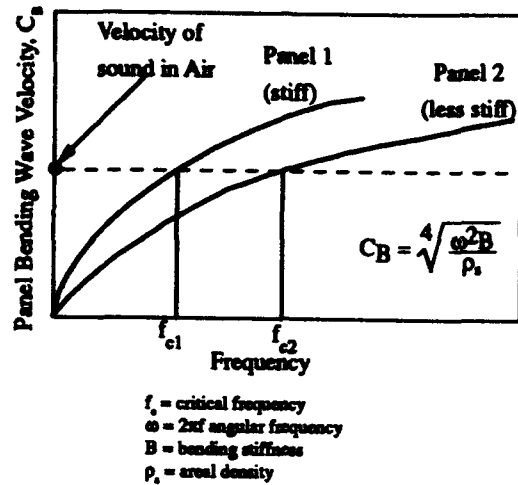
Figure 3. Critical Frequency Relationships

f_c = critical frequency
$\omega = 2\pi f$ angular frequency
B = bending stiffness
ρ_s = areal density

$$C_B = \sqrt[4]{\frac{\omega^2 B}{\rho_s}}$$

C_B, is proportional to the square root of frequency and the fourth root of bending stiffness. In order to move f_c to lower frequency, it is necessary to make the panel stiffer. The design problem, then, was to devise a way of providing high composite panel loss factor while simultaneously making the panel very stiff.

Computer programs were written to calculate the composite panel loss factor, bending stiffness, and critical frequency, f_c, as a function of the structural panel materials and geometry for both symmetrical and unsymmetrical panels, using the modal strain energy method. [4 & 5] A statistical energy analysis (SEA) program was written to predict the TL of a given damped panel design when tested in the Boeing Noise Engineering Laboratory (NEL) anechoic/ reverberant facility (ARF). These programs were used to perform damping design trade studies of various panel configurations and to design panels for testing in the NEL ARF. The first panel tested was a symmetrical panel designed to provide proof-of-concept. Figure 4 shows the construction of this panel, and Figure 5 illustrates the TL test. The test was conducted using an acoustic intensity probe to measure the intensity of sound transiting the test panel from the reverberant room to the anechoic room, which gives a direct measure of TL. [6] Two panels were tested: a baseline panel having no viscoelastic material (VEM) or septum plies, and the damped panel shown in Figure 4. The noise transmission
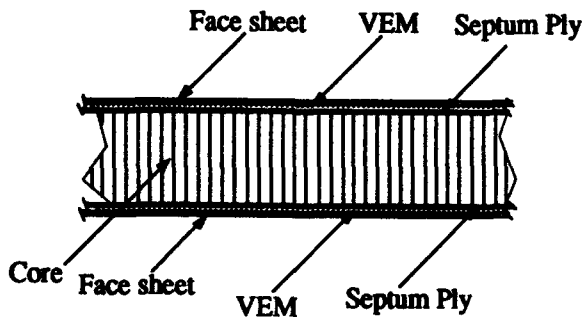
Figure 4. Symmetric Test Panel
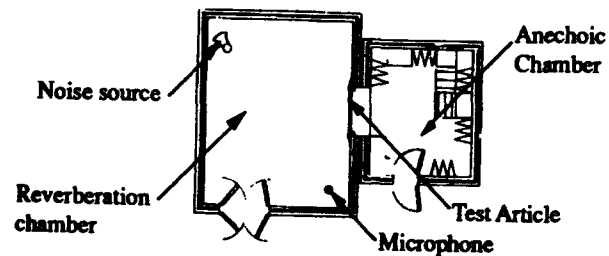
Figure 5. NEL Acoustic TL Test

losses measured during the test for these two panels are shown in Figure 6. The damped panel was designed to increase TL in the 100 to 1000 Hz region. It can be seen that a 5 to 9 dB improvement was, in fact, realized in the frequency band of interest.
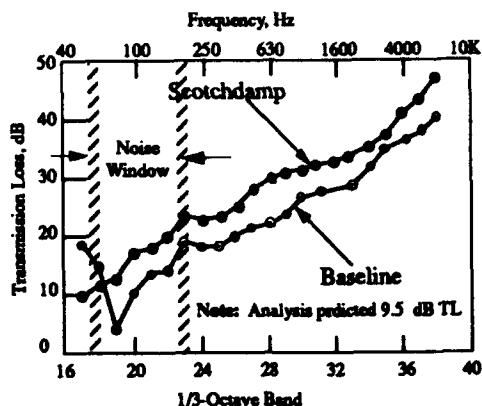
Figure 6. Noise Transmission Test Results

Tuned Cavity Resonators. Increasing TL is a necessary condition to providing acoustic protection at low frequ ;cies, but it is not sufficient in itself. There has to be absorption as well. As long as there is **any** noise transmitted into the interior of the shroud, unless there is absorption, the interior noise level will build up until it equals the exterior noise level. We have already seen that ordinary absorption becomes very ineffective at frequencies below 100 Hz; so, to provide the necessary absorption, an alternative approach is necessary. Tuned cavity resonators seem to provide the only effective means of supplying the necessary absorption at low frequency. These devices are frequently known as Helmholtz resonators (Figure 7), and whether they act as a muffler or a resonator depends upon the value of the acoustic resistance of the passage connecting the cavity and the acoustic space (the interior of the payload shroud in our case). For a given cavity of frequency f_0, there is one value of acoustic resistance that will theoretically provide perfect absorption at f_0. However, the absorption bandwidth of the resonator in this case will be very narrow. In practice, resonators tuned to several frequencies covering the spectral region from 50 to 200 Hz can be used, with acoustic resistances tailored to provide **reasonably** high absorption and **reasonably** wide bandwidth.

The low frequency tuned cavity resonator concept was tested experimentally at Cambridge Collaborative, Inc. using a large impedance tube. The results confirmed theory and indicated that useful absorption could be obtained, even at the low frequencies of interest. Experimental results are shown in Figure 8. The dashed portion of the curves corresponds to a region in which the impedance tube structure had resonances.
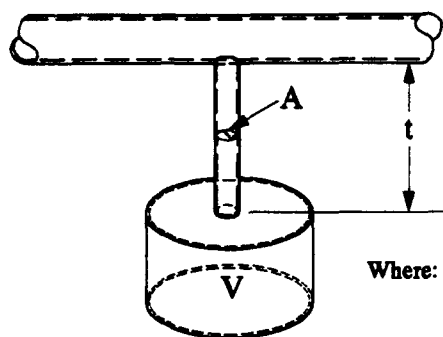
$$f_0 = \frac{C}{2\pi}\sqrt{\frac{A}{Vt}}$$

Where: C is the velocity of sound
        f_0 is cavity resonant frequency

Figure 7. Tuned Cavity Absorbers

Note: Invalid data - - Structural resonances in impedance tube
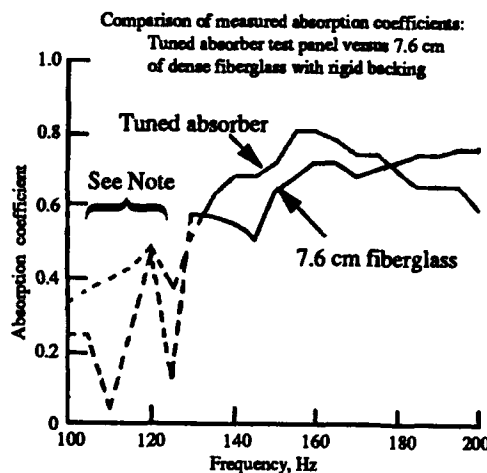
Figure 8. Impedance Tube Test - - Multiple Tuned Absorbers

Macrocore Design Concept

After the acoustic test of the symmetric panel of Figure 4, the panel was cut up into 15.2-cm-wide (6 in) beams and a modal test performed to determine the modes, frequencies, and loss factors. The results corroborated the loss factor predictions, but the inclusion of the VEM reduced the bending wave velocity, and hence, f_c and the mode frequencies. It was felt that, although the principle had been proved satisfactorily, it would not be useful for our purposes unless a structure could be built that had high composite loss factor and low f_c; that is, it would have to be very stiff. Also to satisfy structural and thermal design requirements for the launch vehicle shroud, it was decided that the VEM could only be placed on the interior side of the panel. Consequently, the unsymmetrical panel loss factor analysis program was used to design a panel with both the necessary loss factor and the necessary stiffness to bring f_c down to 100 Hz. The resulting panel was a deep sandwich structure on the order of 15.2 cm (6 in) thick that was constructed with lightweight core and stiff face sheets. It was at this point that the synergism of combining the deep, stiff sandwich panels necessary to achieve TL with the PVD, with the tuned cavity resonators became apparent. The cavity volume required to tune resonators down to the 50-200 Hz region is quite large, and would be impractical to integrate into conventional honeycomb panels with thickness in the 25- to 50-cm (1-2 in) range. But a 15.2 cm (6 in) deep panel gave the necessary room to provide adequate numbers of properly sized resonators.

The resulting sandwich structure, referred to as "macrocore", is shown in Figure 9. The outer face skin of the sandwich provides most of the protection against the launch vehicle external environment and will provide most of the structural strength required to support the combined axial loads and bending moments due to aerodynamic and inertia forces. The outer skin is supported by a very lightweight large-cell core (the "macrocore"). A septum ply, made of a thin sheet of cured, reinforced thermoset or thermoplastic composite, is bonded to the inner surface of the macrocore, acting both to stabilize the thin core walls, and to transmit the shear from the core to the VEM, which lies between the septum and the inner face skin of the macrocore sandwich. Thus, the VEM is placed in full planar shear. The inner skin is relatively thinner and lighter than the outer skin, and holes or orifices through it connect the individual cavities formed by the macrocore hexagonal cells to the inside volume of the payload shroud. The acoustic resistance of the orifices is controlled by their size, length, number, and the mesh-size of the screens covering them.
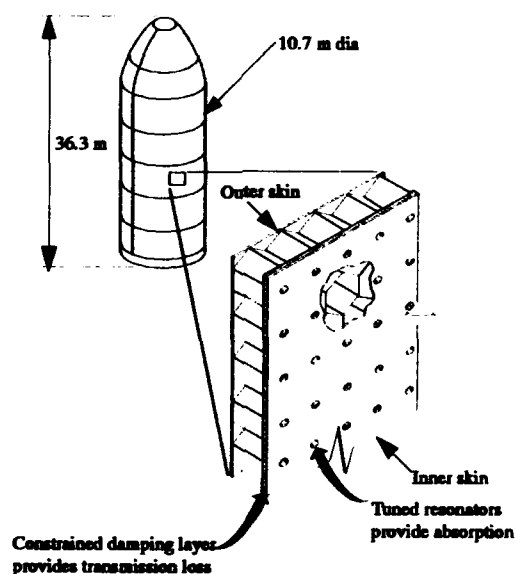
Figure 9. Macrocore Payload Shroud Structural Design Concept

The macrocore design concept illustrated in Figure 10 typifies an all aluminum construction. The macrocore cell walls are constructed from corrugated aluminum ribbon, and the face skins are conventional honeycomb panels. Another design that is under active development is a thermoplastic version, in which the outer face skin is made of thermoplastic honeycomb panel, and the inner face skin and the macrocore are made of relatively lighter weight thermoplastic honeycomb panel. The thermoplastic design is shown in Figure 11.
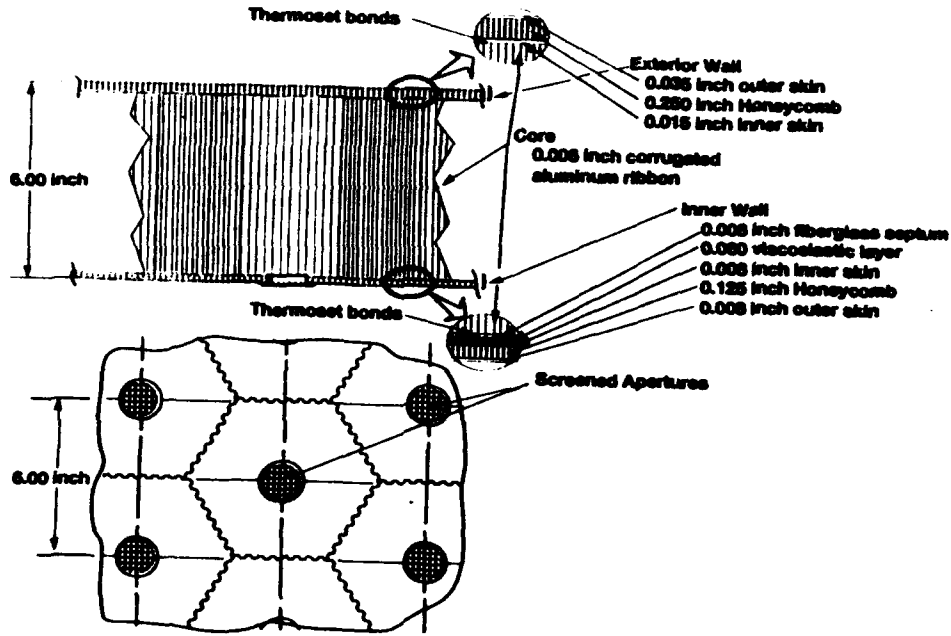
Figure 10. Aluminum Macrocore
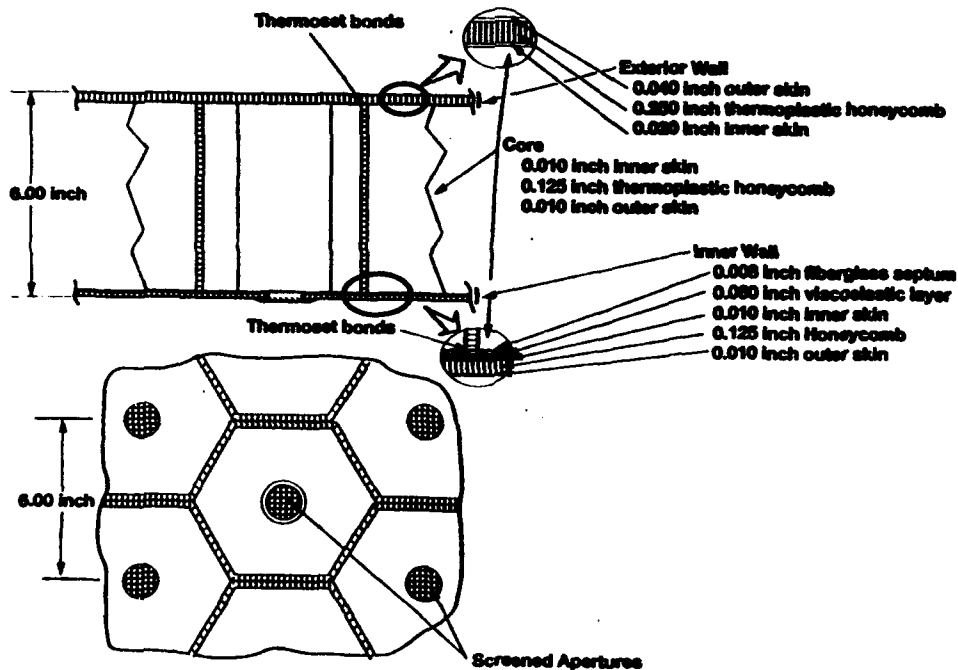
Figure 11. Thermoplastic Macrocore

A large panel was built to test the above concept acoustically. It incorporated the necessary features to reproduce acoustic performance, but the core was structurally somewhat different to reduce cost. The hexagonal core cells were replaced by square cells, allowing a simple, low-cost egg-crate construction to be used. A 1.8 m by 1.8 m (6 ft by 6 ft) panel was constructed for test in the NEL ARF. The panel is shown in Figure 12 and the TL results are shown in Figure 13, along with the results from the prior test of the symmetric panel previously discussed. The upper curves are for tests of the panel with the orifices open, closed, and covered by a screen of known acoustic resistance. The lower curves are those from the symmetric panel, already shown in Figure 6. It is seen that everywhere in the "noise window" the new panel is as good as, and usually much better than the symmetric panel. Interpretation is made somewhat difficult, however, by the fact that the 50 to 200 Hz region lies in the stiffness controlled region of the macrocore panel. Tests with much larger curved panels or large scale shroud sections will be required to completely verify real shroud performance.
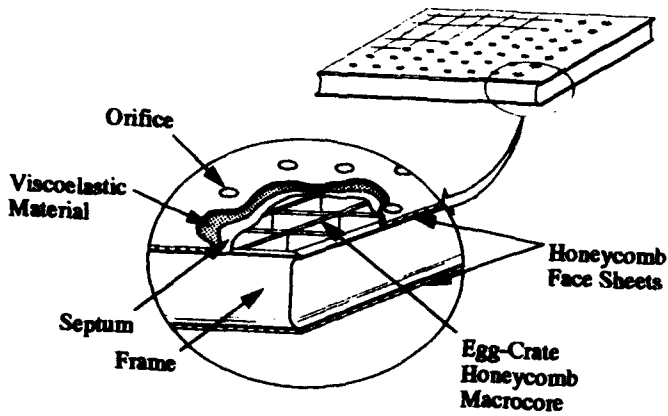
Figure 12. 1.8 m by 1.8 m Panel Fabricated and Tested in 1990
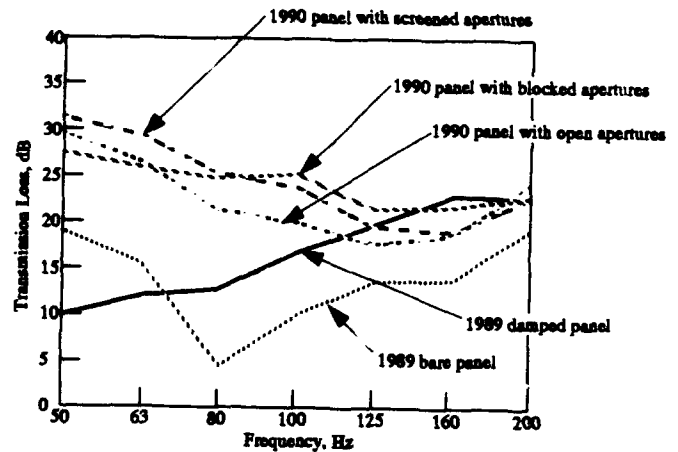
Figure 13. Measured Transmission Loss

In order to evaluate the acoustic performance of the macrocore shroud, Cambridge Collaborative, Inc. performed SEA predictions of noise reduction and shroud internal noise level for a macrocore shroud and an Isogrid-type shroud. (Figure 14) The shrouds were assumed to be one of the NLS "growth" shrouds, 10.7 m in diameter by 36.3 m in length. (35 ft by 119 ft) The Isogrid-type shroud was provided with the usual 7.6 cm (3 inch) thick fiberglass acoustic blankets. It can be seen that the macrocore is predicted to outperform the Isogrid-type shroud by 5 dB in OASPL, with the biggest part of the improvement lying in the desired 50 to 200 Hz region.
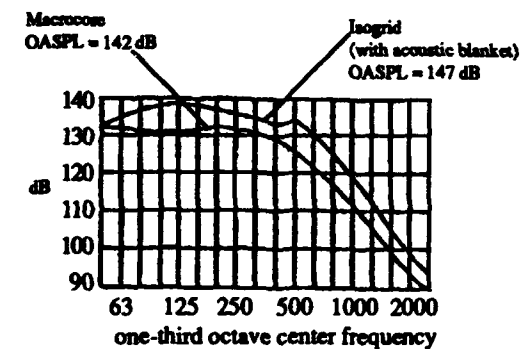
SEA noise prediction performed by Cambridge Collaborative Inc.,

Figure 14. Predicted Shroud Interior Noise Levels

Trade Studies & Structural Tests

After testing and analysis had validated the acoustic performance of the macrocore shroud design concept, the next step was to perform a study to verify such things as structural integrity, manufacturability, weight and cost. Initial steps have been completed to validate the macrocore design including both analysis and testing. Basic structural requirements were taken to be those for a growth NLS vehicle with a 10.7 m diameter by 36.3 m long shroud (35 ft by 119 ft), thus providing a conservative estimate for shrouds likely to be needed in the next 20 years. The macrocore construction was designed to meet the structural loading and acoustic requirements. NLS trajectory analyses gave a value for a maximum compression design lineload of 403 kgm (2250 lb/in), which was used for this study. The outer honeycomb face skin was assumed to carry the total design lineload. The macrocore cell was sized to meet acoustic requirements and stabilize the outer face skin. To keep our estimates conservative, it was initially assumed that the inner face skin carried none of the load. Buckling analyses were performed to determine compression buckling strength of the shroud walls. Core shear tests were conducted to assess the shear strength of the design and determine the shear stiffness properties of the macrocore for the buckling analyses. The shear test setup and some results are shown in Figure 15. In addition, tensile tests and bond strength tests were performed to verify the joining methods. The results of the tests performed to date were universally positive, with the macrocore performing as predicted.

Shear test setup

Shear test force/
displacement plot, L-direction
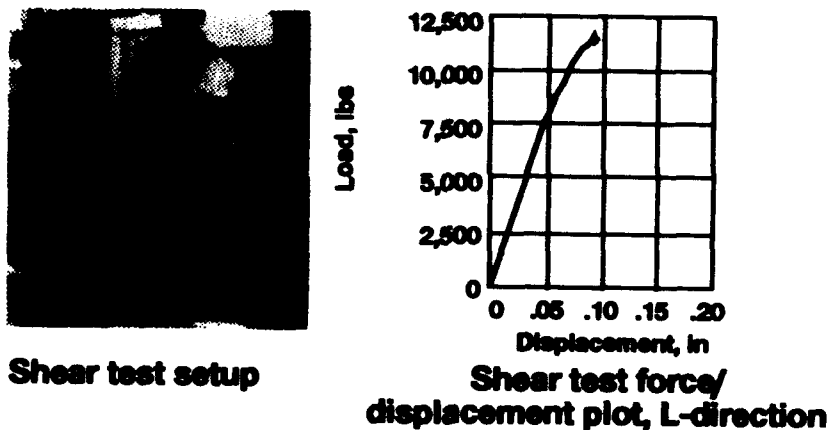
Figure 15. Shear Testing of Macrocore Panels Performed to Determine
Shear Stiffness and Verify Structural Integrity

An important structural consideration was heat transfer to the VEM layer due to aerodynamic heating of the shroud external surface. Analyses were conducted both for a worst case launch trajectory and for heat soak on the launch pad. The results are shown in Figure 16. Due to the thermal lag between the inner and outer face skins, the maximum temperature at the inner surface of the shroud is only 54 degrees C (130 degrees F), which is acceptable for the VEM and within NLS thermal requirements. The temperature history of the inner and outer skins is shown. The inner and outer skins are effectively isolated from each other by the macrocore. The only physical conductor being the thin walls of the core, heat transfer must be accomplished primarily by radiation and convection.
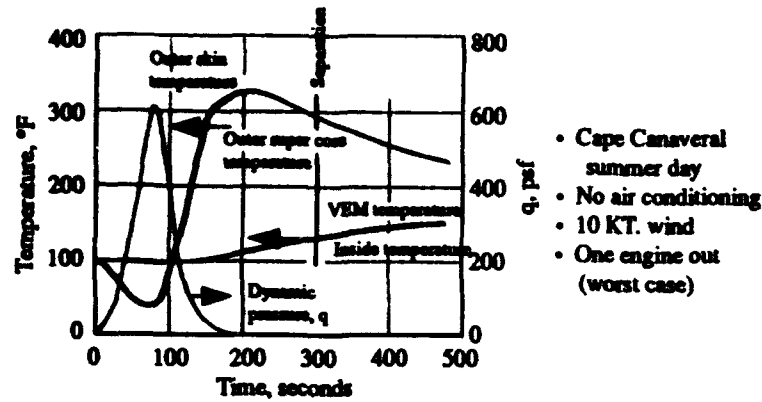
- Cape Canaveral summer day
- No air conditioning
- 10 KT. wind
- One engine out (worst case)

- Inner skin and VEM separation temperature ~ 130°F (54°C) (launch and on pad)
- Outer skin maximum temperature ~ 330°F(166°C)
- Maximum line load occurs near minimum outer skin temperature

Figure 16. Results of Thermal Analysis of Macrocore Shroud

Detailed studies have been conducted of the manufacturing processes for both thermoplastic and aluminum macrocore shrouds. A natural outgrowth of the manufacturability study are cost and weight estimates. These are summarized in Figure 17, where comparisons are made with an Isogrid-type shroud.

- Assumptions
  - 10.7 m diameter x 36.3 m long shroud
  - Stressed for 2250 lb/in lineload
  - Weight of fiberglass blankets included for Isogrid

- Results

Concept	Weight (Kgm)	Cost ($M)
Isogrid	23,000	43
Macrocore	12,300	18

Figure 17. Weight and Cost Trade Study Results

CONCLUSION

In summary, a new structural design concept has been developed for use in launch vehicle payload shrouds. This structure has several unique features, resulting in the following advantages:

Effective noise reduction in the low frequency region of 50 to 200 Hz, where the principal acoustic problem lies for large launch vehicles.

Very high composite panel loss factor effective in reducing structure-borne vibration.

Lighter weight than present shrouds.

Lower cost than present shrouds.

Eliminates the necessity for fiberglass blankets.

Eliminates a major source of contamination.

Highly effective thermal barrier.

The very stiff, lightweight panels can be assembled into an essentially monocoque structure, without the requirement for extensive internal stiffening.

These features and advantages, though aimed specifically at use in launch vehicle payload shrouds, are potentially useful in many other structural applications. The designs are still conceptual in nature and will require additional extensive analysis and testing.

ACKNOWLEDGMENT

The authors wish to acknowledge the assistance of Dr. Jerome Manning of Cambridge Collaborative, Inc. for analysis and testing work performed during the course of this study. The ideas and advice he gave during many discussions were invaluable.

REFERENCES

1. D. Johnson, R. Ikegami & K. Hunziker, "The Application of Statistical Energy Analysis in the Design of Viscoelastic Passive Damping", Paper No. JBA, Proc. DAMPING '89, 8-10 Feb '89, West Palm Beach, Fl.

2. R. Ikegami & D. Johnson, "Reliability for Satellite Equipment in Environmental Vibration (RELSAT)", Final Report (Mar '83 - Mar '88) to Flight Dynamics Laboratory, Air Force Wright Aeronautical Labs., Aug "88.

3. L. Beranek, Noise and Vibration Control, McGraw-Hill, 1971.

4. J. Newton, R. Ikegami & D. Carbery,"Integrally Damped Honeycomb Structural Concepts to Increase Noise Transmission Loss", Paper No. FBA, Proc. DAMPING '91, 13-15 Feb. '91, San Diego, Ca.

5. C. Johnson & D. Kienholz,"Finite Element Prediction of Damping in Structures With Constrained Viscoelastic Layers", AIAA Journal, Vol. 20, No. 9, pp. 1284-1290, Sept. '90

6. Crocker et al, "Measurement of Transmission Loss of Panels by the Direct Determination of Transmitted Acoustic Intensity", Noise Control Engineering, July/August, 1981.

PROTECTION OF ATTITUDE CONTROL THRUSTERS AGAINST PYRO-
TECHNIC STAGE SEPARATION SHOCK

Ernst Hornung, Deutsche Aerospace, ERNO Raumfahrttechnik[*]
Huba Oery, Technical University Aachen[**]

Abstract:

This paper investigates a simplified analysis, simulation and evaluation on violent pyrotechnic shocks. The shock environment at thruster location was specified in terms of a shock response spectrum (SRS) with a maximum level of 35,000 g above 3,000 Hz. These values are far above the strength of the elements of the monopropellant thrusters with flow-control values, transducers, catalyst and wire mesh sieves as potentially critical items. Therefore, the design approach was to use shock mounts between the 5.4 m cylinder and the thrusters. Shock mounts with minimum damping have been found to be efficient against pyrotechnic shocks. The mechanism will be explained by simple idealization as a single degree of freedom system. The shock input is idealized as base motion excitation. Two phases are distinguished which may be typical for a pyro shock environment at a location close to the pyrocharge:

- A single pulse with an extreme high acceleration level and extreme short duration (τ)
- Followed by quasi-cyclic excitation on a much lower level and with a much longer duration at high frequencies

Shock testing of the thruster on a shock machine was rejected because of potential errors in the definition of the specified environment and in the realization of that environment and in the realization of that environment, especially at the lower frequencies. Full model testing for development of the thruster was possible. The test results as well as further numerical simulations approved the "minimum damping concept". Another important issue is that shock severity should be related to the vibration velocity and not to the acceleration itself.

[*] ERNO Raumfahrttechnik GmbH
Deutsche Aerospace
Head of Maindepartment "Structuremechanics"
Hünefeldstr. 1-5
D-2800 Bremen 1
Phone (0421) 539-4382
Fax (0421) 539-5582

[**] University of Aachen
Emeritus
Institut für Leichtbau
Wüllner Str. 7
D-5100 Aachen
Phone (0241) 806830
Fax (0241) 32414

Protection of Attitude Control Thrusters Against Pyrotechnic Stage separation Shock

1.   Introduction

Aerospace structures must be light, consequently they become flexible, thin-walled and susceptile to buckling and vibrations. Considerable analytical progress has been achieved in the last years concerning the dynamic response analyses. Modal or global approaches has been used for arbitrary input excitations.

One area at the response problems, however, has not been deeply dealt with, this is the structural response on very high level very short duration shocks. In this context the attempt is made to summarize some basic knowledges and considerations.

Excessive dynamic responses jeopardize the correct function of the vehicle or lead to structural failure.

Guidance and control sensors can be seriously disturbed by vibration outputs. Large amplitudes hurt the clearance limits between substructures or block the control surfaces, or the gimbaling rocket nozzles.

The most frequent troubles caused by dynamic responses are due to mechanical stresses, such as structural collapse, rupture or fatigue, or also the failure of electronic devices, black-boxes and cables. Mechanical stresses are proportional to the vibrations velocity, therefore the velocity of the vibrations is more suitable to judge the criticality of a dynamic output than the acceleration. This statement will be explained in more details in § 2.

Dynamic excitations cannot be avoided, therefore remedies have to be found in order to reduce the danger of the consequencies. General methods cannot be applied, there are different devices and design rules for different sort of excitations. Here in § 3 we will consider the possibilities to reduce the structural responses on violent pyrotechnic shocks.

2.   The Vibration-Velocity Concept

2.1   The Vibration Propagation in a Uniform Elastic Rod

If the end of a uniform elastic rod see Fig. 1 will be <u>hit by a force</u>

$$P = \sigma A \qquad\qquad (1)$$
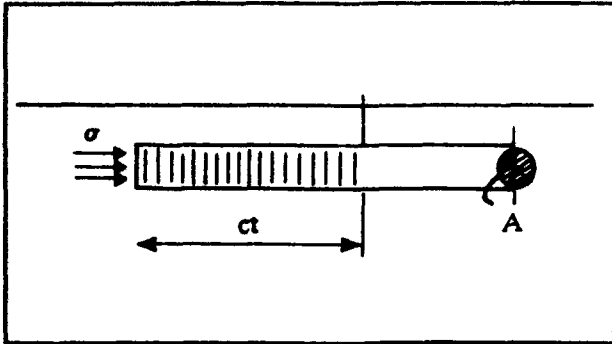
Fig. 1: Propagation of stress in a rod.

the stress will propagate with the velocity of the stress-wave "c". After the time "t" the length l = "ct" will be compressed by the stress σ and, consequently, this length will be shortened by

$$\Delta l = \frac{\sigma}{E} l = \frac{\sigma}{E} ct \qquad (2)$$

giving an end velocity to the initial section of

$$V = \frac{\Delta l}{t} = \frac{\sigma}{E} c \qquad (3)$$

$$\sigma = E \frac{V}{c} \qquad (4)$$

This reasoning enables us to define the stress in an elastic medium, if the vibration velocity is known

The same argumentation shows that all the sections within the shadowed area of the rod, Fig. 1 have the velocity V. This way the momentum-equation will define the stress-wave velocity as follows

$$\int P dt = m \Delta V \qquad (5)$$

$$A \sigma \Delta t = A c t \rho \frac{\sigma}{E} c \qquad (6)$$

$$c^2 = \frac{E}{\rho} \qquad (7)$$

$$c = \sqrt{\frac{E}{\rho}} \qquad (8)$$

Similar analyses can be repeated on a modal basis. We consider now a rod with the finite length of L which experiences a velocity shock with the velocity V_o, given by a very large rigid mass M arriving with this velocity, as shown in Figure 2. The relative velocity $(-V_o)$ can be developed in modal components and used as initial condition.

The absolute velocity will be subsequently defined in each instant as the sum of the local relative modal velocities and of the transport velocity V_o.

In this chapter we found out that for a shock-excited rod the absolute vibration velocity measured in one specific point of the continuum is directly proportional to the stress at
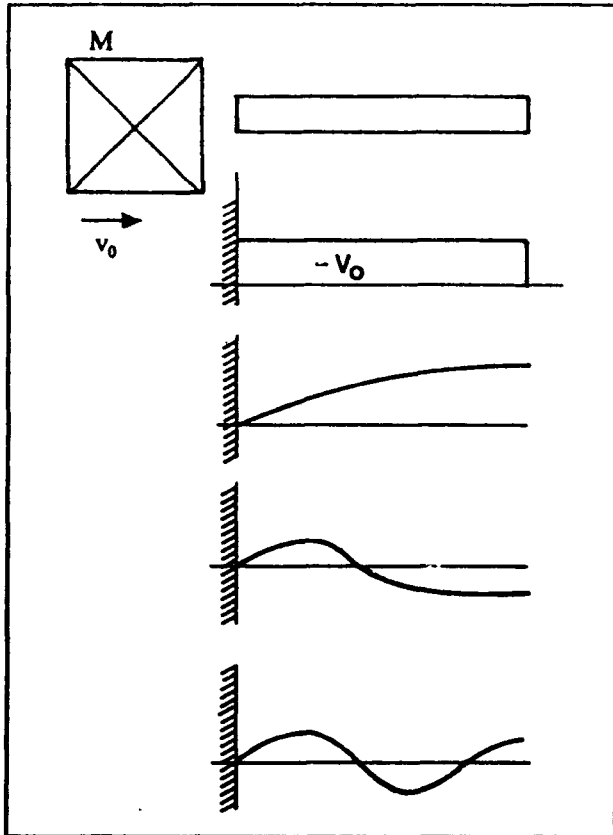
Fig. 2: Development of relative velocity in modal components

the same location in the same direction, if the propagation of the stress is due to an impact force applied.

2.2 The Relation between the Modal Velocity and the Modal Stress in a free Vibration of a Continous Beam

It exists a similar relation between the maximum stress and the maximum vibration velocity in the case of a pure free modal vibration as well:

$$\sigma_{max} = \kappa_i \sqrt{E \cdot \rho \cdot V_i} \tag{9}$$

$$= \kappa_i \sqrt{E \cdot \rho \cdot (a_i \omega_i)} \tag{10}$$

Here, however, the modal velocity $v_i = a_i \omega_i$ and the modal stress $\sigma_{max\,i}$ are measured at different locations as shown in Figure 3. For the formulas in Figure 3 the beam, if bent, is uniform and has a full rectangular cross section. For other cross section forms working in bending holds e.g. for the 1st and 2nd case in Fig. 3:

$$\kappa = \frac{1}{2} \frac{H}{r_g} \tag{11}$$

where H is the height and r_g radius of gyration of the cross section. This formula shows that κ is equal to 1.73; 2; 1 and 1.41 for a rectangular, circular, two-flange, and thin-

walled tube cross section form, respectively. In all cases, only the bending or extensional flexibility (no shear) has been considered.

It is worth noting that for a simply supported beam with a concentrated central mass m (m/m beam = 10) we find κ = 9.7.
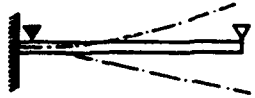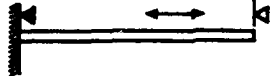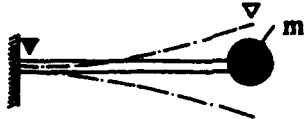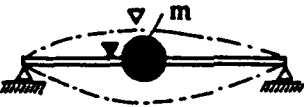
Actual Case	Proportionality: κ
	1,732
	1,732
	1
	$\approx 1{,}48\sqrt{1+4{,}11\dfrac{m}{m\ beam}}$
	$\approx 2{,}12\sqrt{1+2\dfrac{m}{m\ beam}}$

Fig. 3: Relation between the maximum modal vibration velocity and modal stress for uniform beams with full rectangular cross-section and without shear deformations.

location of: ▽ modal displacement (velocity, acceleration) measurement

▼ modal stress measurement

2.3 Correlation between Vibrations Velocity and Stresses for different Materials

Material	ρ Kg/m^3	E Pa	velocity of shock propation $c=\sqrt{\dfrac{E}{\rho}}$ m/s	$\sqrt{E\cdot\rho}$ Ns /m^3
Light alloy 70 75 T6	2800	7.5·10^{10}	5,175.4	1.45·10^7
Steel CroMo	7800	2.1·10^{11}	5,188.7	4.047·10^7
Titanium 6AL4V	4700	1.1·10^{11}	4,837.8	2.27·10^7
CFRP UD T300	1650	1.3·10^{11}	8,876.2	1.464·10^7

Table I: The factor √E ρ is dependent on the structural materials

The formula

$$\sigma_i = \kappa \sqrt{E\rho}\ V_i \qquad (12)$$

has been explained in the chapter 2.1 and in Figure 3. The factor $\sqrt{E\rho}$ is dependent on the structural materials, as shown in the Table I.

Consequently, a vibration velocity of e.g. 1 m/sec and $\kappa = 1$ corresponds to a stress of 1.45·10^7 N/m^2 (or 14.5 N/mm^2) in a light-alloy beam. We recall, however, to § 2.1 where we stated that κ could be for a SDOF system easily as high as 10.

In general, in aerospace structures vibration velocities up to 1-2 m/sec are allowable, depending on the circumstance whether a unique stress peak or an alternating load has to be taken into account.

2.4 Comments to the Shock Environment Definitions per Shock Response Spectra (SRS) Concept

It is common practice to define transient excitations by a shock response spectrum (SRS), calculated with SDOF systems having a standard (say $\zeta = 0.05$ or Q $= 10$) viscous damping. The shock response spectrum gives the maximum response for each resonant frequency of a potential equipment experiencing the base motion excitation, to be specified. This approach (SRS) could be a useful approximation tool, if the shock is not too violent ("violent" i.e. "very high" amplitude for "very short" duration) although also in these cases the SRS cancels and/or distorts some important information. Attention must be payed, in additon to check wether the mathematical model used for the calculation of the shock-response-spectrum is representativ for the specific problem investigated or not.

We believe, however, that pyrotechnic shocks - which are really "Very violent" - need a more precise definition, as this necessity can be proven by the invetigations decribed in this paper.

The specifications of pyrotechnic shocks if based on shock response spectra, belonging to a given damping value (mostly Q $= 10$) should therefore be revised. Indeed, the usualy defined straight lines envelope is not representative, even for the tested structure for many reasons:

i)   it does not consider phase relations and multi DOF generalization

ii) the same shock spectra can belong to an infinite number of excitation time-histories

iii) shock spectra are not complete without the knowledge of the place and direction of the measurement (or prediction)

iv) the enveloping of the response curve ignores the feedback effects of the components and this way can lead to important over- or under-estimations

v)   the establishment of the shock-spectra should consider the different types of shocks (short duration or long lasting shocks: force/motion/velocity or acceleration shocks etc.) and their time histories. Indeed, e.g. the structural damping can be useful or unimportant or even harmful and decisive according to the type and duration of the shock as well as type and location of the damping.

The standard shock spectra are usualy established using a Q-amplification factor of $Q=10$ (strictly speaking a damping of 5 %). It is necessary to do so, because the forcing functions contain sometimes periodic terms which would lead to infinite responses for non damped resonators. However, especialy concerning the point v.), the arbitrarily chosen model and damping value can influence the conclusions in a good or in a bed direction.

3.   The Pyrotechnic Separation of the ARIANE 5. 2nd Stage (EPS)

The actual task was the protection of thrusters for the ARIANE 5 attitude controle system against pyrotechnic stage separation shocks.
Figure 4 shows the configuration of ARIANE 5 with

·   main stage
·   solid propellant booster EAP
·   separation plane

and above separation in a concentric arrangement

            vehicle equipment bay VEB
                at the periphery
            second stage EPS
                in central position.

In our case, the attitude control thrusters are located at the VEB. They are combined to clusters of three. The clusters are located at the lower edge of the VEB, in order to provide maximum lever arms for the attitude control maneuvers. Thus they are very close to the separation plane.

The local cross section to be separated by pyrotechniques is an aluminium cylinder with a 5.4 m diameter, 6 mm thick in the separated section.
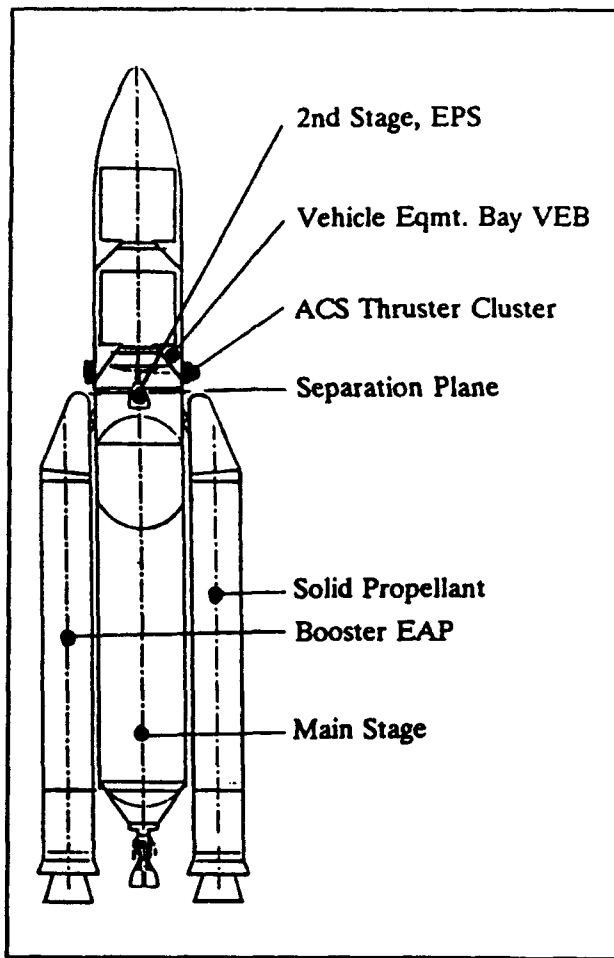
Fig. 4: ARIANE 5 Configuration

The shock environment at cluster location was specified in terms of a classic shock response spectrum (SRS) with a maximum level of 35000 g above 3000 Hz (corresponding to a velocity v = 18.6 m/s at 3000 Hz, and with a structural damping of 5% or Q = 10 of the responding 1 DOF system, see Figure 5. This specification corresponds in order of magnitude to actual measurements made in a pretest, where half sine like shocks with peaks up to 45000 g and duration of 40 μs $\div$ 80 μs have been monitored on the shell.

These response values, even at 3000 Hz with v = 18.6 vibration velocity are far above the strength of the elements of the monopropellant thruster with flow control valves, transducers, catalyst and wire

mesh sieves as potentially critical items. Therefore, the design approach was to use shock mounts between 5.4 m cylinder and cluster.

It must be pointed out, in addition, that these clasic shock spectrum seem to have been calculated with a specific, damped SDOF model. We find this model in the relevant literature Ref. [3] (Harris and Crede) and show it on Fig. 6.

The diagram in Figure 6 shows smaller responses when the damping is increased.

Fig. 5: ARIANE 5, specified shock response spectrum for Zone "Z1"

However, when looking to the equation of motion:

$$\frac{m\,\ddot{x}}{k} + \frac{c\cdot\dot{x}}{k} + x = u_p \sin\frac{\pi}{\tau}t$$

we see that the term which represents the damping force

$$c\cdot\dot{x}$$

here is depending on the absolute displacement of the mass m and on the absolute velocity $\dot{x}$, but not on the relative displacement x-u. I.e. the dashpot is between mass m and inert reference.

Such a system, however, is normally not representative for a shock mount, where stiffness k and damping c are properties of one and the same elastic member between moving base and mass m, see Figure 7 and the shock is a half sine acceleration shock without final remaining displacement and velocity.

With the information so far, we were able to establish the input/output requirement for the shock mount (see Figure 7). The mechanism of the shock mounts be explained by simple idealization as given in Figure 8.

The excited equipment is idealized as a single degree of freedom (SDOF) system, tuned to a low resonant frequency.

Fig. 6: 1DOF system with damping w.r.t. an inert reference per ref. [3] Harris & Crede. Not representative for the present problem.

The low damping of the shock mount is represented by the dashpot with a small damping coefficient c. The shock input is idealized as base motion excitation. Two phases are distinguished which may be typical for a pyro shock environment at a location close to the pyro charge:

o   First a single pulse with extreme high acceleration level and extreme short duration (τ)

o   Followed by quasi-cyclic excitation on much lower level and with much longer duration at high frequencies.

(Such quasi cyclic excitation can arrive with several frequencies at the same time the sonsequencies can be superimposed)

It is understood that no residual displacement and velocity of the base exist after the shock. The response of the SDOF system to the first very short duration pulse is mainly due to the forces transmitted by the dashpot, since the duration is too short (i.e. $f_o\tau << 1$) to build up relevant relative displacement and spring force. Therefore, the response will be low as long as the damping constant c is small.

Input	System	Output
half sine pulse 40000 g	1DOF	SRS < 0.57 f

$\tau = 40 \, \mu s$

$\log a$ 0.57 f

$\log f$

Fig. 7: Input/Output requirement

for $0 < t < \tau$	for $t < 0$ and $t > \tau$
$\ddot{u} = a \sin \Omega t$	$\ddot{u} = \dot{u} = u = 0$

$$\dot{u} = -\frac{a}{\Omega} \cos \Omega t + A$$

$$u = -\frac{a}{\Omega^2} \sin \Omega t + A t + B$$

$$\text{with} \quad A = B = 0$$

$$\text{but} \quad \dot{u}_{max} = \pm \frac{a}{\Omega}$$

$$\text{at} \quad t = 0 \quad \text{and} \quad t = \tau$$

$$\Omega = \frac{\pi}{\tau}$$

Table II: Acceleration shock with no final displacement

response will be low as long as the damping constant c is small.

The response of the SDOF system to the subsequent quasi-cyclic excitation is that to an overcritical stationary excitation, i.e. the responses will be low with the low damping ration $\zeta = c/c_{crit}$.

For extreme short shock pulses and for subsequent quasi-cyclic excitation, which is overcritical, a shock mount with low damping is advantageous.

The second ovservation was that in case of a pyro shock the displacement of the base at the end of the shock event as already stated is and remains zero. (Table II).

For short duration shocks i.e. $\tau f_o << 1$ provided the system is undamped, only the impulse

$$I = \int \ddot{u} dt$$

is important, not the time history. If the system is additionally damped, also the initial velocity $\dot{u}$ (t = 0) can play a considerable role - especially for extreme short durations.

Undamped System

During the time of the shock $0 < t < \tau$ the acceleration is due to the spring force

$$\ddot{x} = \frac{u_o k}{m} = \ddot{u}_o \frac{\omega_o^2}{\Omega^2};$$

$$\left(\frac{\ddot{x}}{\ddot{u}}\right)_{max} = 4(f_o \tau)^2 \qquad (13)$$

$$\text{with} \quad \Omega = \frac{\pi}{\tau}; \quad \omega_o = f_o \cdot 2\pi$$

in the inital phase.

System:

Input:

Response:

$$\left(\frac{\ddot{x}}{\ddot{u}}\right)_{max} = 4\tau \zeta f_o$$

Response is low when:

| f_o | small | f_o | $<< f$ |
| ζ | small | ζ | small |

Fig. 8: Shock mount with minimum damping
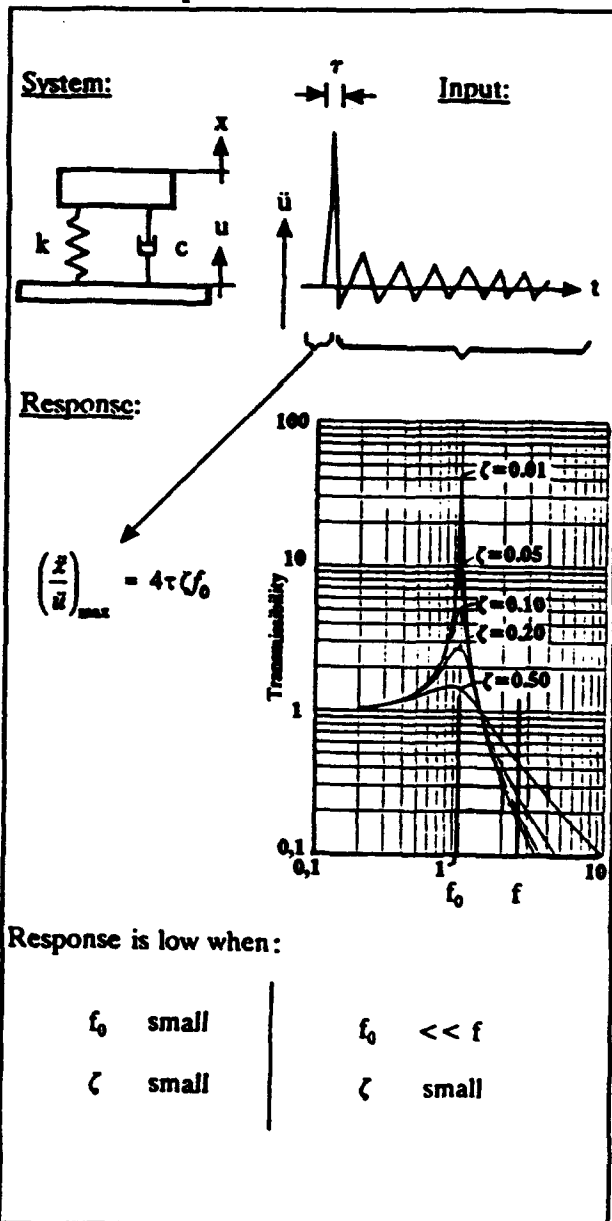
After the shock $(t > \tau)$ the system performs a residual vibration

$$\dot{x} = \frac{\int P dt}{m} = \frac{m\ddot{u}\tau \frac{2}{\pi}}{m} \qquad (14)$$

$$\text{and} \quad \ddot{x} = \dot{x} \cdot \omega_o$$

leading to

$$\left(\frac{\ddot{x}}{\ddot{u}}\right)_{max} = 16 \, (f_o \tau)^3 \qquad (15)$$

in the residual phase.

Damped system

The first observation $\tau f_o << 1$ allows to neglect the spring force and to concentrate on the damping force.

$$F(damp) = \dot{u} \cdot c \qquad at \quad t = 0$$

$$\dot{u}c > F(damp) > -\dot{u}c \qquad at \quad o < t < \tau$$

$$\qquad (16)$$

The second observation; u (final) = 0; allows to define the velocity of the base

$$\dot{u}_{max} = -\frac{a}{\Omega} \qquad (17)$$

at $t = 0$.

Equation (16) and (17) yield the max force within the dashpot at t=0. The resulting acceleration response $\ddot{x}_{max}$ is:

$$F_{max} = \ddot{u}_{max} \cdot c = \frac{1}{\pi} \cdot \ddot{u}_{max} \, \tau \cdot \zeta \, c_{cr}$$

$$\text{with} \quad c_{cr} = 2\omega_0 m = 4\pi f_0 m \tag{18}$$

$$F_{max} = 4 \, \ddot{u}_{max} \, \tau \, \zeta \cdot f_0 \, m$$

$$\ddot{x}_{max} = \frac{F_{max}}{m} = 4 \, \ddot{u}_{max} \, \tau \, f_0 \, \zeta \quad \Longrightarrow \quad \left(\frac{\ddot{x}}{\ddot{u}}\right)_{max} = 4\tau f_0 \zeta \tag{19}$$
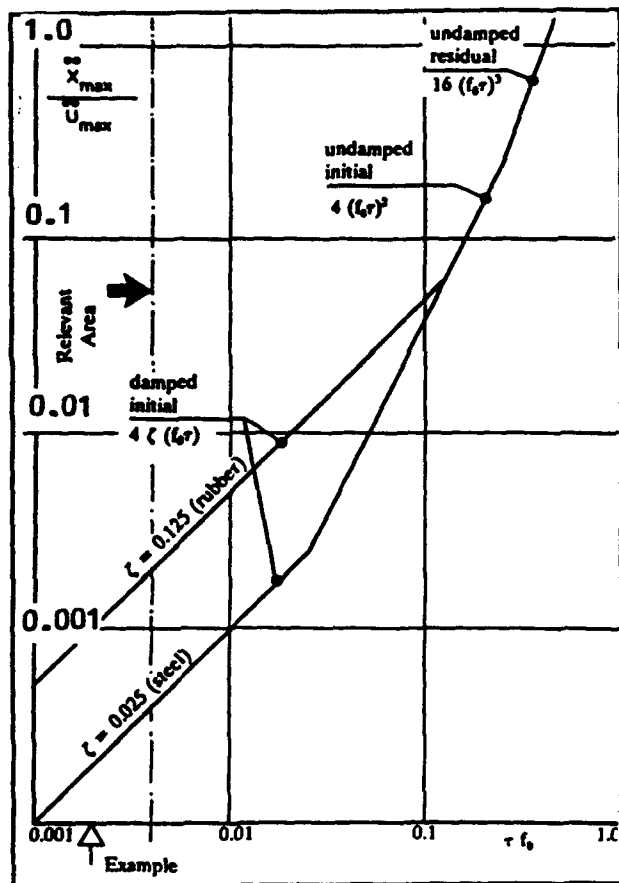
Fig. 9: Response of SDOF system to very short duration half sine pulse.

In the cases where the assumption ($f_0\tau = << \zeta$) is no more fullfilled, both damping force and spring force should be considered, leading to the formula

$$\left(\frac{\ddot{x}}{\ddot{u}}\right) = 4\zeta \, (f_0\tau) \sqrt{1 + \left(\frac{f_0\tau}{\zeta}\right)^2} \tag{20}$$

belonging to the initial short phase.

In the residual phase, the maximum acceleration can be given approximately for the damped system as follows:

$$\left(\frac{\ddot{x}}{\ddot{u}}\right)_{res} = \sqrt{1 + 4\zeta^2} \; 16 \, (f_0\tau)^3 \tag{21}$$

Equations (13), (15) and (19) give the shock response evaluations as shown in principle in Figure 9.

All the measurements on the shell during the simulated stage separation show after the above treated half sine peak a quasi-harmonic motion with very high frequency giving a periodic excitation for the equipments assembled to the shell.

The force transmitted between the mass-point and the base, vibrating in a harmonic motion, is given by the formula

$$(F_p) = c\,(\dot{x}-\dot{u}) + k\,(x-u) \tag{22}$$

and, the acceleration of the mass m

$$\ddot{x} = \frac{c}{m}\,(\dot{x}-\dot{u}) + \frac{k}{m}\,(x-u) \tag{23}$$

The transmissibility T, which is the ratio between the output/input acceleration amplitudes is in stationary motion:

$$T = \frac{\ddot{x}}{\ddot{u}} = \sqrt{\frac{1+(2\zeta\omega/\omega_0)^2}{\left(1-\frac{\omega^2}{\omega_0^2}\right)^2 + (2\zeta\omega/\omega_0)^2}} \tag{24}$$

the phase angle will be defined as follows:

$$\psi = arc\,tg\left[\frac{2\zeta(\omega/\omega_0)^3}{1-\frac{\omega^2}{\omega_0^2} + 4\zeta^2\omega^2/\omega_0^2}\right] \tag{25}$$

These formulas have been plotted in Figure 10.
For very highly overcritical excitation (HOC) i.e. $\omega/\omega_0 \geq 10$ and low or moderate damping, the above formulas can be reduced to

$$T_{HOC} = \left(\frac{\omega_0}{\omega}\right)^2 \sqrt{1+4\zeta^2\left(\frac{\omega}{\omega_0}\right)^2} \qquad for \ \frac{\omega}{\omega o} \geq 10 \tag{26}$$

$$\psi_{(HOC)} = arc\,tg\left(-2\zeta\frac{\omega}{\omega_0}\right)$$
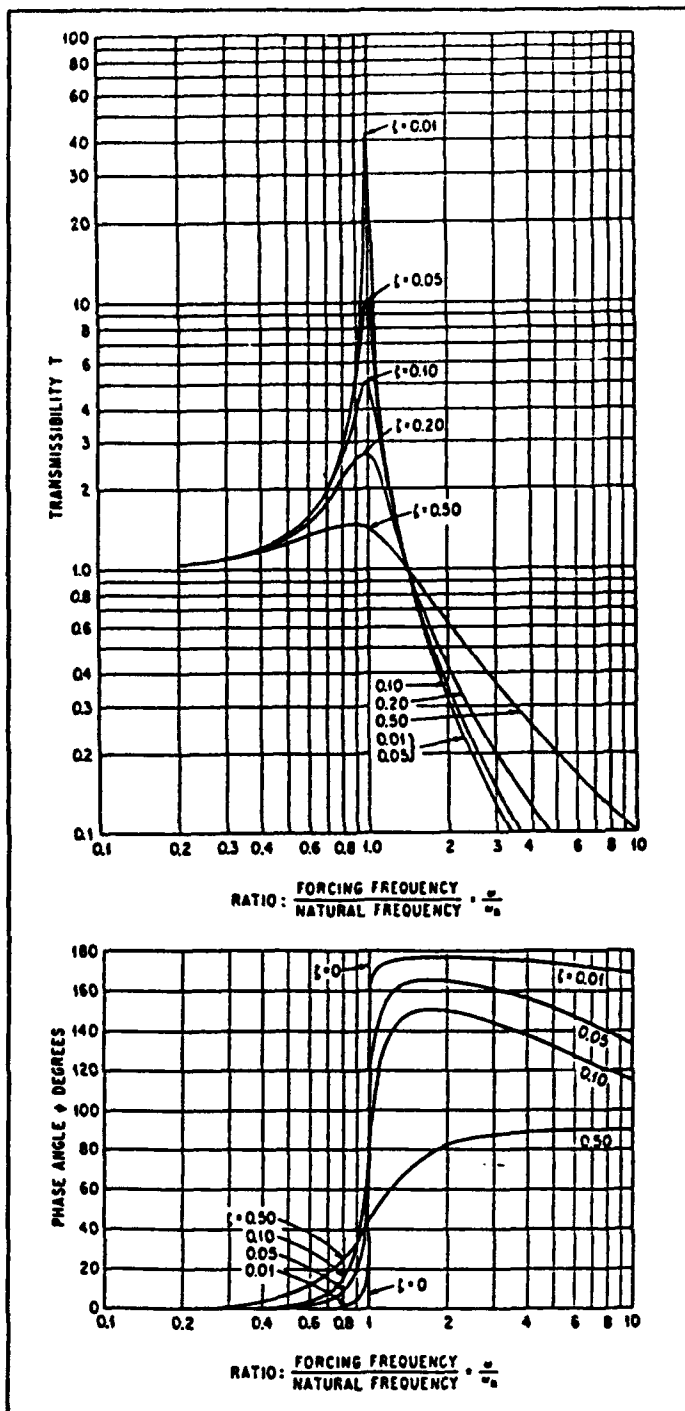
Fig. 10: Transmissibility and phase angle

In the case of even higher excitation frequencies i.e. $\frac{\omega}{\omega_o} > 100$, also the following formula gives a good approximation

$$T_{VHOC} = 2\,\zeta\,\frac{\omega_o}{\omega}\;;\;for\;\frac{\omega}{\omega_o} > 100$$

$$(27)$$

In Figure 10 as well as in the above equations it can be seen that for such excitations the damping is rather harmful, it increases considerable the transmitted force.

The Table III summarizes all the shock response formulas defined in this chapter.

Let us consider a realistic example, with the following input data.

Shock input:

o A half-sine violent peak

   $\ddot{u}_{hs}$ = 40000 g;

   $\tau = 40 \cdot 10^{-6}$ sec

o followed by a quasi-periodic mo tion

   $\ddot{u}_{qp}$ = 5000 g;

   f_{qp} = 10000 Hz

SDOF System
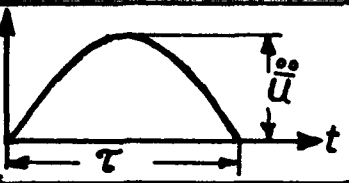
o   f = 50 Hz
o ζ = 0.05

Shock responses

    o   to the half sine peak ($f_0\tau = 50 \cdot 40 \cdot 10^{-6} = 2 \cdot 10^{-3}$)

    -    initial phase

$$\left(\frac{\ddot{x}}{\ddot{u}}\right)_{hs\,i} = 4\,\zeta\,(f_0\tau)\sqrt{1 + \left(\frac{f_0\tau}{\zeta}\right)^2} = 4 \cdot 10^{-4}$$

$$\text{or } \ddot{x}_{hs} = 16\,g$$

Half-sine shock		Harmonic excitation $\ddot{u}\sin\omega t$	
Initial peak $$\left(\frac{\ddot{x}}{-\ddot{u}}\right)_i = P\,(f_o\tau)$$	**Residual amplitude** $$\left(\frac{\ddot{x}}{-\ddot{u}}\right)_r = A\,(f_o\tau)$$	$\ddot{x}\sin(\omega t + \epsilon)$ $$\left(\frac{\ddot{x}}{-\ddot{u}}\right)_R = T\left(\frac{\omega}{\omega_o}\right)$$
$$P\,(f_o\tau) = 4\zeta f_o\tau \cdot$$ $$\cdot \sqrt{1 + \left(\frac{f_o\tau}{\zeta}\right)^2}$$	$$A\,(f_o\tau) = \sqrt{1 + 4\zeta^2} \cdot$$ $$\cdot 16\,(f_o\tau)^3$$	$$T\left(\frac{\omega}{\omega_o}\right) = \sqrt{\frac{1 + \left(2\zeta\frac{\omega}{\omega_o}\right)^2}{\left(1 - \frac{\omega^2}{\omega_o^2}\right)^2 + \left(2\zeta\frac{\omega}{\omega_o}\right)^2}}$$ or if $\quad \dfrac{\omega}{\omega_0} \geq 10$ $$T_{HOC} = \left(\frac{\omega_o}{\omega}\right)^2 \sqrt{1 + 4\zeta^2\left(\frac{\omega}{\omega_0}\right)^2}$$ and if $\quad \dfrac{\omega}{\omega_o} > 100$ $$T_{HOC} = 2\zeta\frac{\omega_o}{\omega}$$

Table III: Shock response formulas

o   residual phase

$$\left(\frac{\ddot{x}}{\ddot{u}}\right)_{Res} = \sqrt{1 + 4\zeta^2} \cdot 16 \, (f_0\tau)^3 = 1.3{\cdot}10^{-7}$$

$$or \quad \ddot{x}_{Res} = 5.2{\cdot}10^{-3} \, g$$

o   to quasi-periodic excitation $(\omega/\omega_0 = \dfrac{10^4}{50} = 200)$ (equ. 24)

$$T\left(\frac{\omega}{\omega_0}\right) = 5 \cdot 10^{-4}$$

$$or \quad \ddot{x}_{qp} = 5 \cdot 10^{-4} \cdot 5000 = 2{,}5 \, g$$

We reproduce now the same values without and with damping:

	without damping	with 5 % damping
$\ddot{x}_{Ast}$ [g]	0.64 g	16 g
$\ddot{x}_{AR}$ [g]	$1.28 \cdot 10^{-7}$ g	$5.2{\cdot}10^{-3}$ g
$\ddot{x}_{qp}$ [g]	0.125 g	2.5 g

Specific Requirements for the Design of Shock Mounts

With the dimensionless acceleration response (Equ. (19))

$$\frac{\ddot{x}_{max}}{\ddot{u}_{max}} = 4 \, \tau \, f_0 \, \zeta \tag{28}$$

the requirement is to design in the first approximation for

o   low resonant frequency f_0
and
o   low damping ration ζ.

<u>Note</u>:

The physical meaning of the above two requirements is to design for a low viscous damping coefficient c.

$$c = c_{cr} \cdot \frac{c}{c_{cr}} = 2\omega_0 m \cdot \frac{c}{c_{cr}} = 4\pi f_0 \, m \, \zeta \qquad (29)$$

In the Fig. 11 we enlarged further this mathematical model, using the same reasoning. Now the platform holds a component. Feed-back effects will be disregarded as before, based on the very low mass relations between the platform and the resonant elements inside the component. It can be seen, that in the component respons we will find besides a shock peak, responses at the eigenfrequencies of the platform, of the component and of the periodic excitation of the shell.

Some numerical examples have been presented on the Table IV. We can conclude that a "very low" suspension frequency for the platform with "very low" damping is the best protection for the components on the platform against very short duration violent acceleration shocks and/or very high frequency excitations. High damping inside the components is desirable.
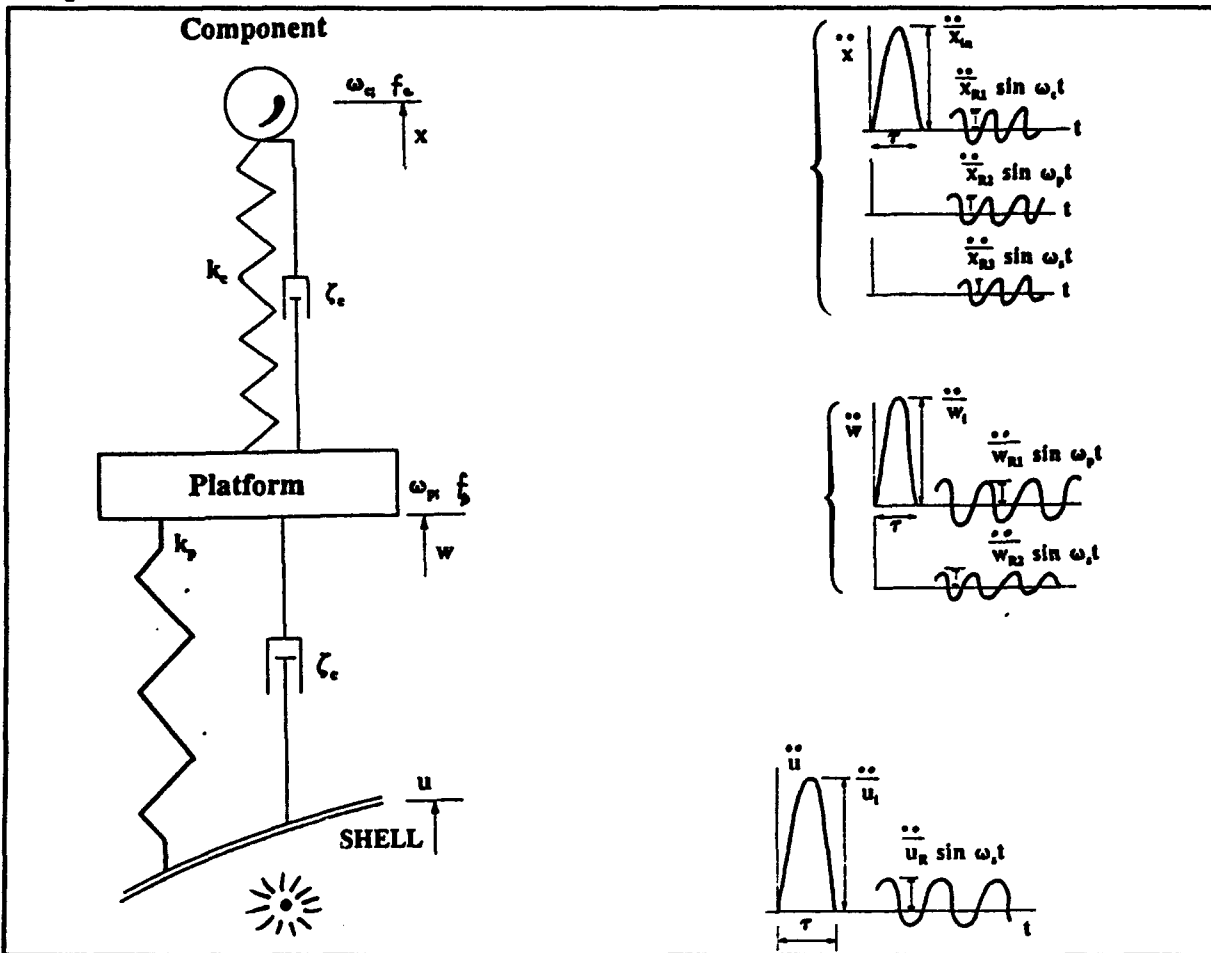
Fig. 11: Output accelerations on platform and component (no feed-back).

	Initial Peak	**Quasi-Harmonic Residuals**
Component	$$\ddot{\bar{x}}_i = P(f_c\tau) * \ddot{\bar{w}}_i =$$ $$= P(f_c\tau) * P(f_p\tau) * \ddot{\bar{u}}_i$$	o free $$\ddot{\bar{x}}_{RI} = A(\zeta\tau) * \ddot{\bar{w}}_i = A(f_c\tau) * P(f_p\tau) * \ddot{\bar{u}}_i$$ o excited (2); (3) $$\ddot{\bar{x}}_{R2} = T\left(\frac{\omega_p}{\omega_c}\right) * \ddot{\bar{w}}_{R4}\ \sin\ \omega_p t =$$ $$= T\left(\frac{\omega_p}{\omega_c}\right) * A(f_p\tau) * \ddot{\bar{u}}_i * \sin\ \omega_p t$$ $$\ddot{\bar{x}}_{R3} = T\left(\frac{\omega_s}{\omega_c}\right) * T\left(\frac{\omega_s}{\omega_p}\right) * \ddot{\bar{u}}_R\ \sin\ \omega_s t$$
Platform	$$\ddot{\bar{w}}_i = P(f_p\tau) * \ddot{\bar{u}}_i$$	o free $$\ddot{\bar{w}}_{R4} = A(f_p\tau) * \ddot{\bar{u}}_i * \sin\ \omega_p t$$ o excited $$\ddot{\bar{w}}_{R2} = T\left(\frac{\omega_s}{\omega_p}\right) * \ddot{\bar{u}}_R * \sin\ \omega_s t$$

$$P(f\tau) = 4\zeta f\tau\ \sqrt{1 + \left(\frac{f\tau}{\zeta}\right)^2}$$

$$A(f\tau) = \sqrt{1 + 4\zeta^2}\cdot 16\ (f\tau)^3$$

o $$T\left(\frac{\omega}{\omega_o}\right) = \sqrt{\frac{1 + (2\zeta\omega/\omega_o)^2}{\left(1 - \frac{\omega^2}{\omega_o^2}\right)^2 + (2\zeta\omega/\omega_o)^2}}$$

o if $\frac{\omega}{\omega_o} \geq 10$

$$T_{HOC} = \left(\frac{\omega_o}{\omega}\right)^2\ \sqrt{1 + 4\zeta^2\left(\frac{\omega}{\omega_o}\right)^2}$$

o if $\frac{\omega}{\omega_o} > 100$

$$T_{THOC} = 2\zeta\ \frac{\omega_o}{\omega}$$

Fig. 11 cont'd: Output accelerations on platform and components (no feed-back)

ζ_p	ζ_s	ζ_c	Platform response [g]			Component response [g]			
			Sharp half sine	harmonic f_p	harmonic f_c	Sharp half sine	harmonic f_c	harmonic f_p	harmonic f_c
10^{-3}			18.06	0.573	62.7	$7.4 \cdot 10^{-3}$	$1.48 \cdot 10^{-4}$	28.68	0.169
5.10^{-2}			113.2	0.576	140.1	$4.65 \cdot 10^{-1}$	$9.29 \cdot 10^{-4}$	28.82	0.378
0.10		0.01	224.7	0.585	258.3	$9.2 \cdot 10^{-2}$	$1.84 \cdot 10^{-3}$	29.24	0.697
0.15	200		336.5	0.599	318.1	0.138	$2.76 \cdot 10^{-3}$	29.94	1.028
0.20			448.3	0.617	505.0	0.183	$3.67 \cdot 10^{-3}$	30.89	1.363
		$1.10-3$				0.058	$1.84 \cdot 10^{-3}$	292.4	0.647
		$2.5 \cdot 10^{-3}$				0.606	$1.84 \cdot 10^{-3}$	116.9	0.65
	200	$5.0 \cdot 10^{-3}$	224.7	0.585	258.3	0.068	$1.84 \cdot 10^{-3}$	58.48	0.66
		$1.0 \cdot 10^{-2}$				0.092	$1.84 \cdot 10^{-3}$	29.24	0.70
0.10		$5.0 \cdot 10^{-?}$				0.361	$1.85 \cdot 10^{-3}$	5.88	1.45
	50					$5.75 \cdot 10^{-3}$	$2.88 \cdot 10^{-5}$	$3.9 \cdot 10^{-2}$	$3.35 \cdot 10^{-2}$
	100					$1.7 \cdot 10^{-2}$	$2.3 \cdot 10^{-4}$	0.195	0.164
	200					0.06	$1.84 \cdot 10^{-3}$	116.9	0.65
	500	$2.5 \cdot 10^{-3}$	224.7	0.585	258.30.	0.362	$2.88 \cdot 10^{-2}$	0.696	4.10
	1000					1.44	0.23	0.610	17.2
0.10	2000					5.75	1.84	0.59	86.1
	4000					23.01	14.72	0.586	$5.17 \cdot 10^{-4}$
10^{-3}	4000	$2.5 \cdot 10^{-3}$	18.06	0.573	62.7	1.85	1.18	0.57	$1.25 \cdot 10^{-4}$
		0.05				1.94	1.18	0.57	630.2

Table IV: Some numerical response examples for the Fig. 14

Indices:	$\tau = 4 \cdot 10^{-5}$ sec
"p" = platform	$\ddot{u}_i = 70\,000.0$ [g]
"c" = component	fs $= 4\,000.0$ [Hz]
"s" = shell	$\ddot{u}_R = 25\,000$ [g]
"i" = initial	$f_P = 200$ [Hz]
"R" = residual	$\zeta_p = ...$

4.   Hardware Development

It was decided to have two shock mount typs during the development phase:

o A typical visco-elastic shock mount
o A steel spring shock mount with low damping

4.1 Viscoelastic Shock Mount

Fig. 12: Visco-elastic shock mount.

The viscoelastic shock mount is shown in Figure 12.

The design principle was

o to use a selected viscoelastic material with good resilient properties in tension and shear in form of washers bonded to the aluminium members

o to use multiple joints i.e. to increase the number of J/F's and to change several times the material of the transmission path for the incoming shock wave

o to change the direction of the transmission path two times by 90°

o to use floating bolts i.e. to protect nut and head by viscoelastic washers.

o to have no row of connection bolts along the lower edge of the dummy in parallel and close to the pyro charge.

Identical number and hole pattern for J/F bolts to the primary structure for visco and steel shock mount was foreseen in order to have the same boundaries. It has to be noted that corresponding to § 3 with the viscoelastic shock mount higher responses were to be expected than with the steel spring design.

4.2 Steel Spring Shock Mount

The steel spring shock mount is shown in Figure 13.
The design principle was to realize the low fundamental resonances for the three degree of freedom of vibration (in translation) and the low damping ratio by

o a steel strip spring design

o made from high strength steel

o dimensioned for conservative displacement

o with minimum J/F damping achieved by use of thin narrow washers at J/F's which efficiently reduce the J/F area. No counter plates.

Counter plates were removed in order to reduce damping

Fig. 13: Steel-spring shock mount in 2 m diameter model.

The shock mount consisted of four L-shaped steel strip springs, which provide elasticity in axial and tangential direction, in combination with four U-shaped steel strip springs, which provide elasticity in radial direction (with respect to the launch vehicle). In order to save space, the steel strip springs are somehow "wrapped" around the edges and corners of the cluster plate. Plus/minus 5 mm dynamic clearance was foreseen in all 3 directions.
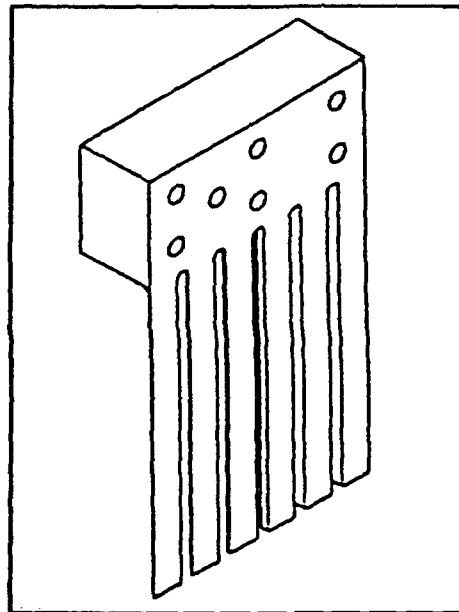
Fig. 14: A resonating comb (an array of reeds) - measurement device.

5. Pyro Shock Tests

5.1 Test Approach

2 m Diameter Model / Development Test

- with two 14 kg cluster dummies
     - one on viscoelastic shock mount
     - one on steel spring shock mount

Full 5 ø Model

- with viscoelastic shock mounts
     - one with thruster dummies
     - one with real thruster

Table V: Test Models for Pyro Shock Tests

Shock testing of the thruster cluster on a shock machine was rejected because of potential errors in the definition of the specified environment and in the realization of that environment, especially at lower frequencies, in this case below 1000 Hz, where the thrusters might become critical.

Full model testing for development of the thruster cluster was possible, since such a test program already existed with the goal to provide an acceptable shock environment for the equipment platform within the VEB.

Thruster cluster hardware became involved in two models of this test program. (see Table V.)

5.2 Test Results

The ACS clusters were instrumented with accelerometers on the dummy plate and thrusters. For the Full-Model-Test an additional mechanical measurement device was installed, a resonating comb (an array of reeds) with different SDOF systems. (see Figure 14). The responses are measured with strain gages. This data allows to proof the shock spectra for components located on the platform.

5.2.1 Evaluation Philosophy

Since acceleration vs. time signals are not directly informative about the damage potential of the shock, they have been transformed into

o   low pass filtered signals with different cut off frequencies in order to obtain structural design loads from low frequency excitation for supports and shock mount itself.

o   Standard shock response spectra (Q=10) (acceleration response of a series of single DOF systems) in order to estimate potential resonant responses at equipment fundamental and higher order modes.

o Velocities from shock response spectra i.e. comparison against "0.80 f" rule in order to check the criticality of the shock for the thrusters on the cluster panel. The allowable vibration velocity of say, 1.25 m/sec can be namely expressed in terms of the acceleration as follows

$$a \ [g] = \frac{\omega V}{g} \sim 0.8 \ f \left[\frac{g}{Hz}\right]$$ (30)

5.2.2 Evaluation at Low Frequencies

Structural Design Load Factor for ClusterPanel

2 m ϕ - Model		5 m ϕ - Model
Visco Panel f_o = 180 Hz	Steel Spring Panel f_o = 50 Hz	Visco Panel f_o = 125 Hz
Filter Cut-Off Frequency		
1 · f_o ≈ 200 Hz	1 · f_o = 50 Hz	≈ 200 Hz
n_L = 64 g	(n_L = < 13 g)	n_L = 15 g
Filter Cut-Off Frequency		
2 · f_o ≈ 400 Hz	2 · f_o = 100 Hz	≈ 400 Hz
n_L = 92 g	n_L = 13 g	n_L = 30 g

The structural design load factor for the cluster panel and the shock mounts themselves is found by low pass filtering of the acceleration signals with a filter cut-off frequency in order to cover conservatively the effects of higher order modes.

The longitudinal load is in the plane of the cluster panel and therefore less critical. The radial load factors n_R are of higher interest. (see Tabel VII)

Table VI: Longitudinal Design Load Factor

2 m ϕ - Model		5 m ϕ - Model
Visco Panel f_o = 180 Hz	Steel Spring Panel f_o = 44 Hz	Visco Panel f_o = 125 Hz
Filter Cut-Off Frequency		
1 · f_o ≈ 200 Hz	1 · f_o = 44 Hz	≈ 200 Hz
n_R = 44 g	(n_R = < 6 g)	n_R = 25 g
Filter Cut-Off Frequency		
2 · f_o ≈ 400 Hz	2 · f_o = 100 Hz	2 · f_o ≈ 400 Hz
n_R = 54 g	n_R = 6 g	n_R = 35 g

With n_R between 35-54 g for the visco panel, the shock is becoming the design driver. Normally one would expect about 40 g as design load factor. Also a stiffness requirement for the panel alone has to be observed.

$$\sqrt{2} \cdot f_2 = \sqrt{2} \cdot 180 Hz = 254 Hz$$ (31)

However, there will be no problem to fulfill the 54 g and 254 Hz requirements.

Table VII: Radial Design Load Factor

5.2.3   Evaluation at Medium Frequencies per SRS
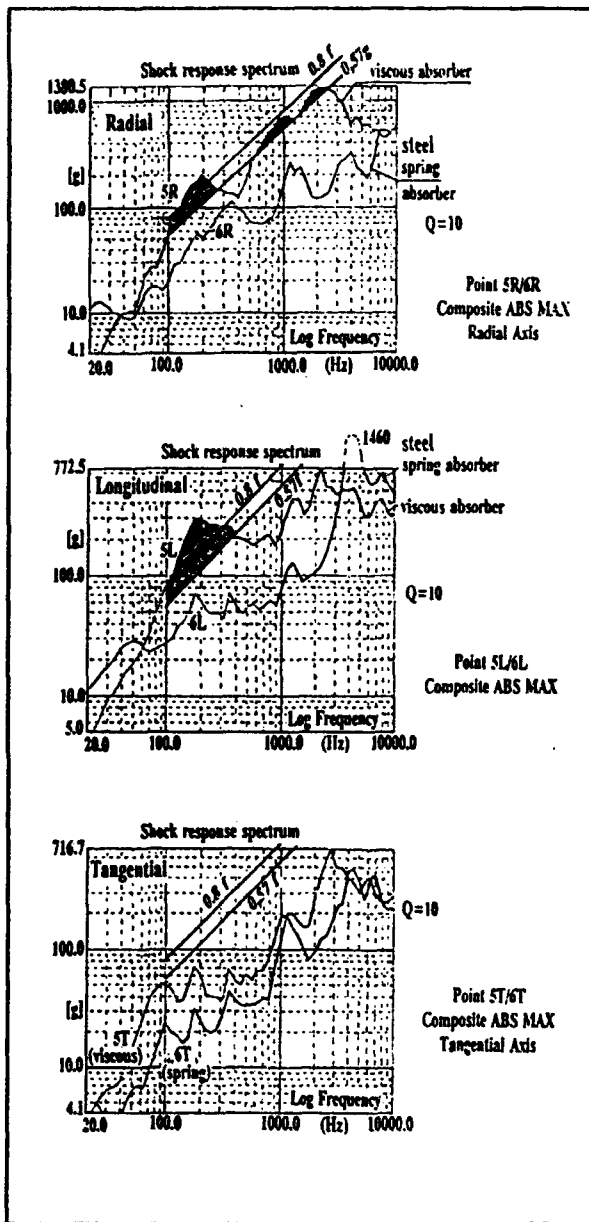
Fig. 15: Test Results from the 2 m Diameter Model Test.
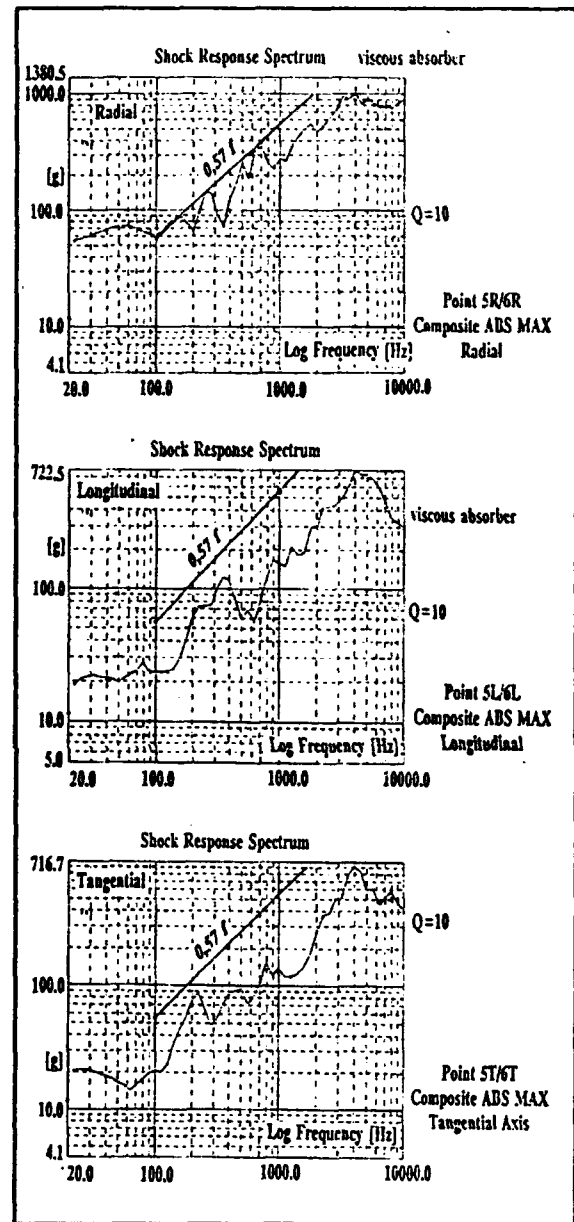
Fig. 16: Test Results from the 5 m Diameter Model Test

Resonant responses for components located on cluster panel.

Test results from 2 m diameter Model Test see Figure 15.

Only the viscous panel SRS is exceeding considerably the 0,8 f/1,4 = 0,57 f equipment limit. When we restrict ourselves to 100-500 Hz, where the hardmounted fundamental resonances of the components might be allocated, then we can compare max values:

Visco Panel	Steel Spring Panel
$n_{comp} = n_L = 280$ g $n_R = 200$ g	$n_L = 70$ g $n_{comp} = n_R = 110$ g

It is obvious that here the design of the components has to be checked against shock loads on a case-by-case basis using the SRS and info on resonant frequencies, for all three axes.

Test results from the 5 m diameter Model Test (see Figure 16) (visco panel only)

The viscos panel SRS fulfills the .57 f requirement. The maximum acceleration responses are
$$n_L = 130 \text{ g}$$
$$n_R = 250 \text{ g}$$

5.2.4   Evaluation at High Frequencies f > 500 Hz per SRS

o 2 m ϕ Model

The steel spring panel SRS is in the hole range below the allowable (0,57 f) line, the viscous panel SRS exceeds it in the range 550 Hz - 2400 Hz.

o 5 m ϕ Model

The visco panel fulfills the .57 f requirement.

5.2.5   Evaluation of the Comb-Device-Measurements on the 5 m Diameter Model

Not yet available. Will be published later on.

6.   Final Conclusion for ARIANE 5

For ARIANE 5 the viscous shock mounts were selected with the following justification

o No problems have to be expected w.r.t
   - stiffness requirement
   - damping requirement
   - sine vibration test responses
   - random vibration test responses
o The shock responses of the thrusters on top of a viscous shock mount are within the actual capability of the thruster and below the 0.57 f requirement for the actual model, they were higher in the previous tests using a $\phi 2$ m model.
o potential general problems with the material characteristics of the viscoelastic material are solved for ARIANE 5.

6. Summary

o Shock is not the only structural dynamic environment. There are also low frequency transients, sine and random vibrations.

o As long as the shock is not a design driver, equipment boxes are protected by conservative requirements w.r.t
  high fundamental frequency   and
  high damping.

These requirement sometimes might be very conservative. However, one has to admit that they always increase the margins of safety of equipments against low frequency transients, sine and random vibrations.

o For shock protection the needs are opposite. When in future high level shocks may become the design driver, then high resonant frequency and high damping will decrease the margins. Then an optimum has to be found which considers vibration and shock.

o Thus for minimum damped shock mount there exist problems with applicable requirements w.r.t. damping $\zeta = 1/2Q$, fundamental frequency f_o and w.r.t. vibration test responses. So the minimum damped shock mount has to be adapted to the applicable requirements of the specific program.

o For the use of viscoelastic material there exist general problems with the material characteristics, as
  scatter in mechanical properties
  creep and permanent set
  sensitivity against temperature
  sensitivity against different chemicals
  (for ARIANE 5 these problems are solved)

o The vibration velocity concept directly relates vibration induced stresses in a structural member to the vibration velocity of the member.

o It has been shown that shock mount with low damping gives the best protection for sensitive components against pyroshock environments.

Reference List:

Ref [1] Mil Std 810
Ref [2] ARIANE 5 "Specification of the Equipment Qualification and Acceptance Environment Test" Document No. A5-SG-1-40-ASAI
Ref [3] Harris and Crede, "Shock and Vibration Handbook"
Ref [4] Timoshenko, "Vibration Problems in Engineering"
Ref [5] Timoshenko, "Theorie of Elasticity"
Ref [6] "Pryro Shock Mount Investigations for ARIANE 5 - Components", E. Hornung, H. Maager, H. Öry, 43rd Congress of the IAF, 1992, Washinton DC

A BOUNDARY ELEMENT FORMULATION FOR DYNAMIC ANALYSIS OF VISCOELASTIC FLUID-DAMPERS

NICOS MAKRIS[1]
University of Notre Dame

G.F. DARGUSH and M.C. CONSTANTINOU
State University of New York at Buffalo

ABSTRACT

A general boundary element formulation is developed to predict the dynamic response of viscous dampers containing viscoelastic fluids with constitutive models containing generalized (fractional or complex order) derivatives.

The fundamental solution of the equation of motion of such fluids is first derived. This solution is used within the framework of integral equations to formulate a boundary element method for the dynamic analysis of generalized viscoelastic fluids. The method is applied for prediction of the response of a viscous damper containing a viscoelastic fluid in the form of silicon gel which is modeled by a fractional derivative Maxwell model. The predicted response is an excellent agreement with experimental results.

1. Presenting Author: Department of Civil Engineering and Geological Sciences, University of Notre Dame, Notre Dame, IN 46556-0767.

INTRODUCTION

Viscous dampers have found wide application in the shock and vibration isolation of industrial machines, equipment, pipework systems and buildings (Huffman 1985, GERB 1986, Makris 1991b,1992). Modeling the behavior of viscous dampers is an increasingly important problem because of their wide range of applicability. The difficulty in constructing realistic mathematical models stems from the strong viscoelastic behavior of the fluid used in such units. The mechanical properties of this viscoelastic fluid are strongly frequency dependent. This frequency dependency is responsible for the significant elastic stiffness that these dampers manifest as frequency increases and a ten-fold decrease of their damping coefficient within the range of 0 to 50 Hz.

Structural engineers are primarily interested in macroscopic models that describe the response of structural elements, including viscous dampers, at the force-displacement level. Although such models are practical and they can be directly used for analyzing the global response of structures, the parameters depend both on the mechanical characteristics of the material as well as on the geometry of the unit. This latter dependency results in calibration of the model parameters for each different damper size, and therefore individual testing of every single configuration is required.

Analytical procedures which can predict the mechanical properties of these devices and, thus, reduce or eliminate the need for comprehensive testing are useful. Particularly, they are useful in the design process of new configurations of such devices. One such attempt has been made by the authors (Makris 1993b) in modeling the behavior of a particular type of viscous damper. In this case, a macroscopic model for the behavior of the damper was proposed and its parameters were determined by analytical means. This involved a series of physically motivated assumptions, which simplified the governing equations to the extent that closed-form solutions were possible.

The procedure described in this paper is general as it can be applied to any geometry. It requires only knowledge of the constitutive law of the fluid. Within the limits of linear viscoelasticity the constitutive law is considered in its most general form, containing fractional or complex order differential operators (Makris 1991a,1993a). The basic fluid dynamics problem of solving the equations of motion and continuity together with the constitutive equations is resolved by application of the boundary element method. These equations are first transformed into the Laplace domain, and an infinite space fundamental solution is obtained. An integral representation is then developed to produce a formulation exclusively in terms of surface variables. The resulting integral equations are solved approximately by employing the method of collocation, along with numerical quadrature. The computed mechanical properties are found to be in excellent agreement with experimental results over a wide range of frequencies.

DESCRIPTION OF VISCOUS DAMPER

Figure 1 shows the geometry of a typical viscous damper. It consists of cylindrical container of radius r_2 which is filled with silicon gel, a high viscosity fluid. Within the container a piston is able to move along all directions. The outer surface of the piston features a smooth top portion and a lower portion containing ribs. The ribs serve the purpose of interlocking the fluid, thus preventing fluid slippage during motion of the piston. The bottom of the piston is hollow and contains a large number of inner pipes of small diameter (usually 15 to 20 mm diameter). This arrangement allows for penetration of the fluid into the pipes and ensures full contact and bond of the fluid with the bottom surface of the piston. The effectiveness of this arrangement is demonstrated in Figure 2 where recorded force displacement loops appear to be perfectly symmetric. This observation also indicates that gravity forces are insignificant in the response of the system. The analyzed damper had the following geometrical properties: $r_1 = 0.062$m, $r_2 = 0.13$m,
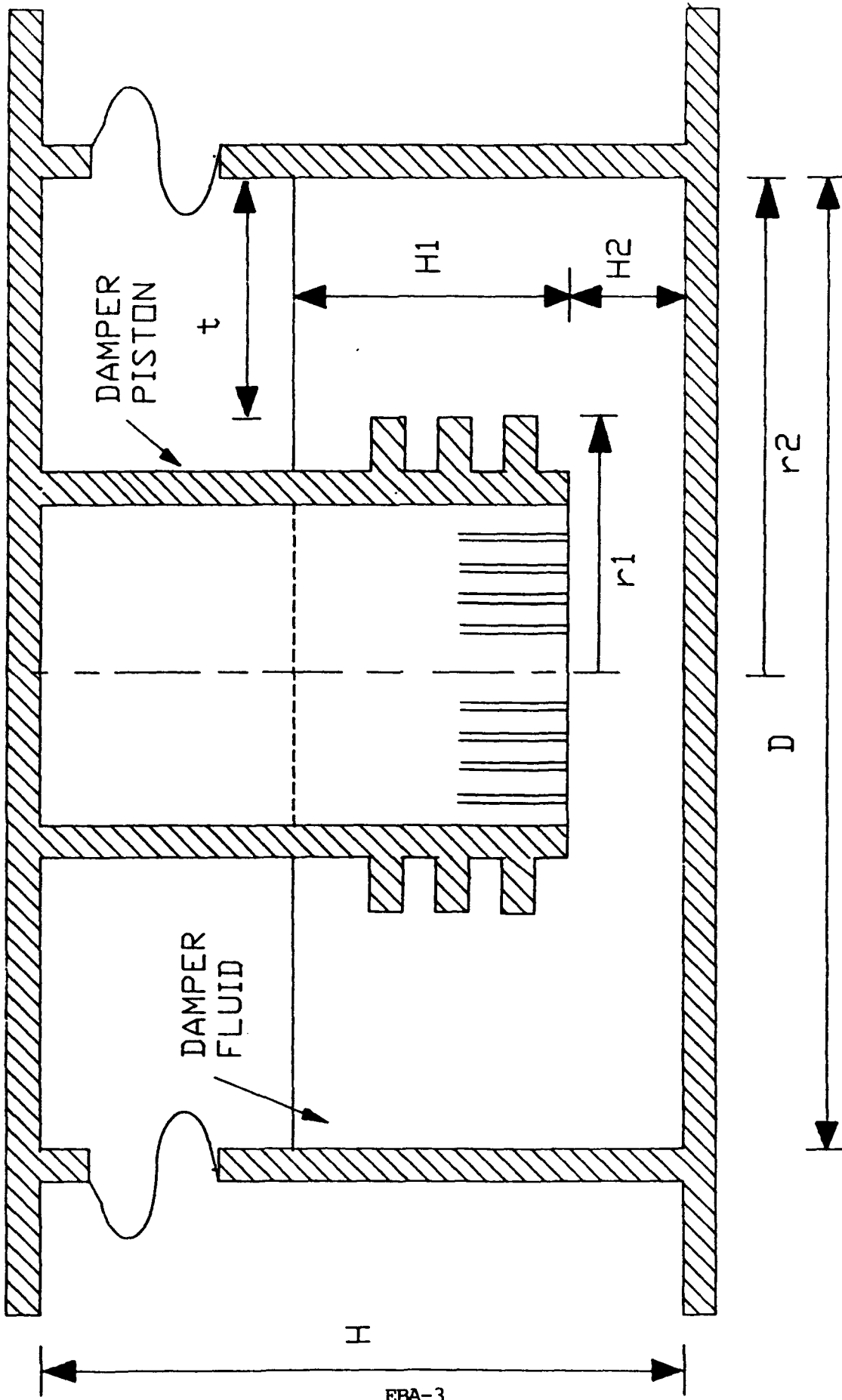
Figure 1: Geometry of Typical Viscous Damper.
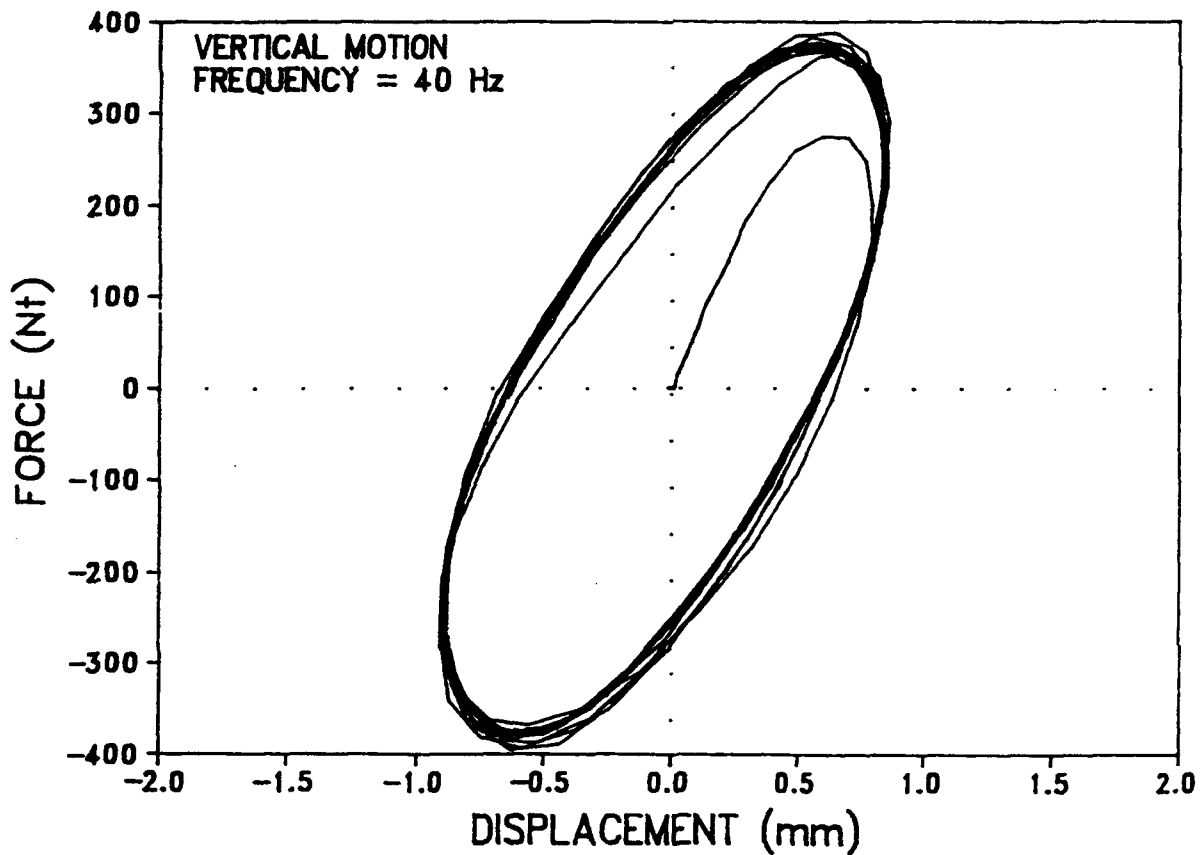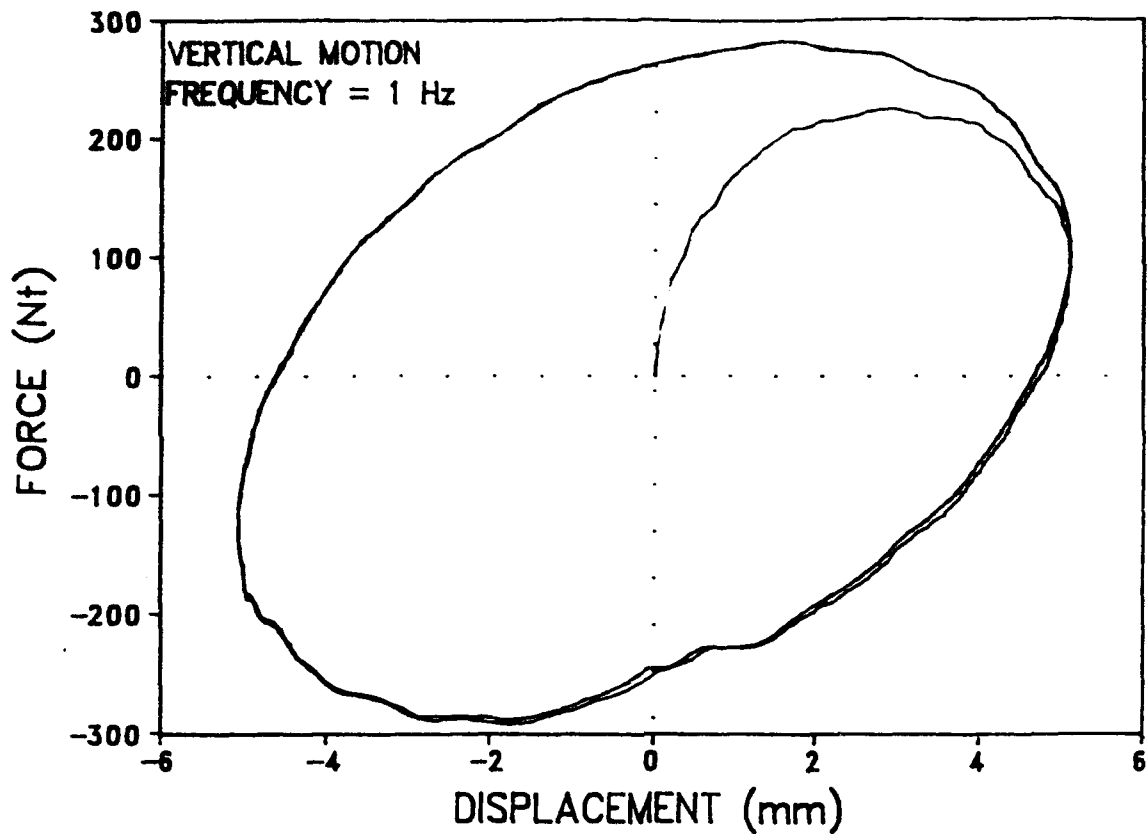
Figure 2: Recorded force displacement loops of damper for vertical harmonic motion at frequencies of 1 and 40 Hz.

$H_1 = 0.12\,\mathrm{m}$ and $H_2 = 0.06\,\mathrm{m}$.

The fluid used in the tested damper is a form of silicon gel with mass density of 930 kg/m^3, which is slightly less than that of water. The rate-dependent and frequency-dependent properties of the fluid were determined in tests employing the cone-and-plate method (Bird 1987).

First, the cone-and-plate method is steady shear flow was used to obtain measurements of the dynamic viscosity of the fluid. Figure 3 depicts measured values of viscosity as function of rate of strain for two samples of the fluid at temperature of 25°C. At low strain rates the viscosity has a value of about 2000 Pa-sec (20,000 poise). Beyond the value of 2 sec^{-1}, the viscosity reduces considerably.

Oscillatory shear flow experiments using the cone-and-plate method were used to measure the *storage and loss shear moduli* of the fluid. In this test, oscillatory shear flow is imposed and measurements of the induced shear stresses are made (Bird 1987). Figure 4 shows measures values of moduli $G_1(\omega)$ and $G_2(\omega)$ as function of frequency at 10% amplitude of shear strain.

Attempts were made to fit the properties of the fluid with conventional models of viscoelasticity (Makris 1991a). It was not possible to achieve satisfactory fit of the experimental data over the entire range of frequencies. However, a very good fit of the experimental data was achieved when the Maxwell model was used with its first order derivatives replaced by fractional order derivatives.

The *shear stress-strain* relationship in the fractional derivative Maxwell model is

$$\tau + \lambda D^r [\tau] = \mu D^q [\gamma] \tag{1}$$

in which τ and γ are the shear stress and strain, respectively, λ and μ are generalized material constants, and $D^r = d^r/dt^r$ is the fractional derivative operator of order r with respect to time. Representations of fractional derivatives in terms of the Riemann-Liouville integral, or the Grunwald infinite series may be found in Oldham and Spanier (1974). Herein we shall define the fractional derivative of order r of a time-dependent function $f(t)$ in terms of its Fourier Transform.

$$F[D^r f(t)] = F\left[\frac{d^r f(t)}{dt^r}\right] = (i\omega)^r F[f(t)] \tag{2}$$

For the calibration of the proposed model, analytic expressions of the storage and shear moduli were determined from equations (1) and (2):

$$G_1(\omega) = \frac{\mu\omega^q \cos\left(\frac{\pi q}{2}\right)\left[1 + \lambda\omega^r \cos\left(\frac{\pi r}{2}\right)\right] + \mu\lambda\omega^{q+r}\sin\left(\frac{\pi r}{2}\right)\sin\left(\frac{\pi q}{2}\right)}{d} \tag{3}$$

$$G_2(\omega) = \frac{\mu\omega^q \sin\left(\frac{\pi q}{2}\right)\left[1 + \lambda\omega^r \cos\left(\frac{\pi r}{2}\right)\right] - \mu\lambda\omega^{q+r}\sin\left(\frac{\pi r}{2}\right)\cos\left(\frac{\pi q}{2}\right)}{d} \tag{4}$$

$$d = 1 + \lambda^2\omega^2 + 2\lambda\omega^r \cos\left(\frac{\pi r}{2}\right) \tag{5}$$
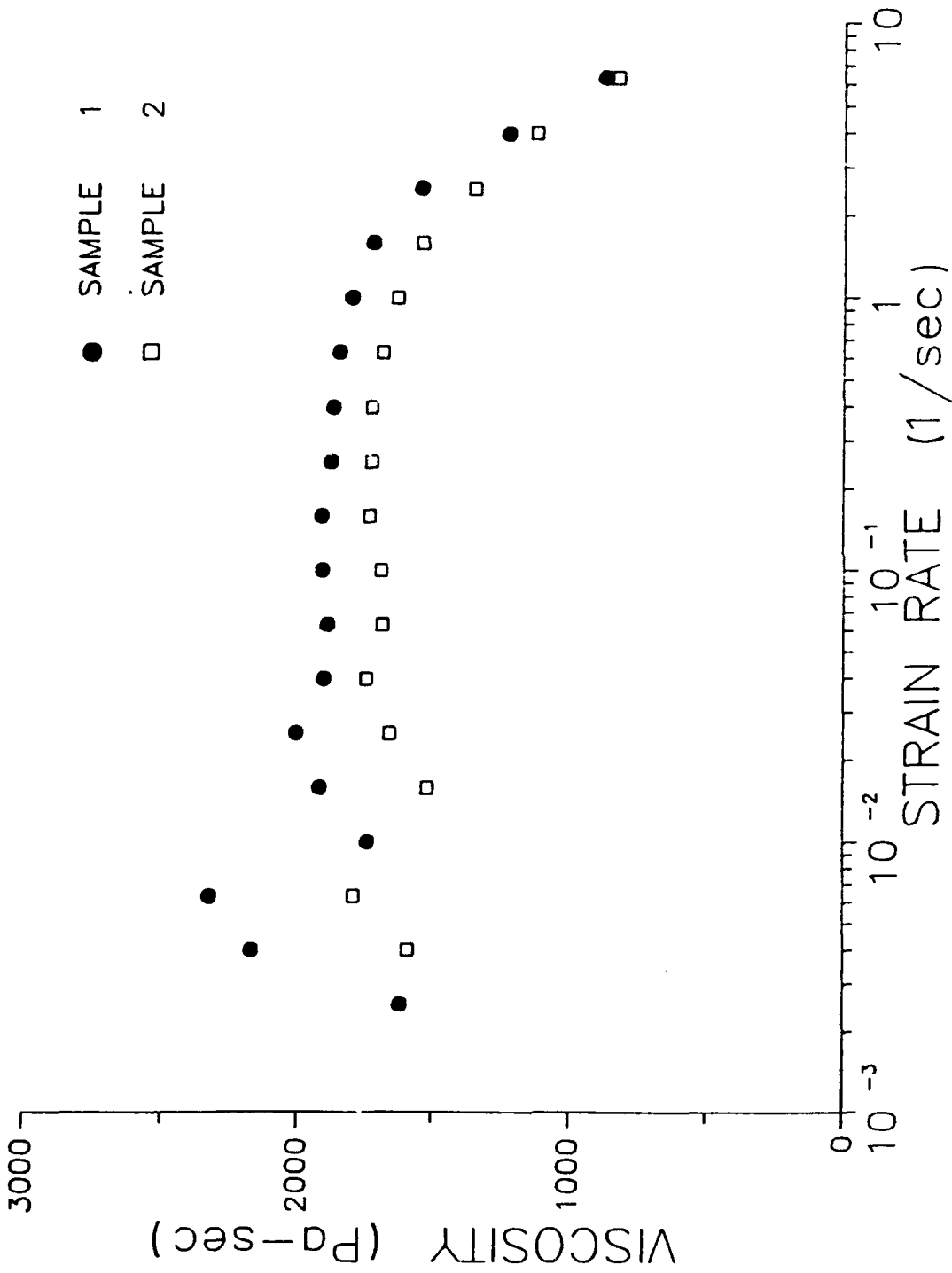
Figure 3: Viscosity of fluid used within the damper as function of strain rate.
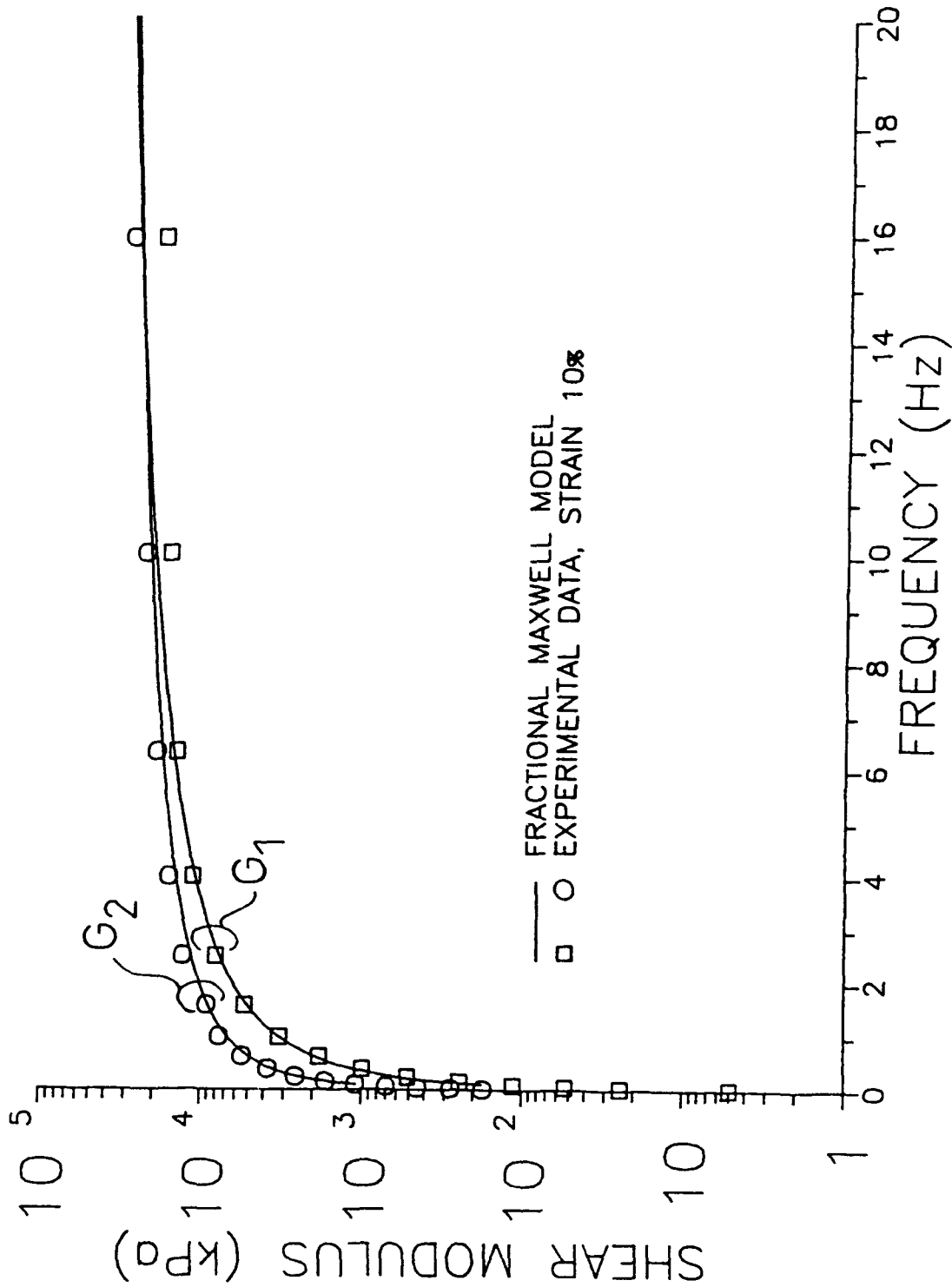
Figure 4: Measured frequency dependent properties of Viscoelastic fluid at 10% strain and comparison of predictions of fractional Maxwell Model.

The four parameters of the model for the silicon gel fluid were determined by the following procedure. Based on the fact that at vanishingly small strain-rates the behavior of the viscoelastic fluid reduces to that of a Newtonian fluid, parameter q was set equal to unity. Accordingly, parameter μ becomes the *zero-shear-rate viscosity* and should be equal to about 2000 Pa-sec (Figure 3). Parameters λ, r and μ were determined in a least square fit of the experimental data on the storage and loss modulus at 5% strain. The result was $\lambda = 0.3$ $(\text{sec})^{0.6}$, $r = 0.6$, $q = 1$ and $\mu = 1930$ Pa-sec. The value of μ is in very good agreement with the experimental results for the viscosity. The values of moduli $G_1(\omega)$ and $G_2(\omega)$ predicted by the calibrated equations (3,4) are plotted against the experimental results in Figure 4. The agreement is seen to be very good.

GOVERNING EQUATIONS AND FUNDAMENTAL SOLUTION

The equations of motion and continuity for an infinitesimal element on the fluid which is assumed incompressible are, in tensor notation,

$$\rho\left(\frac{\partial v_i}{\partial t} + v_j\frac{\partial v_i}{\partial x_j}\right) = \frac{\partial \tau_{ij}}{\partial x_j} - \frac{\partial p}{\partial x_i} \qquad (6)$$

$$\frac{\partial v_j}{\partial x_j} = 0 \qquad (7)$$

where ρ is the density, v_j is the velocity vector, τ_{ij} is the stress tensor due to the viscoelasticity of the material and p is the pressure. The generalized Maxwell model of (1) is now written in tensor form in terms of velocity gradients

$$\tau_{ij} + \lambda\frac{d^r}{dt^r}\tau_{ij} = \mu\left(\frac{\partial v_i}{\partial x_j} + \frac{\partial v_j}{\partial x_i}\right) \qquad (8)$$

Equations (6) to (8) form a set of noninteger differential equations that have to be integrated over the domain occupied by the fluid. Equation (8) describes the behavior of a fluid with memory and therefore in its present form is valid only for infinitesimal displacement gradients. Under this condition, the nonlinear term of the substantial derivative in equation (6) drops for all values of Reynolds number (Landau and Lifshitz 1987), resulting in a linear set of differential equations. Accordingly, this set can be transformed into the Laplace domain by noting the property of the Laplace transform of a fractional derivative

$$L\{D^r[f(t)]\} = s^r L\{f(t)\} - \sum_{k=0}^{n-1} s^k D^{r-1-k}[f(0)], \, n-1 < r < n \qquad (9)$$

where s is the Laplace parameter.

In the Laplace domain the equation of motion and constitutive equation become, respectively

$$\rho s v_i = \frac{\partial \tau_{ij}}{\partial x_j} - \frac{\partial p}{\partial x_i} \qquad (10)$$

$$\tau_{ij} = \mu^*(s)\left(\frac{\partial v_i}{\partial x_j} + \frac{\partial v_j}{\partial x_i}\right) \qquad (11)$$

with $\mu^*(s)$ representing the complex viscosity of the material

$$\mu^*(s) = \frac{G^*(s)}{s} \tag{12}$$

Valuable insight is gained by recalling that $s = \sigma + i\omega$ where ω is the independent variable in the frequency domain and σ is, in general, a real number, its value defining the region in the complex space where the Laplace integral converges. For functions that do not diverge at infinity, $\sigma = 0$ and the two sided Laplace transform can be regarded as a Fourier transform with $s = i\omega$. Substituting (11) into (10) one obtains the linearized Navier-Stokes equation in the Laplace domain with complex viscosity:

$$\mu^*(s)\left(\frac{\partial^2 v_i}{\partial x_j \partial x_j} + \frac{\partial^2 v_j}{\partial x_i \partial x_j}\right) - \frac{\partial p}{\partial x_i} - \rho s v_i = 0 \tag{13}$$

For incompressible material $\partial v_j / \partial x_j = 0$ and the second term in the parenthesis in equation (13) drops.

The linearity of the governing equations makes the boundary element method (Banerjee and Butterfield, 1988) an attractive approach for the solution of this problem. This approach, however, requires the infinite space fundamental solution of equation (13). This solution can be derived in a straightforward manner by employing exponential Fourier transforms (details of the procedure can be found in Shi 1992). For a unit force, $e_j(\xi, s)$, in the j-direction acting at a point ξ in an infinite three-dimensional space, the Laplace domain velocity in the i-direction at point x is

$$v_i(x, s) = G_{ij}(x - \xi, s)\, e_j(\xi, s) \tag{14}$$

where $G_{ij}(x - \xi, s)$ is the velocity kernel

$$G_{ij}(x - \xi, s) = -\delta_{ij}\frac{\partial^2 \Phi(r, s)}{\partial x_k \partial x_k} + \frac{\partial^2 \Phi(r, s)}{\partial x_i \partial x_j} \tag{15}$$

with

$$\Phi(r, s) = -\left(\frac{\pi \mu^*(s)}{\rho}\right)^{1/2}\frac{1}{rs}\left(1 - e^{-r(\rho s/\mu^*)^{1/2}}\right) \tag{16}$$

$$r^2 = y_i y_i \tag{17a}$$

$$y_i = x_i - \xi_i \tag{17b}$$

where δ_{ij} is the Kroneker delta.

The traction field is derived from the velocity field. The rate of infinitesimal strain tensor is

$$\dot{\varepsilon}_{ik} = \frac{1}{2}\left(\frac{\partial v_i}{\partial x_k} + \frac{\partial v_k}{\partial x_i}\right) = \frac{1}{2}\left(\frac{\partial G_{ij}(x - \xi, x)}{\partial x_k} + \frac{\partial G_{kj}(x - \xi, x)}{\partial x_i}\right)e_j(\xi, x) \tag{18}$$

The stresses due to the viscoelasticity of the fluid are

$$\tau_{ik} = 2\mu^* \varepsilon_{ik} \tag{19}$$

and the traction field, t_i, is given from the Cauchy formula

$$t_i = \tau_{ij} n_j - p n_i \tag{20}$$

where n_j is the outward normal to the surface upon which t_i reside.

The pressure, p, that develops due to the same unit force is

$$p(x-\xi, s) = G_{pj}(x-\xi, s) e_j(\xi, s) = \frac{1}{4\pi r^2} \frac{y_j}{r} e_j(\xi, s) \tag{21}$$

Substituting (19) and (21) into (20), the traction in the i-direction due to the unit force is

$$t_i(x, s) = F_{ij}(x-\xi, s) e_j(\xi, s) \tag{22}$$

where $F_{ij}(x-\xi, x)$ is the traction kernel.

Substituting (16) into (15) and carrying out the required differentiation, the explicit form of the velocity and traction kernels in the Laplace domain is derived:

$$G_{ij}(r, s) = -\frac{1}{4\pi\mu^*(s)} \frac{1}{r} \left\{ \delta_{ij} [g(\lambda r) - e^{-\lambda r}] + \frac{y_i y_j}{r^2} [-3g(\lambda r) + e^{-\lambda r}] \right\} \tag{23}$$

$$F_{ij}(r, s) = -\frac{1}{2\pi r^2} \left\{ \left(\frac{y_j}{r} n_i + \frac{y_i}{r} n_j + \delta_{ij} \frac{y_k n_k}{r} \right) [-3g(\lambda r) + e^{-\lambda r}] \right.$$

$$\left. + \frac{1}{2} \left(\delta_{ij} \frac{y_k}{r} n_k + \frac{y_i}{r} n_j \right) (1+\lambda r) e^{-\lambda r} - \frac{y_i y_j}{r^2} [-15g(\lambda r) + (6+\lambda r) e^{-\lambda r}] \frac{y_k}{r} n_k + \frac{1}{2} \frac{y_j}{r} n_i \right\} \tag{24}$$

where

$$g(\lambda r) = \frac{1}{\lambda^2 r^2} - \frac{e^{-\lambda r}}{\lambda^2 r^2} - \frac{e^{-\lambda r}}{\lambda r} \tag{25}$$

$$\lambda = \left(\frac{\rho s}{\mu(s)} \right)^{1/2} \tag{26}$$

In the limiting case of creeping motion or Stokes flow (slow motion where inertial effects are vanishingly small), the dynamic kernels of (23) and (24) must reduce to the incompressible static Kelvin kernels. Accordingly, by taking the limit as λr tends to zero one can easily obtain that

$$\lim_{\lambda r \to 0} G_{ij}(x-\xi, s) = G_{ij}(x-\xi) = \frac{1}{8\pi\mu} \frac{1}{r} \left(\delta_{ij} + \frac{y_i y_j}{r^2} \right) \tag{27}$$

$$\lim_{\lambda r \to 0} F_{ij}(x-\xi, s) = F_{ij}(x-\xi) = -\frac{1}{4\pi} \frac{1}{r^2} \frac{3 y_i y_j}{r^2} \frac{y_k n_k}{r} \tag{28}$$

which are indeed the Kelvin kernels.

For the special case where the viscosity is both real and independent of frequency, the fundamental solution (23) can be transformed analytically back to the time domain. The resulting velocity kernel for an instantaneous pulse force can be written as

$$G_{ij}(x-\xi,t-t') = -\delta_{ij}\frac{\delta^2\Phi(r,t-t')}{\partial x_k \partial x_k} + \frac{\partial^2\Phi(r,t-t')}{\partial x_i \partial x_j} \tag{29}$$

with

$$\Phi(r,t-t') = \frac{1}{r}\int_0^r t^{-1/2}exp\left(-\frac{\rho a^2}{4\mu^*(t-t')}\right)da \tag{30}$$

This is precisely the form given for a Newtonian fluid by Oseen (1927) in his classical monograph.

INTEGRAL FORMULATION

An integral representation for the fractional derivative viscoelastic fluid can be developed directly from the governing differential equations written in the Laplace domain (a similar, more detailed derivation for a Newtonian fluid in the time domain can be found in Dargush and Banerjee 1991a). The governing equation (13) must, of course, hold at all points of the fluid. Therefore, the left hand side of (13), when multiplied by an arbitrary function and integrated over the volume V, must remain equal to zero. That is

$$\int_V \left[A_{ik}\left(\mu^*\frac{\partial v_i}{\partial x_j \partial x_j} + \mu^*\frac{\partial v_j}{\partial x_i \partial x_j} - \frac{\partial p}{\partial x_i} - \rho s v_i\right) + A_{pk}\left(\frac{\partial v_i}{\partial x_j}\right)\right]dV = 0 \tag{31}$$

Next, integration-by-parts can be applied repeatedly to the applicable terms of (31) to transfer the spatial derivatives from v_i and p to A_{ik} and A_{pk}. The result of this operation can be written as

$$\int_S\left[A_{ik}\{\mu^*\left(\frac{\partial v_i}{\partial x_j} + \frac{\partial v_j}{\partial x_i}\right)n_j - pn_j\} - \{\mu^*\left(\frac{\partial A_{ik}}{\partial x_j} + \frac{\partial A_{jk}}{\partial x_i}\right)n_j + A_{pk}n_i\}v_i\right]dS$$

$$+ \int_V\left[\{\mu^*\left(\frac{\partial^2 A_{ik}}{\partial x_j \partial x_j} + \frac{\partial^2 A_{jk}}{\partial x_i \partial x_j}\right) - \frac{\partial A_{pk}}{\partial x_i} - \rho s A_{ik}\}v_i + \{\frac{\partial A_{ik}}{\partial x_i}\}p\right]dV = 0 \tag{32}$$

where S is the surface of the fluid.

An integral equation for the velocity v_i is obtained by letting A_{ik} and A_{pk} correspond to the fundamental solution defined in (23) and (21), respectively. Consequently, for a general location, ξ,

$$C_{ij}(\xi)v_i(\xi,s) = \int_S [G_{ij}(x-\xi,s)t_i(x,s) - F_{ij}(x-\xi,s)v_i(x,s)]dS(x) \tag{33}$$

where the tensor C_{ij} depends only upon the local geometry at ξ, and reduces to the Kroneker delta function δ_{ij} for ξ interior to the surface S. The right-hand-side of (33) involves only velocities and tractions on the surface of the three-dimensional viscoelastic fluid region. Volume integration

has been completely eliminated through the use of the fundamental solution of (13). Additionally, the pressure does not appear explicitly in (33). Due to the imposition of incompressibility, pressure can be determined at any location from the surface velocities and tractions.

Equation (33) represents a general three-dimensional formulation. In some applications, such as the analysis of vertical vibration of viscous dampers, we are primarily interested in purely axisymmetric motion. For this case, it is convenient to introduce a cylindrical coordinate system (r, θ, z) and to consider the surface S to be formed by a generator C, which lies in the $r - z$ plane. Transforming (33) to this system produces

$$\overline{C}_{\alpha\beta}(\xi)\,\overline{v}_{\alpha}(\xi, s) = \int_{C} [\,\overline{G}_{\alpha\beta}(x - \xi, s)\,\overline{t}_{\alpha}(x, s) - \overline{F}_{\alpha\beta}(x - \xi, s)\,\overline{v}_{\alpha}(x, s)\,]\,dC(x) \qquad (34)$$

where $\overline{G}_{\alpha\beta}$ and $\overline{F}_{\alpha\beta}$ are the two-dimensional axisymmetric kernels and the indices α and β show the r or z direction. The axisymmetric kernels $\overline{G}_{\alpha\beta}$ and $\overline{F}_{\alpha\beta}$ are formed from G_{ij} and F_{ij} via circumferential integration.

In order to utilize (34) for the solution of boundary value problems of engineering interest, such as the analysis of viscous dampers, discretization is required. In the present work, the boundary element method is selected for the numerical implementation. Three-noded conforming surface elements are used in conjunction with the method of collocation. Thus, a discretized version of (34) is written at each boundary node. The integration is completed in both the circumferential direction and along the generator C via numerical quadrature. Variable order Gaussian formuli and element subsegmentation are included to insure accuracy of the resulting coefficients. This is of vital importance in the analysis of incompressible media. Furthermore, a modification of the standard indirect method was introduced to obtain strongly similar diagonal block of $\overline{F}$. Additional information concerning various aspects of this numerical implementation can be found in Dargush and Banerjee (1991 a,b,c) and Ahmad and Banerjee (1988).

ANALYTICAL PREDICTION OF MECHANICAL PROPERTIES OF DAMPER

For harmonic input, the dynamic stiffness of the damper is the ratio of the amplitude of the imposed displacement, U_0, to the amplitude of the force, P_0, that develops on the piston in order to maintain the motion. For U_0 being real, P_0 is complex to accommodate the phase difference. Accordingly the calculated dynamic stiffness is

$$K_1 + iK_2 = \frac{P_0}{U_0} \qquad (35)$$

The analytical procedure presented in this paper was employed and the tractions on the surface of the moving piston were calculated. They were subsequently integrated over the piston surface to yield the force needed to maintain harmonic motion. Use of (35) gave the dynamic stiffness.

Dynamic tests of the viscous damper were conducted by imposing to the piston of the damper vertical harmonic motion of specific amplitude and frequency. From records of the force needed to maintain the imposed motion, the mechanical properties of the damper were determined under conditions of steady-state motion. The mechanical properties measured were the storage and loss stiffnesses (defined as the corresponding moduli in a stress-strain relationship). All tests were conducted at room temperature (about 25°C). For description of the test arrangement the reader is referred to Makris (1991a).
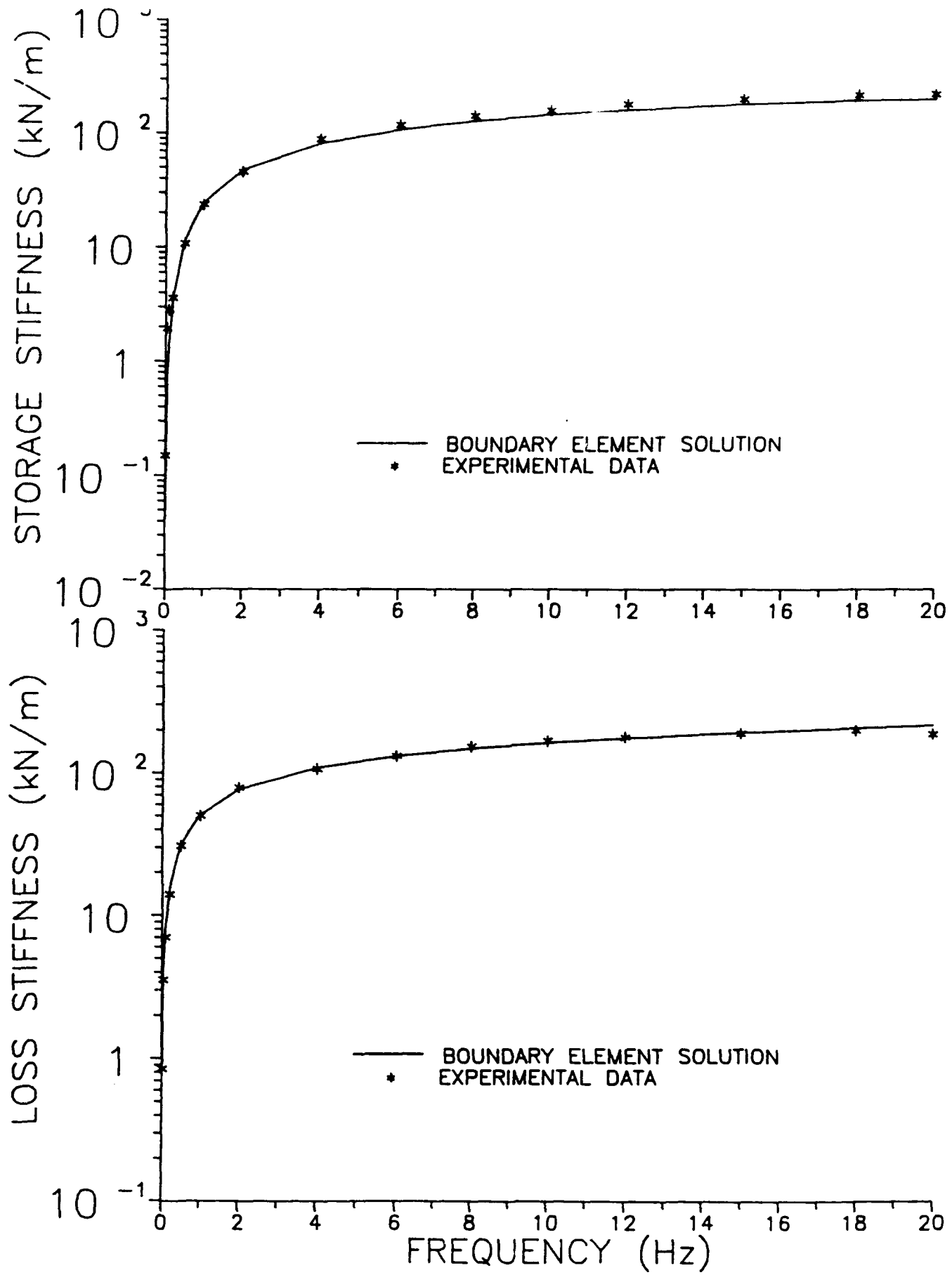
Figure 5: Comparison of Analytically Predicted and Measured Mechanical Properties of Viscous Damper.

Figure 5 compares the analytical results on the storage and loss stiffnesses (continuous line) against experimental data. The model predicts very well the mechanical properties of the device for the entire range of frequencies. The accuracy of the analytical solution demonstrates that it is possible to predict the mechanical properties of devices containing generalized viscoelastic fluids and, thus, reduce and even eliminate the need for comprehensive testing.

SUMMARY AND CONCLUSIONS

A general method for the analysis of linear viscoelastic fluids under dynamic loading has been presented. The material constitutive relation was not restricted to classical models of viscoelasticity. Rather, this constitutive relation was assumed to contain generalized derivatives, that is non-integer order derivatives.

The fundamental solution of the equation of motion of such fluids was derived. This solution was used within the framework of the boundary element method to formulate a method for analysis of generalized viscoelastic fluids. The accuracy of the numerical formulation was verified by comparison to an exact solution of a simple problem. Subsequently, the model was applied in the prediction of the mechanical properties of viscous dampers. The predicted mechanical properties were in excellent agreement with experimental results. It is concluded that the presented procedure may be used, among other problems, to the prediction of mechanical properties of viscous dampers and, thus, reduce or eliminate the need for comprehensive testing.

ACKNOWLEDGEMENTS

REFERENCES

Abramowitz, M. and Stegun, I.A. (1970). *Handbook of Mathematical Functions*, Dover Publications, New York, N.Y.

Ahmad, S. and Banerjee, P.K. (1988). "Multi-domain BEM for Two-dimensional Problems of Elastodynamics", *International Journal for Numerical Methods in Engineering*, 26, 891-911.

Bagley, R.L. and Torvik, P.J. (1983a). "Fractional Calculus - A Different Approach to the Analysis of Viscoelastically Damped Structures", *AIAA Journal*, 21(5), 742-748.

Bagley, R.L. and Torvik, P.J. (1983b). "A Theoretical Basis for the Applications of Fractional Calculus to Viscoelasticity", *Journal of Rheology*, 27(3), 201-210.

Banerjee, P.K. and Butterfield, R. (1981). *Boundary Element Methods in Engineering Science*, McGraw-Hill, London, UK.

Bird, B., Armstrong, R. and Hassager, O. (1987). *Dynamics of Polymeric Liquids*, J. Wiley, New York, NY.

Dargush, G.F. and Banerjee, P.K. (1991a). "A Time-dependent Incompressible Viscous BEM for Moderate Reynolds Numbers", *International Journal for Numerical Methods in Engineering*, 31(8), 1627-1648.

Dargush, G.F. and Banerjee, P.K. (1991b). "Steady Thermoviscous Flow by the Boundary Element Methods", *International Journal for Numerical Methods in Engineering*, 31(8), 1605-1626.

Dargush G.F. and Banerjee, P.K. (1991c). "A Boundary Element Method for Axisymetric Soil Consolidation", *International Journal of Solids and Structures*, 28, 897-915.

Gemant, A. (1938). *"On Fractional Differentials"*, Philosophical Magazine, 25, 540-549.

GERB Vibration Control. (1986). "Pipework Dampers", Technical Report, Westmont, Illinois.

Huffman, G. (1985). "Full Base Isolation for Earthquake Protection by Helical Springs and Viscodampers", *Nuclear Engineering and Design*, 84, 331-338.

Koeller, R.C. (1984). "Applications of Fractional Calculus to the Theory of Viscoelasticity", *Journal of Applied Mechanics*, 51(2), 299-307.

Landau, L.D. and Lifschitz, E.M. (1987). *Fluid Mechanics, Volume 6 of Course of Theoretical Physics*, Pergamon Press, Oxford, UK.

Makris, N. (1991a). "Theoretical and Experimental Investigation of Viscous Dampers in Applications of Seismic and Vibration Isolation", thesis presented to the State University of New York at Buffalo, Buffalo, NY, in partial fulfillment of the requirements for the degree of Doctor of Philosophy.

Makris, N. and Constantinou, M.C. (1991b). "Fractional Derivative Model for Viscous Dampers", *Journal Structural Engineering, ASCE*, 117(9), 2708-2724.

Makris, N. and Constantinou, M.C. (1992). "Spring-Viscous Damper System for Combined Seismic and Vibration Isolation", *Earthquake Engineering and Structural Dynamics*, 21, 649-664.

Makris, N. and Constantinou, M.C. (1993a). "Models of Viscoelasticity with Complex Order Derivatives", *Journal of Engineering Mechanics, ASCE*, in press.

Makris, N., Constantinou, M.C., and Dargush, G.F. (1993b). "Analytical Model of Viscous Dampers", *Journal of Structural Engineering, ASCE*, (submitted).

Oldham, K.B. and Spanier, J. (1974). *The Fractional Calculus*, Academic Press, San Diego, CA.

Oseen, C.W. (1927). *"Neuere Methoden und Ergebnisse in der Hydrodynamik"*, Akad. Verlagsgesellschaft, Leipzig.

Rabotnov, Y.N. (1980). *Elements of Hereditary Solid Mechanics*, Mir Publishers, Moscow, Russia.

Shi, Y. (1992). "Fundamental Solutons and Boundary Element Formulation for Convective Fluid Flow", thesis presented to the State University of New York at Buffalo, Buffalo, NY, in partial fulfillment of the requirements for the degree of Doctor of Philosophy.

Smith, W. and de Vries, H. (1970). "Rheological Models Containing Fractional Derivatives", *Rheological Acta*, 9, 525-534.

VIBRATION RESPONSES OF VISCOELASTICALLY DAMPED PLATES

Yi[1], Sung, Ahmad[2], M. Fouad, Hilton[3], Harry H. and Pollock[4], Gerry D.

Abstract

Dynamic transient responses of plates with free damping layers have been studied in order to evaluate free layer damping treatment performances. The forcing frequencies and temperature effects of free-layer viscoelastic damping treatment on plates are investigated. The damping layer thickness effects are also explored.

Introduction

Vibration and noise control is very important in automobiles, flight vehicle structures and electronic devices, and viscoelastic materials have been and are being used as shock absorbers, vibration and flutter dampers, acoustical barrier, etc. Viscoelastic damping reduces structural fatigue and vibration amplitudes at elastic resonant frequencies and attenuates structure-borne noise.

Damping refers to any form of energy dissipation in any non-conservative system. When the deformation energy is lost as heat through viscous action then this mechanism is known as viscoelastic damping, which is solely due to material properties. Structural damping on the other hand refers to enegy dissipation in joints, fastener, and interfaces. Structural damping is dry solid friction and its constitutive relations are independent of frequency and displacements, velocities and accelerations. In an elastic material, Hook's law is maintained but the elastic moduli are replaced by complex ones. Viscoelastic materials, however, obey differential or integral stresses-strain relationships, which are associated with stresses, strains and their time derivatives. Lazan (1968) has called structural damping rate-independent

---

[1]Post-Doctoral Research Associate at NCSA
[2]Research Scientist at NCSA
[3]Professor Emeritus, AAE Department
[4]Graduate Research Assistant at NCSA

damping since material properties such as Young's modulus and specific damping coefficients are all independent of strain and stress time derivatives, frequency and temperature, while viscoelastic damping corresponds to rate-dependent damping where constitutive relations are functions of those variables.
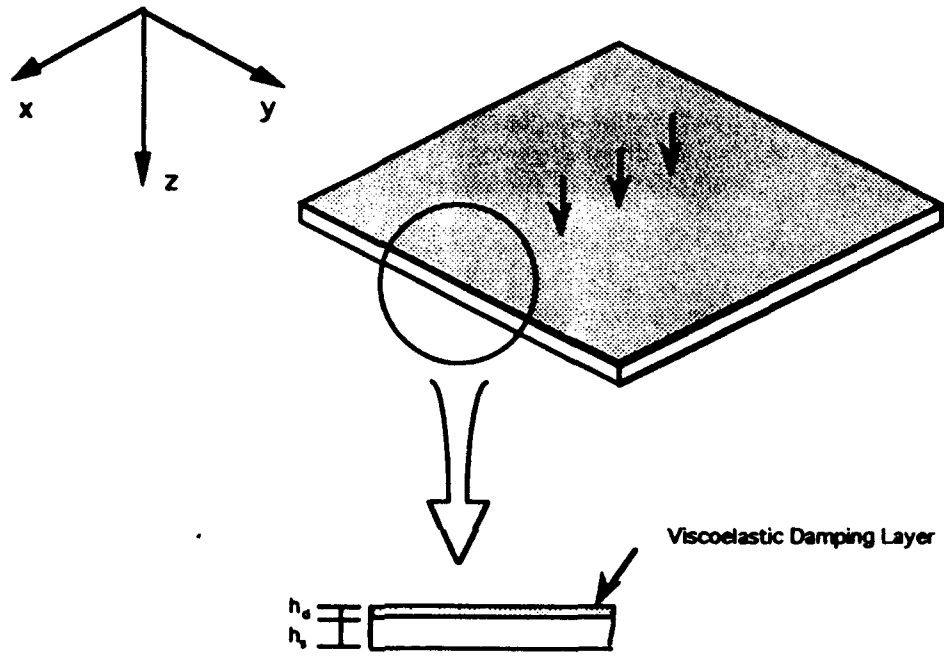
Fig. 1 The plate with free layer damping treatment.

Since damping plays an important role in the proper design of the vibration systems, many studies have been conducted to develop proper viscoelastic damping technologies. Viscoelastic and structural damping have been analyzed by Hilton (1991). In Refs. 3 and 4, expressions for stored and dissipated energies in anisotropic viscoelastic bodies are formulated using generalized Maxwell models, and the relationships between shapes of master relaxation modulus curves and dissipation energy and the latter's influence on passive structural motion control have been investigated. Recently, Yi (1992) also developed more computationally efficient and accurate algorithms for analyzing transient responses of viscoelastically damped composite structures in the real time domain than the previous studies (Bagley and Torvik, 1983; Holzlöhner, 1974; Golla and Hughes, 1985; Johnson and Kienholz,

1982; Yamada *et al.*, 1970; Xie *et al.*, 1989). Recursion formulas also are obtained in order to reduce computer storage, and only the previous time solution is required to compute the next time solution.

Free layer damping treatment is the simplest procedure for introducing light weight damping into structures (see Fig.1). In this paper, we consider the problem of forced oscillations of a plate with viscoelastic damping treatment. Our goal is to evaluate the herditary integral governing vibrations. The vibration responses of plates with free damping layers are calculated using the finite element method. The loading frequencies and temperature effects of free-layer damping treatment on plates are studied and the damping layer thickness effects on the damping performances are also evaluated and discussed.

Viscoelastic Damping Mechanics

The master relaxation modulus curves are the characteristic shapes defining viscoelastic material behavior. Such curves for viscoelastic relaxation moduli can be determined by using the time temperature superposition principle or vibrating beam tests (Hilton, 1964). One way to characterize the material properties of viscoelastic materials is to measure its moduli as functions of temperature and moisture contents, since polymer moduli are functions of time as well as being highly sensitive to temperature and moisture. By using time-temperature superposition, moduli master curves and shift factors can be generated. The superposition principle states that the viscoelastic modulus at one temperature can be related to another one at a different temperature by a change in time scale only. For thermorheologically simple anisotropic materials, the relaxation moduli can be represented in the form:

$$C_{ijkl}[T, M, t] = C_{ijkl}[T_o, M_o, \zeta_{ijkl}(\mathbf{x}, t)] \tag{1}$$

where the subscript o denotes reference conditions and ζ_{ijkl} are reduced times, which are related to the shift functions, a_{ijkl}, in the following manner

$$\zeta_{ijkl}(\mathbf{x}, t) = \int_0^t a_{ijkl}\left[T(\mathbf{x}, s), M(\mathbf{x}, s)\right] ds \tag{2}$$

The C_{ijkl} moduli are now representable by single master relaxation curves.

Experimental data obtained in the time plane at temperatures lower than the reference temperature are shifted to the left of the master curves, while those

obtained at temperatures higher than the reference temperature are shifted to the right. Materials which have such horizontal temperature shift behaviors are referred to as a thermorheologically simple materials and otherwise as thermorheologically complex materials. Shift factors can be determined directly from experimental relaxation curves. Williams, Landel, and Ferry (1955) observed that many polymers exhibit similar temperature dependent behaviors and proposed an empirical shift function relationship

$$\log \ a_{ijkl} = \frac{-\xi_{ijkl}^1 (T - T_o)}{\xi_{ijkl}^2 + (T - T_o)} \quad \text{(no summation)} \tag{3}$$

where a_{ijkl} are shift functions, ξ_{ijkl}^1 and ξ_{ijkl}^2 are universal parameters which vary from polymer to polymer, T is the temperature, and T_o is the reference temperature of the master curves.

Damping material systems may be expressed mathematically in terms of rheological constitutive equations and the general rheological representation for defining the stress-strain relationships for polymeric and rubberlike materials is called viscoelasticity. The constitutive equations for such materials depends not only on the strain and stress but also on the strain and stress rates, and their higer-order derivatives with respect to time, and can consequently stated as

$$\sigma_{ij}(\mathbf{x},t) = \int_{-\infty}^{t} C_{ijkl}[T_o, M_o, \underline{\zeta_{ijkl}}(\mathbf{x},t) - \underline{\zeta_{ijkl}'}(\mathbf{x},\tau)] \frac{\partial}{\partial \tau} \epsilon_{kl}(\mathbf{x},\tau) \ d\tau \tag{4}$$

The complex modulus properties of viscoelastic damping materials are evaluated by the vibrating beam test methods. The dynamic response of the beam with or without the damping layer is measured for several modes of vibration as functions of frequency and temperature. By using vibrating reeds, Bland and Lee (1955) determined complex moduli of isotropic linear viscoelastic materials. Jones (1981) studied complex moduli of damping materials at reduced temperatures as well as reduced frequency domains. Rogers (1981) proposed that the damping characteristics of viscoelastic materials can be analyzed using fractional derivative representations.

The complex moduli are obtained by taking Fourier transforms of the viscoelastic stress-strain relationships in the time domain and master curves for complex moduli are similarly obtained. The stress-strain relationships transformed into the frequency domain become

$$\widetilde{\sigma}_{ij}(\mathbf{x}, \hat{\omega}) = \widetilde{C}^*_{ijkl}(\mathbf{x}, \hat{\omega}) \cdot \widetilde{\epsilon}_{kl}(\mathbf{x}, \hat{\omega}) \tag{5}$$

where $\sim$ denotes Fourier transforms and the complex moduli, $\widetilde{C}^*_{ijkl}(\mathbf{x}, \hat{\omega})$, are related to the relaxation moduli by

$$\widetilde{C}^*_{ijkl}(\mathbf{x}, \hat{\omega}) = \frac{\hat{i}\hat{\omega}}{2\pi} \int_{-\infty}^{\infty} C_{ijkl}(\mathbf{x}, \tau) \cdot e^{\hat{i}\hat{\omega}} d\tau \tag{6}$$

where $\hat{i} = \sqrt{-1}$.

The complex moduli in Eqs. (6) can be decomposed into

$$\widetilde{C}^*_{ijkl}(\mathbf{x}, \hat{\omega}) = \widetilde{C}'_{ijkl}(\mathbf{x}, \hat{\omega}) + \hat{i}\widetilde{C}''_{ijkl}(\mathbf{x}, \hat{\omega}) \tag{7}$$

where the real functions $\widetilde{C}'_{ijkl}(\mathbf{x}, \hat{\omega})$ and $\widetilde{C}''_{ijkl}(\mathbf{x}, \hat{\omega})$ are the real and imaginary parts of complex moduli which are refered to as storage and loss moduli.

Finite Element Equation of Motion

The finite element procedures are formulated based on the variational principles. For the dynamic viscoelastic boundary value problem, the finite element equilibrium equation of motion can be expressed as

$$M_{mn}(\mathbf{x}) \ddot{U}_n(t) + \int_{\tau=-\infty}^{\tau=t} K_{mn}[\zeta_r(\mathbf{x}, t) - \zeta'_r(\mathbf{x}, \tau)] \cdot \frac{\partial U_n(\tau)}{\partial \tau} d\tau = F_m(t) \tag{8}$$

where $m, n = 1, 2, \ldots, N$, N is the number of nodal degrees of freedom, M_{mn} is global mass matix, K_{mn} is stiffness matirx. and F_m represents the nodal force vector due to specified surface tractions.

Since the above equibrium equations are hereditary integral equation, all the previous solutions must be stored in order to evaluate displacements at any specific time. In the previous study, a numerical algorithm is developed for the solution of Eqs.(8) using the Newmark average acceleration method and Prony series representations for relaxation moduli. Recursion formulas also have been obtained in order to reduce computer storage and only two previous time solutions are required to compute the next time solution. Additional detail for the transient viscoelastic finite element formulation can be found in Ref. 4.

Results and Discussion

Consider simply supported plates which are excited by a unit step load. Mindlin-Reissner type theories which account for first order transverse shear deformations are employed in the present study. Twenty five four-node plate elements with three degrees of freedom for each node are used. The material behavior of the plate is linearly elastic with properties for the isotropic plate $E_s = 1 \times 10^7$ psi, $\nu_s = 0.3$ and $\gamma_s = 0.33$ lb/in^3. The plate dimensions are 20 in (lenght) $\times$ 20 in (width) and the thickness is 0.5 in. Isothermal conditions are assumed.
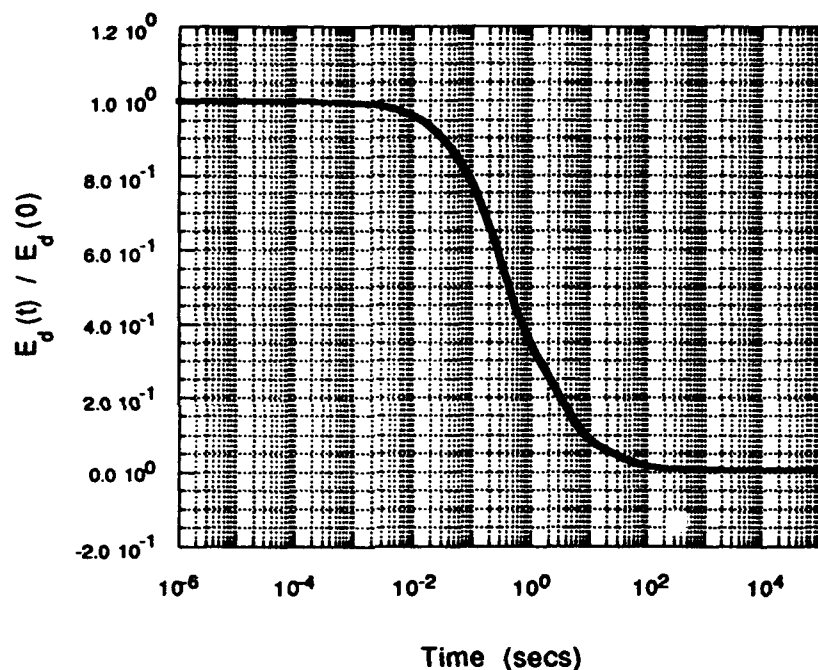
Fig. 2 Time dependent Young's modulus for viscoelastic damping material.

As shown in Fig. 1, the viscoelastic damping layer is attached on top of the plate. The Young's modulus of the viscoelastic damping material is time-dependent. Time variations of the modulus are plotted in Fig. 2. The elastic Young's modulus for the damping material is 2×10^6 psi, Poisson ratio $\nu_d = 0.3$ and material density $\gamma_d = 0.25$ lb/in^3. Time step size is taken as $\Delta t = 0.001$ secs and shift factor is 10 at 40 °C.

First, the effects of free damping layer thickness are studied. Plates with

various damping layer thicknesses (h_d) are considered and their transverse responses of square plates are calculated. At the center of the plate, dynamic transverse deflections of the damped plates with $h_d = 1$, 3 and 5 are plotted in Figs. 3, 4, and 5 respectively. The results show that the vibration amplitudes significantly decrease with increasing damping layer thickness. The vibration is damped out after 1.1 secs for $h_d = .3$ and 0.6 secs for $h_d = 0.5$ respectively. Increasing the damping layer thickness also results in decreasing vibration amplitudes at the initial time and frequencies. For thicker damping layers, the small creep deformations occur because of the degradation of material properties of damping layers. For five different damping layer thicknesses, the vibration responses from t=0 to 0.5 secs are replotted in Fig. 6.

Another numerical example is undertaken in order to evaluate the effects of temperature on the damping performance of viscoelastic free damping treatment. The plate is subjected to a uniformly distributed unit step load at lower temperature (shift factor =1, temperature=18 °C). It can be readily seen from Figs. 7 and 8 that changes in temperature affect both amplitude and frequency responses. This is due to the smaller damping material capabilities with decreasing temperatures. Temperature induced material degradation results in smaller amplitudes and vibration frequencies. As shown in Fig. 7, after 2 secs, the vibration amplitudes at 40 °C are reduced by 95 %, while those at 18 °C decrease only by 56.7 %.

Young's modulus ratio (E_s/E_d) effects on the damping ability are also investigated. Three models ($E_s/E_d = 5$, 10, 100) are used. The results indicate that the damping capacity decreases as the Young's modulus ratio increases as seen in Fig. 9. At $E_s/E_d = 100$, the vibration amplitudes are reduced only by 9 %. However, for larger moduli, the vibration frequency increases since the stiffness of the structure increases.

Next, the time dependent responses of viscoelastically damped plates subjected to uniformly distributed sinusoidal loading, $P(t) = P_o \sin(\omega t)$, are studied. The Young's modulus ratio is 0.2 and a time step $\Delta t = 5 \times 10^{-4}$ secs is used. Two different forcing frequncies $\omega = 10^2$, and 10^3 rad/sec are employed in this study. The results are illustrated in Figs. 10 and 11 which show that vibration amplitudes are significantly influenced by the forcing frequency. Vibration amplitudes at $\omega = 10^3$ rad/sec are much smaller than those at $\omega = 10^2$.
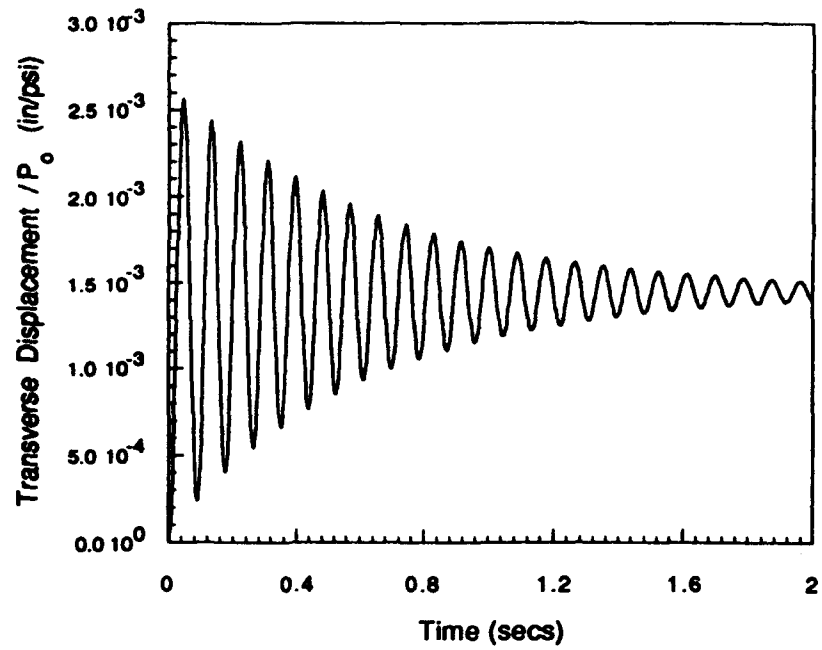
Fig. 3 Vibration response of plate with damping layer ($E_d/E_s = 5$, $h_d = 0.1$, $a_T = 10$).
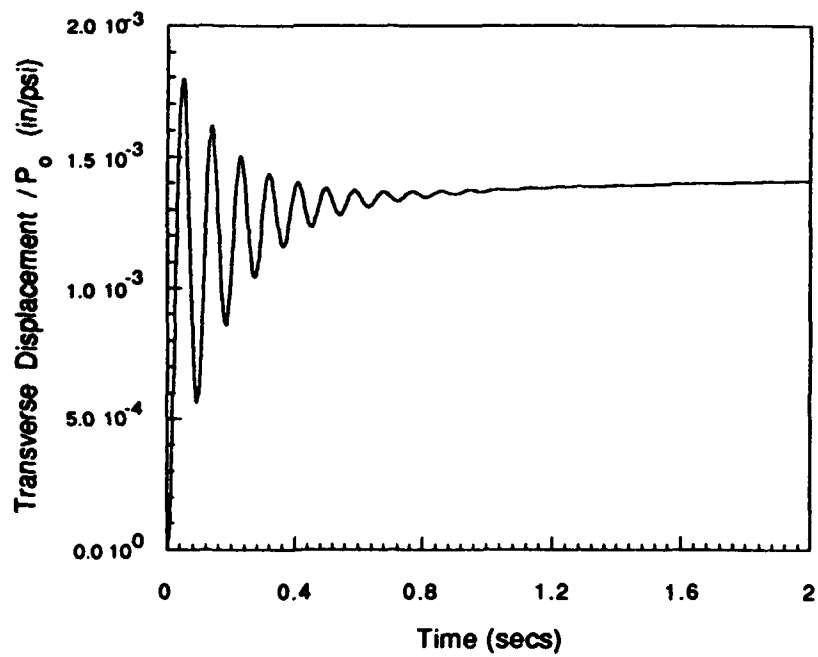
Fig. 4 Vibration response of plate with damping layer ($E_d/E_s = 5$, $h_d = 0.3$, $a_T = 10$).
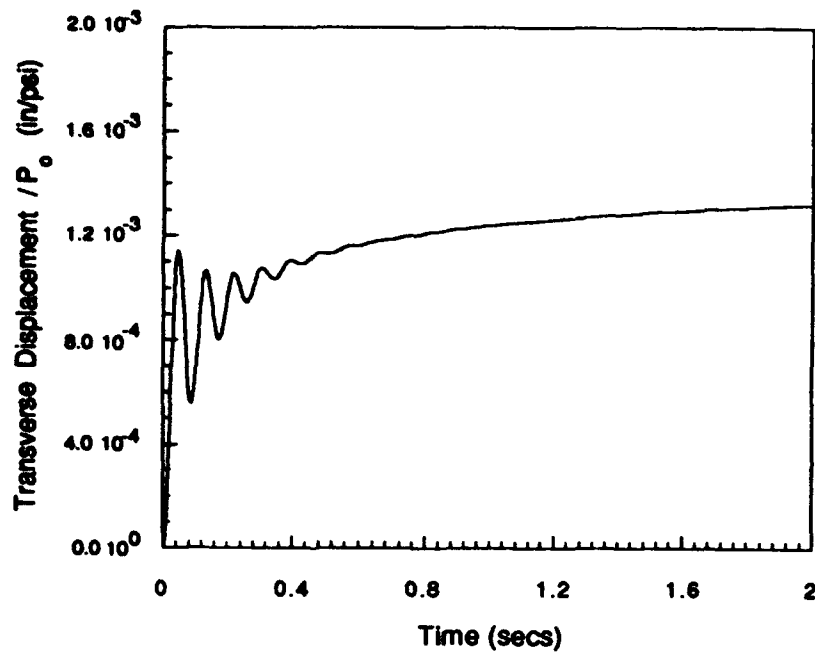
Fig. 5 Vibration response of plate with damping layer ($E_d/E_s = 5$, $h_d = 0.5$, $a_T = 10$).
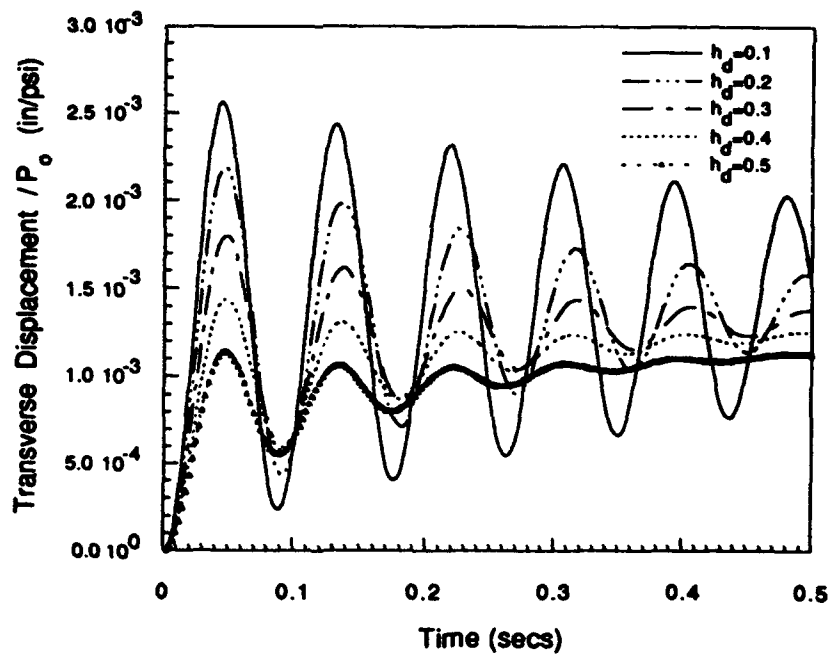
Fig. 6 Vibration response of plate with damping layer ($E_d/E_s = 5$, $a_T = 10$).
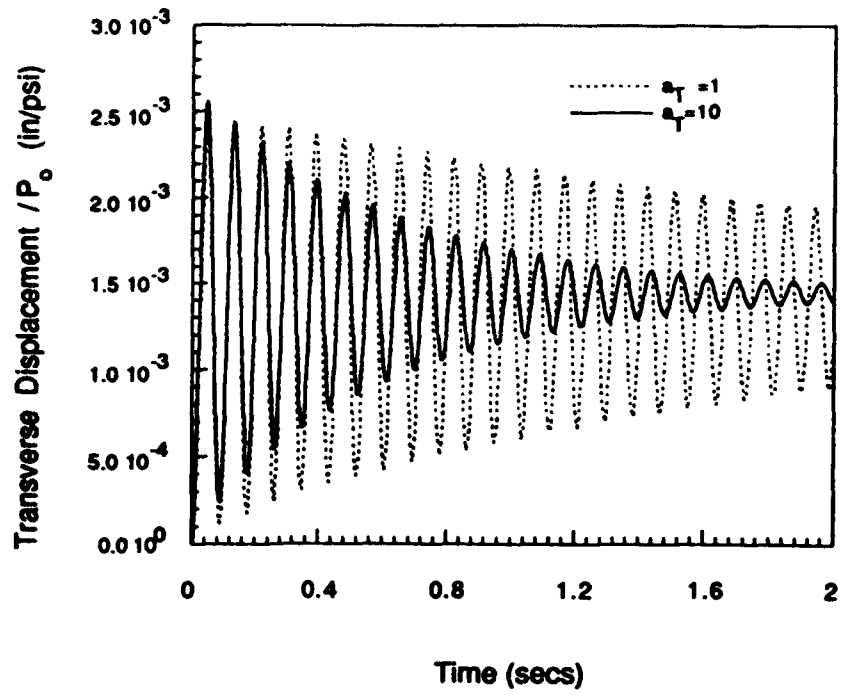
Fig. 7 Vibration response of plate with damping layer ($E_d/E_s = 5$, $h_d = 0.1$).
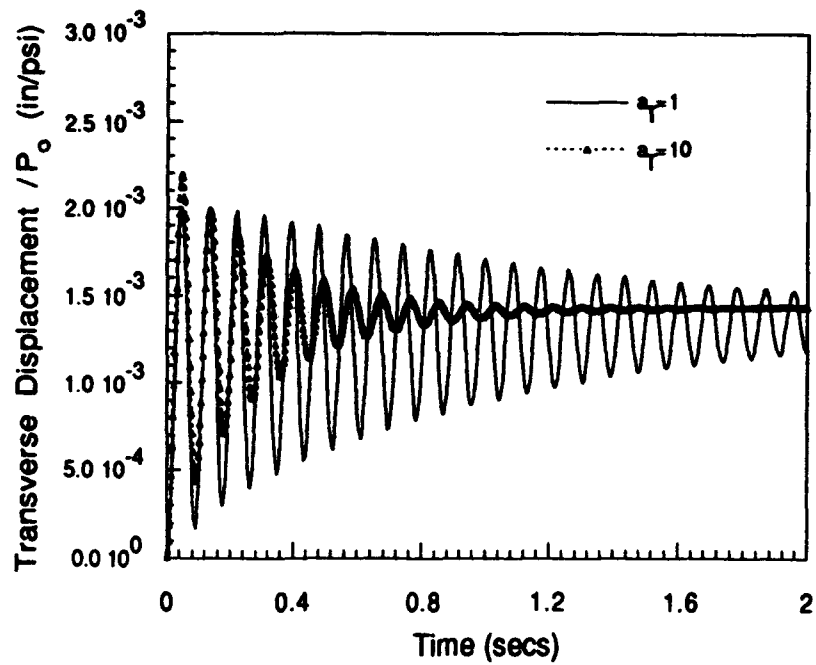
Fig. 8 Vibration response of plate withdamping layer ($E_d/E_s = 5$, $h_d = 0.2$).
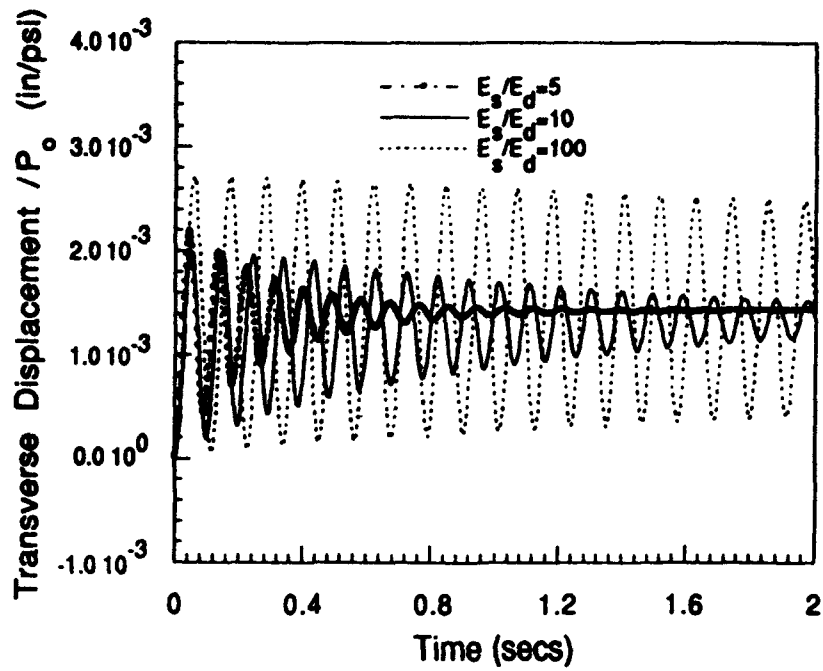
Fig. 9 Vibration response of plate with damping layer ($h_d = 0.2$, $a_T = 10$).
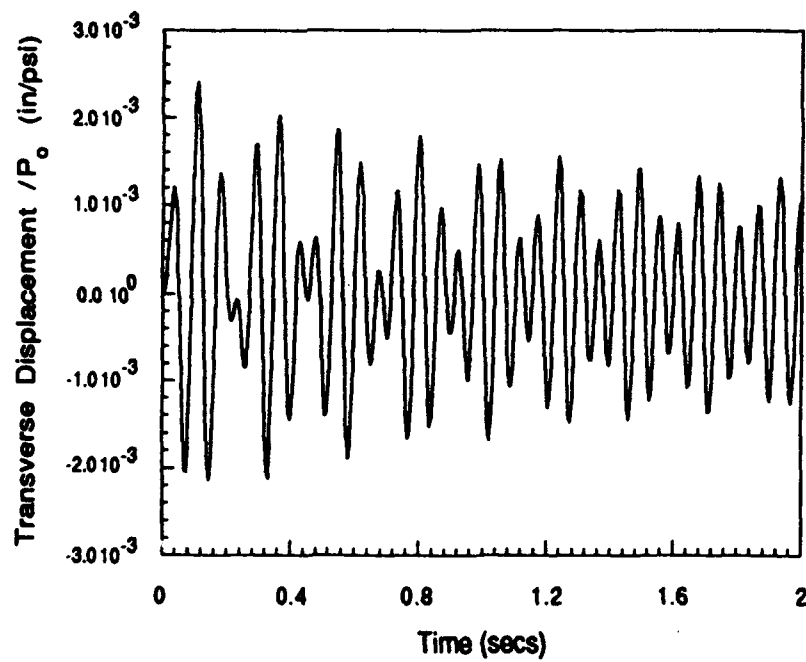
Fig. 10 Vibration response of plate with damping layer ($h_d = .2$, $a_T = 10$, $\omega = 10^2$).
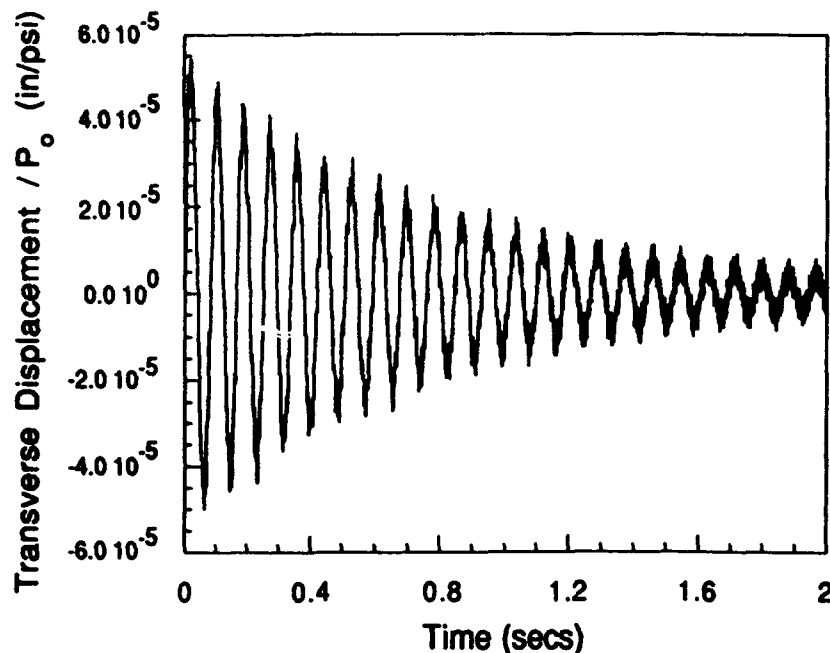
Fig. 11 Vibration response of plate with damping layer ($h_d = 0.2$, $a_T = 10$, $\omega = 10^3$).

Conclusion

The vibration amplitudes are significantly affected by the viscoelastic damping layer thickness, temperature, forcing frequency, and the Young's modulus ratio. The vibration amplitudes remarkablely decrease with increasing damping layer thickness. Since damping material abilities increase with increasing temperatures, increasing temperatures result in decreased vibration amplitudes and frequencies. The damping capacity decreases with smaller damping material Young's moduli. Proper dynamic viscoelastic analysis is important in the design of the viscoelastically damped structures because of the altered nature of vibration amplitudes and frequencies.

References

1. Lazan, B. J. (1968). *Damping of Materials and Members in Structural Mechanics*, Pergamon Press, Oxford.

2. Hilton, H. H. (1991). Viscoelastic and Structural Damping Analysis, *Proceedings of Damping 91 Conference*, WL-TR-91-3078, Wright-Patterson AF Base, Ohio, Vol. III, pp. ICB-1 to ICB-15. *AIAA J.* in press

3. Hilton, H. H. and Yi, Sung (1992). Analytic Formulation of Optimum Material Properties for Viscoelastic Damping, *Smart Materials and Structures*, 1, 113-122.

4. Yi, S. (1992). Finite Element Analysis of Viscoelastic Composite Structures and Analytical Determination of Optimum Viscoelastic Materials, *Ph.D dissertation*, AAE Department, University of Illinois at Urbana-Champaign.

5. Bagley, R. L. and Torvik, P. J. (1983). Fractional Calculus-A different Approach to the Finite Element Analysis of Viscoelastically Damped Structures, *AIAA Journal*, 21, No. 5. 741-748.

6. Golla, D. F. and Hughes, P. C. (1985). Dynamics of Viscoelastic Structures - a Time Domain, Finite Element Formulation," *Journal of Applied Mechanics*, 52, 897-906.

7. Johnson, C. D. and Kienholz, D. A. (1982). Finite Element Prediction of Damping in Structures with Constrained Viscoelastically Damped Structures, *AIAA Journal* 20, 1284-1290.

8. Holzlöhner, U. (1974). A Finite Element Analysis for Time-Dependent Problems, *Int. J. for Num. Meth. in Engr.*, Vol. 8, pp. 55-69.

9. Xie, K., Roystre, L. H. and Ciskowski, R. D. (1989). A Boundary Element Method Formulation for Fractional Operator Modeled Viscoelastodynamic Structures, *Advances in Boundary Elements: Vol.9 Stress Analysis*, Computational Mechanics Publications, Southampton, pp. 55-64.

10. Yamada, Y., Takabatake, H. and Sato, T. (1974). Effect of Time-Dependent Material Properties on Dynamic Response, *Int. J. for Num. Meth. in Engr.*, 8, pp. 403-414.

11. Nashif, A. D., Jones, D. I. G. and Henderson, J. P. (1985). *Vibration Damping*, Wiley-Interscience Publication, New York.

12. Bland, D. R. and Lee, E. H. (1955). Calculation of the Complex Modulus of Linear Viscoelastic Materials from Vibrating Reed Measurements, *Journal of Applied Physics*, Vol. 26, No.12, pp. 1497-1503.

13. Jones D.I.G. (1981). A Reduced-Temperature Nomogram for Characterization of Damping Material Behavior, *The Shock and Vibration Bulletin*, Vol. 51, Part 1, pp. 13-22.

14. Rogers, L. (1981). Temperature Shift Consideration for Damping Materials, *The Shock and Vibration Bulletin*, Vol. 48, Part 2, pp. 55-69.

DAMPING CAPACITY OF SCARF-JOINTS[1]

Mohan D. Rao[2] and Haiming Zhou[3]

Mechanical Engineering-Engineering Mechanics Department

Michigan Technological University

Houghton, MI 49931

ABSTRACT

An analytical model to study the bending vibration of a scarf-jointed beam is formulated in this paper. This model development is based on the concepts of equivalent bending stiffness of the joint, energy method and Hamilton's principle. The adhesive material is modeled using the complex modulus approach and governing equations of motion for a general case of forced motion under arbitrary boundary conditions are derived. The solution for free vibration for the case of a simply supported beam is obtained using finite-difference method. A parametric study has been conducted to observe the effects of various design parameters on the system resonance frequencies and loss factors. It has been found that an increase in the adhesive thickness leads to an increase in the system damping at the same time decreasing the system dynamic stiffness. The joint angle is a key parameter that can be controlled to obtain maximum loss in the system. For a particular joint configuration, there exists an optimum joint angle which maximizes the system damping. Design plots presented in this paper in terms of non-dimensional parameters should be of considerable value in the design of scarf joints.

Adhesive Material

(a) Single Lap Joint

(b) Double-Strap Joint

(c) Stepped-Lap Joint

(d) Scarf Joint

Configurations of Common Adhesively Bonded Structural Joints

Why Scarf Joints?

Scarf and stepped lap configurations are the more efficient joints chosen for joining thick members and are ideal for repair purposes.

Scarf joint is sometimes preferred over other types because of its aerodynamic smoothness, and ability to join adherends of two different materials, such as joining titanium to a composite.

Objectives of This Research

(1) Formulate an Analytical Model for Predicting the Modal Dynamic Parameters of Scarf Joints under Flexural Vibration

(2) Study the Effects of Structural parameters, and Material Properties on the system loss factors and resonance frequencies

Approach

The governing equations of motion of the system, for a general case of forced vibration under transverse distribution load, are first derived using the energy method and Hamilton's principle.

The adhesive material is modeled using the complex modulus approach.

By using finite-difference method, the numerical solutions of the governing equations for free vibration are obtained.
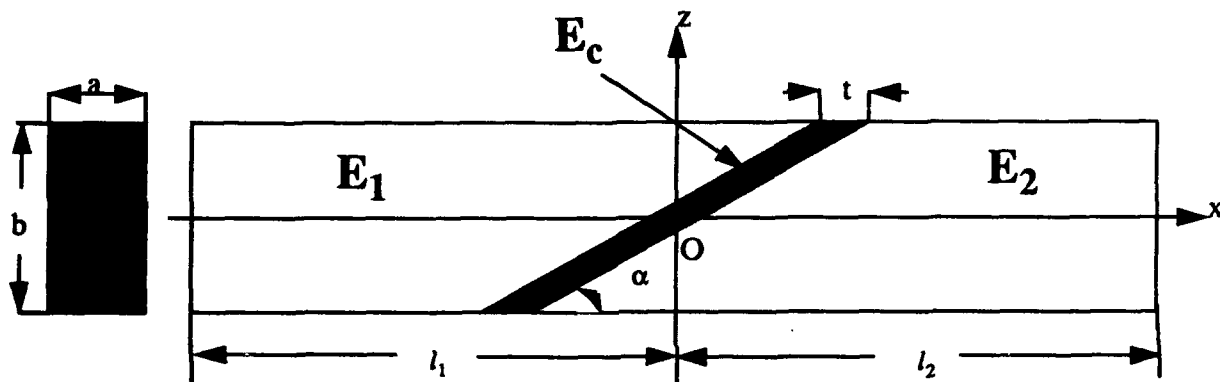
Assumptions

1. The beams are elastic and isotropic. The adhesive layer is viscoelastic whose elastic modulus (assumed constant with frequency) is modeled using the complex modulus approach. Orthrotropic beams could also be analyzed using this model.

2. The cross sections before and after bending, remain plane not only in unbonded areas but also in the scarf joint area. This assumption is quite reasonable as long as the adhesive layer is thin and there is perfect bonding with no slip between the adherends and the adhesive.

3. It is also assumed that the damping of the system comes mainly from the viscoelastic adhesive, and the material damping of the beam material is neglected.

REGION 2

REGION 4

REGION 1   REGION 3   REGION 5

REGION 1   REGION 2   REGION 3   REGION 4   REGION 5
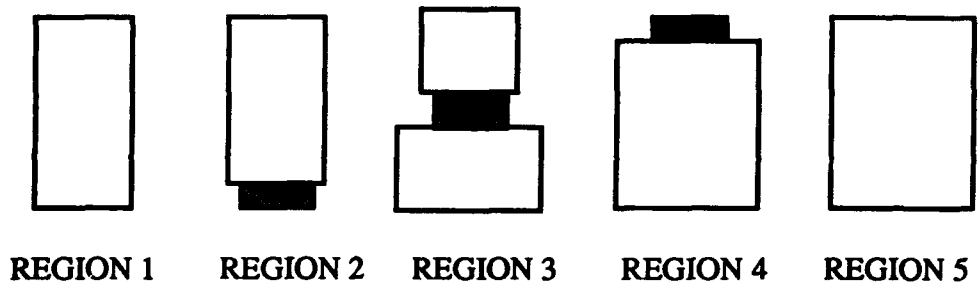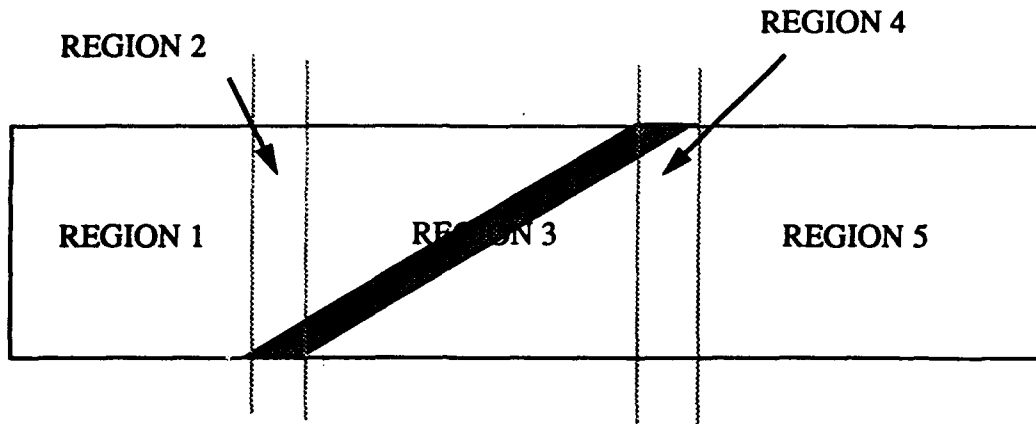
Equivalent Sections of the Scarf Joint for Analysis.

Bending Stiffness

$$K(x) = E_1 \frac{ab^3}{12}$$ **Region 1**

$$K(x) = E_2 \frac{ab^3}{12}$$ **Region 5**

For REGIONS 2, 3 AND 4

Obtain the location of neutral axis for each section, and then determine the area moment of inertia and equivalent bending rigidity for the section as a function of the x- coordinate

EXAMPLE: FOR REGION 2

$$\text{When } x \in \left[-\frac{t}{2} - \frac{b}{2}\cot\alpha, \frac{t}{2} - \frac{b}{2}\cot\alpha \right]$$
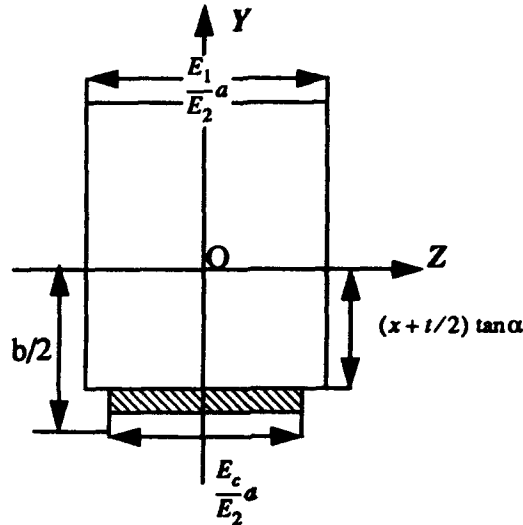
Area A is given by:

$$A = a\,(x+\tfrac{t}{2})\,\tan\alpha\left(\frac{E_c}{E_2} - \frac{E_1}{E_2}\right) + \frac{ab}{2}\left(\frac{E_c}{E_2} + \frac{E_1}{E_2}\right).$$

$$\iint_A y\,dA = \int_{-b/2}^{(x+t/2)\tan\alpha} y\frac{E_c}{E_2}a\,dy + \int_{(x+t/2)\tan\alpha}^{b/2} y\frac{E_1}{E_2}a\,dy = \frac{a}{2}\left(\frac{E_1}{E_2} - \frac{E_c}{E_2}\right)(\frac{b^2}{4} - (x+\tfrac{t}{2})^2\,(\tan\alpha)^2)\,.$$

$$\text{Now, } y^* = \frac{1}{A}\iint_A y\,dA, \quad \text{and}$$

$$I_z = \int_{-b/2}^{(x+t/2)\tan\alpha} y^2\frac{E_c}{E_2}a\,dy + \int_{(x+t/2)\tan\alpha}^{b/2} y^2\frac{E_1}{E_2}a\,dy$$

$$= \frac{a}{3}(x+\tfrac{t}{2})^3\,(\tan\alpha)^3\left(\frac{E_c}{E_2} - \frac{E_1}{E_2}\right) + \frac{ab^3}{24}\left(\frac{E_c}{E_2} + \frac{E_1}{E_2}\right)$$

The moment of inertia with respect to the neutral axis is

$$I_1 = I_z - y^{*2}A = I_z - \left(\iint_A y\,dA\right)^2 / A = \frac{a}{3}\left(x+\frac{t}{2}\right)^3 (\tan\alpha)^3 \left(\frac{E_c}{E_2} - \frac{E_1}{E_2}\right) + \frac{ab^3}{24}\left(\frac{E_c}{E_2} + \frac{E_1}{E_2}\right)$$

$$-\frac{a^4}{4}\left(\frac{E_1}{E_2} - \frac{E_c}{E_2}\right)^2 \left(\frac{b^2}{4} - \left(x+\frac{t}{2}\right)^2 (\tan\alpha)^2\right)^2 / \left(a\left(x+\frac{t}{2}\right)\tan\alpha\left(\frac{E_c}{E_2} - \frac{E_1}{E_2}\right) + \frac{ab}{2}\left(\frac{E_c}{E_2} + \frac{E_1}{E_2}\right)\right).$$

The bending stiffness for this region is $K(x) = E_2 I_1(x)$

Similarly, for region 3,

$$I(x) = \frac{a}{3}\left(x-\frac{t}{2}\right)^3 (\tan\alpha)^3 \left(1 - \frac{E_c}{E_1}\right) + \frac{a}{3}\left(x+\frac{t}{2}\right)^3 (\tan\alpha)^3 \left(\frac{E_c}{E_2} - \frac{E_1}{E_2}\right) + \frac{ab^3}{24}\left(\frac{E_1}{E_2} + 1\right) -$$

$$\frac{\left(\frac{a}{2}\left((x-t/2)\tan\alpha\right)^2 (1 - E_c/E_2) + \frac{a}{2}\left((x+t/2)\tan\alpha\right)^2 (E_c - E_1)/E_2 + \frac{ab^2}{8}(E_1/E_2 - 1)\right)^2}{a\left((x-t/2)\tan\alpha + b/2\right) + a(E_c/E_2)\tan\alpha + a(E_1/E_2)(b/2 - (x+t/2)\tan\alpha)}$$

The bending stiffness is $K(x) = E_2 I(x)$.   for $\left(-\frac{t}{2} - \frac{b}{2\tan\alpha} < x \leq \frac{t}{2} - \frac{b}{2\tan\alpha}\right)$.

and for region 4,

$$K(x) = E_2\left[\frac{a}{3}\left(x-\frac{t}{2}\right)^3 (\tan\alpha)^3 \left(1 - \frac{E_c}{E_2}\right) + \frac{ab^3}{24}\left(\frac{E_c}{E_2} + 1\right) - \frac{\frac{a^2}{4}\left(1 - \frac{E_c}{E_2}\right)^2 \left(\frac{b^2}{4} - \left(x-\frac{t}{2}\right)^2 (\tan\alpha)^2\right)^2}{a\left(x-\frac{t}{2}\right)\tan\alpha\left(1 - \frac{E_c}{E_2}\right) + \frac{ab}{2}\left(\frac{E_c}{E_2} + 1\right)}\right]$$

which encompasses $\left(-\frac{t}{2} + \frac{b}{2\tan\alpha} < x \leq \frac{t}{2} + \frac{b}{2\tan\alpha}\right)$.

In the above equations: $E_c = E_r(1 + i\eta_m)$.

Strain energy in the system due to bending

$$V = \int_{-l_1}^{l_2} \frac{1}{2} K(x) w''^2 dx$$

System Kinetic energy

$$T = \int_{-l_1}^{l_2} \frac{1}{2} \rho_2 A(x) \dot{w}^2 dx$$

The work done by the external forces q(x,t)

$$W = \int_{-l_1}^{l_2} qw dx - (S_1 w - Mw')\big|_{x=-l_1} + (S_2 w - M_1 w')\big|_{x=l_2}$$

Hamilton's principle $\quad \delta \int_{t_1}^{t_2} (T - V + W)\, dt = 0,\quad$ gives

the governing equation of motion

$$K''(x) w'' + 2K'(x) w''' + K(x) w^{(4)} + \rho_2 A(x) \ddot{w} = q(x, t)$$

and the natural boundary conditions are

$$[S - (K'(x) w'' + K(x) w''')]\,\big|_{-l_1}^{l_2} = 0$$

$$[-M + K(x) w'']\,\big|_{-l_1}^{l_2} = 0.$$

Using separation of variables method,

let $w(x, t) = w(x) e^{i\lambda t}$, and get

$$p(x) w'' + q(x) w''' + r(x) w^{(4)} - \lambda^2 w = 0 \qquad \text{where}$$

$$p(x) = \frac{K''(x)}{\rho_2 A(x)}$$

$$q(x) = \frac{2K'(x)}{\rho_2 A(x)} \qquad \text{and}$$

$$r(x) = \frac{K(x)}{\rho_2 A(x)}$$

λ = **damped complex resonance frequency of the system.**

The System loss factor η_i and

Resonance Frequency ω_i for each mode i are

$$\omega_i = real(\lambda_i) \qquad \text{and}$$

$$\eta_i = \frac{imag(\lambda_i^2)}{real(\lambda_i^2)}.$$

SOLUTION OF GOVERNING EQUATIONS

By Finite Difference Method for continuous systems

If the interval $[-l_1, l_2]$ is n aliquot, each part length is $h = \dfrac{l_1 + l_2}{n}$.

$$x_0 = -l_1 \qquad\qquad x_k \; x_{k+1} x_{k+2} \qquad\qquad x_n = l_2$$
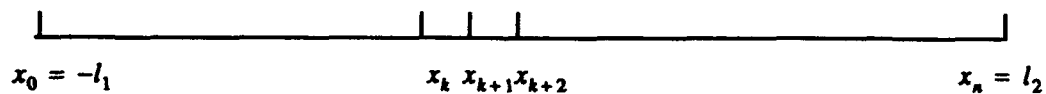
For the division point x_k, we have second, third and fourth derivatives as:

$$(w'')_k = \frac{1}{h^2}(w_{k+1} - 2w_k + w_{k-1})$$

$$(w''')_k = \frac{1}{2h^3}(w_{k+2} - 2w_{k+1} + 2w_{k-1} - w_{k-2})$$

$$(w^{(4)})_k = \frac{1}{h^4}(6w_k - 4(w_{k+1} + w_{k-1}) + w_{k+2} + w_{k-2}).$$

Now the boundary value problem will be changed to a difference equation solution.

$$\left(\frac{q_k}{2h^3}+\frac{r_k}{h^4}\right)w_{k+2}+\left(\frac{p_k}{h^2}-\frac{q_k}{h^3}-\frac{4r_k}{h^4}\right)w_{k+1}-\left(\lambda^2+\frac{2p_k}{h^2}-\frac{6r_k}{h^4}\right)w_k+\left(\frac{p_k}{h^2}+\frac{q_k}{h^3}-\frac{4r_k}{h^4}\right)w_{k-1}-\left(\frac{q_k}{2h^3}-\frac{r_k}{h^4}\right)w_{k-2}=0$$

$$(k = 1, 2, ..., n-1)$$

Input data: $(E_1 = E_2 = 71 GPa, l_1 = l_2 = 0.1 m, b = 0.01 m, \eta_m = 0.1), E_c = 0.1 E_1,$

$$\rho = 2770 kg/m^3, \rho_c = 0.12\rho$$

joint system was simply supported at both ends.

CONCLUSIONS

An analytical model to study the bending vibration of a scarf-jointed beam is formulated in this paper.

This model development is based on the concepts of equivalent bending stiffness of the joint, energy method and Hamilton's principle.

The solution for free vibration for the case of a simply supported beam is obtained using finite-difference method.

It has been found that an increase in the adhesive thickness leads to an increase in the system damping at the same time decreasing the system dynamic stiffness.

The joint angle is a key parameter that can be controlled to obtain maximum loss in the system. For a particular joint configuration, there exists an optim- joint angle which maximizes the system damping.

Fig. 3

Fig. 4

Fig. 7

Fig. 8
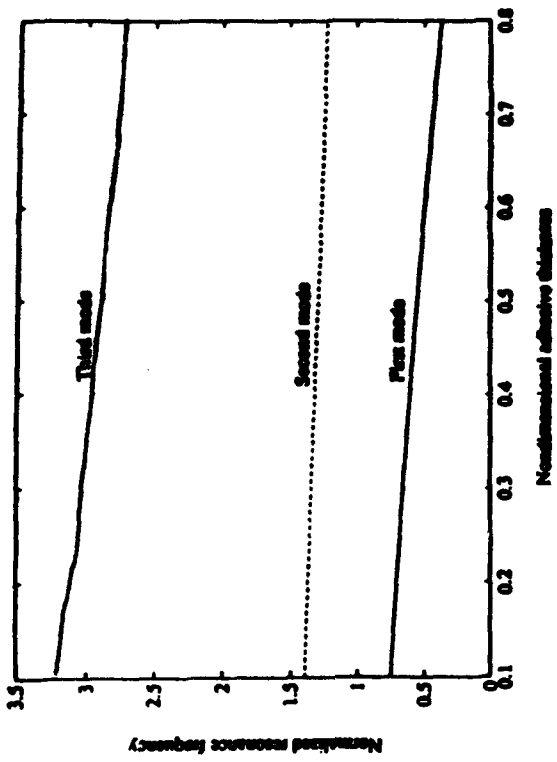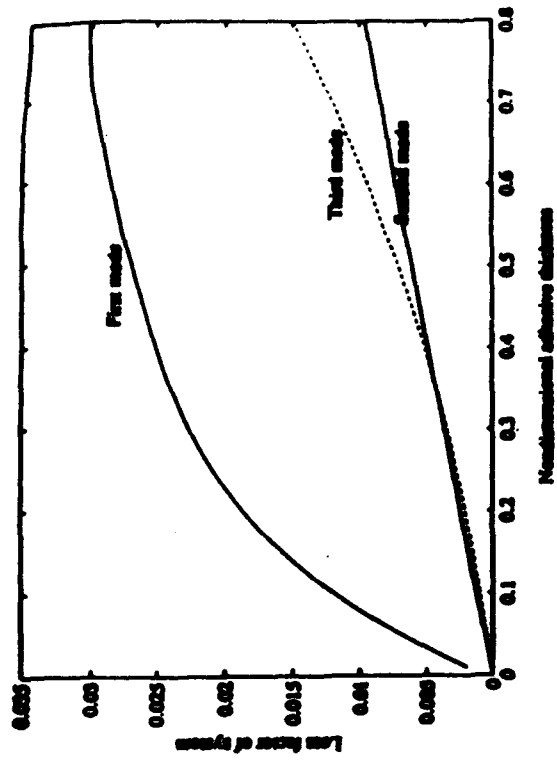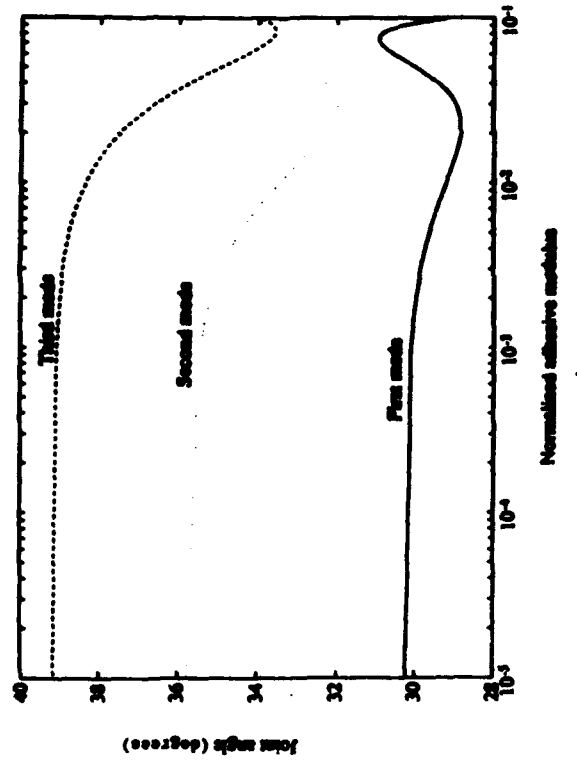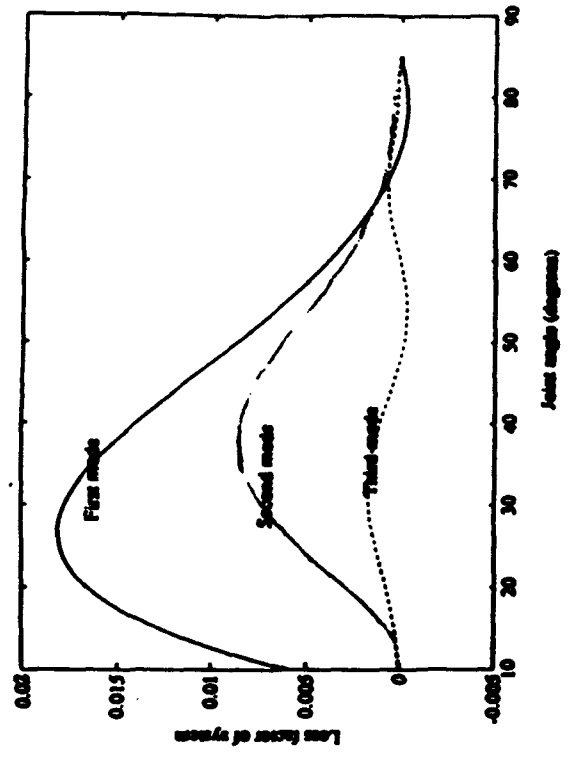
Low Frequency Damping and Ultrasonic Attenuation in Ti3Sn-Based Alloys

Catherine R. Wong,

Carderock Division, Naval Surface Warfare Center*

and

Robert L. Fleischer**

General Electric Research and Development Center

Studies of high-temperature alloys in the Ti-Sn system based on the intermetallic compound Ti3Sn have identified alloys that damp strongly both at low frequencies (0.1 to 10 Hz) and high frequency (5 to 20 MHz). Although the basic mechanism or mechanisms of energy dissipation are presently unknown, the alloys are notable for unusual shapes of microhardness indentations. The deformations imply that large reversible strains can occur at temperatures from 23°C to 1150°C.

* Code 2812 Annapolis, MD 21402-5067 Phone (410)267-2835

** Now at Department of Earth and Environmental Sciences, Rensselaer Polytechnic Institute, Troy, NY 12180-3590

Introduction

Mechanical damping is of interest both because of the need for basic scientific understanding and because energy absorption can be used in many practical applications such as minimizing noise that is distracting or harmful to human beings, minimizing vibrations that would be harmful to equipment, and reducing unwanted acoustic reflections and emissions. A number of metal alloys have long been known for their high damping capacity. These include a variety of dilute Mo alloys[1], Cu-Zn alloys[2] and Mn-Cu alloys[3]. It is also noteworthy that the well-known shape-memory alloy NiTi also shows high damping at room temperature[4]. The purpose here is to report on two alloys in another high-damping system (Ti-Sn) that have some unusual features and a high melting temperature (1590 °C). We describe the damping capacity and what is known structurally about the two alloys studied here and discuss other related compositions that have some key properties in common and are therefore prime candidates for further study.

Motivation

The origin of interest in the alloys studied here was the failure to determine elastic constants in high-frequency (5 to 20 MHz) pulse-echo measurements[5]. Reflections from acoustic pulses could not be identified after a 1 cm travel distance in $Ti_{80}Sn_{20}$, $Ti_{78}Sn_{22}$, and $Ti_{75}Sn_{21}V_4$. Subsequent work with the same technique[6] showed similar attenuation in $Ti_{72}Sn_{18}Al_{10}$ and in a different system, $Ti_{36}Cr_{54}Al_{10}$. Two binary compositions, Ti_3Sn and $Ti_{87}Sn_{13}$, that bracket those that showed the strong attenuation behaved normally in that their elastic constants could be determined.

Experimental Procedure

Preparation Of Samples

Samples were arc melted into disk-shaped ingots using the highest purity components that were reasonably available. Titanium was 99.99% pure and tin >99.999%. Purities of other elements in alloys to be cited for comparison were (Al) 99.9999%, (Cr) 99.99%, (Nb) 99.99%, and (V) 99.9%. Interstitials in weight ppm were (C) 100, (N) 15 and, (O) 500 for $Ti_{80}Sn_{20}$ and (C) 100, (N) 25, and (0) 1000 for $Ti_{78}Sn_{22}$. Samples were annealed at 1350 °C in Ar-filled SiO_2 ampoules that included a small piece of Y to getter oxygen. Microhardness was measured up to 1150 °C using a Nikon-GM tester, a diamond pyramid indenter, and a load of 1000 or 500 g. The pressure during testing was typically less than 10^{-8} atmospheres, with a possible exception at the highest temperature (where outgasing or vaporization may occur).

Phases Present

The expected phases and melting temperatures for both compositions[6] are listed in Table 1, along with the observed phase fractions that were measured using point counts on photographs

of polished metallographic sections. The specific compositions have been checked by traditional wet chemical methods. The results, given in the second column of Table 1, are generally in good agreement with the requested compositions. However, the phase volume fractions imply that the nominal chemical compositions are more accurate than the chemically measured values.

Table 1. Alloy Composition, Phases Expected And Observed, And Properties

Nominal Atomic Composition	Measured Atomic Composition	Melting Temp. (°C)	Specific Gravity	Heat Treatment (°C/H)	Phases Expected Volume Fraction	Volume Fractions Observed (100 Points Counted)
$Ti_{80}Sn_{20}$	79:21	1590	5.76	1350/20	0.79 DO_{19};0.21 A3	0.79;0.21
$Ti_{78}Sn_{22}$	78:22	1590	5.82	1350/20	0.89 DO_{19};0.11 A3	0.90;0.10

Damping Capacity Measurements

The samples tested for damping capacity were electro-discharge machined to approximately 4.0 x 1.0 x 0.1 cm. The damping capacity measurements were carried out at frequencies between 0.01 and 10 Hz and temperatures from -30 °C to 100 °C. The damping capacity and Young's modulus were measured with a Polymer Laboratories Dynamic Mechanical Thermal Analyzer (DMTA) using a fixed-guided cantilevered test configuration. In this configuration, shown in Fig. 1, the clamp on the left holds the sample to a stationary frame while the right clamp attaches the sample to the controlled drive shaft. When the samples are not firmly held, erroneous damping capacity measurements may result due to slip between the sample and clamps. In order to minimize such errors, three-pronged clamps were used. A torque wrench was used to tighten the clamps in order to achieve consistent clamping.

The damping capacity was measured by applying a small sinusoidal mechanical force to the drive shaft and measuring the displacement of the sample. The phase angle, δ, of the lag between the applied load and the measured displacement was calculated. The tangent of δ is a measure of the damping capacity, commonly called the loss factor. Comparison of the amplitude of the load and displacement signals yielded Young's modulus, E'. All samples were tested at three distinct frequencies of vibration: 0.1, 1, and 10 Hz. The dependence of tan δ and E' on temperature was determined by vibrating the samples at 100 microstrain (maximum) while ramping the temperature 1°C per minute from -30 to 100°C and continually alternating the frequencies. The run was then repeated to check for consistency. The dependence of the damping capacity on the strain was found by measuring the damping capacity at 25 °C while continually alternating the frequencies and periodically increasing the amplitude of the vibration. The reported values are the average of the damping capacity over thirty minutes.

The values of E' were corrected to account for error which arose from end-effects at the clamping point of the beam. These effects are due to the uncertainty in the point at which the metal starts to bend in the grips. These "end corrections" are based on the measured modulus and are calculated from an empirically generated curve. Corrections to the tan δ values were made to account for the friction between the air and the moving sections of the DMTA, including the

FIG. 1. Dynamic Mechanical Thermal Analyzer: grip setup.

FIG. 1. Dynamic Mechanical Thermal Analyzer: grip setup.
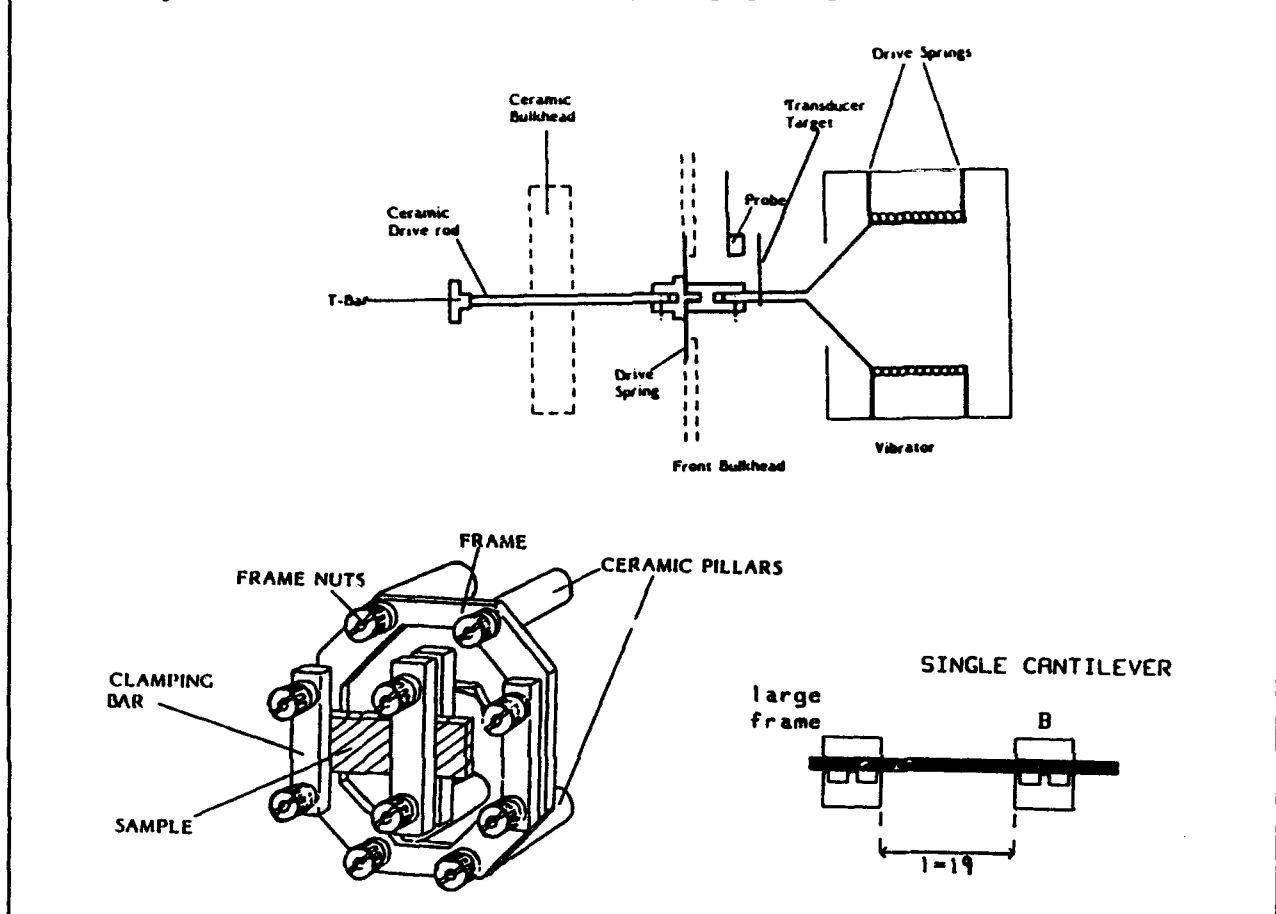
sample, as the sample was vibrated. The correction factor is frequency dependent, and for measured values of the loss factor below 0.01 it was necessary to correct the 10 Hz data. This was done by averaging the loss factor data values over a temperature range in which tan δ was nominally flat. The average of the 1 Hz tan δ data was subtracted from the average of the 10 Hz tan δ data and that number was then subtracted from the 10 Hz tan δ values over the whole temperature range.

Materials Characterization Tests.

In order to determine the stress-strain behavior at ambient temperature a 1.0 x 0.5 x 0.5 cm sample of $Ti_{78}Sn_{20}$ was compressed at a strain rate of 10^{-4} s^{-1} first to a strain, ε, of 3.1% and subsequently to incipient failure. Metallographic and transmission electron microscopic examinations were done on both deformed ($\varepsilon = 3.1\%$) and as-annealed material.

Results

Damping Capacity

Damping capacity measurements at low frequency shown in Fig. 2 revealed a peak in the damping capacity near 20 °C at 0.1 Hz, 30 °C at 1 Hz and 35 °C at 10 Hz for the $Ti_{78}Sn_{22}$ sample and near 15 °C for all three frequencies in the $Ti_{80}Sn_{20}$ sample. The amplitude of the damping capacity peaks decreased with increasing frequency in both samples, from a loss factor of 0.04 at 0.1 Hz to 0.017 at 10 Hz in the $Ti_{78}Sn_{22}$ sample and from a loss factor of 0.025 at 0.1 Hz to 0.015 at 10 Hz for the $Ti_{80}Sn_{20}$ sample. The data from the second runs on each sample closely repeat these values, as shown in Fig. 3. Although distinct discontinuities that are attributed to experimental error appeared in the modulus measurements (Fig. 4), the general trend of the data is thought to be correct. The modulus decreased with increasing temperature until 40 °C in the $Ti_{78}Sn_{22}$ sample and 35 °C in the $Ti_{80}Sn_{20}$ sample and then increased. Since a discontinuity in the curve occurs near the damping capacity peak in the $Ti_{80}Sn_{20}$ in both runs of this sample it would be necessary to repeat that experiment in order to define confidently the damping capacity peak. The plot of the strain dependence of the damping capacity shown in Fig. 5 reveals an unexpected frequency dependence of the $Ti_{78}Sn_{22}$ sample. The loss factor decreases from 0.03 to 0.015 in the $Ti_{78}Sn_{22}$ sample as the strain increases from 50 to 1100 microstrain. Similarly in the $Ti_{80}Sn_{20}$ sample the loss factor decreases from 0.04 to 0.01 as the strain is increased from 50 to 500 microstrain, and the damping capacity at 10 Hz is always higher than the damping capacity at other frequencies. This implies that 25 °C (the temperature at which

FIG. 2. Damping capacity versus temperature for Ti-Sn alloys measured from -30 to 100°C at 100 microstrain.
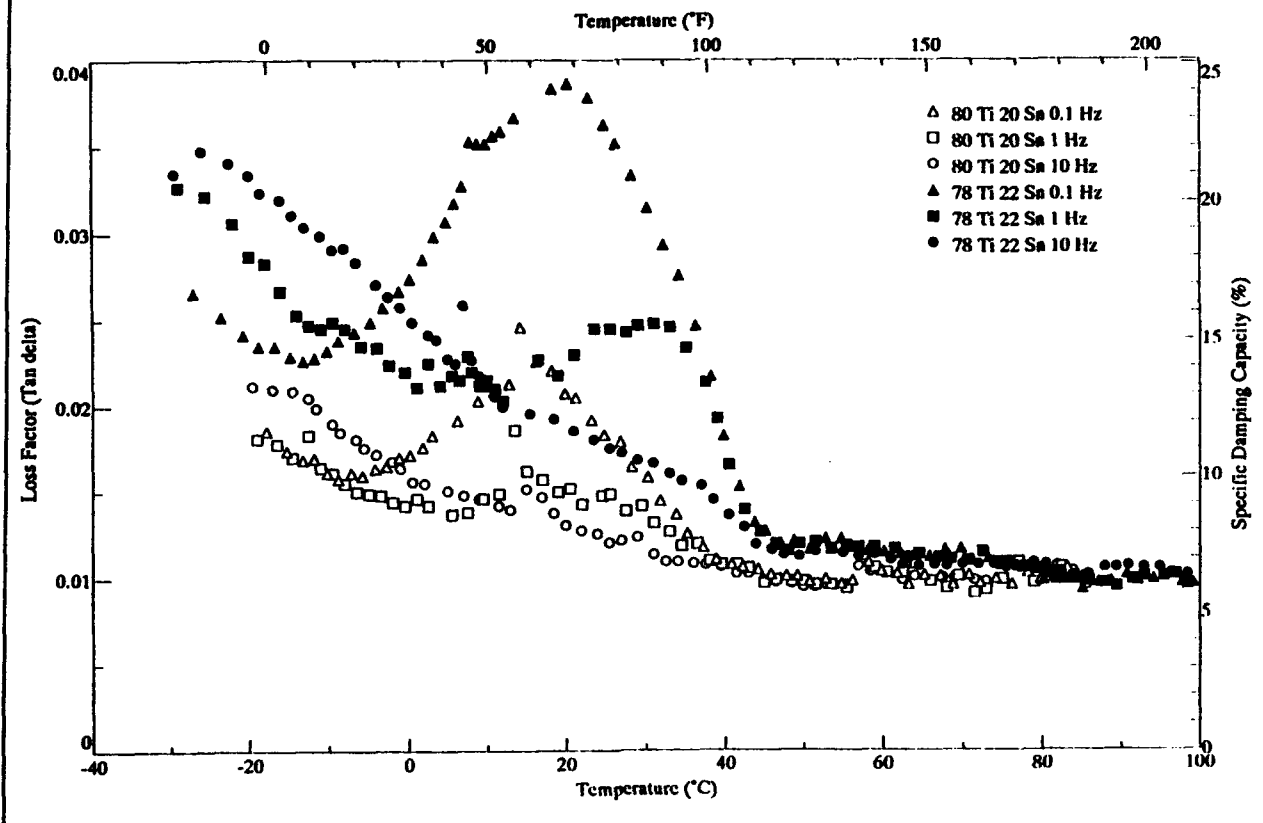
FIG. 3. Duplicate measurements of damping capacity versus temperature for Ti-Sn alloys.

Legend:
- ○ 80 Ti 20 Sn (0.1, 1, 10 Hz) first run
- △ 80 Ti 20 Sn (0.1, 1, 10 Hz) second run
- ● 78 Ti 22 Sn (0.1, 1, 10 Hz) first run
- ● 78 Ti 22 Sn (0.1, 1, 10 Hz) second run
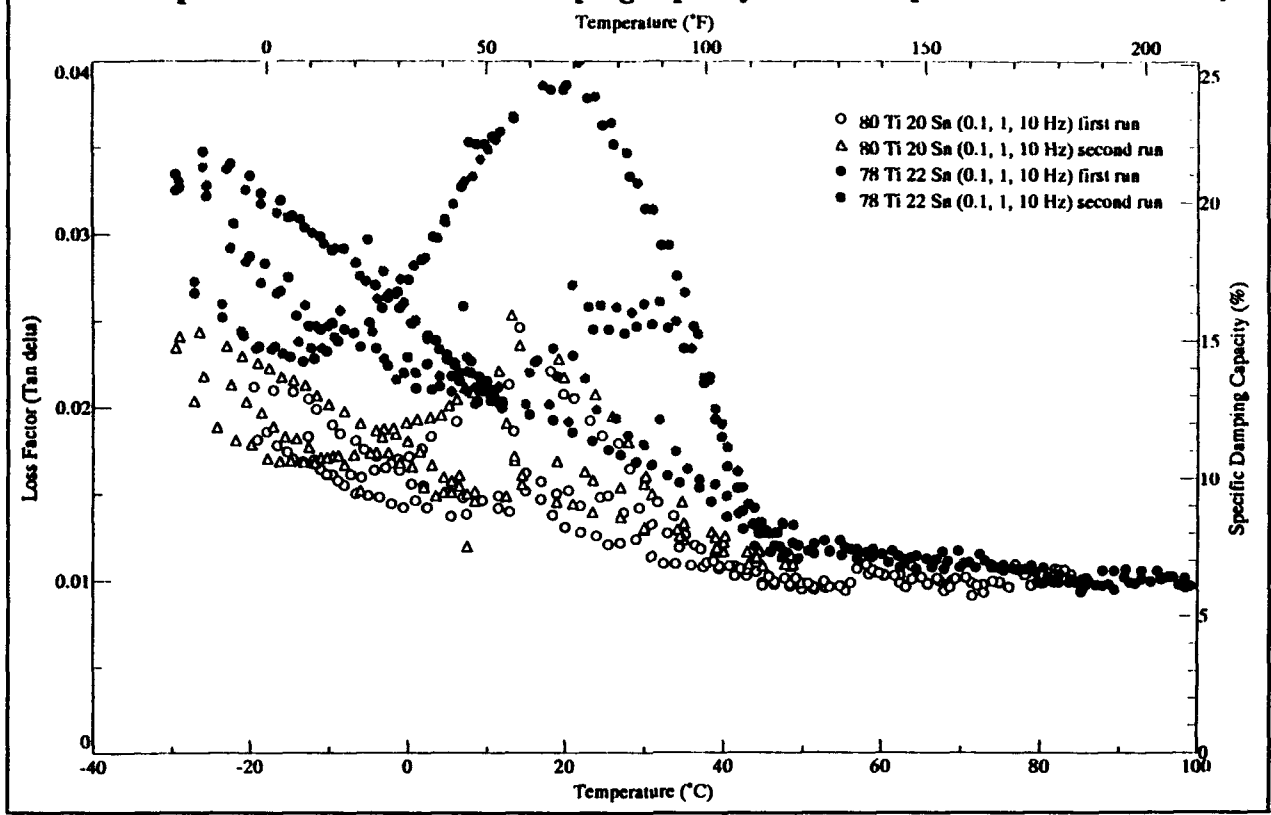
FIG. 4. Bending modulus versus temperature for Ti-Sn alloys measured from -30 to 100°C at 100 microstrain.

Legend:
- ○ 80 Ti 20 10 Hz
- □ 80 Ti 20 1 Hz
- △ 80 Ti 20 0.1 Hz
- ● 78 Ti 22 Sn 10 Hz
- ■ 78 Ti 22 Sn 1 Hz
- ▲ 78 Ti 22 Sn 0.1 Hz

ECA-6
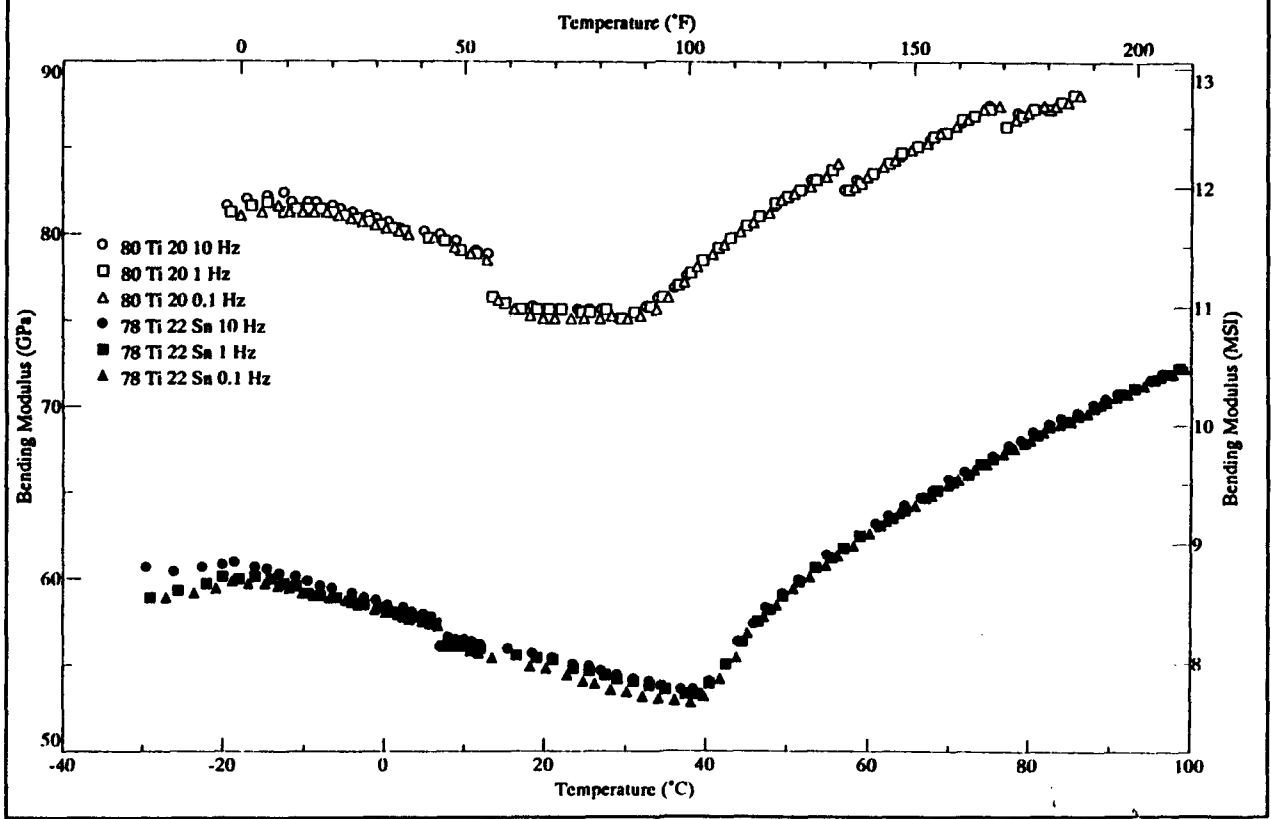
FIG. 5. Damping capacity versus strain amplitude for Ti-Sn alloys measured at 25°C.
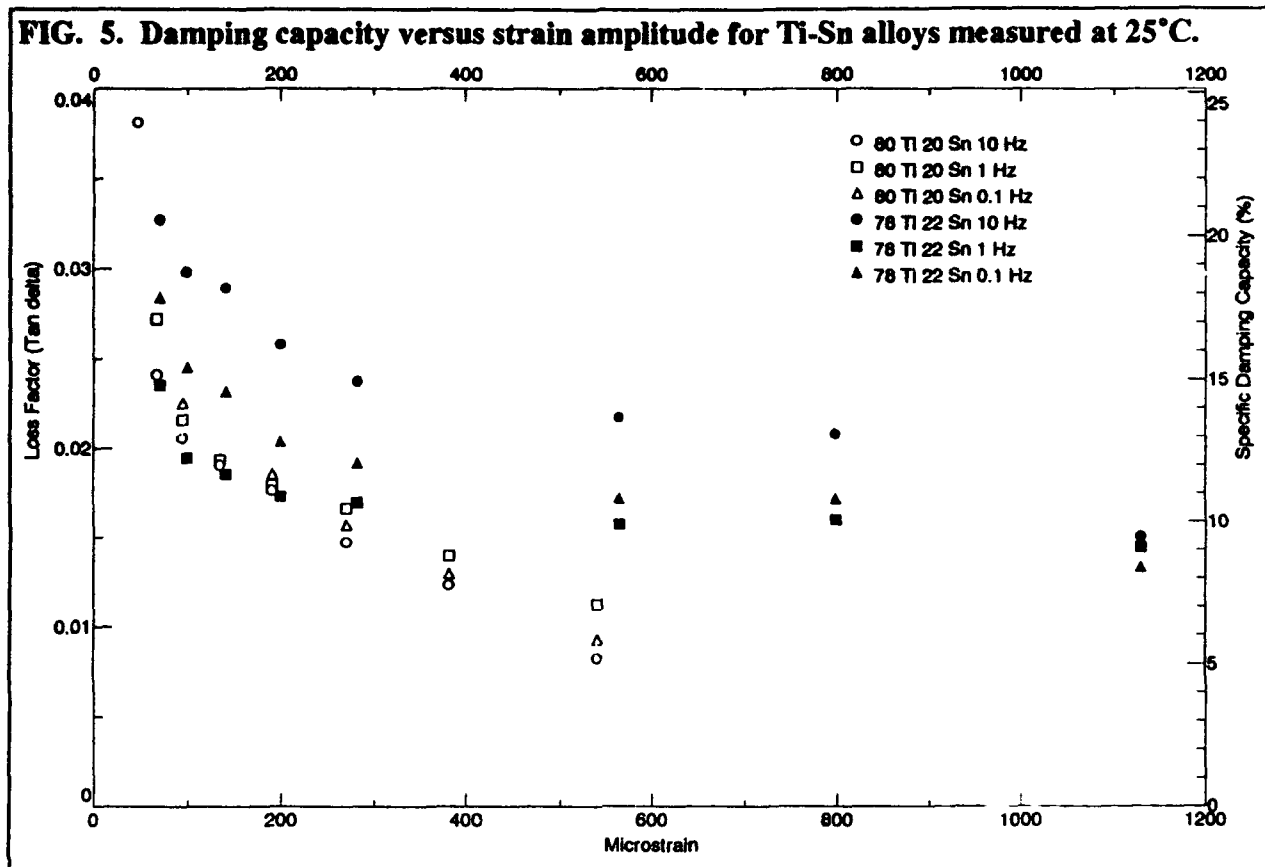
the strain dependence was measured) is higher than the relaxation peak temperature for 0.1 and 1 Hz and below the peak temperature for 10 Hz. This is not confirmed by the temperature scan data. The plot of the strain dependence of the $Ti_{80}Sn_{20}$ sample shows very little frequency dependence, especially at higher strains.

Plastic Mechanical Properties Results

The compressional stress-strain result for $Ti_{78}Sn_{22}$ is shown in Fig. 6. It is doubly noteworthy first for its low work hardening rate and second for the fact that at this low temperature extensive plasticity was present in an alloy that consists of 90 volume percentage of a normally highly brittle intermetallic compound (DO_{19}(hP8) Ti_3Sn). The low work hardening rate is, however, similar to what is seen in Ti-based and Ti_3Al alloys. The moderate strength is in contrast to the very high hardness that has been measured[6] for single-phase Ti_3Sn.

Another noteworthy feature of the deformation of the two alloys is the geometry of the hardness indentations in these materials. Usual Vickers hardness indentations match the square-base diamond-pyramid shape of the indentor, giving a clean regular square shape. Fig. 7 shows indentations that were made at different temperatures in $Ti_{78}Sn_{22}$, and $Ti_{80}Sn_{20}$ shows similar results. These shapes are vastly distorted relative to the conventional square profile, a graphic indication of extensive reverse deformation during the unloading of the indentor.

FIG. 6 Stress-Strain Curve For Compressional Room-Temperature Deformation of Ti78Sn22
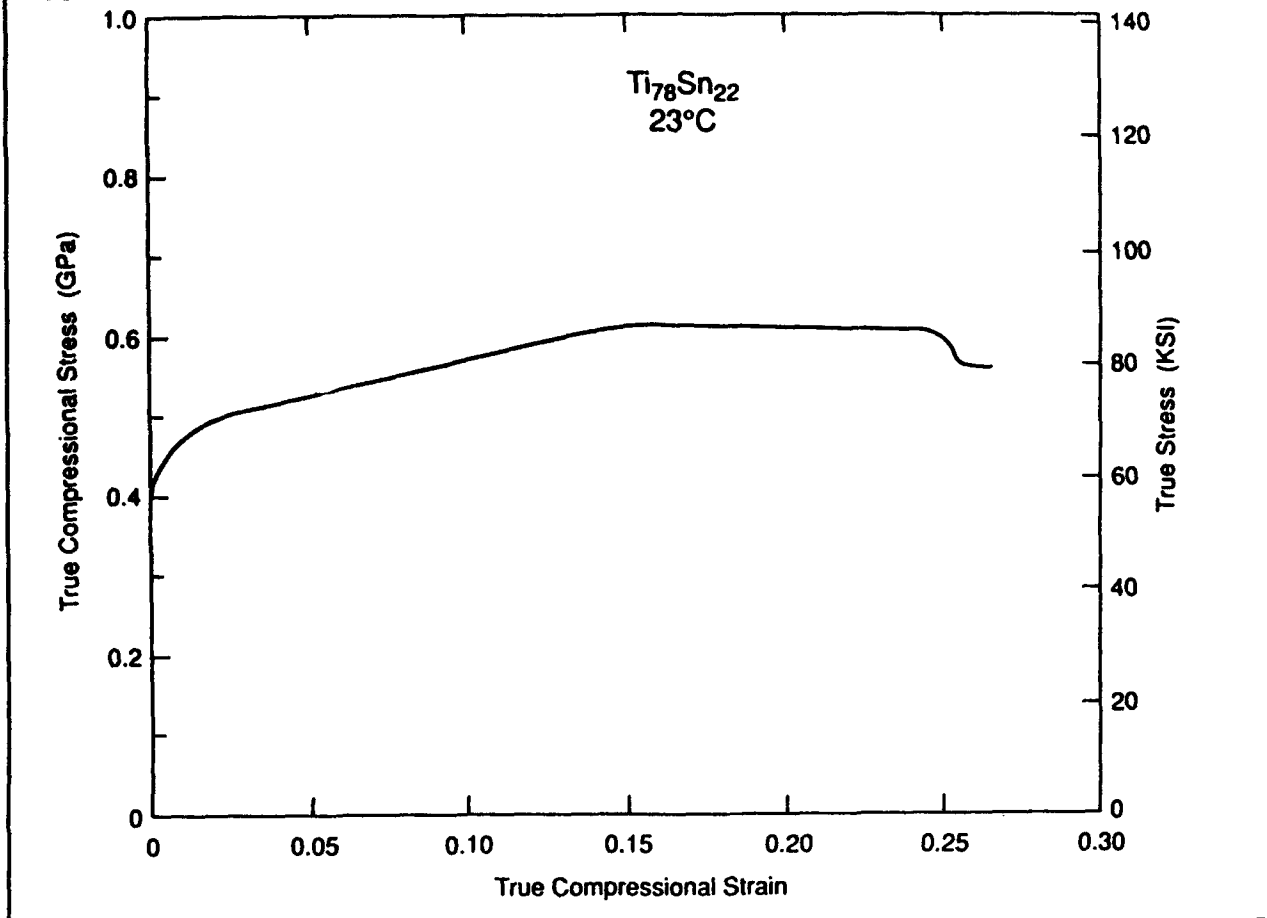
FIG. 6 Stress-Strain Curve For Compressional Room-Temperature Deformation of $Ti_{78}Sn_{22}$

FIG. 7 Vickers diamond-pyramid microhardness indentations in Ti78Sn22 at six temperatures.

FIG. 7 Vickers diamond-pyramid microhardness indentations in $Ti_{78}Sn_{22}$ at six temperatures.
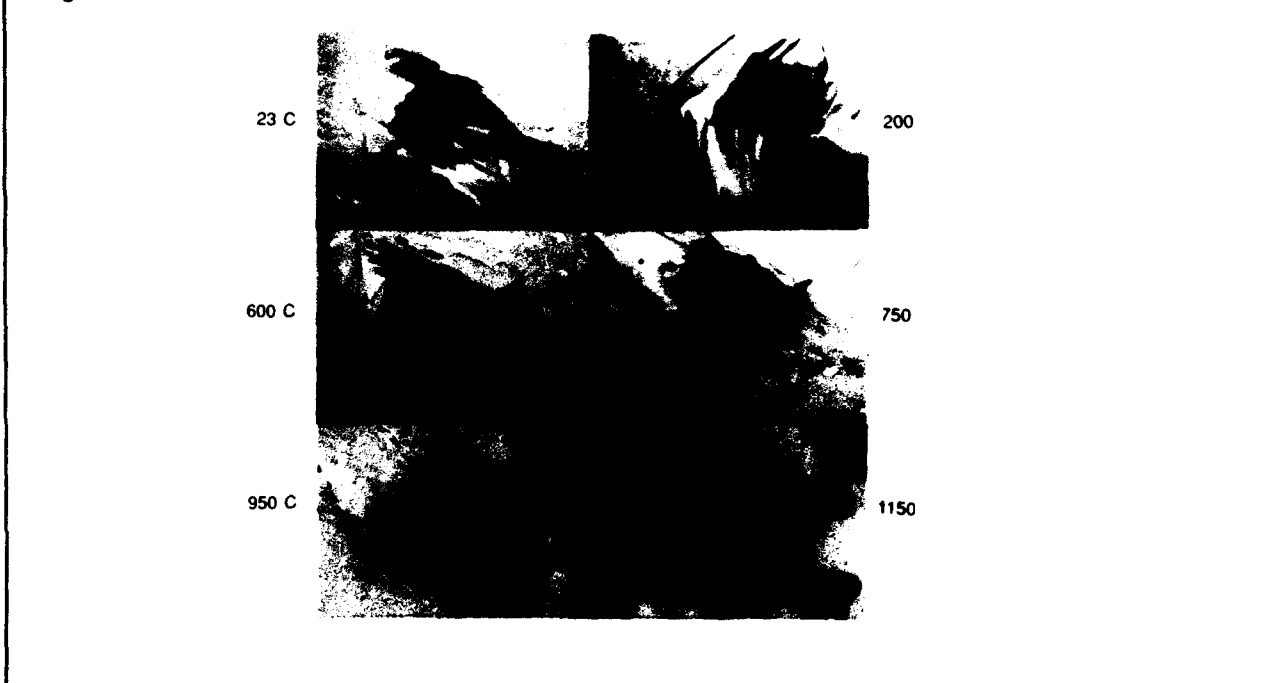
Metallographic And TEM Observations

The deformation markings on a mechanically polished external surface of the compression sample were photographed after a true plastic strain of 0.031. Prominent deformation bands are shown at high and low magnification in Figs. 8 and 9. Deformation proceeds commonly on more than one plane. The dominant slip at room temperature is prismatic with a [0001] slip vector, and only four independent slip systems normally act[7]. TEM (transmission electron microscopy) of undeformed $Ti_{78}Sn_{22}$ and $Ti_{80}Sn_{20}$ confirmed that the expected equilibrium phases were present, hexagonal Ti in a matrix of the ordered hexagonal intermetallic compound Ti_3Sn.

FIG. 8. External surface of compression sample of $Ti_{78}Sn_{22}$ after a strain of 0.031.

10μm
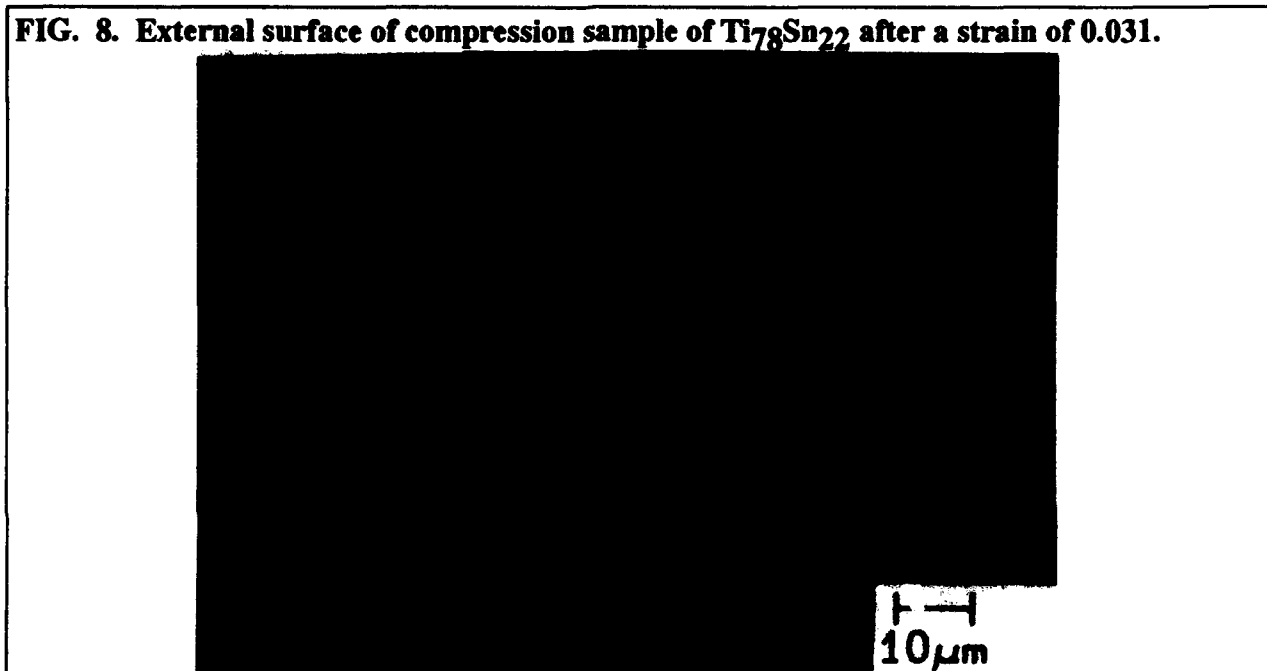
FIG. 9. As in Fig. 8, but at lower magnification, Intersecting bands are prominent.

50μm
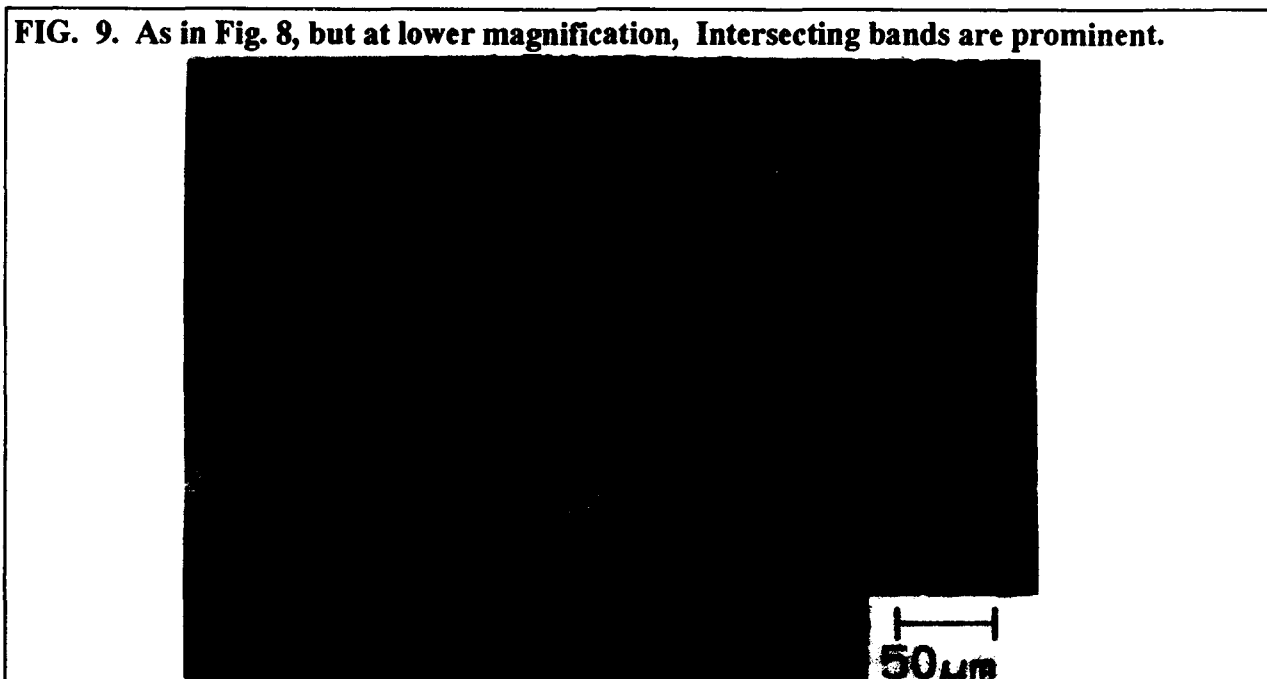
More unusual was the observation of fine-scale twinning on the pyramidal $\{10\overline{1}0\}$ planes, first in the undeformed sample (Fig. 10), but more abundantly present after a strain of 0.031 (Fig. 11). Typical twin widths were 17 ± 5 nm in the undeformed sample and 13 ± 6 in the deformed one, i.e., not meaningfully different. The ordered phase also showed high grown-in dislocation densities in some areas (Fig. 12)

FIG. 10. Twins in undeformed $Ti_{78}Sn_{22}$, DO_{19} phase. The width of the photo is 1.10 mm.

FIG. 11. Twins in deformed $Ti_{78}Sn_{22}$ ($\varepsilon = 0.031$). The width of the photo is 1.80 mm, DO_{19} phase.
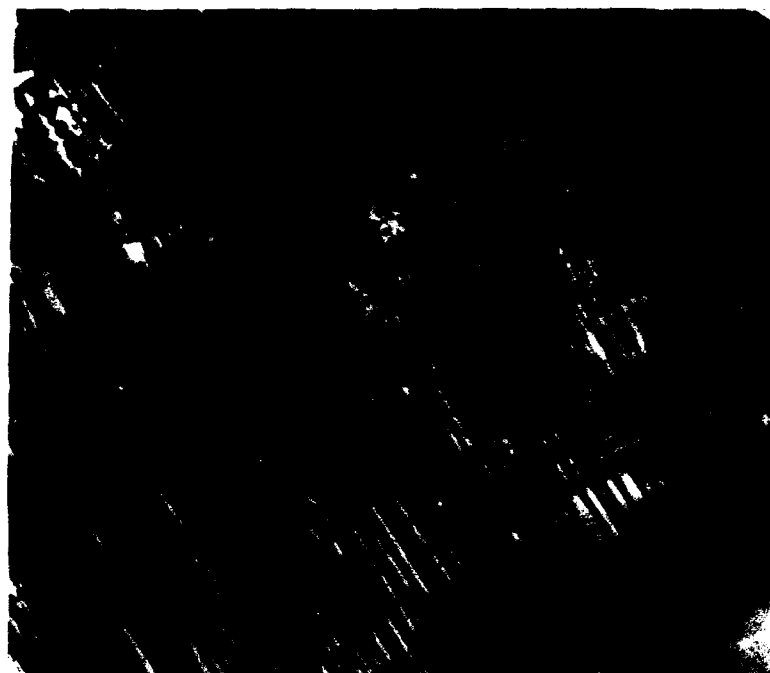
FIG. 12. Dislocations in deformed (ε =0.031) $Ti_{78}Sn_{22}$, DO_{19} phase. 8.10mm = width of the photo.
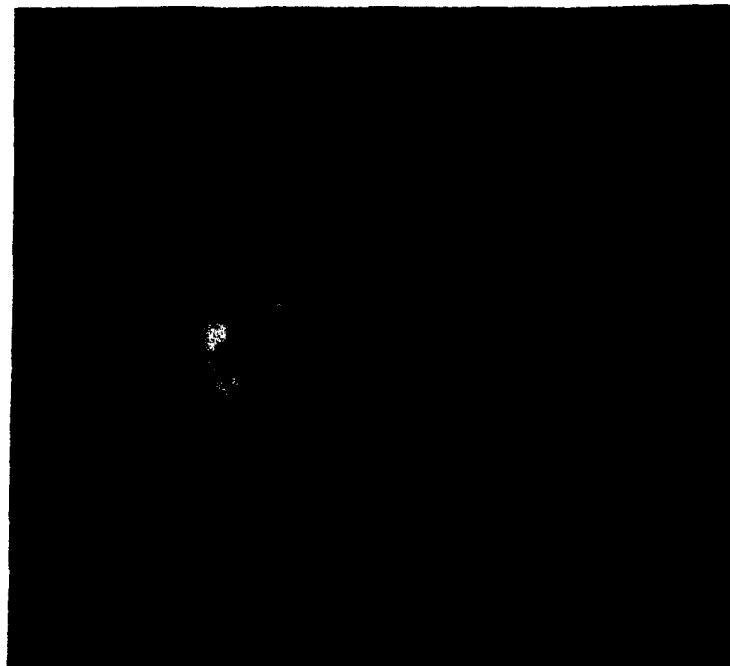
Discussion

Origin Of Damping

The hysteretic process producing energy dissipation in this material has not been identified. The highly asymmetrical Vickers hardness indentations show the mechanism to be anisotropic, which is not uncommon in HCP materials. The abundant fine twins in the deformed sample and the high level of grown in dislocations may point to the mechanism of energy dissipation. They raise the possibility of a stress-induced reversible transformation. The low rate of work hardening and coarse deformation bands are consistent with the high damping capacity of the two alloys.

Systematics -- Possibility Of Identifying Other High Damping Alloys.

The two alloys that were shown here to have high damping capacities at low-frequencies have three other properties in common, high MHz attenuation, misshapen hardness indentations, and fine-scale twinning. Can these characteristics be used to identify other composites that damp well at low frequencies? TEM examination for fine twins is laborious and expensive, but MHz acoustic measurements and hardness tests are far simpler, and we have a body of information on these tests for many intermetallic compositions[6,8]. Table 2 shows some titanium-intermetallic-

based alloys in a sequence of (presumed) descending Young's moduli (E'). Blank lines indicate where attenuation of MHz elastic waves prevented measurement of E'. Values where asterisks appear were derived from the low frequency measurements, which have been done on only two of these alloys. All alloys on the list are two-phase except Ti_3Sn.

Of the five alloys with the high MHz attenuation four have odd hardness impressions; only one of the six samples with the lowest moduli has normal indentations. From this list $Ti_{75}Sn_{21}V_4$ and $Ti_{72}Sn_{18}Al_{10}$ would be the prime candidates as further alloys to study, followed by $Ti_{36}Cr_{54}Al_{10}$ and $Ti_{70}Sn_{16}Al_{14}$.

Table 2. Moduli and hardness shapes for some titanium-based intermetallic compounds

Ultrasonic Young's Modulus (GPa)	Atomic Composition	Indentation Character n=normal; o=odd
207	Ti_3Sn	n
190	$Ti_{36}Cr_{54}Nb_{10}$	n
150	$Ti_{36}Cr_{54}Zr_{10}$	n
120	$Ti_{87}Sn_{13}$	n
106	$Ti_{70}Sn_{16}Al_{14}$	o
--	$Ti_{36}Cr_{54}Al_{10}$	n
--	$Ti_{72}Sn_{18}Al_{10}$	o
--	$Ti_{75}Sn_{21}V_4$	o
77*	$Ti_{80}Sn_{20}$	o
55*	$Ti_{78}Sn_{22}$	o

* From low frequency measurements

Conclusions

Two alloys, $Ti_{78}Sn_{22}$ and $Ti_{80}Sn_{20}$ have been recognized to have unusually strong damping from 0.1 to 10Hz and also from 5 to 20 MHz. If this anisotropy is basic to the damping mechanism then high temperature damping may be possible because the anisotropy persists to 950 °C or 1150 °C.

Acknowledgments

REFERENCES

1. L.R. Stanton and F.C. Thompson, J. Inst. Met. (London) 69, part 1, 29 (1943).

2. R.. Cabaret, L. Guillet, and R. LeRoux, J. Inst. Met. (London) 75, 391 (1949).

3. R.J. Goodwin, J. Inst. Met. (London) 93, 547 (1965).

4. W.J. Buehler, J.B. Gilfrich, and R.C. Wiley, J. Appl. Phys. 34, 1475 (1963).

5. R.L. Fleischer, R.S. Gilmore, and R.J. Zabala, J. Appl. Phys. 64, 2964 (1988).

6. R.L. Fleischer and R.J. Zabala, Metallurgical Trans. 21A, 1951 (1990).

7. P.J. Jones and J.W. Edington, Phil. Mag. 27, 393 (1973).

8. R.L. Fleischer and R.D. Field: "Development Potential of Advanced Intermetallic Materials." Final Report WRDC-TR-90-4046 to U.S. Air Force, Aeronautical Systems Div., Wright - Patterson Air Force Base, Contract f33615-86-C-5055, 1990, 410 pages.

Fully Cyclic Hysteresis of a Ni-Ti Shape Memory Alloy

by

Edward J. Graesser*
Naval Surface Warfare Center
Carderock Division
Machinery Research and Development Directorate
Annapolis, Maryland 21402

and

Francis A. Cozzarelli
State University of New York at Buffalo
Department of Mechanical and Aerospace Engineering
Buffalo, New York 14260

ABSTRACT

A nickel-titanium shape memory alloy (SMA) was subjected to tests for fully cyclic hysteresis in axial tension-compression under strain control. The tests were made in support of a project to examine new materials for added passive damping in earthquake-isolated structures. The material was heat-treated to an extent which produced hysteresis closely approaching room temperature superelasticity. The tests gave results exhibiting markedly different behavior for tension and compression. Various quasi-static rates were used and a rate dependence was exhibited in the inelastic modulus. One sequence of tests showed that the material is able to sustain repeated cycles of axial strain to limits of ±4.5%. This ductility property is of benefit for potential use in the design of energy absorbing devices for large deformation events such as earthquakes.

---

* Presenting Author, Mechanical Engineer, (410) 267-2112

INTRODUCTION

This paper reviews an experimental program which involved the testing of a nickel-titanium shape memory alloy, often referred to as Nitinol (for NIckel-TItanium Naval Ordinance Lab, where it was first discovered). A number of efforts have been devoted to the study of the material behavior of shape memory alloys (SMAs) in either tension or compression. Some of these include [1, 2, 3]. Most studies have involved tensile material characterization tests applied to thin wire samples under conditions of varying temperature, material composition, and heat treatment. Such studies usually focus on phase transformation phenomena and associated deformation behavior for some fixed rate of deformation or change in temperature. In [3] the changing characteristics of superelastic hysteresis in Nitinol were examined after repeated tensile cycling up to 100 cycles. The study in [3] used a constant strain rate for loading and unloading of samples throughout the test program and showed that a fatigue of tensile hysteresis exists above the threshold stress for stress-induced martensite (SIM) formation.

In earthquake engineering energy absorbing devices, the peak levels of strain which can be induced by seismic activity are typically large, extending well into the inelastic range. In addition the strain histories are fully cyclic with non-constant rates of loading. Therefore a program of material characterization was undertaken to evaluate the fully cyclic hysteresis of SMAs to strain levels of ±4.5%. Other work pertaining to the effect of strain rate on the material response of SMAs undergoing fully cyclic large deformation had not been reported in the literature during the period of this research. Thus a program of experimental characterization was undertaken to achieve two goals:

1. Develop uniaxial, fully cyclic hysteresis patterns based upon testing under strain control for the Nitinol SMA to various strain levels.

2. Examine the effect of the applied strain rate on the material response in the fully cyclic loading condition.

The data obtained in Items 1 and 2 also allowed for a comparison with an SMA model from [4]. Studies pertaining to experimental shear characterization or biaxial testing were not pursued in this work and need to be done [5].

Nitinol is perhaps the best known of the SMAs and it is used in a variety of applications (e.g. see [6]). The material response characteristics of SMAs can vary depending on alloy composition, heat treatment and temperature. The basic behavior of the SMA is shown in Fig. 1. The first hysteresis loop (Fig. 1a) has a large area which results from twinning of the martensite microstructure under applied stress. It should be noted that the important transformation temperatures are M_s, M_f, A_s, and A_f, which are the martensite start temperature, martensite finish temperature, austenite start temperature, and austenite finish temperature, respectively. The hysteresis in Fig. 1a is exhibited when $T < M_f$.

The second hysteresis loop (Fig. 1b) is often referred to as superelastic material behavior, and occurs when $T > A_f$. In this material response the unloaded virgin material possesses a stable
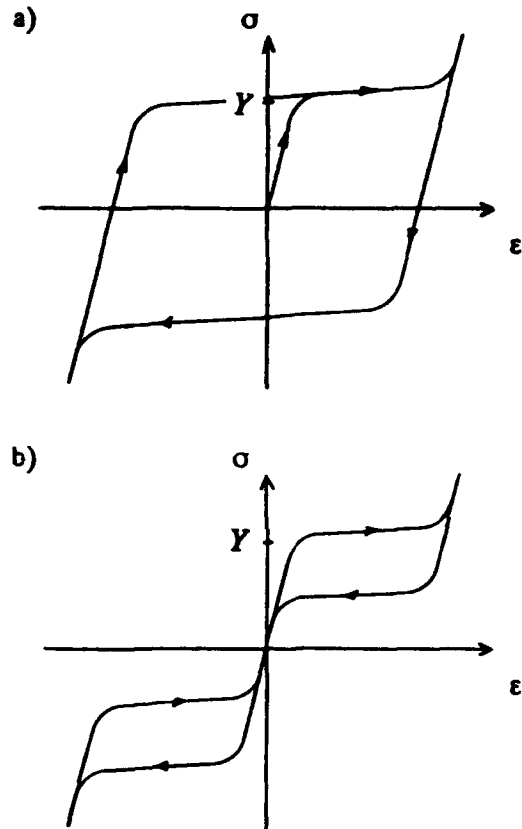
Fig. 1 Schematic stress-strain curves for shape memory alloys

(a) at temperatures below M_f: twinning hysteresis

(b) at temperatures above A_f: superelasticity

austenitic microstructure. Upon applying a stress the austenite is loaded in an elastic manner until a threshold stress as reached whereupon a stress-induced phase transformation begins. Specifically, the austenite is transformed to martensite at stresses above the threshold stress, and causes a long loading stress plateau to develop in the stress-strsin curve. Thus the onset of the phase transformation is also accompanied by a reduction in stiffness giving the appearance of plastic yielding and inelastic deformation. This stress-induced martensite (SIM) is stable due to the applied stress. As unloading is initiated the martensite undergoes a reverse transformation back to austenite. This reverse transformation occurs because the SIM is stable only due to the presence of the applied stress. As such the original undeformed shape will be returned when unloading is complete. The reverse transformation occurs on a lower stress plateau and hysteresis manifested. This potential for absorption of energy may be very useful for the damping of earthquake-induced structural vibration and was the motivation for much of this research.

Some basic mechanical properties of Nitinol are pointed out in Table 1. The high ultimate stress and large elongation at fracture are good properties for an earthquake engineering material to possess. There are however two inhibiting factors regarding the use of Nitinol as an earthquake engineering material. The first is its cost; approximately \$150/lb which is almost six times more expensive than other SMAs (such as Cu based SMAs). The second is its resistance to machining. The aspect of machining will be discussed in detail in a following paragraph. Despite these drawbacks the Nitinol material was nevertheless tested in this research as the advantageous material properties of superelasticity, ductili:y, and high strength are attractive features for application in the fields of base isolation and structural damping. Also, higher material costs may be justified if effective devices can be fabricated for earthquake protection.

Table 1: Selected Properties of Two Shape Memory Alloys

ITEM	UNIT	Ni-Ti	Cu-Zn-Al
Elastic Modulus	10^6 psi	4 - 12	10 - 12
Yield Stress (@ .2%)	10^3 psi	10 - 100	11 - 51
Ultimate Stress	10^3 psi	130	90
Elongation @ Fracture	%	40 - 50	10 - 15
Fatigue Strength (N=10^6)	10^3 psi	51	39
Material Damping Capacity (@ ε amplitude of 10^{-5}	SDC-%	15	30

In the experimental testing of Nitinol, MTS (Mechanical Testing System) servo-controlled electrohydraulic equipment was used for two separate programs of tests. The closed loop servo-controlled axial machine was used in conjunction with a PC based OPTILOG data acquisition system. The MTS machine was used in uniaxial tests on samples which were stressed and strained mechanically using feedback control of either load, strain, or displacement. Loads and displacements were measured by internal electronics. All test sample strain measurements were made using an MTS extensometer, Model 11B-20. This extensometer was able to accurately measure the average strain over a one inch region of the sample test section. During all tests, the OPTILOG data acquisition system received voltage signals from the MTS system

which represented load, strain, and displacement readings. These electronic voltage signals were then converted to appropriate mechanical measurements and subsequently stored computer files.

The first program of material characterization testing involved uniaxial load-unload tests in tension only. These tests were carried out using displacement control. Thus, the first series of tests did not involve fully cyclic loading. These were conducted to determine the effect of heat treatment on the tensile response of Nitinol. These tests also gave preliminary estimates of the elastic modulus and initial tensile yield point for SIM. The load-unload tests were applied to standard tensile-type samples of Nitinol.

The second program of material characterization testing involved fully cyclic strain controlled testing of button-ended Nitinol samples. These tests produced data for the fully cyclic tension-compression hysteretic response of Nitinol to various levels of peak strain. These cyclic tests were also carried out using selected strain-rates to evaluate Nitinol for rate effects in its mechanical response.

All Nitinol test samples were machined from a raw stock of cylindrical bar having a 19/32 inch diameter. The composition of the received material was as follows: Ti - 50.8 atom% Ni in a cold worked condition. This stock was purchased from Raychem Corporation in Menlo Park California. The Nitinol stock was extremely hard and abrasive in machining operations. Triple-coated carbide inserts with a positive relief angle were required for the lathe cutting tools. Lathe turning operations required the application of a positive feedrate and high feed pressure in conjunction with a stiff (heavy) tool holding fixture.

HEAT TREATMENT PROCEDURES AND AXIAL TENSION TESTS

It was known at the outset that the test samples would need to be heat treated prior to mechanical testing. It was also known that variation in heat treatment would lead to a variation in the ultimate mechanical behavior. Measurement of the SMA superelastic material response was a target objective due to the beneficial properties which are associated with this response. Therefore selection of a heat treatment to achieve the superelastic response was pursued in conjunction with uniaxial tests. A technical paper from Raychem Corp. [7] was helpful in the selection of the heat treatment which was ultimately applied to the Nitinol samples.

In the heat treatment of Nitinol, the level of annealing and ageing temperatures, as well as the annealing and ageing times are known to be factors affecting the stress-strain material response characteristics. The ageing treatment has the effect of decomposing Nickel rich alloys through a series of more stable compounds: $Ni_{14}Ti_{11}$, Ni_4Ti_3, Ni_3Ti_2, and finally Ni_3Ti [7]. These precipitates effectively strengthen the Ni-Ti matrix and augment the superelastic response. However they may also have the adverse effect of shifting the transformation temperature away from that which is desired in an application. In the experiments conducted as part of this dissertation research, it was found that the heat treatment which was necessary to approach the superelastic material response involved an annealing treatment followed immediately by a water quench and then an ageing treatment also followed immediately by a water quench.

For annealing treatments which were carried out at high temperatures ($T > 500$ °C) an environment was needed so that corrosion of samples could be avoided. A suitable annealing environment was found to be a salt bath containing Tempering Salt A from Heat Bath Corporation. This salt is a mixture of nitrates and nitrites and was found to give an excellent non-corrosive and uniform temperature environment for annealing of Nitinol. The lower temperature ageing treatments were carried out in a conventional air furnace.

The results of four different tension tests carried out using displacement control will now be discussed. In these tests, each end-tabbed sample was loaded in tension at a constant displacement rate and then unloaded at the same rate to zero stress. These results will show the effect of heat treatment on the material behavior as well as the associated mechanical responses which were achieved. First refer to Fig. 2. The information given above the plot of the stress-strain response gives the heat treatment which was applied to the sample prior to the test. For the experimental response of Fig. 2, the test sample was given a low temperature heat treatment involving annealing only. The annealing temperature was 385 °C and was held for 30 min. after which the sample was quenched.

The uniaxial load-unload tensile test which was then applied was run under displacement control out to a maximum strain of 3.7% at a displacement rate of $\dot{\delta} = 1.6 \times 10^{-4}$ in/sec. For the loading process, the elastic modulus, E, is calculated as 3×10^6 psi. As the sample enters into the inelastic range, the transition proceeds along a smoothly changing curve without passing through a sharply defined yield point. Upon unloading from the maximum strain level, the slope of the stress-strain curve shown in Fig. 2 is initially equal to the slope of the elastic loading branch, as expected. However, upon continued unloading to zero stress there is a reduction in slope which is referred to as the springback effect and is associated with pseudoelastic behavior. Pseudoelasticity is the term generally used when referring to any nonlinearity in the unloading curve of the stress-strain diagram wherein more strain is recovered than that associated with purely elastic unloading [7]. The term superelasticity is used more specifically with pseudoelastic materials which display an unloading plateau stress such that the springback of strain proceeds completely back (or nearly so) to the undeformed geometry. Due to the low modulus, smooth transition to inelasticity, and small springback, it is believed that a mixed phase transformation process took place involving martensite only. Thus for superelastic behavior of the Ti-50.8 at% Ni composition used in this research, a heat treatment which increases the amount of springback from that shown in Fig. 2 was required.

Further heat treatments based upon recommendations from [7] were carried out and then followed by uniaxial load-unload tensile tests. The most profound springback was exhibited after heat treatment processes involving both annealing and ageing treatments. An annealing treatment of 650 °C for 30 minutes followed by a water quench and a subsequent ageing treatment was found to significantly improve the effect of springback in the response of the Nitinol compound. From Fig. 3 it is seen that the material response approached that of superelasticity following ageing at 325 °C for 30 minutes and quenching. In the recorded material response a much more profound transition from elastic to inelastic deformation is observed. The yield stress is $Y \approx$ 45000 psi. Computation of the elastic and inelastic moduli reveals that $E \approx 10 \times 10^6$ psi and $E_y \approx$ 200×10^3 psi. Notice in Fig. 3 that the springback effect is significant. The sample was strained to

Re-Heat Treatment : 385 deg. C for 1/2 hr.

Water Quench

$$\delta \;=\; (.075/T) \; * \; t \quad\quad (T \;=\; 8 \text{ min})$$

Test Section Diameter: D = .249 in

Test Section Length: L = 1.75 in
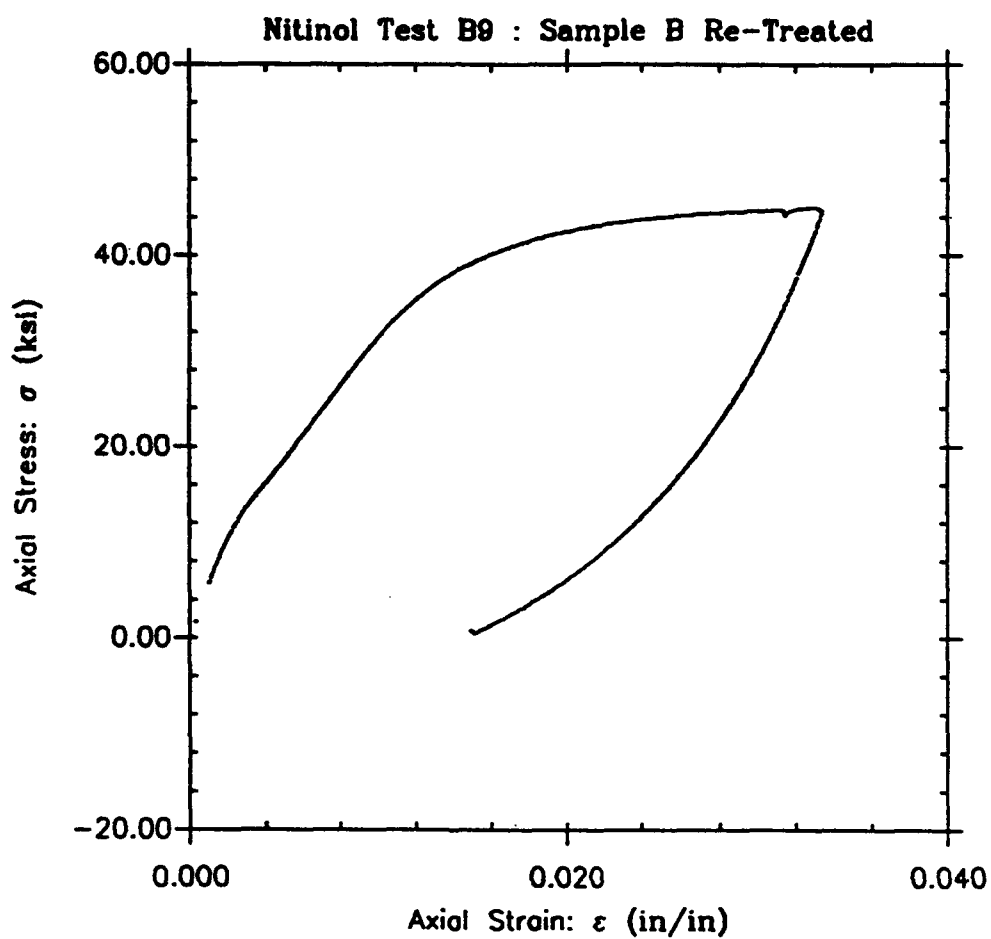
Fig. 2 Tensile load-unload test of Nitinol using displacement control

Re-Heat Treatment : 650 C 1/2 hr. (NaCl), W.Q.

: 325 C 30 min. (Air), W.Q.

$\delta = (.1125/T) * t$ (T = 12.8 min.)

Test Section Diameter: D = .249 in

Test Section Length: L = 1.75 in
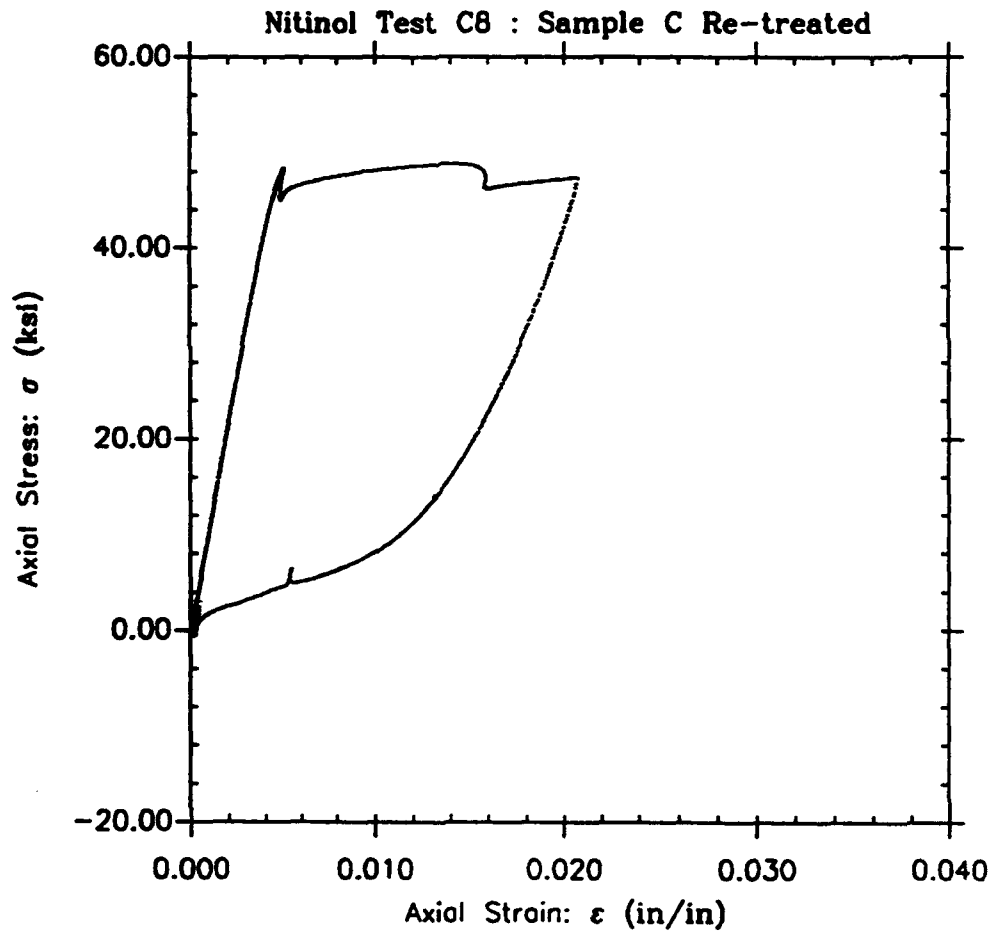
Fig. 3 Load-unload response of Nitinol for a higher annealing temperature

2.1%, and recovery of strain following unloading was essentially complete with no detectable residual strain. The response of the material is short of the superelastic response however since a well defined unloading stress plateau is absent.

Mechanical responses which were obtained during the course of similar tensile tests for variations of heat treatment were unable to attain a clearly defined superelastic response. The cause of this problem is most likely related to the composition of the material. Since the composition is somewhat rich in Nickel, A_f is likely to be higher than room temperature. Recall that A_f is the temperature above which the microstructure is fully austenitic. Differential scanning calorimeter tests were carried out on small Nitinol test samples to test this hypothesis. These tests were conducted at Memry, Inc. with the help of Dr. L. McD. Schetky, Chief Scientist of the company. The results of these tests are as follows:

| Without Heat Treatment: | $A_s = -13\,°C$ | $A_f \approx 35\,°C$ |
| After 600 °C for 1 hr. | $A_s = 3\,°C$ | $A_f \approx 35\,°C$ |

Recall that A_s represents the temperature at which austenite starts to form in the microstructure.

Thus it is seen that the annealing treatment given above has the effect of increasing A_s while giving little change to A_f. Since A_f is well above room temperature the microstructure was not fully austenitic, and a fully superelastic response at room temperature was impossible. However, it was found that through the use of a specific heat treatment the effect of pseudoelastic springback was enhanced to the point wherein fully cyclic hysteresis approached the response seen in superelastic materials. The specific heat treatment range which was used to achieve this end is as follows:

| Annealing Treatment : | 630 - 650 °C, Water Quench |
| Ageing Treatment : | 325 - 350 °C, Water Quench |

The tensile tests which have been discussed here were all carried out using a constant displacement rate for both loading and unloading conditions. In the displacement control tests, samples were found to have a greatly varying strain rate associated with their mechanical response. Since the constant displacement rate did not produce a constant strain rate, use of strain control was mandatory for fully cyclic tests.

CYCLIC AXIAL TESTS ON NITINOL

Cyclic tension-compression testing of Nitinol was carried out using button-ended test samples. These samples were clamped in a split-ring fixture and attached to the MTS axial machine. The design of the button-ended test sample was adequate such that compression buckling was avoided. All samples were heat-treated prior to testing as specified in the last section.

A total of four samples (samples F, G, H, and I) were used in fully cyclic tests. Following initial tests, some samples were re-heat treated and used again in subsequent tests. This recycling of test samples was possible due to the utilization of the memory effect which restores stress induced changes to the sample microstructure via re-application of the original heat treatment.

Axial strains were measured using an MTS strain extensometer, Model 11B-20, which is highly accurate to strain levels of ± 15% over a one inch gage length. In addition, the extensometer is the key instrument for feedback control of strain when operating in the strain control mode. Obviously strain control is the best means of carrying out such cyclic tests. In each cyclic test which was conducted, strain was applied to the sample using ramp loading. This gave a constant strain rate during the loading and unloading processes. In this manner strain rate effects may be evaluated when reducing the data from a variety of different tests.

The first result for cyclic loading of Nitinol pertains to Sample F and is shown in Fig. 4 for Nitinol Test F2. This figure shows two successive cycles of strain controlled loading to different peak strains. The first cycle is given in the inner hysteresis loop wherein the sample was cycled between strain limits of -1.5% and +1.5% using ramp strain loading. Each ramp segment was applied over 500 seconds thus corresponding to a strain rate of $3x10^{-5}$ sec^{-1}. The second cycle of strain applied to the sample during the test is shown in the figure as the outer hysteresis loop. The strain limits for this cycle are ± 2% with a strain rate of $4x10^{-5}$ sec^{-1}. The strain histories for each of these two cycles are given in Fig. 5 and show the ramp loading which was used. It is clear that this mode of strain control gave well defined, constant rates of strain during loading, unloading, and reloading. The use of a different peak strain for the second cycle shows that the material behavior in the second cycle is consistent with that of the first with no apparent plastic deformation. This is seen by noting that there is there is very little residual strain at zero stress following the second full cycle of loading.

In Fig. 4 the shape of hysteretic response is much different than the hysteretic responses of steel, aluminum, or other metals which exhibit plastic deformation once past the proportional limit. The shape exhibited here is unique to the behavior of SMAs and in this case closely approaches a superelastic response. Indeed, note that following two full cycles of relatively large strain deformation, little or no residual strain is detectable. After unloading from the peak strains in either tension or compression, a profound springback of strain takes place. In tension, when zero stress is reached during the unloading process, there still exists a finite amount of residual strain in the test sample, approximately .35%. However, upon continued unloading of strain (through the application of a small compressive force) the remaining amount of residual strain is recovered. Then, compressive strain loading of the sample proceeds along an elastic path as though the sample was in its initial (or virgin) state. This aspect of the hysteretic behavior is repeated during the second cycle of strain loading to strain limits of ± 2%. Thus, during cyclic loading, reloading of the sample from the completely unloaded state takes place along a common elastic line which passes through the origin of the stress-strain coordinates. This line corresponds to the elastic loading line of a virgin sample possessing an identical material composition and heat treatment.

Re-Heat Treatment: 630 C 1/2 hr. (NaCl) W.Q.

: 325 C 30 min (Air) W.Q.

ε Limits : -.015/.015, -.02/.02 (Ramp Time = 500 sec)

Test Section Diameter: D = .40 in

Extensometer Gage Length: L = 1.0 in
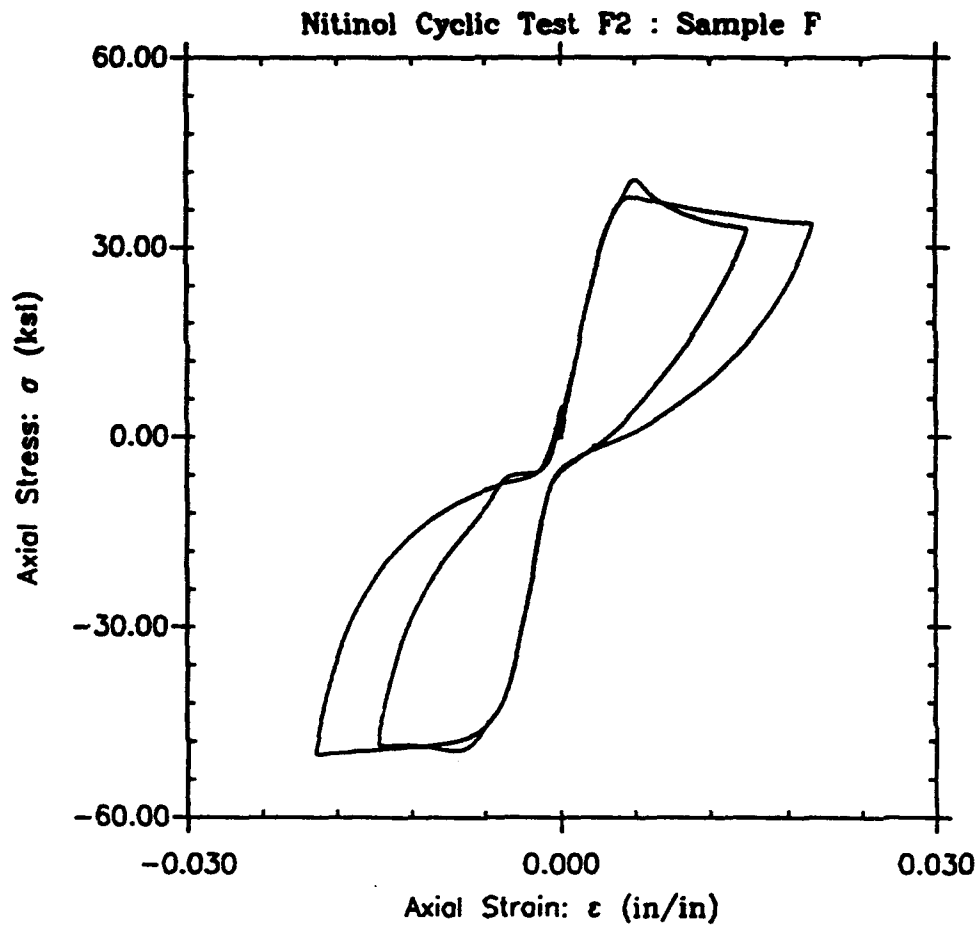
Fig. 4 Two cycles of tension-compression hysteresis for heat treated Nitinol
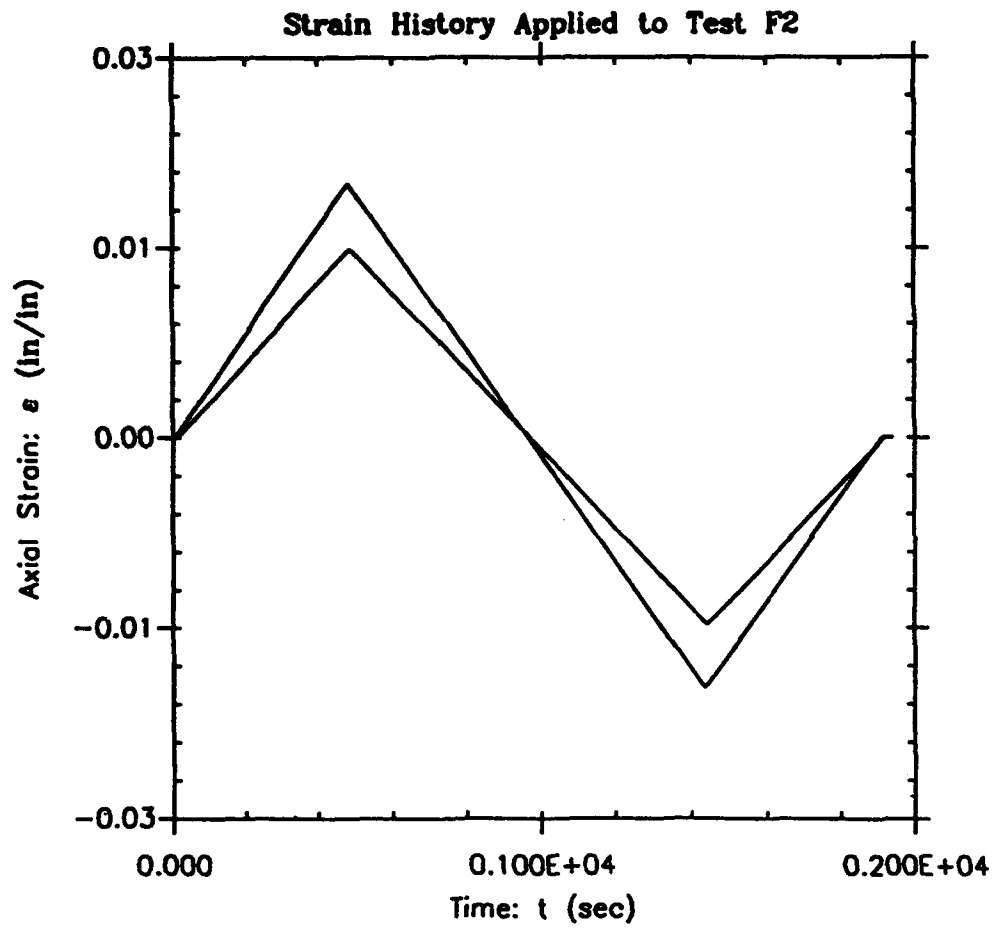
Fig. 5 Ramp loading and unloading used in Test F2: constant strain rate

We will use the word "yield" rather loosely here. The term "yield point" as it applies to SMAs actually corresponds to the stress level at which stress induced phase transformations take place in the material and has nothing to do with plastic deformation. Nevertheless, the generic term "yield" will be retained for the sake of simplicity in this discussion. Inspection of Fig. 4 reveals that the yield points in tension and compression are not the same. During the course of the first cycle, the yield point (corresponding to a .2% offset in strain) in compression exceeds the yield point in tension by 7200 psi. Also, compressive stress levels at peak strains are greater than corresponding tensile stress levels by as much as 16 ksi. These results agree with the findings of Wasilewski [1] which stemmed from separate tests on compressive and tensile Ni-Ti samples for monotonic uniaxial behavior.

Another aspect of the mechanical response which was observed in Fig. 4 is the stress relaxation which occurred following tensile yield. Reports from the literature pertaining to this observed behavior in Nitinol were not found during the course of this research. Similar behavior following initial tensile yield is reported for A-36 steel in [8]. But for steel this effect is attributed to a yield point instability that results from rate dependence of the material combined with geometrical effects associated with sample mounting and alignment. For the behavior of Nitinol in Fig. 4 the relaxation phenomenon is repeated in the second cycle of deformation although it is less pronounced. This aspect of the mechanical response will be addressed again as it pertains to additional test results yet to be discussed.

Next consider a case where repeated cycles of strain were applied as shown in Fig. 6 for the response of Sample G in Test G1. The strain limits were ± 1.5% and strain was applied at the rate of 7.5×10^{-5} sec^{-1}. In this test the hysteresis loop is seen to shift by small increments for each repeated cycle. The trend of this shifting process is indicated by arrows for cycles 2 through 5. The first cycle is indicated separately by the number 1. Note that a relaxation in stress again occurs for deformation past the peak stress at yield in tension. Also the first cycle of the hysteresis pattern differs slightly in its shape as compared to the subsequent cycles 2-5. Furthermore, when examining the tensile quadrant of the plot, the position of the first cycle is not consistent with the trend of hysteresis loop "shifting". This indicates that a hysteretic stabilization takes place during the first full cycle of strain loading. For cycles which follow thereafter any changes in shape which occur from one cycle to the next are incremental. Here, no major changes in shape are manifested once stabilization takes place. Similar stabilization of hysteresis loops are observed in cyclic deformation of metals into the plastic range (e.g. see [8])

Let us now re-examine the portion of the hysteresis loop pattern which corresponds to the inelastic behavior following yield in tension. The stress relaxation which follows yielding is most pronounced for the first cycle of deformation. In the cycles of strain loading which follow thereafter, relaxation of the stress in tension also occurred after the transition from elastic to inelastic behavior. This is indicated by the presence of a negative valued slope in the inelastic region. Thus, in contrast to the behavior of metals which undergo plastic deformation, stress relaxation following initial tensile yielding is maintained for repeated cycles of strain controlled deformation in Nitinol. However the level of stress relaxation is slightly reduced as additional cycles of strain are applied.

Heat Treatment: 650 C 30 min (NaCl) W.Q.

: 350 C 30 min (Air) W.Q.

ε Limits : -.015/.015, (Rate = .000075/sec)

Test Section Diameter: D = .400 in

Extensometer Gage Length: L = 1.0 in
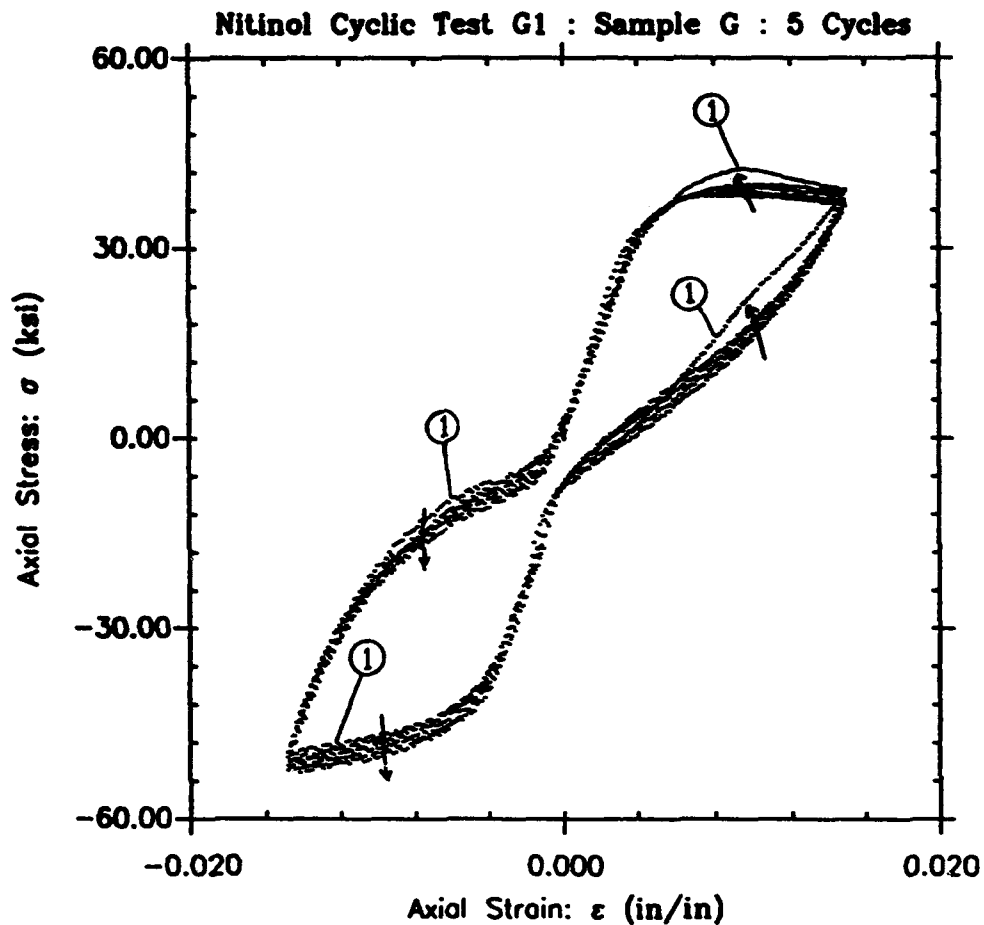
Fig. 6 Five cycle test of heat treated Nitinol using $\dot{\varepsilon} = 7.5 \times 10^{-5} \ sec^{-1}$

What happens to the mechanical response from the previous test for an increased rate of strain application? To address this question Test Sample G was re-heat treated and tested again for five new cycles of strain between the limits of ± 1.5%. However in this test (Test G2) shown in Fig. 7 the strain rate was doubled to 1.5×10^{-4} sec^{-1}. By comparing this response to the previous response it is immediately evident that the slope of the inelastic region is has increased. The yield points in tension and compression do not show a significant variation however. As in the case of Test G1, the first loop of the cyclic pattern is raised slightly above the stabilized loop in the tensile quadrant of the plot. Note that the stabilized loops of the cyclic hysteresis in Test G2 undergo very little variation in shape or position as cycling proceeds. Of all these points, the fact that the inelastic modulus has increased for an increased rate of strain application is the most important because it indicates a change in the overall hysteretic response. More will be said about this as we discuss other test results.

How do we know that the results for Test G2 shown in Fig. 7 are not affected by the previous cyclic test (G1)? First, the test sample had very little residual strain at the end of Test G1 ($\varepsilon = 1.0 \times 10^{-4}$ in/in). Also, the sample was re-heat treated prior to Test G2 thus re-establishing the initial microstructure via the shape memory effect. However, to properly demonstrate that the response given in Test G2 is valid, Sample G was re-heat treated again following the test and was then re-subjected to the conditions of Test G1. The response given previously in Fig. 6 is expected to be reproducible in this case due to the properties of the SMA. In Fig. 8 the mechanical response of Sample G in Test G3 is shown for two cycles of strain ranging between ± 1.5% at a strain rate of 7.5×10^{-5} sec^{-1} (as in Test G1). The first two cycles of Test G1 (Fig. 6) were reproduced in Test G3 as shown in Fig. 8. By superimposing Fig. 8 onto 6 careful comparisons show that the paths of the hysteresis loops in the stress strain diagram are nearly coincident. Thus the response in Fig. 7 is shown to be independent of any previous mechanical response by virtue of the heat treatment/memory effect which was applied prior to the test.

In the next series of figures, the mechanical responses of additional cyclic test samples (H, I) are shown for cases of larger strain. Note that strain rates of 1.0×10^{-4}, 1.5×10^{-4}, and 3.0×10^{-4} sec^{-1} were used to give a measure of the rate dependence of the material response. Sample H was cycled between strain limits of ± 3.0%. Sample I was cycled between strain limits of ± 4.5%. The cyclic responses of Sample H in Tests H1, H2, and H3 are shown in order of increasing strain rate in Figs. 9, 10, and 11 respectively. The cyclic responses of Sample I in Tests I1, I2, and I3 are shown in order of increasing strain rate in Figs. 12, 13, and 14 respectively. These results show that there are four primary effects exhibited in the mechanical response for conditions of increasing applied strain and increasing applied strain rate.

The first effect concerns the yield points in tension and compression. For all test results which have been discussed thus far, variations in the values of the yield stresses do not show a tendency to increase for the variations of strain rate considered herein. The second effect to be pointed out pertains to the changes of the slope of the inelastic response which occurs for increasing strain rates. By viewing the results of Tests H1, H2, and H3 successively in Figs. 9 to 11, the slopes of the inelastic portions of the of the hysteretic stress-strain loops are seen to

Heat Treatment: 650 C 30 min (NaCl) W.Q.

: 350 C 30 min (Air) W.Q.

ε Limits : -.015/.015, (Rate = .00015/sec)

Test Section Diameter: D = .400 in

Extensometer Gage Length: L = 1.0 in

Nitinol Cyclic Test G2 : Sample G : 5 Cycles
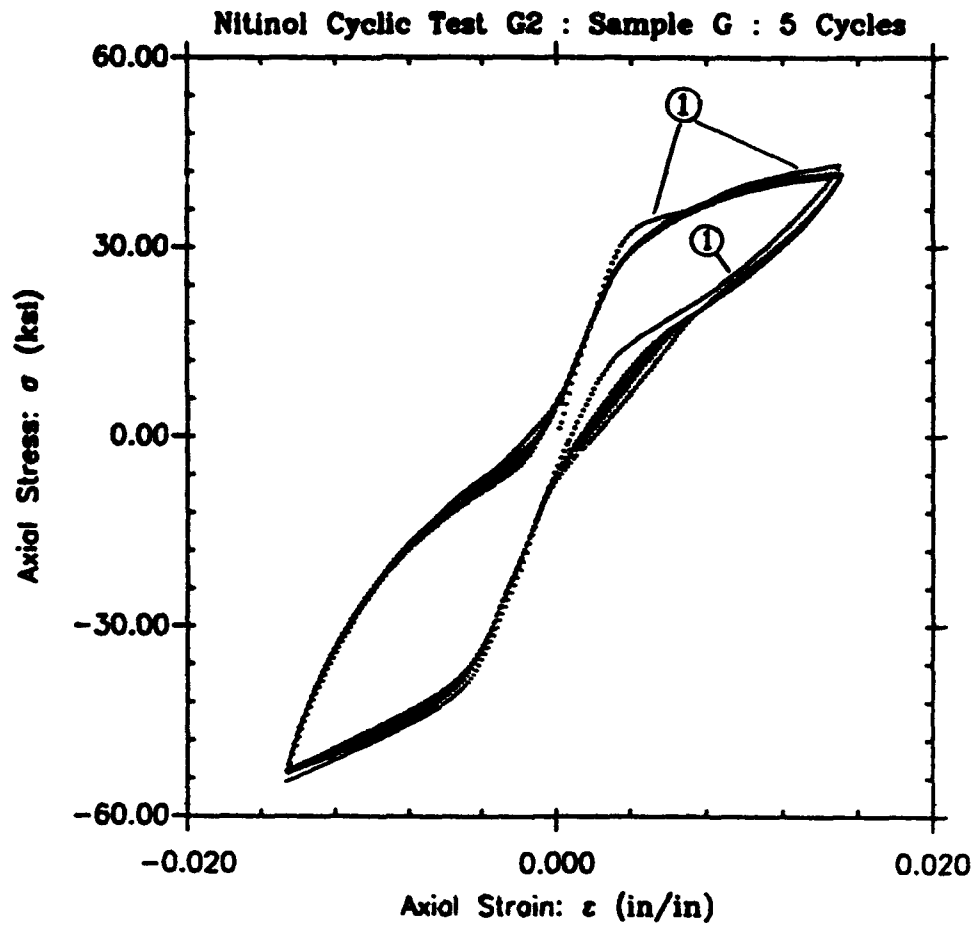
Fig. 7 Five cycle test of heat treated Nitinol using $\dot{\varepsilon} = 1.5 \times 10^{-4}$ sec^{-1}

Heat Treatment: 650 C 30 min (NaCl) W.Q.

: 350 C 30 min (Air) W.Q.

ε Limits : −.015/.015, (Rate = .000075/sec)

Test Section Diameter: D = .400 in

Extensometer Gage Length: L = 1.0 in
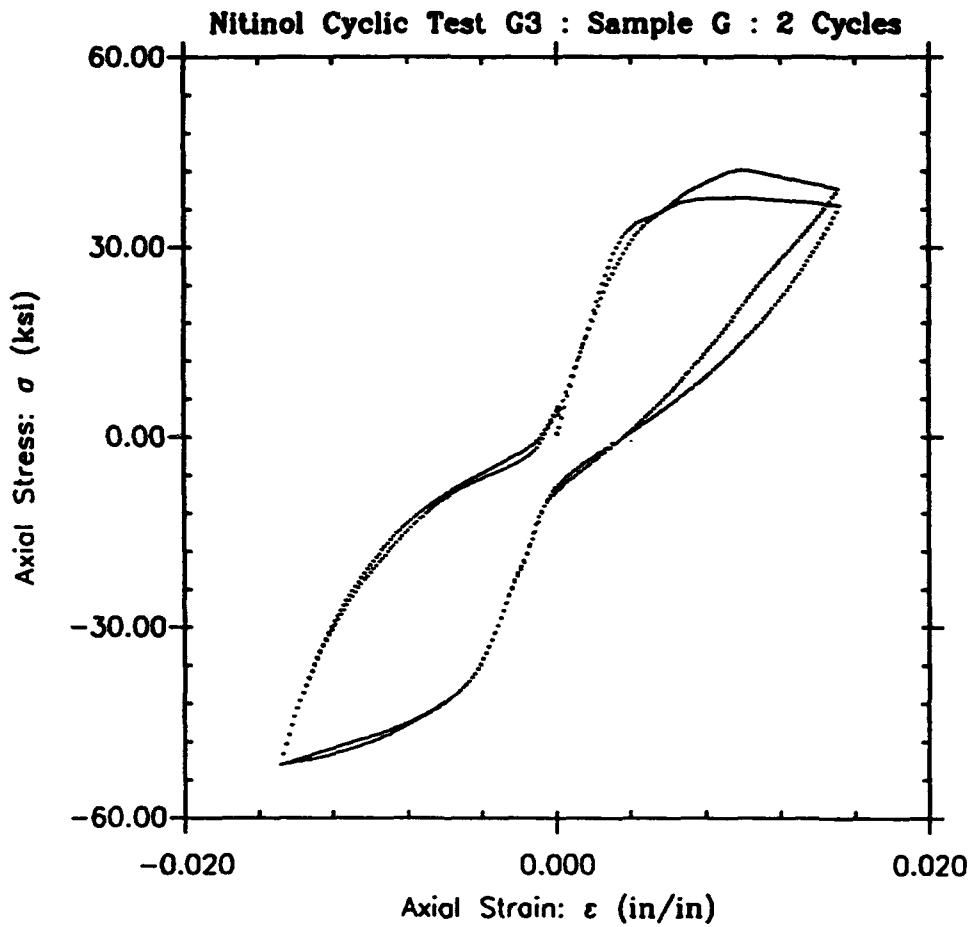
Fig. 8 Two cycle test to reproduce the response of Test G1

increase with increasing strain rate. The same observation can be made for Tests I1, I2, and I3 in Figs. 12 to 14.

The third effect is a by-product of the second effect just discussed. In the sequences of Figs. 9 to 11 and 12 to 14 the peak tensile and compressive stresses corresponding to peak strain levels increase with increasing applied strain rates. The result is much more dramatic, however, in compression. This is due to the fact that the inelastic modulus in compression is significantly larger than that in tension.

The fourth effect which is observed for this sequence of tests pertains to the variation in the shape of the hysteresis loop pattern. In the previously discussed tests of Figs. 5, 6, 7, and 8, the hysteresis loops were, for lack of a better term, tightly pinched. This pinching behavior resulted from the material response which was developed during unloading processes. As the test samples were unloaded from their peak strains, the descending branches of the hysteresis loops approached the origin of the stress-strain diagram. As such those responses approached the superelastic material response. For the sequence of tests just shown in Figs. 9 to 11 and 12 to 14, pinching of the hysteresis loops is less pronounced. Two factors contribute to this effect. The first and primary factor is the level of strain which is applied to the sample. Inspection of the figures shows that the hysteresis loop "opens up" more in the pinched region for Figs. 12 to 14 than for Figs. 9 to 11. That is to say, the hysteresis loop widens in the region of the origin of the stress-strain plot. As such the shape of the full hysteretic response of Nitinol is dependent not only on the strain rate, but also on the level of applied strain.

The second factor which contributes to the change in shape of the hysteresis loop is the level of strain rate applied in the test. Increasing rate of strain application will also tend to open up the hysteresis loop in the pinched region. This is shown by referring to Figs. 12 to 14 wherein the effect is most pronounced. This effect can also be seen, although less dramatically, in Figs. 9 to 11. It is possible that only a limited amount of pseudoelastic springback is available, and once past a certain strain limit load reversal is required to complete the reverse transformation thus widening the hysteresis loop. However a clearer metallurgical basis for these observations is required.

SUMMARY

We will now summarize the results obtained up to this point. For the tests discussed herein, and also for similar tests which were not discussed, two important points regarding strain rate behavior in Nitinol are noted:

1)   Axial tensile and compressive yield point behavior does not show a pronounced sensitivity to the varying levels of strain rate which were applied here.

2)   The inelastic uniaxial response of Nitinol is strongly rate dependent and affects the overall shape of the fully developed cyclic hysteresis.

These points are depicted graphically in Figs. 15 and 16 respectively.

Heat Treatment: 650 C 30 min (NaCl) W.Q.

: 350 C 30 min (Air) W.Q.

ε Limits : $-.03/.03$, (Rate = .0001/sec)

Test Section Diameter: D = .398 in

Extensometer Gage Length: L = 1.0 in

Nitinol Cyclic Test H1 : Sample H : 5 Cycles
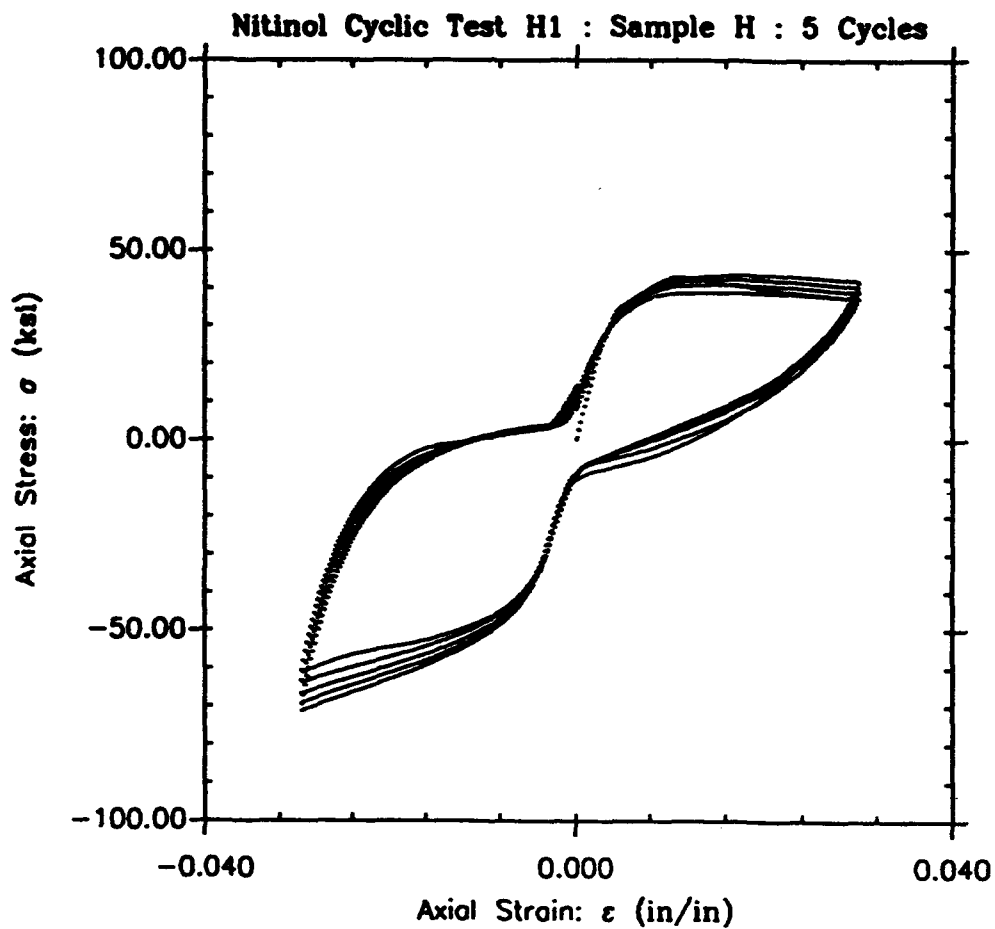
Fig. 9 Hysteretic response to $\pm 3\%$ strain at $\dot{\varepsilon} = 1.0 \times 10^{-4}$ sec^{-1}

Heat Treatment: 650 C 30 min (NaCl) W.Q.

: 350 C 30 min (Air) W.Q.

ε Limits : −.03/.03, (Rate = .00015/sec)

Test Section Diameter: D = .398 in

Extensometer Gage Length: L = 1.0 in

Nitinol Cyclic Test H2 : Sample H : 4 Cycles
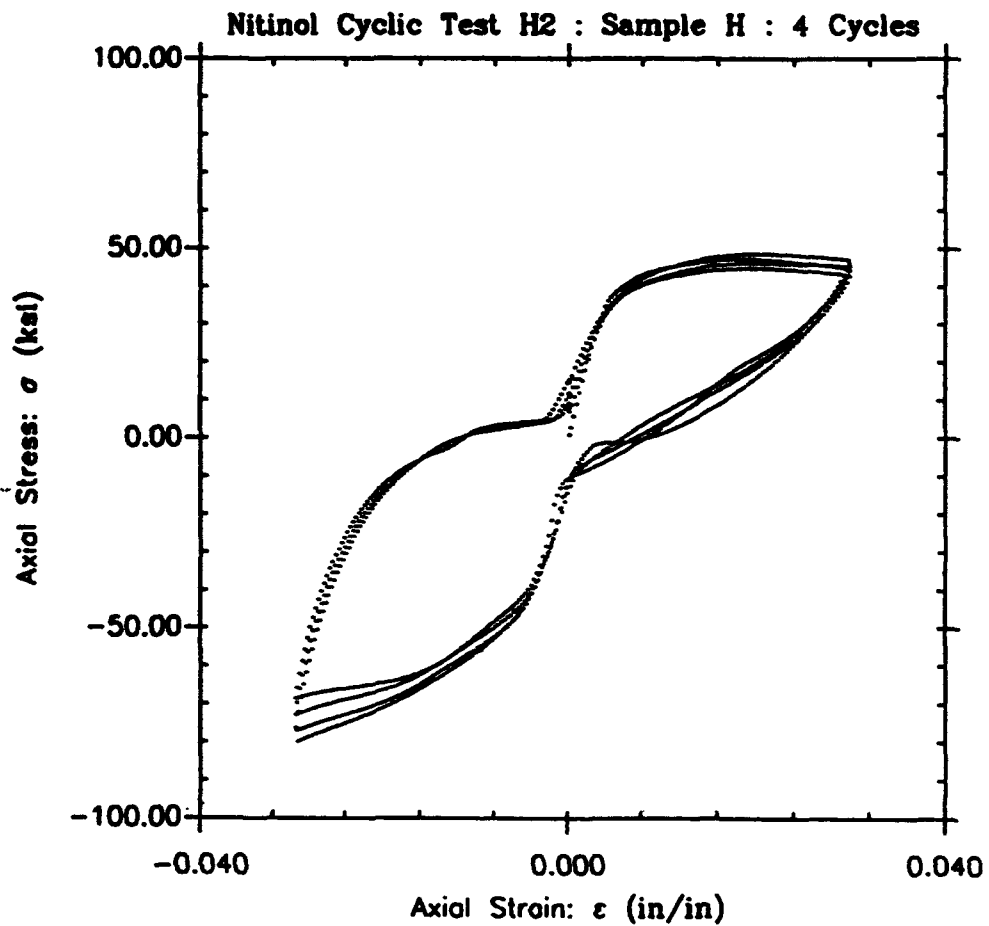
Fig. 10 Hysteretic response to ± 3% strain at $\dot{\varepsilon} = 1.5 \times 10^{-4}$ sec^{-1}

Heat Treatment: 650 C 30 min (NaCl) W.Q.

: 350 C 30 min (Air) W.Q.

ε Limits : $-.03/.03$, (Rate = .0003/sec)

Test Section Diameter: D = .398 in

Extensometer Gage Length: L = 1.0 in
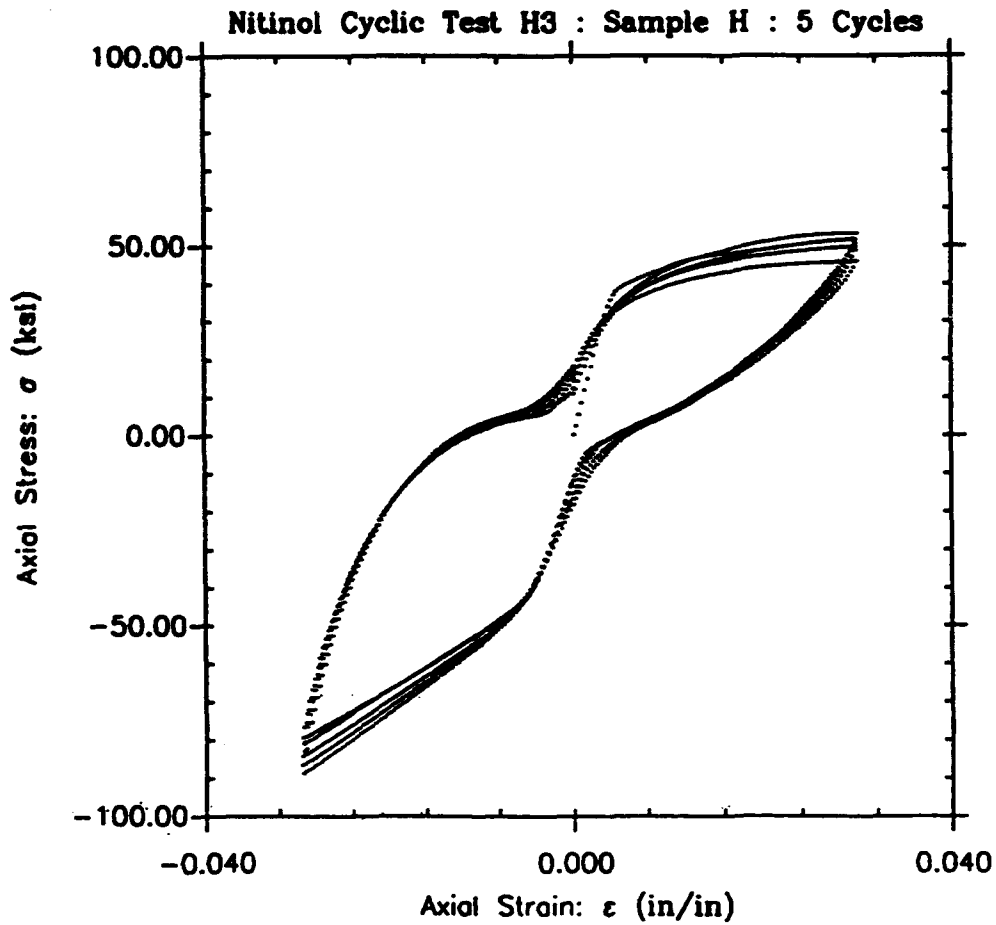
Fig. 11 Hysteretic response to ± 3% strain at $\dot{\varepsilon} = 3.0 \times 10^{-4}$ sec^{-1}

Heat Treatment: 650 C 30 min (NaCl) W.Q.

: 350 C 30 min (Air) W.Q.

ε Limits : $-.045/.045$, (Rate = .0001/sec)

Test Section Diameter: D = .400 in

Extensometer Gage Length: L = 1.0 in
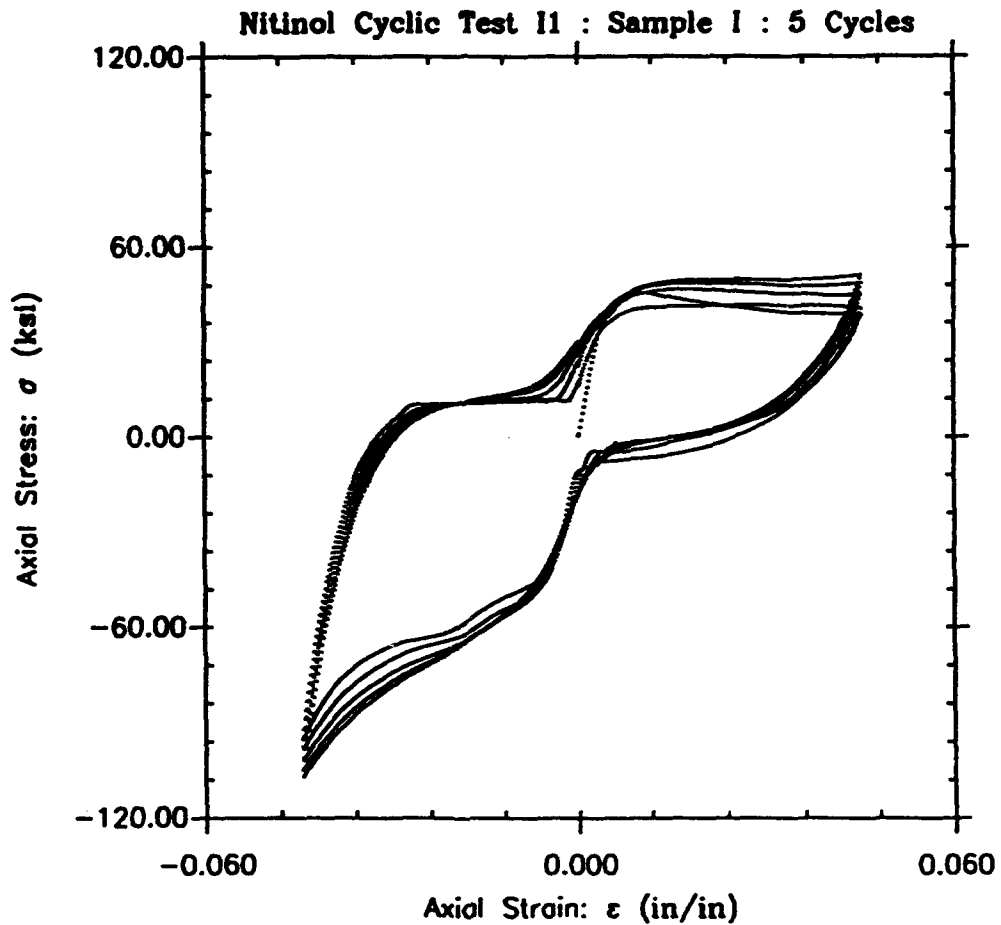
Fig. 12 Hysteretic response to ± 4.5% strain at $\dot{\varepsilon} = 1.0 \times 10^{-4}$ sec^{-1}

Heat Treatment: 650 C 30 min (NaCl) W.Q.

: 350 C 30 min (Air) W.Q.

ε Limits : $-.045/.045$, (Rate = .00015/sec)

Test Section Diameter: D = .400 in

Extensometer Gage Length: L = 1.0 in
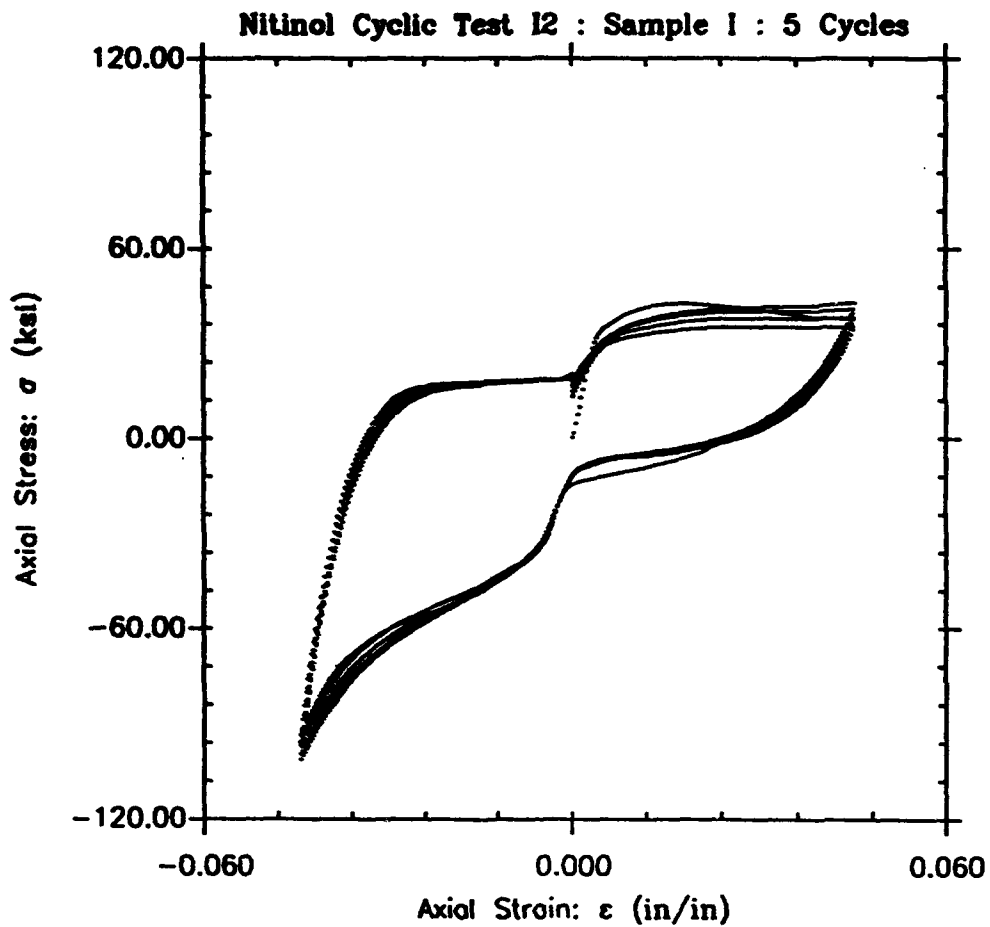
Fig. 13 Hysteretic response to $\pm 4.5\%$ strain at $\dot{\varepsilon} = 1.5 \times 10^{-4} \ sec^{-1}$

Heat Treatment: 650 C 30 min (NaCl) W.Q.

: 350 C 30 min (Air) W.Q.

ε Limits : -.045/.045, (Rate = .0003/sec)

Test Section Diameter: D = .400 in

Extensometer Gage Length: L = 1.0 in

Nitinol Cyclic Test 13 : Sample I : 3 Cycles
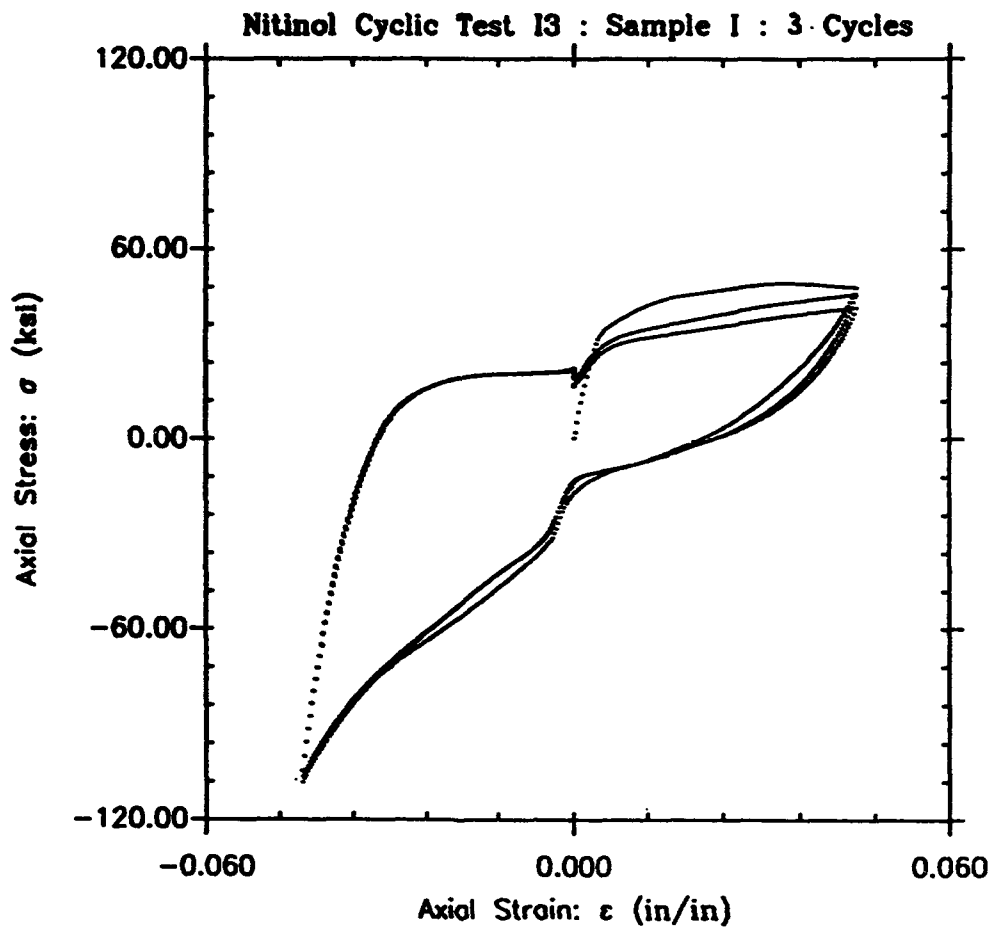
Fig. 14 Hysteretic response to $\pm$ 4.5% strain at $\dot{\varepsilon}$ = 3.0x10^{-4} sec^{-1}

Fig. 15 Tensile (□) and compressive (O) yield stresses vs. strain rate

△ Strain Limit of Test = 1.5%

◇ Strain Limit of Test = 2.0%

□ Strain Limit of Test = 3.0%

○ Strain Limit of Test = 4.5%

Tangent Modulus at 1.5% vs. Strain Rate : Exp. Res.

Least Squares : $y = a_\bullet + a_1 x$

$a_\bullet = -295.63$ ksi

$a_1 = 2537200.0$ ksi-sec

Corr. Coeff. $R = 0.83$

$R^2 = 0.69$
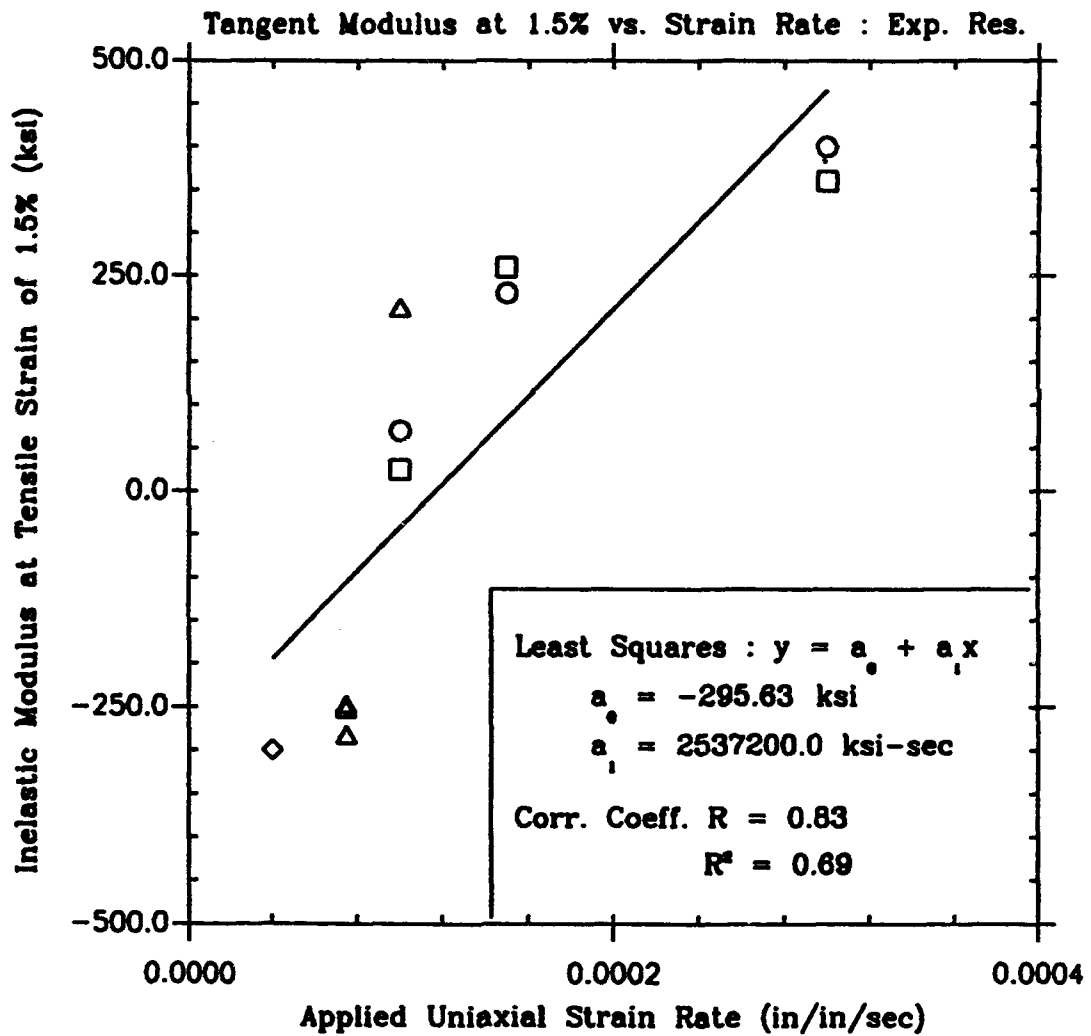
Fig. 16 Inelastic tensile modulus as a measure of shape of hysteresis

In Fig. 15 yield stresses (at .2% strain offset) in tension and compression are plotted versus the applied strain rate. The boxes indicate tensile yield points while the circles indicate compressive yield points. These experimental values do not indicate any pronounced sensitivity of the uniaxial yield point to strain rates varying in the range between 3×10^{-5} and 3×10^{-4} sec^{-1}. However, the data plotted in Fig. 15 shows that the measured compressive yield stresses were consistently larger in magnitude than their counterparts in tension.

A measure of the strain rate dependent shape of hysteresis is taken here as the inelastic modulus of Nitinol in tension. Inelastic moduli were measured using the slope of the line drawn tangent to the stress-strain curve at common tensile strains of 1.5%. The tangent lines were drawn to stress-strain curves of stabilized hysteresis loop patterns. For the sake of consistency, the second loop of each cyclic test was selected for all tangent modulus measurements. The results of this procedure are plotted in Fig. 16. Here, a line representing a least squares linear fit of the experimental data is shown as a solid line. A correlation coefficient of $R = 0.83$ was calculated for the data points of Fig. 16. Even though the data given here are not strongly correlated ($0.9 \leq R \leq 1$) the correlation is adequate to demonstrate an observed trend for the inelastic response. The indicated trend demonstrates a strong rate dependence of the inelastic response properties of Nitinol to the applied strain rates which were used in this research.

It should be noted that the strain rates which were used in these experimental studies are significantly less than actual (earthquake induced) strain rates developed in the energy absorbing devices of seismically protected structures. Higher strain rates were not used in these studies because only a limited number of test samples were available. Nevertheless, the responses of Nitinol given here show that this material has a strong potential for possible use in earthquake engineering energy absorbing applications. This is due to its ability to undergo deformation to large strain levels without succumbing to damage and fatigue resulting from plastic deformation. Also the elastic modulus of the material is high enough to give adequate stiffness for small strain levels. Ultimately, SMAs need to be characterized for cyclic hysteresis properties at larger strains and strain rates, both mechanically and metallurgically. SMA characterization studies also need to be made for cyclic shear and cyclic biaxial behavior.

REFERENCES

1.   Wasilewski, R.J., "The Effects of Applied Stress on the Martensitic Transformation in TiNi," *Metallurgical Transactions*, Vol. 2, November, 1971, pp. 2973-2981.

2.   Miyazaki, S., Otsuka, K., and Suzuki, Y., "Transformation Pseudoelasticity and Deformation Behavior in a Ti-50.6at%Ni Alloy," *Scripta Metallurgica*, Vol. 15, 1981, pp. 287-292.

3.   Miyazaki, S., Imai, Y., Igo, Y., and Oysuka, K., "Effect of Cyclic Deformation on the Pseudoel...icity Characteristics of Ti-Ni Alloys," *Metallurgical Transactions A*, Vol. 17A, January, 1986, pp. 115-120.

4.   Graesser, E.J. and Cozzarelli, F.A., "Shape Memory Alloys as New Materials For Aseismic Isolation," *Journal of Engineering Mechanics*, ASCE, Vol. 117, No. 11, 1991, pp. 2590-2608.

5.   Graesser, E.J. and Cozzarelli, F.A., "A Proposed Three-Dimensional Constitutive Model for Shape Memory Alloys," submitted to *Journal of Intelligent Material Systems and Structures*, 1993.

6.   Borden, T., "Shape Memory Alloys: Forming a Tight Fit," *Mechanical Engineering*, ASME, Vol. 113, No. 10, 1991, pp. .67-72.

7.   Duerig, T.W. and Zando, R., "An Engineer's Perspective of Pseudoelasticity," *Engineering Aspects of Shape Memory Alloys*, ed. by T.W. Duerig, K.N. Melton, D. Stöckel, and C.M. Wayman, Butterworth-Heinemann Ltd., 1990, pp. 369-393.

8.   Chang, K.C. and Lee, G.C., "Biaxial Properties of Structural Steel Under Nonproportional Loading," *Journal of Engineering Mechanics*, ASCE, Vol. 112, No. 8, 1986, pp. 792-805.

DESIGN AND SEISMIC TESTING OF SHAPE MEMORY STRUCTURAL DAMPERS

Peter R. Witting[1]
Department of Mechanical and Aerospace Engineering
State University of New York at Buffalo

Francis A. Cozzarelli
Department of Mechanical and Aerospace Engineering
State University of New York at Buffalo

Different damping designs using the shape memory effect in the alloy Cu-Zn-Al as the principle damping mechanism are examined to determine the best design. The mechanical tests of the finalized design is discussed. Seismic response characteristics of a model five story building, with and without added Cu-Zn-Al shape memory dampers are studied experimentally. The seismic response results of the building with added Cu-Zn-Al shape memory dampers are then compared with the studies of viscoelastic dampers tested on the same model five story building.

[1]State University of New York at Buffalo
Department of Mechanical and Aerospace Engineering
305 Jarvis Hall
Buffalo, New York 14260
716-645-2561

INTRODUCTION

The use of structural dampers and base isolators have been shown to greatly reduce the damage to a structure due to an earthquake [1,2,3,4,5]. The study of these devices is somewhat limited, in terms of the material used in the structural dampers and base isolator devices. Viscoelastic structural dampers have been studied in [1,5], and frictional structural dampers were studied in [2,3,4]. Rubber bearing base isolation devices have also been studied. These are, however, only a few of the many materials which may be used to create the vibration control desired during an earthquake. The emphasis in this study is to research the possible benefits, to passive structural vibration control techniques, of the relatively new class of materials, the shape memory alloy.

Constitutive relationS for the shape memory alloy (SMA) have been developed in [6,7,8,9,10]. In addition, the material properties of a few different shape memory alloys are explored in [11,12,13,14]. The objectives of this study were to design, build and test a structural damper which uses a shape memory alloy. The testing of the SMA damper included a study of the dynamic response of a 2/5 scale five-story steel frame structure with added SMA dampers. These results were then compared to viscoelastic dampers, which were tested on the same structure.

PSEUDOELASTICITY

A shape memory alloy (SMA) undergoes a reversible phase transformation or phase reorientation when deformed. In addition, the SMA can undergo a reversible change in geometry with a change in temperature, which is due to a phase transformation. Pseudoelasticity is the constitutive behavior which describes the above mentioned phenomena. In this study, however, we will only be concerned with stress induced pseudoelastic behavior.

There are two different classes of stress induced pseudoelastic behavior: large area hysteretic behavior and superelasticity. The difference between the two is due to differing A_f and M_f temperatures. The M_f temperature is the temperature below which the alloy has a body centered tetragonal (BCT) martensitic crystal structure. Conversely, above the A_f temperature the alloy has a body centered cubic (BCC) austenitic crystal structure. It should be pointed out that $A_f > M_f$. In addition, if the material temperature falls between A_f and M_f the material will have a mixture of both BCC and BCT crystal structures.

If a SMA at a temperature below its M_f temperature is cyclicly loaded, a large area hysteresis loop is formed. This hysteresis loop, however, is not formed by the dislocation glide mechanism typical of a plastically deforming metal. This loop is due to the growth, shrinkage and rotation of the martensitic crystals. This allows the SMA to undergo many more large strain high damping cycles than a typical plastically deforming metal. In addition to resistance to large strain fatigue, the material reverts back to the original crystal orientation and therefore to its original shape, if the temperature is raised above the A_f temperature. Thus the material exhibits a shape memory effect.

The superelastic constitutive model describes the stress-strain relation of a SMA at a temperature above the A_f temperature. At low stress levels, a material with superelastic properties will behave elastically. However, at some higher stress level, which depends on the material and its heat treatment, a phase transformation from BCC to BCT begins. This transformation will reduce the modulus of the material as seen in Fig. 1. Upon unloading, the material undergoes a reverse transformation at a lower stress level. The difference in the transformation stress level between loading and unloading is due to internal friction in the diffusionless phase transformation. Once the reverse phase transformation is complete, the material behaves elastically, and with complete unloading of the material, a complete recovery is ideally seen. The complete cycle is shown in Fig. 1.
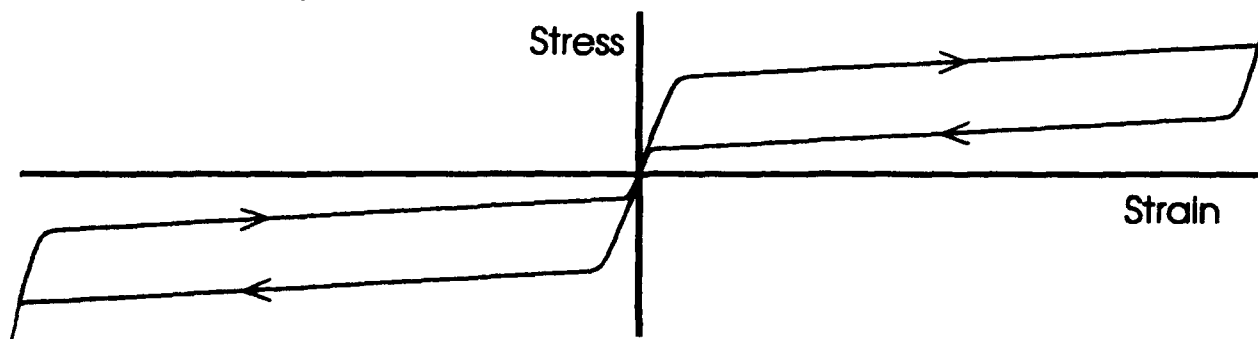
Fig. 1 Superelastic Stress Strain Relationship

REQUIREMENTS OF SMA DAMPER

The essential idea behind the damper design was to create a structural damper that would take advantage of the Cu-Zn-Al superelastic material properties to damp the building's motion and generate a centering force on the building. The Cu-Zn-Al SMA was chosen because it not only has desirable material properties, but it is also easily machined and relatively inexpensive. The purpose of this form of a damper is to minimize the motion of the building during the earthquake, and to restore the building to its original position after the earthquake is over.

The dampers had to be designed to satisfy the requirements of a model five story building at the National Center for Earthquake Engineering Research, where the earthquake tests were performed. This model five story building was built by the joint U.S.-China Cooperative Research Program. The building was designed to allow different dampers to be installed in the cross bracing. Since the building is used for many tests, these tests must of course not damage the building. To prevent such damage, the maximum inter-story drift was limited to .25 inches. Furthermore, since we did not want to drastically change the natural frequency of the building, the maximum additional inter-story stiffness, due to the presence of the dampers, was set at 9000 lbs/inch maximum.

Along with constraints imposed by the building there were also some material constraints to be considered in the design. The maximum strain in the Cu-Zn-Al was set at 2% to guarantee that the material would not yield plastically. However the design had

to ensure that strains up to this 2% maximum would be induced, because larger energy absorbing shape memory hysteresis loops occur at the high strain levels.

SELECTING DAMPER DESIGN

Four designs for producing a damping device using Cu-Zn-Al were investigated. The designs' principal mechanisms were the bar in torsion, beam in bending, axially loaded beam and the clamped plate loaded in the center. In the comparison of these different types of devices, a linear constitutive law was used although it is quite clear that a nonlinear model would more accurately predict the behavior. However, it became clear, from the linear analysis to follow, which design would work the best. A nonlinear model was then used to more accurately determine the exact dimensions of the design.

In the following analysis, the shear and Young's moduli were estimated from tensile tests on Cu-Zn-Al [13]. The shear modulus was taken to be half the Young's modulus. The values gave a rough estimate of the performance of the damper, and was all that was needed to determine which design to use.

The first design considered was the Cu-Zn-Al annular plate clamped at the inside and outside edges. After an examination of the force deflection equation [15], with thicknesses and radii of Cu-Zn-Al washers that were practical to machine, it was found that the annular plate design was much too stiff and resulted in very small strains. The axially loaded beam was also found to be unsuitable, because the constraints of stiffness and strain would cause a beam, made from Cu-Zn-Al with the properties required by the building, to buckle.

The torsional bar and bending beam designs both could be made with suitable stiffness and desirable strains. Therefore an analysis comparing the energy absorbing capabilities of the two designs was completed in order to determine which design is best. Since larger strains clearly result in more energy absorbed during cyclic loading, the strain ranges ε_{low} to ε_{max} that contain 90% of the strain energy was compared between the two designs. Below is the development of the analysis for both the bending beam and torsional bar designs.

The bending beam design (Fig. 2) is clamped in the middle and at the outside edges. Note that the direction of the deflection of the damper (δ) is in the same direction as the applied force (F). The force-deflection equation in terms of the length of the beam (L), width of beam (B), height of beam (H), and modulus of Cu-Zn-Al (E) is [15]

$$F = \frac{2EBH^3}{L^3} \delta \qquad (1)$$

Due to the constraint of stiffness (S) imposed by the building, we shall ensure the proper stiffness S by setting it to the expression

$$S = \frac{2EBH^3}{L^3} \qquad (2)$$

Therefore the force deflection equation reduces to $F=S\delta$. The bending moment equation along the length of the beam [16] is

$$M(X) = \frac{F}{4}[2X-L] \qquad (3)$$

Combining the linear elastic constitutive law $\tau_{xx}=E\varepsilon_{xx}$, the strength of materials flexure formula, and the bending moment equation above, and then solving for the strain yields

$$e_{xx} = \frac{3Fy}{EBH^3}[2X-L] \qquad (4)$$
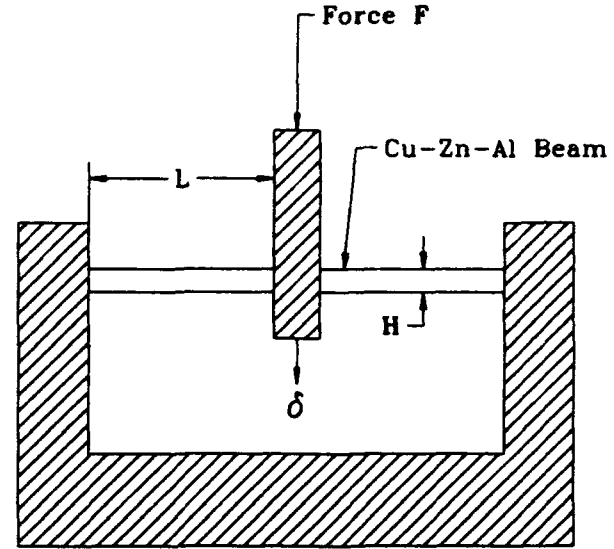
Fig. 2 Bending Beam Design

The maximum strain ε_{max} occurs at $x=L$, $y=H/2$, and the maximum force F equals $S\Delta$, where Δ is the maximum expected displacement of the damper. Substituting these values in Eq. (4) yields

$$e_{max} = \frac{3LS\Delta}{2EBH^2} \qquad (5)$$

Solving Eqs. (2) and (5) for B and H then yields

$$B = \frac{27S\Delta^3}{2E\,e_{max}^3 L^3} \qquad\qquad H = \frac{e_{max}L^2}{3\Delta} \qquad (6)$$

Substituting Eq. (6) back into Eq. (4) yields

$$e_{xx} = \frac{6\Delta(2x-L)y}{L^3} \qquad (7)$$

Eq. (6) and Eq. (7) allow the constraints of stiffness (S), maximum strain (ε_{max}), and maximum deflection (Δ) to be prescribed, so that the height (H) and thickness (B) of the beam is a function of L only.

The strain energy density is given by $U_o=\frac{1}{2}E\varepsilon^2_{xx}$. The strain energy function is symmetric in both the horizontal and vertical directions. Therefore, it is necessary to integrate over only one quarter of one of the beams, then multiply the result by eight. The integral of the strain energy is

$$U = 8\int_{x_{min}}^{x_{max}} \int_{y_{min}}^{y_{max}} \int_{z_{min}}^{z_{max}} \frac{1}{2}E\,e_{xx}^2\,dz\,dy\,dx \qquad (8)$$

In order to integrate over the region of high strain, the limits of integration must be

found. The region of high strain shall be defined as the region with strains between ε_{low} and ε_{max}. Since the strain is not a function of the z direction, the limits become $z_{min}=0$ and $z_{max}=B$. Clearly the end of the beam is the high limit of integration in the x direction thus $x_{max}=L$. The lower limit can be found by substituting into Eq. (7) the values $\varepsilon_{xx}=\varepsilon_{low}$ and $y=H/2$, and solving for x. Substituting Eq. (6) into the resulting expression yields

$$X_{min}=\frac{L}{4}\left[\frac{e_{low}}{e_{max}}+1\right]$$
(9)

The top of the beam is clearly the max limit in the y direction $y_{max}=H/2$. The lower limit can be found as a function of x by setting $\varepsilon_{xx}=\varepsilon_{wow}$ and solving for y. This limit becomes

$$y_{min}=\frac{L^3 e_{low}}{6\Delta(2x-L)}$$
(10)

Integrating Eq. (8) with the above limits and substituting $\beta=\varepsilon_{low}/\varepsilon_{max}$ yields

$$U=\frac{S\Delta^2}{2}[1-\beta^3+3\beta^3\ln(\beta)]$$
(11)

If $\varepsilon_{low}=0$ then $\beta=0$ and Eq. (11) simplifies to $U=\Delta^2 S/2$ which is the total energy of the system.

The strain energy of the torsional bar will now be investigated. The basic dimensions of the damper used in the design are the torsion arm length D, radius of torsion bar R, and length of torsion bar L (Fig. 3). Note that the torsion bar length L is defined as the distance between the torsion arm and the side grips as shown in the drawing of the torsional bar design (Fig. 3). The torsion arm length D is measured from the center of the torsion arm to the center of the pivot. The displacement δ is again in the same direction as the force F (Fig. 3).
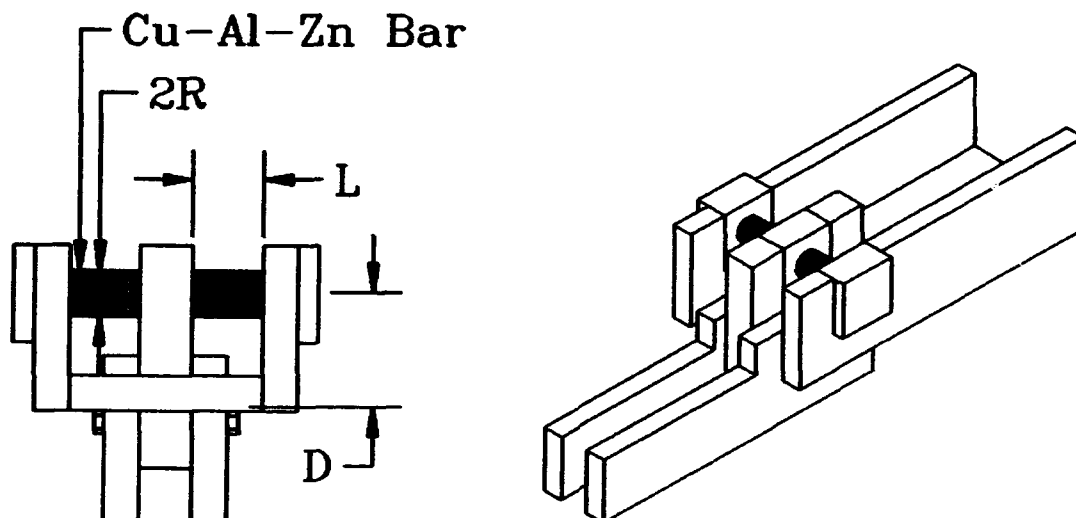
Fig. 3 Torsional Bar Design

The angle of twist θ due to the displacement δ is expected to be small, therefore $\delta=D\sin(\theta)\approx D\theta$. The equation for shear strain ε_{xy}, in terms of the L, D, δ and the radial distance from the center of the Cu-Zn-Al bar r, is

$$\varepsilon_{xy}=\frac{\theta r}{2L}=\frac{\delta r}{2LD} \tag{12}$$

Also, the equation for the force F on the damper in terms of L, D, δ and r is given by

$$F=\frac{\pi G R^4 \delta}{LD^2} \tag{13}$$

As before, the stiffness S is defined so that $F=S\delta$, giving

$$S=\frac{\pi G R^4}{LD^2} \tag{14}$$

The maximum shear strain occurs at $r=R$ when δ is equal to the maximum deflection allowed (Δ). Substitution into Eq. (12) yields

$$\varepsilon_{max}=\frac{\Delta R}{2LD} \tag{15}$$

Solving Eq. (14) and Eq. (15) for L and D yields

$$L=\frac{\Delta^2 S}{4\pi G R^2 \varepsilon_{max}^2}, \qquad D=\frac{2\pi G R^3 \varepsilon_{max}}{\Delta S} \tag{16}$$

Upon substitution of Eq. (16) into Eq. (12) the following simple expression for shear strain results

$$\varepsilon_{xy}=\frac{\varepsilon_{max} r}{R} \tag{17}$$

The equation for strain energy density is $U_o=2G\varepsilon_{xy}^2$. This equation must be integrated over the high strain region in a manner similar to the procedure used for the bending beam design. The strain is independent of the y and θ directions, so those limits become $y_{min}=0$, $y_{max}=L$, $\theta_{min}=0$ and $\theta_{max}=2\pi$. The maximum limit in the r direction is $r_{max}=R$. The minimum value of r can be found by substituting ε_{low} for ε_{xx} in Eq. (17); this limit then becomes $r_{low}=R\varepsilon_{low}/\varepsilon_{max}$. The total strain energy function, after using Eq. (16) to eliminate L, finally becomes

$$U=2\int_0^{2\pi}\int_0^{\frac{\Delta^2 S}{4\pi G R^2 \varepsilon_{max}^2}}\int_{\frac{R\varepsilon_{low}}{\varepsilon_{max}}}^R \frac{2G \varepsilon_{low}^2}{R^2}r^3 dr dy d\theta \tag{18}$$

Integrating and substituting $\beta=\varepsilon_{low}/\varepsilon_{max}$ yields

$$U=\frac{\Delta^2 S}{2}[1-\beta^4] \tag{19}$$

If $\varepsilon_{low}=0$ then $\beta=0$, and Eq. (19) simplifies to $U=\Delta^2 S/2$ which is the total energy put into the system.

The strain energy equations, Eq. (11) and Eq. (19) can be divided by $\Delta^2 S/2$ to yield the percent of the total strain energy $\Delta^2 S/2$ as a function of the strain range β integrated over. Fig. 4 is a comparative plot of the percent total strain energy vs the strain range β for the torsional bar and the bending beam designs. It can be seen from Fig. 4 that for any given β between 0 and 1 the percent of total strain energy contained within that region is higher for the torsional bar damper design. This means that more of the energy is put into higher strain regions in the torsional bar design than, the bending beam design. The larger strain results in a greater amount of energy absorbed, and therefore the torsional bar design apparently results in a more effective damper.
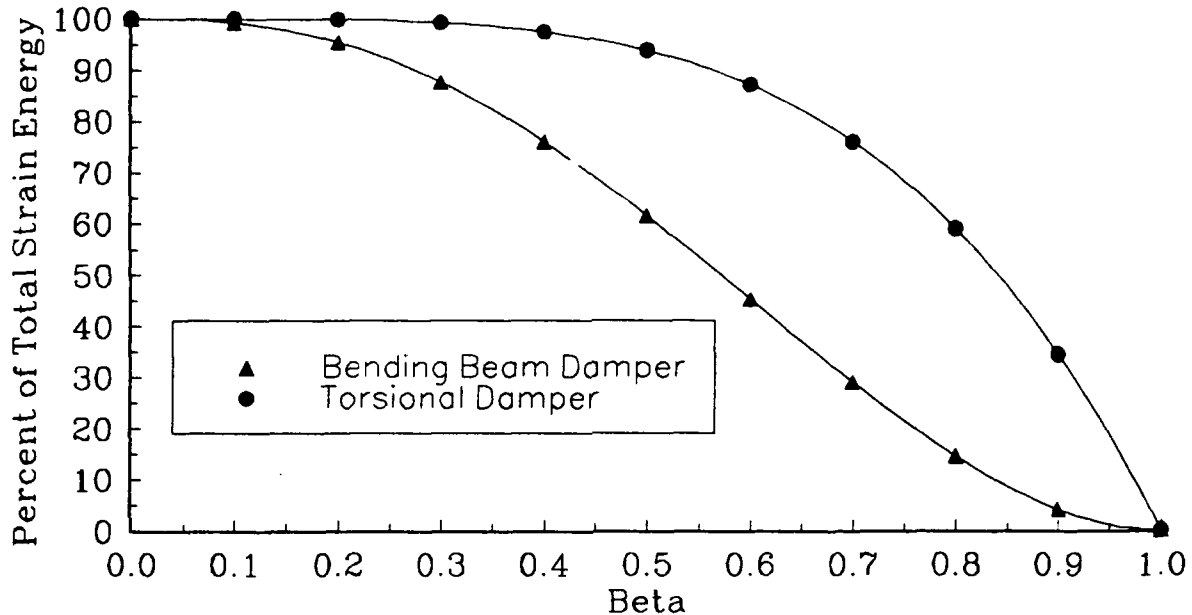
Fig. 4 Percent Strain Energy vs Strain Range β

FINAL DAMPER DESIGN

The finalized damper design was determined though analytical and experimental methods. The first damper was designed by employing available analytical tools and material data. This design was then built and tested on the MTS tensile tester. The results were then used to modify the estimated material properties and determine a new design.

After the torsional bar design was chosen, a more accurate nonlinear model for design was developed. The constitutive law used in the analysis was bilinear, i.e.

$$\tau_{xy}=2G_1\epsilon_{xy}+[2(G_1-G_2)(\epsilon_t-\epsilon_{xy})]U(\epsilon_{xy}-\epsilon_t) \tag{20}$$

Note there are two shear moduli: G_1 which is the elastic shear modulus and G_2 the inelastic shear modulus (see Fig. 5). Also note from the figure that ϵ_t is the value of the strain at which the stress strain curve changes slope. The term $U(\epsilon_{xy}-\epsilon_t)$ is a step function
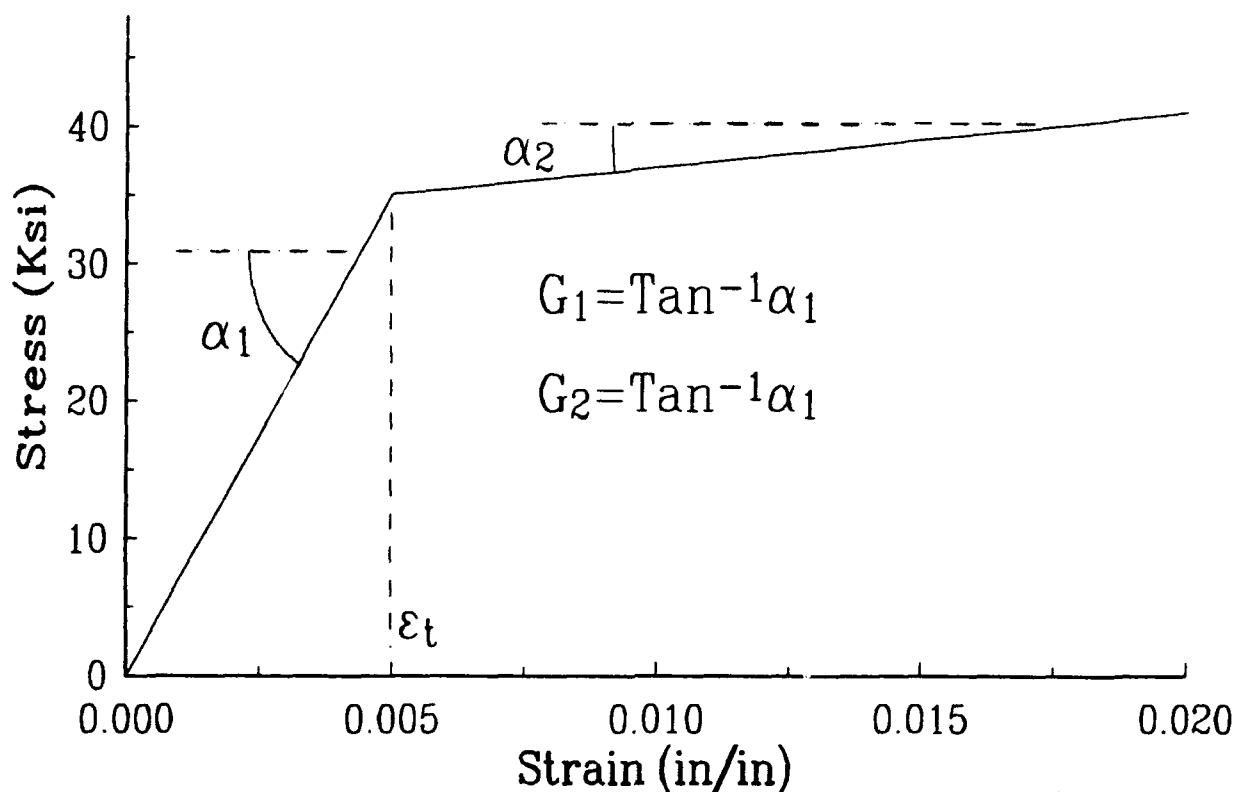
Fig. 5 Stress Strain Curve Used to Model Damper

and is defined as follows:

$$U(x)=\begin{Bmatrix} 0 & \text{If } x\leq0 \\ 1 & \text{If } x>0 \end{Bmatrix}$$

(21)

The torque produced from the two torsional bars in the damper design (Fig. 4) is

$$T=FD=2\int_0^{2\pi}\int_0^R (\tau_{xy}r)rdrd\theta$$

(22)

Substituting in the constitutive law, Eq. (20), and Eq. (12) for the shear strain and assuming that $R>2LD\varepsilon_t/\delta$, the integration of Eq. (22) simplifies after some manipulation to

$$F=\frac{\pi G_2 R^4}{LD^2}\delta+\frac{8\pi\varepsilon_t}{3D}(G_1-G_2)[R^3-\frac{2(LD\varepsilon_t)^3}{\delta^3}]$$

(23)

The above equation gives the force deflection curve for different values of L,D and R. For design, however, we must control the maximum strain ε_{max} and the stiffness S. The stiffness will now be redefined as the force needed to produce the maximum deflection Δ, divided by Δ. With δ equal to Δ and with S as defined above, Eq. (15) and Eq. (23) are solved for D and R in terms of L. The results are as follows:

$$D = \left(\frac{3S\Delta^4}{2^4 \pi L^3 e_{max}[3G_2 e_{max}^4 + e_t(G_1 - G_2)(4e_{max}^3 - e_t^3)]} \right)^{\frac{1}{2}}$$

$$R = \left(\frac{3S\Delta^2 e_{max}}{2^2 \pi L[3G_2 e_{max}^4 + e_t(G_1 - G_2)(4e_{max}^3 - e_t^3)]} \right)^{\frac{1}{2}} \tag{24}$$

The original damper was designed to err on the stiff side, because the radius of the torsional bar could be turned down on the lathe ar.d then retested until the correct stiffness was achieved. After the first damper was built and tested at different radii, the shear modulus was modified to fit the results of the testing and the final design was determined.

It should be noted that in the torsion bar design, the Cu-Zn-Al bar acts as a beam in bending in addition to the desired mechanism of a bar in torsion. Since the Cu-Zn-Al bar is clamped on both ends, the deflection of the Cu-Zn-Al bar due to bending can be modeled as a beam clamped at the ends and loaded at midspan. Using a linear constitutive relationship, the stiffness K of the torsion bar in bending is

$$K = \frac{6\pi E R^4}{L^3} \tag{25}$$

The stiffness due to torsion for the same bar is given in Eq. (14). Dividing Eq. (14) by Eq. (25) and replacing G with E/(1+v) gives with a little rearrangement

$$\frac{S}{K} = \frac{1}{6(1+v)} \left(\frac{L}{D} \right)^2 \tag{26}$$

To ensure that the deflection of the Cu-Zn-Al bar in bending is insignificant in comparison to the deflection due to the torsion, we set S/K<0.1. Assuming v=0.3, D>1.13L would satisfy the above conditions.

Cu-Zn-Al DAMPER TESTING

After the damper had been constructed and the Cu-Zn-Al heat treated, the damper was tested on the MTS machine. Fig. 6 shows the force deflection relationship of the Cu-Zn-Al torsional bar structural damper. The first cycle of the force deflection curve has a much more pronounced superelastic characteristic than the subsequent cycles.

A comparison between the stiffness and energy loss between the SMA damper and the viscoelastic damper can now be made. The stiffness of the SMA damper was 8813 lb/inch, which was near the target stiffness. In addition, the energy loss per cycle was calculated to be 68.1 lb-in. The fourth cycle was used for this calculation since the force deflection curve has stabilized at that cycle. The viscoelastic damper's stiffness and energy loss per cycle varied with frequency, temperature and percent strain [1]. At 0.1 Hz, 5% strain and 40°C, the viscoelastic damper had a energy loss per cycle of 69 lb-in and a stiffness of 322 lb/inch. However at 4 Hz, and 20% strain and 21°C, the same
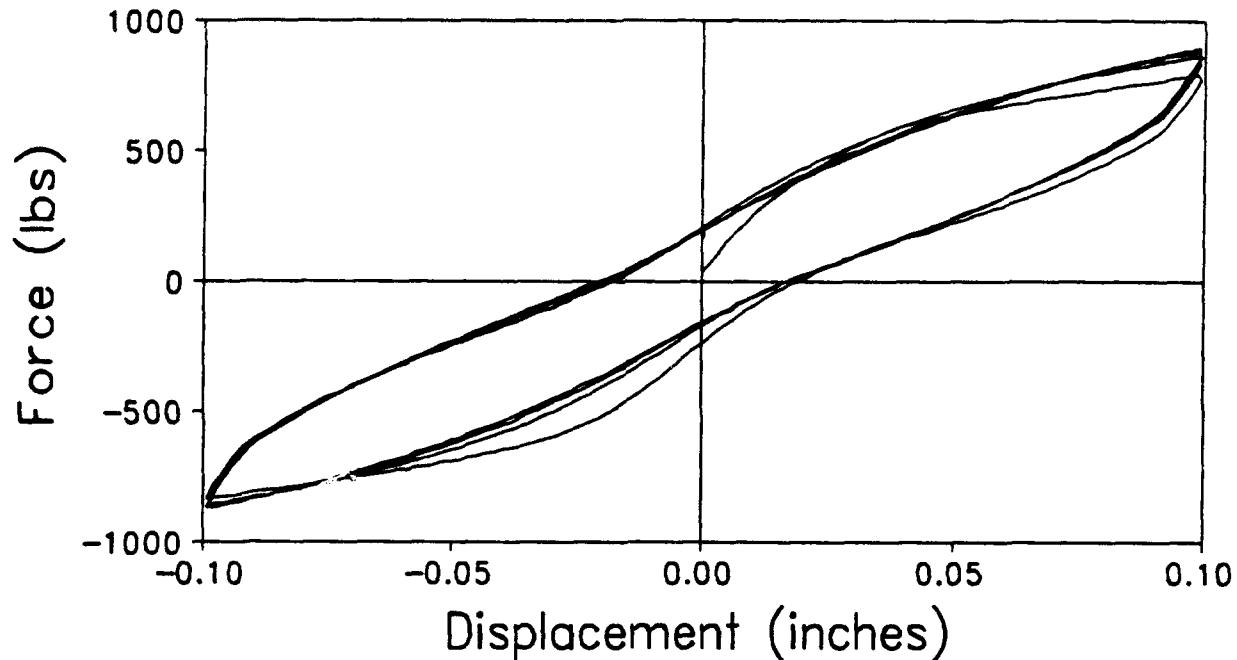
Fig. 6 Force vs Disp. of Cu-Zn-Al Damper

viscoelastic damper had a energy loss per cycle of 28431 lb-in and a stiffness of 5311 lb/inch. These results would indicate that the viscoelastic damper would provide greater damping than the SMA damper.

It should be pointed out that while the SMA damper does not provide as much damping as a viscoelastic damper, it can be used in applications where the viscoelastic damper cannot. The three fundamental advantages of a damper designed with SMA material over viscoelastic material are: SMA are much stronger, relatively insensitive to temperature, and can provide a restoring force. These three factors make SMA materials suitable for a base isolation system. A base isolation system must be strong enough to support the building and should restore the building back to its original position after an earthquake. The viscoelastic damper could not be used for this purpose since the material is much to soft to support this type of load.

EARTHQUAKE SIMULATOR TEST SET UP

As noted earlier, the test structure used was a five-story model building. The model building is 224.0" in height and 52.0" on each side. Diagonal braces with SMA dampers were bolted to the gusset plates welded to the girders. The acceleration and absolute displacement in the horizontal direction were measured on the east and west sides of the concrete base and on each floor of the building. In addition, the displacement δ, across the damper between the second and third floors on both sides of the building, was also measured. The placement of the displacement and acceleration

measurement devices is shown in Fig. 7. Temposonic displacement transducer's and Endevco accelerometer's were used for the displacement and acceleration measurements. Strain was also measured using strain gauges on the top and bottom of the girders of the second and third floors, where the strain was expected to be the largest.

A banded white noise test was run to determine the frequency response function of the structure. This frequency response function was then used to construct simulated ground motions of the Hachinohe, Olympia, El Centro and Quebec earthquake records. To prevent damage to the structure, each ground motion was initially run with a conservatively small peak acceleration of 0.06g's. The magnitudes of the ground motions were then increased until it was determined that the structure would be damaged by any further increase. The maximum inter-story drift and maximum strain measured during the tests

■ Endevco Accelerometer

☐ Temposonic Displacement Transducer

◆ SMA Damper

Fig. 7 Instrumentation of Model Structure

determined whether or not an earthquake of greater magnitude would be run. All four earthquakes and banded white noise were run with peak accelerations of 0.06g, 0.12g, 0.24g and 0.36g. In addition, the structure was subjected to banded white noise and the four ground motions at 0.06g's with no dampers.

SEISMIC TEST RESULTS

Bar graphs, which compare the damped to undamped building responses for the El Centro earthquake record, are given in Figs. 8-10. Fig. 8 presents the maximum relative floor displacements, with and without dampers. Fig. 9 presents the maximum floor accelerations for the same case. Finally, Fig. 10 presents the maximum inter-story drift. Table I summarizes the results of building responses to the four earthquake records, by listing the maximum responses of the undamped structure and the percent reduction of responses of the damped structure.

We have previously noted that larger damper displacements resulted in larger energy absorbing hysteresis loops. It was also noted that the damper stiffness decreases with increasing deflections. This change in stiffness and energy absorbing hysteresis loops with deflection, was expected to cause a change in the natural frequency and damping ratio of the building as the magnitudes of the ground motions increased. Since

Fig. 8 Max Floor Disp. (0.06 El Centro)
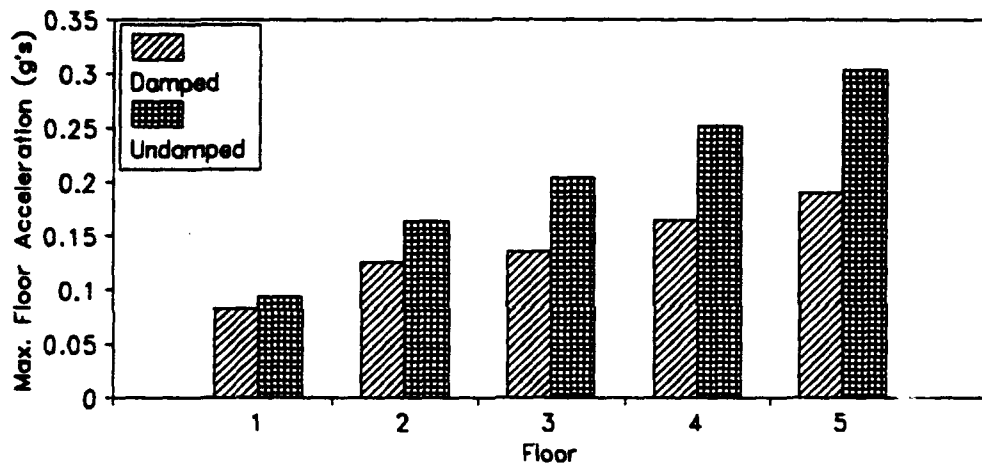
Fig. 9 Max Acceleration (0.06 El Centro)
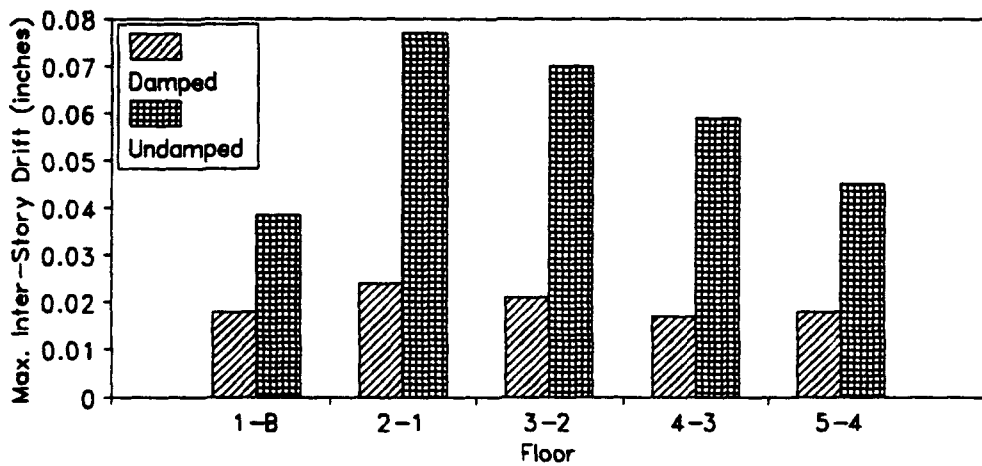
Fig. 10 Max Inter-Story Drift (0.06 El Centro)

Table I Summary of Dynamic Response of Model Building

Maximum Response	Floor Level	Earthquake's with 0.06g max acceleration			
		Hachinohe		El Centro	
		Undamped	% Reduction	Undamped	% Reduction
Relative Floor Disp. (inch)	1	0.074	60.4%	0.039	53.4%
	2	0.211	62.7%	0.113	66.4%
	3	0.237	48.9%	0.182	67.6%
	4	0.436	64.4%	0.238	68.9%
	5	0.507	63.5%	0.283	67.5%
Maximum Floor Acc. (g's)	1	0.119	12.6%	0.093	11.8%
	2	0.267	29.2%	0.163	23.3%
	3	0.387	36.7%	0.203	33.5%
	4	0.461	36.2%	0.251	34.7%
	5	0.554	35.6%	0.303	37.3%
Inter-Story Drift (inch)	1-B	0.074	60.4%	0.039	53.4%
	2-1	0.144	65.3%	0.077	68.8%
	3-2	0.130	64.6%	0.070	70.0%
	4-3	0.100	66.0%	0.059	71.2%
	5-4	0.071	57.7%	0.045	60.0%
		Quebec		Olympia	
		Undamped	% Reduction	Undamped	% Reduction
Relative Floor Disp. (inch)	1	0.015	13.3%	0.032	37.5%
	2	0.039	20.5%	0.088	44.3%
	3	0.053	0.0%	0.136	42.6%
	4	0.060	-8.3%	0.181	44.2%
	5	0.083	4.8%	0.217	44.7%
Maximum Floor Acc. (g's)	1	0.094	33.0%	0.131	32.1%
	2	0.167	37.7%	0.190	28.4%
	3	0.141	13.5%	0.203	15.3%
	4	0.119	-23.5%	0.187	-23.5%
	5	0.182	8.8%	0.292	16.4%
Inter-Story Drift (inch)	B-1	0.015	13.3%	0.032	37.5%
	2-1	0.026	15.4%	0.059	49.2%
	3-2	0.022	4.5%	0.050	42.0%
	4-3	0.021	28.6%	0.048	52.1%
	5-4	0.033	51.5%	0.039	51.3%

the damper stiffness decreases with larger deformation, the natural frequency of the building was also expected to decrease under the larger earthquakes. Fig. 11 shows the decrease in the natural frequency with increase of the base excitation. Under larger deformation, larger energy absorbing force deflection cycles are experienced which causes an increase in the damping ratio. Fig. 12 shows such an increase in damping with larger earthquakes.
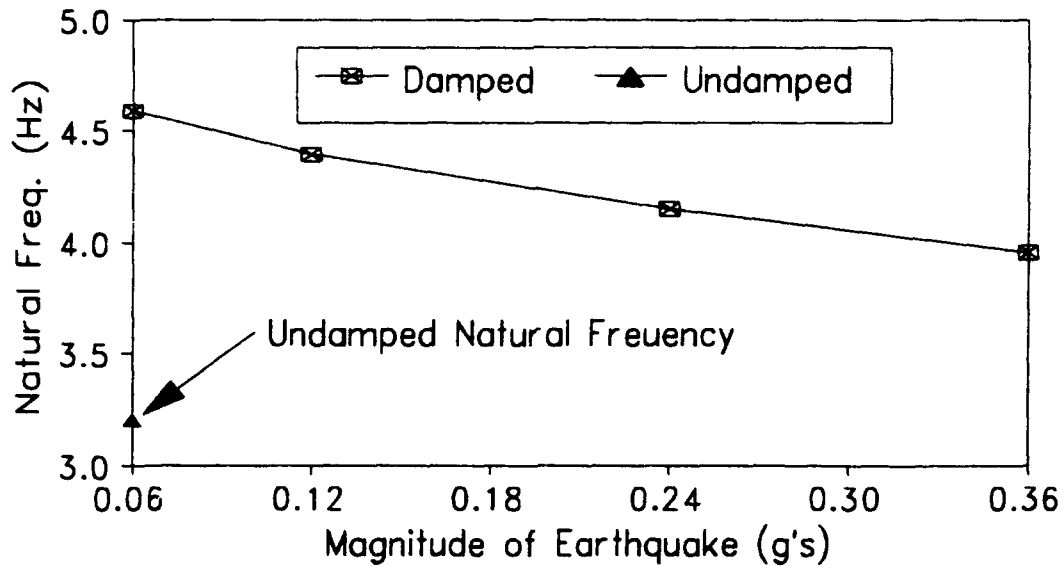
Fig. 11 Natural Frequency vs Base Excitation
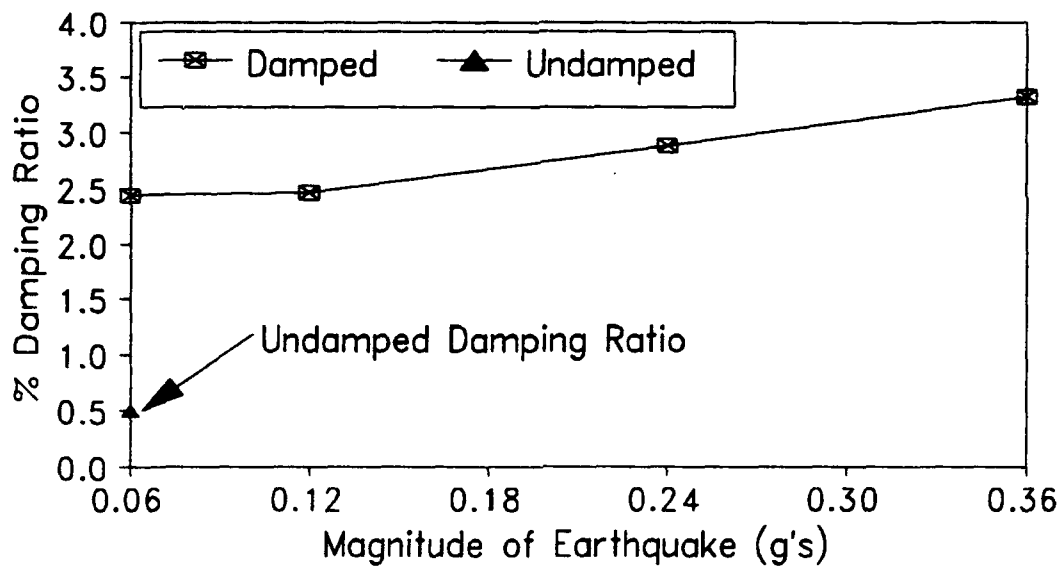
Fig. 12 Damping Ratio vs Base Excitation

It should be noted that the above mentioned damping ratios were calculated by the half-power method [17] for the first mode of vibration only. Since the damping ratio is less than 15%, the half-power method can be considered accurate. A plot of a typical third floor acceleration frequency transfer function with and without SMA dampers (Fig. 13), reveals the first and second modes of vibration clearly. However, the frequency response of the second mode of vibration is less then half that of the first mode. Therefore, the discussion of results will be limited to the first mode of vibration, since it dominates the dynamic response of the structure. The bare frame transfer function is characterized by a tall and narrow spike at 3.2 Hz. This indicates little damping. The frequency response of the SMA damped building is wider and shorter which shows an increased damping from the undamped case.
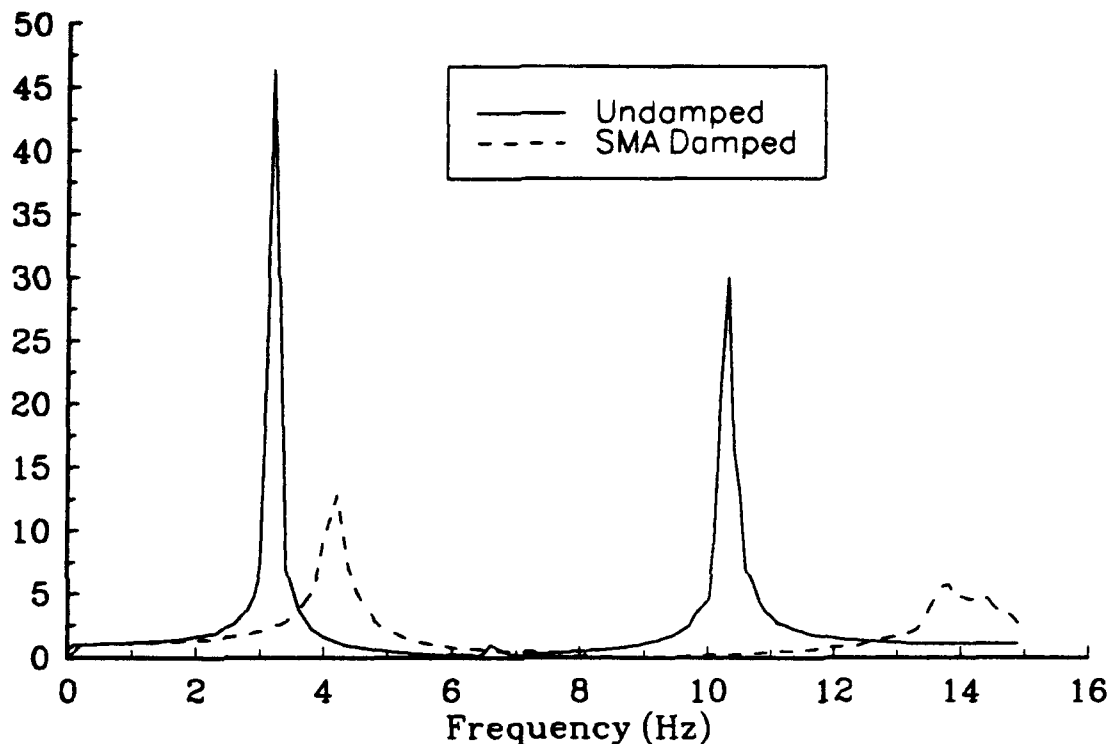
Fig. 13 Frequency Response of Damped and undamped Building

DISCUSSION OF RESULTS

It seems apparent from an examination of Table I that the effectiveness of the damper varies with the earthquake. For instance, the percent reduction of the maximum relative floor displacement due to the Hachinohe ground motion averaged over the five floors is 60.0%, while same averaged percent reduction for the Quebec earthquake case is only 6.1%. In fact, the fourth floor maximum relative floor displacement and maximum acceleration of the damped building was greater then the response of the undamped building in the Quebec earthquake case. The other floor's maximum responses as well as the inter-story drift response for all floors, however, were smaller in the damped case then the undamped case. These sizable differences can be accounted for by noting that the frequency contents of the four ground motions are different. The Quebec earthquake has a larger content of higher frequencies then the Hachinohe earthquake. Since the SMA dampers increase the natural frequencies of the building (Fig. 11), the SMA dampers will be more effective against earthquakes with lower frequencies.

The calculated damping ratios are less dependent upon the frequency content of the earthquake record. Fig. 12 shows an increase of damping over the undamped case. However, the damping for SMA dampers is not as great as for viscoelastic dampers. Viscoelastic dampers have been shown [1] to yield a damping ratio between 5% and 14%, depending on the temperature of the viscoelastic material, for the same five story model building. Whereas the SMA damper properties are not highly temperature dependent, the damping measured was less than for the viscoelastic dampers at their

ECC-16

least favorable temperature. Since the SMA damper was designed to maximize the benefits of the Shape Memory Material properties of Cu-Zn-Al, there is no evidence to indicate that a redesign of the damper would result in improved damping on this test building.

In spite of the above drawbacks, the potential for effective SMA damping is apparent. The dampers did mitigate the building's motion and the building was safely tested with the SMA dampers at levels where the building would have been severely damaged without the dampers. In addition, the test results indicate that the SMA damper is probably best suited for base isolation applications. One of the features of the SMA damper is the potential for a self-centering hysteresis loop. This feature is not effectively utilized in structural damping, because the building's inherent stiffness creates a self-centering force that is much greater than the damper's. However, in base isolation this self-centering property would be of great benefit, since the base isolation device acting alone must restore the building to its original position.

Another indication that the SMA damper would be useful in base isolation is the change in natural frequency of the building with increased levels of base excitation (Fig. 11). A base isolation device should be stiff for small deflection, so that wind loading and small tremors will not cause the building to move excessively. In the event of a large earthquake, the stiffness should reduce and allow the building greater mobility to isolate itself from the ground motion. The decrease in natural frequency of the damped building (Fig. 11) with increased base excitation indicates a corresponding decrease of damper stiffness with increased damper deflection. This same change in damper stiffness was also noted earlier.

SUMMARY AND CONCLUSION

The results of experimental studies on the material properties of the shape memory material (SMA) Cu-Zn-Al have been presented and analyzed. Experimental results on the seismic behavior of a Cu-Zn-Al SMA damped steel-frame 2/5 scale model structure have also been presented. In addition, a discussion of the advantages of the torsion bar SMA damper over other SMA damper designs was included.

The material test results show that this composition of Cu-Zn-Al has a superelastic stress strain relation for a very limited number of cycles. After a few cycles, the internal friction will increase and cause a hysteretic material behavior with a very small amount of spring back. The final hysteretic stress strain behavior was found to be caused by martensitic transformation rather than by slip/glide dislocation motion.

The seismic test results demonstrated that Cu-Zn-Al dampers are effective at mitigating the 2/5 model five story building's response to various ground motions. The results were compared to results of tests done with viscoelastic dampers, and it was concluded that the Cu-Zn-Al dampers were not as effective as the viscoelastic dampers. The test results of the structural dampers indicated that the SMA dampers are better

suited for base isolation.

ACKNOWLEDGEMENT

REFERENCES

1. Chang, K.C., Soong, T.T., Oh, S-T., and Lai, M.L., 1991, "Seismic Response of a 2/5 Scale Steel Structure with Added Viscoelastic Dampers," Technical Report NCEER-91-0012, National Center for Earthquake Engineering Research, Buffalo, NY.
2. Filiatrault, A., Cherry, S., 1988, "Comparative Performance of Friction Damped Systems and Base Isolation Systems for Earthquake Retrofit and Aseismic Design," *Earthquake Engineering and structural Dynamics*, Vol. 16, pp. 389-416.
3. Malushte, S.R., Singh, M.P., "A Study Of Seismic Response Characteristics Of Structures With Friction Damping," *Earthquake Engineering and structural Dynamics*, Vol. 18, pp. 767-783.
4. Roik, K., Dorka, U., Dechent, P., 1988, "Vibration Control of Structures Under Earthquake Loading By Three-Stage Friction-Grip Elements," *Earthquake Engineering and structural Dynamics*, Vol. 16, pp. 501-521.
5. Zhang, Ri-Hui., Soong, T.T. Mahmood, P., 1989, "Seismic Response of steel Frame Structures with Added Viscoelastic Dampers," *Earthquake Engineering and structural Dynamics*, Vol 18, pp. 389-396.
6. Graesser, E.J. and Cozzarelli, F. A., 1989, "Multidimensional Models of Hysteretic Material Behavior for Vibration Analysis of Shape Memory Energy Absorbing Devices," Technical Report NCEER-89-0018, National Center for Earthquake Engineering Research, Buffalo, NY.
7. Graesser, E. J., and Cozzarelli, F. A., 1991, "A Multidimensional Hysteretic Model for Plastically Deforming Metals in Energy Absorbing Devices," Technical Report NCEER-91-0006, National Center for Earthquake Engineering Research, Buffalo, NY.
8. Graesser, E. J., 1990, "Multi-Dimensional Modeling of Hysteretic Materials Including Shape Memory Alloys: Theory and Experiment," Ph.D. Dissertation, SUNY at Buffalo, Buffalo, NY.
9. Graesser, E. J., and Cozzarelli, F. A., 1991, "Shape Memory Alloys as New Materials for Aseismic Isolation," *Journal of Engineering Mechanics*, ASCE, Vol. 117, No. 11, pp. 2590-2608.
10. Graesser, E. J., and Cozzarelli, F. A., 1991, "Extension of a One-Dimensional Model of Hysteresis to Three Dimensions: Procedure and Verification," *High Temperature Constitutive Modeling: Theory and Application*, ASME, MD-Vol. 26/AMD Vol. 121, ed. by A. Freed and K. Walker, pp 365-381.
11. Duerig, T. W., Melton, K. N., Stöckel, D., Mayman, C. M., 1990, *Engineering Aspects of Shape Memory Alloys*, Butterworth-Heinemann Ltd.
12. Fletcher, A. J., Thomas, D. L., 1970, "Solid-State Transformations in Certain Copper-Aluminum-Zinc Alloys." *Journal of the Institute of Metals*, Vol 98, pp 188-192.

13. Witting, P.R. and Cozzarelli, F.A., 1992, "Shape Memory Structural Dampers: Material Properties, Design and Seismic Testing," Technical Report NCEER-92-0013, National Center for Earthquake Engineering Research, Buffalo, NY.

14. Witting, P.R., 1992, "Shape Memory Structural Dampers: Design and Seismic Testing," MS Thesis, SUNY at Buffalo, Buffalo, NY.

16. Shigley, Joseph E., and Mitchell, Larry D., 1983, *Mechanical Engineering Design-Fifth Edition*, McGraw-Hill Inc.

15. Roark, Raymond J., and Young, Warren C., 1975, *Formulas for Stress and Strain fifth edition*, McGraw-Hill Inc.

17. Clough, Ray W., and Penzien, Joseph, 1985, *Dynamics of Structures*, McGraw-Hill Inc.

THE VIBRATION CHARACTERISTICS OF COMPOSITES WITH EMBEDDED SHAPE MEMORY ALLOY

Lee Chin Hai and Dr. C. T. Sun
Dept. of Aero., Mech. & Eng. Science   U of Florida

ABSTRACT

The objective of this paper is to explore new technique to improve dynamic response and vibration characteristics of composite plates or beams by using shape memory alloy wires(SMA wires). Analytical method is developed to predict the natural frequencies at large amplitude under activation or deactivation (heating or cooling).

A dynamic model is also developed in predicting the beam responses at activation /deactivation phases. The model could be used to estimate natural frequencies, damping (loss factor) of SMA hybrid laminated beams at simply-supported boundary conditions. The dynamic response of sandwich beam with SMA embedded were calculated in both time domain and frequency domain.
1

Lee Chin Hai

       Address   231 Aero. Bldg. Dept of Aero., Mech. and Eng. Science, University of Florida, Gainesville, FL32611

       Phone   1-(904)-392-6741 , 1-(904)-334-5890

INTRODUCTION

Smart materials [1] [2] are intelligent materials with special ability to change their physical properties and geometry (i.e, stiffness, damping, viscosity, shape, etc) due to certain stimuli or inputs, such as optical fibers, piezo-electric polymers, piezo-ceramics, electrostrictors, electro-rheological fluids, (SMA)shape memory alloy, and magnetostrictors. Adaptive materials and structures are but a subset of smart materials and structures.

The unique feature of smart material in the latest decade have been shown in a great number of components in large space structures or special mechanical devices comparing to its older generation. The employment of smart materials is the only reason to reach such a full adaptive control effectiveness of the dynamic response of structures, like space crane , robot arms...etc. It not only has reduced the weight of traditional adaptive actuators(as hydraulic actuators), but has evolved to a new concept of dynamic properties tunning in smart structure. Though, the smart materials employed in smart structure have many special advantages yet, the lack of solid test database in some smart materials (as Shape Memory Alloy or Electro-Rheological fluid) [1] applied in structure elements has hindered further research in this area. Besides, this brand new area needs interdisciplinary coordination, such as material properties , structural mechanics, controls, electrical devices, testing engineering and fabrications.

The shape memory alloy used in the past few years on robot arm was indeed an effective control element, its simple construction and the possibility to move smoothly without environmental pollution(shedding lubricant hydraulic oil). We will be able to reduce complexity of mechanical elements if so constructed, also the fact of long fatigue life and corrosion resistent capability made the material more fascinating to engineers. Besides, the only energy it needs is any type of thermal energy such as the application of electric current through SMA wire. The shape memory alloy might also be a good candidate as key element in performing active vibration control, or passive vibration control [3]. We found that its wire type could be embedded in various kinds of composite materials serving different purpose for vibration suppression, changing structure stiffness to avoid the resonance at various vibration mode, acoustic vibration control, working as geometry variation device and so forth.

In general, single rod or beam element may not necessarily have to change stiffness to evade resonance while excited by external disturbance at fundamental mode, but single beam possessing constant mechanical properties could reach resonance at higher modes. A progressive concept in changing stiffness of structures is important for some reasons:

For example, at a global view of a complex structure which contain many spars, rod or beams, we can activate one or few of its elements to alter the global structure natural frequency in order that certain maneuver can be achieved. We could activate some particular SMA wires in rods or beams of a space structure, a crane or jacking arm, to consummate a series of movements. By using the smart material served as adaptive control members is more efficient and weight saving.

A space structure or satellite are flexible bodies in space maneuver. We can stiffen some particular members as it rotates in space, the whole structure will act as rigid body or at least

semi-rigid one such that we could spent less analytical work at flexible structure. Besides,the changing vibrational characteristics of the hybrid structure may be of practical interests too. All in all, the trend is, well tuned elements in natural frequency change of large flexible structure may be imperative for some applications.

SPECIAL FEATURES OF SMA(shape memory alloy)

There are two types of solid state transformation : one is diffusional transformations which a new phase is formed by migrating atoms randomly in all directions, with different chemical composition than the matrix from which it is formed. This progression of transformation is dependent upon both time and temperature. The other is displacive transformations, which do not require atomic migration or change in the chemical nature of the matrix to alter its solid state. Its crystal structure is merely rearranged into a more stable one. This progression of transformation is only dependent upon temperature. [4]

The austenite ←—→ martensite transformation of SMA material is displacive transformation. The progression of transformation from one phase to the other depend on temperature only, volume fraction of martensite increases as temperature decreases from the parent phase (austenite)-each atomic layer packed together in packed shape at austenite phase, and each layer moves a little to achieve the martensite phase, this phenomena is called Bain strain. [9]

In general, shape memory alloy (NITINOL) will undergo an accommodation step: the lattice shape change is not merely caused by Bain stain, owing to the other layers of austenite do not always change to the slant structure described previously. It will accommodate itself to a more relaxed shape dubbed twinning (the general shape after cooling from austenite phase), the twinning process plays a key role in the shape memory effect.

VIBRATION CHARACTERISTICS OF SANDWICH BEAMS

There are two kinds of vibration control technique which were currently applied. One is passive vibration control technique, the other is active vibration control technique. Yet, the emerging smart materials come to the world had create other ramifications in the vibration control studies. It is showed unique abilities of smart materials that could change material viscosity, stiffness, and so forth, while activated by electric current, magnetic field, heating processes. The ability of SMA wire to change stiffness in SMA hybrid laminated beam has been described above, the test results have shown unique potential to shift the structure natural frequencies. Thus, resonant condition of vibration induced by impinging loads, sinusoidal loads, etc, could definitely be subdued by activating the SMA wires embedded in the composite structures. However, the test results in laboratory also showed the lower damping coeficients while SMA hybrid laminated beam was fully activated. All the tests of SMA hybrid laminate beams were done under the clamp-clamp boundary condition, which is not very useful in many engineering applications. We often choose cantilever beam or simply-supported beam as candidates in practical vibration problems. Still, the tests showed vivid evidence of structure stiffening effect and changing of damping properties.

In practical applications, cantilever beams are used commonly, such as moving beams

fixed at one end, a robot arm, helicopter rotor blade, an electric post, a fan blade of jet engine, and miller arm of a milling machine, just name a few. The cantilever beams require strength and bending regidity to serve as sound structure. One of the best choices is sandwich beams construction. There are many advantages of using sandwich structures; (1) sandwich structures have great strength/weight ratio, superior flexural regidity/weight ratio, (2) tailored composite skins perform excellently under various design requirements and, (3) the sandwich core, which is softer and less weight, could be made out of very good damping materials in order to reduce vibrations caused by mechanical loading or acoustic loading...etc. The bonding material could be film adhesive and spray-on primer which serve the purpose to join sandwich faces with core materials. Thicker core can be cut in smaller blocks stringed together for making curved sandwich panels.

VIBRATION SUPPRESSION IN STRUCTURES

Vibration suppression is a very broad subject in which a lot of techniques are available to achieve such purpose. Passive vibration control has simpler technique by using extra mass, spring attached on the main structures or by using vicoelastic damping material on structures. They require predetermined dynamic system analysis and open control scheme. Active vibration control is mainly closed loop control to suppress mechanical vibration. They require more effort in designing feed back control law plus intrigue electronic devices in structure system like large space station.

EQUATION OF MOTION OF SANDWICH PANEL

Our primary goal in this section is to establish the principles of mechanics for sandwich panels, whose faces are made of SMA hybrid composite laminate. A large flexible structures like wind turbine, may face plenty of vibrational problems. We are assuming that this flexible wind turbine panel is the said sandwich panel which vibrate with large amplitude. This large amplitude creates geometric nonlinearity. The structure is under elastic deformation. No normal or in-plane stresses in the core, core thickness is constant The only significant stress in the core is the transeverse shear. The face skins are thin comparing to the core thickness. They take the in-plane forces only with upper skin identical to lower skin. The panel is assumed in perfect bonding between the skins and the core.

A. DERIVATION OF EQUATION OF MOTION

The activation of upper skin shows general approach of unsymmetric plate lay-up. The unsymmetric effect occurs at various boundary condition. The skin stiffness varies with temperature and time, the young's modulus of SMA wire denoted by $E_s(t)$, like that in [5] , could be linearized according to diagram in [4] young's modulus - temperature relation. Since $E_s(t)$ are different at activation and deactivation due to hysteresis effect [4] p.98, thus:

At heating:
$$E_s(\Delta t) = 3.5 + .25 \ (\Delta T/\Delta t) \ \Delta t \quad (Msi) \qquad (1)$$
$$E_s(\Delta t) = 24.13 + 3.10 \ (\Delta T/\Delta t) \ \Delta t \ (Gpa) \qquad T: °C$$
where, $\Delta T = 32°F$, $17.78°C$ respectively

At cooling after activation:

$$E_s(\Delta t) = 11.5 - .34 \, (\Delta T / \Delta t) \, \Delta t \quad (Msi) \qquad (2)$$
$$E_s(\Delta t) = 79.29 - 4.22 \, (\Delta T / \Delta t) \, \Delta t \quad (Gpa)$$

where, $\Delta T = 23.5°F$, $13.07°C$ respectively

$E_s(\Delta t)$: SMA wire Young's modulus
ΔT : temperature range
Δt : time step (sec.)
$\Delta T / \Delta t \propto f(I,V,G)$
   I: electric current
   V: electric voltage
   G: heat flux

We can approach the problem with energy variation to derive the equation of motion of sandwich panel. Assuming that only strain energy of the SMA hybrid skins (upper and lower), and transverse shear energy of the core are considered. We neglect flexural rigidies of the face skins for its small thickness comparing to the core thickness. The recent research on nonlinear analysis of composites by Whitney and leissa [6], Bai [7], and a collective work on geometrically nonlinear analysis Chia [8], can serve as good indication in deriving the equation of motion. The effects of skin stiffness variation at activation/deactivation will also be considered.

The displacement fields are assumed in the following: (starting from 2-D plate approach)

Non-activation:

$$u(x,y,z,t) = u_0(x,y,t) + z \, \psi_x \qquad (3)$$
$$v(x,y,z,t) = v_0(x,y,t) + z \, \psi_y \qquad (4)$$
$$w(x,y,t) = w(x,y,t) \qquad (5)$$

These assumption lead to the conventional results by previously collected work as [9].

Activation mode: upper skin deforms by heating and recovery stresses, assuming that core is good insulator to temperature, and the extra terms appeared in (6),(7) are small.

$$u(x,y,z,t) = u_0(x,y,t) + z \, \psi_x - f(x,t) \qquad (6)$$
$$v(x,y,z,t) = v_0(x,y,t) + z \, \psi_y - g(y,t) \qquad (7)$$
$$w(x,y,t) = w(x,y,t) \qquad (5)$$

where, f, g are the shrinkage of upper skin at activation (cantilever beam)
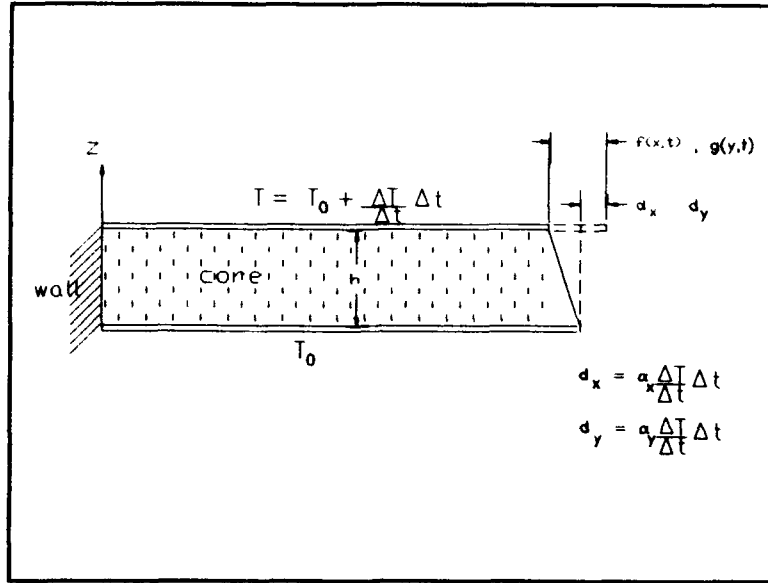
Introducing core shear rotation due to skin activation(cantilever beam)

$$\psi_{sx}(x, t) = \frac{f(x, t) - d_x}{h}$$

$$\psi_{sy}(y, t) = \frac{g(y, t) - d_y}{h}$$

(8)

where,

    $u_0(x,y,t)$: panel neutral plane displacement in x-dir.

    $v_0(x,y,t)$: panel neutral plane displacement in y-dir.

    $w(x,y,t)$: panel neutral plane deflection in z-dir.

    $\psi_x(x,y,t)$: panel neutral plane rotation about y-axis

    $\psi_y(x,y,t)$: panel neutral plane rotation about x-axis

    z   : local normal dir. to neutral plane of panel

    $f(x,t)$: deformation of upper skin at activation in x-dir

    $g(y,t)$: deformation of upper skin at activation in y-dir

    ψ_{sx} : core shear rotation due to upper skin activate in x - dir.

    ψ_{sy} : core shear rotation due to upper skin activate in y - dir.

    d_x : thermal expansion in x-dir.

    d_y : thermal expansion in y-dir.

    α_x : skin thermal expansion coeficient in x-dir.

    α_y : skin thermal expansion coeficient in y-dir.

    T_0 : ambient air temperature

The strains of skins can be expressed as

$$\epsilon_x^u = \frac{\partial u_0}{\partial x} - \frac{h}{2}\frac{\partial \psi_x}{\partial x} + \frac{1}{2}(\frac{\partial w}{\partial x})^2 - \frac{\partial f(x, t)}{\partial x}$$

(9)
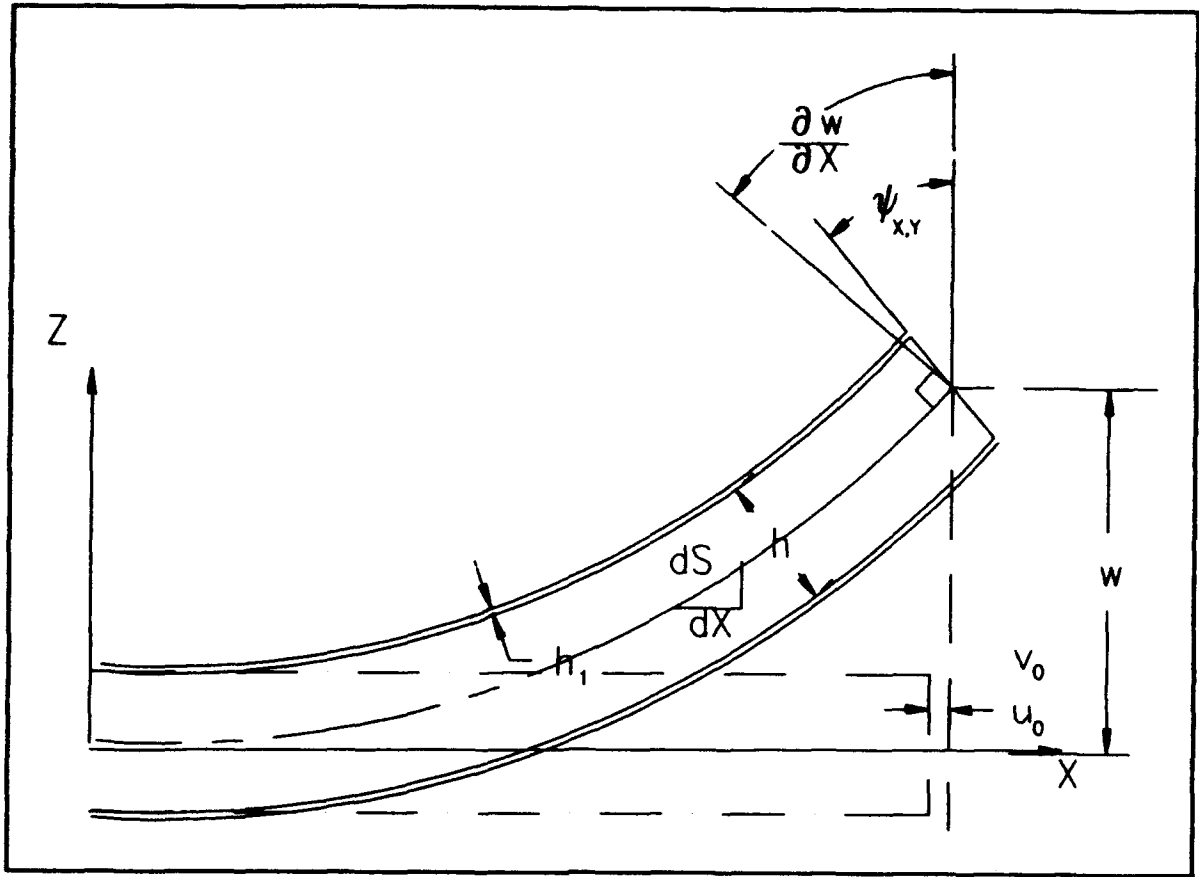
Figure 1   Large deformation of sandwich panel

$$\epsilon_x^1 = \frac{\partial u_0}{\partial x} + \frac{h}{2}\frac{\partial \psi_x}{\partial x} + \frac{1}{2}(\frac{\partial w}{\partial x})^2 \tag{10}$$

$$\epsilon_y^u = \frac{\partial v_0}{\partial y} - \frac{h}{2}\frac{\partial \psi_y}{\partial y} + \frac{1}{2}(\frac{\partial w}{\partial y})^2 - \frac{\partial g(y,t)}{\partial y} \tag{11}$$

$$\epsilon_y^1 = \frac{\partial v_0}{\partial y} + \frac{h}{2}\frac{\partial \psi_y}{\partial y} + \frac{1}{2}(\frac{\partial w}{\partial y})^2 \tag{12}$$

$$\gamma^u = \frac{\partial u_0}{\partial y} + \frac{\partial v_0}{\partial x} - \frac{h}{2}(\frac{\partial \psi_x}{\partial y} + \frac{\partial \psi_y}{\partial x}) + (\frac{\partial w}{\partial x}\frac{\partial w}{\partial y}) \tag{13}$$

$$\gamma^1 = \frac{\partial u_0}{\partial y} + \frac{\partial v_0}{\partial x} + \frac{h}{2}(\frac{\partial \psi_x}{\partial y} + \frac{\partial \psi_y}{\partial x}) + (\frac{\partial w}{\partial x}\frac{\partial w}{\partial y}) \tag{14}$$

The core transeverse shear strains are
According to the asymmetrical skin laminated sandwich panel at activation (upper skin stiffness change) and compare to [7], we find :

$$\gamma^c_{xz} = \psi_x - \psi_{sx} + \frac{\partial w}{\partial x} \qquad (15)$$

Skin strain expressed
in (9) to (14) as

$$[\epsilon^u]^T = [\ \epsilon^u_x \quad \epsilon^u_y \quad \gamma^u\ ]$$

$$[\epsilon^1]^T = [\ \epsilon^1_x \quad \epsilon^1_y \quad \gamma^1\ ]$$

Neutural plane strain (which cause bending by coupling stiffness), and sandwich panel curvature κ as below:

$$[\overline{\epsilon}]^T = [\ \frac{\partial u_0}{\partial x} + \frac{1}{2}(\frac{\partial w}{\partial x})^2 \quad \frac{\partial v_0}{\partial y} + \frac{1}{2}(\frac{\partial w}{\partial y})^2 \quad \frac{\partial u_0}{\partial y} + \frac{\partial v_0}{\partial x} + (\frac{\partial w}{\partial x}\frac{\partial w}{\partial y})\ ]$$

$$[\ \kappa\ ]^T = [\ \frac{\partial \psi_x}{\partial x} - \frac{\partial \psi_{sx}}{\partial x} \quad \frac{\partial \psi_y}{\partial y} - \frac{\partial \psi_{sy}}{\partial y} \quad \frac{\partial \psi_y}{\partial x} + \frac{\partial \psi_x}{\partial y}\ ]$$

Also according to principles of variation, total strain energy of the sandwich panel could be expressed as:

$$V = \frac{1}{2} \int_0^a \int_0^b \ [\epsilon^u]^T \begin{bmatrix} \overline{A}_{11} & \overline{A}_{12} & \overline{A}_{13} \\ \overline{A}_{21} & \overline{A}_{22} & \overline{A}_{23} \\ \overline{A}_{31} & \overline{A}_{32} & \overline{A}_{33} \end{bmatrix} [\epsilon^u]\ dx\ dy$$

$$+ \frac{1}{2} \int_0^a \int_0^b \ [\epsilon^1]^T \begin{bmatrix} A_{11} & A_{12} & A_{13} \\ A_{21} & A_{22} & A_{23} \\ A_{31} & A_{32} & A_{33} \end{bmatrix} [\epsilon^1]\ dx\ dy$$

$$+ \frac{1}{2} \int_0^a \int_0^b \ [\overline{\epsilon}\ \ \kappa]^T \begin{bmatrix} B^* \\ D^* \end{bmatrix} [\kappa]\ dx\ dy$$

$$+ \frac{1}{2} \int_0^a \int_0^b \int_{-\frac{h}{2}}^{\frac{h}{2}} \ [\ \gamma^c_{xz} \quad \gamma^c_{yz}\ ] \begin{bmatrix} G_{13} & 0 \\ 0 & G_{23} \end{bmatrix} \begin{bmatrix} \gamma^c_{xz} \\ \gamma^c_{yz} \end{bmatrix} dz\ dy\ dx \qquad (17)$$

where $\bar{A}_{ij}$, A_{ij} , B^* , D^* are the laminated plate stiffness properties. The superscript u , l , c indicate upper, lower, core respectively.

The kinetic energy form could be derived as following:
from equations (5),(6),(7)

$$T^u = \frac{1}{2} \int_0^a \int_0^b \rho_0 h_1 \ (\ \dot{u}_u^2 + \dot{v}_u^2 + \dot{w}^2 \ ) \ dy \ dx \tag{18}$$

$$T^l = \frac{1}{2} \int_0^a \int_0^b \rho_0 h_1 \ (\ \dot{u}_l^2 + \dot{v}_l^2 + \dot{w}^2 \ ) \ dy \ dx \tag{19}$$

$$T^c = \frac{1}{2} \int_0^a \int_0^b \rho_c h \ (\ \dot{u}_0^2 + \dot{v}_0^2 + \dot{w}^2 \ ) \ dy \ dx \tag{20}$$

where, ρ_0 is SMA hybrid laminate skin density (lb/in^3), ρ_c is Sandwich core density (lb/in^3) u_0, v_0 is neutural plane displacements

Total kinetic energy of sandwich panel is:

$$T = T^u + T^l + T^c \tag{21}$$

External work can be expressed due to a uniform loading q_0 as

$$W = -\frac{1}{2} \int_0^a \int_0^b q_0 \ w \ dy \ dx \tag{22}$$

Thus, employing the variation principle minimizing the total energy, we have the following:

$$
\begin{aligned}
U &= -T + V + W \\
\delta U &= -\delta T + \delta V + \delta W = 0
\end{aligned}
\tag{23}
$$

From Appendix A (A.25),(A.26),(A.27),(A.28), we assume that under simply-supported or cantilever boundary conditions, beams are under cylinderical bending (1-D static condition). Ignoring the coupling stiffness effect of upper, lower skin at activation, and there are no nolinear part containing $N_x^{u,l}$ in the (A.28), We have the following governing equations

$$2 A_{11} \left(\frac{\partial^2 u_0}{\partial x^2} + \frac{\partial w}{\partial x} \frac{\partial^2 w}{\partial x^2} - \frac{1}{2} \frac{\partial^2 f}{\partial x^2} \right) = 0 \tag{24}$$

$$
A_{11} \left(\frac{\partial^2 u_0}{\partial x^2} + \frac{\partial w}{\partial x} \frac{\partial^2 w}{\partial x^2} - \frac{h}{2} \frac{\partial^2 \psi_x}{\partial x^2} - \frac{\partial^2 f}{\partial x^2} \right) + G_{13} \left(\psi_x - \psi_{xx} + \frac{\partial w}{\partial x} \right)
$$
$$
= \frac{D_{11}}{h} \frac{\partial^2 (\psi_x - \psi_{xx})}{\partial x^2}
\tag{25}
$$

$$G_{11}(\psi_x - \psi_{sx} + \frac{\partial w}{\partial x}) = \frac{D_{11}}{h} \frac{\partial^2(\psi_x - \psi_{sx})}{\partial x^2} \qquad (26)$$

$$G_{11} h(\frac{\partial \psi_x}{\partial x} - \frac{\partial \psi_{sx}}{\partial x} + \frac{\partial^2 w}{\partial x^2}) + q_0 = 0 \qquad (27)$$

The above equations of motion are able to draw the same conclusion as Whitney [9] if we neglect equations (24) , (25) and preserve the bending equations (26),(27). The ψ_{sx} varies in different materials, but often it is negligible if the structure is stiff enough.

VIBRATION ANALYSIS OF SANDWICH BEAMS

The recent studies in the analysis of laminated beams and plates are abundant. We have found that a large portion of the researches done in composite structures are devoted to solid laminated beams and plates or shells, and its increasing use in the field of mechanical engineering, aerospace engineering, marine engineering, auto-industry, sporting goods, proved that the realms of application will definitely be expanding.

The paper surveyed by Kapania and Raciti [10],[11] have shown direct evidences of applying Classical Kirchhoff Plate theory on thin plate analysis at early stage of applications on composites. The method proved effective in thin laminate stress-strain analysis, and the classical laminate theory quoted in most of engineering text books are still used by composite engineers. Yet, people learned that CLT (Classical Laminate Theory) would lead to considerable errors in analyzing composite plates. CLT underpredicts plate deflections and overpredict its natural frequencies, especially when transverse shear moduli (interlaminar shear moduli) of laminated composite beams and plates are usually very low compared to in-plane tensile moduli. Therefore, shear effect is crucial in composite laminates and has been acknowledged ever since. There are two categories in shear deformation theory which have been used after CLT; that is, the first-order theory and the higher-order theory. The first-order theory, well known Reissner-Mindlin theory, were developed by Reissner [12], Mindlin [13]. The more extensive work by Yang, Norris, Stavsky [14] and Whitney, Pagano [15], followed the earlier Mindlin theory, has worked well for laminated beams and plates analysis in predicting deflections, natural frequencies, and buckling loads. The higher-order theory, more sophisticated idea, consider through-the-thickness stress response, such as σ_z, τ_{xz}, in regions of discontinueties at the boundaries. Thus, the higher-order theory gives more accurate results than CLT or Mindlin's theory. However, the theory requires higher computing cost which made it impractical. Owing to this limitation, higher-order theories involving higher-order derivatives of transverse displacement (the shear rotations of beams and plates) were developed in the 80's and the more popular applications made by Reddy [16] is a typical one in the higher-order theory for laminated composites.

The survey work in [10],[11] has mensioned a lot of researches on vibration of composite beams and plates also. We could find references in particular papers on the dynamic behavior of composites and sandwich plates by Bert [17]. The said are all pertained to symmetrically laminated plates and linear vibration problems with first-order or higher-order

approach. Their solution methodologies involving analytical (closed form, Galarkin, Rayleigh-Ritz) and numerical (such as FEM method). In recent years, there are considerable amount of researches about the unsymmetric laminated composites (with nonzero B matrix). The reasons of this particular research area evolved may be for the purposes of , 1) providing built-in self-damping mechanism when subjected to dynamic responses, or 2) the results of fabrication error in orienting different plies of a structure component, or 3) for aeroelastic tailoring to control mode shape and frequencies of lifting surfaces. One new reason is 4) to analyse the dynamic characteristics of the unparallel activations of smart material embedded in composites or sandwich structures, such as the sandwich beam, made of SMA hybrid composite skins and soft core. The upper skin is stiffer at full activation than lower skin, indicating that $\underline{B_{11} \neq 0}$. Some analytical approaches to unsymmetric laminates were presented by Whitney [18] and vibration analysis in unsymmetric composite plates were analyzed by Jensen [19].

Selecting first-order shear deformation theory as assumption of sandwich panel dispalcement field is due to its fairly thick and soft core, the thin and stiff SMA hybrid laminated skins are bonded between core. The higher-order theory may not fit for the unprecedented thermal activation and combined core deformations. Long and flexible beam or sandwich beam might confront large-amplitude vibration which lead to nonlinear vibration problems, and its nonlinear governing equations require special technique to obtain fairly good results. The researches in this particular area can be found recently in Kapania & Raciti [20]. They apply FEM technique to obtain the nonlinear governing equations, then using multiple-scale method to solve the nonlinear ordinary differential equations.

Reviewing the work by Bhimaraddi [21] [22] and Eslami & Kandil [23] [24] have helped the author how to solve group of nonlinear partial differential equations. The method assign two known admissible functions for w, ψ_x which satisfy the sturcture boundary conditions, then apply Gelarkin method transforming these nonlinear governing equations into one nonlinear ordinary differential equation take the form as $\ddot{s} + a_1 s + a_2 s^2 + a_3 s^3 = q_0$. The final step is to use multiple-scale technique to solve this nonlinear ordinary differential equation for free vibration analysis.

Reviewing the latest research work have shown that they are mostly related to composite beams,plates,shells, of solid laminates. There are very few work contributed to sandwich structures, especially in sandwich beam with embedded smart materials. The nonlinear vibration problems of SMA hybrid sandwich beam will be studied at different boundary conditions in the following subsections.

SOLUTION OF SIMPLY-SUPPORTED BEAM

The nonlinearity induced by unsymmetric laminates of the sandwich beam ,$\partial/\partial x(N_x{}^u \partial w/\partial x) + \partial/\partial x(N_x{}^l \partial w/\partial x)$,expressed in governing equations($u_0 = 0$) for 1-D beam case, obtaining

$$-G_{13}h\left(\psi_x + \frac{\partial w}{\partial x}\right) + D_{11}\frac{\partial^2 \psi_x}{\partial x^2} + B_{11}\frac{\partial w}{\partial x}\frac{\partial^2 w}{\partial x^2} = I\ddot{\psi}_x \qquad (28)$$

$$G_{13}h\left(\frac{\partial\psi_x}{\partial x}+\frac{\partial^2 w}{\partial x^2}\right)+\frac{3}{2}(\bar{A}_{11}+A_{11})\left(\frac{\partial w}{\partial x}\right)^2\frac{\partial^2 w}{\partial x^2}+\frac{h}{2}(A_{11}-\bar{A}_{11})\left(\frac{\partial\psi_x}{\partial x}\right)\frac{\partial^2 w}{\partial x^2}$$

$$+\frac{h}{2}(A_{11}-\bar{A}_{11})\left(\frac{\partial^2\psi_x}{\partial x^2}\right)\frac{\partial w}{\partial x}+(N_x^{*u}+N_x^{*1})\frac{\partial^2 w}{\partial x^2}+q_0=(2\rho_0 h_1+\rho_c h)\,\ddot{w}$$

(29)

two nonlinear partial differential equations where,

N_x^{*u} Applied inplane load due to SMA wire recovery stress in uper
skin (lb/in)

N_x^{*1} Applied inplane load due to SMA wire recovery stress in lower
skin (lb/in)

Boundary conditions (simply-supported beam) are

x=0

     w = 0   (30a)

     $\partial\psi_x/\partial x=0$ (30b)

x=L

     w = 0   (30c)

     $\partial\psi_x/\partial x=0$ (30d)

We could assume the admmisible functions

w =   S(t) sin(αx)   (31)

ψ_x = -S(t)/L cos(αx)   (32)

        α = nπ/L

        n = 1,2,3,...

        S(t) flexural amplitude (function. of time)

equations (31), (32) satisfy boundary conditions (30a), (30b), (30c), (30d). Take derivative of (28) w.r.t x then add (29), and insert the $\partial\psi_x/\partial x$ of (29) in D_{11} term of $\partial/\partial x$ of (28). Noting that the shear effect and the inplane load effect are included in $D_{11}\partial^2/\partial x^2$ term. Ignoring non-linear part in $D_{11}\,\partial^2/\partial x^2$ [...], then substitute (31), (32) in (29) and apply Gelarkin method for (29) with weighting function sin(αx). The simply supported free vibration beam equation become

α = nπ/L

$$-s\left[\,D_{11}\left(1+\frac{N_x^{*u}+N_x^{*1}}{G_{13}h}\right)\alpha^4+(N_x^{*u}+N_x^{*1})\alpha^2\,\right]\frac{L}{2}+$$

$$s^2\left(\frac{2}{3}\alpha^3 B_{11}-\frac{h\alpha^2}{3L}(A_{11}-\bar{A}_{11})\right)-s^3\left(\frac{3\alpha^4 L}{16}(\bar{A}_{11}+A_{11})\right)$$

(33)

$$+\frac{2q_0 L}{n\pi}=\ddot{s}\left[\,(2\rho_0 h_1+\rho_c h)\left(1+\frac{D_{11}}{G_{13}h}\alpha^2\right)+\frac{I\alpha}{L}\,\right]\frac{L}{2}$$

Illiminate inertia term, we obtain static problem of external uniform load q_0 over span of L. For free vibrational analysis, we delete q_0 and (33) could be simply expressed as

$$a_1 \ddot{s} + a_2 s + a_3 s^2 + a_4 s^3 = 0 \tag{34}$$

$$a_1 = (2\rho_0 h_1 + \rho_c h)(1 + \frac{D_{11}}{G_{13}h}\alpha^2) + \frac{I\alpha}{L} \tag{35}$$

$$a_2 = D_{11}(1 + \frac{N_x^{*u} + N_x^{*l}}{G_{13}h})\alpha^4 + (N_x^{*u} + N_x^{*l})\alpha^2 \tag{36}$$

$$a_3 = (\frac{h\alpha^2}{3L}(A_{11} - \bar{A}_{11}) - \frac{2}{3}B_{11}\alpha^3)\frac{2}{L} \tag{37}$$

$$a_4 = \frac{3\alpha^4 L}{16}(\bar{A}_{11} + A_{11})\frac{2}{L} \tag{38}$$

(34) can also be expressed as

$$\ddot{s} + \omega^2 s + \frac{a_3}{a_1}s^2 + \frac{a_4}{a_1}s^3 = 0 \tag{39}$$

$$\omega^2 = \frac{D_{11}(1 + \frac{N_x^{*u} + N_x^{*l}}{G_{13}h})\alpha^4 + (N_x^{*u} + N_x^{*l})\alpha^2}{(2\rho_0 h_1 + \rho_c h)(1 + \frac{D_{11}}{G_{13}h}\alpha^2) + \frac{I\alpha}{L}} \tag{40}$$

Equation (39) is the Duffin's equation without damping term. The current methods treating (34) include Newton-ralphson approach like Singh & Rao [25], the finite element in time (FET) method in Bauchan & Hong [26], the finite element method in Hou & Yuan [27] and the multiple scale technique in Bhimaraddi [21] [22]. The cubic non-linearity described in $(a_4/a_1)s^3$ is a stiffening factor as vibration amplitude become large enough, or this term can be a softening factor if (a_4/a_1) is negative. The phenomenom could be found in Cartwell [28], Schmidt & Tondl [29] which investigating some parametrically excited systems or coupled nonlinear vibration systems.

DAMPED SYSTEM UNDER HARMONIC EXCITATION

We constructed the nonlinear vibration model illustrated in previous sections for merely the studies of undamped free vibration. It inherit special features of increased natural frequencies with respect to higher vibration amplitude(A/h) under the prescribed condition. Yet, our primary goal , in this section, is to excite the known nonlinear model with harmonic load in order to seek for the dynamic response in either time domain or frequency domain. Hopefully, we are able to obtain the equivalent structure transfer function in refer to Inmman [30]. The phsical model is sandwich beam of composite faces with SMA wires embedded. The core is fairly soft and good damping material. All the properties of the model were mentioned in the previous sections. However, this damped system is not viscously damped but hysterically damped system. The rationale is based on the fact that composite material of polymer matrix are following the elastic-viscoelastic correspondence principle(their moduli could be expressed as complex moduli). In view of [31], [32], the governing equation is adding (34) with a harmonic forcing term at the right hand side, the equation become

$$\ddot{s} + \omega^2 s + d_2 s^2 + d_3 s^3 = \varepsilon q' \cos\Omega t \tag{41}$$

where ω^2 , d_2, d_3, were defined in equation (40), (35) to (38) and ε is small , $q' = 4q_0/(\pi a_1 h)$ (#/slug in) as indicated in (33). Ω is forcing frequency (rad/sec), t is time step, and $\underline{s}$ is nondimensional amplitude (A/h). Since $\underline{I}$ is very small and $\underline{L}$ is large for long beam, (35) can be simplified as

$$a_1 = (2\rho_0 h_1 + \rho_c h)(1 + \frac{\bar{D}_{11}}{G_{13}h}\alpha^2) \tag{42}$$

We then apply correspondence principle from [33] and [34] by substituting (43) in (42) to (46)

$$\bar{G}_{13} = G_{13} + i \eta_c G_{13} \tag{43a}$$
$$\bar{D}_{11} = D_{11} + i \eta_b D_{11} \tag{43b}$$
$$(A_{11} - \bar{A}_{11})^* = (A_{11} - \bar{A}_{11}) + i \eta_e (A_{11} - \bar{A}_{11}) \tag{43c}$$
$$B_{11}^* = B_{11} + i \eta_d B_{11} \tag{43d}$$
$$(A_{11} + \bar{A}_{11})^* = (A_{11} + \bar{A}_{11}) + i \eta_a (A_{11} + \bar{A}_{11}) \tag{43e}$$

where η_b , η_a , η_d , η_e are the loss factors for the composite laminate [34], $\underline{i = \sqrt{-1}}$, the value of η_b , η_a , η_d , η_e are approximately .2 η_m [η_m (loss factor of epoxy matrix) = .015]. core η_c is approx. .4. Therefore, the known values of loss factor can be substitute in the following expressions,

$$\omega^2 = \frac{\bar{D}_{11}(1 + \frac{N_x^{*u} + N_x^{*l}}{G_{13}h})\alpha^4 + (N_x^{*u} + N_x^{*l})\alpha^2}{a_1} \tag{44}$$

$$d_2 = \bar{a}_2 / a_1 \tag{45}$$

$$\bar{a}_2 = (\frac{h\alpha^2}{3L}(A_{11} - \bar{A}_{11})^* - \frac{2}{3}B_{11}^*\alpha^3)\frac{2}{L} \tag{45a}$$

$$d_3 = \bar{a}_3 / a_1 \tag{46}$$

$$\bar{a}_3 = \frac{3\alpha^4 L}{16}(\bar{A}_{11} + A_{11})^*\frac{2}{L} \tag{46a}$$

Therefore, the nonlinear ordinary differential equation (41) with its nondimensional $\underline{s}$ may also be expressed in complex form

$$s = X + i Y$$

we substitute the expression into equation (41)

$$(\ddot{X} + i\ddot{Y}) + (e_5 + ie_6)(X + iY) + (e_7 + ie_8)(X + iY)^2 + (e_9 + ie_{10})(X + iY)^3 = \varepsilon \, q' \, \cos\Omega t \tag{47}$$

separation of the real and imaginary part in equation (47)

real part

$$\ddot{X} + e_5 X - e_6 Y + e_7(X^2 - Y^2) - 2e_8 XY + e_9(X^3 - 3XY^2) + e_{10}(Y^3 - 3X^2 Y) = \varepsilon \, q' \, \cos\Omega t \tag{48}$$

imaginary part

$$\ddot{Y} + e_5 X + e_6 Y + e_8(X^2 - Y^2) + 2e_7 XY - e_9(Y^3 - 3YX^2) + e_{10}(X^3 - 3Y^2 X) = 0 \tag{49}$$

solving (48), (49) system of highly nonlinear and coupled equations with assumed initial conditions as

$$X(0) = \dot{X}(0) = Y(0) = \dot{Y}(0) = 0 \tag{50}$$

we get the calculated dynamic response under harmonic excitation. However, there is no analytical solution for the system of equations except using numeriacl method. Using higher order Runge- Kutta approach to obtain the time response of the physical model. We insert the prescribed SMA sandwich beam model in (48), (49) and (50) and apply ode45 of MATLAB to get the response plot as following Figures. The real part $\underline{X}$ is the physical nondimensional amplitude-time response. Frequency response could also be obtained by applying FFT (fast fourier transform) to the time response.

CONCLUSION AND DISCUSSION

The calculated response showed that how much the vibration can be suprressed through the use of SMA in sandwich beam structure. The beam length, core thickness, and inplane recovery stresses of SMA are important parameters in predicting dynamic response of sandwich beam. Further studies in 2-D SMA hybrid sandwich plate will be pursuited.

The practical use of activated sandwich structures and the realistic boundary conditions in engineering applications demand detailed studies. A more effecient numerical method is essential for predicting large amplitude response of elastic structures and treating SMA wires as sensors could induce more advanced study in vibration control.

References

[1]   Rogers C. A., Selected papers presented at the U.S. Army Research office workshop on "Smart Materials, Structures, and Mathematical Issues", p17-p26, Virginia Polytechnic Inst. and State U. , Blacksburg, Virginia 24061 September 15-16, 1988.

[2]   Hawkins L. E., Vick B., Rogers C. A.," An Investigation of the Transient Thermal Response of Shape Memory Alloy Composite Beam", pp. 1972, from A collection of technical papers of "AIAA/ASME /ASCE/AHS/ASC 31st Structures, Structural Dynamics and materials conf. ", Long Beach, CA, April 2-4, 1990.

[3]   Kaufman L., R. Salzbrenner ,"Internal Vibration Absorption in Potential Structural Materials", Research Contract. DAAG46-74-C-0048, MIT., Section excerpt from "Shape Memory Effects in Alloys", Jeff Perkins, Naval Postgraduate School, Montery, CA . Call no. (UF), TN689.2.i59, 1975.

[4]   Duerig, T. W., K N. Melton, D Stockel, C. M. Wayman, " Engineering Aspects of Shape Memory Alloys", Butterworth-Heinemann Ltd, 1990. pp.5

[5]   Rogers C.A., Barker D. K.," Experimental Studies of Active Strain Energy Tuning of Adaptive Composites", pp. 2234, Fig 9., A collection of technical papers of "AIAA/ASME/ASCE/AHS/ASC 31st Structures, Structural Dynamics and Materials conf. ", Long Beach, CA, April 2-4, 1990.

[6]   Whitney, J.M. and Leissa, A.W., Journal of Applied Mechanics, Vol. 36, 1969, pp. 261-266.

[7]   Bai, C.M. and Sun, C.T., "Nonlinear Flexural Vibration of Sandwich Plates Subjected to In-Plane Forces", 2nd International Conference on Sandwich Construction, held in Gainesville, U of Florida, 1992

[8]   Chia, C.Y., "Nonlinear Analysis of Plates",McGraw-Hill, New York, 1980

[9]   Whitney, J.M., " Structural Analysis of Laminated Anisotropic Plates", Materials Lab., AFWAL, Technomic Publishing Co., 1987, pp.303, (10.161),(10.162)

[10]   Kapania, R. K. & Raciti, S. "Recent Advances in Analysis of Laminated Beams and Plates, Part I: Shear Effects and Buckling", AIAA Journal, Vol. 27, No. 7, July 1989, PP 923-934.

[11]   Rakesh K.K & Stefano R., "Recent Advances in Analysis of Laminated Beams and Plates, PartII: Vibrations and Wave Propagation" ,AIAA Journal, Vol. 27, No. 7, July 1989, PP935-946.

[12]   Reissner, E. "The Effect of Transverse Shear Deformation on the Bending of Elastic Plates" Journal of Applied Mechanics. 12:69-77,1945.

[13]   Mindlin, R.D. "Influence of Rotatory Inertia and Shear on Flexural Motions of Isotropic, Elastic Plates" Journal of Applied Mechanics 18:336-343, 1951.

[14]   Yang P.C. Norris C.H. Stavsky Y. " Elastic Wave Propagation in Heterogeous Plates" International Journal of Solids and Structures, 2:665-684, 1966.

[15]   Whitney J.M., Pagano N.J. "Shear Deformation in Hetergeneous Antisotropic Plates", Journal of Applied Mechanics, 37:1031-1036, 1970.

[16]   Reddy J.N.,"A Simple Higher-Order Theory for Laminated Composites" Journal of Applied Mechanics, Vol.51, 1984.pp.745-752.

[17]   Bert C.W. "Research on Dynamic Behavior of Commmposite and Sandwich Plates", Shock and Vibration Digest, Vol.17, Nov. 1985.pp.3-15.

[18]   Whitney J.M. "Bending-Extensional Coupling in Laminated Plates under Transverse Loading" Journal of Composite Materials, Vol.3, Jan.1969.pp.20-28.

[19]   Jensen D.W. & Crawley E.F. "Frequency Determination Technique for Cantilevered Plates with Bending-Torsion Coupling" AIAA Journal, Vol.22, March 1984.pp.415-420.

[20]   Kapania R.K. & Raciti S. "Nonlinear Vibrations of Unsymmetrically Laminated Beams", AIAA Journal ,Vol. 27, Feb. 1989. pp.201-211.

[21]   Bhimaraddi A." Nonlinear Flexural Vibrations of Rectangular Plates Subjected to In-Plane Forces Using a New Shear Deformation Theory", Elsevier Applied Science Publishers Ltd., 1987.

[22]   Bhimaraddi A. "Nonlinear Free Vibration Analysis of Composit Plate with Initial Imperfections and In-Plane Loading", International Journal of Solids structures, Vol. 25, No.1, pp.33-43, 1989.

[23]   Eslami H. & Kandil O.A. " Nonlinear Forced Vibration of Orthotropic Rectangular Plates Using the Method of Multiple Scales", AIAA Journal, Vol.27, No.7, July 1989.pp.955-960.

[24]   Eslami H. & Kandil O.A. " Two-Mode Nonlinear Vibration of Orthotropic Plates Using Method of Multiple Scales", AIAA Journal, Vol. 27, No.7, July 1989, pp.961-967.

[25]   Singh G & Rao G. V. "Analysis of The Nonlinear vibration of Unsymmetrically Laminated Composite Beams", AIAA Journal, Vol. 29, No. 10, October 1991, pp. 1727-1735.

[26]   Bauchau O. A. & Hong C. H. "Nonlinaer response and Stability Analysis of Beams Using Finite Elements in Time", AIAA Journal, Vol. 26, No. 9, September 1988, pp. 1135-1142.

[27]   Hou J. W. & Yuan J. Z. "Calculation of Eigenvalue and Eigenvector Derivatives for Nonlinear Beam Vibration", AIAA journal, Vol.26, no. ,July 1988, pp. 872-880.

[28]   Cartwell M.,"Introduction to Linear, parametric and Nonlinear Vibration", U of Aberdeen, T.J. Press (Padstow) Ltd, Padstow, Cornwall, Great Britain,1990, TA355. C34

[29]   Schmidt G. & Tondl A. "Nonlinear Vibration", Cambridge University Press., QA935. S263, 1986

[30]   ⌐ Inmman   'structural dynamics and control   ++++++++++++

[31]   Sun C. T. et al, "Internal Damping of Short-Fiber Reinforced Polymer Matrix Composites", Computers and Structures, 20, pp. 391-400 , 1985.

[32]   Gibson R. F., Chaturvedi S. K., Sun C. T. "Complex Moduli of Aligned Discontinuous Fiber-Reinforced Polymer Composites", U of Idaho, U of Florida, Journal of Materials Science, Vol. 17, 1982, pp.3499-3509.

[33]   Suarez S. A., et al. "The Influence of Fiber Length and Fiber Orientation on Damping and Stiffness of Polymer Composite Materials", Conference on Experimental Mechanics in Las Vegas, June 9,1985.

[34]   Sun C. T., Wu J. K. "Prediction of Material Damping of Laminated Polymer Matrix Composites", Journal of Material Science, Vol. 22 (1987), pp. 1006-1012.

Model 2, h=.2", L=120', Simply-Supported Beam

Model 2, h=.2", L=120', Simply-Supported Beam

Model 2, h=.2", L=120', Simply-Supported Beam

Model 2, h=.2", L=120", Simply-Supported Beam

Model 2, h=.2", L=120', Simply-Supported Beam

Model 2, h=.2", L=120', Simply-Supported Beam

Model 2, h=.2", L=120', Simply-Supported Beam

Model 2, h=.2", L=120', Simply-Supported Beam

$N_x^{*u} = N_x^{*l} = 45$ #/in

$N_x^{*u} = N_x^{*l} = 0$

Force freq.= 4 rad/sec

Force freq.= 16 rad/sec

Force freq.= 12 rad/sec

Force freq.= 20 rad/sec

Time Response (sec.)

A/h

A/h real

Loss F.=0.9792--- Loss F.=0.9651 Freq. Response (HZ)

Loss F.=1.0695e-02--- Loss F.=0.1245 Freq. Response (HZ)

Loss F.=3.5077e-02--- Loss F.=0.7241 Freq. Response (HZ)

Loss F.=0.4706--- Loss F.=0.1245 Freq. Response (HZ)

ECD-18

Model 1, h=.2", L=12", Simply-Supported Beam

A MAGNETIC TUNED-MASS DAMPER FOR BUFFET-INDUCED AIRFOIL VIBRATION

Joseph R. Maly
Kevin L. Napolitano

CSA Engineering, Inc.

1. Abstract

Vibrations are an inherent problem for aircraft structures, especially military aircraft that perform high-speed maneuvers causing extreme acceleration levels. A form of unwanted vibration called buffet occurs when an aircraft surface is directly exposed to an unsteady, vortex flow generated upstream during high-angle-of-attack maneuvers. In the case of the F/A-18 aircraft, buffeting of the twin vertical stabilizers excites the bending and torsional modes of these structures, and, over time, fatigue failures occur. Failures of this nature are unpredictable and result in millions of dollars every year in maintenance costs.

A tuned mass damper solution for this problem is proposed. Analysis indicates that an array of dampers employing eddy currents induced by rare earth magnets for the damping mechanism will provide sufficient damping to significantly reduce the dynamic response of the twin-vertical-tail buffet. A prototype damper was built, and it was determined by testing that this concept is a valid approach to solve this problem. The prototype was tested on a simple structure, selected so that the mass ratio with the prototype applied to the structure is equal to the mass ratio of the TMD array applied to the F/A-18 tail. The amplitude of the undamped response was reduced by a factor of 20 when the magnetic TMD was applied.
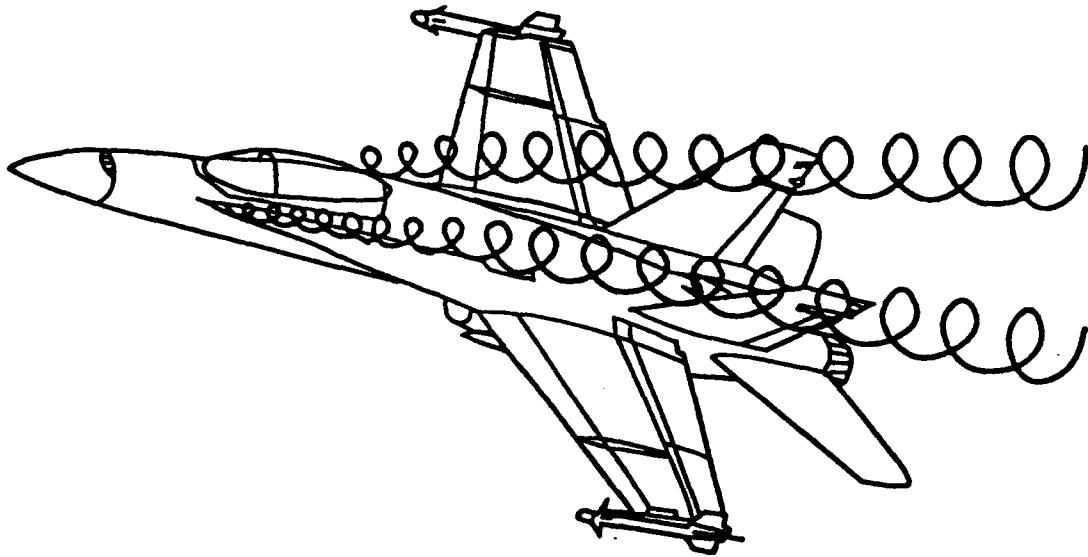
Figure 1: Schematic of vortex flow field generated during F/A-18 maneuver (courtesy McDonnell Aircraft Company)

2. Introduction and Summary

Vibrations are inherent to aircraft structures, especially military aircraft that perform high-speed maneuvers causing extreme acceleration levels. A form of unwanted vibration called buffet occurs when an aircraft surface is directly exposed to an unsteady, vortex flow generated upstream during high-angle-of-attack maneuvers. In the case of the F/A-18 aircraft, buffeting of the twin vertical tails excites the bending and torsional modes of these structures, and, over time, fatigue failures occur. Figure 1 shows a simplified sketch of this flow field and the buffeting of the F/A-18 empennage. Failures of this nature are unpredictable and result in millions of dollars every year in maintenance costs.

Vibration damping is often a preferred solution when resonant vibration cannot be eliminated. Integral damping concepts, which incorporate damping mechanisms into structural designs in the early stages of development, are becoming design tools throughout the aerospace industry, but excessive vibration in existing aircraft requires a solution that can be appended to a current design. Tuned-mass dampers (TMDs) are more feasible for aircraft aerodynamic surface vibration problems than other types of dampers, especially for modifications to existing aircraft. This is because of the capability to add a significant amount of damping to a single mode with a minimal

addition of weight; past research has supported this.[1] [2]

The goal of this effort was to develop a self-contained damping device (capable of mass-production for retrofit to existing aircraft) to attenuate the dynamics due to buffeting of the F/A-18 vertical tail. Research showed that the F/A-18 tail is subjected to such a severe dynamic environment that a single, conventional TMD would require a displacement far in excess of the allowable "rattle" space (the space between the skins) in the tail; this led to the concept of an *array* of TMDs positioned near the top of each tail. Analysis predicted that a 10-pound TMD was needed to achieve a goal of 40% added (structural) damping. The analysis was based on the assumption of 10% baseline (aerodynamic) damping. It was determined that the space limitation that precluded the implementation of a single TMD could be overcome if the moving mass was divided over ten individual units, each weighing one pound.

Previous research has shown that a conventional TMD employing viscoelastic materials (VEMs) would not survive the dynamic environment of the F/A-18 vertical tail, so a design was developed employing eddy currents induced by rare earth magnets for the damping mechanism. A prototype was built, and it was determined by testing that this concept is a valid approach to solve this problem. The prototype was tested on a simple structure, selected so that the mass ratio with the prototype applied to the structure was equal to the mass ratio of the TMD array applied to the F/A-18 tail. The results of this test are plotted in Figure 2; the amplitude of the undamped response was reduced by a factor of 20 when the magnetic TMD was applied.

Magnetic TMDs are unaffected by temperature variations and will have applications in many other fields. This work was performed for the Naval Air Systems Command under the Small Business Innovation Research (SBIR) Program.

3. Background

Design studies have indicated that a tuned-mass damper (TMD) is more feasible for aircraft aerodynamic surface vibration problems than other types of dampers, especially for modifications to existing aircraft. This is because of the high *damping/weight* ratio achievable with this type of damper and its ability to add significant damping to a single vibrational mode.

A TMD is a device consisting of a mass and a damped "spring" attached to a structure at or near an antinode of a troublesome mode of vibration. It is actually a special case of a vibration absorber. The application of a TMD to a structure

---

[1]Gibson, W. C., Maly, J. R., and Austin, E. M., "Conceptual Design of Damping Treatments for the F/A-18 Vertical Tail," CSA Report No. 88-11-02, November, 1988.

[2]Parin, M. and Nashif, A. D., "Development of Vibration Control Measures for the F/A-18 Vertical Tail," Anatrol Report No. 88024, February, 1989.
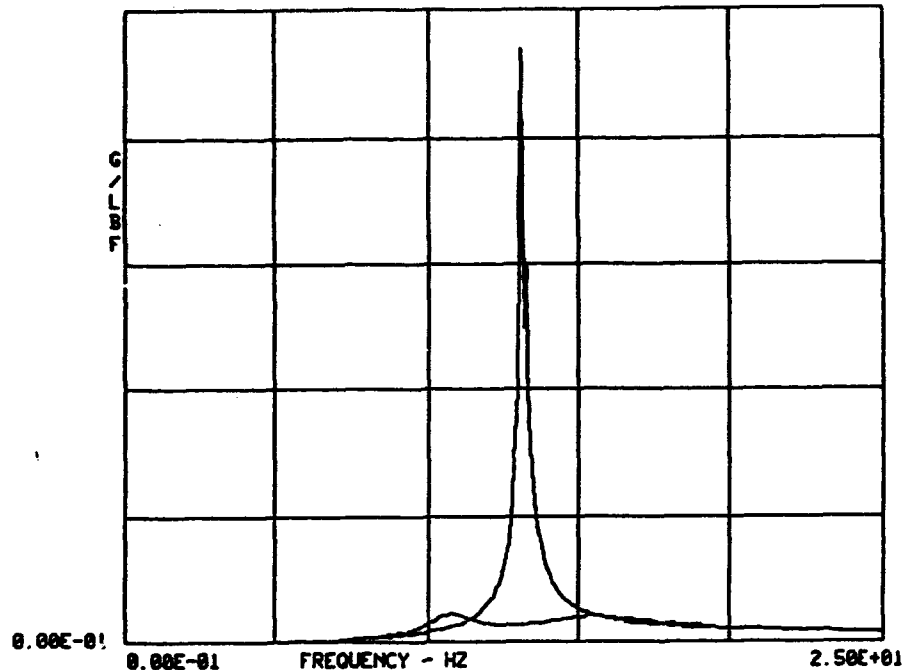
Figure 2: Frequency response for a test structure with and without prototype TMD

results in two coupled modes replacing the original "target" mode. These "split" modes typically have significantly lower amplitudes than the original mode, with the amount of reduction dependent on the loss characteristics of the damped spring. One of the modes has a lower frequency than the original mode, while the other mode is higher in frequency. These effects are shown in Figure 3 for a simple system.

TMDs are constructed using a "tuning mass" and a spring with complex stiffness. The spring is often a simple pad of viscoelastic material in compression or shear, or the TMD can be built as a damped structure such as a cantilever beam with viscoelastic material sandwiched between two face-sheets. The damping mechanism can also be achieved with magnetic or viscous (fluid) damping.

Because of the extreme loading conditions to which the F/A-18 vertical tail is subjected under high-angle-of-attack maneuvers, a traditional viscoelastic-based TMD will not solve this problem. The extreme case of the loading environment is a considerable one; displacements of over 12 inches and accelerations in excess of 500 G's (zero to peak) at the tip of the tail have been observed in flight.[3] There are two reasons why a "standard" TMD cannot be used under these conditions.

1. A TMD composed of VEM would not be able to survive the high G-loads that are generated in the high-angle-of-attack maneuvers. VEMs are soft, polymeric materials, and stress failure of the TMD would occur under the extreme dynamic

---

[3]Liguore, S., Ferman, M., Yurkovich, R., "Integral Damping Treatment for Primary Aircraft Structures," Damping '91 Conference, San Diego, CA, February, 1991.
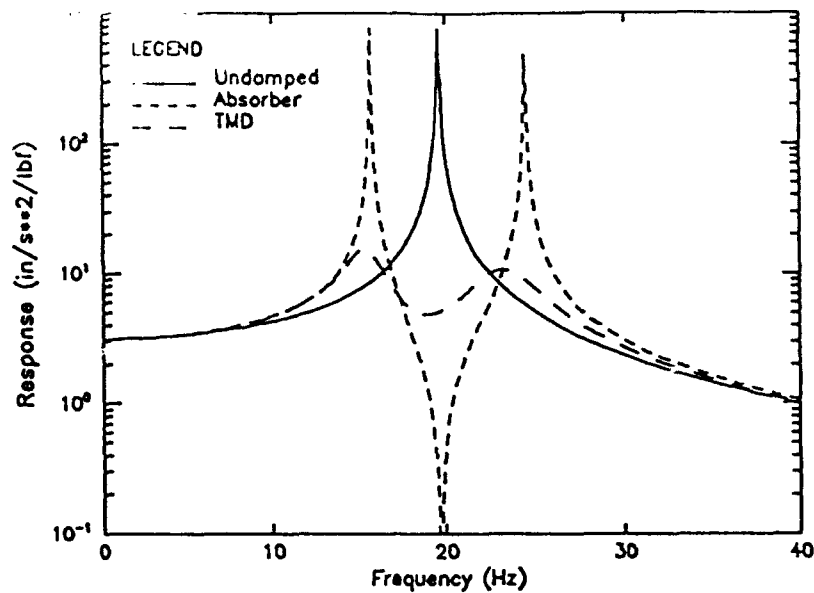
Figure 3: Effects of an absorber and a tuned-mass damper

loads of the buffet environment. This failure would occur whether the TMD spring is a simple pad of VEM in compression or shear (in which case the VEM will fail) or the TMD is a damped structure, such as a damped cantilever beam, with the VEM sandwiched between two face-sheets.[4] In addition, heating of the VEM as the vibration energy is dissipated at these extreme levels would cause unpredictable deterioration of the viscoelastic properties of the material.

2. Under the extreme conditions of the high-angle-of-attack maneuvers, "rattle space" (required displacement of the TMD mass relative to its base, where it is mounted to the aircraft) far exceeds the amount of space available inside the vertical tail.

Because of these reasons, alternative approaches were investigated, but the best approach was still the original TMD concept. The primary concerns associated with employing a TMD solution (enumerated above) were addressed as follows:

1. The damping mechanism for the TMD is magnetic damping, thereby eliminating the need for incorporating VEMs into the design. The details of this damping mechanism are described below.

---

[4]For a damped cantilever beam to be used as the TMD, the facesheets would have to be very thin to achieve the 15-Hz frequency. It has been shown by test that even thin steel facesheets would fail due to stress under dynamic loading at this frequency of about 12 G's.
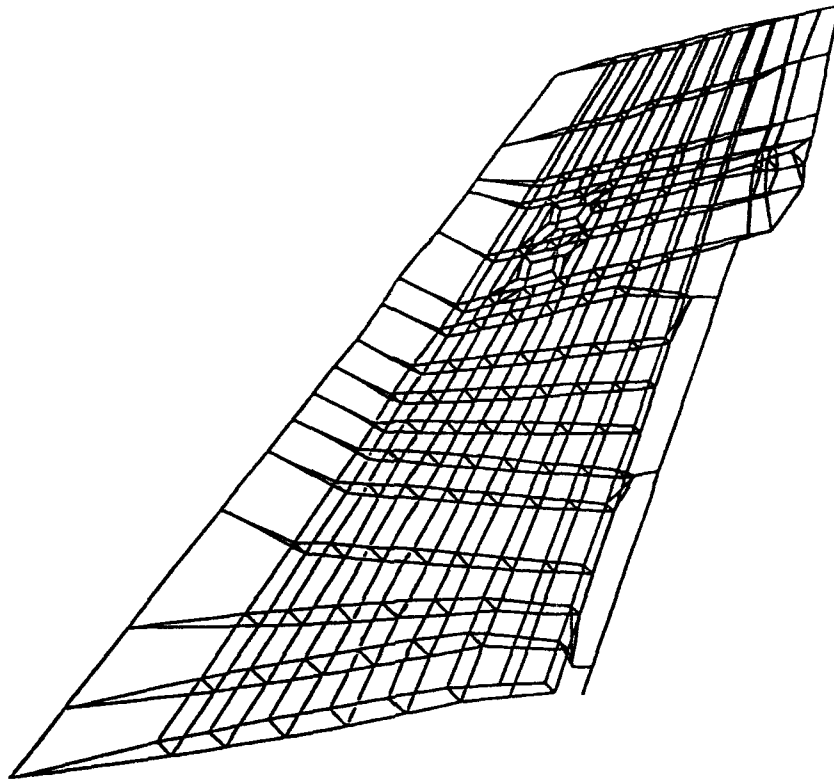
Figure 4: Finite element model of F/A-18 vertical tail

2. The problem of limited rattle space is addressed by employing an array of ten TMDs. By increasing the number of individual TMD units, damping can be obtained for much higher acceleration levels by effectively increasing the TMD moving mass, and, therefore, the associated effective mass ratio. (The effective mass ratio is the ratio of the moving mass of the TMD to the modal mass of the structure for the mode of interest scaled to a unit displacement at the point of attachment of the TMD.) A higher effective mass ratio permits a TMD design with a higher level of damping. Because of this effect combined with distributing the mass over ten individual units, less rattle space is required.

4.   Analysis

The TMD concept was analyzed using the finite element model of the F/A-18 vertical tail shown in Figure 4. This model was developed by CSA Engineering for McDonnell Aircraft Company as a baseline model for damping treatment design; it was based on a more complex finite element model for stress analysis created by Northrop Corporation. Dynamic loading simulating the extreme buffet environment was used to excite the model and make predictions of system performance. A baseline damping level of 10% was assumed due to aerodynamic effects.

The fundamental modes of this structure are the first bending mode, predicted by the finite element model at 15 Hz, and the first torsion mode, at 43 Hz. These are

the primary modes of interest for this problem because of the nature of the loading; the buffet pressure PSD, which is a function of angle of attack, air speed, and air density, typically peaks in the frequency range of 10-50 Hz.[5] These modes occur at frequencies that are far enough apart that a TMD for one of these modes will have virtually no effect on the other mode. Since TMD design for a low frequency is more difficult, this effort focused on a design for the 15-Hz bending mode. A solution for the torsion mode could also be designed.

A TMD was derived for the bending mode that would contribute 10% damping. The parameters for this TMD are the following: weight = 0.8 lbs, spring stiffness = 17.5 lbs/in, loss factor = 0.2.

Eigenanalysis was performed with this TMD applied to determine the response of the vertical tail under the extreme loading conditions (500 G's at the tip of the tail).[6] While the above design did produce 10% damping for the bending mode and the response of the tail below 40 Hz was reduced significantly, the amount of displacement required for the TMD mass (relative to the TMD base) was in excess of 18 inches. If the rattle space is 1 inch, the maximum relative displacement is 0.5 inches, and, assuming linear behavior, the TMD would only be effective for accelerations of up to (500)(0.5)/18, or about 14, Gs.

To solve this problem of high relative displacement in the TMD, the mass of the TMD in the finite element model was increased. Adding mass to the TMD increases the effective mass ratio, and, it can be shown that, as the effective mass ratio increases, the allowable loss factor of the TMD also increases. (If a higher-than-allowable TMD loss factor is used, however, the TMD will not be "tuneable.") The resulting modal loss of the structure also goes up with increasing effective mass ratio.

TMDs with weights of 5, 10, and 15 pounds were analyzed with the finite element model. Iterations on these models were performed, varying the TMD spring stiffnesses and loss factors to "tune" the TMDs. The corresponding spring stiffnesses and loss factors and the resulting modal loss factors and relative displacements under the 500-G loading are listed in Table 1 and shown in graphic form in Figure 5. Obviously, relative displacement decreases as modal damping increases. The corresponding TMD base displacements (at the point on the tail where the TMD is mounted) are 2.9, 2.7, and 2.5 inches, respectively, compared to approximately 8 inches for the baseline model. Figure 6 shows the displacement response plot for the baseline configuration compared to responses with the 0.8-, 5-, 10-, and 15-pound TMDs added.

An auxiliary, but important, advantage to designing a TMD solution with a high effective mass ratio is the resulting low sensitivity to mistuning of the TMD. This

[5]Zimmerman, N. H., and Ferman, M. A., "Prediction of Tail Buffet Loads for Design Application," McDonnell Aircraft Company, July, 1987.
[6]The analyses performed here assumed accelerations of 500 Gs at the tip of the tail for the first mode. It has since been determined that the actual accelerations for the first mode are up to 120 Gs, and that the *second* mode has peak accelerations of 500 Gs. This reduces the order of difficulty for a first-mode TMD, and relaxes the rattle space requirements.

TMD			modal damping	relative displacement (in)
weight (lb)	stiffness (lb/in)	loss factor		
0.8	17.5	0.2	10%	18.
5.0	100.	0.45	26%	6.8
10.0	150.	0.9	42%	3.8
15.0	190.	1.2	48%	2.9

Table 1: Design and modal parameters for three TMDs for the bending mode
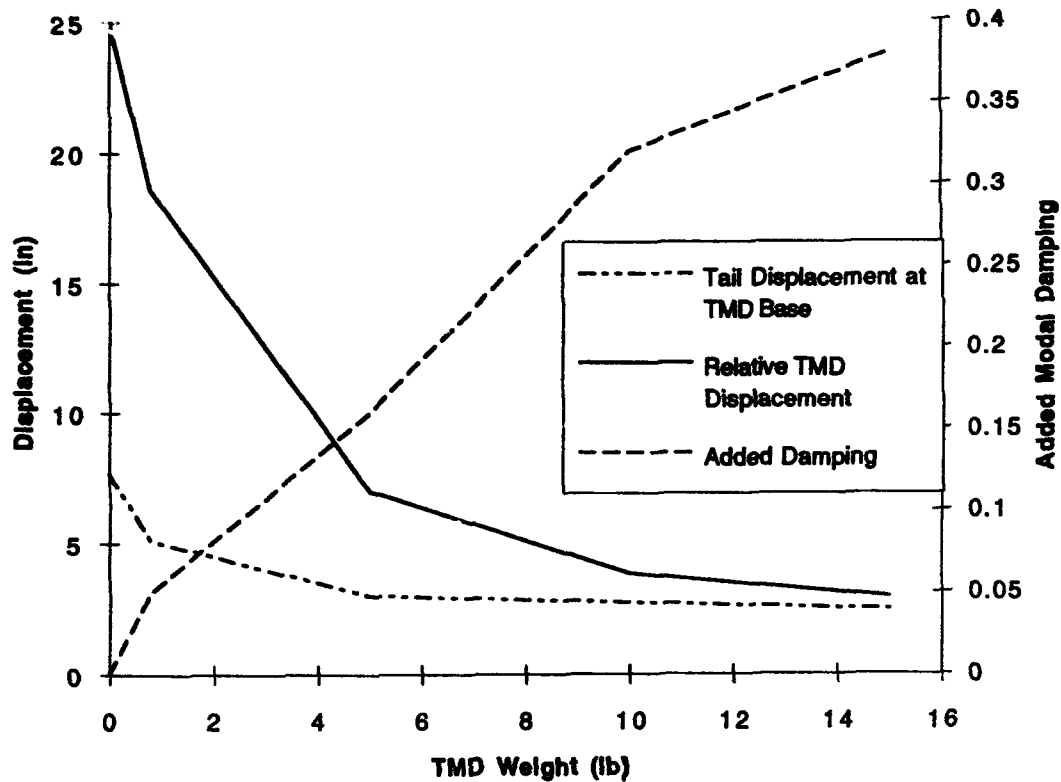
Figure 5: Displacement and damping trends versus TMD weight
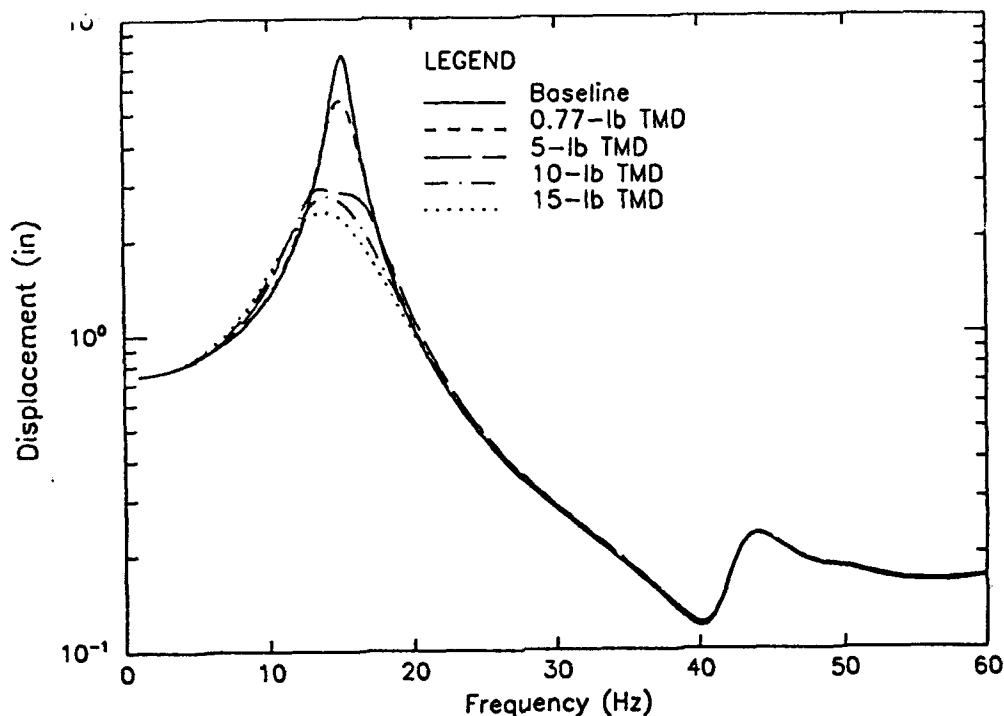
Figure 6: Displacement responses at TMD attachment point with 0.8-, 5-, 10-, and 15-pound TMDs compared to baseline response at attachment point

is illustrated in Figure 7. The displacement response at a point on the tail with the 10-pound TMD is compared to the response at the same point if the TMD were mistuned, with respect to frequency, by 15%. Another perspective on the sensitivity of the TMD to mistuning can be observed in Figure 8. This plot shows the effect on the modal damping of the split modes due to variations in the spring stiffness of the TMD.

It should be pointed out that simply adding mass to a system to increase modal mass does not reduce amplitude of modal response, even though frequency is directly related to mass. Figure 9 shows the effect on the response of a single-degree-of-freedom system when mass is added to the system without also adding the stiffness and damping of the TMD.

4.1   Tuned-Mass Damper Array

To keep the overall weight of the solution as low as possible, a variation of the 10-pound TMD was pursued. Given the space limitations inside the tail, it would be physically impossible to install a single 10-pound TMD, so ten 1-pound TMDs were positioned at discrete nodes of the finite element model, and the analysis sequence was repeated. This group of ten 1-pound TMDs will be referred to as the TMD array. Each TMD had the same loss factor as the 10-pound TMD, with one-tenth the spring stiffness. Figure 10 shows a typical displacement response, for the extreme loading
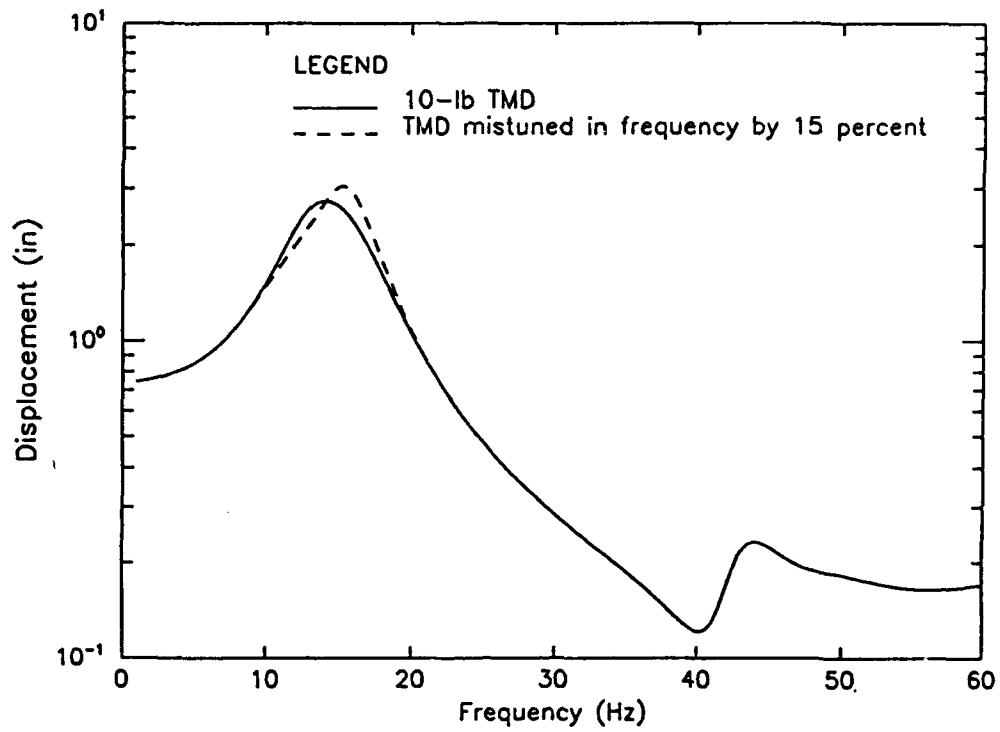
Figure 7: Displacement response with 10-pound TMD compared to response with mistuned TMD
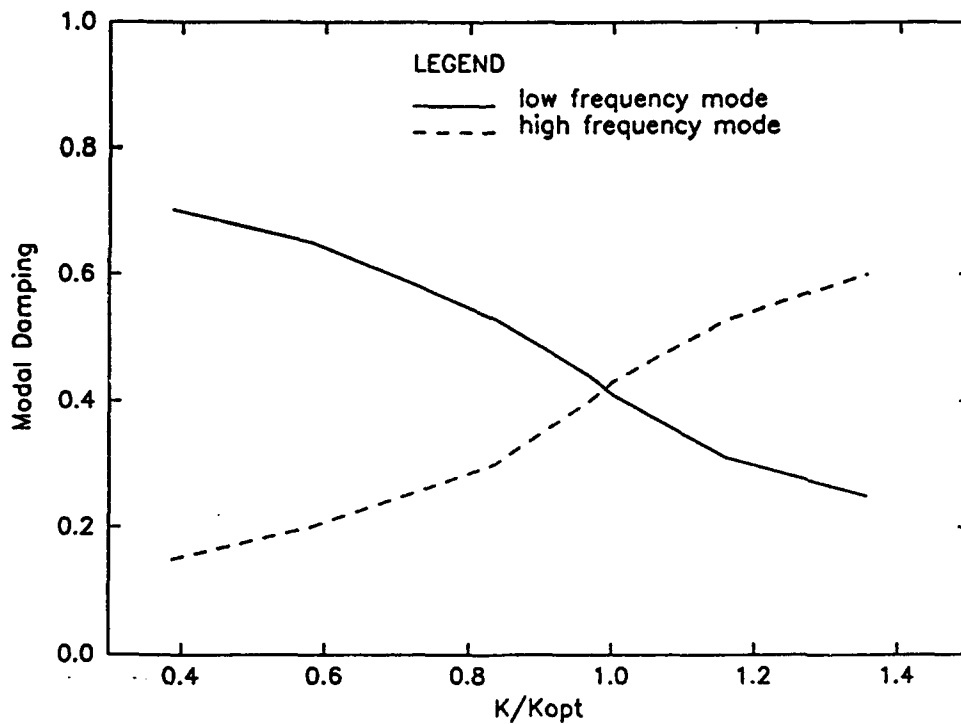
Figure 8: Sensitivity of TMD tuning to TMD stiffness
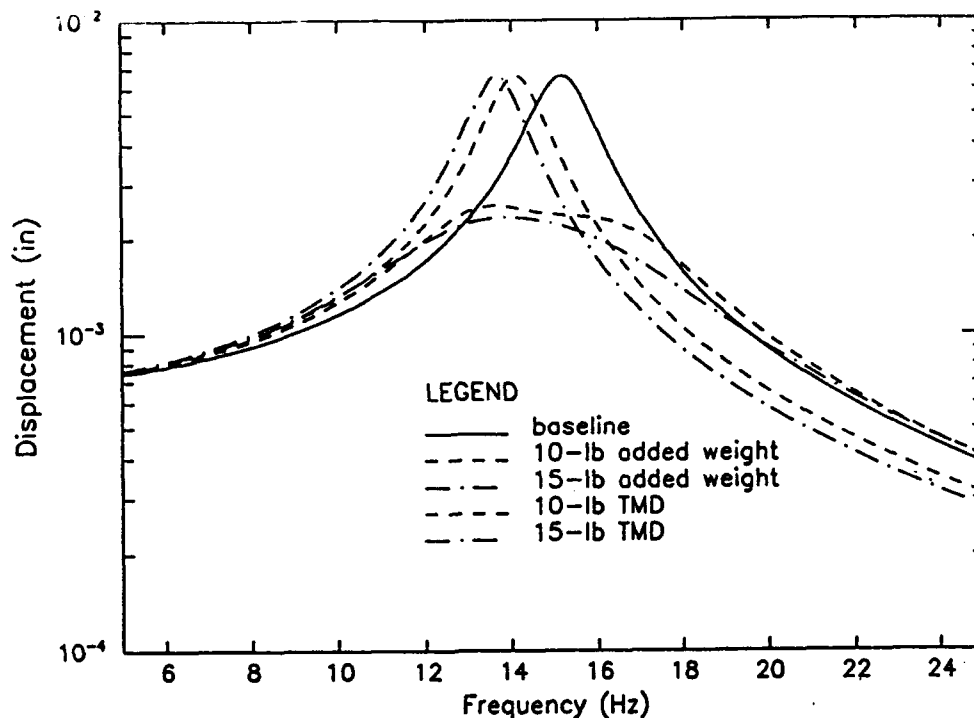
Figure 9: Single-degree-of-freedom system: displacement response with added mass, with and without damped spring

condition, with the TMD array applied compared to the baseline response.

The displacements of the TMD masses relative to the TMD bases for the ten units of the TMD array are shown plotted versus frequency in Figure 11; these displacements represent the required strokes for the TMDs under the maximum loading conditions. The maximum relative displacements vary from 3.4 inches to 4.6 inches, a significant decrease from 18 inches for the 0.8-pound TMD. Since the maximum available stroke for each TMD is about 1 inch (corresponding to a maximum relative displacement of 0.5 inches), the maximum G-load for which each individual TMD will be effective is between (500)(0.5)/4.6, or 54.3, Gs, and (500)(0.5)/3.4, or 73.5, Gs.

4.2 Nonlinear Behavior at High Acceleration Levels

At accelerations greater than these maximum G-levels, the TMD masses will "bottom out" and collide with the TMD end caps. Even though the analyses predict that the TMD array will effectively decrease response levels up to accelerations of 54 to 74 Gs, when the loading exceeds these levels the TMD mechanism becomes ineffective. The behavior of the TMD array at these high acceleration levels was analyzed with nonlinear analysis.

To analyze the non-linear behavior of this TMD mass impact, the F/A-18 vertical tail with the TMD applied was modeled as a simple two-degree-of-freedom system, shown in Figure 12. A FORTRAN code was written to numerically integrate the
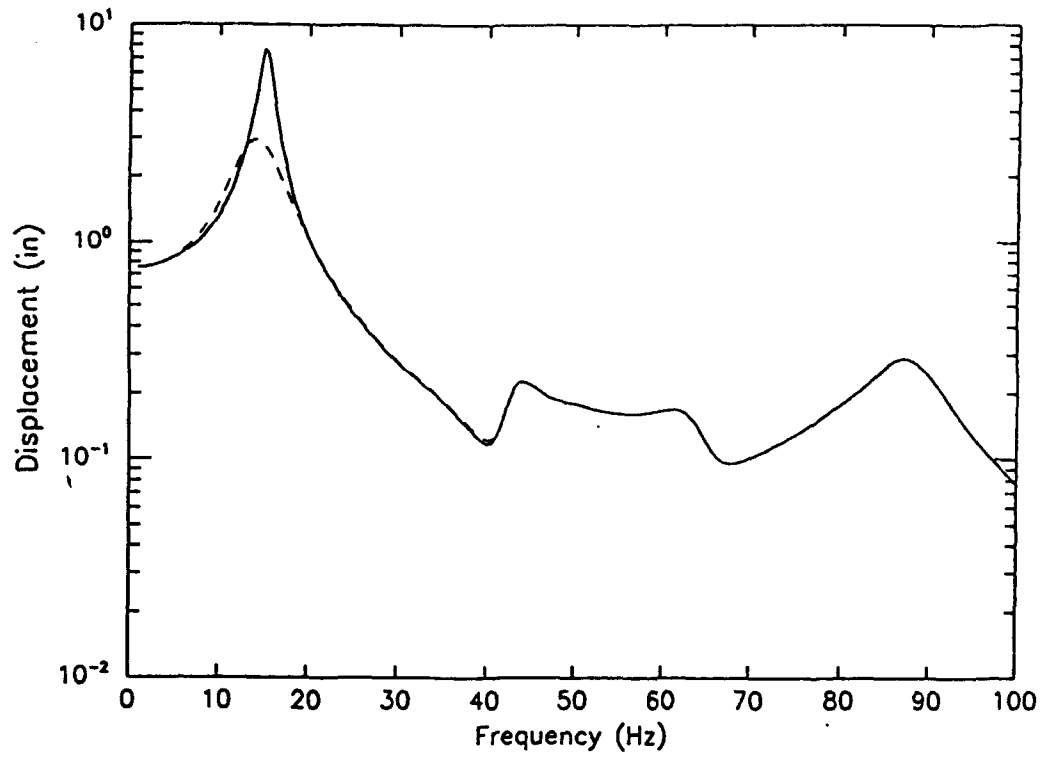
Figure 10: Typical displacement response, for extreme loading condition, with TMD array compared to baseline response
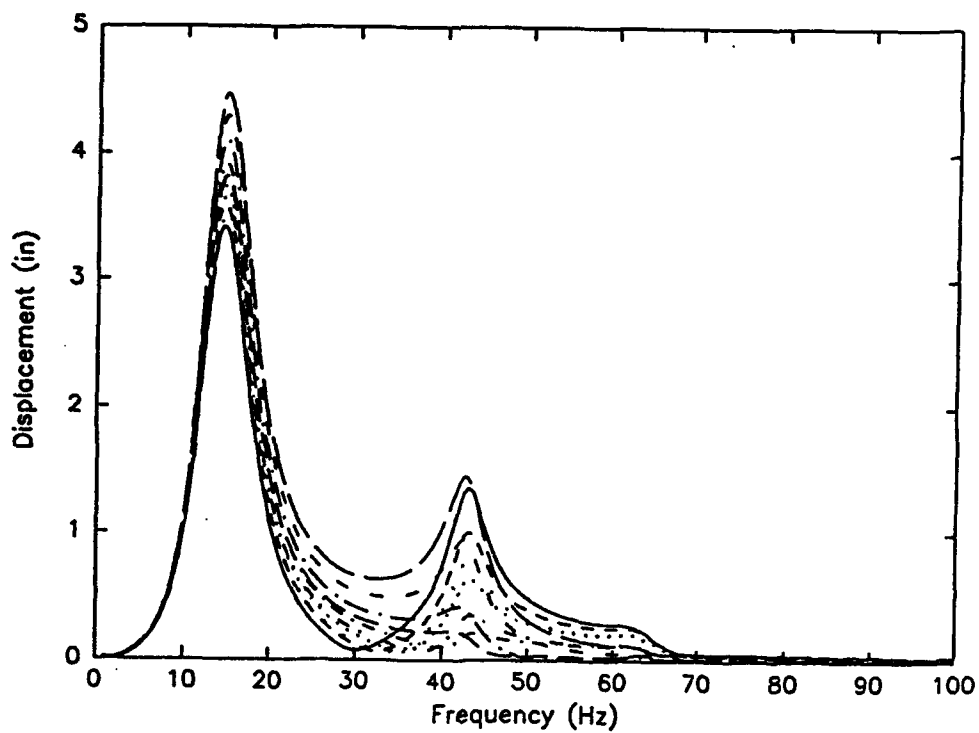
Figure 11: TMD stroke versus frequency for the individual units of the TMD array
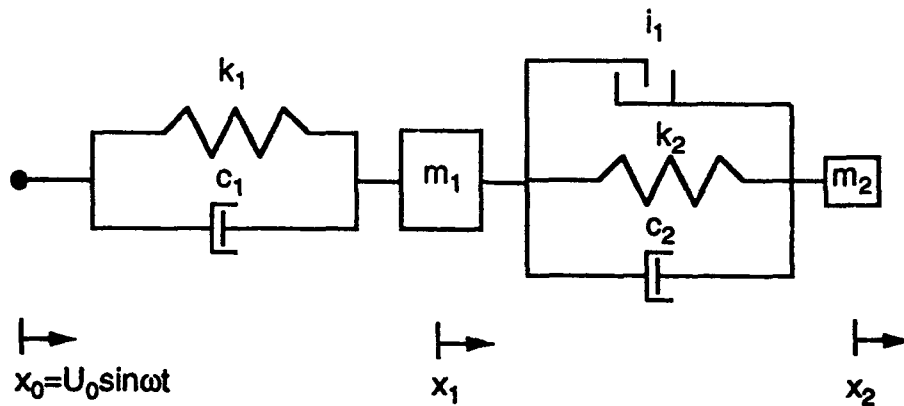
Figure 12: Two-degree-of-freedom model of F/A-18 vertical tail with TMD

time-domain response of this system, based on the following assumptions:

1. Baseline damping is represented by a viscous dashpot, $c_1(\omega)$.

2. A perfectly plastic collision results when the maximum TMD relative displacement is reached.

The variables shown in the Figure are the following:

- m_1 = modal mass of the baseline finite element model = 64.3 lb
- k_1 = modal stiffness of baseline finite element model = $\omega_n^2 m_1$ = 1507 lb/in
- $c_1(\omega)$ = baseline damping of finite element model = $k_1 \eta / \omega$)
- m_2 = TMD mass = 10 lb
- k_2 = TMD stiffness = 155 lb/in
- c_2 = TMD viscous damping = 1.54 lb-sec/in
- i_2 = maximum TMD relative displacement condition, $|x_2 - x_1| < 0.5$ in
- x_0 = input excitation displacement, $x_0 = U_0 sin(\omega t)$
- x_1 = TMD base displacement (the point on the tail where the TMD is mounted)
- x_2 = TMD mass displacement

A mathematical description of this physical system is the following (assuming a

perfectly plastic collision):

$$\left\{\begin{array}{c} \ddot{x}_1 \\ \ddot{x}_2 \end{array}\right\} = \left\{\begin{array}{cc} m_1 & m_2 \end{array}\right\} \left[\begin{array}{cccccc} -k_1 & k_1+k_2 & -k_2 & -c_1 & c_1+c_2 & -c_2 \\ 0 & -k_2 & k_2 & 0 & -c_2 & c_2 \end{array}\right] \left\{\begin{array}{c} x_0 \\ x_1 \\ x_2 \\ \dot{x}_0 \\ \dot{x}_1 \\ \dot{x}_2 \end{array}\right\}$$

$$x_0 = U_0 sin(\omega t)$$
$$\dot{x}_0 = \omega U_0 cos(\omega t)$$
$$|x_2 - x_1| < 0.5$$

Since the system is nonlinear, performance has to be calculated not only over the frequency range but also for a range of input excitation values. The response quantity of interest is x_1, the TMD base displacement; this is the displacement of the tail at the point where the TMD is mounted. The equations of motion were numerically integrated to obtain the steady-state response of the system. The response was calculated over several periods to allow the homogeneous solution to deteriorate and the response to become periodic. The maximum TMD base displacement, x_1, in the last period of response was stored for a given frequency and input excitation. This was done over a frequency range of 1 to 31 Hz. The frequency domain responses are shown in Figures 13 and 14. Two excitation levels are shown:

1. TMD stroke < 1.0 in, with the TMD acting as a linear system (Figure 13), and

2. maximum expected base excitation (undamped base displacement = 7.7 in), with the TMD acting as a nonlinear system (Figure 14).

Three cases were analyzed for each excitation level:

1. baseline (no damping treatment),

2. TMD configuration (spring-mass-damper), and

3. TMD mass only (pure impact absorber, i.e., $k_2 = c_2 = 0$).

These analyses indicate that the nonlinear properties of the TMD, i.e., after it "bottoms out," will not adversely affect the displacement response. However, as base excitation increases, added damping to the system decreases. It is not clear whether damping at high excitation levels is due to the linear behavior of the TMD, the nonlinear behavior, or a combination of these. The operation of the TMD at high acceleration levels will require further investigation.
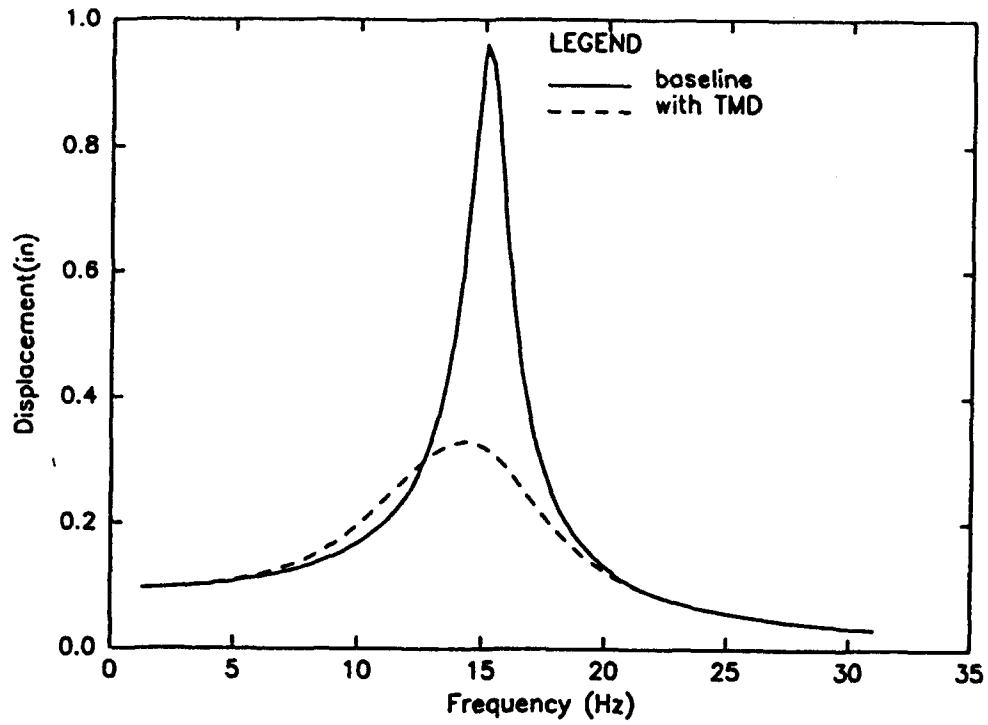
Figure 13: Response at TMD base with TMD in linear mode
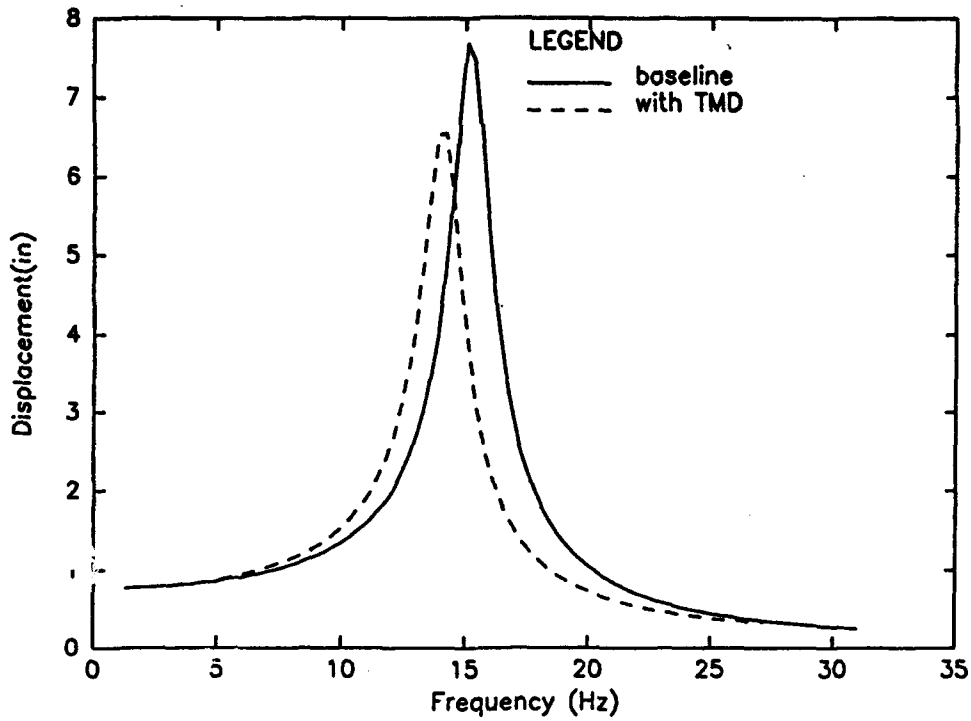
Figure 14: Response at TMD base with TMD in nonlinear mode

5. Design

A prototype TMD was developed subject to the constraints associated with the F/A-18 vertical tail geometry and the specifications derived from the analyses. The prototype was designed and built as one of the ten (identical) units for the proposed TMD array. The design requirements consisted of the following:

- overall dimensions of the TMD:

    - thickness (in the direction of motion of the TMD mass, which is normal to the tail) < 2 in

    - height and width should be kept to a minimum, < 4 in×4 in

- overall weight should be kept to a minimum,

- moving mass of the TMD ∼ 1 lb

- spring stiffness ∼ 15 lb/in

- damping coefficient ∼ 0.14 lbf·sec/in @ 15 Hz (corresponding to a TMD loss factor of ∼ 0.8)

5.1 Magnetic Field Configuration

The basic operating principle of magnetic damping is that energy is dissipated in the form of induced eddy currents in a metal when it moves relative to an established, DC magnetic field. In the case of a TMD, an array of magnets can be built into the moving mass, which is suspended on mechanical springs. When this magnetically charged mass moves relative to the housing of the TMD (composed of a conducting material and oriented so that the field generated by the magnets in the moving mass passes through it), a restraining force is generated proportional to the velocity of the mass. To obtain the desired level of damping in the TMD, the variables that can be manipulated are the magnetic field strength, the volume of intersection of the field with the conductor, and the resistivity of the conductor. More precisely,

$$c \sim (B^2 v)/\rho,$$

where

c = damping coefficient = force/velocity,
B = magnetic field strength,
v = volume of field/conductor intersection, and
ρ = conductor resistivity.

Figure 15: Prototype TMD

5.2 Prototype Fabrication and Testing

The prototype design for the magnetic TMD consists of a combination of mechanical springs and mass to provide the desired natural frequency for the system, and pairs of permanent magnets which move relative to a conductor to provide the damping. Figure 15 shows a photograph of the prototype TMD.

To verify the effectiveness of the prototype design, two tests were performed:

1. The TMD was mounted directly to an electrodynamic shaker, and the transmissibility of the TMD moving mass relative to the TMD base was measured. This test was performed to measure the natural frequency and damping of the TMD.

2. Using as a base structure a cantilevered aluminum beam with a bending frequency approximately equal to the target bending mode frequency of the F/A-18 vertical tail, frequency response functions were measured with and without the TMD. This test was done to verify the effectiveness of the TMD.

5.2.1 Transmissibility Test

For the transmissibility test, an adaptor plate was machined so that the TMD could be bolted directly to the armature of a 50-pound shaker. The TMD was subjected to random excitation with a low-pass cutoff frequency of 50 Hz and a peak
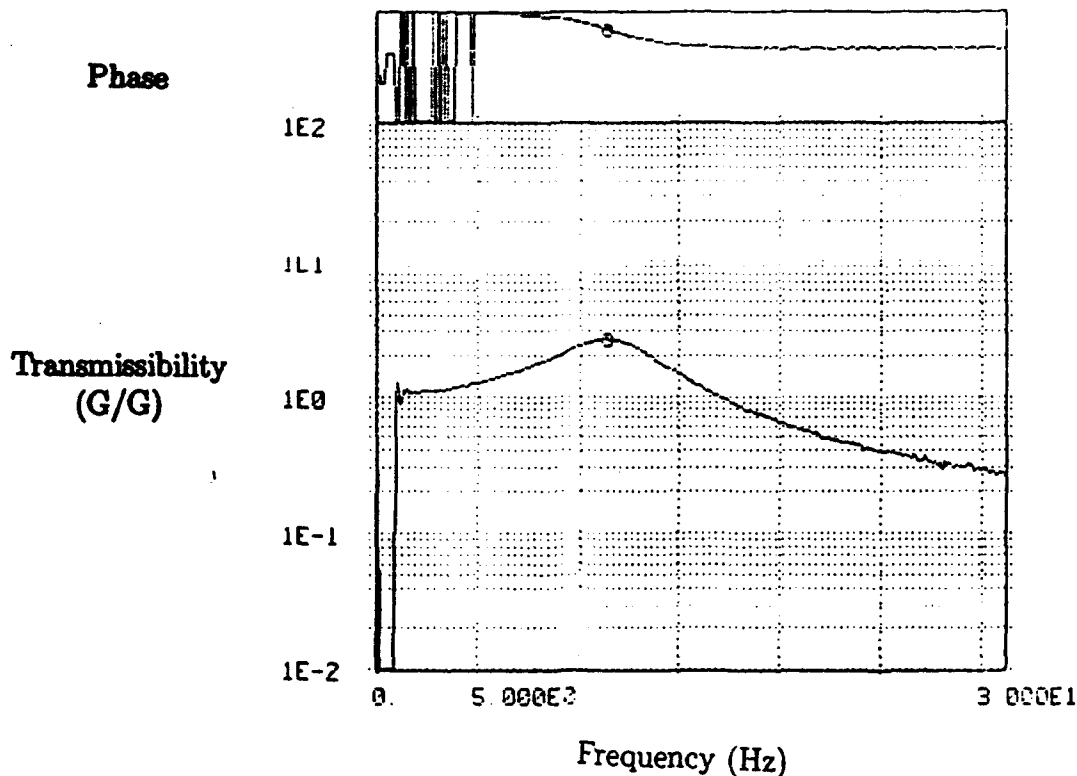
Figure 16: Measured transmissibility of the prototype TMD

3 Gs. Acceleration was measured with accelerometers mounted to the moving mass and the TMD base. The transmissibility was measured with respect to frequency as the ratio of the mass acceleration to the base acceleration.

The measured transmissibility function is shown in Figure 16. The discontinuity in the function below 1 Hz is due to the fact that the function represents the ratio of two accelerations, and both of these approach zero at very low frequencies. The natural frequency of the TMD was observed at 11.3 Hz; the TMD loss factor (structural damping generated by the TMD) was computed as 0.5. These results verified that the prototype design satisfies the requirements for a working TMD.

5.2.2 Frequency Response Measurements

A 48"×4"×1" aluminum beam was used as the base structure for the frequency response measurements. When this beam is mounted in a cantilevered configuration so that the cantilever beam length is 45.5", the first bending frequency of the beam is 13.5 Hz. The TMD was bolted to the beam, and a frequency response function was taken by applying a random excitation (8-lbf peak) to the beam at the location of the TMD attachment; force input and acceleration output were measured at this point. This test configuration is shown in Figure 17. The results of the measurement are shown in Figure 18, compared with an equivalent measurement taken without the TMD. The two lower plots show an amplitude comparison on log and linear scales.

The effect of the TMD on the dynamic response of the beam was dramatic. The

Figure 17: Prototype TMD test configuration
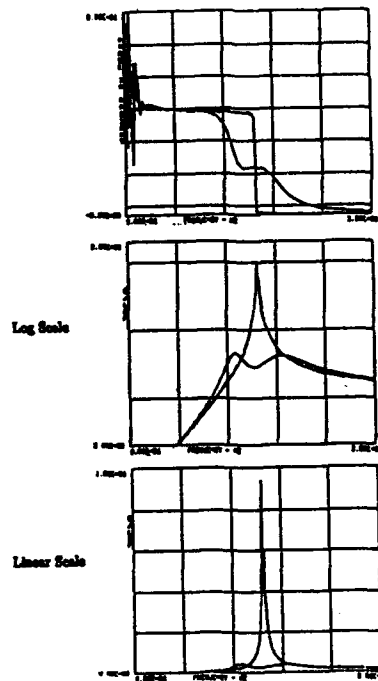
Figure 18: Acceleration/force versus frequency for cantilever beam with and without TMD
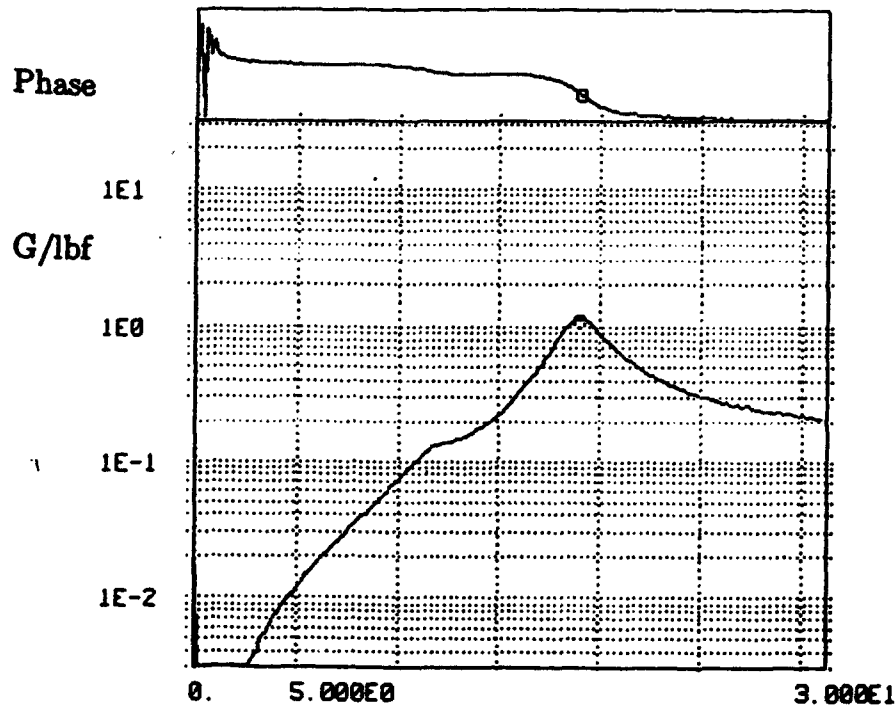
Figure 19: Acceleration/force versus frequency for cantilever beam with mistuned TMD

original 13.5-Hz mode was split into two modes, at 10.9 Hz and 15.7 Hz, and the amplitude of the response was attenuated by a factor of 20. The effective mass ratio of this single TMD applied to the aluminum beam is approximately equal to the mass ratio of an array of ten of these TMDs applied to the F/A-18 vertical tail.

As mentioned previously, a high effective mass ratio permits a high TMD loss factor, which in turn yields a high level of damping as well as a low sensitivity to mistuning of the TMD. The high level of damping obtained is shown in Figure 18. To illustrate this low sensitivity to mistuning, the bending frequency of the cantilever beam was modified by changing the cantilever length to 40", raising the undamped frequency to 15.5 Hz. This represents a frequency change of 15%, but the response of the structure is still attenuated by a factor of 8.5. The response of the beam with the mistuned TMD is shown in Figure 19. (For this test, the beam frequency, not the TMD frequency, was changed, i.e., mistuned.)

6. Summary

Previous efforts at developing damping treatments for the buffet-induced vibration problem associated with the twin-tail configuration of the F/A-18 aircraft were reviewed. Because of the severe dynamic environment and space limitations within the structure, solutions to this problem based on reducing the associated structural dynamics are extremely limited.

An innovative approach involving the well-established vibration suppression technique of the tuned-mass damper (TMD) is suggested. By installing an array of TMDs near the top of each vertical tail, the space limitation can be, to a great extent, overcome, and a high level of damping can be achieved for high-G loading conditions. Limitations on standard TMD design using viscoelastic materials have been overcome with a TMD that employs permanent, rare earth magnets for the damping mechanism.

A prototype tuned-mass damper was designed, built, and tested. The test results, together with the analyses, indicate that this is a viable solution to the problem of the buffet-induced vibrations of twin-tailed aircraft. A magnetic tuned-mass damper could be used to reduce the response of any airfoil; many other aerospace and commercial applications will be found for a magnetic tuned-mass damper.

Attenuation of Empennage Buffet Response Through Active Control of Damping Using Piezoelectric Material

Jennifer Heeg, Jonathan M. Miller, and Robert V. Doggett, Jr.[†]
Structural Dynamics Division
NASA Langley Research Center
Hampton, VA 23681-0001

ABSTRACT

Dynamic response and damping data obtained from buffet studies conducted in a low-speed wind-tunnel by using a simple, rigid model attached to spring supports are presented. The two parallel leaf spring supports provided a means for the model to respond in a vertical translation mode, thus simulating response in an elastic first bending mode. Wake-induced buffeting flow was created by placing an airfoil upstream of the model so that the wake of the airfoil impinged on the model. Model response was sensed by a strain gage mounted on one of the springs. The output signal from the strain gauge was fed back through a control law implemented on a desktop computer. The processed signals were used to "actuate" a piezoelectric bending actuator bonded to the other spring in such a way as to add damping as the model responded. The results of this "proof-of-concept" study show that the piezoelectric actuator was effective in attenuating the wake-induced buffet response over the range of parameters investigated.

[†]Mail Stop 242, NASA Langley Research Center, Hampton, VA 23681-0001.
Phone 804-8642934; Fax 804-864-7792.

INTRODUCTION[§]

Randomly varying pressures produced by such phenomena as separated flow, shock-wave boundary-layer interaction, and wake flows can produce significant buffeting structural response of airplane components. The internal structural loads resulting from these responses are important for two reasons. First, when added to loads from other sources, the resulting total load can approach limiting values. Second, the random nature of the loading can adversely affect the fatigue life of the structure.

Wake-flow-induced empennage buffeting, the subject of this paper, has been a significant area of concern for a number of years, beginning with the crash of the Junkers F13 commercial transport airplane at Meopham, England, in July 1930. This tragic accident, attributed to buffeting by British scientists[1] but blamed on other causes by an independent German investigation[2], precipitated a surge of empennage buffet research in Europe.[3-6] At the same time, independent studies in the United States had begun to focus on empennage buffeting.[7,8] During World War II many military airplanes of both U. S. and British design were affected by empennage buffeting.[9,10] Following the war, buffet studies while continuing to address the buffet problems of specific airplanes were expanded in attempts to gain a better understanding of buffeting and develop empirical means for predicting buffet responses and loads.[11-17] Currently, empennage buffeting is a significant area of concern for the teen-series fighter airplanes such as the F-15[18] and F-18[19,20], although most of the work has focused on the F-18. Even though a large proportion of recent empennage buffeting studies have addressed military airplanes, it can be a problem for commercial airplanes as well. This fact is evidenced by the tail damage due to buffeting that occurred for a DC-10.[21]

Typically, undesirable buffet response of empennage surfaces has been treated by passive means--either adding structure to increase strength or extend fatigue life, or streamlining upstream components to reduce wake flows. An alternative approach would be to use an active control feedback system to attenuate the buffet response. Although active control methods have been evaluated extensively for flutter alleviation and other aeroelastic applications[22], such methods have been virtually ignored for buffeting, the work of Destuynder[23] that treated wing buffeting being a notable exception. Because recent active flutter suppression studies using piezoelectric actuators in feedback control systems have yielded some promising results for controlling wing and panel flutter[24-27], it appeared logical to evaluate this concept as a possible means to attenuate buffet response. Accordingly, a "proof of concept" study was initiated and the results therefrom are reported herein.

In particular, the purpose of this paper is to present buffeting response measurements made on a simple wind-tunnel model that was equipped with an active control feedback system that used a piezoelectric actuator. The tests were conducted in a small, laboratory-type, low-speed wind tunnel. The model was subjected to wake flow produced by an upstream airfoil. The wake produced by this airfoil buffeted the model in much the same way that the wake of the wing might buffet the empennage of an airplane. The model was attached to leaf springs that were configured such that the model was free to respond in a vertical translation degree of freedom thus simulating response in a first elastic bending mode. A strain gage mounted on one of the leaf springs was used to

---

[§]The references cited in the brief historical review presented in the second paragraph of the INTRODUCTION are only a small illustrative sample of the many works that are available in the open literature. A comprehensive historical review with complete bibliography was not intended.

measure the dynamic response of the model. These response signals were fed back through a computer-implemented control law that supplied voltages to a piezoelectric actuator mounted on the other spring. Damping and dynamic response data are presented for three cases--open loop (control system off) and two values of feedback gain.

PIEZOELECTRIC CHARACTERISTICS

Piezoelectric materials generate a mechanical strain when subjected to an applied voltage, or conversely generate a voltage when they are mechanically strained. Certain manmade materials may be made piezoelectric by applying a relative large voltage across a sample of the material. The applied voltage causes the dipoles within the material to become realigned in an orderly fashion such that the positively charged ends of the dipoles are oriented towards the negative pole of the applied voltage. If the voltage is applied for a sufficient length of time, the dipoles retain their orientation when the voltage is removed. The sample is now said to be poled. Subsequent applications of smaller voltages to the sample will cause the dipoles to reorient themselves, positive ends of dipoles attracted to negative pole of applied voltage thus causing the specimen to deform. When this smaller voltage is removed, the dipoles return to their poled alignment and the sample returns to its undeformed shape. This electromechanical coupling is illustrated by the sketch in figure 1 which shows a sample of material that was originally poled in the z direction. If a voltage difference is applied in the z, or 3, direction but in the opposite sense from the original poling voltage, the specimen will, as shown in the figure, thicken and shorten (a Poisson-like effect) in the two in-plane x and y directions. If the applied voltage is in the same sense as the poling voltage, opposite effects take place. The subscripted symbol d is commonly used to represent this coupling.

By attaching small pieces of piezoelectric material to an elastic structure it is possible to create actuators which can be used to deform the structure. By controlling the voltages applied to the piezoelectric patches the structure can be made to deform in a desired manner. A bending actuator (commonly referred to as a bimorph configuration) is illustrated in figure 2. The sketch at the top of the figure illustrates a beam to which a piece of poled piezoelectric material has been bonded to each side. The arrows indicate the direction of the original poling voltage. If excitation voltages are applied to the patches as shown in the bottom sketch, the top patch will expand whereas the bottom patch will contract, thus causing the beam to bend. By controlling the magnitude and sense of the excitation voltages supplied to the actuator the beam can be bent in a prescribed fashion.

An excellent review and extensive bibliography of the use of piezoelectric actuators and other "smart structure" concepts is given in reference 29.

MODEL

The wind-tunnel model was a modified version of the one used by Heeg[25] in a previous study using piezoelectric actuators for active flutter suppression. A photograph of the model system is presented in figure 3. The rectangular-planform wing had a 4-inch span and 4.5-inch chord. The airfoil section was a 5-percent-thick double wedge with the point of maximum thickness at the one-quarter chord. The wing was constructed of an aluminum alloy plate that was covered with balsa wood. Mass balance was provided by aluminum alloy tape. The wing panel was very stiff, rigid in the content of the present study.

As shown in the figure, the wing was attached to a pair of parallel leaf springs mounted outside of the flow. Each steel spring was 0.016 inches thick, 1.25 inches wide, and 6.0 inches long. The springs were clamped at both ends. One end of each spring was clamped to a support strut that was tied to the plastic plate that formed the ceiling of the wind-tunnel test section. The other ends were clamped to a medal block that was in turn attached to a very stiff rod that passed through

a slot in the ceiling plate and attached to the model. This mounting arrangement provided for a vertical translation degree of freedom with a natural frequency of about 8.9 Hz.

A four-active-arm resistance wire strain gage bridge was mounted near the root of one of the leaf springs. The output signal of the gauge was proportional to the vertical displacement of the model.

For the present study a bending actuator made of lead zirconate titanate (PZT), a piezoceramic, was used. This actuator was installed near the root on the spring without the strain gage. A 1.5-inch-long by 1.00-inch-wide by 0.0075-inch-thick PZT plate was bonded to each side of the spring. The actuator can be seen in the figure 3 photograph. A sketch of the installation is shown in figure 4. The plates were bonded to the spring with like poles oriented toward the spring. The 0.005-inch-thick bonding layer electrically insulated the piezoelectric plates from the steel spring. Small copper tabs were attached to the plates during the bonding process to provide a mean of applying voltages to the bonded side of each piezoelectric plate. Additional insulation was applied to the exposed portions of the copper tabs to insulate them from the spring.

WIND TUNNEL

The experiments were conducted in the Langley Flutter Research Experimental Device (FRED) which is a small, low-speed, laboratory-type, open-return wind tunnel. A photograph of the FRED is presented in figure 5. A sketch of FRED is presented in figure 6 as are some of its characteristics. The wind tunnel is powered by a two horsepower, variable speed electric motor connected to a squirrel cage fan located downstream of the 6-inch-square test section. Honeycomb screening at the beginning of the entrance cone is used to ensure smooth flow in the test section. The tunnel speed is continuously controllable up to a speed of about 74 knots. The walls and ceiling in the test section are made of clear plastic so that the model may be easily observed. Models are usually mounted from the ceiling as was the case for this study.

For the present study FRED was modified so that a rigid airfoil could be placed just upstream of the beginning of the test section. A schematic representation of this setup is presented in figure 7. The wake from this airfoil was used to generate buffeting flow. The angle of attack and position of this airfoil could be easily adjusted so that the resulting wake would impinge on the model mounted downstream. The angle of attack and airfoil position selected for the present test was obtained by trial and error. The configuration finally selected was the one that produced the largest buffet response of the model. Once the final position of the airfoil was selected, the wake-generating airfoil was clamped into place. Therefore, all of the buffet response data presented herein were obtained for the airfoil in the same location and orientation. Although no quantitative measurements were made of the characteristics of the wake flows, some qualitative measurements were made using a pressure probe to ensure there were not any unusual peaks in the spectrum of the wake in the frequency range of interest. None were found.

FEEDBACK SYSTEM

A block diagram of the feedback system is presented in figure 8. The output analog signal from the strain gage bridge mounted on one of the support springs was amplified and routed to an analog-to-digital converter which had a sample rate of $1/\tau$. The strain gage signal is proportional to and in phase with the displacement of the model. The digitized signal was then sent to the control law which was implemented on a desktop personal computer. The control law was a simple gain system. That is, the digital signal was only multiplied by a constant value -K. The gained signal was next routed to a one step time delay $e^{-\tau s}$ where s is the Laplace operator and τ the time between samples as indicated above. The time delay provides a means for changing the phase of the feedback signal. The gained- and phased-shifted signal was converted back to an analog signal by

a zero-order-hold digital-to-analog converter. The transfer function of this converter is $(1 - e^{-\tau s})/s$. The converted signal was routed to an operational amplifier. The output signal from this amplifier was used to drive the piezoelectric actuators. The range of output voltage for this amplifier was +/- 80 volts.

For the present study a sampling rate of 400 samples per second was used. This relatively high rate was chosen to ensure that the wave form of the response signal was well defined. The transfer function amplitude and phase that results from this rate are presented in figure 9 as a function of the ratio of frequency to frequency of the vertical translation mode, f/f_{trans}. The magnitude of the transfer function is almost constant over the range of f/f_{trans} shown in the figure. The phase angle gradually decreases from its value of 180° at zero frequency as f/f_{trans} increases. The phase shift at the frequency of the translation mode, $f/f_{trans}=1.0$, is about 168°. Had a lower sampling rate been used, the phase angle at $f/f_{trans}=1.0$ would have been smaller. The closer the phase angle to 90° the more effective the feedback system should be in introducing damping into the system.

Two values of the gain -K were used, namely, 14 and 29. The 29 gain was the value that caused the system to begin to saturate at a tunnel velocity of about 39 knots. The 14 gain was the value that caused saturation to begin at a velocity of about 74 knots.

The feedback system was implemented on a personal computer with a 80386 processor and a 80387 co-processor running in real time under a UNIX operating system. The computer was programmed in C-language. All calculations were made using floating point arithmetic. The analog-to-digital converts were 12 bit units. Some additional information about the components of the computer system is given in reference 29.

TEST PROCEDURE

With the control law gain set to the desired value the tunnel speed was increased to and then held constant at a preselected value. Damping and buffet response measurements were made at velocities of 9.7, 19.4, 29.2, 38.9, and 48.6 knots. Damping data were also obtained at a velocity of 4.4 knots. (Because the present study was conducted at nominal sea level altitude and the speeds were very low, the test section density was essentially the sea level value. Consequently, the true velocity is essentially equal to equivalent airspeed.) The output signal from the strain gage bridge was routed to a transfer function analyzer that was used to calculate the autocorrelation function of the response signal. The final autocorrelation function was an ensemble average of many individual measurements. The root-mean-square value of the response was obtained by taking the square root of the value of the function at time zero. The damping of the response was obtained from the log decrement of the function. A typical autocorrelation function is presented in figure 10. Autospectra of the responses were also obtained to ensure that there was no model response in spurious modes. These spectra showed that the model responded only in the vertical translation mode. The quality of the autocorrelation functions as indicated by the typical one shown in figure 10 supports this fact as well.

RESULTS AND DISCUSSION

Total damping and dynamic response data were acquired over a range of speeds for open loop (control system off), and two values of control system gain, namely, 14 and 29. The results of these measurements are presented and discussed in this section. The data are presented as their respective variations with velocity measured in knots. As discussed previously, the damping and response data were obtained from autocorrelation functions of the model response.

Damping

The variations of damping ratio g with airspeed V in knots are presented in figure 11. The values of damping at zero velocity for the open-loop case correspond to the structural damping ratio. The use of the feedback system increased the structural damping ratio substantially--the higher the gain, the larger the damping. For the open-loop case, circle symbols, the damping increases with increasing velocity. This trend is essentially linear. The curve faired through the data points is a linear least square fit. The increase in damping that occurs with increasing velocity is due to aerodynamic effects. So, for the open-loop case, the difference between the total damping at a given velocity and the structural damping at zero velocity is the aerodynamic damping ratio. The closed-loop gain=14 data also show a linear increase in total damping with velocity. Again, the curve faired through the data is a linear least square fit. There is more scatter in these data than there was for the open-loop data. The difference between the gain=14 data and the open-loop data at the same velocity is the damping increase produced by the feedback system. This increase is constant over the range of velocities studied because the curves through the open-loop and gain=14 data are parallel. The closed-loop gain=29 data, triangle symbols, show a further increase in damping. The curve fared though these data is also a linear least square fit. The scatter in the data for this gain is the worst of the three cases. For this gain, the relative performance of the feedback system deteriorates with increasing velocity. For example, the damping added by the control system at V=29 knots is less than the damping added at 10 knots.

Although for gain=29 the control system began to saturate at about V=39 knots, it was still possible to estimate the damping for this and the higher test velocity, about 49 knots, from the autocorrelation functions. These values are indicated in the figure by the solid triangle symbols. As would be expected, control system performance was adversely affected once saturation began to occur. Note that the estimate of the total damping for the gain=29 case at V=49 knots is lower than it is for the open-loop case.

The effectiveness of the active control system in increasing the damping can be seen also by comparing the three autocorrelation functions presented in figure 11 for V=19.4 knots. A visual inspection of there functions clearly shows the increase in damping that occurs as control system gain is increased. As can be seen from the autocorrelation functions, the frequency of the response in the vertical translation mode differed only slightly from its open-loop wind-off value of 8.9 Hz. For all practical purposes the response frequency remained constant over the range of parameters covered in this study. However, the frequency was observed to decrease slightly with increasing feedback gain.

Response

Variations of the root-mean-square response σ with flow velocity are presented in figure 13. The open-loop data, circle symbols, show an increase in response with increasing velocity. Although the trend appears at first glance to be linear, close examination shows that there is a small amount of nonlinearity present. The curve through the data is a second degree least square fit which fares through the individual data points quite nicely. The closed-loop gain=14 data, square symbols, indicate a similar trend but with a lower response. Again, the faired curve is a second degree least square fit. A similar trend was found for the closed-loop gain=29 data, triangle symbols, with these responses being the lowest of the three cases. A second degree least square fit was also used to fair the curve though these data points. The two solid triangle symbols represent gain=29 data for the two test velocities where some saturation of the feedback system had occurred. As would be expected, saturation adversely affected control system performance. Indeed, the response at the highest velocity, about 49 knots, is higher than for the open-loop case. This is consistent with the damping estimates at this velocity which were lower than the open-loop case.

CONCLUDING REMARKS

Data have been presented from using a piezoelectric actuator in a feedback control system to attenuate the buffet response in low-speed, wind-tunnel tests of a relatively simple model that was free to response in a vertical translation degree of freedom. The vertical translation degree of freedom was provided by two parallel leaf springs. The wake of an upstream-mounted airfoil was used to produce wake-induced buffeting response as might be experienced by an airplane empennage. Model response was measured by a strain gage mounted on one support spring. These signals were feedback through a control law implemented on a desktop computer. The resultant output command signals were routed to a piezoelectric bending actuator mounted to the other support spring. Data were acquired for open-loop and two closed-loop conditions. Over the range of parameters covered, the control system was effective in increasing the damping of the translation mode and attenuating the buffeting response--the higher gain the larger the damping and the smaller the response.

It should be pointed out that this relatively simple study was in the nature of a "proof of concept." It should not be inferred that piezoelectric materials are ready for use in full-scale airplane applications. Such applications will depend on many factors which were not investigated in this study, and many factors which are still unknown. What should be inferred, however, is that piezoelectric materials have the potential for use as "buffet suppressers," but considerably more research and development work is needed before this potential can be realized.

REFERENCES

1. Accident Investigation Sub-Committee: Accident to the Aeroplane G-AAZK at Meopham, Kent, on 21st July, 1930. R. & M. No. 1360, British A. R. C., 1931.
2. Blenk, Hermann; Hertel, Heinrich; and Thalau, Karl: Die deutsche Untersuchung des Unfalls bei Meopham (England). Zeitschrift fur Flugte-chnik und Motorlufschiffahrt, Vol. 23, No. 3, pp. 73-86, Feb. 1932. (Available in English translation as NACA TM 669, The German Investigation of the Accident at Meopham (England), 1932.)
3. Biechteler, Curt: Versuche zur Beseitigung von Leitwerkschutteln. Zeitschrift fur Flugtechnik und Motorluftschiffahrt. Vol. 24, No. 1, pp. 15-21, Jan. 1933. (Available in English translation as NACA TM 710, Tests for the Elimination of Tail Flutter, 1933.)
4. Aerodynamics Staff of the National Physical Laboratory: Two Reports on Tail Buffeting. R. & M. No. 1457, British A. R. C., 1932.
5. Duncan, W. J.; and Ellis, D. S.: Second Report on Tail Buffeting. R. & M. No. 1541, British A. R. C., 1933.
6. Abdrashitov, G.: Tail Buffeting. Central Aero-Hydrodynamical Institute Report No. 385, Moscow, 1939. (English translation available as NACA TM 1041, 1943.)
7. Hood, Manley J.; and White, James A.: Full-Scale Wind-Tunnel Research on Tail Buffeting and Wing-Fuselage Interference of a Low-Wing Monoplane. NACA TN 460, 1933.
8. White, James A.; and Hood, Manley J.: Wing Fuselage Interference, Tail Buffeting and Air Flow About the Tail of a Low-Wing Monoplane. NACA TR-482, 1934.
9. Bartels, R. C. F.: Tail Buffet Characteristics and Longitudinal Oscillation of Combat Airplanes. NAVY Bureau of Aeronautics, Structures Project Report No. 27, Feb. 1, 1945.
10. Kerr, C. E.: Notes on some recent & current aerodynamics research work in U. K. C. T. I. Technical Note No. 183, Feb. 1945.
11. Bouton, I.; and Madrick, A. H.: Structural Criterion for Buffeting Tail Loads. McDonnell Aircraft Corporation Report 1958, Mar. 1951.
12. Huston, Wilber B.: A Study of the Correlation Between Flight and Wind-Tunnel Buffet Loads. Advisory Group for Aeronautical Research and Development, Report 111, Apr.-May 1957.
13. Rainey, A. Gerald; and Igoe, William B.: Measurements of the Buffeting Loads on the Wing and Horizontal Tail of a 1/4-Scale model of the X-1E Airplane. NACA RM L58F25, 1958.

14. Rigby, Robert N.; and Cornette, Elden S.: Wind-Tunnel Investigation of Tail Buffet At Subsonic and Transonic Speeds Employing Dynamic Elastic Aircraft Model. NASA TN D-1362, Sep. 1962.

15. Jones, J. G.: A Survey of the Dynamic Analysis of Buffeting and Related Phenomena. Royal Aircraft Establishment Technical Report 72197, Feb. 1973.

16. Hwang, Chintsun; and Pi, W. S.: Aircraft Wake Flow Effect and Horizontal Tail Buffet. Journal of Aircraft, Vol. 16, No. 4, 1978.

17. Mabey, D. G.: Some Aspects of Aircraft Dynamic Loads Due to Flow Separation. AGARD-R-750, Oct. 1987.

18. Triplett, William E.: Pressure Measurements on Twin Vertical Tails in Buffeting Flow. Journal of Aircraft, Vol. 20, No. 11, November 1983.

19. Zimmerman, N. H.; Ferman, M. A.; Yurkovich, R. N.; and Gerstenkorn, G.: Prediction of Tail Buffet Loads for Design Application. AIAA/ASME/ASCE/AHS/ASC 30th Structures, Structural Dynamics and Materials Conference, Mobile, AL, pp. 1911-19, Apr. 1989. (AIAA Paper No. 89-1378)

20. Lee, B. H. K.; Brown, D.; Zgela, M.; and Poirel, D.: Wind Tunnel Investigation and Flight Tests of Tail Buffet on the CF-18 Aircraft. AGARD Specialists' Meeting on Aircraft Loads Due to Flow Separation, Sorrento, Italy, Apr. 1990.

21. National Transportation Safety Board: Aircraft Incident Report. Aeromexico DC-10-30, XA-DUH Over Luxembourg, Europe, November 11, 1979.

22. Noll, Thomas E.: Aeroservoelasticity. Flight-Vehicle Materials, Structures and Dynamics Assessment and Future Directions. Chapter 3, Vol. 5, Structural Dynamics and Aeroelasticity. ASME, New York, NY, 1993.

23. Destuynder, R.: Active Control of the Buffeting Response on a Large Modern Civil Airplane Configuration in Wind Tunnel. Proceedings of the Second International Symposium on Aeroelasticity and Structural Dynamics, Aachen, West Germany, DGLR-Bericht 85-02, Apr. 1985.

24 Scott, Robert Charles: Control of Flutter Using Adaptive Materials. Master of Science Thesis, Purdue University, May 1990.

25. Heeg, J.: An Analytical and Experimental Investigation of Flutter Suppression via Piezoelectric Actuation. AIAA Dynamics Specialists Conference, Dallas, TX, Apr. 1992. (Also available as NASA TM-107653, July 1992.)

26. Lazarus, K.: Multivariable High-Authority Control of Plate-like Active Lifting Surfaces. Ph. D. Thesis, Massachusetts Institute of Technology, May 1992.

27. Paige, Derek A.: Composite Panel Flutter Suppression Using Piezoelectric Materials. Master of Science Thesis, Purdue University, May 1992.

28. Active Structuresw Technical Committee: A State-of-the-Art Assessment of Active Structures. NASA TM 107681, Sep. 1992.

29. Dunn, H. J.: Experimental Results of Active Control on a Large Structure to Suppress Vibration. J. of Guidance, Control, and Dynamics, Vol. 15, No. 6, Nov.-Dec. 1992, pp. 1334-1342.
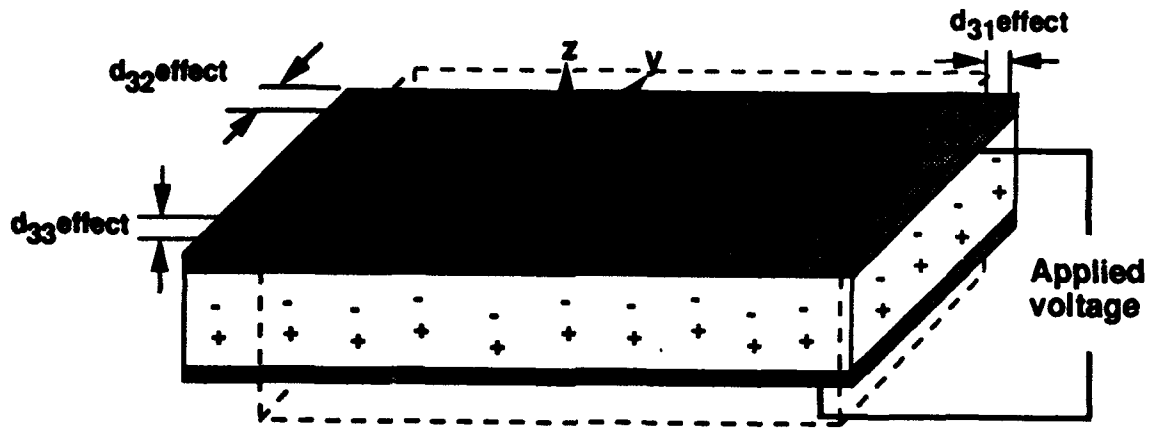
Figure 1. - Piezoelectric characteristics.
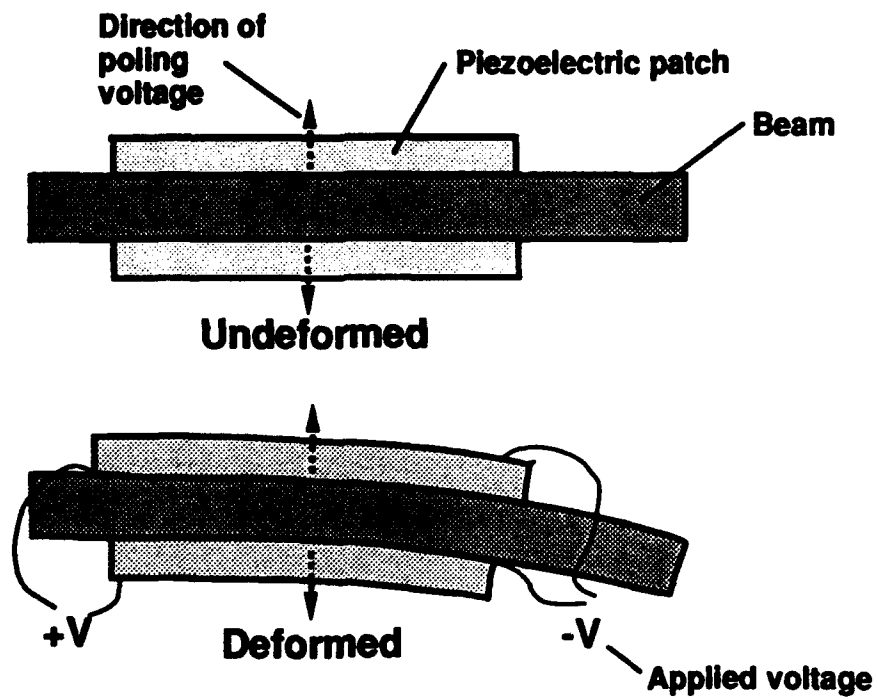
Figure 2. - Piezoelectric bending actuator.
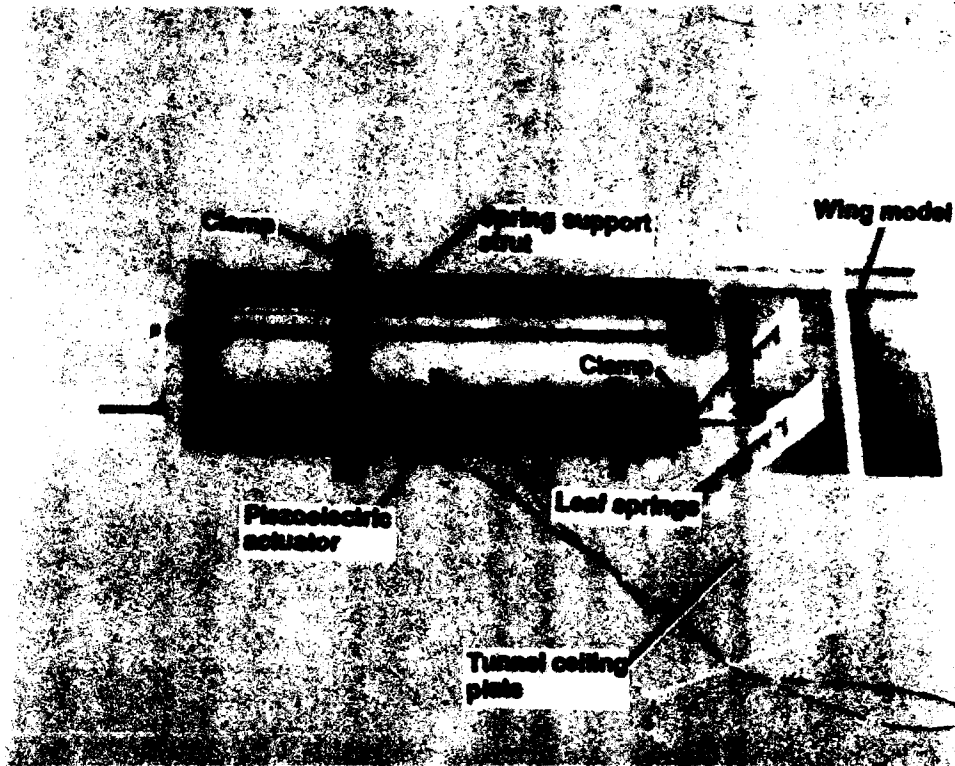
Figure 3. - Wind-tunnel model and support system.
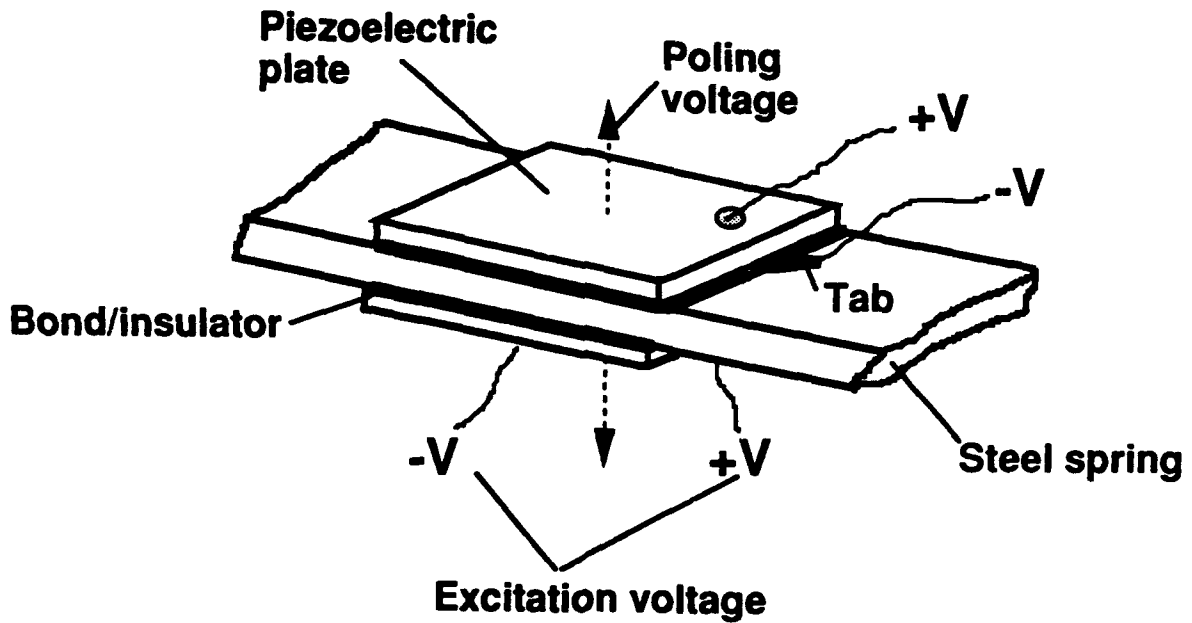
Figure 4. - Installation of PZT piezoelectric bending actuator.
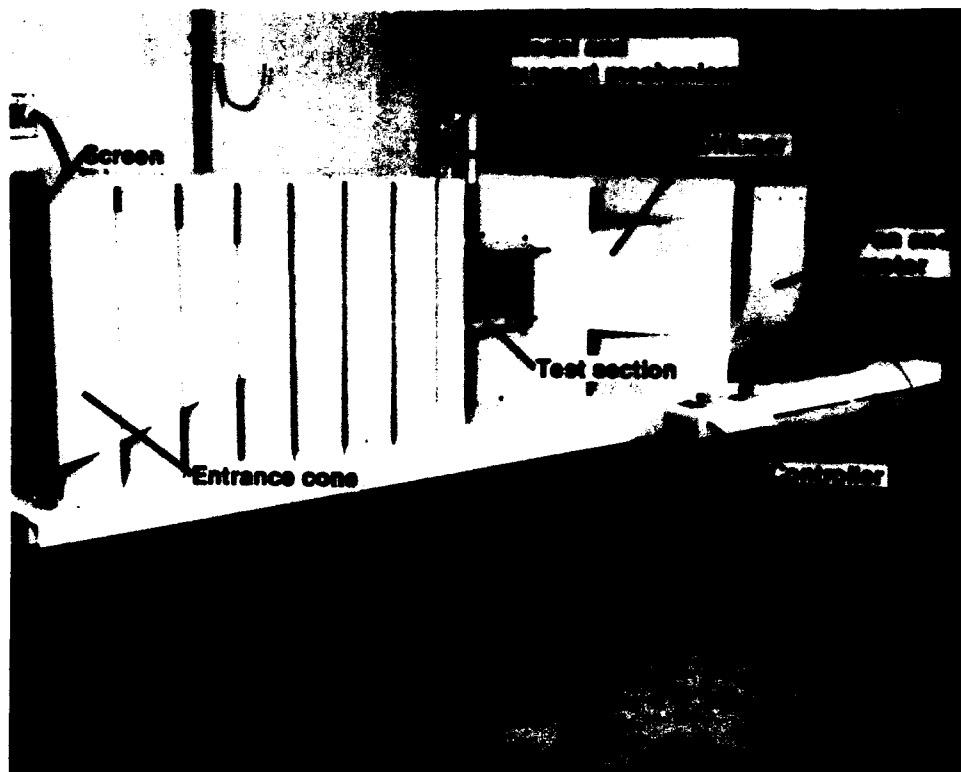
Figure 5. - Flutter Research Experimental Device (FRED).
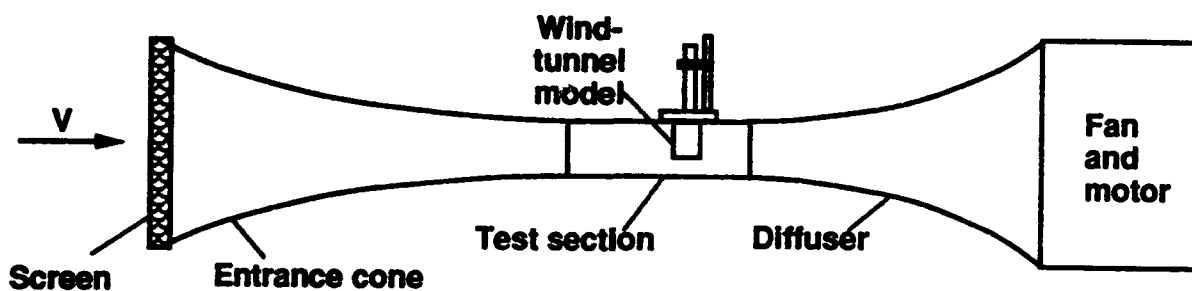
Type: Low speed, open return

Power: 2hp electric motor

Pressure: Atmospheric

Speed: 125 ft/sec, 74 knots

Test section: 6-inch-square

Model mounting: ceiling

Figure 6. - Sketch of Flutter Research Experimental Device (FRED).
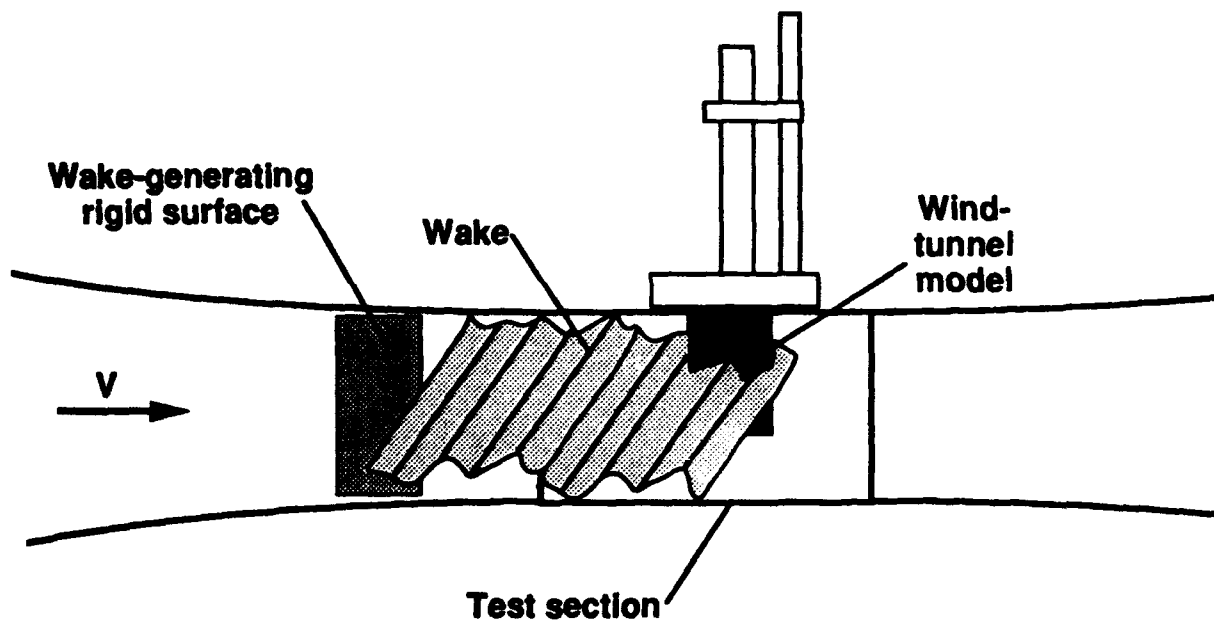
Figure 7. - Wake generator.
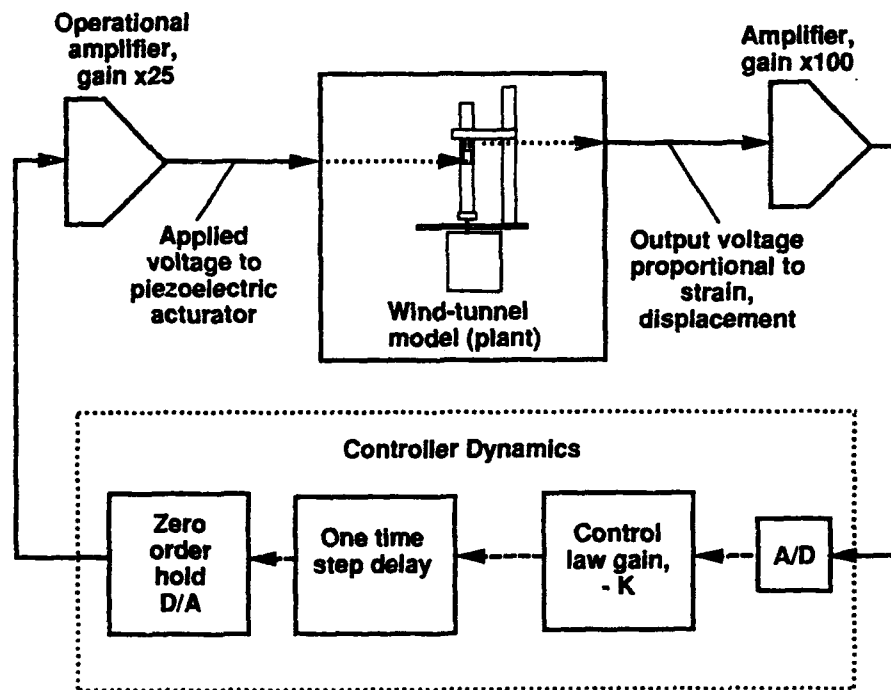
Figure 8. - Block diagram of feedback system.
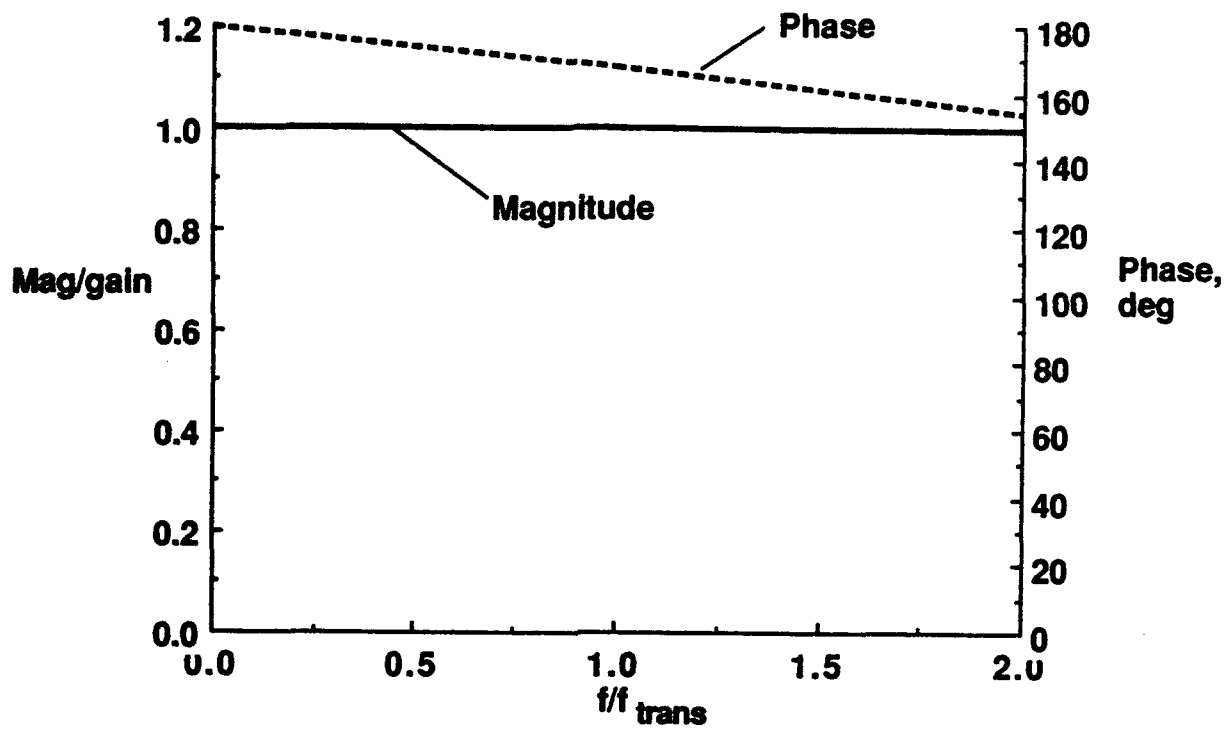
Figure 9.- Transfer function.
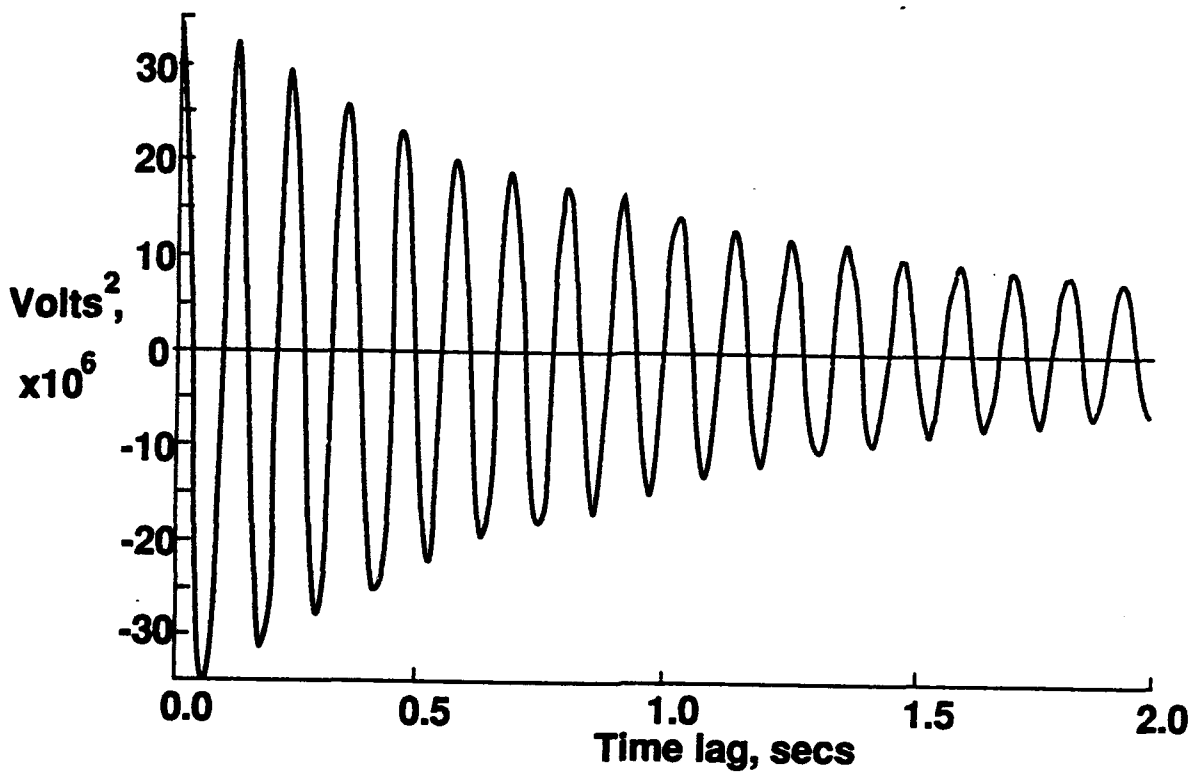
Figure 10. - Typical autocorrelation function.
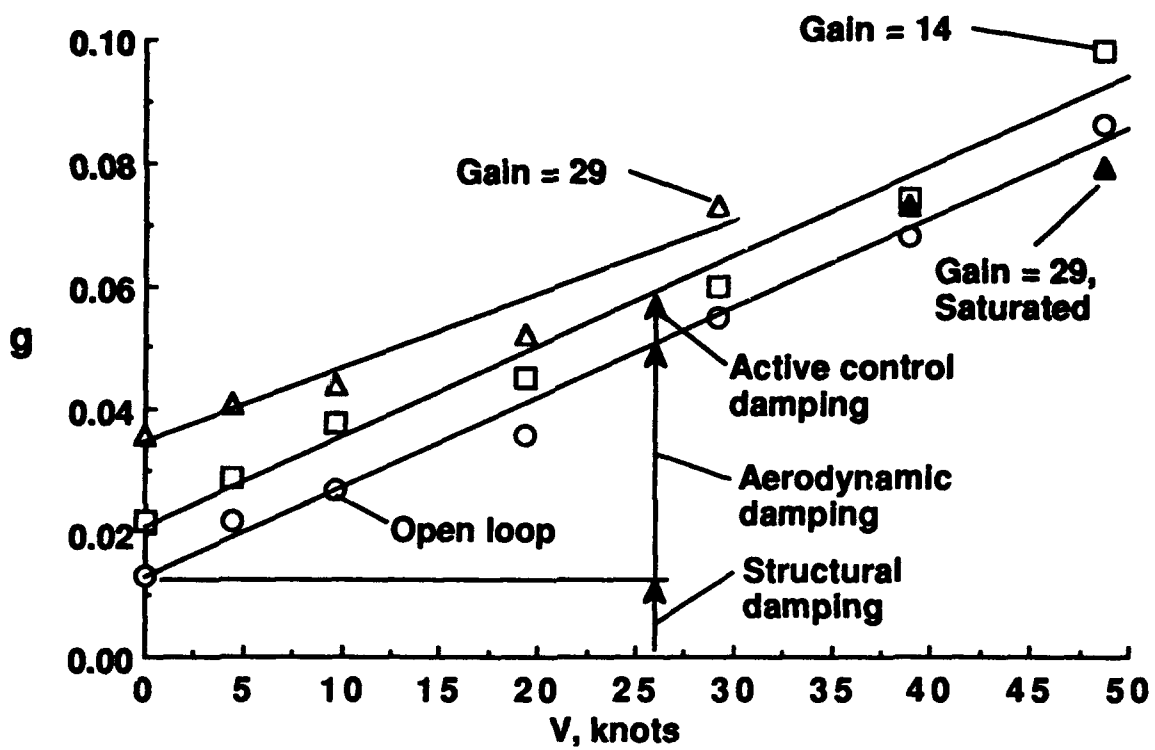
Figure 11. - Variation of damping with velocity.
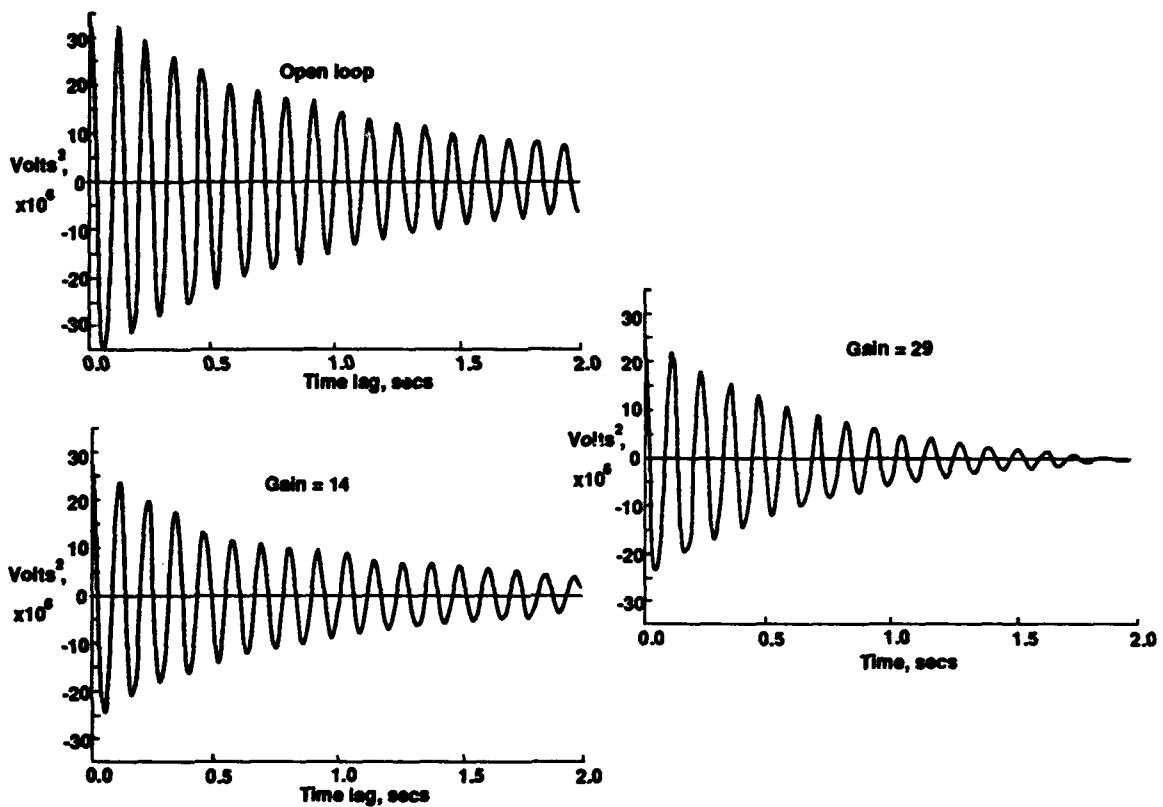
Figure 12. - Autocorrelation functions for a velocity of 19.4 knots.
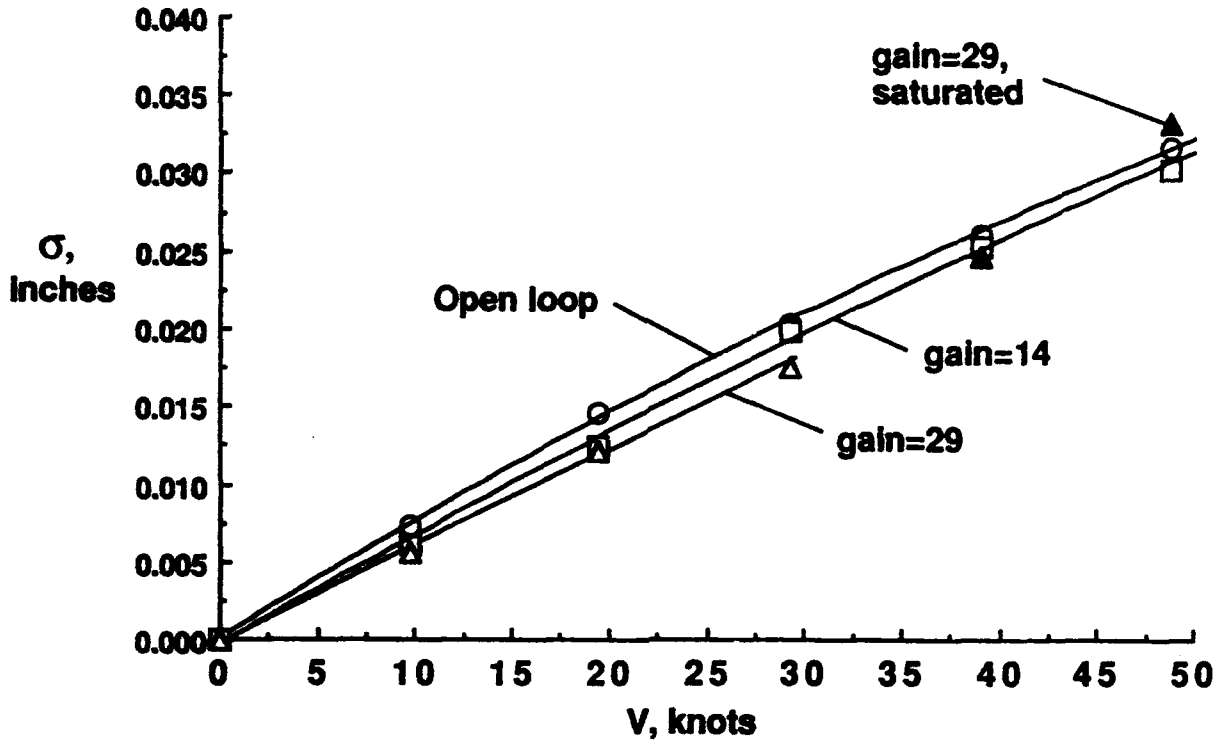
Figure 13. - Variation of root-mean-square response with velocity.

Analytical Evaluation of
Damping Treatments for F-15 Wing

Scott R. Schroeder

CSA Engineering, Inc.
2850 West Bayshore Road
Palo Alto, CA 94303
(415)494-7351

Presented February 25, 1993
Damping '93, San Francisco, CA

The work documented in this presentation was done at CSA Engineering, under Air Force contract number F33615-89-C-3201 (Passive Damping Design Methods and Applications).

Objective

- Determine through analysis and testing the effectiveness of damping treatment for F-15 wing

  - Treatment was designed by
    Air Force Flight Dynamics Directorate

  - Effectiveness measured by fatigue life extension for
    wing with damping treatment

CSA's job was to analyze the effectiveness of a damping treatment that was previously designed by the Flight Dynamics Directorate of the Air Force.

The dynamic material properties of the materials used in the damping treatments were needed for the analysis.

Palgren-Miner Cummulative Fatigue Law:[1]

where:

Nd=damped life

Nu=undamped life

Sd=damped stress

Su=undamped stress

$$\left[\frac{N_d}{N_u}\right] = \left[\frac{S_d}{S_u}\right]^{-3.323}$$

[1] Lavrea, Vincent, Lynn Rogers, Arnel Pacia, and Mike Parin, "Add-On Damping Treatment for the F-15 Upper-Outer Wing Skin," Paper No. WL-TR-92-3069, July 1992.

Cracks have been found across entire upper-outer wing skin, typically near the rivets. According to the Flight Dynamics Directorate, these cracks are caused by vibratory stresses induced from separated flow.[1]

The Air Force conducted flight and modal tests to identify the problem modes. The flight tests shows the frequency range of high stresses in wing skin, and modal tests identified stiffener-rocking and local panel modes in the frequency range of interest.[1]

Wing-skin cracking has significantly limited the service life of the F-15. Designed for a service life of 8000 hours, the F-15 A/B aircraft only realized service lives of 250 hours. The C/D versions, with reinforced skins and stiffeners, only realized service lives of 1250 hours.[1]

[1] Lavrea, Vincent, Lynn Rogers, Arnel Pacia, and Mike Parin, "Add-On Damping Treatment for the F-15 Upper-Outer Wing Skin," Paper No. WL-TR-92-3069, July 1992.

External Treatment
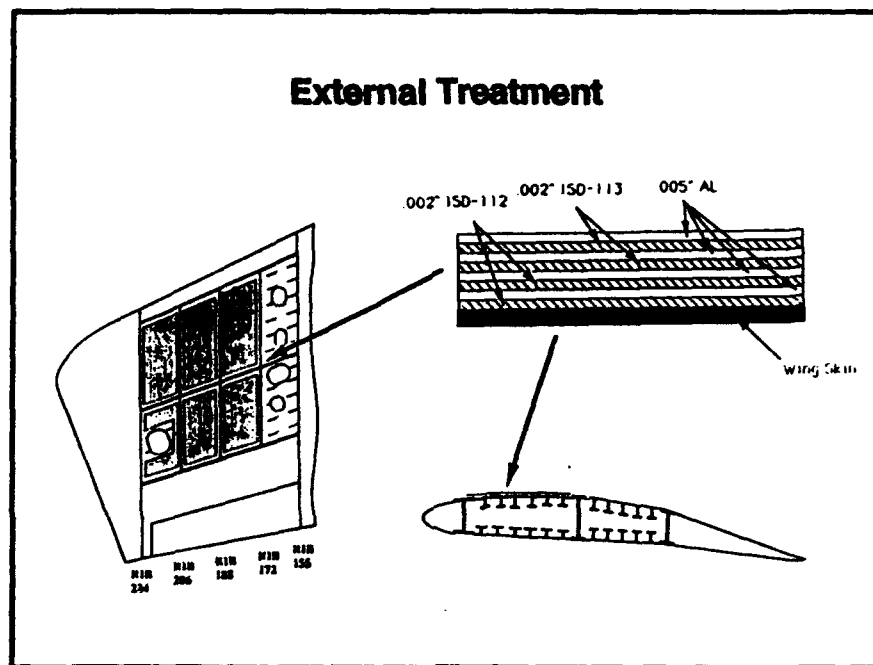
The external treatment covers entire upper-outer wing skin exterior. All constraining layers are made of aluminum. Alternating layers of ISD 112 and 113 viscoelastics provide a wide temperature range of effectiveness.

Internal Treatment
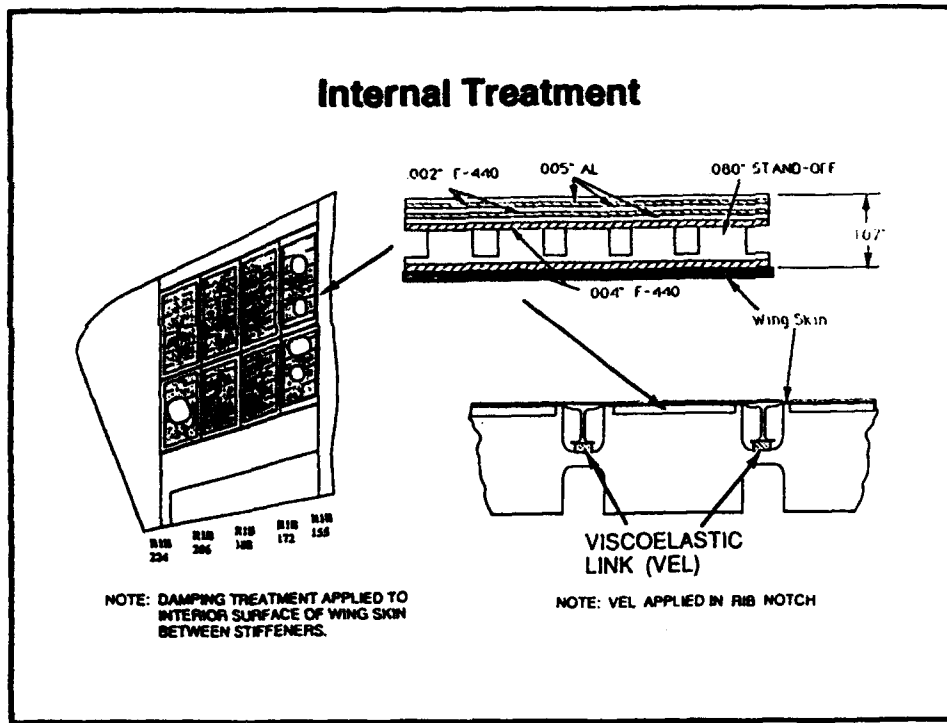
The internal treatment covers entire upper-outer wing skin interior. There are three aluminum constraining layers. FD-440 viscoelastic, manufactured by Hueston Industries, is used. The viscoelastic links damp relative motion between ribs and spars.

The stand-off syntactic foam acts as a mechanical amplifier of surface strain into viscoelastic.

Characterization of Material Properties

- **Need dynamic material properties of syntactic foam, FD-440, and viscoelastic links**
  - ISD 112 and 113 properties obtained from database
- **Syntactic foam properties found from cantilever-beam resonance test**
  - Foam samples pulled from production line
  - Found a Young's modulus of 200,000 psi, nearly constant over frequency range of 0-3000 Hz

The material properties needed are real modulus, poisson's ratio, loss factor, and density. The VEM Database was used to obtain ISD material properties.

The properties of the syntactic foam were found by a cantilever-beam test. The nearly constant modulus of the foam over the frequency range indicates low loss.

Characterization of Material Properties (cont)

- FD-440 viscoelastic tested at CSA
  - DCS (direct complex stiffness) test
  - Stiffness tested at several temperatures
  - Properties characterized in nomogram
- Viscoelastic links tested at CSA in DCS test
  - Tested at room temperature
  - 150 Hz is upper bound of accuracy for this test
  - Quick, inexpensive test

Temperature range is 50° to 75° Fahrenheit for F-15 wing under damaging flight conditions.[1]

[1] Lavrea, Vincent, Lynn Rogers, Arnel Pacia, and Mike Parin, "Add-On Damping Treatment for the F-15 Upper-Outer Wing Skin," Paper No. WL-TR-92-3069, July 1992.

Simplifications Needed to Model
Damping Treatment

- Simplify the model of triple constraining layer

  - Attempted to lump three layers into one equivalent layer

    - adjusted equivalent VEM and constraining-layer
      thickness

    - Looked for agreement in results between detailed
      and simplified models of a damped beam specimen

  - The simplification of multiple constraining layers did not
    produce acceptable agreement with detailed model

The analysis will look for local modes; thus significant detail is needed across the planform of the wing.

The initial plan of this project was to model the entire F-15 wing, with and without the damping treatments. However, modeling every layer of damping treatment would create too many degrees of freedom. Thus a simplification was pursued for the multiple-layer treatment.

A simplified model of a multiple-layer treatment was made by grouping all layers into a single layer. For this single layer, the equivalent VEM and constraining-layer thicknesses were adjusted to match the frequency and loss predicted by a detailed, multiple-layer model. Unfortunately, the simplified constraining-layer model did not predict the same modal frequencies or modal damping as the detailed model. The multiple-layer treatment would have to be modeled in detail, with a single layer of solid elements for each layer of the treatment.

Modeling Simplifications (cont)

- **Simplify the model of stand-off foam**
  - **A single solid element was used for foam cut with grooves**
    - **Material properties first estimated then optimized**
  - **Accuracy checked with detailed model of beam specimen**
  - **Analytical agreement was excellent after a number of iterations on material properties**

Grooves are cut into plane of foam to minimize shear stiffness while maintaining out-of-plane stiffness. These grooves would require too much detail in the finite element model of the wing. Thus a simplification was needed for the foam cut with grooves.

An analytical study was done to develop a simplified element for the foam cut with grooves. First, a detailed model of a damped beam was created. Next, a simplified model of the same damped beam was created with a single layer of solid elements through the thickness of the stand-off foam. For the simplified model, the stiffness of solid elements was reduced in directions affected by grooves, and the properties were modified until the simplified model agreed with the detailed model. The agreement between the two analytical models gave confidence in the modeling simplification.

Verification of Modeling Technique

• Test and analysis correlation of a beam specimen

 – Test specimen built and modal tested

 – Predictions from NASTRAN complex eigenvalue
    analysis compared well to test results

Beam	Mode 1		Mode 2	
	freq (Hz)	loss factor	freq (Hz)	loss factor
Test	106	0.220	330	0.316
Analysis	114	0.207	329	0.319

A final verification of the modeling technique was needed. This verification was found through a test and analysis correlation on a sample damped beam. A sample beam was layered with a layer of FD-440, the stand-off foam, another layer of FD-440, and an aluminum constraining layer. This test specimen was modal tested. In parallel, a finite element model was created of the test specimen. The excellent agreement between test and analytical results gave confidence in the modeling technique.

**Finite Element Model of
Typical Section of F-15 Wing**

• Typical section of the upper-outer wing skin was modeled

• Typical section includes two ribs and three stiffeners

• Each layer of treatment was modeled with a single layer of
   solid elements

• Simplification used for stand-off foam

   – Used equivalent properties from study
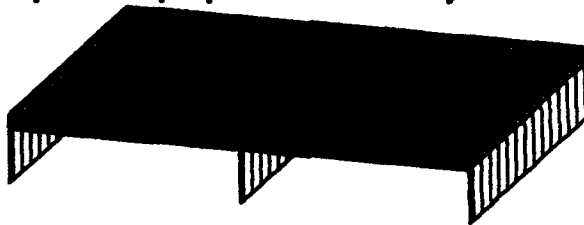
The multiple-layer damping treatment requires many degrees of freedom in the finite element model, too many degrees of freedom to model the entire wing. Therefore, a typical section of the outer wing was modeled. This typical section included two ribs and three stiffeners. The ribs were modeled as pinned connections to ground, since the ribs are much more stiff than the rest of the structure. Symmetric and antisymmetric boundary conditions were applied at the other edges in order to model the continuation of the structure.

The damping treatment on the typical section was modeled according to the previously-verified technique. The stand-off foam was modeled with single layer of solid elements through the thickness and the equivalent material properties. Each layer in the multiple constraining layer was modeled with a layer of solid elements. The viscoelastic links were modeled as springs to ground. This model contained 12,000 degrees of freedom.

Solution Using Typical Section Model

- Used typical-section model to predict ratio of damped to undamped RMS stress response

- NASTRAN modal random response

- Symmetric and antisymmetric boundary conditions were run in separate analyses

- Broad-band, unit PSD pressure applied to wing exterior

The finite element model was analyzed in a NASTRAN modal random response. One percent structural damping was assumed. RMS stresses were output for the damped and undamped models at various locations across the section.

Results

- Ratio of damped to undamped RMS stress calculated at elements with largest stresses
- Palgren-Miner cummulative fatigue law used to calculate fatigue life extension
- The treatment works!
  - Fatigue life of wing extended beyond 8000 hours

Treatment	External Only		Internal Only (Recommended)		VELs Only	
Boundary	antisym	sym	antisym	sym	antisym	sym
(Sd/Su)	0.555	0.606	0.332	0.437	0.347	0.477
(Nd/Nu)	6.93	5.27	39.0	15.7	33.7	11.7
Life (hours)	9,010	6,850	50,700	20,400	43,800	15,300

For the calculation of damped to undamped RMS stress, the location with the greatest undamped RMS stress was used.

The analytical predictions for the service life show a large margin of safety.

THE INFLUENCE OF CONSTRAINED-LAYER DAMPING TREATMENT ON PARAMETRIC AND AUTOPARAMETRIC RESONANCES IN NONLINEAR AND INTERNALLY RESONANT NONLINEAR STRUCTURES

Lawrence D. Zavodney*
Cedarville College

Joseph A. Schudt
Department of Engineering Mechanics
Ohio State University

1.0 ABSTRACT

The influence of viscoelastic constrained-layer damping treatment on parametric resonances of single-degree-of-freedom (SDOF) systems and autoparametric resonances of multiple-degree-of-freedom (MDOF) nonlinear systems possessing autoparametric coupling was investigated. The results show that commercially available aluminium-backed treatment is effective in suppressing parametric resonances in SDOF systems by moving the regions of parametric resonance away from the frequency axis. In the MDOF systems the damping affects the highly nonlinear response characteristics of each mode and the nonlinear coupling between modes; it can suppress the modulation between modes. In general, the effect of increased application of damping treatment is to contract the regions of nonlinear modal interaction and, in some cases, actually suppress the nonlinear modal coupling entirely with a sufficient amount of damping treatment. Experimental results include slow swept-sine excitations at constant amplitude and slow swept-amplitude excitations at constant frequency. Particular attention was paid to the nonlinear resonances and the modal interaction regions bounded by the Hopf bifurcation.

* Chairman, Department of Engineering, Cedarville, Ohio, 45314, (513) 766-7682

2.0 Introduction

Parametric resonances are not uncommon in structural vibrations. Zavodney [1] and Zavodney, et al [2-4] have provided a summary of parametric resonance in SDOF nonlinear structural systems. Damping is a common method of controlling or reducing vibration for externally excited resonances. However, damping plays quite a different role in parametrically excited systems. When systems exhibit nonlinear behavior, the analysis is more complicated; the nonlinearity and the damping together affects the system response so it is not always obvious what part the damping plays in the response. Zavodney and Shihada [5] investigated the influence of linear viscous damping on the fundamental and principal parametric resonances of SDOF systems possessing quadratic and cubic nonlinearities. The results showed that linear viscous damping plays a significantly different role than in the externally excited oscillator; if reduction in amplitude at resonance is the objective, then in some cases certain critical levels of damping must be exceeded--otherwise one can increase the damping by an order of magnitude but realize less than 5% reduction in the response amplitude.

When the structure possesses more than one mode, as is usually the case, there is the possibility of nonlinear modal coupling. When modes are coupled, it is possible to exchange energy from a directly excited mode to another mode. The end result is that more than one mode is participating in the response and, hence, the structure is vibrating at other frequencies in addition to the frequency of the excited mode--which is not always the same as the excitation frequency. As a result the analysis becomes even more complicated. Attempting to find appropriate mathematical models for these behaviors is extremely difficult. One particular mathematical model may describe one type of behavior, but when the excitation frequency is changed by only 0.1 Hz, the behavior is something else--qualitatively and quantitatively--i.e., a bifurcation has occurred. The nonlinear coupling responsible for this behavior is further enhanced if the structure possesses an internal resonance; an internal resonance occurs whenever any natural frequencies are commensurate (i.e., in a 2:1, 3:1, 3:2, etc. ratio). When a structure simultaneously possesses an internal resonance and appropriate nonlinear coupling terms, it is possible for one mode to parametrically excite another mode; this phenomenon is called an autoparametric resonance. When this happens, the nonlinear effects are greatly intensified and completely dominate the response. Nayfeh and Zavodney [6] and Balachandran and Nayfeh [7] provided a theoretical model and experimental results showing that such behavior can lead to long-time responses that are not steady-state; mathematically a Hopf bifurcation has occurred.

The objective of this paper is to investigate theoretically and experimentally the effects of damping on parametric and autoparametric resonance in nonlinear SDOF and MDOF flexible structures. The experiments were performed on structures fabricated from prismatic beams and lumped masses. These types of structures were easy to prepare and tune--i.e., by adjusting the position of the masses the resonant

frequencies could be changed. This was essential for the MDOF structure when an internal resonance was desired.

3.0 Single-Degree-of-Freedom Structure
3.1 Theoretical Analysis

Many structural elements can be modelled as slender beams and lumped masses. When the support undergoes motion, the beam is subject to vibration—either external or parametric, or both. In this section the governing equations are derived for inplane flexural vibration of a thin elastic prismatic cantilever beam subject to parametric vibration at the base. The nonlinear terms arising from the curvature and coupling effects are retained. Galerkin's method is used to discretize the governing nonlinear partial differential equation of motion. The linear eigenvalue problem is solved to determine the eigenvalues, and the eigenfunction is used to determine the coefficients of the time modulation equation. A multiple-scales perturbation solution is obtained for the temporal modulation equation.

The governing equation of motion is derived using Euler-Bernoulli beam theory. The beam, shown in Figure 1, is cantilevered at the oscillating support, has a length L, and carries a concentrated mass m at an arbitrary distance s = d along the neutral axis of the beam. We assume that the thickness of the beam is so small compared with the length that the effects of shearing deformation and rotatory inertia of the beam can be neglected. Since we are investigating parametric resonances (transverse vibration), we will not consider axial resonances of the beam since the frequency of excitation will be far below the first axial resonance. If the beam is kept relatively short (< 30 beam widths), the transverse vibration is purely in-plane (if the lumped mass is symmetrical with the centerline); if the excitation frequency is far below the first torsional mode, then we can neglect the torsional modes of the beam in the analysis. These assumptions are consistent with observations in the laboratory. Also, we do not observe any combination or internal resonances. When the mass is removed and the length is increased by an order of magnitude, combination resonances do occur.

Using Euler-Bernoulli beam theory, the governing equation of motion is given by Zavodney and Nayfeh [8] as

$$
EI\left(v_{ssss} + \frac{1}{2}v_{ssss}v_s^2 + 3v_sv_{ss}v_{sss} + v_{ss}^3\right) + \left(1 - \frac{1}{2}v_s^2 - ...\right)(\rho + m\delta(s - d))\ddot{v}
$$

$$
- \frac{\partial}{\partial s}(Nv_s) + v_sv_{ss}\int_s^L (\rho + m\delta(\xi - d))\ddot{v}d\xi - \frac{\partial}{\partial s}(J\delta(s - d)[\ddot{v}_s\left(1 + \frac{1}{2}v_s^2 + ...\right)
$$

$$
+ v_s\dot{v}_s^2]) + \left(1 - \frac{1}{2}v_s^2 - ...\right)c\dot{v} + v_sv_{ss}\int_s^L c\dot{v}d\xi = 0.
$$

$$(1)$$

where N is given by

$$N = \frac{1}{2}\rho \int_s^L \left[\int_0^\xi \left(v_\eta^2 \right)_{tt} d\eta \right] d\xi - \frac{1}{2} m \int_s^L \delta(\xi - d) \left[\int_0^\xi \left(v_\eta^2 \right)_{tt} d\eta \right] d\xi$$

$$+ m(\ddot{z} - g) \int_s^L \delta(\xi - d)\, d\xi + \rho L \left(1 - \frac{s}{L} \right)(\ddot{z} - g)$$

(2)

and the following nomenclature has been used:

x,y	-	Newtonian Cartesian reference frame
g	-	acceleration of gravity
s	-	reference variable along beam
ξ	-	variable of integration along beam
$d\xi$	-	differential length of beam element
L	-	beam length
w	-	beam width
t	-	beam thickness
d	-	position of mass center of mass m
ρ	-	mass density of homogeneous beam per unit length
c	-	coefficient of viscous damping
m	-	mass of concentrated weight on beam
J	-	polar moment of inertia of mass m
$v(\xi,t)$	-	lateral displacement of beam element dx
$u(\xi,t)$	-	longitudinal displacement of beam element $d\xi$
$\phi(s)$	-	angle with respect to vertical of beam at s
$\kappa(s)$	-	curvature of beam at s
I	-	cross-sectional moment of inertia of beam
E	-	modulus of elasticity of beam.

This field equation is subject to the following boundary conditions:

$$v(0,t) = 0, \ v_s(0,t) = 0, \ v_{ss}(L,t) = 0, \ v_{sss}(L,t) = 0 \ . \qquad (3),(4),(5),(6)$$

The governing problem (1)-(6) is nonlinear and does not admit a closed-form solution. An approximate solution was sought that satisfies both the equation and the boundary conditions. Since the boundary conditions are spatial and independent of time, the solution of the nonlinear problem is assumed to take the form

$$v(s,t) = \sum_n r\, y_n(s)\, G_n(t) \qquad (7)$$

where r is a scaling factor, $y_n(s)$ is the shape function of the nth linear mode, and $G_n(t)$ is the time modulation of the nth mode.

The general solution for the shape function can be stated as the composite function

$$y(s) = C_1\left[\left(\sin\frac{k}{L}s - \sinh\frac{k}{L}s\right) - L\left(\cos\frac{k}{L}s - \cosh\frac{k}{L}s\right)\right] + C_1 U(s-d)\{h_1$$

$$\left[\sin\frac{k}{L}(s-d) - \sinh\frac{k}{L}(s-d)\right] + h_3\left[\cos\frac{k}{L}(s-d) - \cosh\frac{k}{L}(s-d)\right] - Lh_2$$

$$\left[\sin\frac{k}{L}(s-d) - \sinh\frac{k}{L}(s-d)\right] - Lh_4\left[\cos\frac{k}{L}(s-d) - \cosh\frac{k}{L}(s-d)\right]\}, \tag{8}$$

where C_1 is an arbitrary constant and k is the characteristic root of the frequency equation [8]. The frequency of oscillation is given by

$$\omega^2 = \frac{EI}{\rho}\left(\frac{k}{L}\right)^4 . \tag{9}$$

Galerkin's method was used to obtain a non-linear differential equation governing the temporal modulation of the beam which contained cubic stiffness terms.

3.2 Experimental Analysis

Experiments were performed on the structure shown in Figure 1. The excitation was a base displacement (along the axis in the vertical direction) at a frequency nearly twice that of the first flexural mode of the cantilever beam. The resonant response that ensues is called a principal parametric resonance. The experiments consisted of frequency sweeps at constant-amplitude acceleration and amplitude sweeps at constant frequency. The amplitude was held constant by a computer-controlled feedback loop; as the frequency was changed, the corresponding excitation amplitude required adjustment to keep the acceleration level constant. The excitation level was chosen as large as possible without causing excessive amplitudes of displacement; a maximum level of 0.350 g's was selected. The response was measured by strain gages mounted on the beam.

The experimental frequency response of the undamped structure (where undamped means before any damping treatment was applied) for two levels of excitation is shown in Figure 2. It shows that the system is softening because it bends to the left. This behavior was neither expected nor predicted. These experiments were conducted by increasing the frequency of excitation very slowly while simultaneously keeping the table acceleration constant. The arrows indicate jumps; for example, when the excitation level is 0.350 g's (denoted by the circles), the response jumps up to the large amplitude and then slowly decreases as the frequency is increased. When the frequency is decreased, the response follows the same curve and extends it into an overhang. The response eventually jumps down to the trivial response. The response for the 0.250-g excitation level is qualitatively the same but at a lower amplitude.

Additional experiments at the same levels of excitation were performed with one and two strips of viscoelastic damping treatment applied, as shown in Figures 3 and 4. For the 0.250-g excitation level, the principal parametric resonance was completely

suppressed with only two strips of damping treatment applied. Two 0.10-inch strips of damping treatment covers only 5% of the surface area of the beam between the support and the lumped mass and has an equivalent viscous damping coefficient of 0.0073.

The regions of parametric resonance in the excitation-amplitude versus the excitation-frequency plane were also determined. These experiments were performed by repeating the frequency response experiments for different levels of excitation and plotting only the bifurcation points where either the trivial response becomes unstable (during both a sweep up and a sweep down) or a nontrivial response jumps to the trivial response. An example is shown in Figure 5. This figure shows three boundaries which divide the domain into two interior regions; the inner-most region (bounded by the center curve and the right curve) represents the loss of trivial stability for the linear system. The additional curve on the far left represents the extension of the instability region caused by the overhang due to the softening nonlinearity in the system. Because nontrivial responses exist at excitation frequencies below those predicted by linear theory, the system is said to possess a subcritical instability. The amount of overhang is reduced for increased damping levels, as shown in Figures 6 and 7.

A summary of the bifurcation boundaries showing only the region where nontrivial responses exist is shown in Figure 8. As the equivalent linear viscous damping coefficient increases, the instability regions move away from the frequency axis. The bifurcation boundaries predicted from the theory using the experimentally measured damping coefficients are also shown in Figure 8. The values of the equivalent damping coefficient were obtained from the free response data. The Eigensystem Realization Algorithm (ERA) [11] was used to estimate the damping coefficients and natural frequencies. The agreement between theoretical curves and experimental data in Figure 8 is excellent.

3.3 Discussion of Experimental Results

Principal parametric resonances can be attenuated by the application of constrained-layer damping treatment. The experiments show that just a small quantity of the material can be effective. The theoretical model using a first-order perturbation solution did a good job in predicting the stability boundaries for the parametric resonance, but did not predict the softening behavior of the beam nor predict the jump down.

In summary, increased application of the damping treatment reduces the amplitude of the resonant response, and reduces the region of parametric instability. The only way to completely suppress a parametric resonance is to move the instability region far enough away from the axis so that it is completely removed from the area of interest.

4.0 Multiple-Degree-of-Freedom Structure
4.1 Theoretical Analysis

Several researchers have investigated this model and have developed mathematical models. The equations describing the displacement of m_1 and m_2 are given by [10]

$$v_1(x,t) = \varepsilon l_1 f_{11}(x)u_1(t) + \varepsilon l_1 f_{12}(x)u_2(t) \tag{10}$$

$$v_2(y,t) = \varepsilon l_1 f_{21}(y)u_1(t) + \varepsilon l_1 f_{22}(y)u_2(t) \tag{11}$$

where the u_i are given by

$$\ddot{u}_1 + 2\varepsilon\mu_1\dot{u}_1 + \omega_1^2 u_1 + \varepsilon X_{11}(\dot{u}_1)^2 + \varepsilon X_{12}\dot{u}_1\dot{u}_2 + \varepsilon X_{13}(\dot{u}_2)^2 + \varepsilon Y_{11}u_1\ddot{u}_1$$
$$+ \varepsilon Y_{12}u_1\ddot{u}_2 + \varepsilon Y_{13}u_2\ddot{u}_1 + \varepsilon Y_{14}u_2\ddot{u}_2 + 2\varepsilon Z_{11}F\,\Omega\,u_1\cos\Omega t$$
$$+ 2\varepsilon Z_{12}F\,\Omega u_2\cos\Omega t = 2FK_1\cos\Omega t \tag{12}$$

$$\ddot{u}_2 + 2\varepsilon\mu_2\dot{u}_2 + \omega_2^2 u_2 + \varepsilon X_{21}(\dot{u}_1)^2 + \varepsilon X_{22}\dot{u}_1\dot{u}_2 + \varepsilon X_{23}(\dot{u}_2)^2 + \varepsilon Y_{21}u_1\ddot{u}_1$$
$$+ \varepsilon Y_{22}u_1\ddot{u}_2 + \varepsilon Y_{23}u_2\ddot{u}_1 + \varepsilon Y_{24}u_2\ddot{u}_2 + 2\varepsilon Z_{21}F\,\Omega\,u_1\cos\Omega t$$
$$+ 2\varepsilon Z_{22}F\,\Omega u_2\cos\Omega t = 2FK_2\cos\Omega t \tag{13}$$

The two cases of particular interest are when $\Omega \approx \omega_1$ and $\Omega \approx \omega_2$ which corresponds to a direct excitation to the first mode and to the second mode.

For the case of an internal resonance and excitation to the first mode, the detuning parameters are defined as

$$\omega_2 = 2\omega_1 + \varepsilon\sigma_1 \quad\text{and}\quad \Omega = \omega_1 + \varepsilon\sigma_2 \ , \tag{14}$$

From a multiple-scales perturbation analysis, the steady-state equations are obtained:

$$\dot{a}_1 = \sigma_2 \tag{15}$$

$$\dot{a}_2 = 2\sigma_2 - \sigma_1 \tag{16}$$

$$a_2 = a_1^2 / \left(\mu_2^2 + (2\sigma_2 - \sigma_1)^2\right)^{1/2} \tag{17}$$

$$a_1^6 + 2[\mu_1\mu_2 - \sigma_2(2\sigma_2 - \sigma_1)]a_1^4 + [\mu_2^2 + (2\sigma_2 - \sigma_1)^2][(\sigma_2^2 + \mu_1^2)a_1^2 - F^2] = 0 . \tag{18}$$

The stability of these solutions is obtained by perturbing each steady-state solution and studying the behavior of the disturbance. Any solution of (15)-(18) is stable if the real parts of all eigenvalues are less than zero.

For the case of internal resonance and an excitation to the second mode, we put

$$\omega_2 = 2\omega_1 + \varepsilon\sigma_1 \quad\text{and}\quad \Omega = \omega_2 + \varepsilon\sigma_2 \tag{19}$$

and obtain the following steady-state equations:

$$a_1(\mu_1 - a_2\sin\gamma_1) = 0, \tag{20}$$

$$a_1[(\sigma_1 + \sigma_2)/2 + a_2\cos\gamma_1] = 0, \tag{21}$$

$$\mu_2 a_2 + a_1^2 \sin\gamma_1 - F\sin\gamma_2 = 0, \tag{22}$$

$$\sigma_2 a_2 + a_1^2 \cos\gamma_1 + F\cos\gamma_2 = 0. \tag{23}$$

There are two possible solutions to these equations: the solution which corresponds to the linear problem given by

$$a_1 = 0 \quad \text{and} \quad a_2 = F / \sqrt{\sigma_2^2 + \mu_2^2} \,, \tag{24}$$

and the nonlinear solution which corresponds to

$$a_1^2 = \frac{1}{2}[\sigma_2(\sigma_1 + \sigma_2) - 2\mu_1\mu_2] + \sqrt{F^2 - \left[\mu_1\sigma_2 + \mu_2\left(\frac{\sigma_1 + \sigma_2}{2}\right)\right]^2}\,, \tag{25}$$

$$a_2 = \sqrt{\mu_1^2 + \left(\frac{\sigma_1 + \sigma_2}{2}\right)^2}\,. \tag{26}$$

The stability of the solutions for a direct excitation to the second mode is obtained in a similar fashion. The nature of the response predicted from these equations will be discussed later.

4.2 Experimental Analysis

Experiments were performed on a multiple-degree-of-freedom (MDOF) structure. The structure used for these experiments is shown in Figure 9; it has been studied by several researchers [6,7,8,9]. It was chosen because it was easy to fabricate and could be easily tuned (to create an internal resonance) by adjusting the lengths of the beams and position of m_2. The shaker was an Unholtz-Dickie model 200 which has a capacity of 1100-lb force. Data was obtained by strain gages attached to the structure. The signals were monitored on a digital oscilloscope and captured by a Hewlett-Packard data acquisition system attached to a PC. The experiments consisted of the following: a) random excitation to determine resonant frequencies and damping coefficients; b) harmonic excitation at constant frequency and amplitude to determine steady-state response levels; c) harmonic excitation at constant amplitude of acceleration and small changes in the frequency of excitation to effectively cause a slow frequency sweep; d) harmonic excitation at constant frequency and small changes in the amplitude of excitation to effectively cause a slow amplitude sweep; e) impulse response resulting from a sudden release from a deformed position approximating the first mode shape, the second mode shape, and a combination of the two; and f) impulse response resulting from an impact to the lower mass. The nature of the response was quite complicated at times, so a variety of the above techniques was used throughout the experimental phase.

The procedure used for applying damping treatment to the SDOF structure was used for the MDOF structure: thin strips of 0.10-inch width damping treatment were applied in increasing numbers to each beam, increasing the damping of the structure.

The responses of this structure--both to impulse and harmonic excitation--were very complicated. The primary source of the quadratic modal-coupling nonlinearity in this structure was due to the asymmetrical geometry. When an internal resonance existed, the nonlinear coupling was significantly intensified and would dominate the response; when this happened, the response amplitudes were three to four times larger than the linear response. Internal-resonance detuning is a measure of the difference between the frequency of the second mode and two times the frequency of the first mode; the detuning parameter is defined by equation (14) or (19).

Because the results of the SDOF experiments showed that a parametric resonance could be suppressed with a small amount of damping treatment, the experiments on the MDOF structure were performed at very high levels of excitation. Studies [6,7,9,10] have shown that under some conditions, nonlinear responses can be achieved with very small levels of excitation (on the order of 20 mili-g's). In the experiments performed here, the excitation levels were on the order of 100 mili-g's -- five times that required to solicit a nonlinear response. This large excitation level was used to extend the range for which damping treatment could be applied; in other words, more damping treatment could be applied before the nonlinear motion was expected to be suppressed.

Damping treatment was applied in five steps. With each application of damping treatment the model was adjusted (i.e., the length of the lower beam) to return it to the original amount of detuning. This was a painstaking procedure because it sometimes required more than a dozen adjustments in the length of the lower beam just to get the results reported here.

The labels in the subsequent figures correspond to the following amounts of damping treatment: the unmarked or "O" for none, "I" for one strip on each beam, "II" for two strips on each beam (17% of the surface area), "III" for four strips on each beam, "IV" for six strips on each beam (50%), and "V" for 100% coverage.

The structure shown in Figure 9 was tuned such that the first resonance occurred at 4.012 Hz and the second resonance occurred at 8.040 Hz; this corresponded to an internal resonance detuning of +0.016 Hz, or +0.20% (of the second resonant frequency). This was as close as practically possible to perfect tuning on a real structure; a tuning closer to 0% could be accomplished at the expense of more painstaking effort (i.e., moving the lower beam into the clamped support in 0.001-inch increments and repeating the experiments until the desired detuning is achieved). After each application of damping treatment, the model was retuned to get nearly 0.0% detuning.

The structure was forced with low-level random excitation; the input acceleration was measured by an accelerometer mounted on the base clamp and the response displacement was measured by the strain gages. The roots were estimated by a

complex exponential curve fit. The estimates of the natural frequencies and damping coefficients are listed in the figure captions and summarized in Table 1.

The frequency responses for the structure without treatment and for three of the five cases of damping treatment are shown summarized in Figures 10 and 11. This 3-D perspective plot aids in visualizing the qualitative and quantitative changes caused by the increase in the damping. The frequency axis is shown normalized with respect to the excitation frequency because the addition of the damping treatment caused the frequencies to shift slightly. The response amplitude (displacement of m_1) is represented in units corresponding to the ratio of the lower mass displacement amplitude to the length of the lower beam. This scaling provides a convenient comparison of all of the results for all of the experiments. For example, the peak amplitude of the response of the first mode is approximately 8% of the length of the lower beam.

When the first mode is directly excited with a large-amplitude excitation at a frequency near the first resonance, the response is nonlinear, as shown in Figure 10. Figure 10(a) shows the first mode response and Figure 10(b) shows the second mode response. The response of the untreated structure shows the most interesting behavior. As the frequency of excitation is increased from 0.90, the amplitude initially grows until the second mode is also excited; this happens at a frequency near 0.97. As the frequency is increased further, the amplitude of the first mode decreases dramatically—almost four times! When a Hopf bifurcation occurs near a frequency of 1.0, no steady-state responses are possible. This region is denoted by dots which represents an "average" amplitude. Actual bounds on the modulation are shown later in the amplitude response curves. As the frequency is increased further, the amplitude of response increases until it jumps down (at the first mode frequency of 1.072) to the linear response amplitude. The linear response consists only of the directly excited mode—no other modes are present. If the frequency is decreased from above, the jump up occurs at a lower frequency (i.e., 1.044) than did the jump down during a sweep up. This indicates an overhang or double-valued steady-state response. Theory shows that these two solution branches are connected by an unstable solution branch; this is shown by the dashed line on the response (note—there are no data points for this dashed line because they cannot be realized in the laboratory). Further decreases in the excitation frequency cause the response to follow the same path as that followed during the sweep up. The frequency response is almost symmetrical; because it is slightly skewed to the right, it indicates that a slight positive detuning of the internal resonance is present.

The frequency response curve for the undamped structure shows four distinct types of motions that are possible when the excitation frequency is near the first mode: (1) the linear solution where only the directly excited mode participates in the response, (2) a region where nonlinear coupling is present and causes two steady-state solutions to co-exist—the linear one and a nonlinear one, (3) only a nonlinear response where the

modes achieve one steady-state amplitude, and (4) a region bounded by a Hopf bifurcation where no steady-state solutions exist.

As damping treatment was applied to the structure, response amplitudes were attenuated. Certain trends can be observed in Figure 10. The second application of damping treatment [II] consisted of two strips on each beam (17%). Both response peaks are significantly attenuated. The peak at a frequency below the resonance is almost completely eliminated while the response peak at the upper frequency is reduced in amplitude sufficiently to eliminate the hysteresis. The fourth application of damping treatment [IV] consisted of six strips (50%) and caused further peak broadening and smoothing, resulting in a frequency response that was so broad that it appeared as if it had a large damping coefficient. The fifth application (100%) almost completely eliminated the modal coupling; however, when one compares the harmonic response (i.e., Figure 10) to the stochastic response, it is obvious that linear-based modal analysis techniques (i.e., random excitation) cannot be used to identify this type of nonlinearity. This figure shows that damping treatment can attenuate the nonlinear hysteretic behavior and eliminate the amplitude of the response.

A direct excitation to the second mode is shown in Figure 11. Similar observations can be made from these curves. The frequency axes have been nondimensionalized with respect to the excitation frequency; hence the second mode has a resonance at 1.0 and the first mode, representing a frequency nearly one-half that of the excitation, has a resonance at 2.0 (representing a subharmonic resonance of order 1/2). The indirectly excited mode (i.e., the first mode) remains trivial until it is strongly (and nonlinearly) coupled to the second mode; when it is, the amplitude of the second mode is drastically attenuated. Furthermore, during a sweep down, there is no jump up in the second mode response—only a jump down—because the lower branch merges with the upper branch; it is not a turning point bifurcation as was the case for a direct excitation to the first mode as seen in Figure 10. The first mode response demonstrates both a jump up and a jump down during a frequency sweep. For the fifth application of damping treatment, the nonlinear coupling between the modes is completely suppressed; the end result is that the system behaves like a moderately damped linear system.

Experiments were also conducted to measure the amplitude response at selected frequencies of excitation; these curves are cuts across a particular frequency response curve shown in Figures 10 and 11. For the case of no damping treatment, a cut at a frequency of 1.004 (first-mode excitation) passes through the modulation region. The amplitude response at this frequency is shown in Figure 12. As the amplitude of excitation is increased, the system experiences a Hopf bifurcation and begins to modulate; i.e., energy begins to flow back and forth between the two modes. As the amplitude of excitation is increased, the "average" amplitude tends to increase and the maximum excursions increase.

At a frequency of 1.067 the first-mode frequency response curve (for no damping treatment) in Figure 11(a) shows a double-value steady-state amplitude. An amplitude sweep through this region, as shown in Figure 13, reveals a jump phenomenon. When starting on the lower branch, increasing the amplitude of excitation causes a jump up to the upper branch; decreasing the amplitude of excitation causes a jump down at a lower value of the amplitude of excitation.

When the maximum damping treatment was applied, there was essentially one response; Figure 14 shows an amplitude sweep through this resonance at a frequency of 0.979. Although the curves are quite tame, they still show nonlinear coupling because the second mode is excited. Even though the excitation is driving the first mode, some of the energy is channeled into the second mode.

Amplitude-excitation experiments were also performed for a direct excitation to the second mode. Figure 15 shows a cut across the 0.998 frequency line (the 1.999 frequency line for the first mode) in Figure 10 for the structure with no damping treatment applied. Although the second mode is directly excited, its response is attenuated; instead, the energy goes into the first mode which responds like a parametrically excited SDOF system. An amplitude sweep at the 1.057 frequency line (2.119 for the first mode) in the region of the overhang is shown in Figure 16. During the experiment, the amplitude of the excitation was increased slowly. At 0.32 g's rms, the linear solution became unstable. However, the divergence growth rate was so slow that it was possible to stay on the unstable branch long enough to locate some of the equilibrium points. These are shown in the figure as isolated circles. However, by waiting long enough, the response went to the steady-state nonlinear solution which is shown as a solid line. During a sweep down, the response followed the upper curve rather than the lower curve. At an excitation level of 0.075 g's rms, the response jumped down to the linear response on the lower branch and remained there. Note that the overhang region in Figure 10 is qualitatively different than the overhang region in Figure 11; hence, it is not surprising to see a qualitative difference in the double solution region of Figures 13 and 16.

When damping treatment was applied to the structure, the regions of multiple solutions contracted and eventually disappeared. For small levels of excitation the linear solution appeared; this is shown in Figure 17. At this frequency of excitation (0.992 for the first mode, 1.991 for the second mode), when the excitation level exceeded 0.09 g's, the second mode saturated. The energy that was put into the system at the second-mode was channeled into the first mode; essentially the second mode frequency was parametrically exciting the first mode. Hence, the first mode response appears to have a parametric type response.

4.3 Discussion of Results and Comparison with Theory

The experimental results were compared with the theoretical results using values of the damping coefficients and natural frequencies shown in Table 1 obtained

from the random excitation experiments and complex exponential curve fits. The response of the structure to a direct excitation of the first mode is given by equations (17) and (18); typical results are shown in Figure 18-O. Two additional theoretical curves were generated for increasing amounts of damping; these are shown in Figures 18-III and 18-V. These curves also capture the qualitative behavior seen in the experimental results.

5.0 Summary and Conclusions

Analysis and experiments were performed to study the effect of commercially available viscoelastic damping treatment on parametric and autoparametric resonances in nonlinear systems. Both SDOF and MDOF structures were used; they consisted of flexible beams and masses.

For the SDOF structure, experiments were conducted at several levels of excitation and it was found that the damping treatment was particularly effective in reducing--and even suppressing--the resonance entirely. The first-order theory predicts the region of the loss of trivial stability very well, but failed to predict the softening behavior of beam 2 and the closing (i.e., merging of the two branches) of the frequency response curves.

For the 2DOF system, the particular case of an internally resonant structure was considered. The qualitative and quantitative effects of the damping treatment were determined for very large excitation levels; it was observed that increased amounts of damping treatment reduces the nonlinear modal coupling and modulation regions and reduces the amplitude of response. For the case of direct excitation to the second mode, a large amount of damping treatment was capable of eliminating the nonlinear coupling.

6.0 Acknowledgements

7.0 References

1. Zavodney, L.D., "A Theoretical and Experimental Investigation of Parametrically Excited Nonlinear Mechanical Systems," Ph.D. Dissertation, Virginia Polytechnic Institute and State University, 1987.
2. Zavodney, L.D. and Nayfeh, A.H. "The Response of a Single-Degree-of-Freedom System with Quadratic and Cubic Nonlinearities to a Fundamental Parametric Resonance," *Journal of Sound and Vibration*, 1988, Vol 120, 63-93.

4. Zavodney, L.D., Nayfeh, A.H. and Sanchez, N.E., "Bifurcations and Chaos in Parametrically Excited Single-Degree-of-Freedom Systems," *Nonlinear Dynamics*, 1990, Vol 1, 1-21.

5. Zavodney, L.D. and Shihada, S.M., "The Role of Damping in the Suppression of Parametric Resonances in Nonlinear Systems," *Proceedings of Damping '89*, West Palm Beach, Florida, February 8-10, 1989, FBD-1 - FBD-22.

6. Nayfeh, A.H. and Zavodney, L.D., "Experimental Observation of Amplitude- and Phase-Modulated Responses of Two Internally Coupled Oscillators to a Harmonic Excitation," *Journal of Applied Mechanics*, 1988, Vol 110, 706-710.

7. Balachandran, B. and Nayfeh, A.H., "Nonlinear Motions of Beam-Mass Structure," *Nonlinear Dynamics*, 1990, Vol 1, 39-62.

8. Zavodney, L.D. and Nayfeh, A.H., "The Non-Linear Response of a Slender Beam Carrying a Lumped Mass to a Principal Parametric Excitation: Theory and Experiment," *International Journal of Nonlinear Mechanics*, 1989, Vol 24, 105-125.

9. Zavodney, L.D. and Hollkamp, J.J., "Experimental Identification of Internally Resonant Nonlinear Structures Possessing Quadratic Nonlinearity," *Proceedings of the 32nd Structures, Structural Dynamics and Materials Conference*, Baltimore, Maryland, 8-10 April, 1991, 2755-2765.

10. Haddow, A.G., Barr, A.D.S., and Mook, D.T., "Theoretical and Experimental Study of Modal Interaction in a Two-Degree-of-Freedom Structure," *Journal of Sound and Vibration*, 1984, Vol 97, 451-473.

11. Junag J-N. and Pappa R.S., "An Eigensystem Realization Algorithm for Modal Parameter Identification and Mode Reduction," *Journal of Guidance, Control and Dynamics*, Vol 8. 1985, pp 620-627.

Table 1. Natural frequencies (Hz) and damping coefficients (percent of critical) estimated from complex exponential curve fits to the frequency response data for low-level random excitation of the 2DOF tuned and slightly detuned structure.

Damping	ω_1	ω_2	$\omega_1\zeta_1$	ζ_1	$\omega_2\zeta_2$	ζ_2	$|a_1|$	$|a_2|$
0	4.012	8.040	0.410	0.016	0.191	0.004	0.012	0.022
I	4.091	8.050	0.569	0.022	0.396	0.008	0.006	0.020
II	4.062	8.161	0.485	0.019	0.531	0.010	0.010	0.022
III	4.131	8.220	0.476	0.018	0.863	0.017	0.011	0.026
IV*	4.175	8.283	0.593	0.023	1.135	0.022		
V	4.278	8.620	1.425	0.053	1.731	0.032	0.007	0.011

* Estimated from sinusoidal-dwell data because random excitation data unavailable.
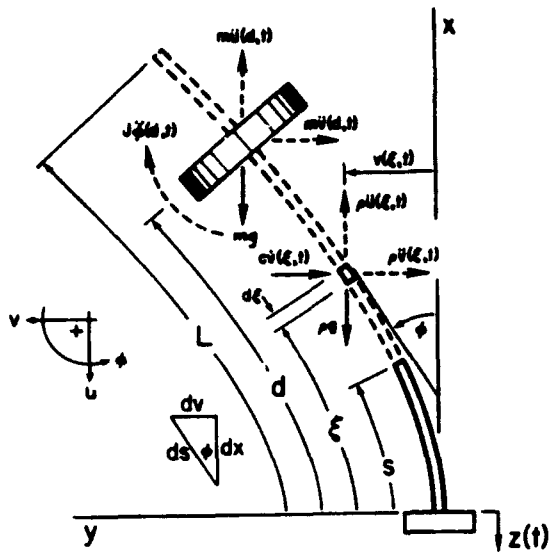
Figure 1. Structure consisting of a flexible beam carrying a lumped mass used for the SDOF experiments. Constrained-layer damping treatment was applied in thin 0.10-inch strips on both sides to incrementally increase the level of damping in the structure. The model was attached to a shaker head that was oscillating in the vertical direction.
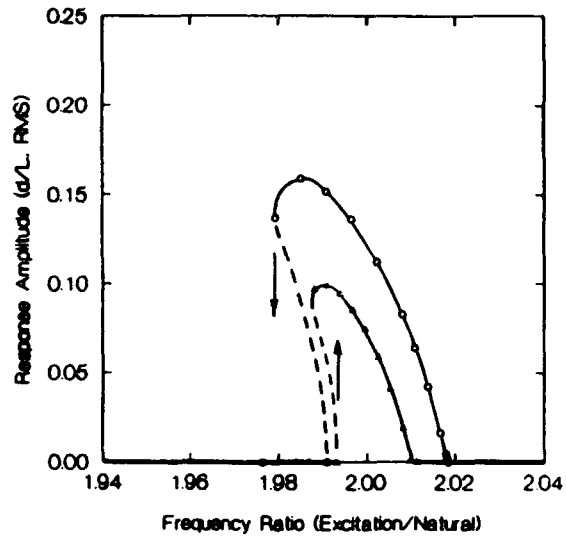
Figure 3. Frequency-Response at two levels of excitation for the SDOF structure with one strip of damping treatment applied.
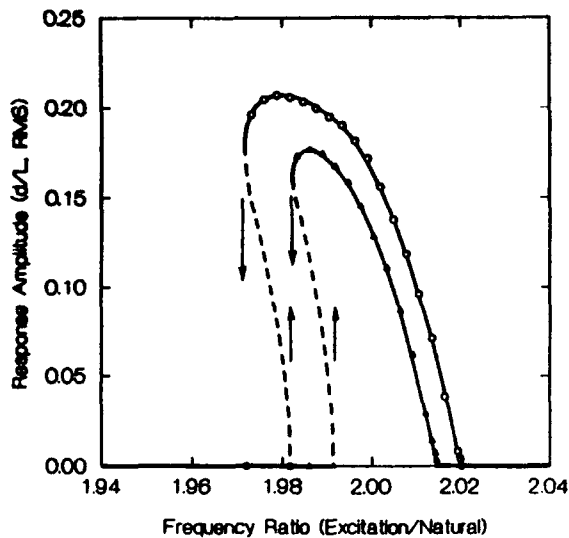
Figure 2. Frequency-Response for the SDOF structure before damping treatment was applied for two levels of excitation (0.25 and 0.35 g's rms). The bending of the curves to the left indicates that the system is softening. These curves were obtained by sweeping the frequency up and down through the region of principal parametric resonance at a rate slow enough such that a steady-state amplitude was maintained.
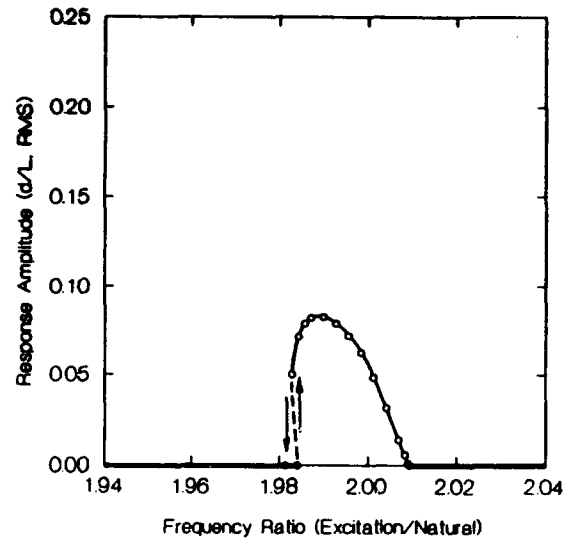
Figure 4. Frequency-Response at two levels of excitation for the SDOF structure with two strips of damping treatment applied. Note that the resonance for the smaller excitation level is completely suppressed.
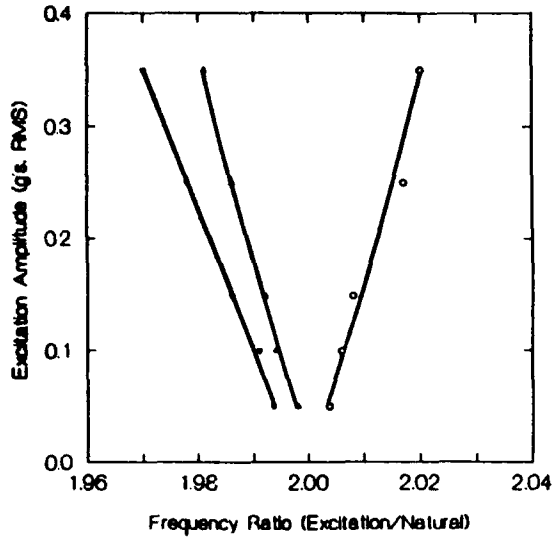
Figure 5. Bifurcation diagram showing the instability regions of the principal parametric resonance for the beam before the damping treatment was applied. The curve on the far left represents the bifurcation boundary caused by the overhang observed in Figure 2 which is caused by the softening behavior. It represents a subcritical instability.
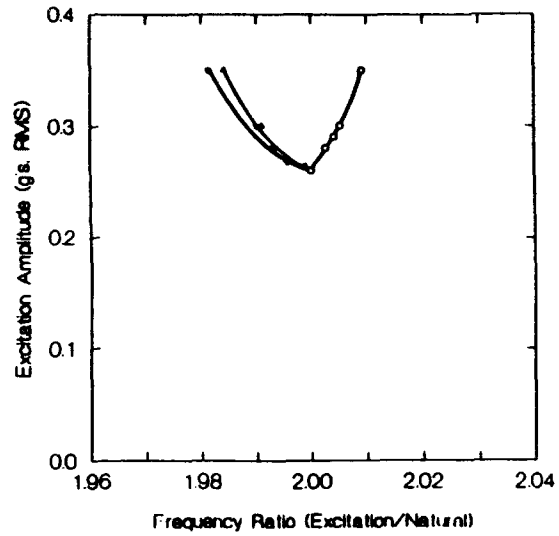
Figure 7. Bifurcation diagram showing the instability regions of the principal parametric resonance for the beam with two strips of damping treatment.
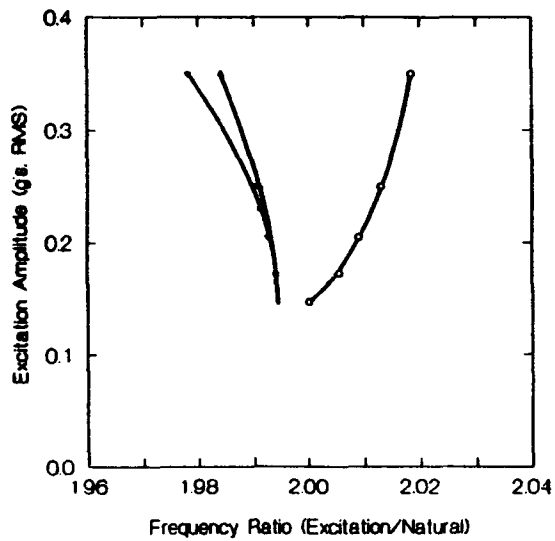
Figure 6. Bifurcation diagram showing the instability regions of the principal parametric resonance for the beam with one strip of damping treatment.
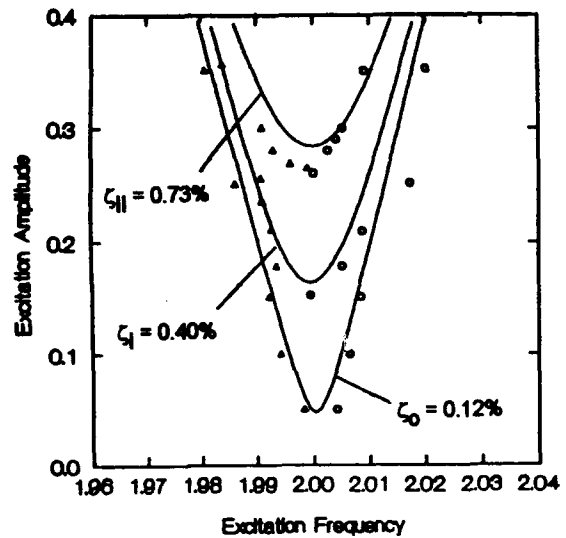
Figure 8. Comparison of the bifurcation boundaries indicating the loss of stability of the trivial solution as predicted by theory and measured during experiment for three different applications of damping treatment.

FBA-16
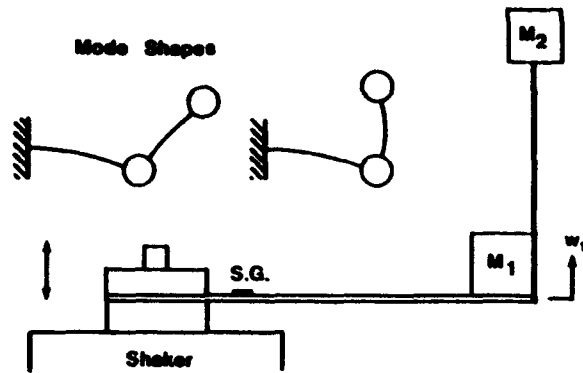
Figure 9. Structure used for the MDOF experiments. By adjusting the length of the lower beam and the position of the second mass, the first and second resonant frequencies could be adjusted. The higher modes and out-of-plane modes were not excited during the experiments; hence a 2DOF model can be used to adequately describe the observed behavior.
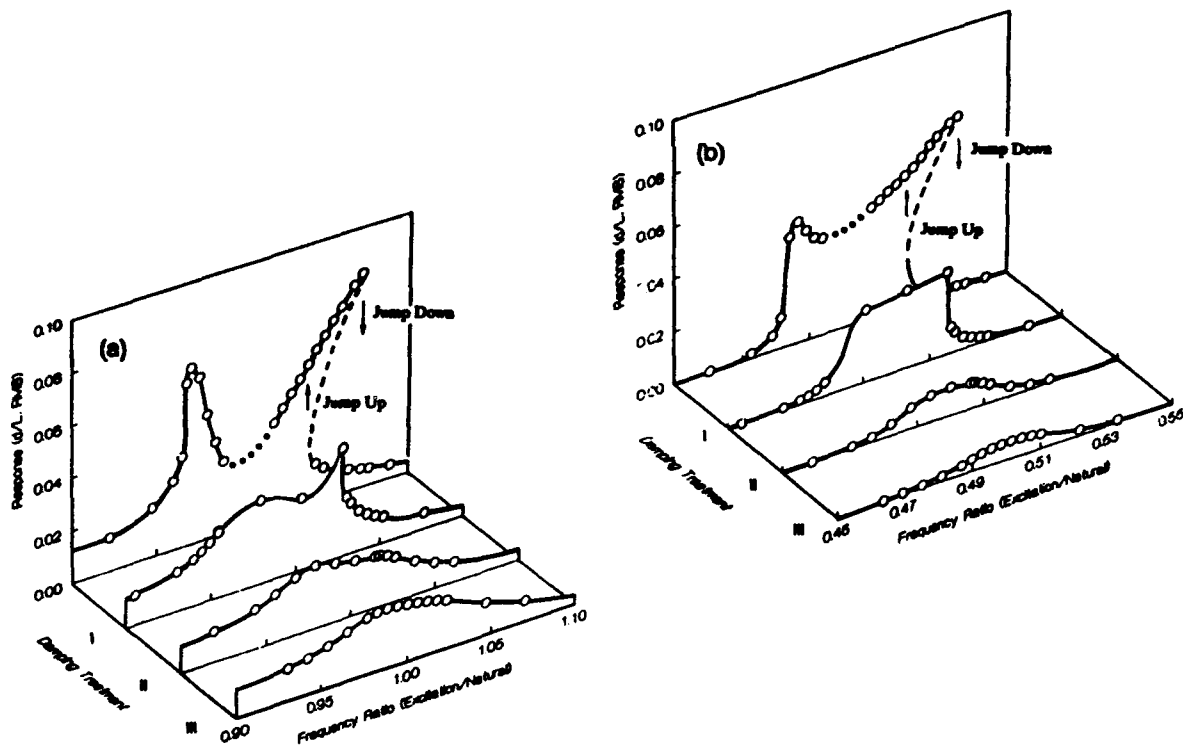
Figure 10. Frequency response of the 2DOF structure with +0.20% detuning (for no damping treatment) for a direct excitation to the first mode: (a) shows the first mode response and (b) shows the second mode response. Although attempts were made to have a perfect internal resonance, there is some small amount of detuning as evidenced from the unsymmetrical nature of the response curves.

FBA-17
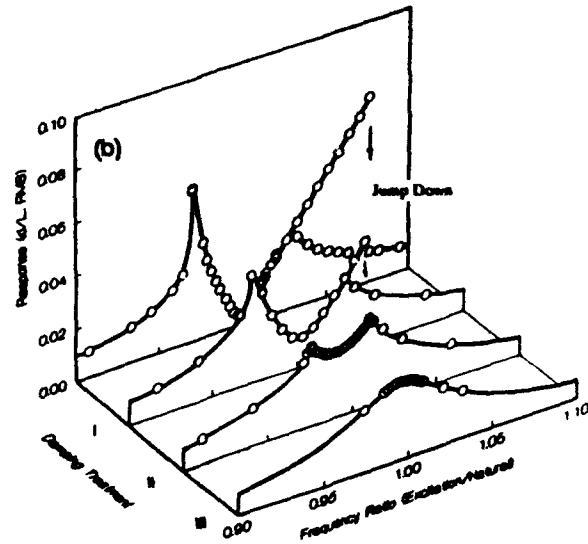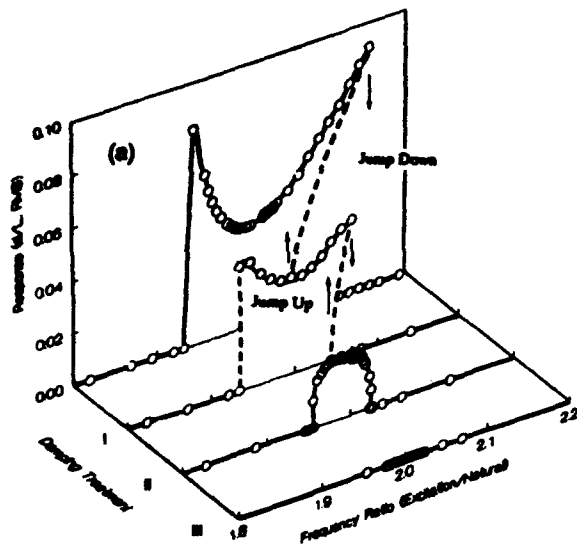
Figure 11. Frequency response of the 2DOF structure with +0.20% detuning (for no damping treatment) for a direct excitation to the second mode: (a) shows the first mode response and (b) shows the second mode response.
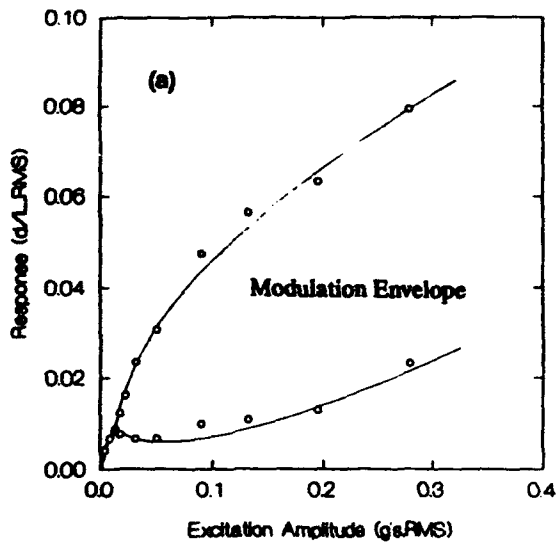
Figure 12. First mode amplitude response of the 2DOF structure with +0.20% detuning and no damping treatment for a direct excitation to the first mode at a frequency of 1.004. This frequency corresponds to the modulation region in Figure 10. The curves approximate the bounds on the modulation. The second mode amplitude is qualitatively similar.
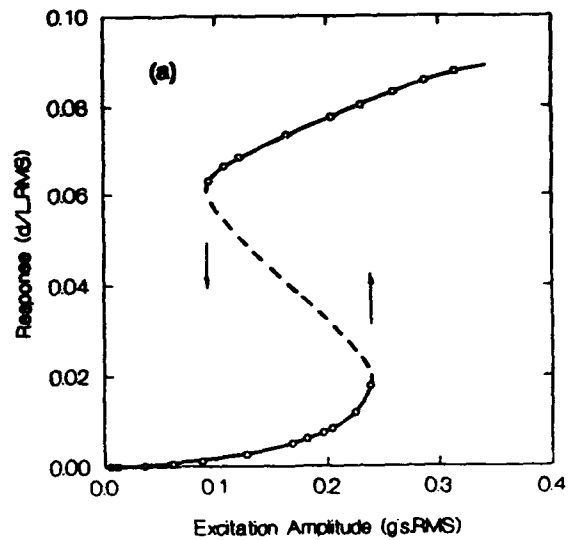
Figure 13. First mode amplitude response of the 2DOF structure with +0.20% detuning and no damping treatment for a direct excitation to the first mode at a frequency of 1.067. This frequency corresponds to the overhang region in Figure 10. The curves approximate the bounds on the modulation. The second mode amplitude is qualitatively similar.
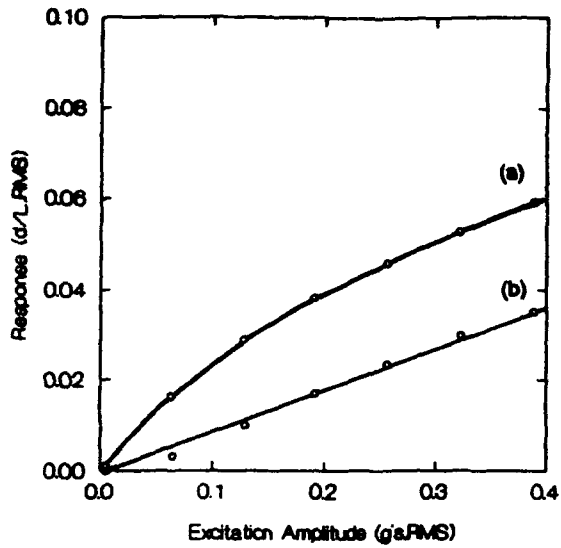
Figure 14. Amplitude of the response of the 2DOF structure with the +0.29% detuning for the highly damped case for a direct excitation to the first mode at a frequency of 0.979. This frequency corresponds to the resonance in Figure 10. The curves approximate the bounds on the modulation: (a) first mode, (b) second mode.
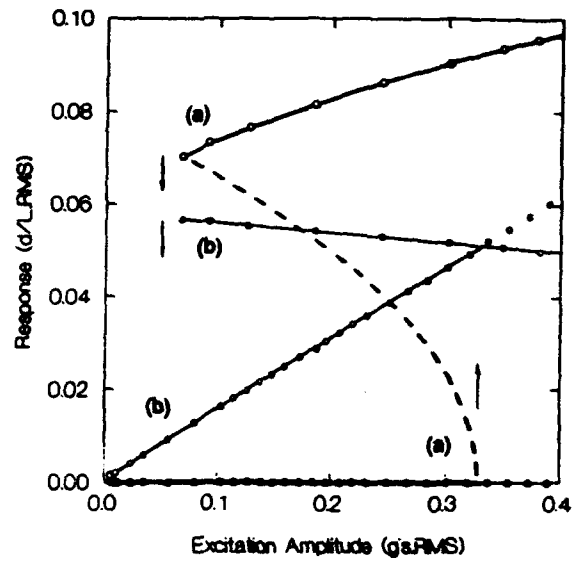
Figure 16. Amplitude response of the 2DOF structure with +0.20% internal resonance detuning for the case with no damping treatment for a direct excitation to the second mode at a frequency of 1.057. This frequency corresponds to the overhang region in Figure 11(b): (a) first mode, (b) second mode.
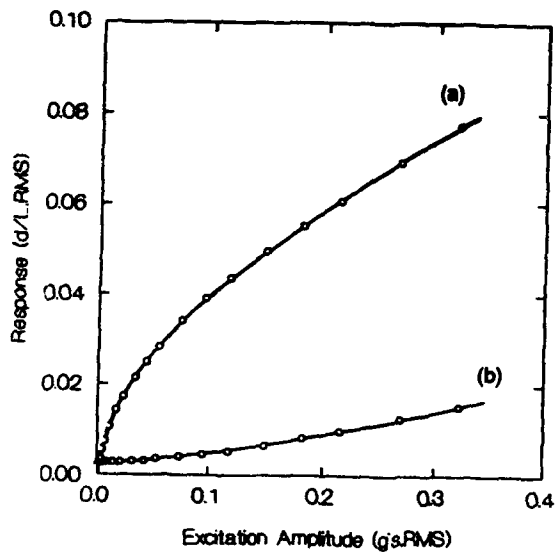
Figure 15. Amplitude response of the 2DOF structure with +0.20% internal resonance detuning for the case with no damping treatment for a direct excitation to the second mode at a frequency of 0.998. This frequency corresponds to the resonance region in Figure 11(b): (a) first mode, (b) second mode.
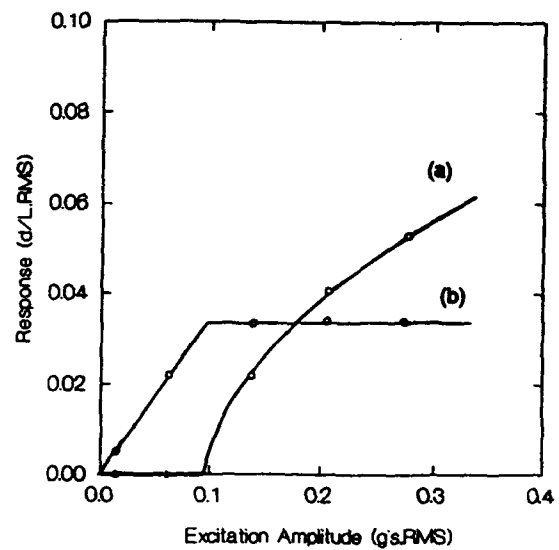
Figure 17. Amplitude response of the 2DOF structure with 0.29% internal resonance detuning for the highly damped case for a direct excitation to the second mode at a frequency of 0.992. This corresponds to the peak response in Figure 11: (a) first mode, (b) second mode.
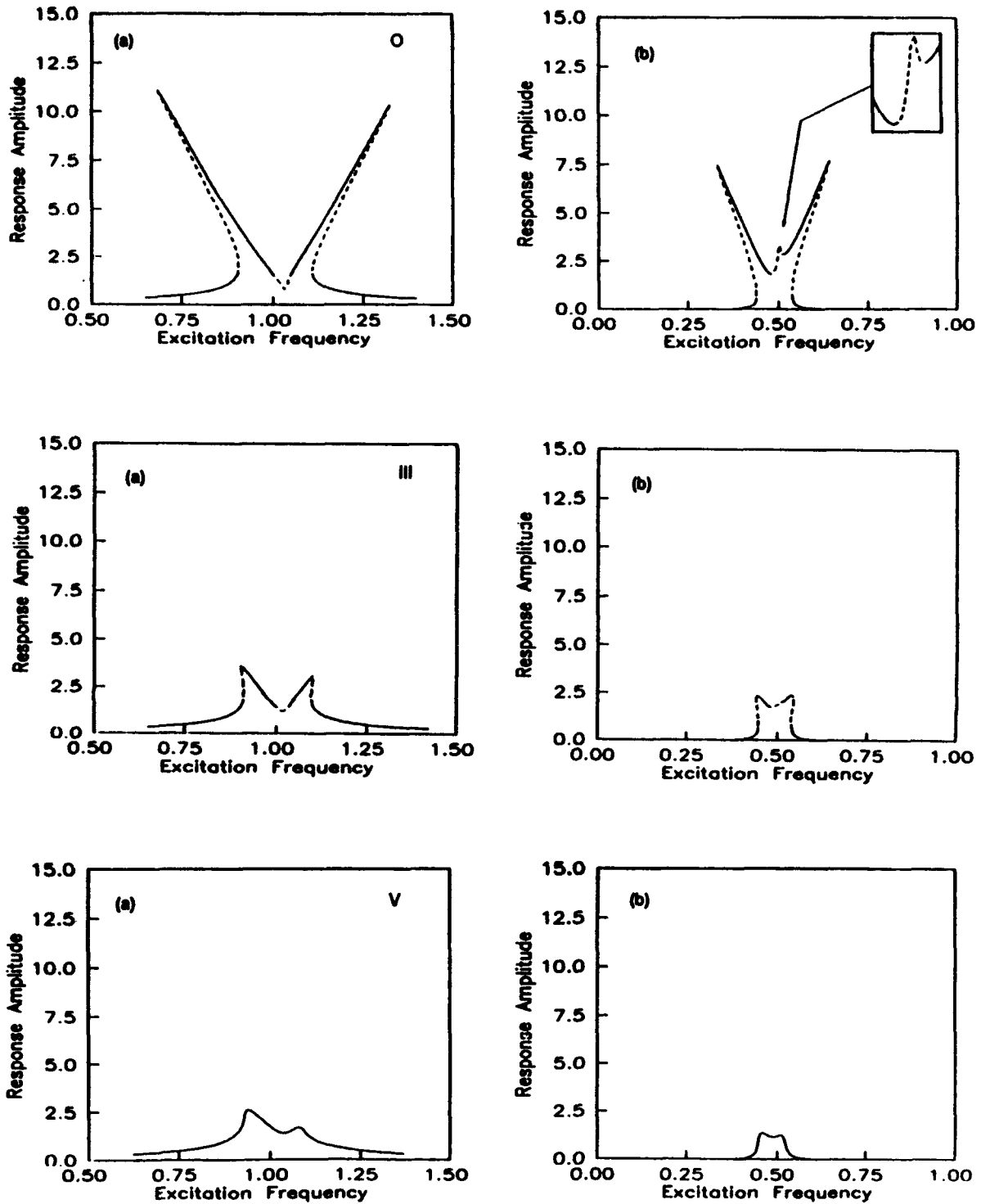
Figure 18. Theoretical frequency response for a direct excitation to the first mode of a slightly detuned structure for three different values of damping, corresponding to the undamped beam (no treatment applied), damping treatment III and damping treatment V: (a) first mode response, (b) second mode response.

Incorporating a Full Damping Matrix in the Transient Analyses of Nonlinear Structures

J. Michael Chapman*
Boeing Defense & Space Group†

Damping '93 Conference
February 24-26, 1993

Abstract

The common practice in the aerospace industry of diagonalizing the damping matrix to obtain approximate solutions for the transient response of large structures is in many cases inappropriate. While most aerospace structures are lightly damped and constructed from component structures having modal damping, the composite damping matrix constructed using the "triple matrix product" is usually not diagonally dominant. Here it is shown that large errors in the transient response will occur when two modes of the component structures have identical or nearly identical frequencies but different assigned modal damping.

This paper then gives an efficient numerical algorithm to include the full damping matrix in the transient response without calculating the complex eigenvalues and eigenvectors of the structure. The algorithm also permits the efficient calculation of any nonlinear forces by reducing the size of the nonlinear problem down to the number of nonlinear forces while eliminating repeated calculations involving the full damping matrix. The algorithm also uses a numerically attractive "differencing" technique to calculate the transient response thereby increasing the precision of the results. Finally, several criteria are presented to determine which off-diagonal terms in the damping matrix to retain. The performance of the integrator is then enhanced by using sparse matrix multiplies.

---

*Principal engineer, Boeing, M/S 8M-80, ph. (206) 773-1846
†PO Box 3999, Seattle, Wa. 98124-2499

1 Introduction

In the aerospace industry, transient analyses are generally performed to calculate the response and maximum expected loads for large multiple degree-of-freedom structures experiencing various dynamic environments such as liftoff, buffet, or main engine cutoff. These analyses are initiated by constructing dynamic models for all the sub-structures composing the total vehicle, and by specifying the forcing functions and equations of motion that apply to this system. The dynamic response is then determined by integrating these equations of motion for the composite vehicle.

The construction of the composite structural model from the component models is accomplished using modal synthesis techniques. The component models specify the mass, stiffness, and damping of each sub-structure. While the specification of the mass and stiffness of the component models is clearly defined and gives consistent results using a variety of modal synthesis techniques, inconsistent results have been obtained using the various techniques generally accepted in the industry for constructing the damping models. The purpose of this paper is to discuss and resolve some of the inconsistencies that arise when using these different damping models.

Damping is generally specified for the composite system model in either one of two ways. First and simplest, the modal damping for the system modes is specified directly. The equations of motion for the system model then has the form:

$$\ddot{Q} + 2\xi\omega\dot{Q} + \omega^2 Q = \phi^T F \tag{1.1}$$

where the modal damping ξ is specified for each mode directly according to the frequency of the mode.

The second most common method for generating the system damping matrix is to specify the damping for each of the component models and to use modal synthesis techniques to construct the composite damping matrix. This technique is usually referred to as the TMP (triple matrix product) method and the resulting system damping matrix is generally full. The equations of motion for the system model then has the form:

$$\ddot{Q} + D\dot{Q} + \omega^2 Q = \phi^T F \tag{1.2}$$

where the damping matrix D is constructed using:

$$D = \phi^T C \phi \tag{1.3}$$

and C contains the damping matrices for the component models.

The integration of the equations of motion in Eq. 1.2 generally requires the inclusion of all terms in the matrix D to obtain accurate results. An inexpensive method to do this *without* calculating the complex eigenvalues and eigenvectors of Eq. 1.2 is given in Section 3. The common practice of only using the diagonal of D to obtain

an approximate and inexpensive solution of Eq. 1.2 is useful in many situations but can lead to erroneous solutions when applied indiscriminately as demonstrated in the next section. A criterion specifying when the diagonalization procedure can be used is discussed in Section 4. Conclusions and summary are given in Section 6.

2 Erroneous Results Using the Diagonal of D for Identical Frequency Modes

Consider a two degree of freedom system having identical frequencies but arbitrary damping given by:

$$\begin{bmatrix} 1 & 0 \\ 0 & 1 \end{bmatrix} \begin{bmatrix} \ddot{x}_1 \\ \ddot{x}_2 \end{bmatrix} + \begin{bmatrix} 2\xi_1\omega & 0 \\ 0 & 2\xi_2\omega \end{bmatrix} \begin{bmatrix} \dot{x}_1 \\ \dot{x}_2 \end{bmatrix} + \begin{bmatrix} \omega^2 & 0 \\ 0 & \omega^2 \end{bmatrix} \begin{bmatrix} x_1 \\ x_2 \end{bmatrix} = \begin{bmatrix} 0 \\ 0 \end{bmatrix} \qquad (2.1)$$

The dependent variables x_1 and x_2 in Eq. 2.1 are uncoupled and the modal damping values ξ_1 and ξ_2 are arbitrary. The natural frequencies of both x_1 and x_2 are identical and equal to ω.

The exact solution to Eq. 2.1 is given by:

$$x_i(t) = X_i e^{-\xi_i\omega t} \cos(\sqrt{1 - \xi_i^2}\,\omega t + \varphi_i) \qquad (2.2)$$

where $i = (1,2)$ and X_i and φ_i are constants determined by the initial conditions.

Now apply an orthonormal transformation $x = \phi q$ to Eq. 2.1 to obtain:

$$\ddot{q} + 2\omega[\phi^T \xi \phi]\dot{q} + \omega^2 q = 0 \qquad (2.3)$$

where $\phi^T\phi = \phi\phi^T = I$ is the identity matrix and

$$x = \begin{bmatrix} x_1 \\ x_2 \end{bmatrix}, \quad q = \begin{bmatrix} q_1 \\ q_2 \end{bmatrix}, \text{ and } \quad \xi = \begin{bmatrix} \xi_1 & \\ & \xi_2 \end{bmatrix} \qquad (2.4)$$

In practice, the damping matrix obtained using the TMP method is generally coupled for identical frequency modes since the eigensolver when applied to the composite mass and stiffness matrices is only required to generate a set of eigenvectors that are orthonormal. The eigenvectors obtained for the repeated eigenvalues are linearly independent and made to be orthogonal using techniques such as Gram-Schmidt Orthonormalization. An infinite number of choices for the eigenvectors are possible and the choice made by the eigensolver will generally not diagonalize the damping matrix for those repeated eigenvalues. Eq. 2.3 is therefore representative of the normal case obtained from the eigensolver since the damping matrix is generally not considered in the process.

Let the orthonormal transformation ϕ be expressed in terms of an angular rotation θ so that:

$$\phi = \begin{bmatrix} \cos\theta & -\sin\theta \\ \sin\theta & \cos\theta \end{bmatrix} \tag{2.5}$$

The transformed matrix of modal damping coefficients can then be expressed as:

$$\phi^T \xi \phi = \begin{bmatrix} \xi_1 + \sin^2\theta\,(\xi_2 - \xi_1) & \cos\theta\sin\theta\,(\xi_2 - \xi_1) \\ (symmetric) & \xi_1 + \cos^2\theta\,(\xi_2 - \xi_1) \end{bmatrix} \tag{2.6}$$

The transformed matrix of damping coefficients $\phi^T \xi \phi$ is therefore diagonal for arbitrary θ only when $\xi_1 = \xi_2$.

Let η_1 and η_2 represent the diagonal terms in Eq. 2.6 and let $\tilde{q}$ represent the solution of Eq. 2.3 when the off-diagonal terms in Eq. 2.6 are ignored. The equation governing $\tilde{q}$ is then:

$$\ddot{\tilde{q}} + 2\eta\omega\dot{\tilde{q}} + \omega^2\tilde{q} = 0 \tag{2.7}$$

The exact solution of Eq. 2.7 is given by:

$$\tilde{q}_i(t) = e^{-\eta_i\omega t}\left\{ \tilde{q}_i(0)\cos(\sqrt{1-\eta_i^2}\,\omega t) + \frac{\dot{\tilde{q}}_i(0) + \eta_i\omega\tilde{q}_i(0)}{\omega\sqrt{1-\eta_i^2}}\sin(\sqrt{1-\eta_i^2}\,\omega t) \right\} \tag{2.8}$$

where $i = (1,2)$ and $\tilde{q}_i(0)$ and $\dot{\tilde{q}}_i(0)$ are constants determined by the initial conditions and are given by:

$$\tilde{q}(0) = \phi^T x(0) \quad \text{and} \quad \dot{\tilde{q}}(0) = \phi^T \dot{x}(0) \tag{2.9}$$

Construct diagonal matrices κ and σ using the terms:

$$\kappa_i = e^{-\eta_i\omega t}\left\{ \cos(\sqrt{1-\eta_i^2}\,\omega t) + \frac{\eta_i}{\sqrt{1-\eta_i^2}}\sin(\sqrt{1-\eta_i^2}\,\omega t) \right\} \tag{2.10}$$

and

$$\sigma_i = e^{-\eta_i\omega t}\frac{1}{\omega\sqrt{1-\eta_i^2}}\sin(\sqrt{1-\eta_i^2}\,\omega t) \tag{2.11}$$

Let $\tilde{x}$ represent the solution obtained for x when the off-diagonal terms in Eq. 2.6 are ignored. Then using $\tilde{x} = \phi\tilde{q}$ the solution for $\tilde{x}$ becomes:

$$\tilde{x} = \left[\phi\kappa\phi^T\right]x(0) + \left[\phi\sigma\phi^T\right]\dot{x}(0) \tag{2.12}$$

Using the orthonormal properties of ϕ, Eq. 2.12 can be re-expressed as:

$$\begin{bmatrix} \tilde{x}_1 \\ \tilde{x}_2 \end{bmatrix} = \begin{bmatrix} \kappa_1 + \sin^2\theta\,(\kappa_2 - \kappa_1) & -\sin\theta\cos\theta\,(\kappa_2 - \kappa_1) \\ (symmetric) & \kappa_2 - \sin^2\theta\,(\kappa_2 - \kappa_1) \end{bmatrix}\begin{bmatrix} x_1(0) \\ x_2(0) \end{bmatrix}$$
$$+ \begin{bmatrix} \sigma_1 + \sin^2\theta\,(\sigma_2 - \sigma_1) & -\sin\theta\cos\theta\,(\sigma_2 - \sigma_1) \\ (symmetric) & \sigma_2 - \sin^2\theta\,(\sigma_2 - \sigma_1) \end{bmatrix}\begin{bmatrix} \dot{x}_1(0) \\ \dot{x}_2(0) \end{bmatrix}$$

$$\tag{2.13}$$

This equation demonstrates that the solution for $\tilde{x}_1$ is strongly coupled to the initial conditions for $x_2(0)$ when $\eta_1 \neq \eta_2$ or equivalently when $\xi_1 \neq \xi_2$. This result clearly contradicts the exact solution given in Eq. 2.2. Moreover, since the initial conditions for $x_i(0)$ and $\dot{x}_i(0)$ are arbitrary, the solutions for $\tilde{x}(t)$ can differ dramatically for $t > 0$ from the exact solution for $x(t)$ as given in Eq. 2.2. Therefore, $\tilde{x}$ obtained by diagonalizing the equations of motion in Eq. 2.3 and given by Eq. 2.12 does not closely approximate the exact solution for $x(t)$ given in Eq. 2.2 when $\xi_1 \neq \xi_2$. This conclusion also follows for the nonhomogenious solutions of Eq. 2.3 as can be demonstrated by examining the transfer function.

The preferred method to solving Eq. 2.3 is simply to calculate an orthogonal transformation ϕ that will diagonalize the damping matrix. So instead of having a fully coupled set of equations to solve as in Eq. 2.3, uncoupled equations are obtained as in Eq. 2.1. The technique of diagonalizing the damping matrix obtained from the TMP procedure for general aerospace structures should therefore include provisions for modes having identical frequencies.

In this section it was shown that large off diagonal terms in the damping matrix will arise for identical frequency modes having different assigned modal damping when the modes are subjected to some arbitrary orthonormal transformation. This is also the case for modes having different modal frequencies, and it is reasonable to expect that these modes will also be strongly coupled. In section 4, criteria are given specifying when diagonalization can and cannot be used. In particular, it is shown that the off diagonal terms cannot be ignored for nearly identical frequency modes when the frequency separation is of the "same order of magnitude" as the off diagonal terms in the damping matrix. Since this is generally the case for most aerospace structures having a high modal frequency density and constructed from components having different modal damping schedules, an inexpensive numerical integration technique to determine the transient response for the these structures must be developed. The next section gives a numerically efficient algorithm that can be used to include all terms in the damping matrix for linear and nonlinear structures.

3   An Inexpensive Algorithm to Incorporate the Full Damping Matrix in the Transient Response

Techniques integrating Eq. 1.1 when the forcing function F is permitted to be a non-linear function of time t and the dependent variables $Q, \dot{Q}$, and $\ddot{Q}$ have been in use by the aerospace industry for some time [1, 2, 3, 4]. The integration algorithm used in [1, 2, 4] can be used to include all terms in the damping matrix D in Eq. 1.2 without an excessive increase in computation time. If n represents the number of modal coordinates in Eq. 1.2, the algorithm requires that an (n by n) matrix inverse

be performed prior to the integration, and $n^2 + O(n)$ multiplications at every time step. For comparison, the numerical solution of Eq. 1.2 using a fourth-order fixed step Runge-Kutta algorithm requires $O(4n^2)$ multiplications per time step as demonstrated in section 5. An improved version of the algorithm presented in [1, 2] will be presented here.

The exact solution of Eq. 1.1 when $F = F(t)$ is a prescribed function of time can be expressed as:

$$Q_i = e^{-\xi_i \omega_i t} \left\{ Q_i(0) \cos(\sqrt{1 - \xi_i^2}\omega_i t) + \frac{\dot{Q}_i(0) + \xi_i \omega_i Q_i(0)}{\omega_i \sqrt{1 - \xi_i^2}} \sin(\sqrt{1 - \xi_i^2}\omega_i t) \right\}$$

$$+ \frac{1}{\sqrt{1 - \xi_i^2}\omega_i} \int_0^t e^{-\xi_i \omega_i (t-\tau)} \sin\left(\sqrt{1 - \xi_i^2}\omega_i(t - \tau)\right) \mathcal{F}_i(t - \tau) d\tau \qquad (3.1)$$

Assume the force $\mathcal{F}$ varies linearly in time from time step t_1 to t_2. Then knowing all quantities at time t_1, the solution at time t_2 can be expressed as:

$$Q_i^{(2)} = a_i Q_i^{(1)} + b_i \dot{Q}_i^{(1)} + c_i \mathcal{F}_i^{(1)} + d_i \mathcal{F}_i^{(2)} \qquad (3.2)$$

$$\dot{Q}_i^{(2)} = \alpha_i Q_i^{(1)} + \beta_i \dot{Q}_i^{(1)} + \gamma_i \mathcal{F}_i^{(1)} + \sigma_i \mathcal{F}_i^{(2)} \qquad (3.3)$$

$$\ddot{Q}_i^{(2)} = \mathcal{F}_i^{(2)} - 2\xi_i \omega_i \dot{Q}_i^{(2)} - \omega_i^2 Q_i^{(2)} \qquad (3.4)$$

where $\mathcal{F} = \phi^T F$ and the vector coefficients $(a, b, c, d, \alpha, \beta, \gamma,$ and $\sigma)$ are defined in terms of ξ_i, ω_i and $\delta = t_2 - t_1$ and are given by:

$$a_i = e^{-\xi_i \omega_i \delta} \left(\frac{\xi_i}{\sqrt{1 - \xi_i^2}} \sin \tilde{\omega}_i \delta + \cos \tilde{\omega}_i \delta \right) \qquad (3.5)$$

$$b_i = e^{-\xi_i \omega_i \delta} \frac{\sin \tilde{\omega}_i \delta}{\tilde{\omega}_i} \qquad (3.6)$$

$$c_i = \frac{1 - a_i}{\omega_i^2} - d_i \qquad (3.7)$$

$$d_i = \frac{e^{-\xi_i \omega_i \delta}}{\delta \omega_i^3} \left(\frac{2\xi_i^2 - 1}{\sqrt{1 - \xi_i^2}} \sin \tilde{\omega}_i \delta + 2\xi_i \cos \tilde{\omega}_i \delta \right)$$

$$+ \frac{1}{\omega_i^2} - \frac{2\xi_i}{\delta \omega_i^3} \approx \frac{\delta^2}{6} + O(\delta^3) \qquad (3.8)$$

$$\alpha_i = -\omega_i^2 b_i \qquad (3.9)$$

$$\beta_i = a_i - 2\xi_i \omega_i b_i \qquad (3.10)$$

$$\gamma_i = b_i - \sigma_i \qquad (3.11)$$

$$\sigma_i = \frac{c_i + d_i}{\delta} = \frac{1 - a_i}{\omega_i^2 \delta} \approx \frac{\delta}{2} + O(\delta^2) \qquad (3.12)$$

$$\tilde{\omega}_i = \sqrt{1 - \xi_i^2}\, \omega_i \tag{3.13}$$

The Eqs. 3.2 to 3.4 can be cast into a superior form by calculating the differences in Q and $\dot{Q}$ from time t_1 to t_2. Doing so gives:

$$\Delta Q_i = \frac{1 - a_i}{\omega_i^2}\left(\tilde{Q}_i^{(1)} + 2\xi_i\omega_i\dot{Q}_i^{(1)}\right) + b_i\dot{Q}_i^{(1)} + d_i\Delta\mathcal{F}_i \tag{3.14}$$

$$\Delta\dot{Q}_i = b_i\tilde{Q}_i^{(1)} + (a_i - 1)\dot{Q}_i^{(1)} + \sigma_i\Delta\mathcal{F}_i \tag{3.15}$$

where Δ is an operator giving changes in the operand from t_1 to t_2, e.g., $\Delta\mathcal{F}_i = \mathcal{F}_i^{(2)} - \mathcal{F}_i^{(1)}$. Eqs. 3.14 and 3.15 are numerically attractive because the differences in large nearly identical quantities are not required in the evaluations of ΔQ and $\Delta\dot{Q}$. In contrast, Eqs. 3.2 and 3.3 do not have this advantage and a loss of precision can be expected for computer calculations using a finite number of decimals. Nevertheless, numerical studies performed on large aerospace structures (such as the Shuttle or the Titan vehicles) have shown acceptable agreement between the two methods for linear analyses using diagonal damping. Precision advantages for full damping and/or nonlinear problems remains to be demonstrated.

To apply Eqs. 3.14 and 3.15 to the solution of Eq. 1.2, identify the diagonal and off-diagonal terms of the damping matrix D as D_d and D_o, respectively, so that:

$$D = D_d + D_o \tag{3.16}$$

The modal damping values are then obtained using $2\xi_i\omega_i = [D_d]_{ii}$. The off-diagonal terms are carried over to the right hand side of Eq. 1.2 and are treated as a damping force prescribed by

$$\mathcal{F}^{(damp)} = -D_o\dot{Q} \tag{3.17}$$

Separately identify the applied, nonlinear, and damping force contributions to the generalized force so that

$$\mathcal{F} = \mathcal{F}^{(applied)} + \mathcal{F}^{(nonlinear)} + \mathcal{F}^{(damp)} \tag{3.18}$$

Substituting Eqs. 3.15 and 3.18 into Eq. 3.17 and solving for $\Delta\mathcal{F}^{(damp)}$ gives:

$$\Delta\mathcal{F}^{(damp)} = -\left[I + D_o\sigma\right]^{-1} D_o\left(\Delta\dot{Q}^{(applied)} + \sigma\Delta\mathcal{F}^{(nonlinear)}\right) \tag{3.19}$$

where

$$\Delta\dot{Q}^{(applied)} = b\tilde{Q}^{(1)} + (a - 1)\dot{Q}^{(1)} + \sigma\Delta\mathcal{F}^{(applied)} \tag{3.20}$$

As can be seen in Eq. 3.19, when $\mathcal{F}^{(nonlinear)} \equiv 0$, the only additional labor required to include the full damping matrix into the transient response as governed by Eq. 1.2 is to calculate the inverse of a matrix and to multiply this matrix times

a vector of known quantities at each time point. The matrix inverse needs only to be performed once, prior to actual integration. When the modal coupling is small, the inverse in Eq. 3.19 can be expanded into a Taylor series and $\Delta \mathcal{F}^{(damp)}$ can be determined using predictor-corrector algorithms. While these algorithms will work when the modal coupling is small, they will in general require more work to ensure convergence.

Now let the generalized force $\mathcal{F}$ have a nonlinear dependence on a small subset of displacements, velocities, and accelerations so that

$$\mathcal{F}^{(nonlinear)} = \phi_{nl}^T F_{nl}(t, x_d, \dot{x}_v, \ddot{x}_a) \tag{3.21}$$

where F_{nl} is permitted to be a nonlinear function of selected physical displacements x_d, velocities $\dot{x}_v$, and accelerations $\ddot{x}_a$ given by:

$$x_d = \phi_d Q + G_d^{(residual)} F_{nl} \tag{3.22}$$

$$\dot{x}_v = \phi_v \dot{Q} \tag{3.23}$$

$$\ddot{x}_a = \phi_a \ddot{Q} \tag{3.24}$$

where $G_d^{(residual)}$ is the residual flexibility at the x_d locations due to the nonlinear forces F_{nl} and is included within Eq. 3.22 to account for modal truncation effects.

The numerical algorithm given in Eqs. 3.14 and 3.15 will now be modified to permit an efficient calculation of the nonlinear forces and the modal transient response. Let

$$\Delta \mathcal{F}_{applied}^{(damp)} = -[I + D_o \sigma]^{-1} D_o \Delta \dot{Q}^{(applied)} \tag{3.25}$$

$$\Delta \mathcal{F}^{(nl)} = \tilde{\phi}_{nl}^T \Delta F_{nl} \tag{3.26}$$

$$\tilde{\phi}_{nl} \equiv \phi_{nl}[I + \sigma D_o]^{-1} \tag{3.27}$$

Eq. 3.19 can then be expressed in the form:

$$\Delta \mathcal{F}^{(damp)} + \Delta \mathcal{F}^{(nonlinear)} = \Delta \mathcal{F}_{applied}^{(damp)} + \Delta \mathcal{F}^{(nl)} \tag{3.28}$$

Substituting Eqs. 3.18 and 3.28 into Eqs. 3.14 and 3.15 and using Eq. 3.4 evaluated for times t_1 and t_2 then gives:

$$\Delta \mathcal{F} = \Delta \mathcal{F}^{(linear)} + \Delta \mathcal{F}^{(nl)} \tag{3.29}$$

$$\Delta Q = \Delta Q^{(linear)} + d \Delta \mathcal{F}^{(nl)} \tag{3.30}$$

$$\Delta \dot{Q} = \Delta \dot{Q}^{(linear)} + \sigma \Delta \mathcal{F}^{(nl)} \tag{3.31}$$

$$\Delta \ddot{Q} = \Delta \ddot{Q}^{(linear)} + \mathcal{L} \Delta \mathcal{F}^{(nl)} \tag{3.32}$$

where

$$\mathcal{L} \equiv \left[I - 2\xi \omega \sigma - \omega^2 d \right] \tag{3.33}$$

and

$$\Delta \mathcal{F}^{(linear)} \;=\; \Delta \mathcal{F}^{(applied)} + \Delta \mathcal{F}^{(damp)}_{applied} \tag{3.34}$$

$$\Delta Q^{(linear)} \;=\; \frac{1-a}{\omega^2}\left(\ddot{Q}^{(1)} + 2\xi\omega\dot{Q}^{(1)}\right) + b\dot{Q}^{(1)} + d\Delta\mathcal{F}^{(linear)} \tag{3.35}$$

$$\Delta \dot{Q}^{(linear)} \;=\; \Delta \dot{Q}^{(applied)} + \sigma\Delta\mathcal{F}^{(damp)}_{applied} \tag{3.36}$$

$$\Delta \ddot{Q}^{(linear)} \;=\; \Delta\mathcal{F}^{(linear)} - 2\xi\omega\Delta\dot{Q}^{(linear)} - \omega^2\Delta Q^{(linear)} \tag{3.37}$$

The modal responses at time t_2 can then be expressed as:

$$\mathcal{F}^{(2)} \;=\; \mathcal{F}^{(1)} + \Delta\mathcal{F} \;=\; \mathcal{F}^{(linear)} + \Delta\mathcal{F}^{(nl)} \tag{3.38}$$

$$Q^{(2)} \;=\; Q^{(1)} + \Delta Q \;=\; Q^{(linear)} + d\Delta\mathcal{F}^{(nl)} \tag{3.39}$$

$$\dot{Q}^{(2)} \;=\; \dot{Q}^{(1)} + \Delta\dot{Q} \;=\; \dot{Q}^{(linear)} + \sigma\Delta\mathcal{F}^{(nl)} \tag{3.40}$$

$$\ddot{Q}^{(2)} \;=\; \ddot{Q}^{(1)} + \Delta\ddot{Q} \;=\; \ddot{Q}^{(linear)} + \mathcal{L}\Delta\mathcal{F}^{(nl)} \tag{3.41}$$

$$\quad\;\; \mathcal{F}^{(2)} - 2\xi\omega\dot{Q}^{(2)} - \omega^2 Q^{(2)} \tag{3.42}$$

where

$$\mathcal{F}^{(linear)} \;=\; \mathcal{F}^{(1)} + \Delta\mathcal{F}^{(linear)} \tag{3.43}$$

$$Q^{(linear)} \;=\; Q^{(1)} + \Delta Q^{(linear)} \tag{3.44}$$

$$\dot{Q}^{(linear)} \;=\; \dot{Q}^{(1)} + \Delta\dot{Q}^{(linear)} \tag{3.45}$$

$$\ddot{Q}^{(linear)} \;=\; \ddot{Q}^{(1)} + \Delta\ddot{Q}^{(linear)} \tag{3.46}$$

$$\;=\; \mathcal{F}^{(linear)} - 2\xi\omega\dot{Q}^{(linear)} - \omega^2 Q^{(linear)} \tag{3.47}$$

The initial value for $\mathcal{F}^{(1)}$ is the initial value for $\mathcal{F}$ given by Eq. 3.18. Note that Eqs. 3.44 and 3.45 are numerically more efficient than Eqs. 3.2 and 3.3 since less multiplications per time step are required. Note also that the modal accelerations calculated using Eqs. 3.42 and 3.47 accommodates all numerical round off errors that may creep into the calculated responses, and therefore maintains numerical consistency at each time step between the modal displacements, velocities, and accelerations. Since the numerical algorithm given in Eqs. 3.38–3.47 explicitly calculates the accelerations using the modal stiffness and displacements, the technique will be referred to as a "stiffness" technique.

An alternative numerical algorithm using a "flexibility" technique is also possible. The algorithm is nearly identical to that given above except that numerical consistency is maintained by using:

$$Q^{(2)} = \frac{1}{\omega^2}\left(\mathcal{F}^{(2)} - 2\xi\omega\dot{Q}^{(2)} - \ddot{Q}^{(2)}\right) \tag{3.48}$$

for the flexible displacements where the accelerations are obtained using:

$$\ddot{Q}^{(2)} = \ddot{Q}^{(linear)} + \mathcal{L}\Delta\mathcal{F}^{(nl)} \tag{3.49}$$

and the linear accelerations are obtained by substituting Eq. 3.35 and 3.36 into Eq. 3.37 with the result:

$$\ddot{Q}^{(linear)} = (a - 2\xi\omega b)\dot{Q}^{(1)} - \omega^2 b Q^{(1)} + \mathcal{L}\Delta\mathcal{F}^{(linear)} \tag{3.50}$$

It is interesting to note that for linear problems this technique does not require the calculations of the displacements during the integration and that these may be determined during post processing or only for the data recovery times. However, the "flexibility" and the "stiffness" techniques have yielded essentially identical results when both are performed in double precision.

To determine the nonlinear forces specified in Equations 3.21–3.24, use Eqs. 3.38–3.47 to obtain the following expressions:

$$x_d = x_d^{(linear)} + G_d\Delta F_{nl} \tag{3.51}$$

$$\dot{x}_v = \dot{x}_v^{(linear)} + G_v\Delta F_{nl} \tag{3.52}$$

$$\ddot{x}_a = \ddot{x}_a^{(linear)} + G_a\Delta F_{nl} \tag{3.53}$$

$$\Delta F_{nl} = \Delta F_{nl}(t, x_d, \dot{x}_v, \ddot{x}_a) \tag{3.54}$$

where

$$x_d^{(linear)} = \phi_d Q^{(linear)} \tag{3.55}$$

$$\dot{x}_v^{(linear)} = \phi_v \dot{Q}^{(linear)} \tag{3.56}$$

$$\ddot{x}_a^{(linear)} = \phi_a \ddot{Q}^{(linear)} \tag{3.57}$$

and the matrices G_d, G_v and G_a are defined as

$$G_d = \phi_d d\tilde{\phi}_{nl}^T + G_d^{(residual)} \tag{3.58}$$

$$G_v = \phi_v \sigma \dot{\phi}_{nl}^T \tag{3.59}$$

$$G_a = \phi_a \mathcal{L}\tilde{\phi}_{nl}^T \tag{3.60}$$

The nonlinear forces ΔF_{nl} are determined by solving Eqs. 3.51–3.54. Note that these equations have only as many unknowns as there are nonlinear forces and that the terms $x_i^{(linear)}$ for $i = (d, v, a)$ are constants during the nonlinear solution. Many existing nonlinear solution techniques can be employed to solve these equations inexpensively.

Once the nonlinear forces have been determined, the modal responses are determined using Eqs. 3.38–3.41. Note that the only expensive operation in the algorithm

is the calculation of $\mathcal{F}_{applied}^{(damp)}$ in Eq. 3.25 and that this calculation is *not required* in the iterative nonlinear solution of Eqs. 3.51–3.54.

Various approximation techniques can be used to calculate $\mathcal{F}_{applied}^{(damp)}$ inexpensively when the modal coupling terms in $[D_o]_{ij}$ are small compared to $[D_d]_{ii}$. Given a representative maximum modal velocity $\dot{Q}^{(max)}$ selected elements in the symmetric matrix $H \equiv -[I + D_o\sigma]^{-1}D_o$ can be ignored and set to zero whenever

$$[D_o]_{ij}\dot{Q}_j^{(max)} \ll 2\xi_i\omega_i\dot{Q}_i^{(max)} \tag{3.61}$$

A sparse matrix multiply of H and $\Delta\dot{Q}$ can then be used in Eq. 3.25. More on this subject will be given in the next section.

4   Diagonalization of the Damping Matrix

In a recent paper by Ma and Hwang[5], approximate solutions to Eq. 1.2 for periodic excitation can be obtained by diagonalizing the damping matrix when the normalized damping matrix is strongly diagonally dominant; *i.e.* when

$$\frac{\sigma_i}{2\xi_i\omega_i} \ll 1, \text{ for all } i = 1, \cdots, n \tag{4.1}$$

where

$$\sigma_i = \sum_{\substack{k=1 \\ k \neq i}}^{n} | D_{ik} | \tag{4.2}$$

and D is the (n by n) damping matrix as defined in Eq. 1.3. Note that when the damping matrix is strongly diagonally dominant, that no additional criterion specifying adequate frequency separation between the modes is necessary. Moreover, the paper goes on to state that when the damping matrix is not diagonally dominant, then additional conditions on the modal damping values and frequency separation are needed to neglect the modal coupling for periodic or harmonic excitation.

While diagonal dominance is a sufficient condition to neglect the off diagonal terms for periodic excitation, the condition is overly restrictive for many transient analyses of aerospace structures. Examples include ignition and burnout events which are generally characterized by forcing functions that are nearly step functions. Since the transient response to these forcing functions is governed primarily by the initial conditions, less restrictive conditions to ignore the off diagonal terms of the damping matrix can be derived by examining the homogeneous response of Eq. 1.2 for lightly damped structures.

Using the perturbation technique of multiple time scales, Kevorkian and Cole give the homogeneous response to Eq. 1.2 for lightly damped structures [6]. The

results will be summarized here for convenience. The response for each mode $Q_i(t)$ is represented by a power series in ξ_i so that

$$Q_i(t) = Q_i^{(0)}(\tilde{t}_i, \tau_i) + \xi_i Q_i^{(1)}(\tilde{t}_i, \tau_i) + \xi_i^2 Q_i^{(2)}(\tilde{t}_i, \tau_i) + \cdots \qquad (4.3)$$

where

$$\tilde{t}_i \;=\; \xi_i \omega_i t \text{ is the "slow" time,} \qquad (4.4)$$

$$\tau_i \;=\; \omega_i t (1 + \xi_i^2 \mu_i + \cdots) \text{ is the "fast" time.} \qquad (4.5)$$

The formula for μ_i is given below. The elements D_{ik} are assumed to be $O(\xi_i)$ (order of ξ_i) for all k so that

$$D_{ik} = \xi_i d_{ik} \text{ and } d_{ik} \text{ is assumed } O(1). \qquad (4.6)$$

The solutions for $Q_i^{(0)}(\tilde{t}_i, \tau_i)$, $Q_i^{(1)}(\tilde{t}_i, \tau_i)$, and μ_i are given by

$$Q_i^{(0)}(\tilde{t}_i, \tau_i) \;=\; e^{-\tilde{t}_i} \left(A_i^{(0)} \cos \tau_i + B_i^{(0)} \sin \tau_i \right) \qquad (4.7)$$

$$Q_i^{(1)}(\tilde{t}_i, \tau_i) \;=\; e^{-\tilde{t}_i} \left(A_i^{(1)} \cos \tau_i + B_i^{(1)} \sin \tau_i \right)$$

$$+ \sum_{k=1, k \neq i}^{n} d_{ik} \frac{\omega_k}{\omega_i^2 - \omega_k^2} e^{-\tilde{t}_k} \left[A_k^{(0)} \sin \tau_k - B_k^{(0)} \cos \tau_k \right] \qquad (4.8)$$

$$\mu_i \;=\; \frac{1}{2} \sum_{k=1, k \neq i}^{n} \frac{d_{ik}^2}{\omega_i^2 - \omega_k^2} \qquad (4.9)$$

The constants $A_i^{(m)}$ and $B_i^{(m)}$ for all i and $m = 0, 1$ are determined from the initial conditions.

Some observations are worth noting. First, the solution response for $Q_i^{(0)}$ for $t < O(1/\xi_i)$ is obtained using only the diagonal elements of D. Second, the solution response for $Q_i^{(1)}$ is valid only when the quantity

$$d_{ik} \frac{\omega_k}{\omega_i^2 - \omega_k^2} \text{ is } O(1) \text{ or smaller.} \qquad (4.10)$$

And third, whenever $\omega_i = \omega_k$ the condition $D_{ik} = 0$ must be satisfied which is always possible by using an orthonormal transformation as discussed in Section 2.

Let $Q_i^{max} = \max |Q_i^{(0)}|$ for all $t > 0$. The perturbation solution to $Q_i(t)$ given above will then be valid whenever the following condition is satisfied.

$$\sum_{k=1, k \neq i}^{n} |D_{ik}| \frac{\omega_k}{|\omega_i^2 - \omega_k^2|} Q_k^{max} \ll Q_i^{max} \text{ , for all } i \qquad (4.11)$$

Eq. 4.11 provides a convenient test for demonstrating the adequacy or inadequacy of only using the diagonal of D to obtain a close approximation for the homogeneous solution to Eq. 1.2. Also, since the transient analysis of Eq. 1.2 at any time t can be considered the superposition of the homogeneous solution determined by the displacements and velocities at that time point and the particular solution with zero initial conditions, Eq. 4.11 must be satisfied for any transient analysis of Eq. 1.2 if the solution obtained using only the diagonal of the damping matrix is to be a close approximation to the solution obtained using all terms in the damping matrix.

Note that Eq. 4.11 is generally a much less stringent requirement for decoupling than Eq. 4.1. Qualitatively, Eq. 4.11 only requires $D = O(\xi)$ when the frequencies are adequately separated to obtain a $O(1)$ solution that has an error of only $O(\xi)$, whereas Eq. 4.1 requires $D = O(\xi^2)$ to permit a harmonic response that is $O(1/\xi)$ for selected modes while having an error that is $O(\xi)$ for all modes. Therefore, Eq. 4.11 may be satisfied permitting diagonalization of the damping matrix even when the damping matrix does not satisfy Eq. 3.61 or Eq. 4.1.

Note also in Eq. 4.11 that the inequality is violated for frequencies that are sufficiently close; i.e., whenever $D_{ik}/(\omega_i - \omega_k) = O(1)$. The approximate solution will therefore be invalid whenever $\omega_i - \omega_k = O(\xi_i)$ and $D_{ik} = O(\xi_i)$. Unfortunately, this is precisely the case for many structures analyzed in the aerospace industry.

Given that all off-diagonal terms in the damping matrix cannot generally be neglected, it would be desirable to determine which terms that must be retained. Then assuming that a substantial number of terms can be neglected, the transient response as determined by the numerical integrator in Section 3 can be made more efficient by using a sparse matrix multiply.

One criterion to determine which off-diagonal terms to neglect is given by Eq. 3.61 discussed in Section 3. A less restrictive criterion can be developed using Eq. 4.11; i.e., elements D_{ik} can be ignored whenever

$$|D_{ik}| \frac{2\omega_i\omega_k}{|\omega_i^2 - \omega_k^2|} Q_k^{max} \le 2\omega_i\xi_i Q_i^{max} \qquad (4.12)$$

Note that this expression requires D_{ik} to be only $O(\xi_i)$ when the frequencies are adequately separated, but requires D_{ik} to be $O(\xi_i^2)$ when $(\omega_i - \omega_k)/\omega_i = O(\xi_i)$. The assumed expansion for D_{ik} given in Eq. 4.6 is therefore violated for frequencies that are very close. The perturbation solution when the off-diagonal elements are $O(\xi_i^2)$ and the frequency differences are allowed to be $O(\xi_i)$ or smaller remains to be performed.

One other common technique to determine the insignificant terms in the damping matrix is to explicitly calculate the modal coupling that exists between the modes and to neglect those terms that have very small coupling. In [5] the modal coupling c_{ik} between any two modes i and k during sinusoidal excitation at frequency ω is

shown to be given by:

$$c_{ik} = \frac{j\omega D_{ik}}{\sqrt{\omega_i^2 - \omega^2 + j2\xi_i\omega_i\omega}\sqrt{\omega_k^2 - \omega^2 + j2\xi_k\omega_k\omega}} \tag{4.13}$$

where $j = \sqrt{-1}$. Notice that the maximum modal coupling in Eq. 4.13 will be at a frequency between ω_i and ω_k and will satisfy

$$|c_{ik}| \leq C_{ik} \equiv \frac{|D_{ik}|}{\sqrt{2\xi_i\omega_i}\sqrt{2\xi_k\omega_k}} \tag{4.14}$$

and that C_{ik} is unity along the diagonal. Note also that the larger the frequency separation between two modes, the smaller the ratio of $|c_{ik}|$ to C_{ik} and as a result the smaller the modal coupling. Using Eq. 4.13, this ratio can be shown to be $O(1)$ until the frequency separation becomes prohibitively large. The technique of ignoring elements in the damping matrix whenever the modal coupling is small can then be stated most simply as

$$C_{ik} \ll 1. \tag{4.15}$$

This condition thus requires C_{ik} to be $O(\xi_i)$ and is consequently more restrictive than Eq. 4.12. In [5] it is also shown that the modal coupling will always be small whenever the damping matrix is strongly diagonally dominant.

In conclusion, several criteria have been given to determine which terms in the damping matrix that must be retained. The criterion given by Eq. 4.12 is generally the least restrictive and only requires the off-diagonal elements to be $O(\xi)$ when the response of all the modes are of the same order of magnitude and the frequencies are adequately separated. This criterion is invalid, however, when the frequency differences of selected modes become close in value. Alternatively, the frequency independent criteria given by Eqs. 3.61 and 4.15 are also acceptable but generally require the off-diagonal elements to be $O(\xi^2)$ and are therefore more restrictive than necessary for modes having large frequency differences.

5   Results

Proof that the diagonalization of the damping matrix leads to erroneous results has now been demonstrated for both the Shuttle and Titan IV liftoff loads analyses. In both of these analyses the payload has 1% modal damping while the booster has modal damping generally greater than 1 percent. The Shuttle is generally assigned modal damping values of 1% and 2% for modes less than and greater than 10 Hz, respectively, while the Titan IV vehicle is generally assigned 1.5% modal damping for modes less than 14.5 Hz and increasing to 3% for modes greater than 20 Hz.

Exceptions to this Titan IV damping schedule are also given for slosh modes and the first three pitch and yaw bending modes with assigned modal damping values less than one percent.

Peak payload accelerations during a Shuttle liftoff carrying a TDRS spacecraft attached to an Inertial Upper Stage have been calculated both by diagonalizing the full damping matrix and by retaining all terms in the damping matrix. The result that the diagonalization approximation both over and under predicts the peak acceleration levels can be demonstrated by examining the peak lateral accelerations of a single TDRS antenna rib tip. The two lateral accelerations of 27.2 and 12.8 G's calculated using the diagonalization approximation change to 7.3 and 14.3 G's when all terms in the damping matrix are retained. Similar results are also demonstrated for all phases of flight of the Titan IV vehicle; *e.g*, a critical payload acceleration during the T=35 seconds buffet flight event changes from 40.0 to 2.9 G's when the transient response is calculated first with and then without the diagonalization approximation.

The above results for both the Shuttle and Titan IV vehicles clearly demonstrates that the diagonalization approximation grossly over and under predicts the peak acceleration levels of selected payload components and that all terms in the damping matrix must be accounted for. Efficient numerical integrators that can accommodate the full damping matrix are then desired.

The algorithm described in section 3 was coded in FORTRAN on a SGI IRIS workstation. The algorithm was validated by requiring the peak modal accelerations for a typical Titan IV flight event to converge *(as the step size is reduced)* to the results obtained using two different but highly precise integrators. The first validation integrator chosen was as a variable step 5th order Runge-Kutta-Fehlberg algorithm and the second was a 12th order Adam's predictor-corrector algorithm. Both had tight error control bounds to control the internal step size. In addition, to ascertain the relative efficiency of the algorithm proposed here, a fixed step 4th order Runge-Kutta integrator was also used.

The Titan IV buffet flight event at T=35 seconds was used in the validation and efficiency studies. The system model was cutoff at 40 Hz giving a model size of 202 modes. The prescribed buffet aero forces consisted of 30 seconds of data given every 5 milli-seconds. The data recovery step size was selected as 2.5 milli-seconds to ensure ten points of response data during the period of the highest frequency mode. Peak modal accelerations over the 30 seconds were obtained.

Results from the two validation integrators agreed to less than 0.05%. The integration times, however, were 3:09:01 (hrs:min:secs) for Adam's method and 42:00 (min:secs) for the 5th order Runge-Kutta algorithm. By contrast, the faster fixed step 4th order Runge-Kutta algorithm took 26:33 (13:27) using an integration step size of 1.25 (2.5) milli-seconds and had a maximum percentage error of 0.3% (5.1%). The modified closed form algorithm presented in section 3 had integration times of

13:30, 7:03, and 3:47 (min:secs) when the integration step size was selected as 0.625, 1.25, and 2.5 milli-seconds, respectively. The maximum percentage errors on any modal acceleration was likewise calculated as 0.1%, 0.6%, and 2.5%, respectively. These results clearly indicate not only that the new algorithm is approximately four times faster than the fixed step 4th order Runge-Kutta algorithm using the same step size, but also can achieve greater precision in less time. Similar results for nonlinear problems can also be expected.

6   Summary

The common practice in the aerospace industry of diagonalizing the damping matrix to obtain approximate solutions to Eq. 1.2 is in many cases inappropriate. While most aerospace structures are lightly damped and constructed from component structures having modal damping, the composite damping matrix constructed using the TMP (triple matrix product) is usually not diagonally dominant even though the modal coupling between any two modes is small. Moreover, structures having high modal coupling between modes having identical frequencies are frequently not re-orthogonalized to diagonalize the damping matrix for these modes. Many cases can be cited whereby the inappropriate diagonalization of the damping matrix led to large spurious loads and accelerations.

The proper course of action is, of course, to determine prior to the integration of the equations of motion, whether the damping matrix is strongly diagonally dominant. For the usual case when this is not so, inexpensive integration techniques can be used to determine the transient response without the need to calculate the complex eigenvalues and eigenvectors for the system. Furthermore, several criteria can be used to determine which off-diagonal terms in the damping matrix to retain, thereby permitting sparse matrix multiplies to be used to further enhance the performance of the integrator.

References

[1] J.M. Chapman, *A Friction Methodology for Space Shuttle/Payload Transient Loads Analyses,* Proceedings of the Shuttle Payload Dynamic Environments and Loads Prediction Workshop, Jan. 24-26, 1984, JPL D-1347, Vol. 2, pages 543-572.

[2] I-Min Yang and R.F. Hruda, *Transient Responses for Space Shuttle with Trunnion Friction,* Proceedings of the Shuttle Payload Dynamic Environments and Loads Prediction Workshop, Jan. 24-26, 1984, JPL D-1347, Vol 2, pages 573-579.

[3] E.E. Henkel, J.E. Misel, and D.H. Frederick, *A Methodology To Include Static and Kinetic Friction Effects In Space Shuttle Payload Transient Loads Analyses*, Proceedings of the Shuttle Payload Dynamic Environments and Loads Prediction Workshop, Jan. 24-26, 1984, JPL D-1347, Vol 2, pages 581-588.

[4] E.E. Henkel and R. Mar, *Improved Method for Calculating Booster to Launch Pad Interface Forces*, AIAA Journal of Spacecraft and Rockets, November-December 1988, Vol. 25, pp 433-438.

[5] F. Ma and J.H. Hwang, *Approximate Solutions of Nonclassically Damped Systems*, Computers in Engineering, Vol. 2, ASME 1991

[6] J. Kevorkian and J.D. Cole, *Perturbation Methods in Applied Mathematics*, Applied Mathematical Sciences, Vol. 34, Springer-Verlag New York Inc., 1985, pp. 212-217.

ANALYSIS OF DRY FRICTION HYSTERESIS IN CABLES UNDER UNIFORM BENDING

By Xiaolun Huang[1] and *Oleg Vinogradov*[2]

ABSTRACT: A cable is considered as a system of interacting wires with distributed dry friction forces at the interfaces. Deformations of the cable subjected to a uniform bending are analyzed. It is shown that there is a critical bending curvature when a slip between the wires starts. It starts in the neutral axis of the cross section of the cable and then spreads symmetrically over the cross section with the increase of bending. The effect of the interwire slippage on the cable stiffness is investigated. This model is also used to analyze a cable under the quasi-static cyclic bending. Explicit expression for the hysteretic losses per cycle of bending is derived. Numerical examples are given to show the influence of the interwire friction and helix angle on the bending stiffness and hysteretic losses in the cable.

---

[1] Research Associate, Department of Mechanical Engineering, The University of Calgary, Calgary, Alberta, Canada T2N 1N4.

[2] Professor, Department of Mechanical Engineering, University of Calgary, Calgary, Alberta, Canada T2N 1N4.

INTRODUCTION

Internal damping in vibrating cables has been of interest for a long time (Pipes, 1936; Yu, 1952; Claren and Diana, 1969; Luchansky, 1969; Hobbs and Raoof, 1984; Vinogradov and Pivovarov, 1986). Although it is clear that the interaction between the wires is the cause of energy losses and Sturm (1936) had postulated it long time ago, a precise mechanism of slippage in a deformed cable still remains unknown in many respects. One of the reasons is the difficulty of analyzing a complex structural system with internal degrees of freedom, which is due to the internal discontinuity of displacements at the interfaces in the presence of finite friction forces. Because of that, most researches analyzed two extreme cases of the cable model: either infinite-friction (solid bar model) or friction-free (loose wire model) (Hruska, 1951; Machida and Durelli, 1973; Costello and Phillips, 1976; Knapp, 1983). Neither of the models assumes internal structural losses. LeClair and Costello (1988) calculated the friction forces in a cable by assuming that each helical wire is deformed like a free spiral spring. But this approach cannot be applied to study the hysteretic behaviour of cables either.

Another approach, in which a multilayered cable is modelled by a system of coaxial orthotropic shells, has been developed by Hobbs and Raoof (1984), Blouin and Cardou (1989). This approach was also used by Raoof and Huang (1991) to analyze the damping in uniformly bent cables. But the model of coaxial shells does not include the twisting and bending deformations of wires in the cable.

An attempt to relate the internal friction to the damping properties of a cable was made by Vinogradov and Atatekin (1986). In their study, a cantilever cable was bent under a transverse load applied at the free end, and the interwire slip was assumed to occur due to the twisting of helical wires. Later they justified such an assumption in responding to the discussion by Sathikh and Pathasarathy (1988). In the paper by Lanteigne (1985), slippage was assumed to occur only between the layers in a bent cable. According to the recent theoretical paper by Ramsey (1988), twisting slippage was confirmed to be an inevitable mechanism of slippage in an uniformly deformed cable. Twisting strains were also used by Knapp (1983) as a criterion of occurrence of interwire slippage. More recently, an axially loaded cable in the presence of dry friction was studied by Vinogradov and Huang (1991). They considered the effect of the interwire slip on the macro-properties of the cable. This model was applied to investigate the hysteresis in a cyclically stretched cable (Huang and Vinogradov, 1992).

The objective of this paper is to analyze the friction hysteresis in cables subjected to uniform bending. The paper will study the origination and development of the interwire slippage in the uniformly bent cable and the slipping effect on the macro-properties of the cable. An approach employed here is based on Love's theory for thin rods. The mathematical model incorporates interwire friction and slippage into the existing cable mechanics. Numerical examples are used to show the friction effect on the cable stiffness and hysteresis.

CABLE MODEL

The fundamental structure that has most features of cable geometries is a single layered cable (see Fig.1). Such a basic model of a cable allows simplifying mathematical derivations without loosing the characteristic features associated with the slip and energy losses. The following assumptions are used in this study:

(1) Wires in the same layer are identical in geometrical and material properties.

(2) Cable is subjected to a uniform bending, and the deformations are assumed to be small so that only the elastic properties of the material are important.

(3) Constituent wires in the cable are treated as thin rods with the initial shape of a straight helix.

(4) The Poisson effect on changing transverse dimensions of the wires is neglected.

(5) Local contact deformations in wires are ignored.

(6) Cable is considered to be initially pre-stretched, and the interwire friction forces caused by the pretension are much larger than those induced by the fluctuating component of the bending.
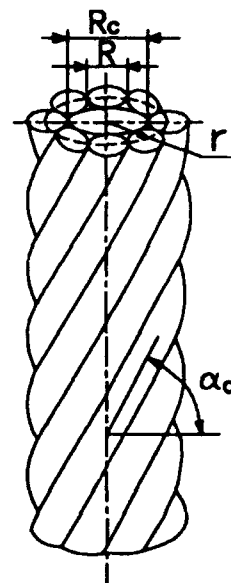
Figure 1 A six-wire cable.

A global system of Cartesian coordinates (x, y, z) is placed in the cable, with the z-axis coinciding with the cable axis and the bending is in the (y, z) plane. A local system of coordinates is introduced by a trihedron (t, n, b) moving along the centerline of the helical wire; the unit vectors of the trihedron are as follows: t is the tangent vector, n is the vector in the principal normal direction, and b equals to $t \times n$ and is called the binormal vector. The location of the wire's centerline in the cross section of the cable can be also determined in the polar coordinates (r, φ). The global and local coordinate system are shown in Fig.2.

When the bending of the cable is small that the interwire friction forces is sufficient enough to hold the wires together, the cable behaves like a solid beam. In such a case, the centerline of each wire can be described as a helix embedded in a torus. Then the curvatures in the principle normal and binormal directions of the helical wire, denoted by κ and κ', and the torsion, denoted by τ, are given by (Huang, 1992)
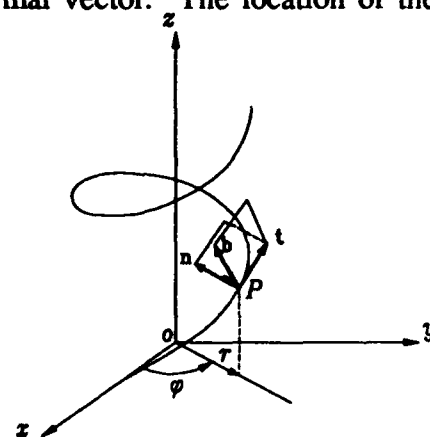
Figure 2 Coordinate systems for helix.

$$\kappa = -\frac{\sin\alpha_0 \cos^2\alpha_0}{\rho}\cos\varphi \qquad (1)$$

$$\kappa' = \frac{\cos^2\alpha_0}{r} + \frac{\sin^2\alpha_0}{\rho}\sin\varphi \qquad (2)$$

FCA-3

$$\tau = (\frac{1}{r} - \frac{\sin\varphi}{\rho}) \sin\alpha_0 \cos\alpha_0 \qquad (3)$$

where α_0 is the helix angle of the wire in initial configuration, r is the radius of the centerline of the wire as a helix, ρ is the bending radius of the cable, φ is the polar coordinate of the wire's center at the cross section of the cable.

When the bending is such that the dry friction forces between the wires cannot hold them together any more, a slip occurs. As a result, continuity of deformations in the slipping region would be violated. Also, once interwire slippage occurs, a wire will be bent and twisted around its own neutral axis, instead of around the cable axis when the cable behaves as a solid beam. In this situation, each wire, because of its dimensions, should be treated as a thin rod, and thus the cable is considered as a system of interacting helical thin wires.

It should be noted that due to the presence of dry friction at the interfaces between the wires, the helical wire may behave differently from a free spring. In general, the procedure of solving the problem can be outlined as follows:

(1)   For a given bending deformation of the cable, check if the interwire friction is sufficient to prevent any slippage between the wires.
(2)   If the friction forces are exceeded, a slip occurs. Then each wire in the slipping region of the cable is treated as a thin rod, and the internal loads and deformations in the wire are found from the equations of equilibrium.

Let us denote the components of the interwire force acting on the cross section of the wire by F_t, F_n and F_b and the components of the moments acting on the cross section by M_t, M_n and M_b. The components of the distributed force per unit length of the wire are p_t, p_n and p_b and the components of the distributed moment per unit length are m_t, m_n and m_b. If the tangential strain in the wire is denoted by ε_t, then the axial force of the wire is represented by

$$F_t = A\varepsilon_t \qquad (4)$$

where $A = E\pi R^2$. For small deformations, the components of internal moments acting on the cross section of the wire are related to τ, κ and κ' by

$$(a) \ M_t = \frac{B}{1+\nu} (\tau - \tau_0), \qquad (b) \ M_n = B(\kappa - \kappa_0), \qquad (c) \ M_b = B(\kappa' - \kappa_0'). \qquad (5)$$

where $B = E\pi R^4/4$, E is the Young's modulus of the wire material, R is the radius of the cross section of the wire, and the subscript "0" refers to the initial configuration.

Furthermore, considering the fact that there is no radial shear force in the cable's cross section when it is subjected to the axial loads, the shear force component in the principle normal direction of the wire, F_n, should be equal to zero. This fact was also noted by Costello (1990). When a cable is under pure and small bending, this shear component of the internal force in the wire is equal to zero, in both cases a cable behaves as a solid beam or as an assembly of free springs. Also, since the wire and core are in cross contact, the component of the distributed friction moment m_n should be equal to zero.

For small deformations of the cable, the difference between the deformed wire and undeformed one is so small that we may always take the undeformed state of the wire as our reference. Then the length of an infinitesimal element of the helical wire can be approximated by

$$ds \approx ds_0 = \frac{r d\phi}{\cos\alpha_0} \tag{6}$$

Note that F_t, M_t, M_n and M_b, can be expressed by Eqs.4 and 5 as functions of ϵ_t, τ, κ and κ'. Then substitution of the above relationships into the six equations of equilibrium (Love, 1944) give the following

$$A\frac{d\epsilon_t}{ds_0} + p_t = 0 \tag{7}$$

$$\kappa_0' F_t - \tau_0 F_b + p_n = 0 \tag{8}$$

$$\frac{dF_b}{ds_0} + p_b = 0 \tag{9}$$

$$\frac{1}{1+v}\frac{d\tau}{ds_0} - \kappa_0'\kappa + \frac{m_t}{B} = 0 \tag{10}$$

$$\frac{d\kappa}{ds_0} - \tau_0(\kappa'-\kappa_0') + \frac{\kappa_0'(\tau-\tau_0)}{1+v} - \frac{F_b}{B} = 0 \tag{11}$$

$$\frac{d\kappa'}{ds_0} + \tau_0\kappa + \frac{m_b}{B} = 0 \tag{12}$$

where τ_0, κ_0 and κ_0' are the torsion, curvatures in principle normal and binormal direction of the wire in the initial straight state, and are given by

$$\tau_0 = \frac{\sin 2\alpha_0}{2r}, \qquad \kappa_0 = 0, \qquad \kappa_0' = \frac{\cos^2\alpha_0}{r} \tag{13}$$

In most engineering applications cables are pre-stretched. Under small deformations, each outer wire remains in contact with the core, so that the centerline of the wire is always on the cylindrical surface with the radius $r=R_c+R$. From this observation, the expression for the binormal curvature, κ', may be shown to be the same as Eq.2 which is valid for any curve on the torus. In fact, comparison of Eq.2 for the helix on a torus to that for a free spring (Huang, 1992) shows that the expressions for the binormal curvature κ' in these two cases are very close for the helix angle α_0 is nearly equal to $90°$ (which is valid for most structural cables). Therefore, it is reasonable to approximate the binormal curvature κ' by Eq.2 for a helical wire in the cable for any friction conditions.

SLIPPING MECHANISM

In order to understand the mechanism of the interwire slippage in a bent cable with dry friction, it is helpful to examine the deformations of the wire in a friction-free cable.

From the condition of no-friction, the following external forces and moments on the helical wire vanish

$$p_t = p_b = m_t = m_n = m_b = 0 \tag{14}$$

Then from Eqs.2, 12 and 13, the curvature in the principle normal direction is found to be

$$\kappa = -\frac{\sin\alpha_0}{\rho}\cos\varphi \tag{15}$$

When the latter is substituted into Eq.10, the following is obtained

$$\frac{d\tau}{ds_0} = \frac{1+v}{r\rho}\sin\alpha_0\cos\varphi \tag{16}$$

Integration of this equation, subject to the boundary condition that $\tau=\tau_0$ at $\varphi=0$ (in the neutral axis of the cross section), leads to

$$\tau = \frac{\sin 2\alpha_0}{2r} - \frac{(1+v)\sin 2\alpha_0}{2\rho}\sin\varphi \tag{17}$$

Finally, when these expressions for κ', κ and τ from Eqs.2, 15 and 17 are substituted into Eq.11, it is found that

$$F_b = 0 \tag{18}$$

It is of interest to compare these results to those for the free spiral spring (Huang, 1992). As could be expected, they have similar forms. For the case that $v\cos^2\alpha_0 \ll 2$ which is satisfied for most structural cables, they are identical.

From Eqs.7 and 14 it follows that the tangential force component F_t should be constant, because its derivative with respect to the wire length is equal to zero. From the analogy between the wires in a friction-free cable under pure bending and the free spiral spring, it is found that

$$F_t = 0 \tag{19}$$

Now let us consider the possible modes of slipping in a friction-free cable. Slip is a discontinuity of displacements between the two surfaces in contact. According to the geometry of
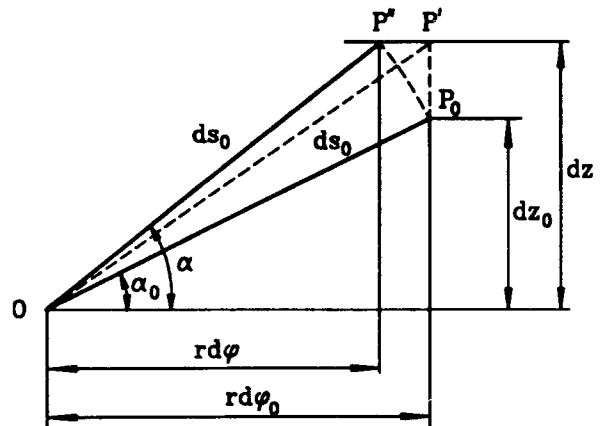
Figure 3 Displacement of the wire's centerline.

a developed helix shown in Fig.3, it is easy to obtain the following relationship between the tangential strain, ε_t, and the stain along the cable axis, ε_c, in the helical wire

$$\varepsilon_c = (1+\varepsilon_t)\frac{\sin\alpha}{\sin\alpha_0} - 1 \qquad (20)$$

Considering that the change of the helix angle before and after bending is small, the above can be linearized as follows

$$\varepsilon_c = \varepsilon_t + \frac{\Delta\alpha}{\tan\alpha_0} \qquad (21)$$

where $\Delta\alpha = \alpha - \alpha_0$. It follows from Eq.19 in a friction-free cable ε_t will be zero as well. Using Eq.15 and the boundary condition that $\alpha = \alpha_0$ at $\varphi = 0$, $\Delta\alpha$ can be found to be

Figure 4 Displacement of wire's centerline on the cylindrical surface.

$$\Delta\alpha = \int_0^{\varphi} -\kappa\frac{r d\varphi}{\cos\alpha_0} = \frac{r\tan\alpha_0}{\rho}\sin\varphi \qquad (22)$$

Then the strain ε_c in Eq.21 for the wire in a friction-free cable can be found to be

$$\varepsilon_c = \frac{r}{\rho}\sin\varphi \qquad (23)$$

which is exactly the same as when a cable is considered as a solid beam. It suggests that there is no slipping tendency between the wire and the core along the direction of cable axis.

On the other hand, when the cable is uniformly bent, the wire in the very top and bottom of the cross section of the cable will not move. However, the wires between these points could move. In Fig.4 the displacement is shown schematically. Fig.3 can help to understand how the wire on the upper part of the cable would move. Because there is no internal force in the helical wire, the length of the wire would not change ($OP_0 = OP''$); in order to incorporate the bending of the cable, therefore, the wire have to slip on the core's surface by increasing the helix angle (line OP' moves to OP''). As a result, the trace of the centerline of the wire would be like that being schematically shown in Fig.4. In addition, the twisting and bending deformations of the helical wires are also the source of slippage. It is known that a twisting deformation is always associated with the bending in a helical wire; in contrast, there is no twisting deformation in the core whose initial shape is a straight rod. Thus slipping tendency due to the twisting of the wire always exists in a deformed cable.

CRITICAL BENDING CURVATURE AND SLIPPING BOUNDARY

Bending of a cable without slipping

For some level of bending when slippage does not take place, the helical wire's centerline is simply a helix embedded on a torus. Consequently, the three geometrical parameters, κ, κ' and τ, can be described by Eqs.1, 2 and 3, respectively.

Recalling Eq.21, ε_t can be expressed as a function of ε_c and $\Delta\alpha$. For the wire described
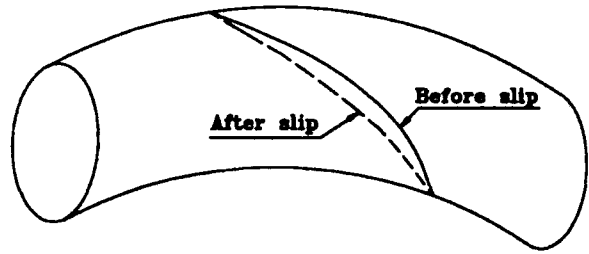
in a polar coordinate system in the cross section of the cable, the axial strain along the cable axis, ε_c, can be presented from the simple beam theory

$$\varepsilon_c = \frac{r}{\rho}\sin\varphi \tag{24}$$

which is the same as Eq.23 for the wire in a friction-free cable. Note that $\Delta\alpha$ can be found by integrating the equation $d\alpha/ds = -\kappa$ (Eq.1) subject to the boundary condition $\alpha = \alpha_0$ at $\varphi = 0$. The result is

$$\Delta\alpha = \int_0^{\bullet} -\kappa\frac{rd\varphi}{\cos\alpha_0} = \frac{r}{2\rho}\sin2\alpha_0\sin\varphi \tag{25}$$

Substitution of the above two formulas into Eq.21 yields

$$\varepsilon_t = \frac{r}{\rho}\sin^2\alpha_0\sin\varphi \tag{26}$$

Then, after substituting ε_t together with τ, κ and κ' into the equilibrium equations in Eqs.7-12, the following results for the external distributed forces and moments are found

$$p_t = -\frac{Ad\varepsilon_t}{ds} = -\frac{A\sin^2\alpha_0\cos\alpha_0}{\rho}\cos\varphi \tag{27}$$

$$p_n = \frac{\sin^2 2\alpha_0}{4r^2\rho}\left[\frac{B(\sin^2\alpha_0 - \nu\cos2\alpha_0)}{1+\nu} - Ar^2\right]\sin\varphi \tag{28}$$

$$p_b = \frac{B\sin\alpha_0\cos^2\alpha_0}{(1+\nu)r^2\rho}(\sin^2\alpha_0 - \nu\cos2\alpha_0)\cos\varphi \tag{29}$$

$$m_t = \frac{B\sin\alpha_0\cos^2\alpha_0}{r\rho(1+\nu)}(\sin^2\alpha_0 - \nu\cos^2\alpha_0)\cos\varphi \tag{30}$$

$$m_b = -\frac{B\sin^4\alpha_0\cos\alpha_0}{r\rho}\cos\varphi \tag{31}$$

Criterion of slippage

Since the wire is treated as a thin rod, the slippage is defined as the relative displacement of the wire's cross section with respect to its neighbouring wires and the core. Such a displacement becomes possible if on a surface of the wire, the traction force from all the external loads exceeds the resultant of the interwire friction forces. From Fig.5 we can present the condition causing an interwire slip by

$$q_f^2 \leq (p_t - \frac{m_b}{R})^2 + (p_b + \frac{m_t}{R})^2 \tag{32}$$

where q_f is the resultant distributed friction force.
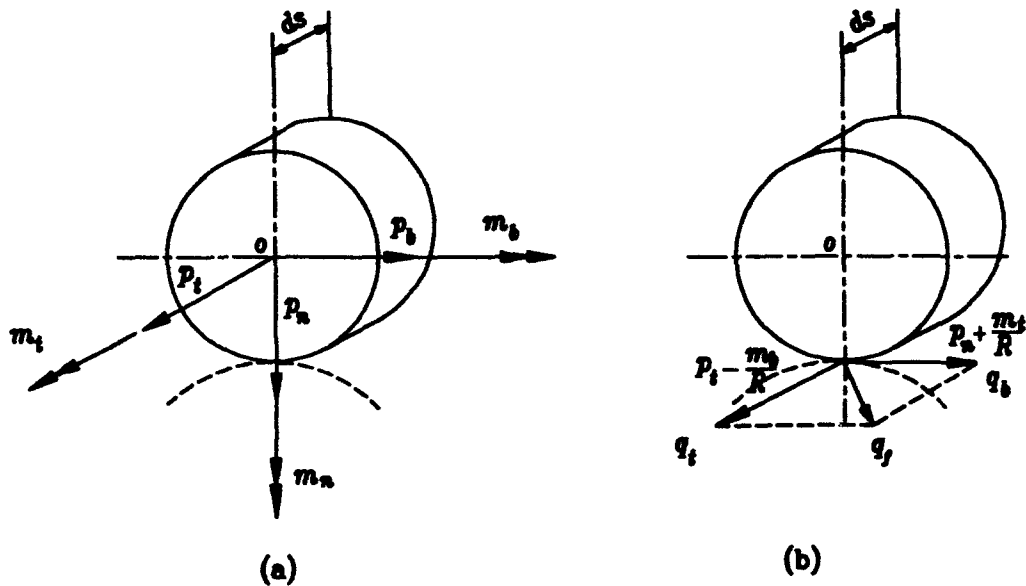
Figure 5 External loads acting on the wire. (a) force and moment components; (b) equivalent traction forces.

Critical bending radius and slipping boundary

From Eqs.27, 29-31, we can see that all the friction force components are in inverse proportion to the bending radius and is direct proportion to $\cos\varphi$. Therefore, for a given bending radius of the cable, ρ, the resultant friction force will achieve its maximum at $\varphi=0$. This result shows that the onset of slip is most will take place at the neutral plane in the bending cable.

After taking the equal sign in Eq.32, we can obtain the critical bending radius associated with the onset of slip from

$$q_f(\rho_c) = \sqrt{(p_t - \frac{m_b}{R})^2 + (p_b + \frac{m_t}{R})^2}$$

$_{,)}$

When the results in Eqs.27, 29-31 are substituted in Eq.33, it is found

$$\rho_\sigma = \frac{B\sin 2\alpha_0}{2rq_f}\sqrt{\sin^2\alpha_0 (\frac{rA}{B} - \frac{\sin^2\alpha_0}{R})^2 + \cos^2\alpha_0 (\frac{\sin^2\alpha_0 - v\cos^2\alpha_0}{R} + \frac{\sin^2\alpha_0 - v\cos 2\alpha_0}{r})^2}$$

(34)

As the bending increases, the slip spreads symmetrically from the neutral plane towards the top and bottom of the cross section of the cable. The slipping boundary can be determined from the consideration of equilibrium and compatibility of the internal loads (forces and moments) at the interface of the slipping and non-slipping regions. Obviously, from the concept of dry friction, the distributed friction forces and moments acting on the wire in the slipping region will be constant. We will identify the forces and moments acting on the wire's cross section by adding a bar over the notation.

Taking into account the symmetry of cable structure, only the first quarter part of the cross section of the cable, that is $\varphi \in [0, \pi/2]$, is necessary to analyze. Let us consider, for example, the tangential component of the internal force. Inside the slipping region, the corresponding distributed friction force p_t is found from Eq.27 by taking $\rho = \rho_c$ and $\cos\varphi = 1$. The result is

$$F_t = \int_0^\varphi -\bar{p}_t \frac{r d\varphi}{\cos\alpha_0} = \frac{A r \sin^2\alpha_0}{\rho_c} \varphi \tag{35}$$

At the slipping boundary, which is characterized by the polar angle φ_s on the cross section, the force component F_t should be equal to that of the wire in the non-slipping region given by Eq.27. Then it follows that

$$\frac{\varphi_s}{\rho_c} = \frac{\sin\varphi_s}{\rho} \tag{36}$$

Similar relationship can be also found from the equilibrium conditions for other components of internal forces and moments. In Fig.6 a scheme is shown for the slipping boundary φ_s as a function of the bending radius ρ. The slipping regions in the cross section of the cable are described by $[-\varphi_s, \varphi_s]$ and $[\pi-\varphi_s, \pi+\varphi_s]$, duo to the symmetry of the structure (see Fig.7).
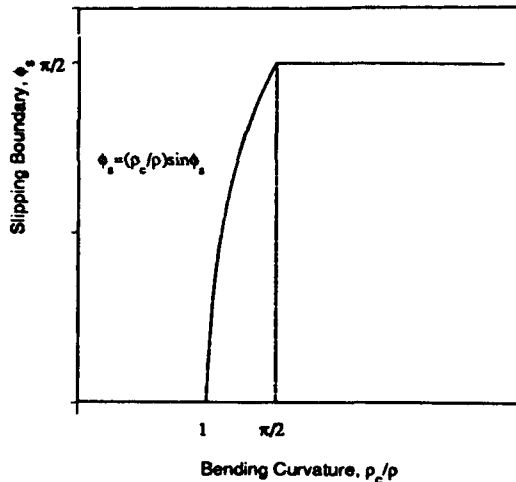
Figure 6 Slipping boundary as a function of the bending radius ρ.
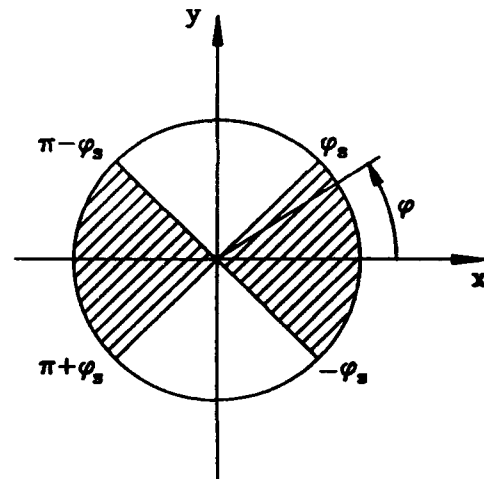
Figure 7 Slipping regions (hatched portions) in the cross section of the cable.

BENDING OF CABLE WITH FINITE FRICTION

In a cable, the friction forces are finite. So there is always some critical bending curvature $1/\rho_c$, below which slip does not occur, as discussed in the previous sections. When the bending increases above this level, an interwire slip will inevitably occur. In this case, the continuity conditions for displacements on the surfaces in contact will be violated.

In the following the equations of equilibrium are used to find the deformations of the wire, including the axial strain, torsion and bending curvatures of the wire, as well as the internal forces and moments in the cross section of the wire. The derivation will focus on the wire in the first quarter part of the cross section, and then the results are extended to the entire cross section.

Note that the distributed friction forces and moments for the wire in the slipping region have been found in Eqs.27, 29-31. Substitution of these results into Eqs.7-12 will lead to

$$\frac{d\overline{\epsilon}_t}{ds_0} = \frac{\sin^2\alpha_0\cos\alpha_0}{\rho_c} \tag{37}$$

$$\overline{P}_n = \tau_0\overline{F}_b - \kappa_0'\overline{F}_t \tag{38}$$

$$\frac{d\overline{F}_b}{ds_0} = -\frac{B\sin\alpha_0\cos^2\alpha_0}{(1+v)r^2\rho_c}(\sin^2\alpha_0 - v\cos2\alpha_0) \tag{39}$$

$$\frac{1}{1+v}\frac{d\overline{\tau}}{ds_0} - \kappa_0'\overline{\kappa} = -\frac{\sin\alpha_0\cos^2\alpha_0}{r\rho_c(1+v)}(\sin^2\alpha_0 - v\cos^2\alpha_0) \tag{40}$$

$$\frac{d\overline{\kappa}}{ds_0} - \tau_0(\overline{\kappa}' - \kappa_0') + \frac{\kappa_0'(\overline{\tau} - \tau_0)}{1+v} - \frac{\overline{F}_b}{B} = 0 \tag{41}$$

$$\frac{d\overline{\kappa}'}{ds_0} + \tau_0\overline{\kappa} = \frac{\sin^4\alpha_0\cos\alpha_0}{r\rho_c} \tag{42}$$

Recalling that $\overline{\epsilon}_t$ can be found from Eqs.21 and 23, we can rewrite Eq.37 as follows

$$\frac{\cos\alpha_0}{\rho}\cos\varphi + \frac{\overline{\kappa}}{\tan\alpha_0} = \frac{\sin^2\alpha_0\cos\alpha_0}{\rho_c} \tag{43}$$

from which $\overline{\kappa}$ is found to be

$$\overline{\kappa} = \frac{\sin^3\alpha_0}{\rho_c} - \frac{\sin\alpha_0}{\rho}\cos\varphi \tag{44}$$

Substituting the latter into Eq.42, we obtain

$$\frac{d\overline{\tau}}{ds_0} = -\frac{\sin\alpha_0\cos^2\alpha_0}{r\rho}[(1+v)\cos\varphi - v\frac{\rho}{\rho_c}] \tag{45}$$

from which $\bar{\tau}$ is found to be

$$\tau = \tau_0 - \frac{\sin 2\alpha_0}{2\rho}[(1+v)\sin\varphi - v\frac{\rho}{\rho_c}\varphi] \tag{46}$$

From Eqs.42 and 44, we can see that Eq.2 is still applicable for the binormal curvature of the wire in the slipping region, *i.e.*

$$\bar{\kappa'} = \kappa' = \kappa_0' + \frac{\sin^2\alpha_0}{\rho}\sin\varphi \tag{47}$$

The tangential force $\bar{F_t}$ has been derived in Eq.35. Another force component, $\bar{F_b}$, is easily found by integrating Eq.39. That is

$$\bar{F_b} = -\frac{B\sin\alpha_0\cos\alpha_0}{(1+v)r\rho_c}(\sin^2\alpha_0 - v\cos 2\alpha_0)\varphi \tag{48}$$

Now let us check the two bounds of the theoretical model of the cable. First, consider the case where the interwire friction is absent. In this extreme condition Eq.34 shows that the critical bending radius becomes infinite, which means that slip starts immediately when the cable is bent. Then Eq.44 yields, when $\rho_c \to \infty$,

$$\bar{\kappa} = -\frac{\sin\alpha_0}{\rho}\cos\varphi \tag{49}$$

Similarly, when $\rho_c \to \infty$, the torsion τ in Eq.46 is found to be

$$\bar{\tau} = \tau_0 - \frac{1+v}{2\rho}\sin 2\alpha_0\sin\varphi \tag{50}$$

These two equations are the same as Eqs.15 and 17 for the wire in a friction-free cable.

Alternatively, if the interwire friction is infinite, the slipping would never occur, no matter how severe the bending is. It means that the critical bending curvature is always as large as the given bending radius, *i.e.*, $1/\rho_c = \cos\varphi/\rho$ (see the derivation of Eq.33). Then Eqs.44 and 46 will be reduced to

$$\bar{\kappa} = -\frac{\sin\alpha_0\cos^2\alpha_0}{\rho}\cos\varphi \tag{51}$$

$$\bar{\tau} = (\frac{1}{r} - \frac{\sin\varphi}{\rho})\frac{\sin 2\alpha_0}{2} \tag{52}$$

which are the same as those in Eqs.1 and 3 for the helix fixed on a torus for the condition of an absolute friction.

The above results for a wire in the slipping region ($\varphi \in [0, \varphi_s]$ and $0 < \varphi_s < \pi/2$) can be easily extended to other parts of the cross section. As mentioned before, the slipping regions are symmetrical to the neutral axis and defined by $[-\varphi_s, \varphi_s]$ and $[\pi - \varphi_s, \pi + \varphi_s]$. Recalling Eq.27, we can see that the distributed friction force p_t takes opposite signs in two different parts of the cross section $\varphi \in (-\pi/2, \pi/2]$ and $\varphi \in (\pi/2, 3\pi/2]$. It implies that the friction force changes its direction

at these two regions. Therefore, the tangential force component F_t should be written in the form

$$\bar{F}_t = \begin{vmatrix} \dfrac{Ar\sin^2\alpha_0}{\rho_c}\varphi & -\dfrac{\pi}{2}<\varphi<\dfrac{\pi}{2} \\ \\ \dfrac{Ar\sin^2\alpha_0}{\rho_c}(\pi-\varphi) & \dfrac{\pi}{2}<\varphi<\dfrac{3\pi}{2} \end{vmatrix} \qquad (53)$$

Following the same approach, the other terms of the internal forces and moments can be found. From Eqs.29 and 39, it is obtained that

$$\bar{F}_b = \begin{vmatrix} -\dfrac{B\sin 2\alpha_0}{2(1+\nu)r\rho_c}(\sin^2\alpha_0-\nu\cos^2\alpha_0)\varphi & -\dfrac{\pi}{2}<\varphi<\dfrac{\pi}{2} \\ \\ -\dfrac{B\sin 2\alpha_0}{2(1+\nu)r\rho_c}(\sin^2\alpha_0-\nu\cos^2\alpha_0)(\pi-\varphi) & \dfrac{\pi}{2}<\varphi<\dfrac{3\pi}{2} \end{vmatrix} \qquad (54)$$

Similarly, the torsion $\bar{\tau}$ and normal curvature $\bar{\kappa}$ can be found, and then the corresponding components of the internal moment are equal to

$$\bar{M}_t = \begin{vmatrix} -\dfrac{B\sin 2\alpha_0}{2\rho}[(1+\nu)\sin\varphi-\nu\dfrac{\rho}{\rho_c}\varphi] & -\dfrac{\pi}{2}<\varphi<\dfrac{\pi}{2} \\ \\ -\dfrac{B\sin 2\alpha_0}{2\rho_c}[(1+\nu)\sin\varphi-\nu\dfrac{\rho}{\rho_c}(\pi-\varphi)] & \dfrac{\pi}{2}<\varphi<\dfrac{3\pi}{2} \end{vmatrix} \qquad (55)$$

$$\bar{M}_n = \begin{vmatrix} -\dfrac{B\sin\alpha_0}{\rho}(\cos\varphi-\dfrac{\rho}{\rho_c}\sin^2\alpha_0) & -\dfrac{\pi}{2}<\varphi<\dfrac{\pi}{2} \\ \\ -\dfrac{B\sin\alpha_0}{\rho}(\cos\varphi+\dfrac{\rho}{\rho_c}\sin^2\alpha_0) & \dfrac{\pi}{2}<\varphi<\dfrac{3\pi}{2} \end{vmatrix} \qquad (56)$$

One exception is the binormal component of the internal moment M_b. As shown in Eq.47, the expression for the binormal curvature κ' of the wire does not change in the slipping region, so that the corresponding component of the moment will remain the same as in the case of no slippage. That is

$$\bar{M}_b = M_b = \dfrac{B\sin^2\alpha_0}{\rho}\sin\varphi \qquad (57)$$

BENDING STIFFNESS OF CABLE

If no slip inside the cable takes place, then it behaves as a solid beam, and the corresponding bending stiffness is calculated as the sum of the inertia moments of all the wires in the cable's cross section. Note that for the wire wound around the core with large helix angle, its cross sectional area is nearly an ellipse. Taking this into account, the bending stiffness of the cable comprising n helical wires and a core can be represented by (see Fig.8)

$$EI_a = \frac{E_c \pi R_c^4}{4} + \sum_{i=1}^{n} EI_i \qquad (58)$$

where

$$EI_i = \frac{B}{2\sin^3\alpha_0}(1+\sin^2\alpha_0) + \frac{B}{2\sin\alpha_0\tan^2\alpha_0}\cos2\varphi_i + \frac{Ar^2}{\sin\alpha_0}\sin^2\varphi_i \qquad (59)$$

$$\varphi_i = \frac{2\pi}{n}(i-1) \qquad i=1, 2, \ldots n \qquad (60)$$

Since, for $n>2$,

$$\sum_{i=1}^{n}\cos2\varphi_i = 0, \qquad \sum_{i=1}^{n}\sin^2\varphi_i = \frac{n}{2} \qquad (61)$$

Eq.58 can be reduced to

$$EI_a = \frac{E_c \pi R_c^4}{4} + \frac{nB}{2\sin\alpha_0}\left(1+\frac{1}{\sin^2\alpha_0}+\frac{A}{B}r^2\right) \qquad (62)$$
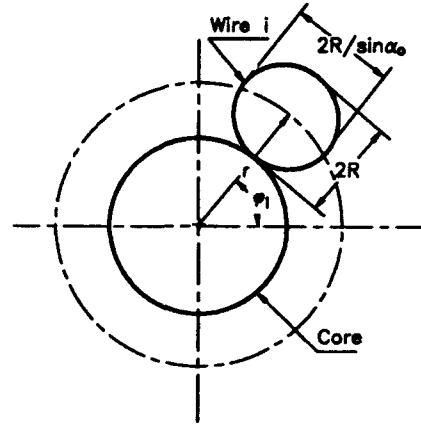
Figure 8 A cross section of the cable.

However, when bending exceeds the critical value and slip occurs, the bending stiffness of the cable will be different. In the slipping part of the cable, wires will deform individually and the cable can not be considered as a solid beam any more. If the ith wire is located in the slipping part of the cable, its contribution to the bending stiffness can be presented by

$$EI_i = M_i \rho \qquad (63)$$

where

$$M_i = (M_{bi}\sin\alpha_0 - M_{ti}\cos\alpha_0 + rP_{ti}\sin\alpha_0 + rP_{bi}\cos\alpha_0)\sin\varphi_i - M_{ni}\cos\varphi_i \qquad (64)$$

in which all the components of the internal force and moment in the wire's cross section have been given by Eqs.53-57.

Therefore, the bending stiffness may be in general written as

$$EI = \frac{E_c \pi R_c^4}{4\rho} + \sum_{\substack{i=1 \\ \varphi_i < \varphi_s}}^{n} EI_i + \sum_{\substack{i=1 \\ \varphi_i < \varphi_s}}^{n} EI_i \qquad (65)$$

When Eqs.59, 63 and 64 are substituted into Eq.65, the following is obtained

$$EI = EI_a - \sum_{\substack{i=1 \\ -\varphi_s \le \varphi_i \le \varphi_s \\ \pi-\varphi_s \le \varphi_i \le \pi+\varphi_s}}^{n} \frac{B}{\sin\alpha_0}\left[\frac{1}{2}+\frac{1}{2\sin^2\alpha_0}+(\frac{A}{B}r^2-\sin^2\alpha_0)\sin^2\varphi_i\right.$$

$$\left.-\sin^2\alpha_0\cos^2\varphi_i+\frac{\cos2\varphi_i}{2\tan^2\alpha_0}\right] + \frac{\rho}{\rho_c}\left(\sum_{\substack{i=1 \\ -\varphi_s\le\varphi_i\le\varphi_s}}^{n}(C\varphi_i\sin\varphi_i-B\sin^3\alpha_0\cos\varphi_i)\right.$$

$$\left.+\sum_{\substack{i=1 \\ \pi-\varphi_s\le\varphi_i\le\pi+\varphi_s}}^{n}[C(\pi-\varphi_i)\sin\varphi_i+B\sin^3\alpha_0\cos\varphi_i]\right) \quad (66)$$

where

$$C = B\sin\alpha_0(\frac{A}{B}r^2\sin^2\alpha_0-\nu\cos^2\alpha_0-\cos^2\alpha_0\sin^2\alpha_0+\frac{\nu}{1+\nu}\cos^4\alpha_0) \quad (67)$$

Obviously, as Eq.66 shows, the stiffness of a cable with the interwire slip would be a function of the bending curvature ρ.

Two extreme cases are of interest here: absolute and zero interwire friction conditions. When the interwire friction is absolute, it will prevent any slip and the cable will behave like a solid beam. Then Eq.66 gives an upper bound for the bending stiffness

$$EI = EI_a \qquad \text{for } \varphi_s=0 \quad (68)$$

On the other hand, if the cable is free of friction, it would behave as an assembly of helical springs. Such a condition can be described by $1/\rho_c=0$ and $\varphi_s=\pi/2$. Then Eq.66 will give the lower bound of the bending stiffness

$$EI_b = \frac{E_c\pi R_c^4}{4}+nB\sin\alpha_0 \quad (69)$$

The ratio $EI_b:EI_a$ depends on the cable structure. To get an impression of the magnitude of this ratio, let us consider a numerical example: a cable with a single layer of 6 wires around the core, i.e., $n=6$, $R_c=0.788$mm, $R=0.737$mm, $\alpha_0=70°$, $E=E_c=207$GPa, $\nu=0.25$ and $r=R+R_c$ for the wire-core touching situation. Using Eqs.62 and 69 we can find that $EI_b:EI_a$ is about 0.11. This shows that slippage would cause significant reduction in the bending stiffness.

In general, friction always exists in some degree, so that the stiffness given by Eq.66 lays between the two extremes. From Fig.6 it is found that, once a slip starts, it will easily spread over the entire cross section of the cable. When the slip occurs in the entire cable, the bending stiffness in Eq.66 yields, after using the results from Eq.61,

$$EI_s = EI_a -\frac{nB}{2\sin\alpha_0}\left[1+\frac{1}{\sin^2\alpha_0}+\frac{A}{B}r^2-2\sin^2\alpha_0\right) + \frac{\rho}{\rho_c}\mu \quad (70)$$

where

$$\mu = \sum_{\substack{i=1 \\ -\pi/2\le\varphi_i<\pi/2}}^{n}(C\varphi_i\sin\varphi_i-B\sin^3\alpha_0\cos\varphi_i)+\sum_{\substack{i=1 \\ \pi/2\le\varphi_i<3\pi/2}}^{n}[C(\pi-\varphi_i)\sin\varphi_i+B\sin^3\alpha_0\cos\varphi_i] \quad (71)$$

Taking into account Eqs.62 and 69, the above can be rewritten as

$$EI_a = EI_b + \frac{\rho}{\rho_c}\mu \qquad (72)$$

HYSTERESIS OF A CABLE UNDER CYCLIC BENDING

A symmetrically cyclic mode of bending deformations in cables is characterized by two phases: loading and unloading phases. In the last section, it was shown (Eqs.62 and 71) that the bending stiffness of a cable is constant for a non-slipping state and is a linear function of the bending radius for the slipping state. During the range of transition from a non-slipping state to fully slipping state, the relationship becomes non-linear (Eq.66). However, the transition range is usually short (see Fig.6).

As shown in Fig.9, the bending moment may be approximated as a piece-wise linear function. The turning point of the moment-curvature function, denoted by $1/\rho_e$, is determined from the condition that the moments for the two different states are equal and it can be found from Eqs.62 and 71

$$\frac{EI_a}{\rho_e} = \frac{EI_b}{\rho_e} + \frac{\mu}{\rho_c} \qquad (73)$$

It follows form the latter

$$\frac{1}{\rho_e} = \frac{\rho_c}{\mu}(EI_a - EI_b) \qquad (74)$$

$$EI_b = EI_a - \mu\frac{\rho_e}{\rho_c} \qquad (75)$$
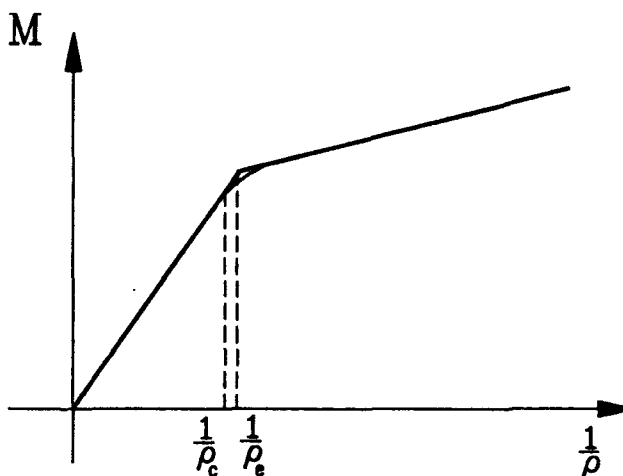
Figure 9 Approximation of the bending-curvature relation as a piece-wise linear function.

After this simplification, a bending moment-curvature relationship for the cable under cyclic bending can also be simplified as shown schematically in Fig.10.

The loading and unloading phases of the cycle comprise two stages: one without slip and the another with slipping. In the non-slipping stage of the loading phase, the bending moment is related to the curvature by

$$M_1 = -M^{max} + EI_a[\frac{1}{\rho} + (\frac{1}{\rho})^{max}], \qquad -(\frac{1}{\rho})^{max} \le \frac{1}{\rho} \le -(\frac{1}{\rho})^{max} + \frac{1}{\rho_e} \qquad (76)$$

In the slipping stage of the loading phase, the bending moment can be written as

$$M_1 = -M^{max} + EI_b[\frac{1}{\rho} + (\frac{1}{\rho})^{max}] + \frac{\mu}{\rho_c}, \qquad (\frac{1}{\rho})^{max} - \frac{1}{\rho_e} \le \frac{1}{\rho} \le (\frac{1}{\rho})^{max} \qquad (77)$$

Since $M_1 = M^{max}$ at $1/\rho = (1/\rho)^{max}$, it is found from Eq.77 that

$$M^{max} = EI_b(\frac{1}{\rho})^{max} + \frac{\mu}{2\rho_c} \tag{78}$$

Using Eq.78, Eqs.76 and 77 can be rewritten as

$$M_1 = \frac{\mu}{\rho_c}[\rho_e(\frac{1}{\rho})^{max} - \frac{1}{2}] + \frac{EI_a}{\rho}, \quad -(\frac{1}{\rho})^{max} \leq \frac{1}{\rho} \leq -(\frac{1}{\rho})^{max} + \frac{1}{\rho_e} \tag{79}$$

$$M_1 = \frac{EI_b}{\rho} + \frac{\mu}{2\rho_c}, \quad (\frac{1}{\rho})^{max} - \frac{1}{\rho_e} \leq \frac{1}{\rho} \leq (\frac{1}{\rho})^{max} \tag{80}$$

Similarly, the moment-curvature relationship for the cable in the unloading phase are found

$$M_2 = -\frac{\mu}{\rho_c}[\rho_e(\frac{1}{\rho})^{max} - \frac{1}{2}] + \frac{EI_a}{\rho}, \quad (\frac{1}{\rho})^{max} - \frac{1}{\rho_e} \leq \frac{1}{\rho} \leq (\frac{1}{\rho})^{max} \tag{81}$$

$$M_2 = \frac{EI_b}{\rho} - \frac{\mu}{2\rho_c}, \quad -(\frac{1}{\rho})^{max} \leq \frac{1}{\rho} \leq -(\frac{1}{\rho})^{max} + \frac{1}{\rho} \tag{82}$$

The energy dissipated per cycle of bending is defined by

$$W_f = \int_{-(1/\rho)^{max}}^{(1/\rho)^{max}} (M_1 - M_2) d(\frac{L}{\rho}) \tag{83}$$

where L is the length of the cable. After substituting Eqs.79-82 into Eq.83, it is found

$$W_f = L\frac{\mu}{\rho_c}[2(\frac{1}{\rho})^{max} - \frac{1}{\rho_e}] \tag{84}$$

which shows that, (a) a bending will cause energy dissipation if the amplitude of bending curvature exceeds the equivalent critical curvature $1/\rho_e$, and (b) the energy dissipation in a cable due to the interwire slippage is a linear function of the bending curvature. This is a typical characteristic of frictional damping.
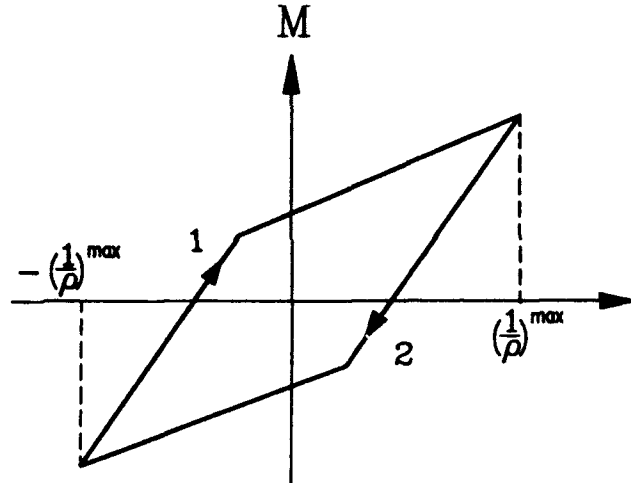
Figure 10 Moment-curvature relationships for the cable under cyclic bending.

NUMERICAL EXAMPLE

To compare the theoretical model to experimental results, a sample cable used by Yu (1952) in experiment is used. The specification is: $n=6$, $R_c=R=1.524$mm, $L=1.016$m, $E_c=E=200$GPa, $v=0.25$.

In Fig.11 the effect of the interwire friction on bending stiffness is shown. In this case, the bending curvature exceeds a critical value, slip occurs inside the cable and it leads to great reduction in stiffness. The transition, in terms of bending deformations, from the non-slipping to fully slipping state is relatively short, as shown by the rugged segments in the curves (note:

the horizontal axis is in logarithm scale). The bending moment-curvature relationships for the cable having various interwire friction forces and helix angles are shown in Figs.12 and 13. They are piece-wise linear functions, and the hysteresis loops are caused by the unloading and reloading phases. Fig.12 shows that, for a given bending curvature, the higher the friction, the larger the bending moment. However, as far as damping is concerned, the effect of friction is not monotonous. The areas enclosed by the hysteretic loops in Fig.12 represent the energy losses. It is clear from the picture that when the friction is too small or too large it could lead to reduction of energy dissipation. Similar effect of the helix angle can be found from Fig.13.

Comparison of the results from the present model with the experimental data by Yu (1952) is shown in Figs.14 to 16. When the interwire friction force is assumed to be 480N/m, the comparison between the results from the theoretical model and the experiment in relationships between the bending moment and

Figure 11 Stiffness-Curvature relationships for bending cables.

angular displacement (see Fig.14), the energy dissipation and angular displacement (see Fig.15), shows good agreement. Fig.16 also indicates a qualitative agreement between the theory and experiment.
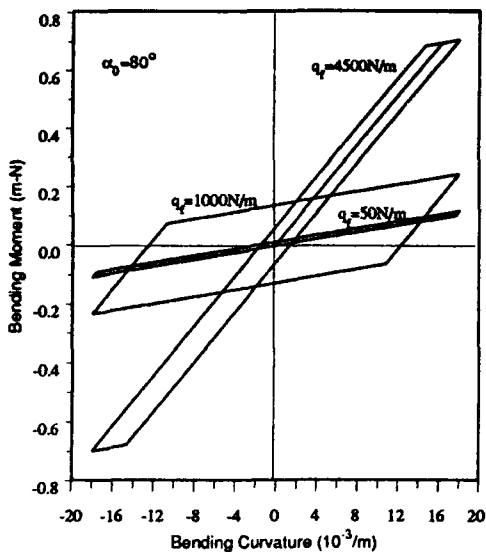
Figure 12 Moment-curvature relationship in bent cables with various friction forces.
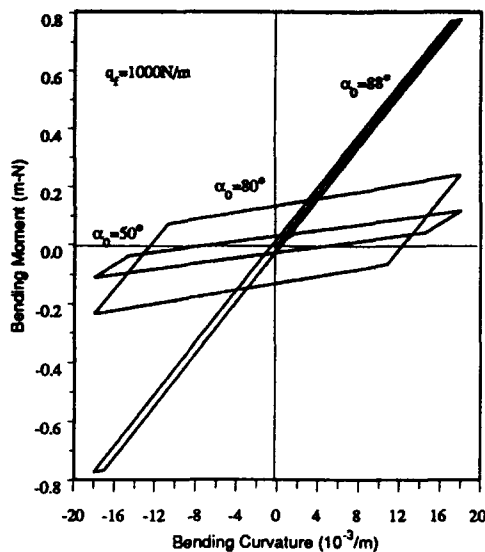
Figure 13 Moment-curvature relationship in bent cables with various helix angles.
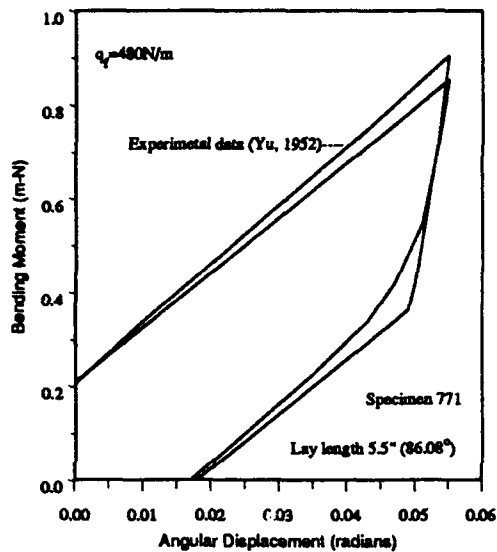
Figure 14 Comparison of moment-displacement relationship between theory and the experiment by Yu (1952).
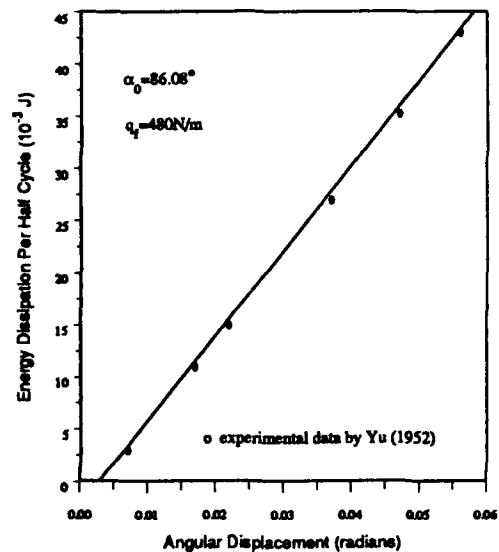
Figure 15 Comparison of energy dissipation from theory and the experiment (Yu, 1952).

CONCLUSIONS

A theoretical model of a cable which takes into account the interwire friction and slippage is developed. It allows analysis of the hysteretic behaviour in cables. It is found that there exists a critical bending curvature causing interwire slippage. A slip starts at the neutral axis and then spreads symmetrically over the entire cross section of the cable. As a result, hysteretic loops are formed in the moment-curvature chart of a cable under cyclic bending. The interwire slippage, slipping boundary, as well as its effect on the internal forces and deformations of the component wires, the reduction of bending stiffness and energy losses of the cable, are theoretically investigated. It is shown that the energy dissipation is linearly proportional to the deflection. Comparison of the model with the experimental results is very encouraging.

Figure 16 Comparison bending stiffness obtained from theory and the experiment by Yu (1952).

ACKNOWLEDGMENTS

REFERENCES

1. Blouin, F. and Cardou, A. (1989), "A study of helically reinforced cylinders under axial symmetric loads and application to strand mathematical modelling," *Int J Solids Structures*, 25(2),pp.189-200.
2. Claren, R. and Diana, G. (1969), "Mathematical analysis of transmission line vibration," *IEEE Transaction on Power Apparatus and Systems*, Vol.pas-88, No.12, pp.1741-1767.
3. Costello, G. A., and Phillips, J. W. (1976), "Effective modulus of twisted wire cables," *J of Eng Mech*, ASCE, 102, pp.171-181.
4. Costello, G. A.(1990), "Theory of Wire Rope," Springer-Verlag New York, Inc.
5. Hobbs, R. E., and Raoof, M. (1984), "Hysteresis in bridge strand," *Proc Inst Civ Engrs*, Part 2, 77, pp.445-464.
6. Hruska, F. H. (1951), "Calculations of stresses in wire rope," *Wire and Wire Products*, 26, pp.766-767, 799-801.
7. Huang, X. (1992), "Mechanics of Cables with Interwire Friction," Ph.D. dissertation, Dept. of Mech. Eng., the University of Calgary, Calgary, Canada.
8. Huang, X. and Vinogradov, O. (1992), "Interwire slip and its influence on the dynamic properties of tension cables," *2nd International Offshore and Polar Engineering Conference*, Paper No. ISOPE-92-T5-01, San Francisco, USA, June 14-19.
9. Lanteigne, J. (1985), "Theoretical estimation of the response of helically armored cables to tension, torsion and bending," *J of Applied Mechanics*, ASME, 52, pp.423-432.
10. LeClair, R. A., and Costello, G. A. (1988), "Axial, bending and torsional loading of strand with friction," *J of Offshore Mech and Arctic Engrg*, ASME, 110, pp.38-42.
11. Luchansky, M. (1969), "Axial stresses in armor wires of bent submarine cables," *J of Engineering for Industry*, ASME, 91, pp.687-693.
12. Knapp, R. H. (1983), "Simple bending models for helically armored cables," *Proc 2nd Int Off-shore Mech and Arctic Engrg*, New York, pp.360-364.
13. Machida, S., and Durelli, A. J. (1973), "Response of a strand to axial and torsional displacements," *J of Mech Eng Sci*, 15, pp.241-251.
14. Phillips, J. W., and Costello, G. A. (1973), "Contact stresses in twisted wire cables," *J of Eng Mech*, ASCE, 99, pp.331-341.
15. Ramsey, H. (1988), "A theory of thin rods with application to helical constituent wires in cables," *Int J Mech Sci*, 30(8), pp.559-570.
16. Raoof, M. and Huang, Y.P. (1991), "Upper-Bound prediction of cable damping under cyclic loading," *J of Eng Mech*, ASCE, 117, pp.2729-2747.
17. Sathikh, S., and Pathasarathy, N. S. (1988), Discussion on Ref.19, *J of Eng Mech*, ASCE, 114(4), pp.727-728.
18. Sturm, R. G. (1936), "Vibration of cables and dampers-I," *AIEE Transactions*, 55, pp.455-465.
19. Vinogradov, O. G., and Atatekin, I. S. (1986), "Internal friction due to twist in bent cable," *J of Eng Mech*, ASCE, 112(9), pp.859-873.
20. Vinogradov, O. and Huang, X. (1991), "Dry friction losses in axially loaded cables," Report #462, Dept. of Mechanical Engineering, University of Calgary, Calgary, Canada.
21. Vinogradov, O. and Pivovarov, I. (1986), "Vibration of A system with non-linear hysteresis," *J of Sound and Vibration*, Vol.111(1), pp.145-152.
22. Yu, A. (1952), "Vibration damping of stranded cable," *Proc Soc Exp Stress Analysis*, 9, 141-158.

ON THE LINEARIZATION OF STRUCTURES CONTAINING LINEAR-FRICTION DISSIPATING DEVICES

Jose A. Inaudi[*]

Earthquake Engineering Research Center, University of California at Berkeley

James M. Kelly

Earthquake Engineering Research Center, University of California at Berkeley

ABSTRACT

This paper deals with the response of structures containing linear-friction energy dissipating devices (EDD). This type of EDD exhibit triangular hysteresis loops when loaded cyclically, dissipating energy proportionally to the square of the deformation amplitude and independently of the deformation frequency. The free-vibration response of single-degree-of-freedom structures with linear-friction elements is studied. Two linearization techniques are applied to estimate the response of structures with linear-friction elements to harmonic and broad-band excitation: the harmonic linearization method, and a linearization based on a linear hysteretic element. Both linearizations show excellent accuracy.

EERC, 1301 South 46th Street, Richmond, CA 94804; Tel.: (510) 231-9519.

INTRODUCTION

Several energy dissipating devices (EDD) show triangular hysteresis loops when loaded cyclically. The energy dissipation per cycle in these devices is quadratic in the deformation amplitude and independent of the frequency of the deformation. Such type of hysteretic behavior is encountered, for example, in the Energy Dissipating Restraint (EDR) proposed by Richter et al. (1990). This passive device, based on a friction mechanism, has been proposed to provide damping in structures with the aim of reducing earthquake induced vibrations. The EDR can be configured to provide a piece-wise linear force-deformation relation with stiffness vK in the loading stroke, and stiffness $1/v\ K$ in the unloading stroke, where K the stiffness of the spring contained in the device, and $v\ (> 1)$ is a parameter that depends on the configuration of the EDR (Richter et al., 1990). Inaudi and Kelly (1992) have recently proposed a hysteretic mass damper in which a friction damper device acting transversely to the direction of the motion of the mass damper provides the energy dissipation mechanism. The mechanical behavior of this frictional system can be approximated by the following memoryless force-deformation relation:

$$f(\Delta, \dot{\Delta}) = K_h\ \Delta(t)\ sgn(\Delta(t)\dot{\Delta}(t)) \tag{1}$$

where f represents the force in the mechanical device, Δ represents the deformation in the EDD; the constant K_h is given by $K_h = 2\ T/L$, where T is the capacity of the frictional device, and L is the length of the the rods where the frictional devices are embedded.

Reid (1956) has suggested the use of this piece-wise linear relation (Eq. (1)) for the constitutive relation of materials presenting hysteresis energy loss per cycle proportional to the square of the strain amplitude and independent of the frequency. Caughey and Vijayaraghavan (1970, 1977) have studied the free-vibration response and the response to sinusoidal excitation of structures with nonlinear elements that satisfy the memoryless relationship described by Eq. (1). This nonlinear model was given the name of Reid's model (Caughey et al., 1970).

In certain occasions the EDD with triangular hysteresis exhibits memory: the element presents a finite stiffness in the transition between loading and unloading. This occurs, for example, due to finite stiffness of the connections of the mechanical device to the structure. A hysteresis loop of a linear-friction element with memory is shown in Figure 1. In the figure K_1 represents the stiffness in loading ($\Delta\dot{\Delta} > 0$) (State 1), K_2 is the stiffness in unloading (State 2), and K_3 is the tangent stiffness of the transition between loading and unloading (from State 1 to State 2 or vice versa). When unloading occurs ($\Delta\dot{\Delta} < 0$) at a certain deformation Δ_l, the tangent stiffness of the element is finite and given by K_3 (State 3). If the deformation reaches Δ_u the tangent stiffness changes to K_2 (State 2). The memory of the element affects the force-deformation relationship when the deformation Δ satisfies

$$\Delta_l(t) < \Delta(t) < \Delta_u(t) \tag{2}$$

where Δ_l is the previous unloading deformation, and Δ_u satisfies

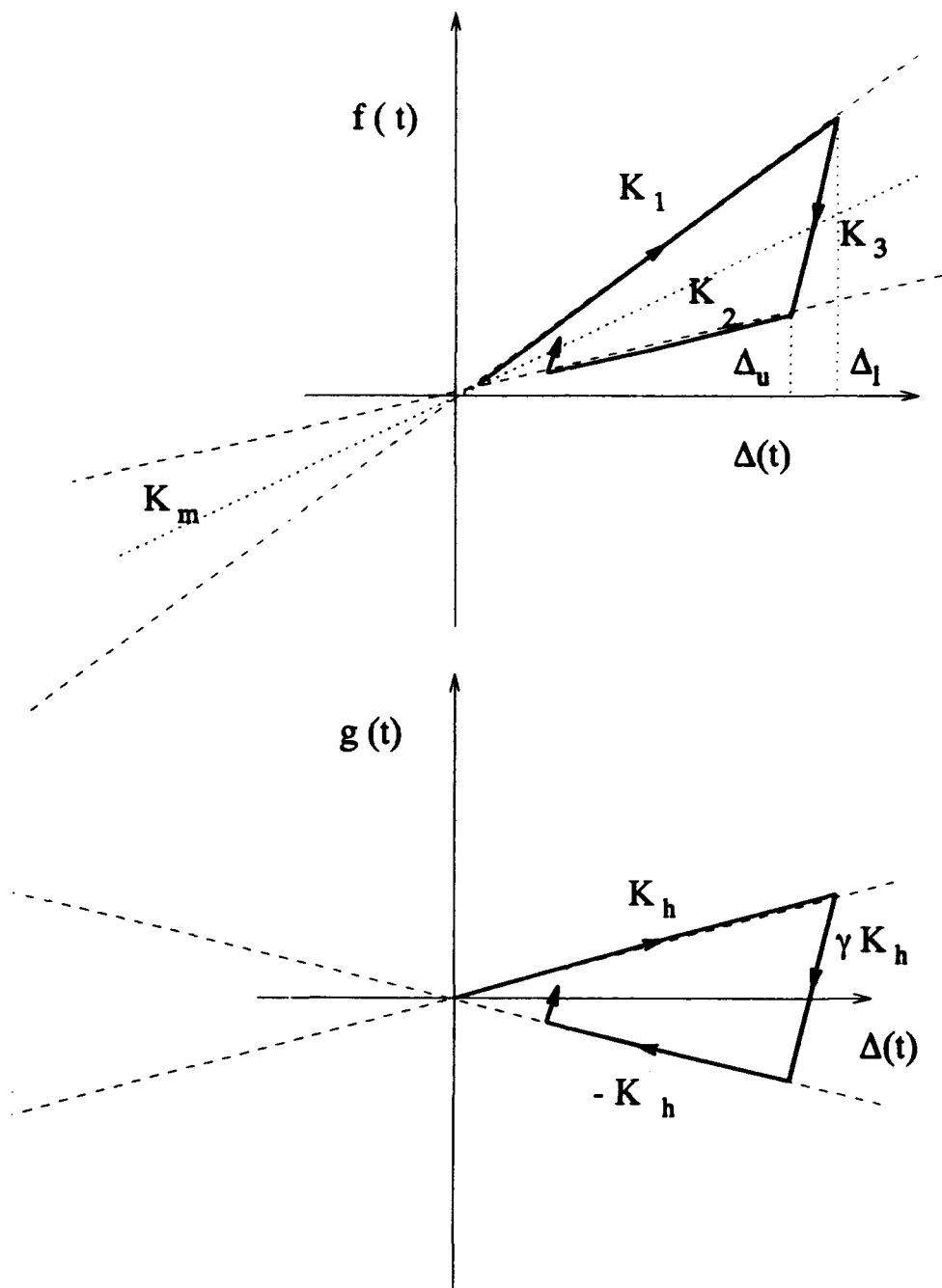$$\frac{\Delta_u}{\Delta_l} = \frac{K_3 - K_1}{K_3 - K_2} \tag{3}$$

Figure 1. Force-deformation relation of a linear-friction EDD with memory.

Similarly, when loading starts at a deformation Δ_u, the tangent stiffness of the element is K_3 (State 3) provided the deformation satisfies Eq. (2) with Δ_l satisfying Eq. (3). If the deformation reaches Δ_l in the loading process, the tangent stiffness changes to K_1 (State 1). This memory transforms the mechanical element into a dynamic element in which past deformations affect the force-deformation relationship of the element. Clearly the memory of the element "decreases" with an increase in the ratios K_3/K_1 and K_3/K_2. For dissipativeness we require $K_2 < K_1 < K_3$.

The force in a linear-friction element with memory can then be represented by

$$f(\Delta, z, l) = \begin{cases} K_1 \Delta(t) & \text{if } l(t) = 1 \text{, and } |\Delta(t)| > \Delta_l(t) \\ K_2 \Delta_u(t) + K_3 (\Delta(t) - \Delta_u(t)) & \text{if } l(t) = 1 \text{ and } z(t) = \Delta_u(t) < \Delta(t) < \Delta_l(t) \\ K_2 \Delta(t) & \text{if } l(t) = -1 \text{, and } |\Delta(t)| < \Delta_u(t) \\ K_2 \Delta_u(t) + K_3 (\Delta(t) - \Delta_u(t)) & \text{if } l(t) = -1 \text{ and } \Delta_u(t) < \Delta(t) < \Delta_l(t) = z(t) \end{cases} \quad (4)$$

where $z(t)$ is the element state variable storing the information of the previous unloading deformation or previous loading deformation, and $l(t) = sign(\Delta \, \dot{\Delta})$. It is convenient to write Eq. (4) as

$$f(\Delta, z, l) = K_m \Delta(t) + g(\Delta(t), l(t), z(t), K_h, \gamma) \quad (5)$$

where $K_m = \frac{1}{2}(K_1 + K_2)$, K_h is defined as $K_h = \frac{1}{2}(K_1 - K_2)$, and $\gamma = \dfrac{K_3 - K_m}{K_h}$. The force-deformation relation $g(\Delta, l(t), z(t))$ is illustrated in the bottom figure of Fig. 1. Clearly $1 < \gamma < \infty$ and in the limit case of $\gamma = \infty$, Eq. (5) reduces to the memoryless relation (Reid's model):

$$f(\Delta, \dot{\Delta}) = K_m \Delta(t) + K_h \Delta(t) \, sgn(\Delta(t)\dot{\Delta}(t)) \quad (6)$$

The Reid's model is then a special case of the linear friction model described in Eq. (4).

The authors refer to the model of Eq. (4) as 'linear friction' not without reason: as it will become apparent the adjective linear in the expression 'linear friction' refers not only to the fact that this model can be realized by means of frictional forces increasing linearly with deformation, but also to the fact that structures containing this type of nonlinear devices exhibit some characteristics typical of linear systems. The purpose of this paper is to analyze the characteristics of structures containing this type of nonlinear dissipating devices and to apply different linearization techniques for the estimation of the response of these structures. The harmonic linearization method and a linearization based on a hysteretic linear element are used to estimate the response of these systems subjected to deterministic and random excitation. These linearization procedures and be used in the preliminary design of structures containing energy dissipating devices exhibiting triangular hysteresis.

FORMULATION OF THE PROBLEM

Consider a linear, undamped N-degree-of-freedom system containing linear-friction dissipating devices. The system can be described by the following differential equation

$$\mathbf{M}\ddot{\mathbf{y}}(t) + \mathbf{K}\,\mathbf{y}(t) + \sum_{i=1}^{N_e}\mathbf{L}_i^T f_i(t) = \mathbf{L}_w\,\mathbf{w}(t)\,, \qquad \mathbf{y}(0) = \mathbf{y}_o\,, \qquad \dot{\mathbf{y}}(0) = \dot{\mathbf{y}}_o \qquad (7)$$

where $\mathbf{M}$ and $\mathbf{K}$ represent the positive-definite mass and stiffness matrices, respectively; $\mathbf{L}_w\,\mathbf{w}$ represents the excitation, f_i is the force in the i-th energy dissipating device, $\mathbf{L}_i^T$ is the appropriate force transformation, and N_e is the number of energy dissipating devices. The force in the i-th EED can be expressed as

$$f_i(t) = K_m^{(i)}\,\Delta(t) + g\left(\Delta_i(t),\,l(t),\,z(t),\,K_h^{(i)},\,\gamma_i\right) \qquad (8)$$

where $K_m^{(i)}$, $K_h^{(i)}$ and γ_i are the parameters of the i-th EDD previously defined; $z_i(t)$ represents the state (memory) of the i-th EDD, $l_i(t) = sgn(\Delta_i\,\dot{\Delta}_i)$, and the element deformation Δ_i in the i-th element is given by

$$\Delta_i(t) = \mathbf{L}_i\,\mathbf{y}(t) \qquad (9)$$

By defining $\bar{\mathbf{K}} = \mathbf{K} + \sum_{i=1}^{N_e}\mathbf{L}_i^T K_m^{(i)}\mathbf{L}_i$, Eq. (7) can be written as

$$\mathbf{M}\ddot{\mathbf{y}}(t) + \bar{\mathbf{K}}\,\mathbf{y}(t) + \sum_{i=1}^{N_e}\mathbf{L}_i^T \mathbf{L}_i\; g\left(\Delta_i(t),\,l_i(t),\,z_i(t)\,K_h^{(i)},\,\gamma_i\;\right) = \mathbf{L}_w\,\mathbf{w}(t) \qquad (10)$$

The analysis of the response of this nonlinear system to deterministic or random loading requires numerical integration. The use of response-spectrum techniques in the preliminary design of structures subjected to dynamic loading is common practice in the engineering community. The earthquake-resistant design of structures, for example, is typically based on a seismic response spectrum. Obtaining a linearized system of equations which approximates Eq. (10) for a given type of excitation is then highly desirable. In the following sections different linearization techniques are employed to approximate the response of this nonlinear system to harmonic and random excitation.

The linear-friction element is homogeneous of order one in its input variables $[\Delta\;\dot{\Delta}]$. This property is transferred to a system such as that of Eq. (7). It can be easily shown that, if the initial conditions and the input excitation are scaled by a factor μ, the response of the system is simply μ times the response of the original system. This property is typical of linear systems. It is also simple to show that Eq. (7) fails to satisfy the addition principle of linear systems (superposition). Owing to the dissipation of energy-per-cycle of this nonlinear element is quadratic in the deformation amplitude, excellent accuracy is obtained with the linearization methods. In fact, the accurate predictability of the response of this nonlinear system by means of equivalent linear systems is a very convenient characteristic of EED with triangular hysteresis.

FREE VIBRATION OF SDOF SYSTEMS WITH LINEAR-FRICTION EDDs

Consider a SDOF system with a linear-friction EDD described by

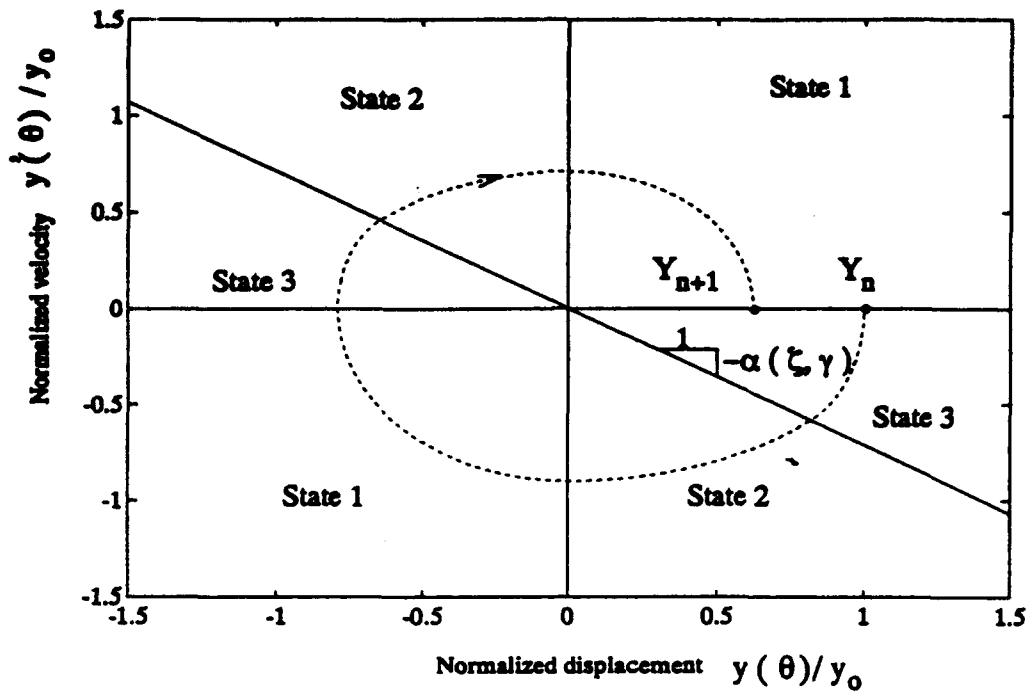$$\ddot{y}(t) + \omega^2 y(t) + \frac{1}{m}\, g\left(y(t),\,l(t),\,z(t),\,K_h,\,\gamma\right) = 0 \qquad (11)$$

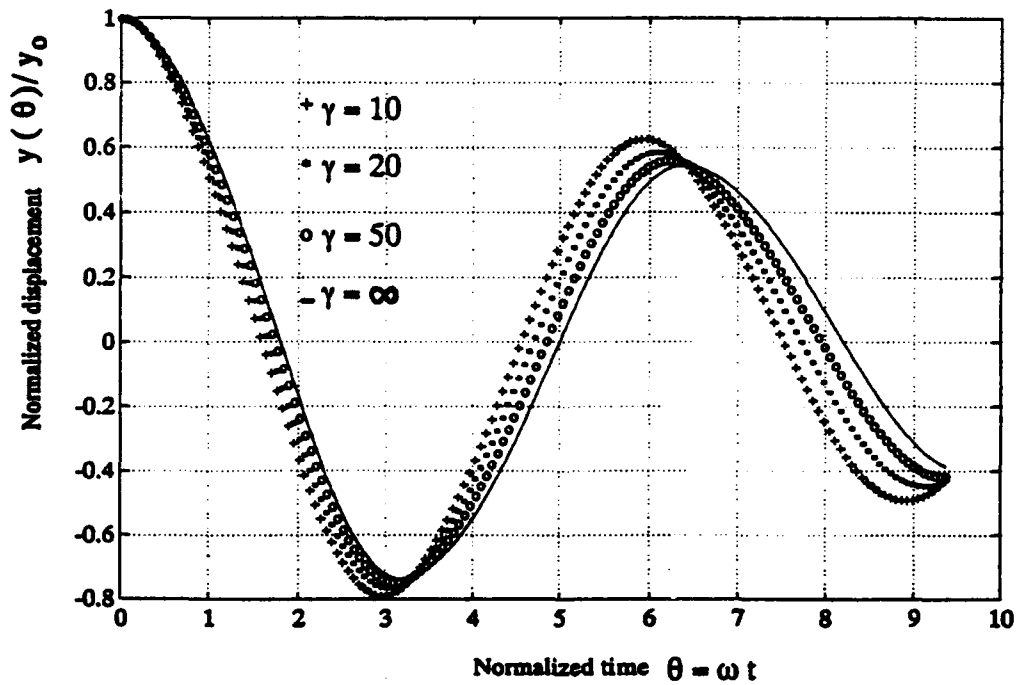Figure 2. Free vibration of a SDOF in the phase plane ($\zeta = 10, \gamma = 0.3, \alpha = 0.713$)

Figure 3. Free vibration of a SDOF with a linear-friction element.

with initial conditions $y(0) = y_o$, $\dot{y}(0) = 0$, and $z(0) = y_o$. In Eq. (11) $\omega^2 = (K + K_m)/m$, where K and m are the stiffness and mass of the oscillator. The function $g(t)/m$ takes three different expressions in the state space depending upon the variable $z(t)$, the deformation, y, and the deformation rate $\dot{y}$. These expressions are

$$\frac{g(t)}{m} = \zeta\omega^2 y(t) \quad (State\,1) \tag{12}$$

$$\frac{g(t)}{m} = -\zeta\omega^2 y(t) \quad (State\,2)$$

$$\frac{g(t)}{m} = \zeta\omega^2 z(t) - \gamma\zeta\omega^2(z(t) - y(t)), \quad z(t) = y_l \quad (State\,3)$$

where $\zeta = K_h/(\omega^2 m)$, and y_l is the current unloading deformation (Δ_l in Eq. (2)). Defining the dimensionless variable $\theta = \omega t$, Eq. (11) can be written as

$$y''(\theta) + y(\theta) + u(y(\theta),\, l(\theta),\, z(\theta),\, \zeta,\, \gamma) = 0 \tag{13}$$

where $u(t) = \dfrac{g(t)}{m\,\omega^2}$ and $y' = dy/d\theta$. Equation (12) can be written as

$$y'' + (1 + \zeta)\,y = 0 \quad (State\,1) \tag{14}$$

$$y'' + (1 - \zeta)\,y = 0 \quad (State\,2)$$

$$y'' + (1 + \gamma\zeta)\,y = z(\theta)\,\zeta\,(\gamma - 1) \quad (State\,3)$$

Equation (13) can be solved exactly for specific initial conditions by solving the corresponding linear system in each region of the state space and ensuring the corresponding continuity conditions. It can be shown that, in free vibration, the system presents fixed switching lines in the reduced state space defined by $y(\theta)$ and $y'(\theta)$. As shown in Fig. 2, the switching lines are given by

$$y(\theta) = 0, \quad y'(\theta) = 0 \quad \text{and} \quad y'(\theta) = -\alpha\,y(\theta) \tag{15}$$

where the constant α can be computed as

$$\alpha(\zeta,\,\gamma) = \frac{\gamma+1}{\gamma-1}\,[\,2\zeta\,\frac{(\gamma-1)^2}{\gamma+1} + 1 + \gamma\,\zeta - 2\,\zeta\,(\gamma - 1) - (1 + \gamma\,\zeta)\,(\frac{\gamma-1}{\gamma+1})^2\,]^{\frac{1}{2}} \tag{16}$$

In the case of the Reid's model ($\gamma = \infty$) the differential equation of the SDOF system is

$$y''(\theta) + y(\theta) + \zeta\,y(\theta)\,sgn\,(y(\theta)y'(\theta)) = 0 \tag{16}$$

The lines $y(\theta) = 0$ and $y'(\theta) = 0$ of the state space constitute the switching lines between two different linear systems with dimensionless frequencies $\sqrt{1+\zeta}$ and $\sqrt{1-\zeta}$. The Ried's oscillator shows a periodic response with a constant decay ratio between consecutive peaks (Caughey et al., 1970). The dimensionless period of the oscillator, T_θ, is independent of the amplitude of oscillation and given by

$$T_\theta(\zeta) = T\,\omega = \pi\,(\frac{1}{\sqrt{1-\zeta}} + \frac{1}{\sqrt{1+\zeta}}) \tag{17}$$

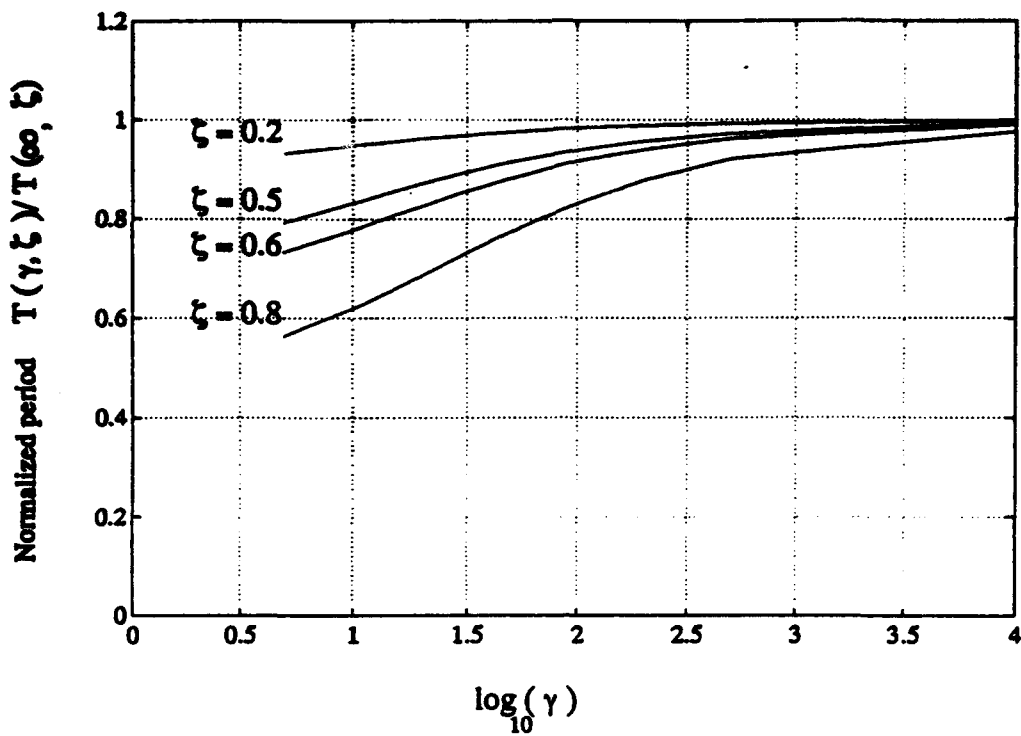where T represents the period of the system in units of time. The ratio of peaks Y_i between

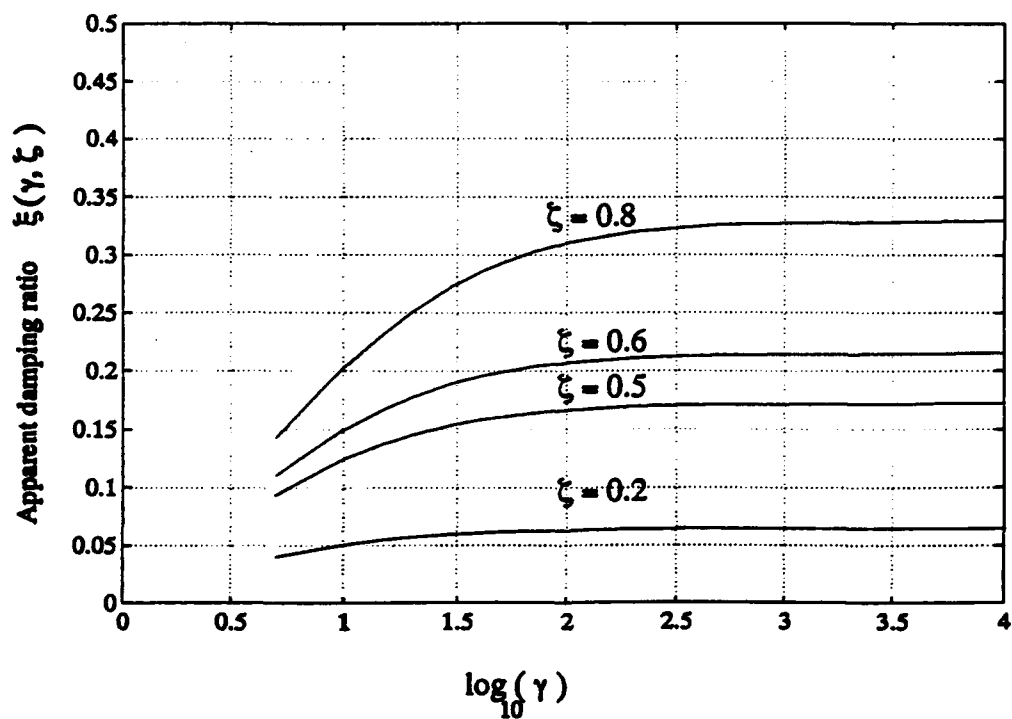Figure 4. Effect of γ on the period of oscillation.

Figure 5. Effect of γ on the apparent damping ratio of the system.

two successive cycles, n and $n+1$, is constant and given by

$$\frac{Y_{n+1}}{Y_n} = \frac{1-\zeta}{1+\zeta} \tag{18}$$

In the case of finite γ (Eq. (13)) this nonlinear system still exhibits a vibration period independent of the amplitude of oscillation, $T_\theta(\zeta, \gamma)$. Naturally, the period is a function of γ and ζ. The effect of γ in the free vibration response of a SDOF system described by Eq. (13) is illustrated in Fig. 3 for $\zeta = 0.30$ and $\gamma = 10, 20, 50$ and ∞. Small values of γ yield a reduction of the period (stiffening effect) and an increase in the ratio between consecutive peaks (effective damping reduction). Figure 4 shows the variation of the period $T_\theta(\zeta, \gamma)$ with γ for different values of ζ. The results are normalized by the period of the system without memory, $T_\theta(\zeta)$ (Eq. (17)), and given for $\zeta = 0.2, ,0.5, 0.6$ and 0.8.

Like the Reid's oscillator, the linear-friction oscillator (Eq. (13)) shows a constant decay ratio between peaks in free vibration. To analyze the effect of γ in the decay ratio of the oscillator, an apparent damping ratio is computed based on the well known result of linear viscously damped systems

$$\frac{Y_{n+1}}{Y_n} = e^{2\pi\frac{\xi}{\sqrt{1-\xi^2}}} \tag{19}$$

Given the decay ratio $h(\gamma, \zeta) = Y_{n+1}/Y_n$ as a function of γ and ζ, The apparent damping ratio of this nonlinear system, $\xi(\gamma, \zeta)$, can be computed using Eq. (19) as

$$\xi(\gamma, \zeta) = \frac{-\frac{1}{2\pi} \ln(h(\gamma, \zeta))}{[1+\frac{1}{4\pi^2} \ln^2(h(\gamma, \zeta))]^{\frac{1}{2}}} \tag{20}$$

where the decay ratio $h(\gamma, \zeta) = Y_{n+1}/Y_n$ is obtained by solving the free vibration problem over one cycle of oscillation. Figure 5 shows the apparent damping ratio $\xi(\gamma, \zeta)$ as a function of γ for $\zeta = 0.2, 0.5, 0.6$ and 0.8. The effect of a reduction in γ is to decrease the effective damping ratio. For $\gamma > 100$ the effect of memory on the equivalent damping ratio is negligible and ξ could be taken, without significant error, as that of the Reid's oscillator (which can be computed using Eqs.(18) and (20)).

Two characteristics of time-invariant linear structures are exhibited by SDOF structures with linear-friction elements: the free vibration period and the logarithmic decrement are independent of the amplitude of oscillation.

HARMONIC LINEARIZATION

This technique, often called the describing function method or the method of harmonic balance (Siljak, 1969), seeks for a linear element that approximates the response of a nonlinear element when the input to the nonlinear element is harmonic. Caughey et al. (1970)

have used this technique in the case of the memoryless element described by

$$f(\Delta, \dot{\Delta}) = K_h \, \Delta(t) \, sgn(\Delta(t)\dot{\Delta}(t)) \tag{21}$$

to obtain an equivalent viscous damper $\bar{f} = c_e \, \dot{\Delta}$ that approximates Eq. (21). The parameter c_e that minimizes

$$J(c_e) = \int\limits_{0}^{\frac{2\pi}{\bar{\omega}}} (\bar{f}(\dot{\Delta}) - f(\Delta, \dot{\Delta}))^2 \, dt \tag{22}$$

for $\Delta(t) = A \, \sin(\bar{\omega}t)$, is given by

$$c_e = \frac{2K_h}{\bar{\omega}\pi} \tag{23}$$

Naturally, the equivalent viscous parameter is inversely proportional to the deformation frequency, $\bar{\omega}$, (since the response of the nonlinear element is rate-independent) and independent of the deformation amplitude, A, (since the energy dissipation per cycle is quadratic in the deformation amplitude). As noted by Beucke and Kelly (1985), the result of Eq. (23) can also be obtained by matching the dissipation of energy in a cycle of harmonic deformation of the equivalent viscous damper, E_v, to that of the nonlinear element, E_h; where

$$E_v = \bar{\omega} \, c_e \, A^2 \, \pi \, , \qquad E_h = 2A^2 K_h \tag{24}$$

In this work we seek for an approximate linear element of the form

$$\bar{f} = k_e \, \Delta(t) + c_e \dot{\Delta}(t) \tag{25}$$

to replace the nonlinear hysteretic element (linear-friction model with memory)

$$f(\Delta, \dot{\Delta}, z) = g(\Delta, l(t), z(t), K_h, \gamma) \tag{26}$$

Letting the deformation $\Delta(t) = A \, \sin(\bar{\omega}t)$, we seek for the parameters k_e and c_e such that the integral of the mean square error is minimized; i.e.,

$$minimize \quad J(c_e, k_e) = \int\limits_{0}^{\frac{2\pi}{\bar{\omega}}} [\, \bar{f}(\Delta(t), \dot{\Delta}(t)) - g(\Delta(t), l(t), z(t))]^2 \, dt \tag{27}$$

After some algebra, the following expressions are obtained for k_e and c_e

$$k_e = K_h \, \rho_k(\gamma) \tag{28}$$

$$c_e = \frac{2 K_h}{\bar{\omega}\pi} \, \rho_c(\gamma) \tag{29}$$

where the functions $\rho_k(\gamma)$ and $\rho_c(\gamma)$ are given by

$$\rho_k(\gamma) = \frac{1}{\pi} \, [\, acos(\frac{\gamma-1}{\gamma+1}) \, (1+\gamma) - 2\sqrt{\gamma} \, \frac{\gamma-1}{\gamma+1}] \tag{30}$$

$$\rho_c(\gamma) = \frac{1}{2} \, [\, 1 + 4\frac{\gamma-1}{\gamma+1} - \frac{4\gamma^2}{(\gamma+1)^2} + (\frac{\gamma-1}{\gamma+1})^2 \,] \tag{31}$$
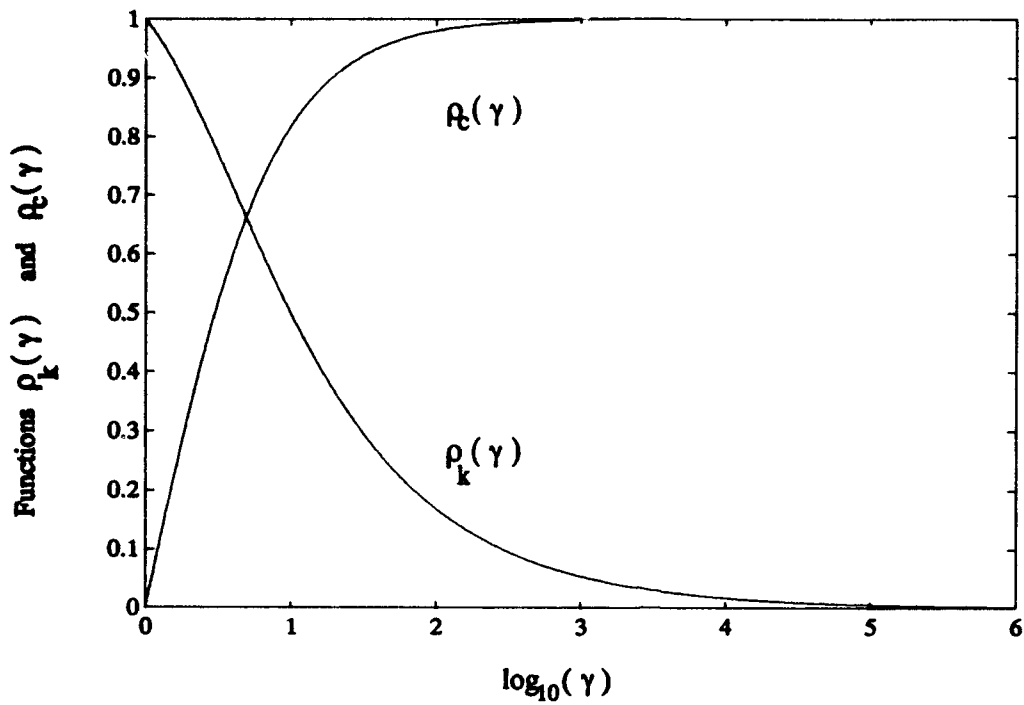
Figure 6. Functions $\rho_k(\gamma)$ and $\rho_c(\gamma)$ (harmonic linearization).
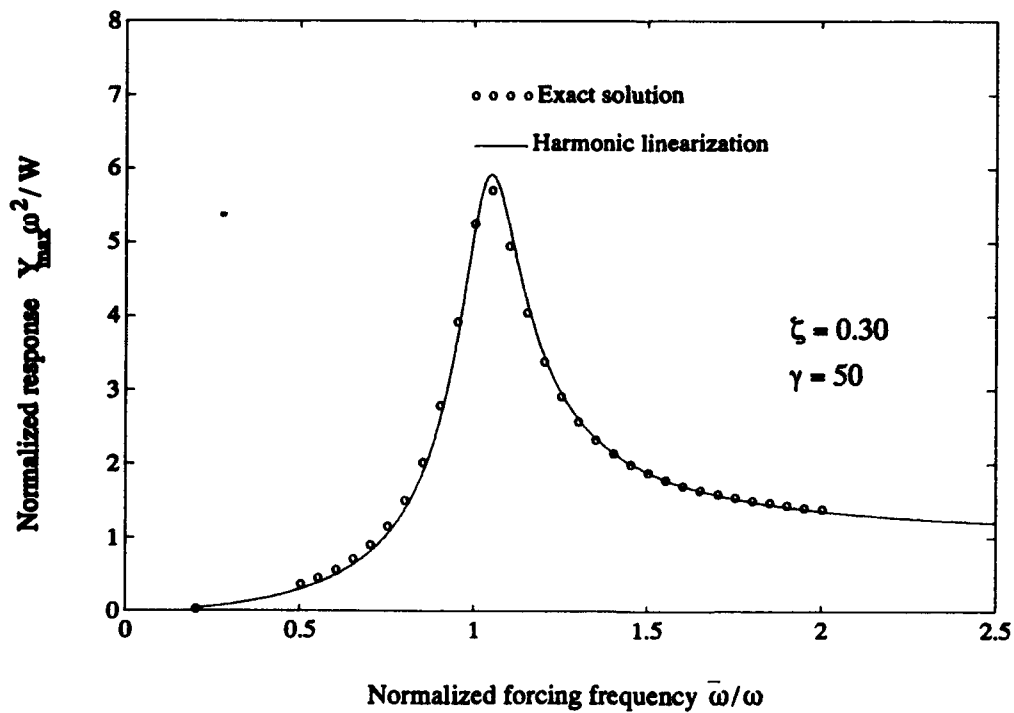

Figure 7. Frequency response of the nonlinear SDOF and of its equiv. linear oscillator.

The functions $\rho_k(\gamma)$ and $\rho_c(\gamma)$ are plotted in Fig. 6. $\rho_k(\gamma)$ is a monotonically decreasing function of γ and $\rho_k(1) = 1$, $\rho_k(\infty) = 0$. On the contrary, $\rho_c(\gamma)$ is a monotonically increasing function of γ and $\rho_c(1) = 0$, $\rho_c(\infty) = 1$. For $\gamma = \infty$, k_e is zero and c_e naturally coincides with the result obtained for the memoryless element (Eq. (23)). It can be shown that the same value of c_e can be obtained by matching the dissipation of energy in a cycle of deformation of the equivalent viscous damper to that of the linear friction element (Eq. (26)), E_h. Therefore, E_h can be written as

$$E_h = 2 A^2 K_h \, \rho_c(\gamma) \tag{32}$$

A characteristic frequency of the deformation response is required to define c_e in Eq. (29). In the case of narrow-band excitation an appropriate selection of $\bar{\omega}$ is the forcing frequency since the steady-state response of this nonlinear system to harmonic loading is periodic with the same period of the excitation. To approximate the steady-state response of the nonlinear system to harmonic excitation, the following equivalent linear system is proposed:

$$\ddot{y}(t) + 2 \, \xi_e \, \omega_e \, \dot{y}(t) + \omega_e^2 \, y(t) = W \, e^{j\beta\omega t} \tag{33}$$

where the equivalent frequency $\omega_e = \sqrt{\omega^2 + K_e/m}$ is computed using Eq. (28) as

$$\omega_e = \omega \sqrt{1 + \zeta \, \rho_k(\gamma)} \tag{34}$$

and the equivalent damping ratio is computed from $\xi_e = \dfrac{c_e}{2m\,\omega_e}$ with c_e given by Eq. (29) and $\bar{\omega}$ equal to the forcing frequency $\bar{\omega} = \beta\omega$,

$$\xi_e = \frac{\zeta}{\pi\beta} \, \frac{\rho_c(\gamma)}{\sqrt{1 + \zeta \, \rho_k(\gamma)}} \tag{35}$$

Figure 4 illustrates the exact and approximate response of a SDOF system to harmonic loading for of $\gamma = 50$ and $\zeta = 0.30$. As shown in the figure good accuracy is obtained.

In the case of broad-band excitation, the natural frequency of the oscillator is an appropriate choice for $\bar{\omega}$ in Eq. (29); the equivalent damping ratio in this case can be obtained from Eq. (29) taking $\bar{\omega} = \omega_e$ as

$$\xi_e = \frac{\zeta}{\pi} \, \frac{\rho_c(\gamma)}{1 + \zeta \, \rho_k(\gamma)} \tag{36}$$

To illustrate the accuracy of the harmonic linearization method in the estimation of the response to broad-band excitation, the response of the nonlinear SDOF to support excitation was obtained and compared with that of the linearized system. The support acceleration is the recorded acceleration in the NS direction during El Centro earthquake (Fig. 8). The exact and approximate response spectra are shown in Fig. 8 for $\gamma = 5$ and 50, and $\zeta = 0.1, 0.3$ and 0.6. The spectra show the normalized maximum deformation of the system $Y_{max}\omega^2/g$, where g represents the acceleration of gravity and ω the natural frequency of the structure without the linear-friction element. As shown in the figure, good accuracy is obtained in the estimation of
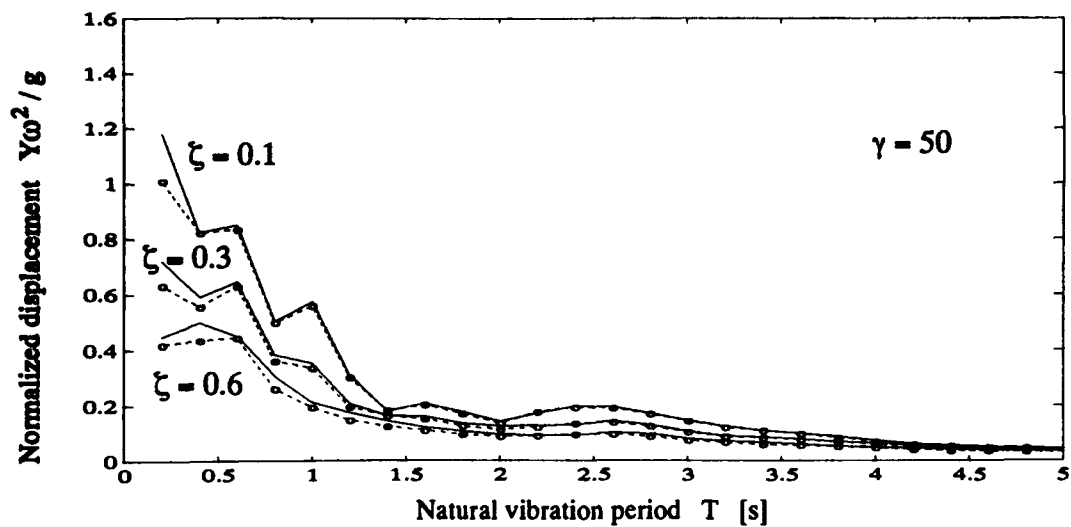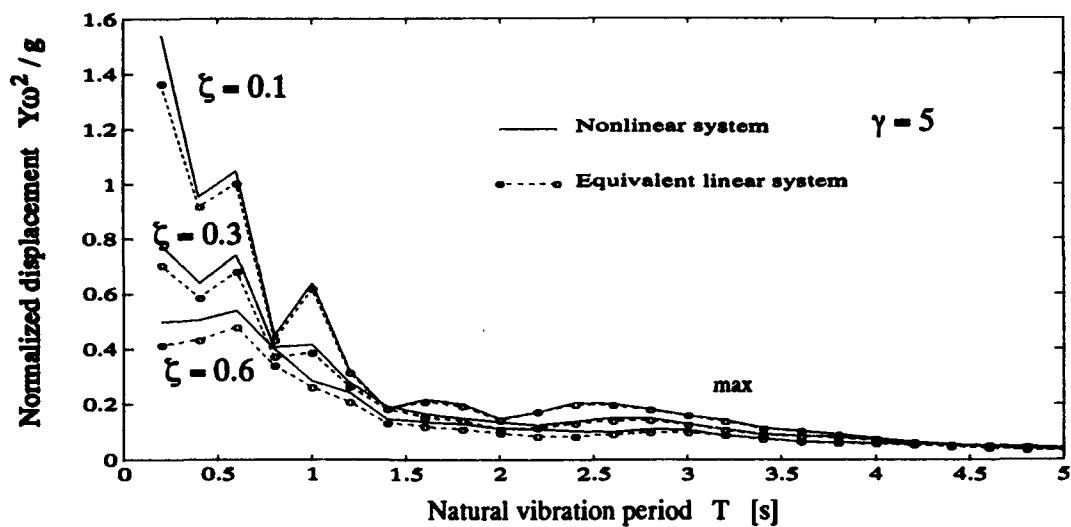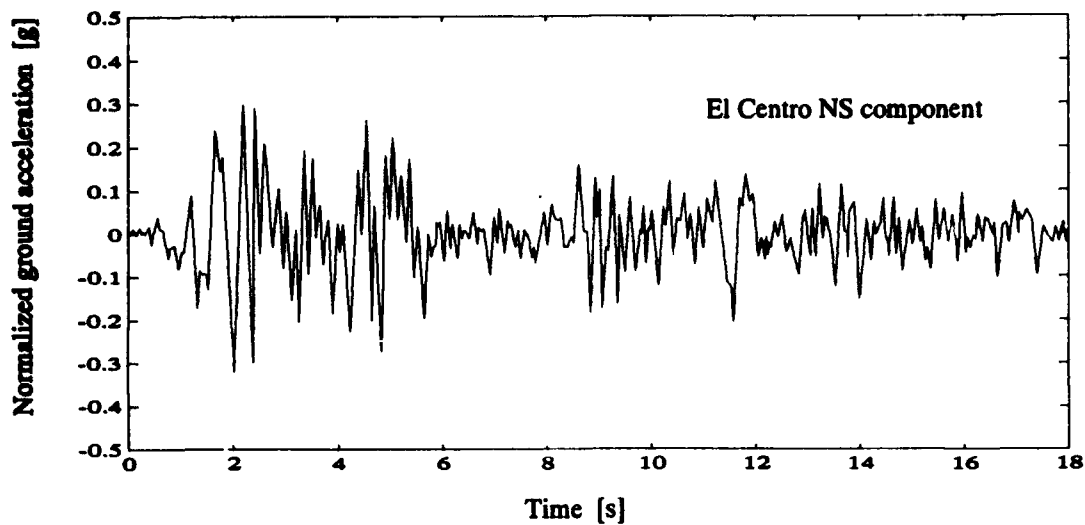
Figure 8. Ground motion signal and deformation response spectra for γ = 5 and γ = 50

the peak deformation response using the linearized system.

In MDOF systems with well separated frequencies the Modal Strain Energy method in combination with the harmonic linearization technique can be used to estimate the response of the nonlinear system described by Eq. (7) under broad-band excitation. We seek for a set of decoupled differential equations that approximates the response of the nonlinear system. Let us define the real-values modes shapes, ϕ_i and modal frequencies, ω_i by replacing the non-linear term of Eq. (7) by the corresponding linear spring elements, $K_e^{(i)}$, and neglecting the equivalent damping elements, $C_e^{(i)}$,

$$\omega_i^2 \, \mathbf{M} \, \phi_i = (\bar{\mathbf{K}} + \sum_{i=1}^{N_e} L_i^T \, K_e^{(i)} \, L_i \,) \, \phi_i \tag{37}$$

$$\phi_i^T \, \mathbf{M} \, \phi_j = \delta_{ij} \tag{38}$$

where $K_e^{(i)}$ is given by Eq. (28) with $K_h = K_h^{(i)}$ and $\gamma = \gamma_i$. By defining the modal coordinates, q, as

$$\mathbf{y}(t) = \Phi \, \mathbf{q}(t) \tag{39}$$

and using the orthogonality property of the modal matrix, $\Phi = [\phi_1 \cdots \phi_N]$, the equivalent linear system can be described by

$$\ddot{\mathbf{q}}(t) + \Omega^2 \, \mathbf{q}(t) + \Phi^T \sum_{i=1}^{N_e} L_i^T \, C_e^{(i)} \, L_i \, \Phi \, \dot{\mathbf{q}}(t) = \Phi^T L_w \, \mathbf{w}(t) \tag{40}$$

where Ω is a diagonal matrix with ω_i^2 in the diagonal. Neglecting the interaction between the modal coordinates we obtain the following N decoupled equations of motion for the system

$$\ddot{q}_l(t) + \omega_l^2 \, q_l(t) + \phi_l^T \sum_{i=1}^{N_e} L_i^T \, C_e^{(i)} \, L_i \, \phi_l \, \dot{q}_l(t) = \phi_l^T L_w \, \mathbf{w}(t) \qquad l = 1, 2,..., N \tag{41}$$

In the case of broad-band excitation, the equivalent damping constant $C_e^{(i)}$ in the l-th equation of Eq. (41) is taken as

$$C_e^{(i)} = \frac{2 \, K_h^{(i)} \, \rho_c(\gamma_i)}{\omega_l \, \pi} \tag{42}$$

Finally, the following modal equations are obtained to approximate the response of the non-linear system

$$\ddot{q}_l(t) + 2\omega_l \xi_l \, \dot{q}_l(t) + \omega_l^2 \, q_l(t) = \phi_l^T L_w \, \mathbf{w}(t) \qquad l = 1, 2,..., N \tag{43}$$

where the equivalent modal damping ratios, ξ_l, are given by

$$\xi_l = \frac{1}{\pi \omega_l^2} \sum_{i=1}^{N_e} \phi_l^T L_i^T \, K_h^{(i)} \, \rho_c(\gamma_i) \, L_i \, \phi_l \,, \qquad l = 1, 2,..., N \tag{44}$$

Figure 9 shows a comparison of the exact and approximate response of a 2DOF system under El Centro earthquake. The properties of the 2DOF system are

$$\mathbf{M} = m \begin{bmatrix} 1 & 0 \\ 0 & 1 \end{bmatrix} \qquad \mathbf{K} = m \begin{bmatrix} 200 & -100 \\ -100 & 100 \end{bmatrix} \, 1/s^2 \qquad L_1^T = \begin{bmatrix} 1 \\ 0 \end{bmatrix} \qquad L_2^T = \begin{bmatrix} 1 \\ -1 \end{bmatrix} \qquad L_w = \begin{bmatrix} -m \\ -m \end{bmatrix}$$
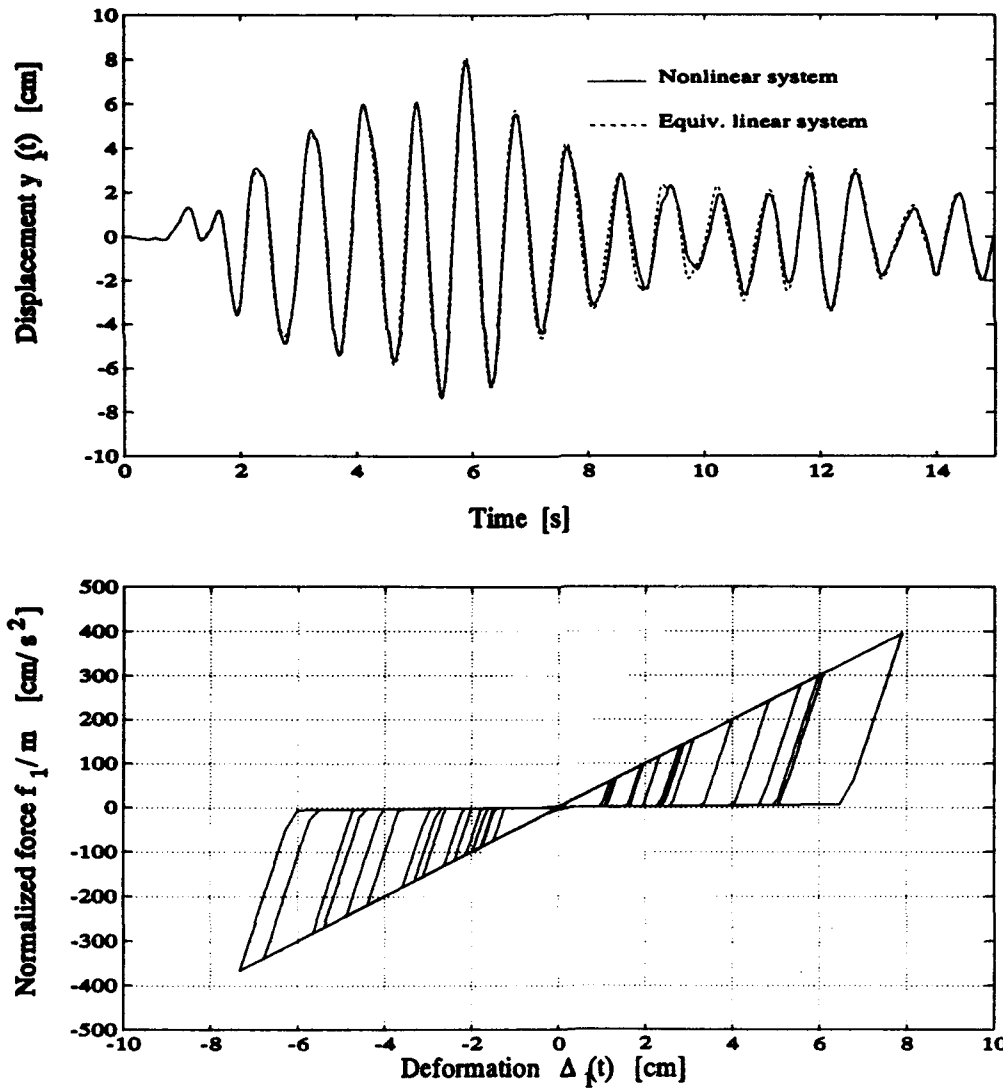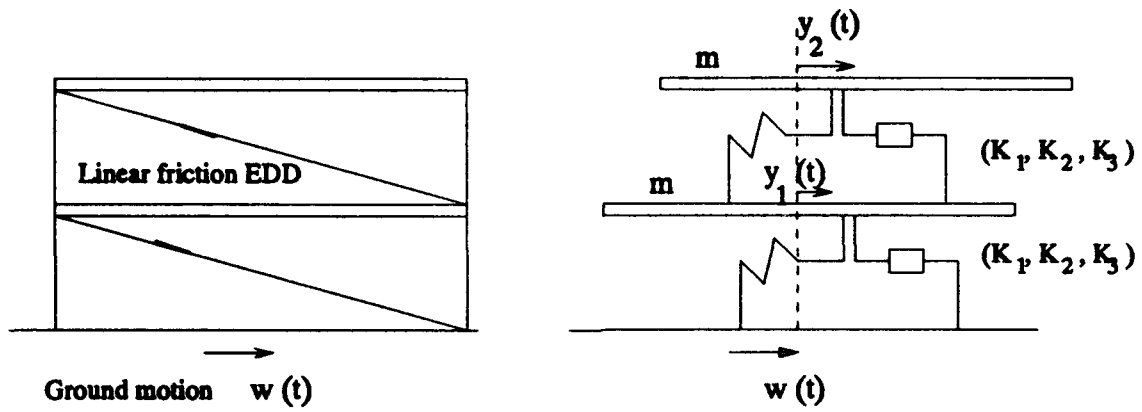
Figure 9. Comparison of the response of a 2DOF nonlinear structure and its linearization.

Two linear-friction elements with parameters $K_1/m = 50\ 1/s^2$, $K_2/m = 1\ 1/s^2$, and $K_3/m = 300\ 1/s^2$ are connected to the structure (top figure in Fig. 9). The natural frequencies of the structure without the EED are $\omega_1 = 6.18\ rad/s$ and $\omega_2 = 16.18\ rad/s$. Using Eqs. (30) and (31) and the assumed parameters K_1, K_2 and K_3, we can compute $\gamma = 11.204$, $\rho_k = 0.474$, $\rho_c = 0.836$. $K_m/m = 25.5\ 1/s^2$ and the equivalent stiffness of each EDD is $K_e/m = 11.608\ 1/s^2$. The mode shapes, modal frequencies and modal damping ratios of the equivalent linear system are obtained as

$$\phi_1^T = [0.5257 \quad 0.8507] \quad \omega_1 = 7.237\ rad/s \quad \xi_1 = 0.0476$$

$$\phi_2^T = [-0.8507 \quad 0.5257] \quad \omega_2 = 18.946\ rad/s \quad \xi_2 = 0.0476$$

As showed in Fig. 9 excellent accuracy is obtained using the linearization technique. The bottom figure of Fig. 9 shows the force-deformation relation of the linear friction element of the first story of the structure obtained in the simulation of the response of the nonlinear system. It is worth mentioning that the relative accuracy of this linearization (maximum error in a certain response quantity normalized by the maximum response value) does not depend on the amplitude of the excitation since both this nonlinear system and the equivalent linear system are homogeneous (of order one) in the input excitation.

STATISTICAL LINEARIZATION OF THE REID'S MODEL

The statistical linearization method is used in this section to estimate the mean square response of structures containing memoryless elements with triangular hysteresis subjected to stationary random excitation. Let us obtain the equivalent damping constant, c_e, of a linear damper that approximates the nonlinear element of Eq. (21) by minimizing the mean square error assuming a stationary jointly-Gaussian deformation deformation-rate process. The coefficient of the equivalent linear element can be computed by solving the following minimization problem:

$$minimize \quad \Lambda[c_e] = E[\varepsilon^2] \tag{45}$$

where the error ε is given by

$$\varepsilon = K_h\ \Delta(t)\ sgn(\Delta(t)\ \dot{\Delta}(t)) - c_e\ \dot{\Delta} \tag{46}$$

and the expectation operator $E[.]$ is taken as

$$E[(.)] = \frac{1}{2\pi\sigma_\Delta\sigma_{\dot{\Delta}}} \int_{-\infty}^{\infty} \int_{-\infty}^{\infty} e^{-\frac{x^2}{2\sigma_\Delta}} e^{-\frac{\dot{x}^2}{2\sigma_{\dot{\Delta}}}} (.)\ dx\ d\dot{x} \tag{47}$$

After some algebra, the equivalent damping parameter is obtained as

$$c_e = \frac{2\,K_h}{\pi}\ \frac{\sigma_\Delta}{\sigma_{\dot{\Delta}}} \tag{48}$$

The stationary response of the nonlinear system described in Eq. (7) (with $\gamma_i = \infty$) under random loading can be estimated using this linearization technique; Inaudi and Kelly (1992) have shown that excellent accuracy in the estimation of mean square response of MDOF structures

with memoryless linear-friction devices is obtained with this technique.

HYSTERETIC LINEARIZATION OF THE LINEAR-FRICTION ELEMENT

The method of statistical linearization is a convenient technique to treat memoryless non-linearities. The mechanical element described by Eq. (26), however, shows dynamic behavior through the state variable $z(t)$. If a differential equation were written for the dynamics of $z(t)$, the statistical linearization method could still be used since Eq. (26) would represent a function of the variables Δ, $\dot{\Delta}$, and z associated to which we could assume a Gaussian distribution (Roberts and Spanos, 1990). In this section a linearization based on a linear hysteretic model is proposed to estimate the response of the nonlinear system to stationary random excitation.

A pure imaginary spring is a linear model that presents energy loss per cycle quadratic in the deformation amplitude and independent of the frequency. In the frequency domain this linear element is represented by

$$f_l(j\bar{\omega}) = j\ sgn(\bar{\omega})\ S_h\ \Delta(j\bar{\omega}) \tag{49}$$

The energy dissipation in a deformation cycle of amplitude A in this linear, non-causal element, E_{lh} is given by

$$E_{lh} = \pi A^2 S_h \tag{50}$$

As noted Eq. (32), the dissipation of energy per cycle in the nonlinear element (Eq. (26)) is quadratic in the amplitude and independent of the deformation frequency. It naturally follows that a complex-valued spring element is a suitable candidate for the linearization of the linear-friction element with memory. The following linear model is proposed in the frequency domain

$$\bar{f}(j\bar{\omega}) = (K_e + j\ sgn(\bar{\omega})\ S_e\ )\ \Delta(j\bar{\omega}) \tag{51}$$

where K_e is given by Eq. (28) and S_e is obtained by matching the energy dissipation of both models. From Eqs. (32) and (50) we obtain

$$S_e = \frac{2K_h}{\pi}\ \rho_c(\gamma) \tag{52}$$

The stationary response of the equivalent hysteretic system can be computed using frequency domain techniques for a given power spectral density of the the excitation process. The dynamics of the equivalent linear structure can be expressed in the frequency domain as

$$[(j\bar{\omega})^2 M + \bar{K} + \sum_{i=1}^{N_e} L_i^T (K_e^{(i)} + j\ sgn(\bar{\omega})\ S_e^{(i)})L_i\ ]\ y(j\bar{\omega}) = L_w\ w(j\bar{\omega}) \tag{53}$$

where $K_e^{(i)}$ and $S_e^{(i)}$ are given by Eqs. (28) and (53), respectively, with the parameters of the i-th element. The stationary mean square response to a stationary excitation can be computed as

$$E[\ y\ y^T\ ] = \int_{-\infty}^{\infty} H_{wy}(j\bar{\omega})\ S_w(\bar{\omega})\ H_{wy}^*(j\bar{\omega})\ d\bar{\omega} \tag{54}$$
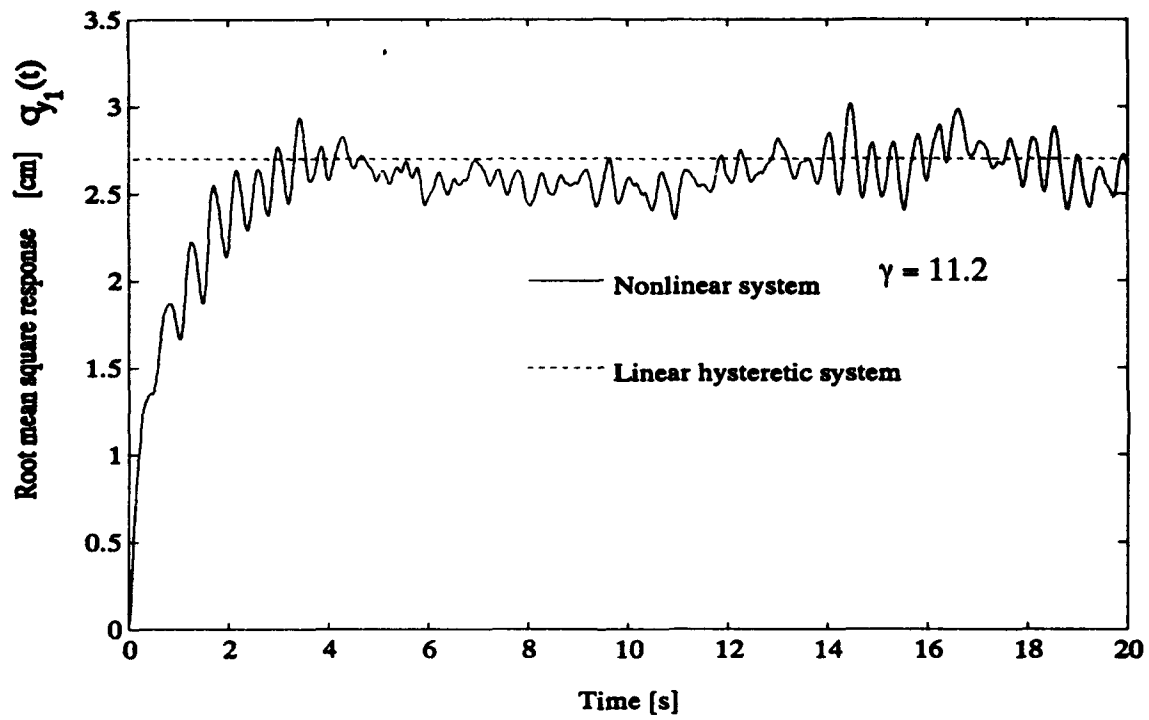
Figure 10. Comparison of Monte Carlo simulation result with hysteretic linearization result.

where $H_{wy}(j\bar{\omega})$ is the transfer function from w to y, $S_w(\bar{\omega})$ is the power spectral density of the excitation, and $()^*$ represents complex transposition.

A simple numerical example is developed to illustrate the accuracy of this method in the estimation of the mean square response of the nonlinear system containing linear friction elements with memory. The mean square response of the nonlinear system described by Eq. (7) subjected to support acceleration modeled by a zero-mean white process with autocorrelation function

$$E[w(t)\,w(t+\tau)] = W\,\delta(\tau) \tag{55}$$

is computed using Monte Carlo simulation techniques. The 2DOF system described previously was subjected to white noise excitation of intensity $W = 1000\ cm^2/s^3$. The parameters of the linear friction elements are $K_1/m = 50\ 1/s^2$, $K_2/m = 1\ 1/s^2$, and $K_3/m = 300\ 1/s^2$. The stationary root mean square displacement of the nonlinear system was computed by averaging in time the mean square deformation response obtained in a Monte Carlo simulation (250 simulations) between $t = 10\ s$ and $t = 20\ s$, giving

$$\sigma_{y_1} = \sqrt{E[y_1^2]} = 2.66\ cm$$

The hysteretic linearization procedure is used to estimate the mean square response of the system. For parameters assumed we can compute $\gamma = 11.204$, $\rho_k = 0.474$, $\rho_c = 0.836$, $K_e/m = 11.609\ 1/s^2$, and $S_e/m = 13.041\ 1/s^2$. The stationary root mean square displacement of the equivalent linear hysteretic system, σ_{y_1}, is computed using Eqs.(53) and (54) as

$$\sigma_{y_1} = 2.70\ cm$$

Again, the accuracy is excellent. Figure 9 shows the results obtained in the Monte Carlo simulation and compares them with the stationary value estimated by means of the hysteretic linearization procedure.

CONCLUDING REMARKS

The free vibration response of SDOF structures with linear-friction EDDs has been investigated. This nonlinear system shows period of oscillation and decay ratio independent of the amplitude of vibration.

The harmonic linearization technique has shown excellent accuracy in the estimation of the response of MDOF structures with linear-friction elements subjected to harmonic and broad-band excitation.

A linearization using a linear hysteretic element has been proposed to estimate the mean square response of structures containing linear-friction elements subjected to random excitation. Using Monte Carlo simulation techniques the excellent accuracy of the hysteretic linearization method has been demonstrated. Both linearization techniques are valuable tools for the preliminary design of structures with energy dissipating devices exhibiting triangular hysteresis loops.

ACKNOWLEDGEMENTS

REFERENCES

Beucke K.E., and Kelly, J.M., 1985, "Equivalent linearizations for practical hysteretic systems", *Int. J. Non-Linear Mechanics,* Vol. 23, No. 4, pp. 211-238.

Caughey, T.K., and Vijayaraghavan, A., 1970, "Free and forced oscillation of a dynamic system with 'linear hysteretic damping' (non-linear theory)", *Int. J. Non-Linear Mechanics,* Vol. 5, pp. 533-555.

Caughey, T.K., and Vijayaraghavan, A., 1977, "Forced oscillations of a piecewise-linear nonlinear dynamic system with several degrees of freedom", *Int. J. Non-Linear Mechanics,* Vol. 12, No. 6, pp. 339-353.

Inaudi, J.A., and Kelly, J.M., 1992, "A friction mass damper for vibration control", *Report No. UCB/EERC-92/15, Earthquake Engineering Research Center,* University of California at Berkeley.

McFarland, B.C., and Bronowicki, A.J., 1989, "Coupled Model Damping in Transient Solutions", *Proc. of Damping'89,* Vol III, pages IDB-1 to IDB-12, National Technical Information Service, February.

Reid, T.J., 1956, "Free vibration and hysteretic damping", *J. Aero. Soc.,* Vol. 69.

Richter, P.J., Nims, D.K., Kelly, J.M., and Kallenbach, R.M., 1990, "The EDR-Energy Dissipating Restraint, a New Device for Mitigating Seismic Effects", *Proc. of the 1990 Structural Engineers Association of California at Lake Tahoe,* September.

Roberts, J.B. and Spanos, P.D., 1990, "Random Vibration and Statistical Linearization", *John Wiley & Sons,* New York.

Siljak, D.D., 1969, "Nonlinear Systems, The Parameter Analysis and Design", *John Wiley & Sons, Inc.,* New York.

ANALYSIS OF DRY FRICTION HYSTERESIS
IN TENSION CABLES

by Xiaolun Huang[1] *and Oleg G. Vinogradov*[2]

ABSTRACT: An analysis of hysteretic losses in tension cables is presented. A basic model of a cable which comprises a core with several wires around it, is used in the analysis.   Deformations of the cable in loading, unloading and reloading phases of the first loading cycle are investigated. As a result, formulas for the energy losses during a symmetric cycle are derived. It is shown that the energy dissipation per cycle is proportional to the cube of the axial load and is in inverse proportion to the distributed friction force. In the paper, the influence of the helix angle of the wires on energy losses is investigated numerically. It is suggested that in applications a cable may be modeled as a solid rod with amplitude-dependent damping properties. The corresponding damping coefficient is obtained by using the equivalent linearization technique.

---

[1] Research Associate, Dept. of Mech. Eng., Univ. of Calgary, Calgary, AB, Canada T2N 1N4.

[2] Professor, Dept. of Mech. Eng., University of Calgary, Calgary, AB, Canada T2N 1N4.

INTRODUCTION

Cables are commonly used as tension members in light and flexible structures. Recently, increasing interest has been shown in utilizing the unique damping characteristic of cables in large space engineering structures and robot arms (Vranish, 1990).

A conventional way to deal with the energy dissipation in a cable is to assume it to be a viscous type of damping. However, as shown in many experimental studies (Yu, 1952; Claren and Diana, 1969; Vinogradov and Pivovarov, 1986), damping in a cable is virtually amplitude-dependent, which is a characteristic of frictional losses.

The problem of frictional hysteresis in tension cables was considered by Hobbs and Raoof (1982), who modelled a multi-layered cable as a set of coaxial orthotropic shells and predicted losses resulting from the slip between the wires along the contact lines. The possibility of an interwire slip in a tension cable was also investigated by Utting and Jones (1989). An attempt to explain the frictional hysteresis in a bent cable was made by Vinogradov and Atatekin (1986), who proposed that the losses are caused by the twisting slippage of the helical wires. More recently, Vinogradov and Huang (1991) developed a model of a cable, in which the cable is treated as a system of thin wires with the dry friction at the interfaces. This model allows the analysis of the interwire slip and its influence on various mechanical properties of cables to be mode (Huang and Vinogradov, 1992, Huang, 1992).

In this paper, the cable model developed by Vinogradov and Huang (1991) is used to analyze the dry friction hysteresis in tension cables. Since this type of hysteresis is caused by the interwire slip, the analysis of deformations of the cable in each phase of the symmetric cycle is presented in full. The results are then extended to determinate the equivalent coefficients of stiffness and damping of the cable as a solid rod. Since frictional damping is not frequency- but amplitude-dependent, the problem will be assessed in a quasi-static approach.

CABLE MODEL

A fundamental structure that has all the features of most cable geometries is that of a number of wires wound helically around a cylindrical core, as shown in Fig.1. Each wire in the cable may be treated as an elastic thin rod, and thus a cable is considered as a system of interacting thin rods.

As shown by Phillips and Costello (1973) using Love's theory of thin rods (Love, 1944), a tensile load on the cable can cause distributed contact forces between the wires. Consequently, any slip at the interfaces will be constrained by the friction forces. Considering that cables are subjected to pretension in most applications and that the amplitude of the fluctuating loads are relatively small, it is reasonable to assume that the interwire friction is constant and determined by the pretension.

Due to the space limitation, some results from Vinogradov and Huang (1991), and Huang (1992) are briefly summarized in following.

When the interwire traction force caused by the tensile load on a cable does not exceeds the interfacial friction, no slip takes place and the cable behaves as a solid rod. In this case the extension stiffness of the cable with n helical wires around the core, K_n, is equal to

$$K_n = E_c \pi R_c^2 + \frac{n E_w \pi R_w^2}{\sin \alpha_0} \qquad (1)$$

where E is the elastic modulus of the material, and R is the radius of the circular cross-section, whereas the subscripts "c" and "w" refer to the core and the outer wires, respectively.

Since dry friction is finite, interwire slip could occur at some part of the cable where the interfacial traction force exceeds the friction constraint. In that part of the cable, deformations in the wires should be found from the conditions of equilibrium for thin rods.

From the geometry of an elementary length of the developed helical wire (see Fig.2), it is easy to obtain the following relationship between the axial strain of the wire, ε_t, and the axial strain of the core (or say the cable), ε_c,

$$\varepsilon_c = (1 + \varepsilon_t) \frac{\sin \alpha}{\sin \alpha_0} - 1 \qquad (2)$$

Taking into account that the change in the helix angle is small, which is valid for most metallic cables, the above can be linearized as

$$\varepsilon_c = \varepsilon_t + \frac{\Delta \alpha}{\tan \alpha_0} \qquad (3)$$

where $\Delta \alpha = \alpha - \alpha_0$.

The rotational deformation of the helical centerline around the cable axis is defined by (see Fig.2)

$$\omega_s = \frac{r_0 (d\varphi - d\varphi_0)}{dz_0} \qquad (4)$$

where r_0 is the radius of the helix in the initial configuration. For the case when the helical wires are in contact with the core, r_0 is equal to $R_c + R_w$. According to the geometry of a developed helix, see Fig.2, Eq.4 can be expressed by
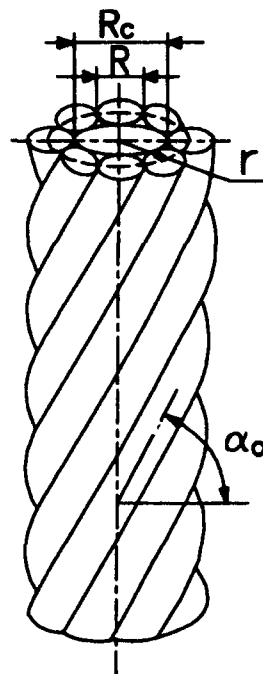
Figure 1 A six-wire cable.

$$\omega_z = \frac{r_0}{r} \frac{1+\varepsilon_\sigma}{\tan\alpha} - \frac{1}{\tan\alpha_0} \tag{5}$$
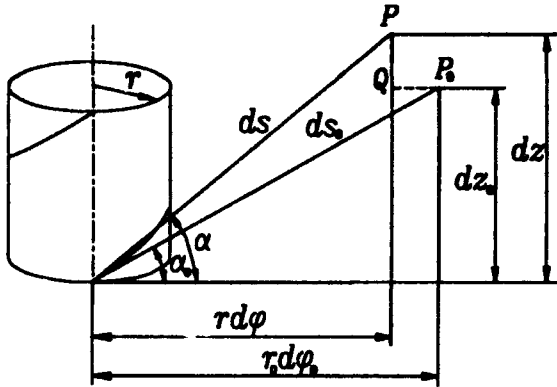
Figure 2 Deformation of an elementary length of helix.

Since the effect of Poisson's ratio on changing the diameter of the wires is negligible (Utting and Jones, 1987), it is assumed that $r=r_0$. If the cable is fixed at the ends, no rotation is allowed. Then Eq.5 yields

$$\varepsilon_\sigma = \frac{\tan\alpha}{\tan\alpha_0} - 1 \tag{6}$$

After linearization of the latter it is obtained

$$\Delta\alpha = \frac{\sin 2\alpha_0}{2}\varepsilon_c \tag{7}$$

It should be noted that the relationship between the change in the helix angle and axial strain in the cable, given by Eq.7, is valid for any part of the tension cable, with slip or without slip. In the non-slipping part of the cable, the axial strain in the cable, ε_{cn}, is simply equal to

$$\varepsilon_{cn} = \frac{P}{K_n} \tag{8}$$

where P is the tensile load on the cable. Correspondingly, the change of the helix angle in the non-slipping part of the cable is obtained from Eq.7

$$\Delta\alpha_n = \alpha_n - \alpha_0 = \frac{\sin 2\alpha_0}{2}\frac{P}{K_n} \tag{9}$$

where subscripts "n" and "0" refer to the non-slipping and initial states, respectively.

In the slipping part of the cable, the change in the helix angle is the sum of two components: $\Delta\alpha_n$, corresponding to the cable as an equivalent solid rod, and $\Delta\alpha_s = \alpha_s - \alpha_n$, which takes into account the interwire slippage. If the axial strain in the slipping part of cable is denoted by ε_{cs}, the following is obtained from Eq.7

$$\Delta\alpha_n + \Delta\alpha_s = \frac{\sin 2\alpha_0}{2}\varepsilon_{cs} \tag{10}$$

Although in a tension cable, the centerline of each outer wire has the same displacement in the direction of the cable axis as that of the core, a slip may still appear due to the twisting and bending deformations of the wire as a helical thin rod. This mechanism can be understood from the deformations of a spiral spring subjected to stretching. Because the twisting and bending deformations of the helical wire and the core are different, a slip can occur at the

interface when the friction constraint is exceeded. The corresponding deformations of the helical wire are governed by the equilibrium conditions. In an ideal situation when the cable is uniform in geometrical and material properties, and the local effect at the fixed ends is negligible, the slip is expected to start at the middle of the cable and then propagate towards the two ends as the tensile load increases.

If the distributed friction force is given by q_f, the change of the helix angle along the axial length of the cable can be found from Love's equations of equilibrium for thin rods (Vinogradov and Huang, 1991; Huang, 1992)

$$\frac{d\alpha}{dz} = Cq_f \qquad (11)$$

where C is a constant related to the cable structure

$$C = -\frac{\sin\alpha_0}{\sqrt{(A\tan\alpha_0 + \frac{B}{r_0 R_w}\sin2\alpha_0)^2 + \frac{B^2}{(1+v)^2 r_0^4}[\frac{r_0}{R_w}\cos2\alpha_0 - \cos^2\alpha_0(1+2v\sin^2\alpha_0)]^2}} \qquad (12)$$

in which $A=E_w\pi R_w^2$, $B=E_w\pi R_w^4/4$ and v is the Poisson ratio of the wire material.

Let us denote the length of the slipping section, or simply called the slipping length, by H_s. At the boundary of the slipping section where $z=H_s$ (origin of the z-axis is set at the middle of the cable), the helix angle must be equal to that in the non-slipping part of the cable, i.e., $\alpha_s=\alpha_n$ at $z=H_s$. Solving Eq.11 subjected to this boundary condition will give

$$\alpha_s = \alpha_n + Cq_f(H_s-z) \qquad (13)$$

Furthermore, from the principle of energy conservation, the slipping length can be found (Vinogradov and Huang, 1991) to be proportional to the tensile load

$$H_s = \frac{DP}{q_f} \qquad (14)$$

where D is the constant determined by the cable structure and is equal to

$$D = -\frac{1}{2a}(b+\sqrt{b^2-4ac}) \qquad (15)$$

in which

$$a = C(a_0+a_2) \qquad (16)$$

$$b = \frac{2}{\sin 2\alpha_0} - 3a_1(a_0 + a_2) \tag{17}$$

$$c = -3a_0 a_1^2 + \frac{3}{2}\frac{1}{K_n} \tag{18}$$

$$Ea_0 = \frac{nB}{r_0^2 \sin\alpha_0}\left(\frac{\cos^2 2\alpha_0}{1+v} + \sin 2\alpha_0\right) + \frac{nA}{2}\tan^2\alpha_0 + \frac{2E_c\pi R_c^2}{\sin^2 2\alpha_0}. \tag{19}$$

$$a_1 = \frac{\sin 2\alpha_0}{2K_n} \tag{20}$$

$$a_2 = \frac{nB}{r_0^2}\left(\frac{4r_0^2}{R_v^2}\tan^2\alpha_0 + \frac{\cos^2 2\alpha_0}{(1+v)\sin\alpha_0} + 4\sin\alpha_0\cos^2\alpha_0\right) \tag{21}$$

The axial strain in the slipping part of the cable in slip can be found by substituting Eqs.9, 13 and 14 into Eq.10

$$\ell_{cs} = \frac{P}{K_n} + \frac{2Cq_f}{\sin 2\alpha_0}\left(\frac{DP}{q_f} - z\right) \tag{22}$$

After this introduction of the cable model, the hysteretic behaviour of cables subjected to cyclic stretching will be investigated in the following sections.

HYSTERESIS

The beginning of a cyclic loading is characterised by three phases: loading, unloading and reloading. The result of the first cycle is the hysteretic loop formed by the unloading and reloading phases of the cycle. However, to find out the hysteretic behaviour, the load-elongation characteristics during the entire first cycle must be analyzed. The behaviour of a tension cable in the loading phase has actually been introduced in the last section. In this section, the treatment of the following unloading phase of the cycle is based on the results obtained for the loading phase. In other words, the state of the cable at the end of the loading phase will be used as the initial conditions for the unloading phase. Similarly, the state of the cable at the end of the unloading phase will be used as the new initial conditions for the following reloading phase. Thus the problem is solved as the initial value problem. For this reason, the state of the cable at the end of the loading phase is presented first. Parameters related to the three phases of a cycle are identified by the subscripts 1, 2 and 3, for the loading, unloading and reloading phases, respectively.

Loading

In general, at the end of the loading phase the cable comprises two parts: one in which the slip took place, and another one where it did not (see Figs.3a and 3b, where, due to the symmetry, only a half-length of the cable is considered). The length of the slipping region during the loading is proportional to the axial load and is given by, from Eq.14,

$$H_{s1} = \frac{DP_1}{q_f} \tag{23}$$

In the nonslipping part of the cable, the helix angle is given by Eq.9

$$\alpha_{n1} = \alpha_0 + \frac{\sin 2\alpha_0}{2K_n} P_1 \ , \tag{24}$$

whereas in the slipping part of the cable, the helix angle is, from Eq.13,

$$\alpha_{s1} = \alpha_{n1} + Cq_f(H_{s1} - z) \tag{25}$$

A sketch of the variability of the helix angle along the cable at the intermediate state of the loading phase is shown in Fig.3b.

For the cable with length 2H, the total elongation is a sum of the elongations from the slipping and non-slipping parts of the cable. Let us denote the cable elongation by δ_1. Then, from Eqs.8 and 22, it follows that

$$\delta_1 = 2\int_{H_s}^{H} \varepsilon_{cn} dz + 2\int_0^{H_s} \varepsilon_{cs} dz = \frac{2HP_1}{K_n} + \frac{2CD^2 P_1^2}{q_f \sin 2\alpha_0} \tag{26}$$

From Eq.26 it is found that $d^2\delta_1/dP_1^2 > 0$, so that the load-elongation curve $\delta_1 = \delta_1(P_1)$ is convex.

Unloading

The unloading is considered as a process of loading which starts at the end of the loading phase, during which the load changes according to the following relationship

$$P_2 = P^{max} + P_2' \qquad\qquad 0 \le P_2 \le P^{max} \tag{27}$$

where P^{max} is the amplitude of the cyclic tension force, and P_2' is the relative load in the unloading phase, $-P^{max} \le P_2' \le 0$.

The state of the cable at the end of the loading phase is used as an initial state for the following unloading phase. Under the action of a compressive load, a slip in the direction opposite to that of the loading phase will start again at the middle of the cable. As a result, the cable at any intermediate state of unloading will have three distinguished segments (see Fig.3c):

(1) a nonslipping segment, denoted by H_{n1}^{min}, whose length is equal to the nonslipping segment at the end of stage one; (2) a new nonslipping segment, denoted by H_{n2}, with respect to the state of the cable at the end of stage one; and (3) a new reverse slipping segment, H_{s2}. It is seen from Fig.3c that H_{n2} is related to H_{s2} by

(28)

$$H_{n2} = H_{s1}^{max} - H_{s2}$$

The objective of the following analysis is to find the relationship between the relative axial force P'_2 and the corresponding relative elongation of the cable.
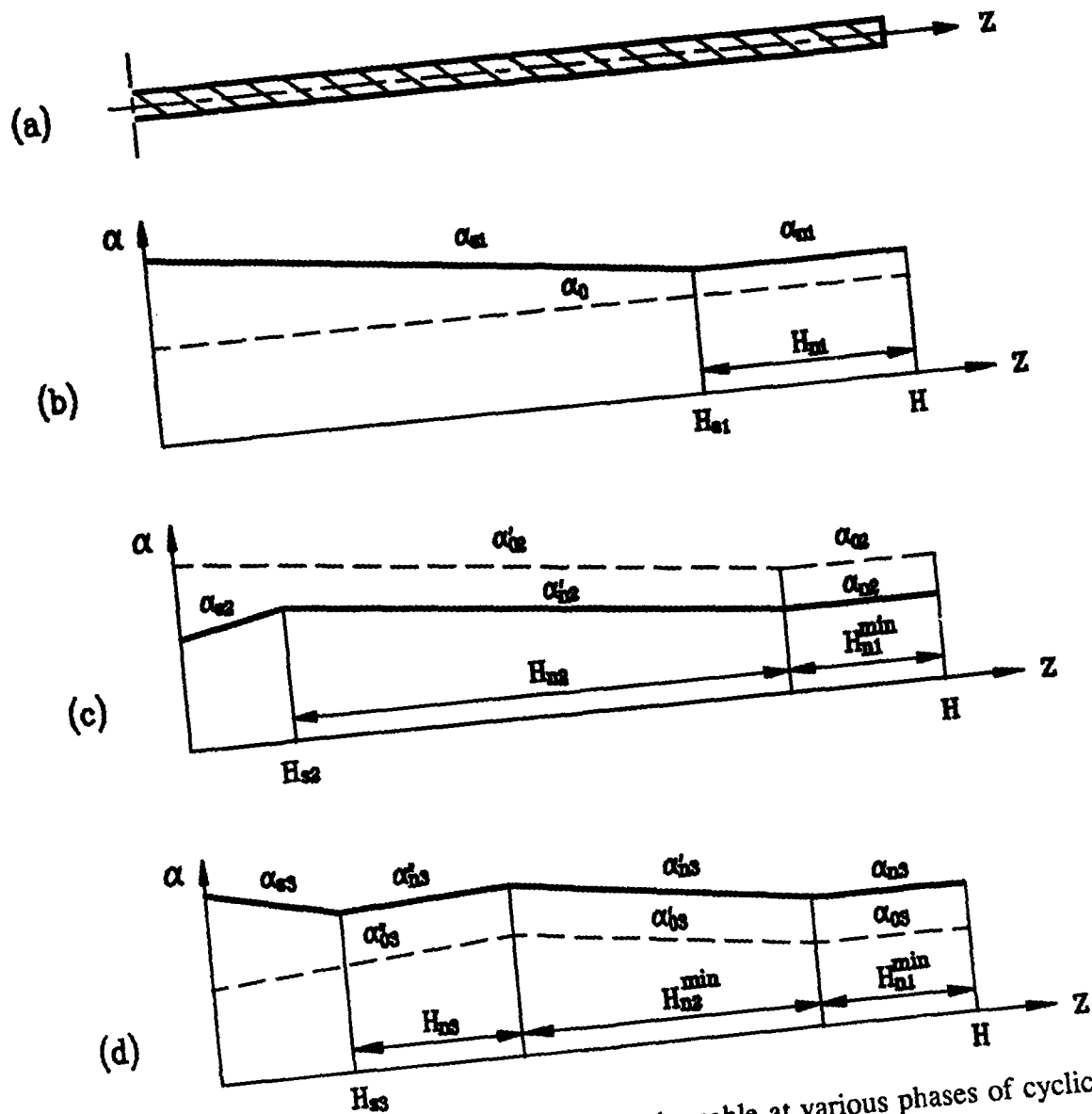

Figure 4.1 Variability of helix angle along the cable at various phases of cyclic loading: (a) a half cable; (b) loading phase; (c) unloading phase; (d) reloading phase.

Consider the helix angle first. At the beginning of the unloading phase, the helix angles in various segments should be equal to those at the end of the loading phase, *i.e.* from Eqs.24 and 25,

$$\alpha_{02} = \alpha_0 + \frac{\sin 2\alpha_0}{2K_n} P^{max} \qquad H_{s1}^{max} \leq z \leq H \qquad (29)$$

$$\alpha_{02}' = \alpha_{02} + Cq_f \ (H_{s1}^{max} - z) \qquad 0 \leq z \leq H_{s1}^{max} \qquad (30)$$

where α_{02} and α_{02}' are the initial helix angles in the nonslipping and slipping parts of the cable at the beginning of unloading, respectively.

In the nonslipping segments, the relative axial strain in the cable caused by load P_2' can be found to be

$$\varepsilon_{cn2} = \frac{P_2'}{K_n} \qquad (31)$$

By substituting Eqs.29 through 31 into Eq.9, the helix angles in the two nonslipping segments are found to be

$$\alpha_{n2} = \alpha_{02} + \frac{\sin 2\alpha_0}{2} \frac{P_2'}{K_n} \qquad H_{s1}^{max} \leq z \leq H \qquad (32)$$

$$\alpha_{n2}' = \alpha_{02}' + \frac{\sin 2\alpha_0}{2} \frac{P_2'}{K_n} \qquad H_{s2} \leq z \leq H_1^{max} \qquad (33)$$

It is seen that the varying components in Eqs.32 and 33 are equal. Correspondingly, the solid lines in Fig.3c, representing α_{n2} and α_{n2}', are at the equal distance from the dashed lines for α_{02} and α_{02}'.

In the new slipping segment H_{s2}, the process of a reversed slip would not start until the slip which occurred at the previous stage has been recovered. It is equivalent to having a double friction force along the length H_{s2} resisting the new slip. In addition, the friction force acts in the direction opposite to that at the initial phase. Therefore,

$$q_{f2} = -2q_f \qquad (34)$$

After taking Eq.34 into account, the helix angle in the new slipping region H_{s2} can be represented by, from Eq.13,

$$\alpha_{s2} = \alpha_{n2}' - 2Cq_f(H_{s2} - z) \qquad 0 \leq z \leq H_{s2} \qquad (35)$$

After substituting Eqs.30, 31, 33 and 34 into Eq.35, the latter can be written in the form

$$\alpha_{s2} = \alpha_{s2} + Cq_f(H_{s1}^{max} - 2H_{s2} + z) \qquad 0 \le z \le H_{s2} \qquad (36)$$

The relative axial strain in the new slipping region is found by substituting Eqs.32 and 36 into Eq.10

$$\epsilon_{as2} = \frac{P_2'}{K_n} - \frac{4Cq_f}{\sin 2\alpha_0}(H_{s2} - z) \qquad (37)$$

Note that the only difference between the unloading and loading phases is in the magnitude and direction of the friction force, as given by Eq.34. Consequently, the relationship between ΔH_{s2} and $\Delta P_2'$, char terising the propagation of the slip during unloading, can be found in a way similar to that in the loading phase. As a result, the length of the reversed slipping segment H_{s2} is found to be directly proportional to the relative load P_2' in the unloading phase

$$H_{s2} = \frac{DP_2'}{q_{f2}} \qquad (38)$$

or, after substitution of q_{f2} from Eq.34,

$$H_{s2} = -\frac{DP_2'}{2q_f} \qquad (39)$$

Then the relative elongation, δ_2', with respect to that at the end of the loading phase, is obtained by integrating the cable's relative strains in the nonslipping and slipping parts given by Eqs.31 and 37

$$\delta_2' = \frac{2P_2'H}{K_n} - \frac{C(DP_2')^2}{q_f \sin 2\alpha_0} \qquad (40)$$

The actual elongation is equal to the elongation at the beginning of the unloading phase (which is also the elongation at the end of the first loading phase) plus the relative elongation δ_2', i.e.

$$\delta_2 = \delta_1^{max} + \delta_2' \qquad (41)$$

Since δ_1^{max} can be found from Eq.26 by setting $P_1 = P^{max}$ and δ_2' by Eq.40, the above equation can be expressed as

$$\delta_2 = \frac{2HP_2}{K_n} + \frac{2C(DP^{max})^2}{q_f \sin 2\alpha_0} - \frac{CD^2(P^{max} - P_2)^2}{q_f \sin 2\alpha_0} \qquad 0 \le P_2 \le P^{max} \qquad (42)$$

At the end of unloading, when $P_2 = 0$, the elongation, given by Eq.42, equals to

$$\delta_2^{min} = \frac{C(DP^{max})^2}{q_f \sin 2\alpha_0} \ne 0 \qquad (43)$$

The fact that $\delta_2^{min} \ne 0$ indicates at the existence of residual strains. This is understandable because

the interwire resistance forces during the unloading becomes twice as large and so a complete recovery of the initially deformed wires cannot be achieved. Note that in this phase, $d^2\delta_2/dP_2^2<0$, and thus the response curve $\delta_2=\delta_2(P_2)$ is concave.

Reloading

During the reloading phase, the load P_3 increases from 0 to P^{max}. Again, the state at the end of the previous phase, the unloading phase, is taken as the initial state of the cable for the reloading phase.

In Fig.3d it is shown that at the beginning of the reloading phase, the cable can be characterized by three distinguished segments: (1) segment H_{n1}^{min} where the cable behaves like a solid rod during the cycle, (2) segment H_{n2}^{min} where the wires slip only once and that is in the first loading phase, and (3) segment H_{s2}^{max} where the wires experience alternate slippage. Correspondingly, the initial helix angles in these segments are found, by using Eqs.32, 33, and 36 and setting $P'_2=-P^{max}$ and $H_{s2}=H_{s2}^{max}$, to be

$$\alpha_{03}=\alpha_{02}-\frac{\sin 2\alpha_0}{2}\frac{P^{max}}{K_n} \qquad H_{s1}^{max}\leq z\leq H \qquad (44)$$

$$\alpha'_{03}=\alpha'_{02}-\frac{\sin 2\alpha_0}{2}\frac{P^{max}}{K_n} \qquad H_{s2}^{max}\leq z\leq H_{s1}^{max} \qquad (45)$$

$$\alpha''_{03}=\alpha'_{03}-2Cq_f(H_s-z) \qquad 0\leq z\leq H_{s2}^{max} \qquad (46)$$

When the relative load increases in the reloading phase, a slip reversed with respect to the previous phase will start again at the middle of the cable and then spread out. For a symmetrical loading, a new region with a relative slip will not exceed the slipping limits of the previous unloading phase, which means that

$$H'_{n3}+H_{s3}=H_{s2}^{max} \qquad (47)$$

Note also that the axial load at the beginning of the reloading phase is equal to zero. Then the relative load at this phase is equal to the absolute value of the load on the cable, namely

$$P_3=P'_3 \qquad (48)$$

In the nonslipping region, the relative axial strain in the cable caused by the load P'_3 is equal to

$$\varepsilon_{an3}=\frac{P'_3}{K_n} \qquad (49)$$

The helix angles in the various nonslipping segments are found to be, by substituting Eqs.44-46

and 49 into 9,

$$\varepsilon_{s3} = \varepsilon_{03} + \frac{\sin 2\alpha_0}{2} \frac{P_3'}{K_n} \qquad (50)$$

$$\varepsilon_{s3}' = \varepsilon_{03}' + \frac{\sin 2\alpha_0}{2} \frac{P_3'}{K_n} \qquad (51)$$

$$\varepsilon_{s3}'' = \varepsilon_{03}'' + \frac{\sin 2\alpha_0}{2} \frac{P_3'}{K_n} \qquad (52)$$

These relationships are shown in Fig.3d by the solid lines equally spaced from the dashed lines characterising the initial angles α_{03}, α_{03}' and α_{03}''.

The helix angle in the new slipping segment H_{s3} is found to be similar to Eq.35 for the unloading phase

$$\alpha_{s3} = \alpha_{s3}'' + 2Cq_f(H_{s3} - z) \qquad 0 \le z \le H_{s3} \qquad (53)$$

In arriving at Eq.53, it has been taken into account that the friction force acts in an opposite direction with respect to the previous phase.

The strain in the new slipping segment, found after substituting Eqs.52 and 53 into 22, is equal to

$$\varepsilon_{as3} = \frac{P_3'}{K_n} + \frac{2Cq_{f3}}{\sin 2\alpha_0}(H_{s3} - z) \qquad (54)$$

where

$$q_{f3} = 2q_f \qquad (55)$$

The relationship between H_{s3} and P_3' is found to be similar to that in the unloading phase

$$H_{s3} = \frac{DP_3'}{q_{f3}} \qquad (56)$$

or, after substituting q_{f3} from Eq.55,

$$H_{s3} = \frac{DP_3'}{2q_f} \qquad (57)$$

The relative elongation δ_3', with respect to the previous phase, is obtained by integrating Eqs.49

and 54 and using H_{t3} given by Eq.57

$$\delta_3' = \frac{2P_3'H}{K_n} + \frac{C(DP_3')^2}{q_f \sin 2\alpha_0} \qquad (58)$$

The actual elongation is then

$$\delta_3 = \delta_2^{min} + \delta_3' \qquad (59)$$

where δ_2^{min} is the residual elongation at the end of the unloading phase given by Eq.23 for $P_2=0$. Thus, using Eqs.43 and 58, the actual elongation (Eq.59) can be written as

$$\delta_3 = \frac{2HP_3}{K_n} + \frac{CD^2}{q_f \sin 2\alpha_0} \left((P^{max})^2 + P_3^2 \right) \qquad 0 \leq P_3 \leq .$$

$$(60)$$

Note that $d^2\delta_3/dP_2^3 > 0$, so that the response curve $\delta_3 = \delta_3(P_3)$ is convex during the reloading phase.

Figure 4 Scheme of the relationship between load and elongation during the first cycle.

Obviously, at the end of the reloading phase, when $P'_3 = P^{max}$, the cable elongation is

$$\delta_3^{max} = \frac{2HP^{max}}{K_n} + \frac{2CD^2}{q_f \sin 2\alpha_0} (P^{max})^2 \qquad (61)$$

that is it is equal to that at the end of the first loading phase. Therefore, the load-elongation curve in a cyclic loading will form a hysteretic loop enclosed by the unloading and reloading curves, as shown schematically in Fig.4. For this reason, in the analysis of cyclic loading the two phases — unloading and reloading — are of interest, since in an ideal multi-cyclic loading the hysteretic loop will repeat itself.

Thus, as far as hysteretic losses are concerned, only the unloading and reloading phases are important. In this sense, the residual elongation, shown in Fig.4, can be excluded from the consideration. This is achieved by subtracting Eq.43 from Eqs.42 and 60 for unloading and reloading phases. As a result, the load-elongation relationship for the cable in a cyclic loading can be written in the form

$$\delta = \begin{cases} \dfrac{2H}{K_n}P + \dfrac{CD^2P^2}{q_f \sin 2\alpha_0} & \text{for loading} \\[4mm] \dfrac{2H}{K_n}P + \dfrac{CD^2(2P_{max}-P)P}{q_f \sin 2\alpha_0} & \text{for unloading} \end{cases} \qquad (62)$$

This equation includes two nonlinear functions forming a closed loop as shown in Fig.5.
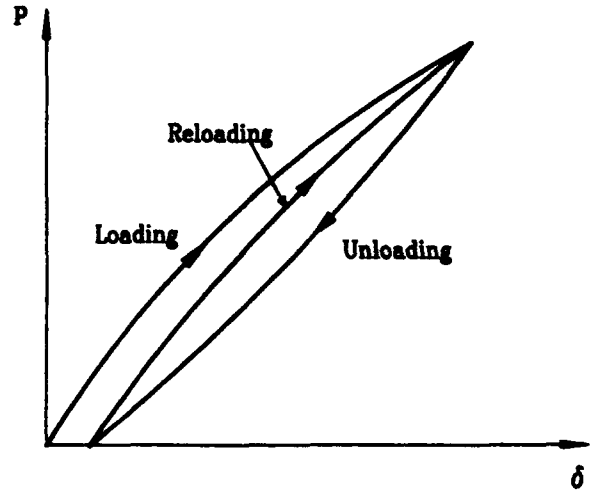
The energy loss in a half-cable subjected to cyclic loading is defined by

$$W_f = \int P d(\delta_3 - \delta_2) \qquad (63)$$

After substitution of δ_2 (Eq.42) and δ_3 (Eq.60), the integration in Eq.64 leads to the following expression

$$W_f = \gamma \frac{(P^{max})^3}{q_f} \qquad (64)$$

where

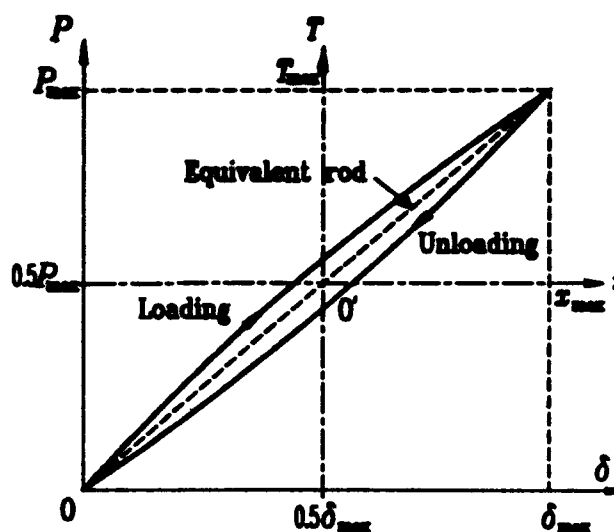$$\gamma = \frac{CD^2}{3 \sin 2\alpha_0} \qquad (65)$$

Figure 5 Hysteretic loop from the cable.

which is a constant characterizing structural and material properties of the cable. Eq.64 indicates that the energy dissipation is proportional to the cube of the load amplitude and in inverse proportion to the interwire friction force, which is a classic energy dissipation pattern in lap joints (Goodman, 1959).

CABLE AS AN EQUIVALENT ROD

As it has been shown above, a model of a cable with finite friction between the wires has nonlinear stiffness characteristics and amplitude-dependent damping properties. In this section a model of a cable as a rod, having material properties such that the properties of a cable and those of the rod are equivalent, is introduced. This is done for the simplest situation when a cable in a system serves as a nonlinear spring and dashpot element. In other words, an equivalent rod can be found by considering oscillations of a single-degree-of-freedom system, shown in Fig.6. The forced oscillation of this system is governed by the equation of motion
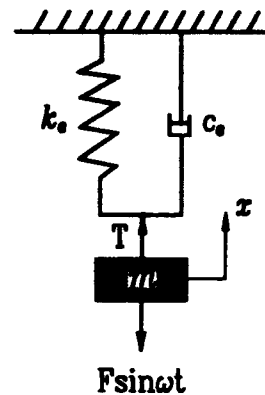
Figure 6 SDOF model.

$$m\ddot{x} + T = F \sin \Omega t \qquad (66)$$

where F and Ω are the amplitude and frequency of excitation, respectively; x is the elongation of the cable, and T is the force in the cable.

Note that in Eq.66, $T=T(x)$. The force-elongation relationship can be found by using Eq.62. However, the latter should be rewritten in a symmetrical form to be used in Eq.66. This is done by using a substitution: $x=\delta-x_{max}$ and $T=P-T_{max}$, in which $x_{max}=\delta/2$ and $T_{max}=P^{max}/2$ (see

Fig.5). As a result, the load-elongation relationship can be written in a form

$$
x = \begin{cases} 2\left[\dfrac{H}{K_n}+\dfrac{CD^2(T+T_{max})}{2q_f\sin 2\alpha_0}\right](T+T_{max})-x_{max} & \text{for loading} \\[4mm] 2\left[\dfrac{H}{K_n}+\dfrac{CD^2(3T_{max}-T)}{2q_f\sin 2\alpha_0}\right](T+T_{max})-x_{max} & \text{for unloading} \end{cases} \tag{67}
$$

From the latter it is found that

$$
T = \begin{cases} -(T_{max}+B_1)+\sqrt{B_1^2+B_2(x+x_{max})} & \text{for loading} \\[4mm] T_{max}+B_1-\sqrt{(2T_{max}+B_1)^2-B_2(x+x_{max})} & \text{for unloading} \end{cases} \tag{68}
$$

where

$$
B_1=\frac{Hq_f\sin 2\alpha_0}{CK_nD^2}, \qquad B_2=\frac{q_f\sin 2\alpha_0}{CD^2} \tag{69}
$$

Now the equivalent linearization technique (Minorsky, 1974) is used to find the equivalent damping, c_e, and stiffness, k_e, coefficients in the linearized equation corresponding to Eq.66. The equivalent linearized equation is

$$
m\ddot{x}+c_e\dot{x}+k_e x=F\sin\Omega t \tag{70}
$$

where

$$
c_e=-\frac{1}{\pi\Omega x_{max}}\int_{-\pi}^{\pi}T(x_{max}\cos\phi)\sin\phi\,d\phi \tag{71}
$$

$$
k_e=\frac{1}{\pi x_{max}}\int_{-\pi}^{\pi}T(x_{max}\cos\phi)\cos\phi\,d\phi \tag{72}
$$

First of all, since $B_1^2 >> 2B_2 x_{max}$[1], it follows from Eq.68 that there exists a nearly linear relation between the load and elongation. When $x=x_{max}$, T will be equal to T_{max} and can approximately be expressed from Eq.68 in a linear form

$$
T_{max}\approx\frac{B_2}{2B_1}x_{max}=\frac{K_n}{2H}x_{max} \tag{73}
$$

where B_1 and B_2 are constants given by Eq.69.

---

[1] It follows from the comparison of the elongations of the cable treated as a solid rod (without slip) and the component of the elongation due to the interwire slip.

The equivalent coefficient of damping is found, by substituting Eq.68 into 71 and again taking into account that $B_1^2 >> 2B_2 x_{max}$, to be

$$c_e = \frac{2 T_{max} B_2}{3\pi\Omega B_1^2}$$ (74)

The latter expression, after substituting T_{max} from Eq.73, is reduced to

$$c_e = \frac{B_2^2 x_{max}}{3\pi\Omega B_1^3}$$ (75)

Similarly, k_e is found from Eq.68 and 72 to be

$$k_e = \frac{B_2}{4} \left(\frac{1}{B_1} + \frac{B_1 B_2}{B_1^2 + B_2 x_{max}} \right)$$ (76)

As it is seen, both c_e and k_e are functions of the amplitude of vibration x_{max}. These functions are shown qualitatively in Figs.7 and 8. However, since x_{max} is very small in comparison with B_1^2, k_e can be approximated by, from Eqs.69 and 76,

$$k_e \approx \frac{B_2}{2B_1} = \frac{K_n}{2H}$$ (77)

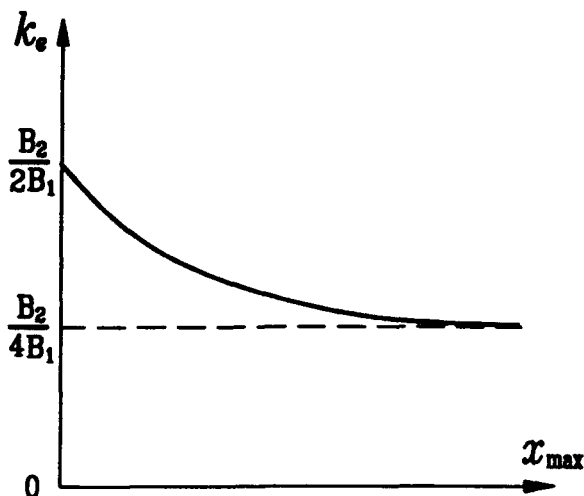The latter shows that k_e is constant and equal to the stiffness of the equivalent solid rod.
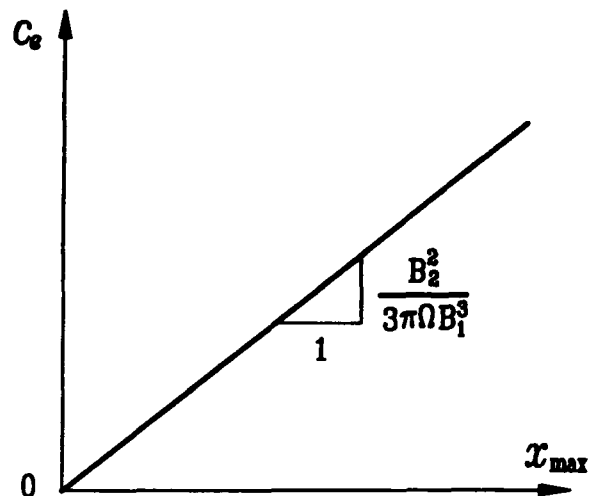

Figure 7   Stiffness-elongation relation.

Figure 8   Damping-elongation relation.

EXAMPLES

In this section some numerical examples are given to demonstrate the theory and present some results. The structural data for a single layered cable given by Utting and Jones (1987) are used, specifically, $n=6$, $R_c=1.97$mm, $R=1.865$mm, $\alpha_0=76.16°$, $H=0.75$m, $E=E_c=197.9$GPa, $v=0.3$. The interwire distributed friction force is assumed to be constant and equal to 1kN/m, except where it is indicated otherwise.

The elongation of the cable during a cycle of loading is shown in Fig.9, where one can see a closed loop formed by the unloading and reloading curves. The enclosed area indicates, therefore, the energy losses during the cycle. The broken line is shown for the case of the friction-free cable (Costello's model). Note that due to the interwire slip the cable's elongation is not equal to zero at the end of the unloading phase.

Fig.10(a)-(c) show the changes of the helix angle during the various phases of the cycle, calculated by using the present theory. In Fig.10(b) one can see that at the end of the unloading phase, when the axial load is equal to zero, the helix angle (shown by the solid line) does not return to a constant value. The reason is that in a slipping region a reversed slip cannot occur until the initial state is restored and only then a slip in an opposite direction becomes possible. This is why the recovering process driven by the elastic strain energy can not be completed, and half of the previous deformation is "locked" in the slipping region.
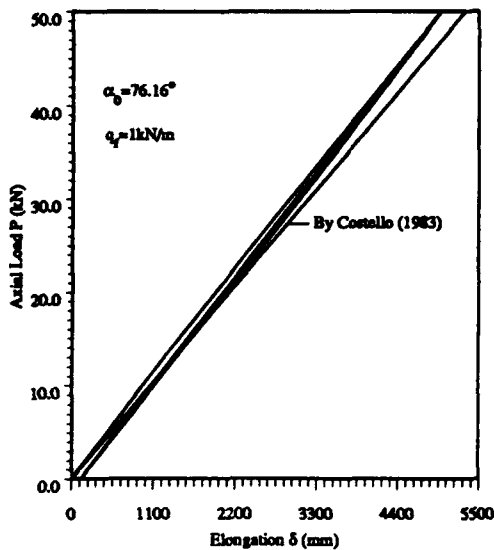
Figure 9 Load-elongation relationship under cyclic loading.
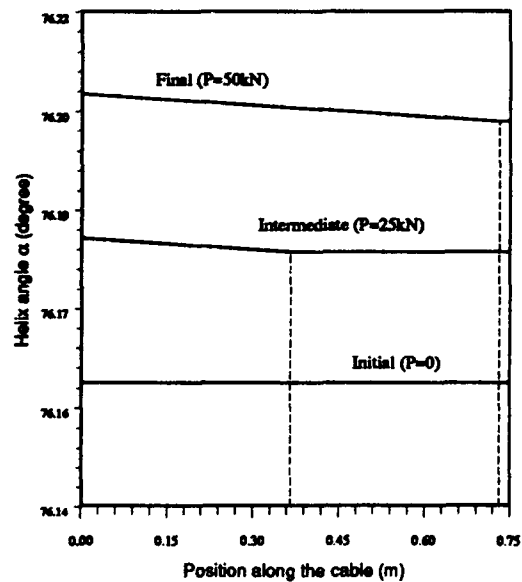
Figure 10a Variability of helix angle during the loading phase of a cycle.

Figure 10b Variability of helix angle during the unloading phase of cycle.

Figure 10c Variability of helix angle during the reloading phase of cycle.

Figure 11 Energy dissipated per cycle—the influence of friction forces.
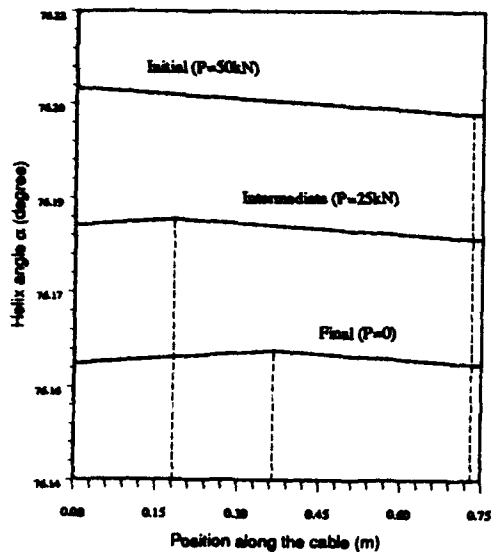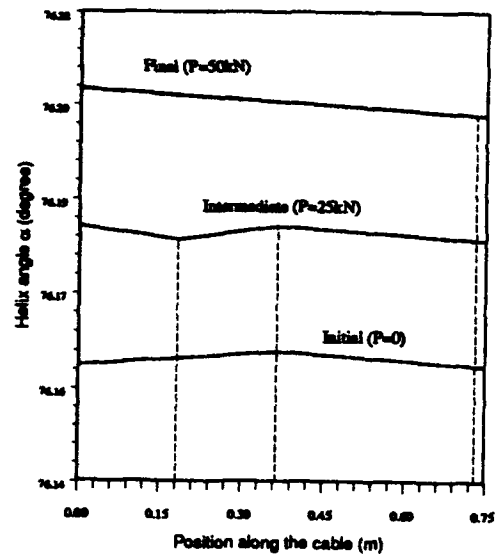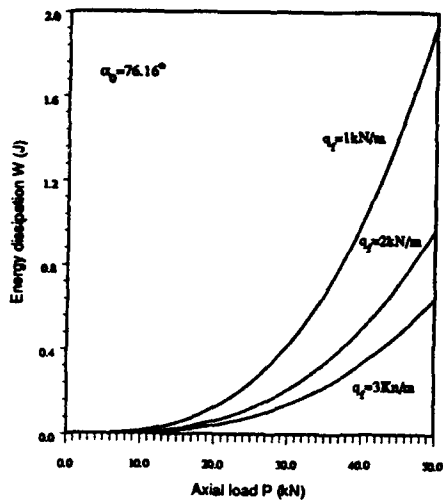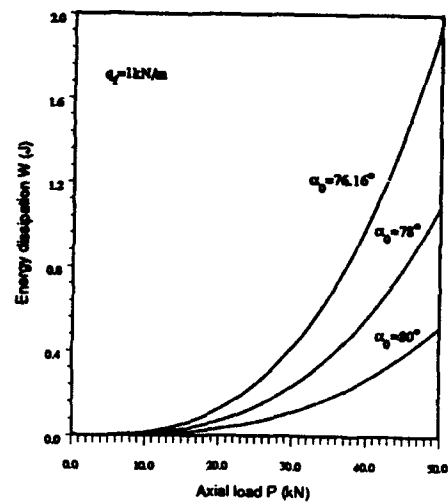

Figure 12 Energy dissipated per cycle—the influence of helix angle.

Eq.64 indicates that the energy dissipation per cycle is proportional to the cube of the axial load and is in inverse proportion to the friction, the type of relationship characterising energy dissipation in the lap joints (Goodman, 1959). In Fig.11 the influence of friction, and in Fig.12 the effect of the initial helix angle on energy losses are shown. Note, that smaller helix angles lead to larger slipping lengths and thus larger energy losses.

CONCLUSIONS

The friction hysteresis in a cable subjected to cyclic tension loading is analytically investigated. The cable model takes into account the friction and slip at the interfaces between wires, and thus it allows analysis of energy dissipation. Explicit load-elongation relationships are derived for the loading, unloading and reloading phases of the cycle. It is shown that these relationship are weakly nonlinear. It is also shown that the unloading and reloading phases of a symmetric cycle form a closed loop characterising the energy losses in a cable. Explicit expression for these losses is obtained, showing they are proportional to the cube of the amplitude of the tensile force and in inverse proportion to the friction forces.

It is suggested that in applications a model of cable as a solid rod with amplitude-dependent damping properties, can be used. Using the equivalent linearization technique, explicit expression for the equivalent coefficient of damping is derived. The given numerical examples show the presence of residual strains in a cyclically loaded cable, and the effect of the magnitude of friction forces and the initial helix angles on the friction hysteresis.

ACKNOWLEDGMENTS

REFERENCES

1.   Claren, R. and Diana, G.(1969), "Mathematical analysis of transmission line vibration," *IEEE Trans. on Power Apparatus and Systems*, Vol.pas-88, No.12, pp.1741-1767.

2.   Goodman, L. E. (1959), "A review of progress in analysis of internal slip damping," **Structural Damping**, Ruzicka, J.E. ed., ASME, New York, pp.35-48.

3.   Hobbs, R. E. and Raoof, M. (1984), "Hysteresis in bridge strand," *Proc Inst Civ Engrs*, Part 2, 77, pp.445-464.

4.   Huang, X. (1992), "Mechanics of Cables with Interwire Friction," Ph.D. dissertation, Department of Mechanical Engineering, The University of Calgary, Canada.

5.   Huang, X. and Vinogradov, O. G. (1992), "Interwire slip and its influence on the dynamic properties of tension cables," *Proc. of the 2nd (1992) International Offshore and Polar Engineering Conference*, Vol.2, pp.392-396, San Francisco, USA, 14-19 June 1992.

6.   Minorsky, N. (1974), **Nonlinear Oscillations**, Basle:Krieger.

7.   Phillips, J. W. and Costello, G. A.(1973), "Contact stresses in twisted wire cables," *J. of Eng. Mech.*, ASCE, Vol.99, pp.331-341.

8.   Utting, W.S. and Jones, N.(1987),"The response of wire rope strands to axial tensile loads — part

I: Experimental results and theoretical predictions," *Int. J. Mech. Sci.*, 29,pp.605-619.

9.   Vinogradov, O. G. and Atatekin, I. S. (1986), "Internal friction due to twist in bent cable," *J. of Eng. Mech.*, ASCE, 112(9), pp.859-873.

10.   Vinogradov, O. G. and Huang, X. (1991),"Dry friction losses in an axially deformed strand cable," *Proc. of 1991 ASME Pressure Vessel & Piping Conf.*, PVP-Vol.211, San Diego, USA.

11   Vinogradov, O. G. and Pivovarov, I.(1986), "Vibration of a system with non-linear hysteresis," *J. of Sound and Vibration*, Vol.111(1), pp.146-152.

12.   Vranish, J.M. (1990), "Advanced mechanisms for robotics," NASA *Conference Publication*, 3109, Vol.1, **Technology 2000**, November 27-28.

13.   Yu, A. (1952),"Vibration damping of stranded cable," *Proc. Soc. Exp. Stress Analysis*, 9, 141-158.

INCREASING THE IMPACT ENERGY ABSORPTION OF CONTAINMENT STRUCTURES WITH VISCOELASTIC MATERIALS

R. D. Holm
S. S. Sattinger
M. A. Mendelsohn

Westinghouse Science and Technology Center[*]

ABSTRACT

Measurements performed with a unique dynamic bending test apparatus showed that steel ring specimens with a constrained viscoelastic damping material absorbed two times more impact energy than comparable rings of plain steel for a given amount of permanent set. Ring specimens with an unconstrained viscoelastic damping material absorbed four times more impact energy than plain steel rings for a given amount of permanent set. Further increases in absorption may be attainable through improvements in material property combinations. These measurements of energy absorption demonstrate that viscoelastic-layered metal construction could be especially well suited for shell structures such as ships, railroad tank cars, tank trucks, and other containers used for the transportation or storage of hazardous substances. The energy absorption benefits of adding constrained or unconstrained viscoelastic layers onto existing structures in retrofit applications is clear. For new construction, optimization studies with constraints such as equal weight, equal cost, or equal volume will be required to compare the energy absorption of damped structures versus that of thicker, undamped structures. A major benefit that will be more difficult to quantify is the puncture protection of the container shell that will be provided by the external damping layers.

*1310 Beulah Road
Pittsburgh, PA 15235
(412) 256-1327

Introduction

Hazardous material spills due to derailment, collisions, and break-ups of railroad cars, trucks, and ships have become a concern of both the environmentalist and the average citizen. Carriers of hazardous materials must improve the impact protection for their hazardous material containers. Cylindrical shells are the basic structural components of many of the containers used for shipping and storing these substances. Needed are new structural materials, design configurations, and manufacturing methods for shell structures having increased impact energy absorption so that these containers will be more likely to withstand accidents without spillage.

The use of viscoelastic materials and damping treatments to reduce vibration and structureborne noise is well-known, and their use for controlling earthquake-induced vibrations in structures is also being explored. Vibrational energy is absorbed passively in these treatments by oscillatory strains that occur in layers of these lossy materials. However, little work has been reported regarding viscoelastic material applications for energy absorption during impact transients. We speculated that with appropriate choices of materials and dimensions, large overall increases in impact energy absorption might be obtained by dissipating the energy in viscoelastic material layers that are well-bonded to the main structural layers. Because most present-day hazardous-substance containers are fabricated from ductile metals, their energy absorption is determined by their behavior in the post-yield range of strains.

Thus the objective of this investigation was to evaluate the feasibility of substantially improving the impact energy absorption of shell-like containment vessels using suitable layers of viscoelastic materials in combination with main structural layers of ductile metals. Our approach was as follows:

- Using simple calculational models, examine the effect of damping additions on load-deflection profiles for pulse-like elastic/plastic bending.
- Develop procedures for installing the viscoelastic layers with good mechanical bonding to the main structural layers.

- In lieu of detailed analytical predictions, perform experiments on simple ring specimens to further quantify gains in impact energy absorption and to provide data for possible future use in validating detailed modeling.
- Compare the measured energy-absorption performance of specimens having free-layer and constrained-layer configurations.

In this paper we show the promising results on impact energy absorption that we obtained by comparing transient time-stepping response solutions for simple dynamic models of damped and undamped elastic/plastic beam bending. We describe the configurations of three different types of ring specimens (one undamped and two damped specimen types) which we constructed to evaluate the energy absorption experimentally, and we show how pulse-transient bending loads were applied to these specimens using our unique dynamic bending test apparatus. We describe the two Westinghouse-formulated polyurethanes which we used as damping materials, including a lower-modulus material for constrained damping layers and a higher-modulus material for unconstrained damping layers, and the procedure we used for casting these layers in place. Finally, we present the measured load-deflection results for the three different types of specimens for varying amounts of initial kinetic energy, and we draw conclusions about the effectiveness of the damping layers that we tested.

Simplified Dynamic Models of Elastic/Plastic Beam Bending

Yielding and Plastic Hinge Formation

To gain some initial insights into the issues of applying damping materials to ductile structures which undergo yield under impact loadings in accident situations, we considered the case of a beam in bending. Figure 1 shows the elastic strain and stress distribution through the cross section of a beam under constant-moment bending load. As the load on the beam increases the strain and stress also increase, but as long as the stress (or strain) is less than the yield stress (or strain), the beam will return to its unloaded deflection when the load is removed. The elastic limit is attained when the highest-stressed fiber just

begins to strain inelastically. The moment, M_e, at which the highest stressed fiber of the beam will just begin to strain inelastically is[1]

$$M_e = \frac{s_e I}{c} \qquad (1)$$

where s_e = Yield stress for the material, psi

I = Moment of inertia for the beam cross section, in^4

c = Half height of the beam, in
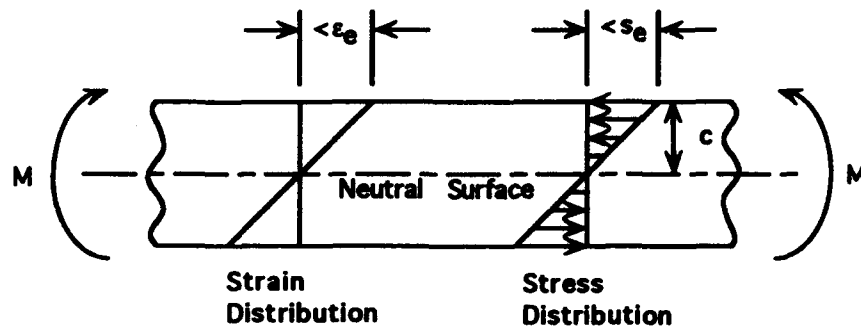
Fig. 1 — Elastic stress and strain in a beam subjected to bending.
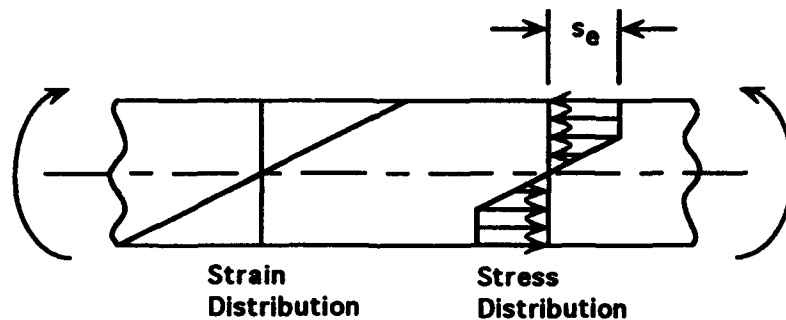
Fig. 2 — Inelastic stress and strain in a beam subjected to bending.

Figure 2 shows the strain and stress distribution in the cross section of a beam subjected to a bending moment which causes inelastic (plastic) strain in the outer fibers. We assume a perfectly plastic beam material which has the same stress-strain curve in tension and compression. The beam will not return to its unloaded deflection when the load is removed. If the beam is further loaded, it will exhibit plastic deformation over its entire cross section (see Fig. 3). Reference 2 shows that a rectangular beam

will develop a so-called plastic hinge or yield hinge, when the moment reaches 1.5 M_e. This limit on load-carrying capability occurs when the material becomes fully plastic over the entire cross section.
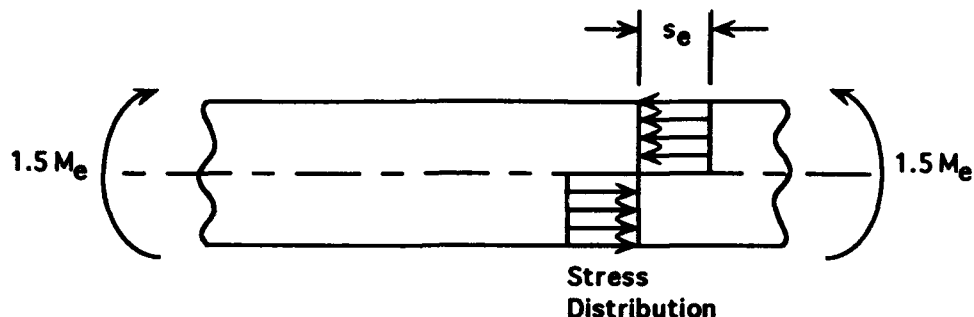
Fig. 3 — Stress distribution of a plastic hinge.

Load-Deflection Relationship for a Pinned-Pinned Beam

As an example of a beam structure in which the bending-moment loading varies from location to location within the structure, Figure 4 shows a pinned-pinned beam with a rectangular cross section which is loaded statically at mid span with a load P. The highest stress will occur at mid span. If the load is below the elastic limit, the deflection, y, at mid span is[3]

$$y = \frac{1}{48} \frac{PL^3}{EI} \qquad (2)$$

where L = beam length, in
      E = Young's modulus, psi

If the load is above the elastic limit and below the plastic limit, the deflection, y_p, at mid span under monotonically increasing static load is[4]

$$y_p = \frac{4M_e^3}{3P^2EI} \left[5 - \frac{2}{\sqrt{2}} \left(3 + \frac{PL}{4M_e} \right) \sqrt{\frac{3}{2} - \frac{PL}{4M_e}} \right] \qquad (3)$$

When the load reaches the plastic limit a plastic hinge occurs at the middle of the beam and it collapses.

$$b = 2.0 \text{ in}$$
$$L = 4.52 \text{ in}$$
$$c = \frac{t}{2} = \frac{0.11}{2} = 0.055 \text{ in}$$
$$I = \frac{bt^3}{12} = 2.218 \times 10^{-4} \text{ in}^4$$
$$E = 30 \times 10^6 \text{ psi}$$
$$s_e = 70,000 \text{ psi}$$
$$M_e = \frac{s_e I}{c} = 282.3 \text{ in-lb}$$

$$P_e = \frac{4M_e}{L} = 249.9 \text{ lb}$$
$$y_e = \frac{1}{48}\frac{P_e L^3}{EI} = 0.0737 \text{ in}$$
$$M_p = 1.5 M_e = 423.5 \text{ in-lb}$$
$$P_p = \frac{4M_p}{L} = 374.7 \text{ lb}$$
$$y_p = \frac{4M_e^3}{3P^2 EI}\left[5 - \frac{2}{\sqrt{2}}\left(3 + \frac{PL}{4M_e}\right)\sqrt{\frac{3}{2} - \frac{PL}{4M_e}}\right] = 0.1638 \text{ in}$$

Fig. 4 — Pinned-pinned beam loaded at mid span.

Shown in Fig. 4 are the loads and mid-span deflection corresponding to the formation of a central plastic hinge in a particular pinned-pinned beam. This beam is a flattened and foreshortened version of the undamped ring specimen which is described in a later section of this paper.
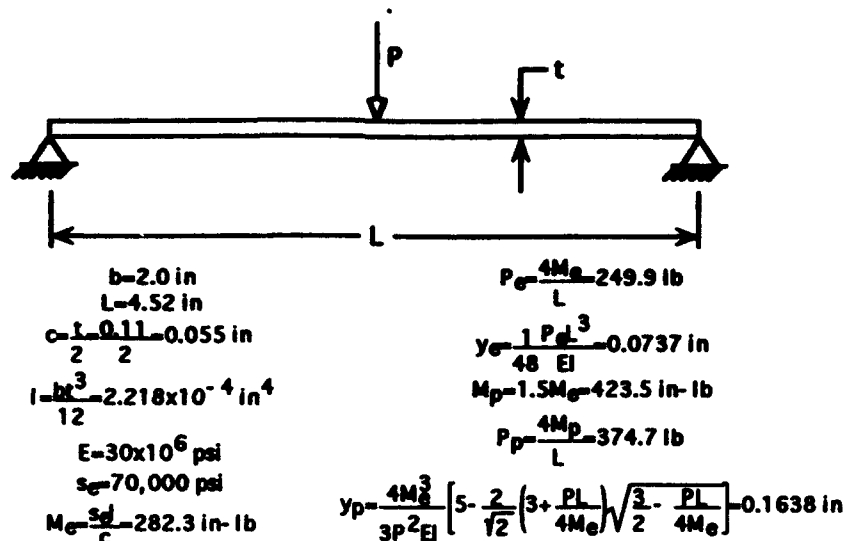
Simple Dynamic Bending Models for a Mass-Loaded Beam

The foregoing descriptions of elastic/plastic behavior apply to beams under monotonically increasing, statically applied loading. Dynamic loading brings the complications of distributed inertia forces and loading reversals. Major complexity would be encountered in making a detailed representation of a damped beam under elastic/plastic bending because of the concentration of strains in those regions of the beam that are beyond the elastic limit.

Because our goal was to make an initial evaluation of impact energy absorption by bonded layers of viscoelastic materials, we needed to generate load-deflection profiles for damped and undamped versions of a simple dynamic model that would take account of elastic/plastic bending. The approach we took was to model the case of a point mass suspended at the center of the pinned-pinned beam using the very simple models shown schematically in Fig. 5. Stiffness K_B in each of these models is a deflection-dependent, effective beam stiffness that is determined as outlined in

the next paragraph. The series spring and dashpot in Fig.
5(b) provide a simple representation of a constrained-layer
damping treatment that provides a beam loss factor of 0.29
at the 23-Hz damped natural frequency of the system with the
beam vibrating elastically. Again for simplicity, we
ignored the effect of plastic strain concentration in the
beam on the behavior of the damping treatment. The value
of the point mass was very large in comparison to that of
the beam itself and corresponds to the loader mass of the
dynamic bending tester, which is described later. This
choice enabled us to represent the beam itself as an
elastic/plastic spring without concern for beam modes of
vibration. The mass is given an initial velocity,
corresponding to an initial kinetic energy, which, if
sufficiently high, causes plastic deformation in the beam.

$M = 0.179 \frac{lb\,sec^2}{in}$ (W = 69.1 lb)

K_B defined in text

$K_D = 5,000 \frac{lb}{in}$

$C = 7.76 \frac{lb\,sec}{in}$

a) Undamped beam   b) Damped beam
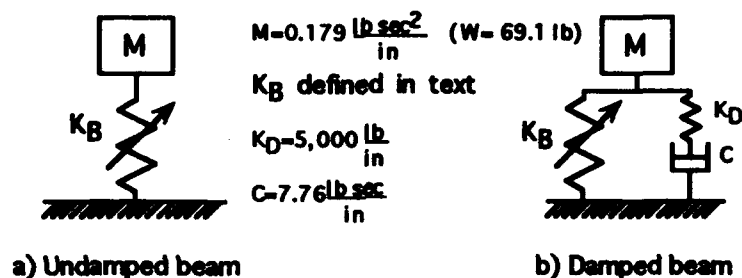
Fig. 5 - Simple dynamic models of a mass suspended on an
         elastic/plastic, simply supported beam.

Calculated Effects of Damping on Energy Absorption in Beam Bending

To calculate the response of the simple beam model,
we used the Newmark Beta = 1/4 or constant-average-
acceleration method given in Reference 5. We repetitively
evaluated the deflection-dependent stiffness,

$$K_B = \frac{\Delta P}{\Delta y} \qquad (4)$$

by alternatively using Equation (2), Equation (3) with
spread-sheet solver routine, or zero stiffness (plastic
hinge), as appropriate.

Fig. 6 plots the instantaneous total reaction force
acting on the suspended mass versus its displacement during
the portion of the transient up to the first zero-crossing
of force for both the undamped and the damped configuration.

The area under the load-deflection curve for the undamped
beam represents the energy absorbed by plastic deformation,
and the area for the damped beam is the combined total of
the energies absorbed by the damping treatment and by
plastic deformation. For nearly identical values of
permanent set and with a smaller amount of peak deflection,
the damped beam absorbed significantly more kinetic energy
than did the undamped beam.

The simple model of the damped system provided
insight as to how a damping treatment could become more and
more effective in absorbing energy as a structure goes
progressively further into yield. As the effective beam
stiffness, K_B, becomes smaller with further progression into
the plastic range, the system begins to behave as a point
mass suspended totally on the damping treatment, i.e., the
stiffness K_B no longer dilutes the system loss factor to the
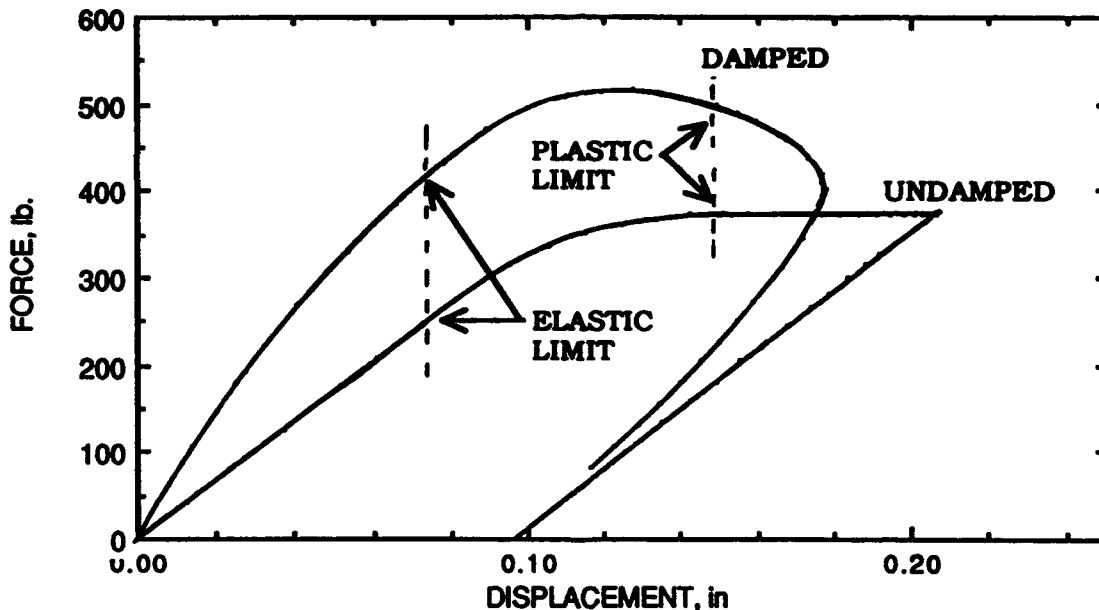extent that it did in the elastic range.

Fig. 6 - Load-deflection results for the dynamic models
shown in Fig. 5.

Design of Ring Bending Specimens

Although the beam example provided a good
illustration of impact energy absorption in damped, ductile
structures undergoing large deformations, we felt that
cylindrical rings would be a better choice for experiments

to represent the responses of containers and other shell-like structures.

Yielding and Plastic Hinge Formation in Rings

The onset of yielding and plastic deformation in rings is somewhat more involved than for beams. Fig. 7 shows a ring with a diametral load P. The highest negative moment occurs under the load (Points 1 and 2 in Fig. 7) and is given by[6]

$$M = -0.159 \, PD \qquad (5)$$

where D is the mean diameter of the ring. The highest positive moment is at 90° to the load (Points 3 and 4 in Fig. 7) and is given by[6]

$$M = 0.091 \, PD \qquad (6)$$

As the load increases, the stress at the load reaches the elastic limit. With further increase in the load, a plastic hinge will develop under the load P_p and the elastic limit will be reached 90° to the load. With plastic hinges at points 1 and 2 the ring will not be as stiff but it will not collapse. The ring will collapse when plastic hinges also develop at the 90° points. The collapse load P_c is given by[7]

$$P_c = \frac{8M_p}{D} \qquad (7)$$

Shown in Fig. 7 are the loads corresponding to the formation of the initial plastic hinge and the collapse of a particular ring; this is the undamped specimen for the ring bending experiments which we describe next.

Description of Test Specimens

We evaluated the energy absorption of a set of steel rings having no damping material and of sets of rings having both unconstrained- and constrained-layer damping configurations. The base structure of the unconstrained-layer rings was kept identical to the undamped rings to enable direct performance comparisons to be made. Being of double-wall construction, the design of the constrained-

layer rings had to strike a compromise between the
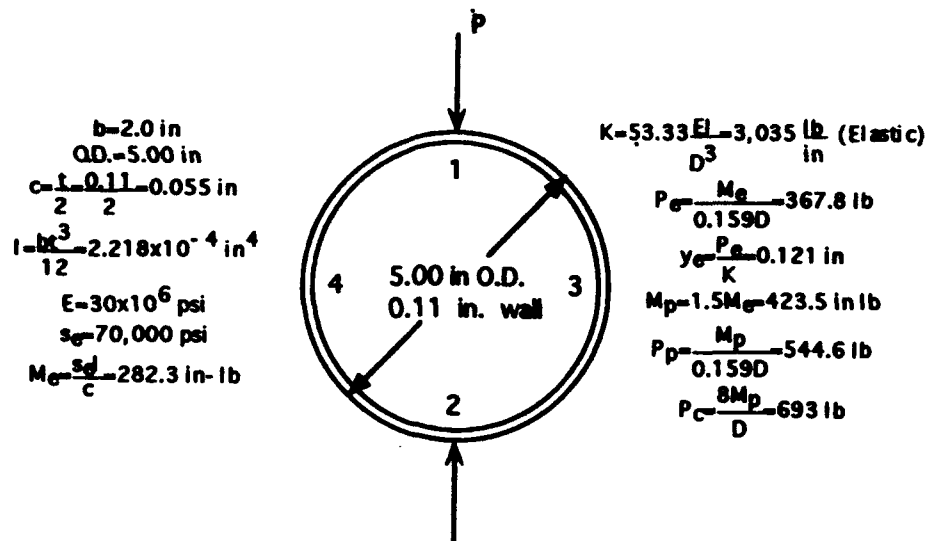conflicting criteria of maintaining the same global damping

$b = 2.0$ in
$O.D. = 5.00$ in
$c = \frac{t}{2} = \frac{0.11}{2} = 0.055$ in
$I = \frac{bt^3}{12} = 2.218 \times 10^{-4}$ in^4
$E = 30 \times 10^6$ psi
$s_\sigma = 70,000$ psi
$M_\sigma = \frac{S_\sigma I}{c} = 282.3$ in-lb

$K = 53.33 \frac{EI}{D^3} = 3,035 \frac{lb}{in}$ (Elastic)
$P_\sigma = \frac{M_\sigma}{0.159D} = 367.8$ lb
$y_\sigma = \frac{P_\sigma}{K} = 0.121$ in
$M_p = 1.5 M_\sigma = 423.5$ in lb
$P_p = \frac{M_p}{0.159D} = 544.6$ lb
$P_c = \frac{8M_p}{D} = 693$ lb

Fig. 7 — Ring loaded across diameter.

stiffness as for the undamped rings (i.e., simultaneous
bending about a common diametral axis) and maintaining the
same local bending stiffness (i.e., combined stiffnesses of
the two walls in bending about their individual mid-wall-
thickness axes). The dimensions chosen for the specimens
are shown in Figs. 7 through 9. Target values for the
storage moduli of the viscoelastic materials were
established by assuming that the response to a nearly half-
sine loading pulse could be approximated by applying damping
treatment design formulas for steady-state sinusoidal
vibration at the corresponding frequency condition. A
decision to use two different viscoelastic materials (a
softer material for the constrained-layer specimens and a
harder material for the unconstrained specimens), both of
which were polyurethanes formulated by Westinghouse, arose
from these calculations.

The two-inch-long ring test specimens were fabricated
from available thicknesses of cold drawn, low carbon,
seamless mechani _ tubing. The yield stress for the tubing
is listed as 70,000 psi. The undamped ring test specimens
(shown in Fig. 7) had a 5.00 in. O.D. and a 0.11 in. wall
thickness. The plain steel ring has a calculated stiffness
of 3,035 lb/in. The calculated collapse load of the plain
steel ring, assuming perfect plastic material and a yield
limit of 70,000 psi, is 693 lb. The damped ring specimens

were cut from tubing subsequent to the molding operations described in the next section.

Description of the Viscoelastic Materials and the Molding Process

Molds

The constrained-layer ring specimens were cut from two concentric steel tubes which functioned as molds during the casting process, forming an annular space for the softer polyurethane damping resin. A base plate with grooves supported the tubes in an upright position and spacers at the top maintained their parallel alignment. Fig. 8 shows the constrained system in which the cast polymer is adhered to both rings.

In the case of the unconstrained system, a special outer mold was coated with mold release, and was split and held together by bolted longitudinal lips so as to facilitate its removal from the harder polyurethane casting. Fig. 9 shows a cross sectional view of the unconstrained coating in which the cast polyurethane is adhered only to the inner tube.

In order to provide for good adhesion of the resin, the outer surface of the inner tube for both the constrained and constrained specimens and the inner surface of the outer tube for the constrained system were sandblasted, cleaned with toluene, and stored under nitrogen until use.

A threaded hole in the bottom of the outer tube for both types of molds provided the connection for the piston driven resin injector. The piston required only hand pressure to force the liquid resin into the mold.

Casting Process

The polyurethanes employed in both the constrained and unconstrained layer damping were prepared from specially formulated p,p'-diphenylmethane diisocyanate (MDI) terminated polyether based prepolymers. Although their chemical formulations differed, both prepolymers were coreacted with the same chain extending polyol mixture. The castings were prepared by adding with stirring and under a

nitrogen atmosphere the extender solution, which was at room
temperature, to the prepolymer which was at approximately
80°C. After thorough mixing for one minute the material was
evacuated at 2-5 Torr for about three minutes, at which time
the foaming and bubbling had subsided. The reacting mixture
was then injected into the bottom of the cylindrical mold,
which had been preheated to 80°C, until the annular space
had been filled. This was followed by casting a flat sheet
of material, 0.080 in. thick, which was used to provide
specimens for dynamic mechanical properties testing. The
castings were cured for 16 hr at 80°C and then demolded.

Dynamic Properties

The dynamic mechanical properties were measured in
shear with a Rheometrics Mechanical Spectrometer. Frequency
scans of the shear moduli and loss factors of the two
materials are shown in Figs. 10 and 11 and a temperature
scan of the constrained layer specimen is shown in Fig. 12.
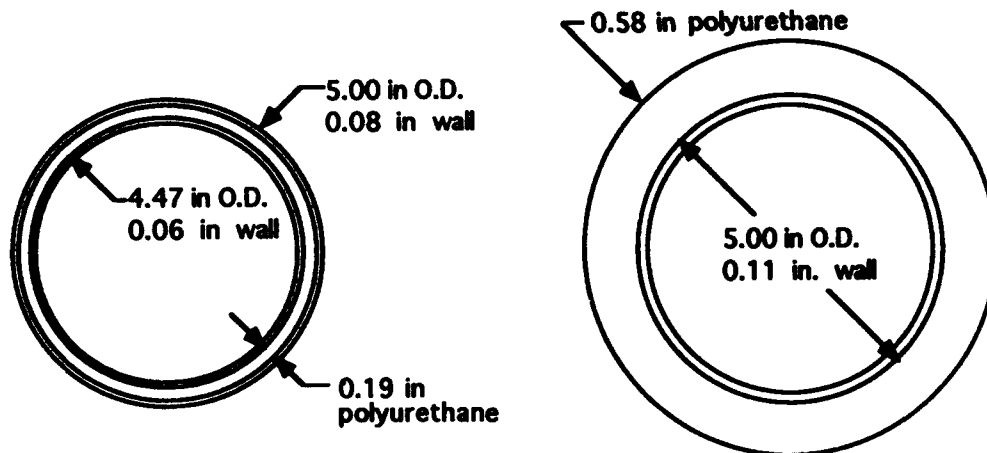
Fig. 8 — Constrained layer   Fig. 9 — Unconstrained layer
     damping ring test   damping ring test
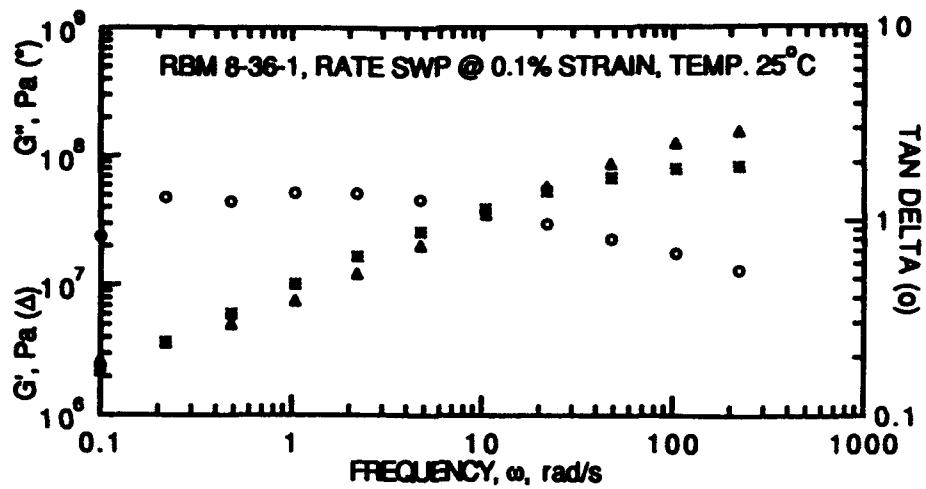   specimen.   specimen.

Fig. 10 — Effect of frequency on the shear properties of
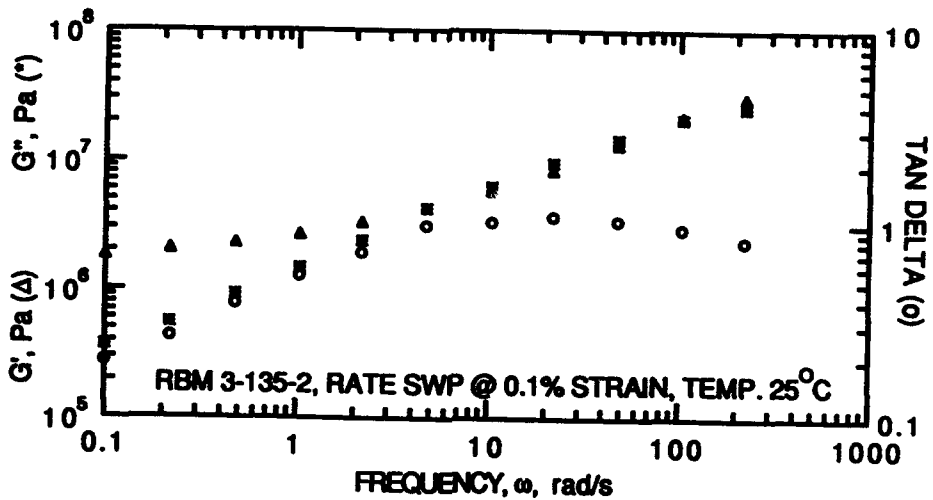the polyurethane used in the unconstrained layer.

Fig. 11 — Effect of frequency on the shear properties of
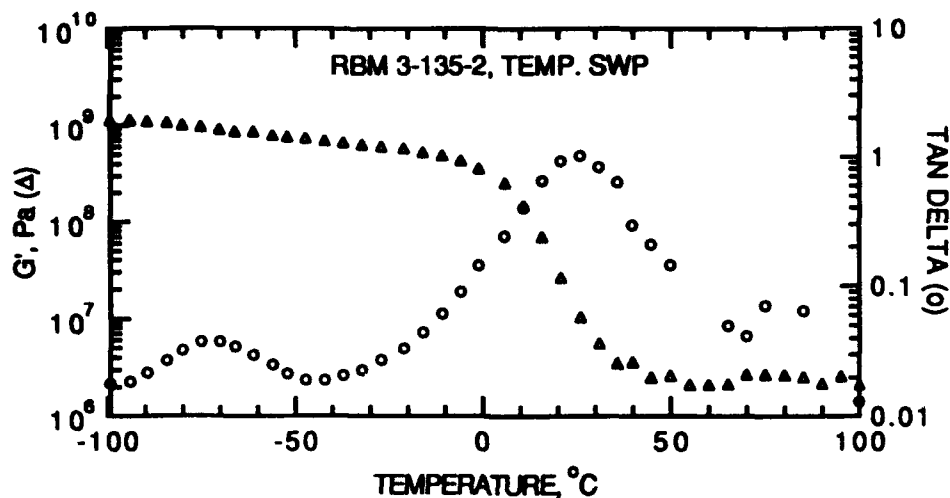the polyurethane used in the constrained layer.

Fig. 12 — Effect of temperature on the shear properties of
the polyurethane used in the constrained layer.

Specimen Test Procedure and Test Results

The ring specimens were tested in a unique dynamic
bending test apparatus that is shown in Fig. 13 and is
described in Reference 8. A schematic of the test apparatus
is shown in Fig. 14. The transfer of kinetic energy from
the drop weight, or exciter mass, to the intermediate or
loader mass is smoothed by means of a rebound spring
inserted between the two masses. The loader mass, after
receiving kinetic energy from the exciter mass, temporarily
interacts with the specimen as a mass-spring oscillator.
Thus, the load rise-time on the specimen is controlled by
the mass-spring oscillator. The peak strain is directly
controlled by choice of the exciter mass drop height and
weight. The exciter mass and loader mass are guided
laterally by ball bushings and cylindrical rails. Vertical
motions are arrested by a pneumatically actuated brake plate
that bears against cemented-on brake shoes.

The test specimen is mounted on a force gage which
measured the impact force. A linear variable differential
transformer (LVDT) measured the deflection of the ring
diameter. The force gage and LVDT signals were captured,
stored, analyzed and plotted with a Norland Digital
Oscilloscope.

The test specimens were given light, medium and heavy
impacts. An attempt was made to have 0.02 in. permanent

Fig. 13 — Dynamic bending tester.

GUIDE RAIL

EXCITER MASS

LOADER MASS
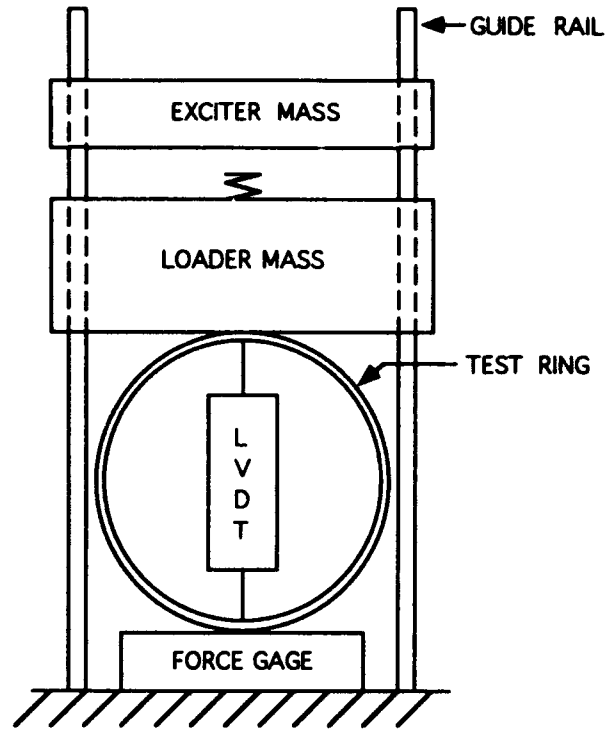
TEST RING

L V D T

FORCE GAGE

Fig. 14 — Principle of operation of the dynamic tester.

Fig. 15 — Constrained layer damping ring test specimen after heavy impact.

Fig. 16 — Unconstrained layer damping ring test specimen after heavy impact.

deformation of the diameter after the light impact, .25 in. deformation after the medium impact, and 0.5 in. deformation after the heavy impact. Figs. 15 and 16 show the constrained and unconstrained rings, respectively, after the heavy impact test. A new specimen was used for each impact.

The loading transients approximated half-sine pulses having roughly 20 Hz frequency content. Typical impact load-deflection curves for the heavy impacts of the undamped specimen and the specimens with constrained layer and unconstrained layer damping are shown in Fig. 17. The area under the load-deflection curve was measured to determine the impact energy absorbed by each specimen. The test results are summarized in Table 1 and the impact energy absorbed versus permanent deformation is plotted in Fig. 18.

Conclusions

The constrained-layer-damped specimens had approximately double the impact energy absorption of the undamped ring test specimen for the same permanent deformation. The unconstrained layer specimens had approximately four times the impact energy absorption of the undamped ring test specimen for the same permanent deformation.

The material loss factors and possibly the moduli of the selected polyurethane damping materials under the conditions of these tests do not necessarily represent the most favorable property combinations. Additional impact energy absorption may be obtained if the desired viscoelastic material characteristics are better matched.

This approach to increasing impact energy absorption is feasible. Applications could include ships, railroad tank cars, tank trucks, and other containers for the transportation or storage of hazardous substances. Our testing made no attempt to optimize the energy absorption per pound, per volume or per dollar spent. We envision that this kind of systems-oriented optimization would best govern the damping design for containment shells. A major benefit that will be more difficult to quantify is the puncture protection of the container shell provided by the external damping layers.

Good adhesive bonding of the viscoelastic materials to the structural layers will be vital to the success of these applications. We have demonstrated a viable procedure for casting these materials in place with excellent bond strength.
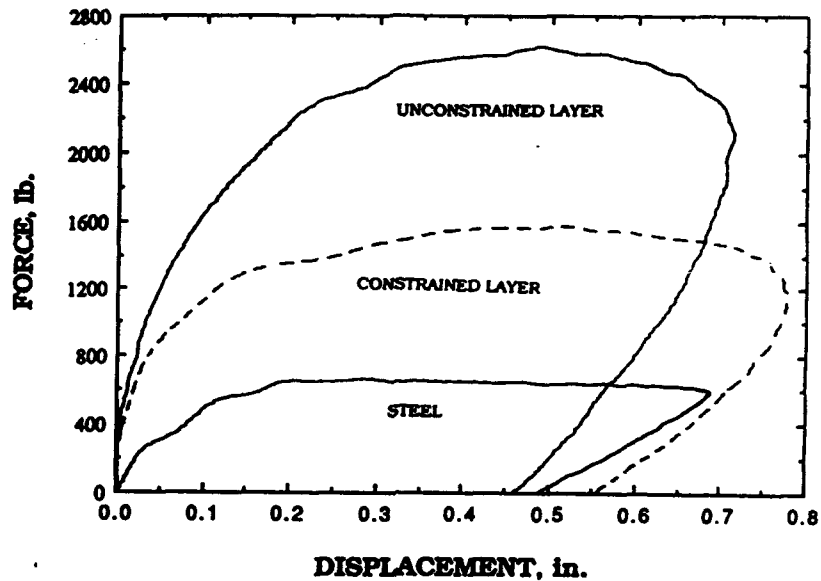
Fig. 17 — Load-deflection for the ring test specimens with a heavy impact.
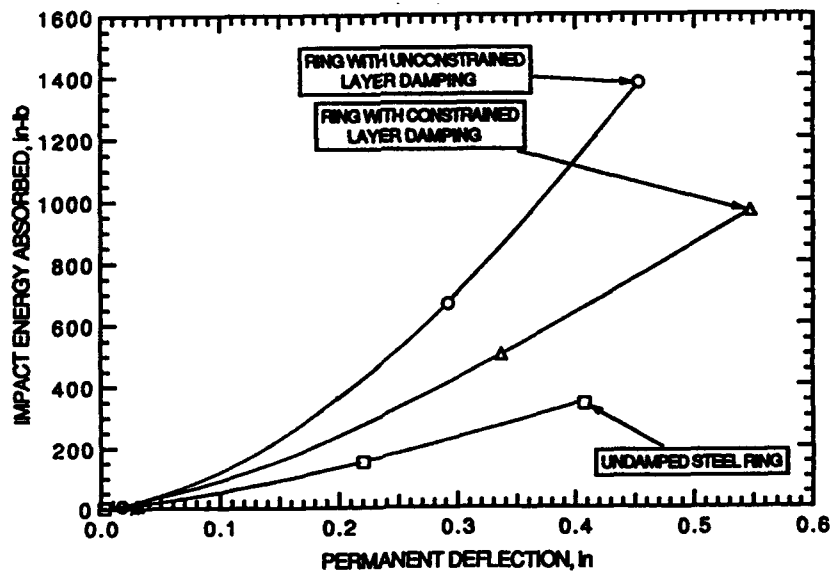
Fig. 18 - Impact energy absorption vs. permanent deformation of damped and undamped rings.

Table 1 - Results of the impact energy absorption tests on the ring specimens.

SPECIMEN	STEEL	CONS. LAYER	UNCONS. LAYER
LIGHT IMPACT			
INITIAL POTENTIAL ENERGY, in-lb	10.75	10.75	10.75
PEAK FORCE, lb.	257.1	284.6	384.6
PEAK DISP., in.	0.071	0.063	0.048
DISP. @ FIRST FORCE ZERO, in.	0.003	0.031	0.018
IMPACT ENERGY ABSORBED, in-lb	1.27	8.78	8.22
MEDIUM IMPACT			
INITIAL POTENTIAL ENERGY, in-lb	191.9	539.5	747.0
PEAK FORCE, lb.	638.0	1265.0	1985.0
PEAK DISP., in.	0.391	0.538	0.487
DISP. @ FIRST FORCE ZERO, in.	0.220	0.337	0.292
IMPACT ENERGY ABSORBED, in-lb	152	501	665
HEAVY IMPACT			
INITIAL POTENTIAL ENERGY, in-lb	373.5	996.0	1481.0
PEAK FORCE, lb.	646.5	1549.0	2598.0
PEAK DISP., in.	0.684	0.780	0.710
DISP. @ FIRST FORCE ZERO, in.	0.408	0.548	0.453
IMPACT ENERGY ABSORBED, in-lb	341	965	1377

References

1. Seely, F. B. and Smith, J. O., Advanced Mechanics of Materials, Second Edition, John Wiley & Sons, New York, pp. 529 (1952).

2. Ibid., pp. 533.

3. Ibid., pp. 445.

4. Ibid., pp. 547.

5. Craig Jr., R. R., Structural Dynamics, John Wiley & Sons, New York, pp. 154-160, (1981).

6. Roark, R. J., Formulas for Stress and Strain, Fourth Edition, John Wiley & Sons, New York, pp. 172, (1965).

7. Seely, op. cit., pp. 577.

8. Sattinger, S. S., "A Dynamic Bending Test Method for Generator-coil Insulation," Experimental Techniques, pp. 18-23, (August 1987).

The Effect of Viscoelasticity on the Performance of Reaction Mass Actuators

by

Lawrence A. Bergman, Harry H. Hilton, and Tsu-Chin Tsao
University of Illinois
Urbana, Illinois, USA 61801

1.0 INTRODUCTION

Recently Pang, Tsao and Bergman, 1992, developed exact transfer functions for elastic and single Kelvin model Euler-Bernoulli beams with external viscous (air) damping in order to study active and passive damping and the effect of their interaction upon performance. In particular, a cantilevered beam carrying a reaction mass actuator at its free end was analyzed. Their analysis is now generalized by using the elastic-viscoelastic analogy (Christensen, 1982; Hilton, 1964) to extend the formulation to include generalized linear viscoelastic behavior. This removes the severe restrictions inherently imposed by a single Kelvin model (SKM) viscoelastic representation through the introduction of a generalized Kelvin model (GKM) material characterization and makes the present analysis applicable to all real linear viscoelastic materials. Two related problems are discussed. The first addresses the identification of the coefficients of the viscoelastic damping terms in the governing equation of motion from vibration test data. The second is the performance of a co-located sensor/reaction mass actuator on a viscoelastic Euler-Bernoulli beam.

2.0 ANALYSIS

Consider an elastic Euler-Bernoulli beam with viscous damping due to its motion in air, shown in Fig. 1. Its governing equation has been derived by Pang, *et al.*, 1992, in nondimensional form as

$$\frac{\partial^4 w^e}{\partial x^4} + a_0 \frac{\partial w^e}{\partial t} + \frac{\partial^2 w^e}{\partial t^2} = f(x, t) \tag{1}$$

where a_0 is the distributed viscous damping coefficient and f is the forcing function. The deformation of the elastic beam neutral axis is represented by $w^e(x, t)$. The Laplace transform of (1) yields

$$\frac{\partial^4 \overline{w}^e}{\partial x^4} + (a_0 s + s^2) \overline{w}^e = \overline{f}(x, s) \tag{2}$$

A general viscoelastic material can be readily described by an equivalent viscoelastic modulus $\overline{E}$ in the Laplace s-plane in terms of the generalized Kelvin model (GKM) material representation. Application of the elastic-viscoelastic analogy requires the substitution of $E_0 \overline{E}$ for E_0 in the dimensional governing equation, leading to the nondimensional equation for a general viscoelastic material,

$$\frac{\partial^4 \bar{w}}{\partial x^4} + \bar{\lambda}\bar{w} = \frac{\bar{f}}{\bar{E}} \tag{3}$$

Consistent with the notation of Pang, *et al.*, 1992, the complex eigenvalues $\bar{\lambda}$ now become

$$\bar{\lambda} = \left(-\frac{a_0 s + s^2}{\bar{E}}\right)^{1/4} \tag{4}$$

with the attendant boundary conditions and transfer functions given by substitution of (4) into the corresponding Pang, *et al.*, 1992, elastic results in the Laplace domain.

The transfer function for a GKM viscoelastic cantilevered beam with a co-located actuator/sensor pair placed at its free end becomes

$$G(1,1;s) = \frac{1}{\bar{E}}\left(\frac{\sin\bar{\lambda}\cosh\bar{\lambda} - \cos\bar{\lambda}\sinh\bar{\lambda}}{\bar{\lambda}^3(1 + \cos\bar{\lambda}\cosh\bar{\lambda})}\right) \tag{5}$$

The Laplace transform variable s is complex and can be represented by

$$s = b + i\omega \tag{6}$$

where b and ω are real, and ω is the motion frequency. When $b = 0$, the equivalent viscoelastic modulus $\bar{E}$ reduces to the complex modulus $\tilde{E}$ with

$$\tilde{E}(\omega) = E_R(\omega) + iE_I(\omega) \tag{7}$$

where the real functions E_R and E_I are, respectively, the storage and loss moduli. A GKM modulus can readily be represented by a Prony series in the time plane which has a Laplace transform $\bar{E}$ and a Fourier transform $\tilde{E}$ such that

$$\bar{E}(s) = E^{(0)} + \sum_{n=1}^{N}\frac{E^{(n)}}{s + 1/\tau_n} \tag{8}$$

and

$$\tilde{E}(\omega) = \bar{E}(s)\big|_{s=i\omega} \tag{9}$$

where the coefficients $E^{(n)}$, relaxation times τ_n, and their number N represent the mechanical properties of an actual viscoelastic material. A special (degenerate) viscoelastic material representation, that of a single Kelvin model (SKM), reduces $\bar{E}$ to

$$\bar{E}(s) = 1 + a_4 s \tag{10}$$

Typical actual viscoelastic material GKM and SKM complex modulus components E_R and E_I are shown in Fig. 2. It is readily seen that any SKM describes an unrealistic characterization of an actual viscoelastic material, as neither its storage nor its loss modulus resembles its counterpart for real damping materials. Figure 2 and Eq. (10) clearly show the SKM's behavior consisting of a constant E_R and an asymptotically increasing E_I governed by the value of the single relaxation time a_4. Moisture and temperature effects can be represented by a

time shift function a_T (Christensen, 1982, Hilton, 1964, and Nashif, et al., 1985), which shifts the time scale to the left or right depending on increasing or decreasing temperatures and/or moisture contents. The equivalent and complex moduli in the s and ω planes, respectively, are affected by changing the denominators of (8) to $s + a_T/\tau_n$ for the GKM's and a_4 in (10) to a_4/a_T for the SKM. This leads to shifting of the omega scale in opposite directions to the shifts in the time scale, i.e. increased temperatures and/or moistures shift E_R and E_I to the right in the direction of increasing frequencies.

Historically, the SKM has found favor because, in many instance, it simplifies analytical solutions thus making them realizable. In the present and past (Pang, et al., 1992) analyses, despite the obtainability of analytical transfer function representations (5), root loci can only be determined numerically even for the simplest case of an elastic beam. Thus the introduction of a GKM modulus in place of an SKM or elastic modulus offers no additonal analytical difficulty and, consequently, readily provides damping solutions for real viscoelastic materials. It is to be noted that (8) embodies characterizations for the SKM when $N = 1$ and for elastic materials with $N = 0$. Extensive catalogues of complex moduli and shift functions for real viscoelastic materials have been presented by Nashif, et al., 1985 and Lazan, 1968. The effects of various shape modifications, or changes in E_R and E_I, on time and frequency responses as well as on damping have been studied by Hilton and Yi, 1992 and by Hilton, 1991.

The effect of passive damping upon the performance of a cantilevered Euler-Bernoulli beam with a co-located sensor/reaction mass actuator at the free end (see Fig. 3) has been examined by Pang, et al., 1992. Here, the distributed structural damping was modeled using a SKM viscoelastic representation. In particular, the stability of the system was examined under P, D, and PD control via examination of the root locus behavior. The characteristic equation of the closed loop system is given by

$$Q(s) = \left[D(s) + N(s)M_p s^2\right]\left[M_a s^2 + C_a s + K_a\right] + N(s)M_a s^2 \left[(C_a + K_d)s + K_a + K_p\right] = 0 \quad (11)$$

where

$$N(s) = (\sin\bar{\lambda}\cosh\bar{\lambda} - \cos\bar{\lambda}\sinh\bar{\lambda})/\bar{\lambda}^3 \quad (12)$$

and

$$D(s) = (1 + a_4 s)(1 + \cos\bar{\lambda}\cosh\bar{\lambda}) \quad (13)$$

Replacement of $1 + a_4 s$ in (13) by $\bar{E}$, with $\bar{E}$ given by (8), leads to the characteristic equation for the system incorporating a general linear viscoelastic material.

An additional topic of interest is the distribution of poles and zeros of the open loop transfer function. As discussed in Pang, et al., 1992, the open loop poles and zeros of the elastic beam in vacuo lie on the imaginary axis, with poles and zeros interlaced. These poles and zeros, denoted s_μ, are related to $\bar{\lambda}$ through

$$s_\mu^2 = -\bar{\lambda}^4 \quad (14)$$

In the presence of distributed viscous damping, $\bar{\lambda}$ is replaced by

$$\bar{\lambda}^4 = -s_\mu^2 = -(s^2 + a_0 s) \quad (15)$$

leading to roots given by

$$s = -\frac{a_0}{2} \pm \frac{\sqrt{a_0^2 + 4s_u^2}}{2}$$ (16)

Here it can be seen that viscous damping shifts the poles and zeros on the imaginary axis into the left half plane by $a_0/2$ and is uniform for all modes.

When the SKM viscoelastic model is employed, in vacuo, $\bar{\lambda}$ is related to s through

$$\bar{\lambda}^4 = -s_u^2 = \frac{-s^2}{1 + a_4 s}$$ (17)

leading to damped poles and zeros given by

$$s = \frac{a_4 s_u^2}{2} \pm \frac{s_u \sqrt{(a_4^2 s_u^2 + 4)}}{2}$$ (18)

From the leading term of (18), it is clear that the effect of the SKM model is to provide increasingly more damping with mode number. In fact, beyond a certain mode number, all modes are overdamped. It can be shown that the open loop locus breaks into two branches upon returning to the real axis, one approaching negative infinity and the other approaching $-1/a_4$. Furthermore, the imaginary portion is bounded by $1/a_4$. In fact, it is readily demonstrated that the mapping of poles and zeros forms a circle centered at $(-1/a_4, 0)$ with radius $1/a_4$, as shown in Fig. 4.

The combination of the SKM material with viscous effects leads to a modification of the mapping to a circle centered at $(-1/a_4, 0)$ with radius $\sqrt{1 - a_0 a_4}/a_4$ if $1 - a_0 a_4 > 0$. This open loop pole-zero mapping can be used for direct identification of distributed damping coefficients appearing within the differential equation of motion by curve fitting the open loop poles and zeros to a circle in the s-plane. However, this presumes that materials essentially conform to the SKM model, which can easily be shown to be in error, as evidenced by Fig. 2.

For the GKM beam, a relation corresponding to (17) is obtained from Eqs. (4) and (8), resulting in

$$\bar{\lambda}^4 = -s_u^2 = \frac{-(a_0 s + s^2)}{E^{(0)} + \sum_{n=1}^{N} \frac{E^{(n)}}{s + 1/\tau_n}}$$ (19)

where $a_0 = 0$ in vacuo. The solution for the damped poles and zeros of (19) involves extracting the roots of an $N-th$ order polynomial. For an actual viscoelastic material, where the complex modulus of Eqs. (8) and (9) is fitted to experimental data, a realistic value of N lies between twenty and thirty in order to ensure a reasonably accurate fit. The analytical solution of (19) is therefore not attainable, even for lower values of N, and numerical strategies must be employed.

As can be seen from Eq. (6), s is a complex variable, and Eq. (19) is thus a complex algebraic equation for the roots b and ω. These can be found from the simultaneous solution of

the two real equations which correspond to the real and imaginary parts of (19). The IMSL nonlinear equation solver routine DNEQNF was employed for this study as well as for the SKM analysis.

3.0 DISCUSSION OF RESULTS

The root loci for a typical closed loop system employing both the elastic and SKM beam models in air with parameters given in Table 1 are shown for several values of gain ratio $\alpha = K_d/K_p$ in Fig. 5. It is apparent that, with the sensor applied to the beam at the base of the RMA, the system can be destabilized in the presence of D control. Furthermore, it can be shown that, in the SKM beam, instability is a 'first system mode' phenomenon and that the system can be stabilized by the addition of P control. For the system examined (see Table 1), a critical gain ratio can be found, in this case $\alpha = 0.318$, above which the system destabilizes and below which the system is unconditionally stable. The instability problem is, of course, exacerbated in the case of the purely elastic beam, also shown in Fig. 5. Somewhat similar results are likely for the GKM beam, although this work is still in progress.

4.0 CONCLUSIONS

The open and closed loop performance of a viscoelastic Euler-Bernoulli beam has been examined. In the former, employing a SKM beam, the poles and zeros are seen to map to a circle, providing a method by which the damping coefficients a_0 and a_4 in the equation of motion can be determined form experimental data. In the latter, it is shown that a critical gain ratio can be determined below which the system is unconditionally stable. Assessment of this method as a means to determine the parameters of a more general viscoelastic model continues, as does the stability analysis of the closed loop system employing the GKM beam.

5.0 REFERENCES

1. Pang, S.T., Tsao, T-C., and Bergman, L.A., 1992. "Interaction Effects in the Hybrid Control of Euler-Bernoulli Beams," *Proceedings of the Ninth ASCE Engineering Mechanics Conference*, College Station, May 25-27, pp. 820-823.

2. Pang, S.T., Tsao, T-C., and Bergman, L.A., 1992. "Active and Passive Damping of Euler-Bernoulli Beams and Their Interactions," *Proceedings of the American Control Conference*, Chicago, June 24-26, pp. 2144-2149. *ASME Journal of Dynamics, Measurement, and Control*, in press.

3. Christensen, R.M., 1982. *Theory of Viscoelasticity, An Introduction, 2nd Edition*, Academic Press, New York.

4. Hilton, H.H., 1964. "Viscoelastic Analysis," *Engineering Design for Plastics* (Eric Baer, Ed.), Reinhold Publishing Co., New York, pp. 199-276.

5. Nashif, A.D., Jones, D.I.G., and Henderson, J.P., 1985. *Vibration Damping*, John Wiley & Sons, New York.

6. Lazan, B.J., 1968. *Damping of Materials and Members in Structural Mechanics*, Pergamon Press, New York.

7. Hilton, H.H. and Yi, S., 1992. "Analytical Formulation of Optimum Material Properties for Viscoelastic Damping," *International Journal of Smart Materials and Structures*, Vol. 1, pp. 113-122.

8. Hilton, H.H., 1991. "Viscoelastic and Structural Damping Analysis," *Proceedings of Damping '91, Air Force TR WL-TR-91-3078*, Vol. 3, pp. ICB 1-15. *AIAA Journal*, in press.

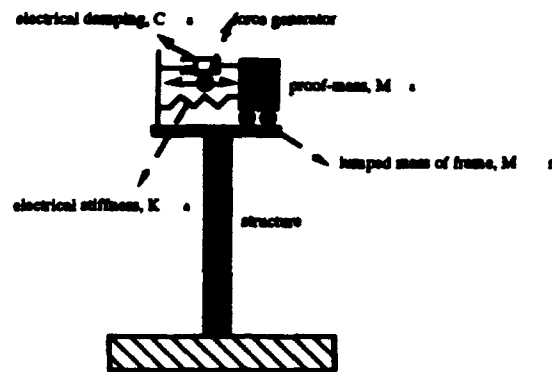| Air Damping Coefficient	a_0	0.01
SKM Coefficient	a_4	0, 0.01
Frame Mass	M_f	0.10
Actuator Mass	M_a	0.10
Actuator Passive Damping	C_a	$\sqrt{2}$
Actuator Passive Stiffness	K_a	5

Table 1: Parameters of Typical Closed Loop System (Nondimensionalized).
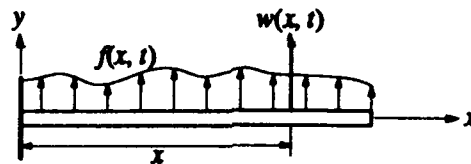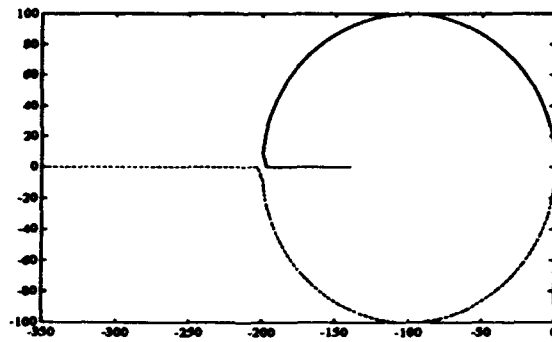

Figure 1. Euler-Bernoulli Beam.
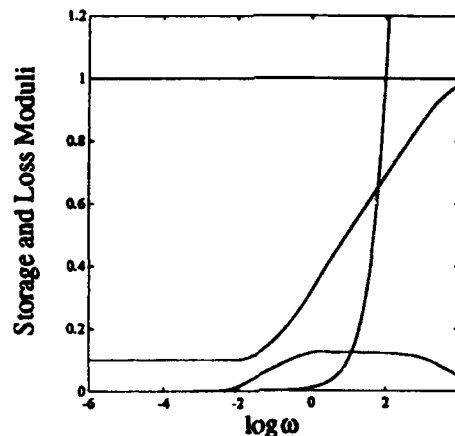
Figure 2. Storage and Loss Modulus for
Single Kelvin and GKM

Figure 3. Euler-Bernoulli Beam with Co-located Sensor/PMA.
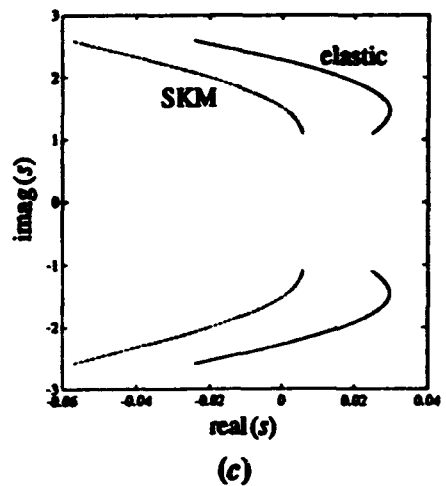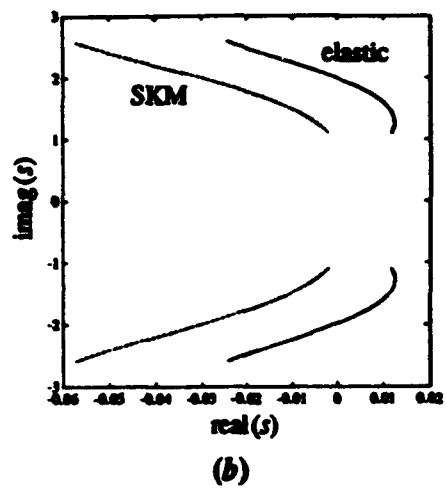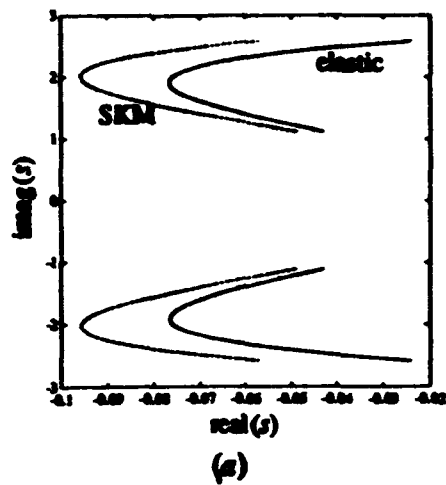

Figure 4. Open Loop Poles and Zeroes for SKM Beam.

Figure 5. Root Loci of Closed Loop System:

Enhanced Passive Vibration Absorbers
Using Acceleration Feedback

Capt. Daniel Stech [1]
Frank J. Seiler Research Laboratory
US Air Force Materiel Command

Dr. Ralph Quan
Frank J. Seiler Research Laboratory
US Air Force Materiel Command

Abstract

A modification to the standard vibration absorber by addition of acceleration feedback is proposed. The modification gives the absorber additional information on the state of the structure which results in an increase in performance. Hyperstability theory is used to derive the bounds on the acceleration feedback which guarantee global stability of the combined structure absorber system. The enhanced absorber is implemented electronically as a simple gain feedback controller. Performance of the enhanced absorber on a simple experimental structure is shown to be double that of the standard absorber. Additional increases in performance are limited by the stroke length of the absorber.

[1]FJSRL/NA, USAF Academy, CO 80840
phone: 719-472-3122

Introduction

A spring - mass - damper coupled to a vibrational system is classified as a vibration absorber. Passive vibration absorbers have a number of advantages for vibration suppression the most important of which is their stability property. Addition of a vibration absorber to a vibrational system such as a flexible structure, results in an overall system which is still guaranteed to be stable. This stability is guaranteed regardless of the fidelity of the structural model upon which the vibration absorber was based. This property is usually referred to as stability robustness. It is generally agreed that models of structures which will be deployed into space will have a high degree of uncertainty, raising questions of stability for vibration suppression systems designed using model based methods. For flexible structures deployed into space, stability robustness of the vibration suppression system will be a valuable property.

The design of a vibration absorber system is an optimization problem. In the general case, it is desired to couple multiple vibration absorbers to a structure with multiple vibrational modes. The design parameters in this problem are the absorber mass, the stiffness of the absorber spring, and the absorber damping coefficient. If the mass of the absorber is fixed to some small fraction of the overall structure - absorber mass, then the problem is finding the stiffness and damping coefficients which minimize or maximize some design criteria.

In the 1950's Den Hartog [1] investigated the vibration absorber design problem. For the case of a single vibrational mode and single vibration absorber he found a closed form solution for the stiffness and damping coefficients which would minimize the maximum value of the transfer function. Juang attempted to minimize a quadratic cost [2]. Both of these approaches gives similar tuning values. Duke attempted to solve the problem of multiple vibration absorbers coupled to multiple vibrational modes. He used a numerical optimization of the system transfer functions [3]. This proved to be very computationally intensive, even for a small system. Posbergh reformulated the tuning problem as a feedback control problem and showed H_∞ techniques could be used to tune the system [4]. Miller and Crawley gave an experimental technique for tuning multiple actuators [5]. Stech showed H_2 methods could be used for the tuning problem [6]. Bruner [7] used a virtual form of the vibration absorber to design a stable compensator which filtered the acceleration measurements, the acceleration measurements were not fed directly back to the structure.

It has been shown that the passive absorber tuning problem can be formulated has a feedback control problem. [4] Viewing the problem in this way, it becomes apparent that the passive vibration absorber belongs to the class of energy dissipative controllers. Hyperstability theory has been used in the stability analysis of dissipative systems [8]. Fundamental to hyperstability theory is the concept of positive dynamic systems. Hyperstability theory allows for the straightforward stability analysis of interconnected positive systems. The idea is simple, two positive real systems may be interconnected and the

overall result is a positive real system. This guarantees global stability. Passive vibration absorbers are in the class of positive real dynamic systems.

Unfortunately, the performance available from vibration absorbers is limited. Since the available measurements are restricted to relative position and relative velocity, only the relative phasing between the absorber and structure mass is known. If it were possible to incorporate absolute phase information about the structure mass into the absorber without destroying its positive real nature, then increased performance could be expected while still maintaining the stability robustness of the vibration absorber.

Researchers have implemented passive vibration absorbers electronically [5, 4]. By actually measuring relative position and relative velocity and multiplying these signals by a stiffness and damping gain, a linear motor can be made to behave as a spring - mass - damper system with electronically tunable stiffness and damping coefficients. Since this implementation of a passive vibration absorber is analogous to a mechanical spring - mass - damper system, it is globally stable. In this research it is shown that by introducing acceleration feedback to this system, absolute phase information can be incorporated into the controller, greatly enhancing performance without losing the property of global stability.

First, the feedback formulation for passive vibration absorbers developed by Posbergh [4]is reviewed. Next, the stability of the standard and enhanced vibration absorber is investigated. Finally, the resulting enhanced absorber is implemented on a simple experimental structure.

Feedback Formulation of the Vibration Absorber

A feedback formulation of the passive absorber problem was developed by Posbergh [4]. The following is a summary of this formulation. Consider the simple case of a single degree of freedom structure coupled to a single vibration absorber. This is represented in Figure 1. The force $f(t)$ can be viewed as an input to an augmented structure - absorber system given by,

$$\begin{bmatrix} m_s & 0 \\ 0 & m_a \end{bmatrix} \ddot{z}(t) + \begin{bmatrix} k_s & 0 \\ 0 & 0 \end{bmatrix} z(t) = \begin{bmatrix} 1 \\ -1 \end{bmatrix} f(t) \tag{1}$$

where $z(t) = [x_s(t) \ x_a(t)]^T$. The force exerted on both the structure mass and the absorber mass by $f(t)$ couples the two systems together. It is given by,

$$f(t) = k_a(x_s(t) - x_a(t)) + c_a(\dot{x}_s(t) - \dot{x}_a(t)) \tag{2}$$

Equation (2) can be written in matrix form

$$f(t) = Ky(t) \tag{3}$$

where $K = [k_a \ c_a]$ is a gain matrix, and

$$y(t) = \begin{bmatrix} y_1(t) \\ y_2(t) \end{bmatrix} = \begin{bmatrix} x_s(t) - x_a(t) \\ \dot{x}_s(t) - \dot{x}_a(t) \end{bmatrix} \tag{4}$$
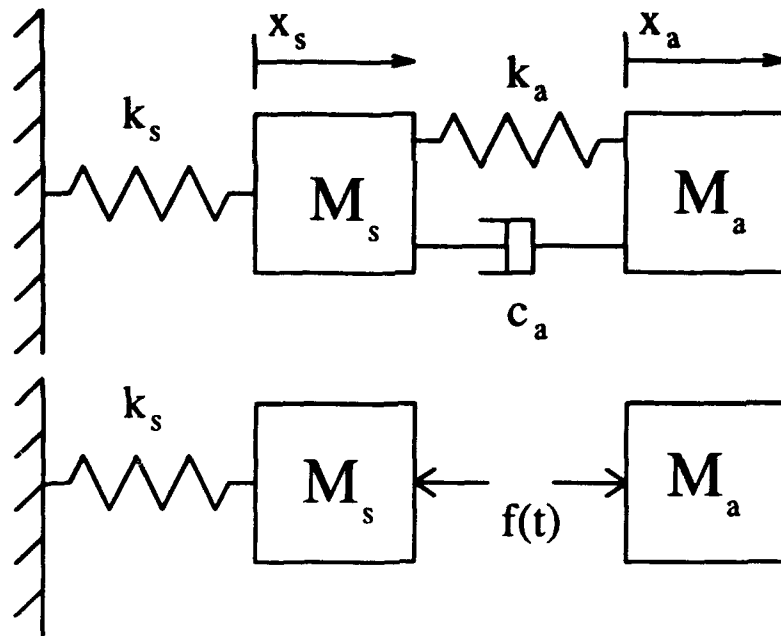
Figure 1: Model of a single vibration absorber coupled to a single degree of freedom structure.

or

$$f(t) = KCx(t) \qquad (5)$$

where

$$C = \begin{bmatrix} 1 & 0 & -1 & 0 \\ 0 & 1 & 0 & -1 \end{bmatrix}$$

and $x(t) = [x_s(t) \ \dot{x}_s(t) \ x_a(t) \ \dot{x}_a(t)]^T$.

Choosing the absorber stiffness and damping which minimize some design criteria is an output feedback problem which has the following first order form,

$$\dot{x}(t) = Ax(t) + Bf(t) \qquad (6)$$

where A and B are the augmented matrices

$$A = \begin{bmatrix} 0 & 1 & 0 & 0 \\ -\frac{k_s}{m_s} & 0 & 0 & 0 \\ 0 & 0 & 0 & 1 \\ 0 & 0 & 0 & 0 \end{bmatrix} \qquad B = \begin{bmatrix} 0 \\ \frac{1}{m_s} \\ 0 \\ -\frac{1}{m_a} \end{bmatrix}$$

These two systems are coupled by the output feedback,
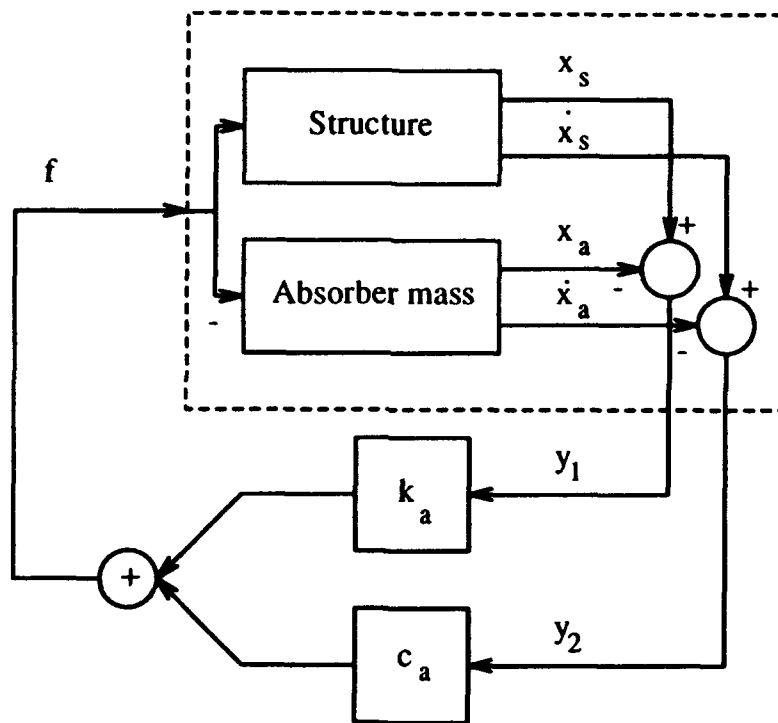
$$f(t) = KCx(t) \qquad (7)$$

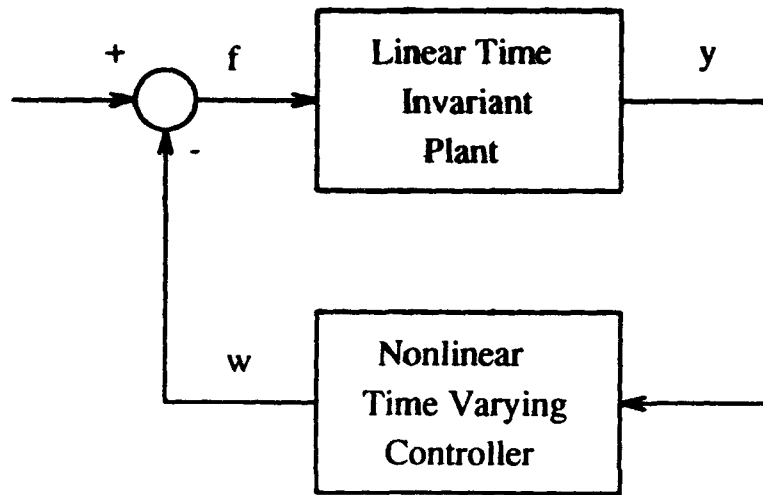Figure 2: Feedback formulation of a passive vibration absorber

Figure 3: Nonlinear and/or time varying feedback system

Figure 2 gives a graphical representation of the feedback formulation. Notice that although the feedback formulation was developed based on the SDOF case, it is equally valid for the multiple degree of freedom case.

Passive Vibration Absorber Stability Analysis

Once the design of the passive vibration absorber is viewed as a feedback control problem, the concept of hyperstability can be used to show stability of the combined structure - absorber system. The following is a review of some useful results from hyperstability theory [8, 9].

Hyperstability mainly deals with the class of feedback systems which can be put in the feedback form shown in Figure 3. The hyperstability concept allows the stability of the total system to be investigated by dealing with the stability of the feedforward and feedback block separately. The combined system is stable if the feedback block satisfies the Popov integral inequality,

$$\eta(0, t_1) \triangleq \int_0^{t_1} y^T w dt \geq -\gamma_o^2 \text{ for all } t_1 \geq 0 \tag{8}$$

where y is the input vector, w is the output vector, and γ_o^2 is a finite positive constant which does not depend on t_1, and the feedforward block is positive real. For the more specific case of linear time invariant blocks, positive real transfer functions satisfy the Popov integral. Therefore, if both blocks are linear time invariant and both are positive real, the system is stable. Landau [9] showed that a proportional integral derivative feedback block with positive gains will satisfy the Popov integral.
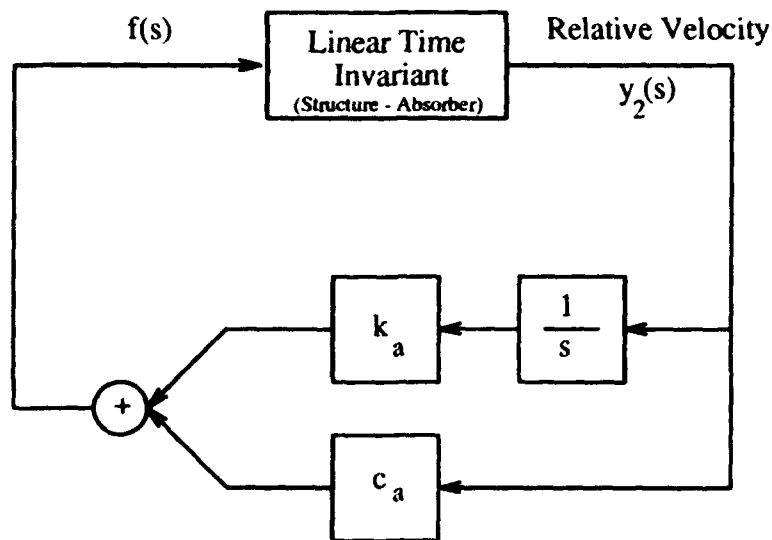
Figure 4: Vibration absorber as a feedback control problem

Definition 1 *A transfer function $H(s)$ is "positive real" if*

1. $H(s)$ is real for real s.

2. $Re[H(s)] \geq 0$ for all $Re[s] > 0$.

Definition 2 *A real rational transfer function is "reactive" if all of its poles and zeros are simple, lie on the jw-axis, and alternate with each other.* [10]

A reactive transfer function is passive [10]. Passive transfer functions also satisfy the Popov integral [11]. Finally, there are two useful properties for the combination of hyperstable blocks.

Lemma 1 *Any block obtained from the feedback combination of two hyperstable blocks is hyperstable.*

Lemma 2 *Any block obtained by the parallel combination of two hyperstable blocks is hyperstable.*

The proofs of the above lemmas can be found in Popov [8].

Given the above, the feedback formulation for the vibration absorber needs only the slight modification shown in Figure 4 to show its hyperstability. It is equivalent to the formulation given previously. To guarantee the stability of the system, the feedforward block must be positive real. Since the feedback block is a PI controller with positive gains,

by Landau [9], it is positive real. Using the feedback formulation given by Equations (6,7), the feedforward transfer function for relative velocity to force is,

$$g_v(s) = \frac{Y_2(s)}{F(s)} = \frac{k_s + (m_a + m_s)s^2}{m_a s(k_s + m_s s^2)}$$ (9)

The zeros of the transfer function are

$$s = \pm j \sqrt{\frac{k_s}{m_a + m_s}}$$ (10)

The poles of the transfer function are

$$s_1 = \pm j \sqrt{\frac{k_s}{m_s}} \qquad s_2 = 0$$ (11)

The transfer function will be reactive and passive if the poles and zeros alternate on the imaginary axis,

$$0 < \sqrt{\frac{k_s}{m_a + m_s}} < \sqrt{\frac{k_s}{m_s}}$$ (12)

Equation (12) is true for $m_a > 0$. As mentioned previously, since the feedback block is a PI compensator, the feedback block is positive real, (according to Landau) and the combined system is stable.

Enhanced Vibration Absorber Stability

The addition of acceleration feedback offers the potential for a significant increase in the performance of a vibration absorber. In the previous section, the stability of passive vibration absorbers was proven using the concept of hyperstability. In this section, it is shown that with certain bounds on the acceleration feedback, the hyperstability of the system is not effected. As before, the modified vibration absorber can be put in the feedback system form. The key is to show that the acceleration feedback does not destroy the passivity of the feedforward block.

Consider a collocated acceleration feedback added to the augmented form given by Equation (1),

$$f(t) = [g \ \ 0]\ddot{z}(t)$$ (13)

Closing the loop gives,

$$\begin{bmatrix} m_s - g & 0 \\ g & m_a \end{bmatrix} \ddot{z}(t) + \begin{bmatrix} k_s & 0 \\ 0 & 0 \end{bmatrix} z(t) = \begin{bmatrix} 1 \\ -1 \end{bmatrix} f(t)$$ (14)

and the feedforward transfer function with collocated acceleration feedback becomes,

$$g_v(s) = \frac{Y_2(s)}{F(s)} = -\frac{k_s + (m_a + m_s)s^2}{m_a s(-k_s + (g - m_s)s^2)} \tag{15}$$

The zeros of the transfer function are

$$s = \pm j \sqrt{\frac{k_s}{m_a + m_s}}, \tag{16}$$

The poles of the transfer function are

$$s_1 = \pm j \sqrt{\frac{k_s}{g - m_s}} \quad s_2 = 0 \tag{17}$$

The transfer function will be reactive if,

$$0 < g < m_s \tag{18}$$

The system is passive, and thus globally stable if $g < m_s$. Since the combined feedback system is passive, then it may be combined with multiple vibrational modes and still remain passive. Next a demonstration of the enhanced absorber is given by simulation and implementation on an experimental structure.

Simulation and Experimental Verification

The enhanced vibration absorber coupled to a flexible structure was simulated. The structure of interest is an aluminum "T" with two attached lead weights. Total weight of the structure is 200 lbs. A diagram of the structure is shown in Figure 5. This structure was designed to produce two isolated low frequency modes, a torsion mode at 6.8 Hz, and a bending mode at 5Hz. Since the third mode of the structure occurs around 40-50 Hz, the isolation of the lower modes makes the structure simple to model.

The vibration absorber is implemented electronically. A linear motor consisting of a rare earth magnet sliding over a coil provides an electromagnetic force to both the structure and the actuator mass. A Kaman position sensor provides relative position between the absorber mass and the structure. A linear velocity transducer provides relative velocity measurements. Relative position and relative velocity signals are multiplied by two gains, actuator stiffness and actuator damping, respectively. The gain amplified signals are summed and fed to a current amplifier which feeds back to the linear motor coil. With this feedback loop in place the linear motor behaves like a mechanical spring - mass - damper system. The absorber stiffness and damping are electronically tunable. The absorber mass
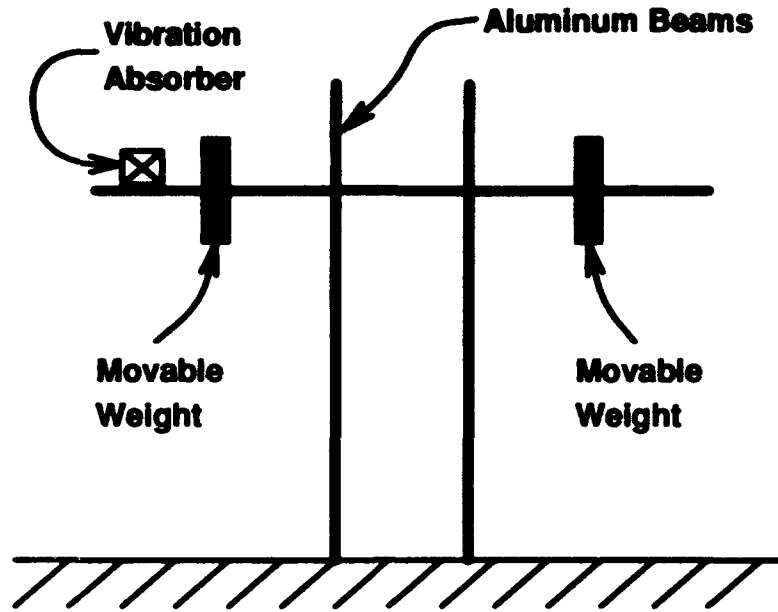
Experimental Structure

Figure 5: Experimental Structure

is 4 lbs, making the absorber to structure mass ratio .02, a realistic mass ratio for space structure applications.

First, a simulation is performed. An undamped model of the structure is damped using a standard vibration absorber. Using the procedure developed in [6], the absorber is tuned to minimize an H_2 cost. For the simulation, the position of the structure is initially displaced at the location of the actuator. Figure 6 shows the free response of the structure compared to the response with the H_2 optimal vibration absorber attached. Next acceleration feedback is introduced and the absorber is retuned. Figure 7 shows the response of the structure with the enhanced passive vibration absorber attached. A considerable increase in performance can be realized by using acceleration feedback. Table

CASE	ω_a	ζ_a	H_2 cost	Absorber Stroke
Free Response	0	0	∞	0
Standard Vibration Absorber	5.31	.1094	.28	.085
Enhanced Vibration Absorber	4.61	.7726	.067	.23

Table 1: Summary of simulation results, ω_a = actuator frequency, ζ_a = actuator damping
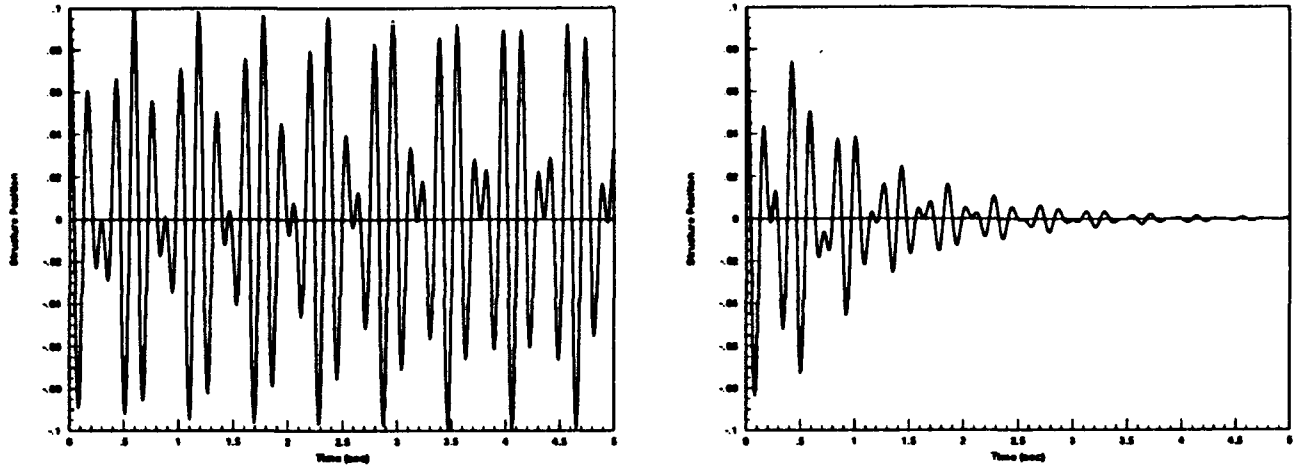
Figure 6: Free response of the structure vs. response with vibration absorber attached.
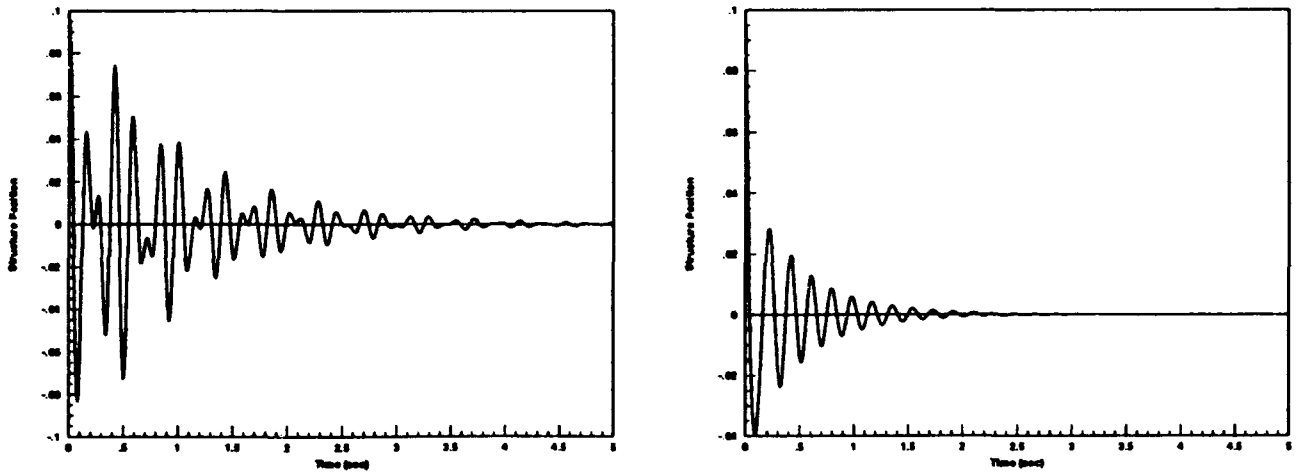

Figure 7: Structure response of standard vibration absorber vs enhanced vibration absorber.
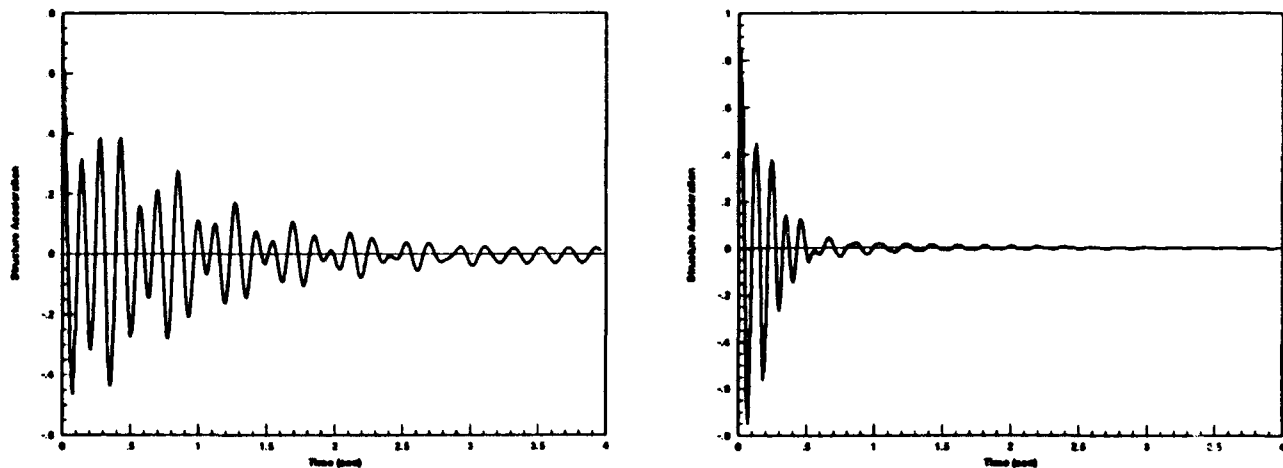
Figure 8: Experimental structure response of standard vibration absorber vs enhanced vibration absorber.

1 summarizes the performance increase at the expense of stroke length.

The above simulation was verified experimentally. Figure 7 shows the actual response of the experimental structure with standard vibration absorber compared with the enhanced vibration absorber. The stroke length of the absorber will limited the performance of the absorber.

Summary

Passive vibration absorbers have the desirable property of global stability. Unfortunately they do not typically exhibit high performance. Standard vibration absorbers can be modified by the use of acceleration feedback to greatly increase performance. Hyperstability theory shows this modification does not affect the stability of the system, provided that the acceleration feedback gain does not exceed the modal mass at the acceleration sensor. The resulting positive real controller exhibits high robustness and performance. The simple gain feedback formulation of the controller allows for simple implementation and requires minimal computation.

References

[1] J. P. Den Hartog. *Mechanical Vibrations.* McGraw - Hill, New York, 1956.

[2] J. Juang. Optimal design of a passive vibration absorber for a truss beam. *AIAA Journal of Dynamics, Guidance, and Control*, 7(6):733–739, 1984.

[3] J. P. Duke, S. Webb, and H. Vu. Optimal passive control of multi-degree of freedom systems using a vibration absorber. In *AIAA Conference on Guidance and Control*, 1990.

[4] T. A. Posbergh, M. S. Trimboli, and J. P. Duke. A control formulation for vibration absorbers. In *Proceedings of the 1991 American Control Conference*, June 1991.

[5] D.W. Miller and E.F. Crawley. Theoretical and experimental investigation of the space-realizable inertial actuation for passive and active structural control. *AIAA Journal of Dynamics, Guidance, and Control*, 11(5):449–458, 1988.

[6] D.J. Stech and S.G. Webb. An H_2 approach for optimally tuning passive vibration absorbers to flexible structures. In *AIAA Conference on Guidance, Navigation, and Control, AIAA-92-4611-CP*, 1992.

[7] L.G. Horta, A.M. Bruner, W.K. Belvin and J.N. Juang. Active vibration absorber for the csi evolutionary model: Design and experimental results. *AIAA Journal of Dynamics, Guidance, and Control*, 15(5):1253–1257, 1992.

[8] V.M. Popov. *Hyperstability of Control Systems*. Springer - Verlag., 1973.

[9] Y.D. Landau. *Adaptive Control*. Marcel Dekker, Inc., 1979.

[10] N. Balabanian and T. Bickert. *Electrical Network Theory*. Jonh Wiley and Sons, Inc., 1969.

[11] D. Wang and M. Vidyasagar. Passive control of a single flexible link. In *IEEE International Conference on Robotics and Automation*, 1990.

PIEZOELECTRIC COMPOSITES FOR USE IN

ADAPTIVE DAMPING CONCEPTS

Wayne T. Reader
and
David F. Sauter

Vector Research Company, Inc.[1]

ABSTRACT

Piezoelectric actuators are frequently employed as the active element in adaptive or active systems used to eliminate or "damp" structural vibrations. Piezoelectric composites of the 1-3 type consist of piezoelectric rods embedded in a polymeric matrix and can provide strain coefficients comparable to those of the solid ceramic with less than 20% of the weight. Most 1-3 composites designed to operate in the thickness mode, e.g. maximize the d_{33} strain coefficient, select the matrix polymer to be in its glassy regime. The primary objective of this paper is to show that this conventional approach does not provide the optimal strain coefficients. The rigid matrix constrains the rod motion sufficiently to cause significant reduction of the effective strain coefficients. It is shown that improved performance is achieved by choosing for the matrix a rubbery polymer containing gaseous inclusions and applying a lightweight cap plate to the composite's surface.

1   Suite 700, 2101 East Jefferson Street, Rockville, MD 20852.
    Tel: (301) 816-5500; Fax: (301) 816-5517.

INTRODUCTION

Piezoelectric composites of the 1-3 type consist of piezoelectric rods encapsulated within a polymeric matrix (Figure 1). The "1-3" designation[1] indicates that the piezoelectric ceramic is connected to itself in one dimension, whereas the matrix encapsulant is connected to itself in all three spatial dimensions.

The electromechanical coupling factor k is defined by [2]

$$k^2 = \frac{\text{electrical energy converted to mechanical energy}}{\text{input electrical energy}} \qquad (1)$$

It is generally accepted as the most important single measure of the performance of a piezoelectric material. Examining the coupling coefficient presented in Figure 2 for a 1-3 composite[3], one may readily understand a primary attraction for the 1-3 composites used in the thickness mode. The coupling coefficient applicable to the thickness mode of the composite, k_t, exceeds that of the solid ceramic for ceramic volume fractions greater than about 5%.

Additional advantages offered by the composites for structural damping applications are light weight and flexibility. Composites weigh a fraction of solid ceramic, and therefore add significantly less loading to light structures. The flexibility achieved by manufacturing the composite with a rubbery polymer enables the sensor or actuator to be installed upon complex structural shapes.

Traditionally, 1-3 composites for ultrasonic uses are manufactured with a relatively rigid matrix encapsulant to ensure that the matrix is carried along with the rod motion to provide a uniform surface motion. However, as will be shown in some detail in subsequent sections of this paper, these rigid polymers may constrain the motion of the rods to less than 50% of their free motion. The use of soft, compliant matrix encapsulants will be shown to allow essentially unconstrained motion of the rods.

THEORETICAL CHARACTERIZATION

It is assumed in this paper that the piezoelectric elements will be used in an active damping scheme to excite the structure perpendicularly to the surface, as shown in Figure 3. Hence, the composite element will be driven in the thickness mode.
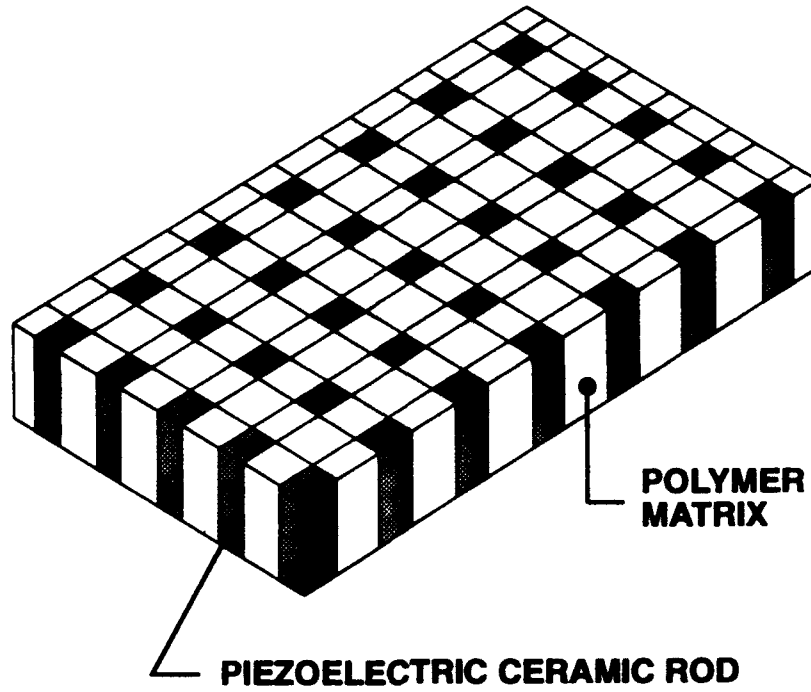
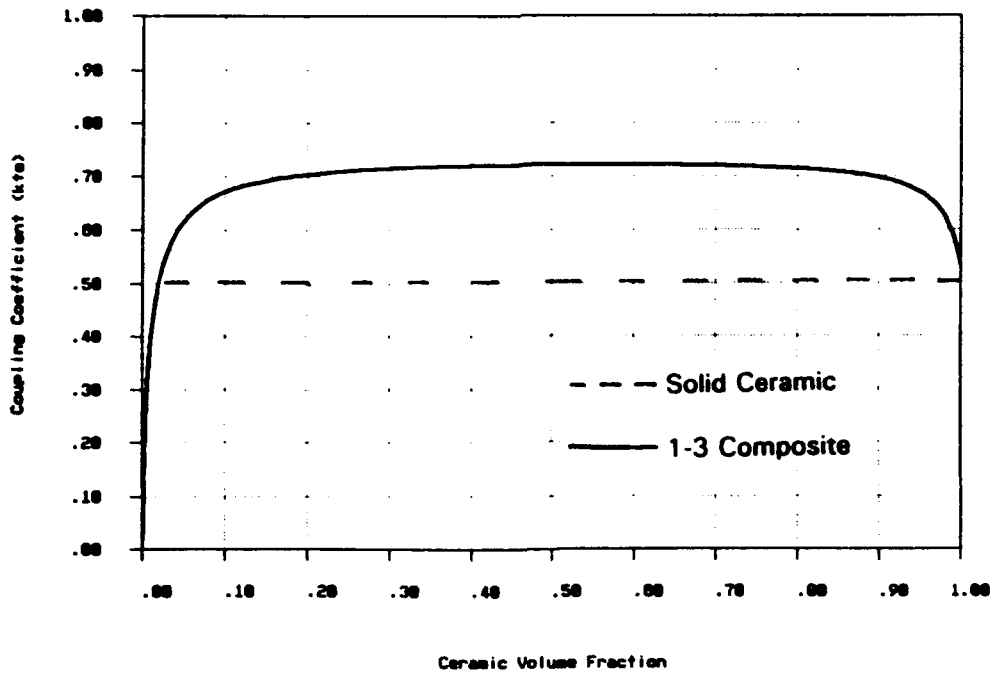Figure 1. A piezoelectric composite of the 1-3 type

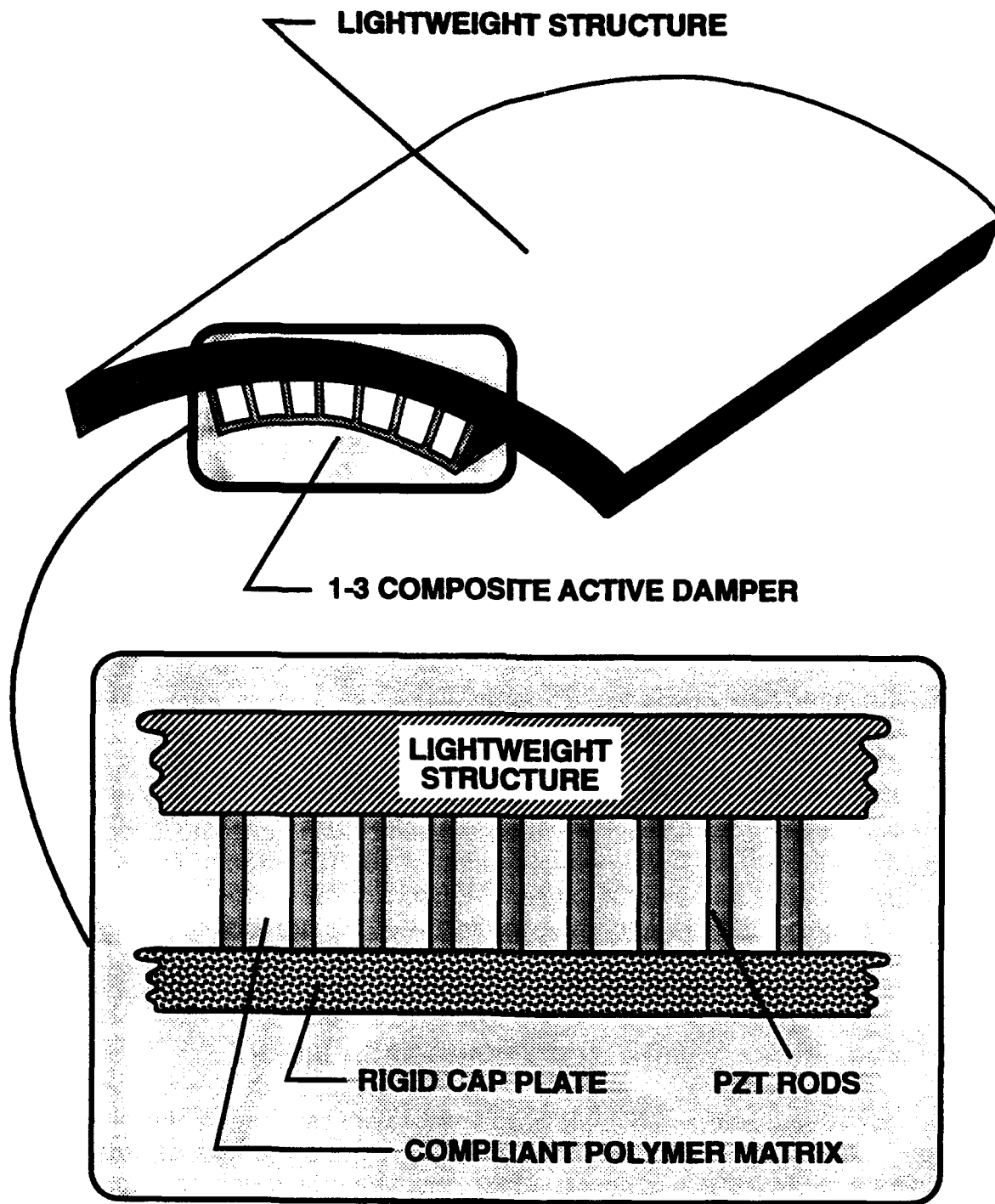Figure 2. $\bar{k}_t$ vs. υ_c predicted for PZT5H rods and a polymer matrix

Figure 3.   1-3 composite element used to impart loads perpendicular to a
structural surface

ANALYTICAL MODEL

Smith and Auld[3] have developed a simple analytical model to describe thickness mode oscillations of 1-3 composite layers.

Locating the layer, electroded on its top and bottom surfaces, in the x-y plane, their simplifying assumptions include:

1. The strain and electric field are independent of lateral position (x-y plane) throughout the individual ceramic and polymer phases.

2. Symmetry exists in the x-y plane, for example elastic constants $c_{12} = c_{21}$, electric field $E_1 = E_2 = 0$, etc.

3. The ceramic and polymer phases move together in the thickness direction.

4. The electric fields are identical in the ceramic and polymer phases.

5. The lateral stresses are equal in both the ceramic and polymer phases, and the composite is laterally clamped.

6. The effective stress and electric displacement in the thickness direction (parallel to the z axis) are obtained as weighted (volume fraction) averages over the ceramic and polymer phases.

The resulting theory has proven to be extremel, useful for designing effective 1-3 composites - particularly for medical ultrasonics applications where relatively rigid transducers of several square centimeter area can be used. One example of the vast utility of this theory are the results presented in Figure 2 which illustrate the possibility of obtaining or even exceeding the coupling performance of a solid ceramic with the small volume fractions in a 1-3 composite.

Transducers intended for applications such as structural damping may not abide by these assumptions if optimal designs are to be developed. For example, if flexible transducers are needed, the polymer stiffness may not be sufficient to follow the motion of the ceramic rods. Further, as suggested previously, the use of rigid polymers may severely constrain the rod motion - producing surface motions which may be as little as 50% of the unconstrained rod motion.

In either of these examples, it is apparent that assumption 3, and probably 1 and 5, would be violated. Therefore, analysis of these cases requires the use of numerical procedures such as Finite Element Analyses.

FINITE ELEMENT ANALYSIS

Advantages Over Analytical Model

The finite element representation of 1-3 composite behavior holds a significant advantage over the analytical model described previously. While the analytical model views the composite as a "macro" system by applying simplifying assumptions, the finite element model describes the detailed response of the composite. For example, solution of the analytical model yields quantities such the average surface displacement, whereas the finite element solution provides the entire displacement field for the model. Other quantities, such as the stress, strain, voltage, and current may be obtained at all nodal points within the finite element model. The effective or average quantities are then readily computed from the nodal fields. Hence, from this detailed information the investigator may both evaluate the performance potential of candidate 1-3 designs, and also gain valuable insight as to the parameters which influence the performance.

A second advantage is that the finite element method is very flexible. A wide variety of 1-3 composite configurations (i.e., addition of a rigid cap plate) and loading conditions may be modeled with simple modeling changes.

Finite Element Models

The displacement response of piezoelectric 1-3 composite materials has been predicted using finite element models. Piezoelectric and standard structural finite elements are used to represent the piezoelectric rods and polymer matrix respectively. Piezoelectric material properties are defined in terms of the elastic stiffness coefficient matrix, piezoelectric matrix, and dielectric matrix, while the polymer properties are defined by Young's modulus and Poisson's ratio. A symmetrical model with nine piezoelectric rods is used to model a 1-3 composite plate of larger lateral extent as shown in Figure 4. Symmetrical displacement boundary conditions are applied at the $x = 0$, $y = 0$, and $z = 0$ planes. Uniform displacement fields are enforced in the lateral directions at the $x = w$ and $y = w$ boundaries to simulate the condition of a larger lateral extent. A sinusoidally varying potential boundary is applied at the $z = t/2$ and $z = -t/2$ plane, for a total applied potential of 100 Volts.

The finite element analysis is conducted using a forced harmonic analysis procedure. The average surface displacement is then computed from the surface nodal displacement field ($z = t/2$).

ALTERNATIVE 1-3 COMPOSITE DESIGNS

Several alternative designs will be examined with finite element analysis to determine a better design to be used for structural damping applications. Included are: (1) the traditional design which employs a rigid epoxy to force uniform surface motion, (2) a variant of the traditional design which replaces the rigid
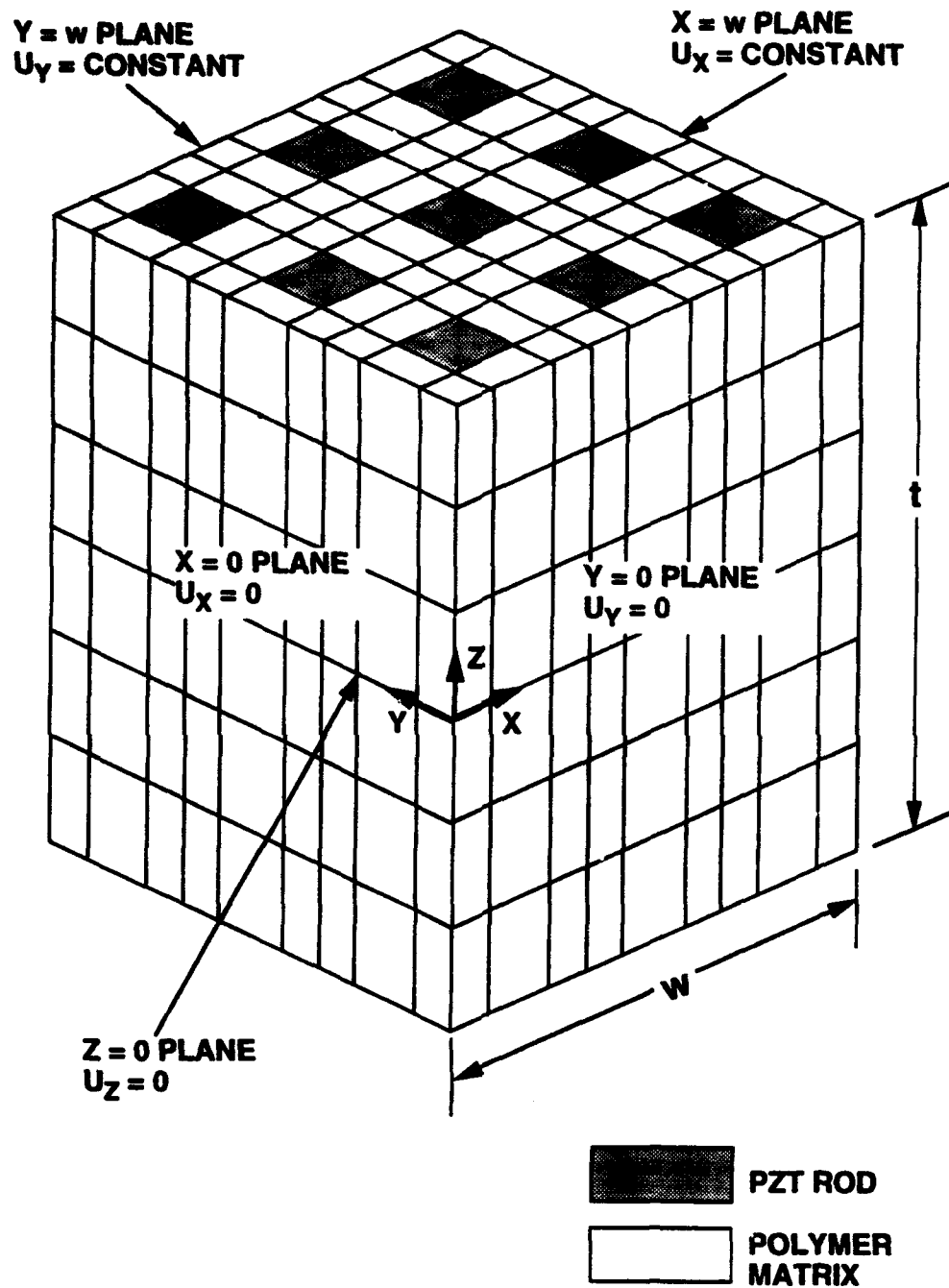
Figure 4. Symmetric finite element model representing a 1-3 composite plate

matrix with a softer urethane, and (3) and a design in which the urethane is voided to increase the compressibility.

TRADITIONAL DESIGNS

The traditional 1-3 composite is comprised of Lead Zirconate Titanate (PZT) rods embedded in a rigid epoxy matrix. The 1-3 composite's displacement performance is a function of both the matrix material mechanical properties and the composite geometrical properties.

Matrix Material

The epoxy matrix promotes the formation of a relatively uniform displacement profile and decreases the effective density of the composite. The rigid epoxy possesses a relatively high shear modulus which helps to produce a uniform displacement field, as shown in Figure 5. However, there is a trade-off because the correspondingly large elastic modulus (Table 1) constrains the rods to as little as 45% of the motion of a free PZT rod. Figure 6 shows this constraining effect for 5 - 20% volume fraction composites. The effective density is reduced because the polymer matrix is typically 85% lighter than piezoelectric ceramics. For example, the effective density of a 12% PZT volume fraction 1-3 composite with an epoxy matrix is 25% of that of a solid PZT ceramic.

Geometric Properties

The geometric parameters which influence 1-3 composite performance are the ceramic volume fraction and the rod length-to-width aspect ratio. Previous investigations[5] show that the displacement performance of the traditional 1-3 composite increases proportionally with volume fraction increases as shown in Figure 6. However, increasing the rod aspect ratio produces only slight performance increases.

REPLACEMENT OF THE RIGID EPOXY MATRIX WITH A RUBBERY POLYMER

The Young's modulus of a commercially available urethane is compared in Figure 7 with the modulus of an epoxy which has been used to manufacture 1-3 composites. For high frequencies, e.g. above a megahertz, both polymers are in their glassy regime and are seen to be comparable in magnitude. However, for audio and subaudio frequencies, the urethane is in its transition region and the moduli differ by at least an order of magnitude. Hence, one might expect the motion of the rods embedded in the urethane to be significantly greater than that of the rod embedded in the epoxy.

The finite element analysis procedures summarized in a previous section are used to predict the performance of alternative 1-3 composite designs. The parameters
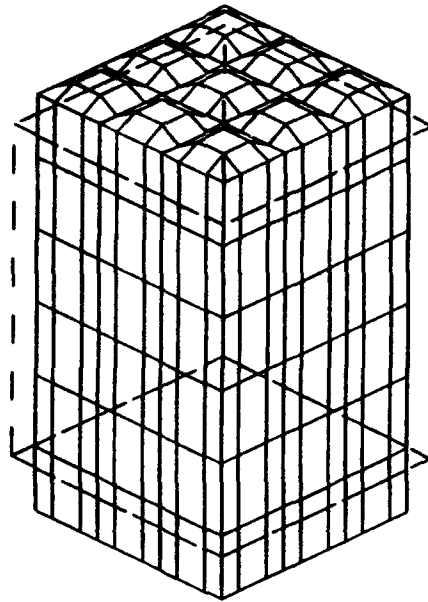
Figure 5.   Finite element displaced shape depicting relatively uniform surface
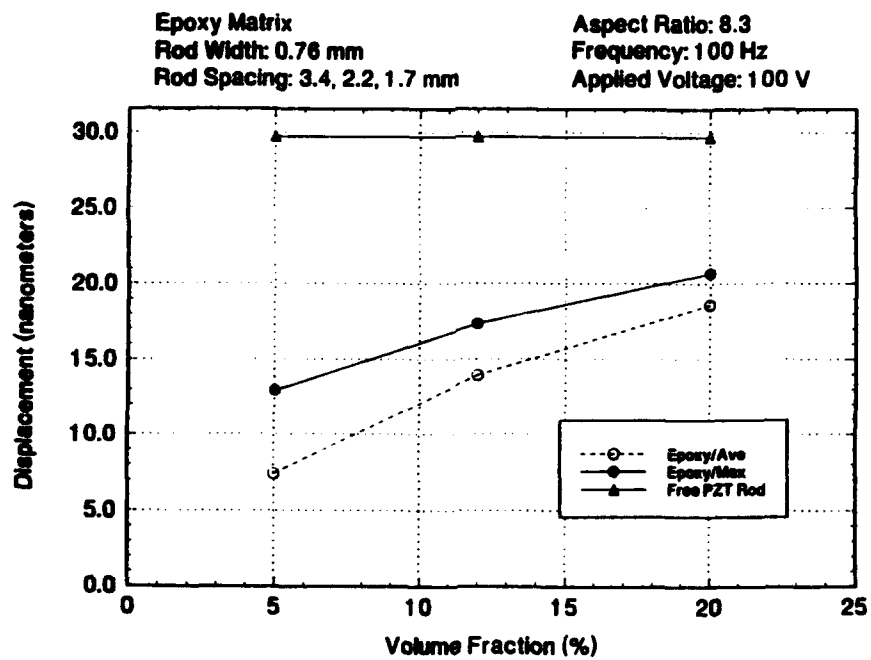motion of an epoxy matrix 1-3 composite

Figure 6.   Influence of epoxy matrix on rod displacement as compared to a free
PZT5H rod.

PIEZOELECTRIC RODS – PZT 5H

ROD SIZES: 0.040" (1 mm), 0.30" (0.76 mm), 0.020" (0.5 mm)
ROD LENGTH: 0.25" (6.4 mm)
VOLUME FRACTION: 5%, 12%, 20% (except 0.5 mm)

MATRIX MATERIALS

EPOXY MATRIX: $E' = 6.9$ GPa
                  $\sigma = 0.35$
                  $\rho = 1140$ Kg/m^3

URETHANE MATRIX: $E' = 0.3$ GPa @ 100 Hz
                  $\sigma = 0.49$
                  $\rho = 1120$ Kg/m^3

VOIDED URETHANE MATRIX: $E' = 0.2$ GPa @ 100 Hz
                          $\sigma = 0.35$
                          $\rho = 560$ Kg/m^3

REINFORCING TOP PLATE USED IN PREDICTIONS

GRP PLATE: $E' = 36$ GPa
                  $\sigma = 0.30$
                  $\rho = 1800$ Kg/m^3

Table 1.   Parameters used to characterize 1-3 composite specimens
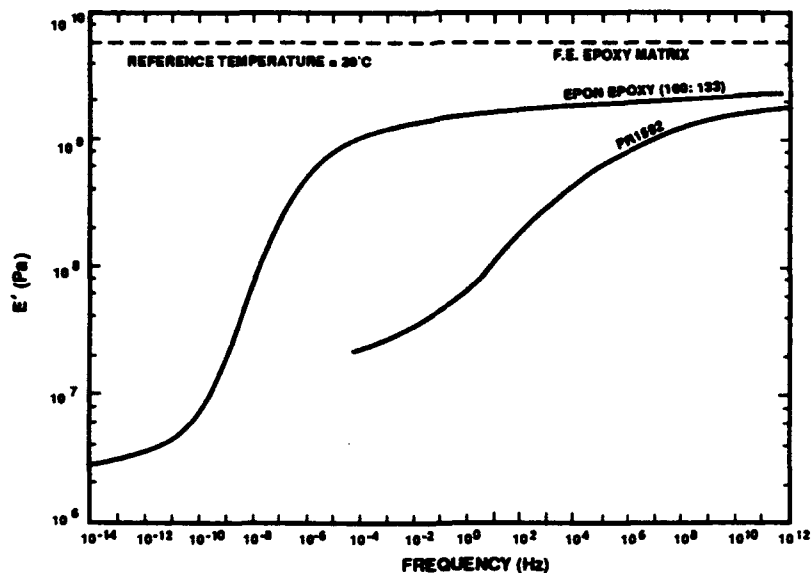

Figure 7.   Moduli of EPON® epoxy and PR 1592 polyurethane[4]

used to characterize the 1-3 composites in the finite element calculations are summarized in Table 1.

Figure 8 presents the displacements of 0.76 mm PZT5H rods embedded in either an epoxy or a urethane matrix when excited with a 100 volt potential. The 0.76 mm PZT5H rods are spaced 3.4 , 2.2, and 1.7 mm apart to form ceramic volume fractions of 5 - 20 %. The maximum rod displacements generated for the urethane matrix are as much as 115% greater than for the epoxy matrix.

However, upon bonding a 1 mm thick GRP (glass reinforced plastic) cap plate to the composite to simulate attaching it to a light structure, Figure 9 shows that the maximum displacement decreases to that predicted for the epoxy matrix. The reason for this decrease can be shown to be caused by the incompressibility, and hence Poisson ratio of approximately 1/2, which characterizes the urethane. The laterally stiff cap plate prevents significant expansion of the composite, essentially enforcing a constant volume condition (i.e., $U_{lateral} = 0$). To illustrate this effect, consider a urethane composite without a cap plate, subjected to a zero lateral displacement condition. Figure 10 shows that the free surface of the incompressible urethane matrix must contract over part of the surface to balance the expansion which occurs in the vicinity of the rod. However, when bonded to the cap plate, the urethane is constrained from contracting, which in turn constrains motion of the rod.

COMPRESSIBLE MATRIX

The effect of the bond between the matrix and cap plate can be alleviated by increasing the compressibility of the matrix, and hence decreasing the Poisson ratio, by adding voids to the matrix. The influence of voids upon the matrix compressibility K and Poisson ratio σ can be estimated using the effective Lame', constants calculated from the theory developed by Chaban.[6] Defining the effective Lame', constants to be λ_e and μ_e, they are expressed in terms of the Lame' constants of the constituent polymer, λ and μ, and the void content ϕ as

$$\mu_e = \frac{\mu}{1 + 15\phi \frac{\lambda+2\mu}{9\lambda+14\mu}} \tag{2}$$

$$\lambda_e = \frac{\lambda + 2\mu}{1 + \phi \left[\frac{3\lambda+2\mu}{4\mu} + \frac{20\mu}{9\lambda+14\mu} \right]} - 2\mu_e \tag{3}$$
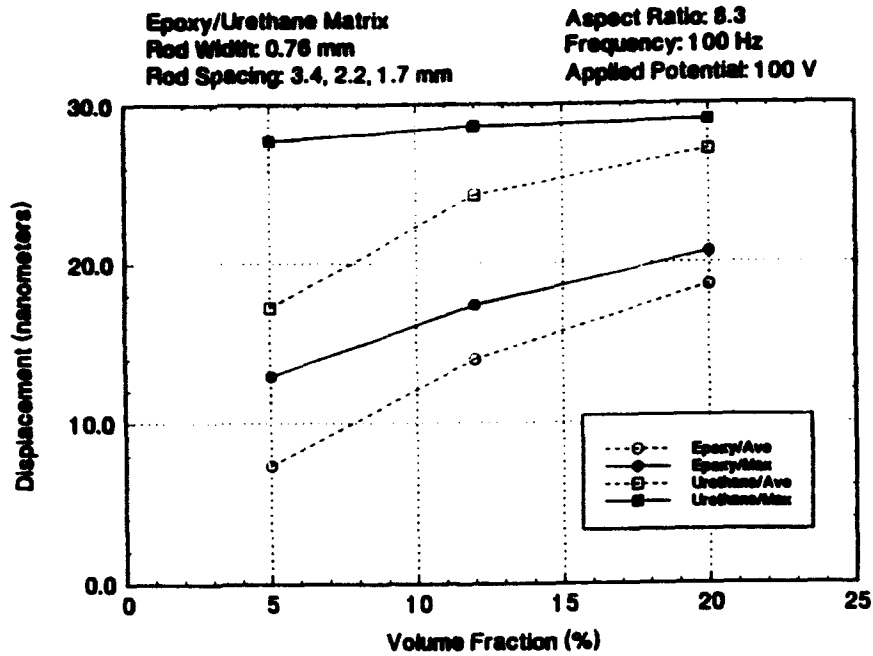
Figure 8.   Comparison of the maximum rod displacement and average surface
displacement for epoxy and urethane matrix polymers.
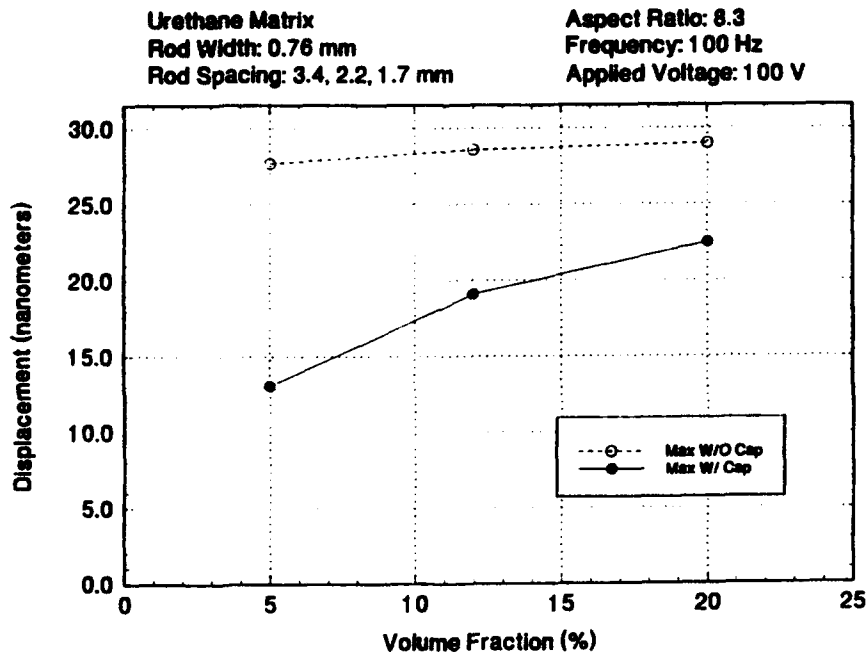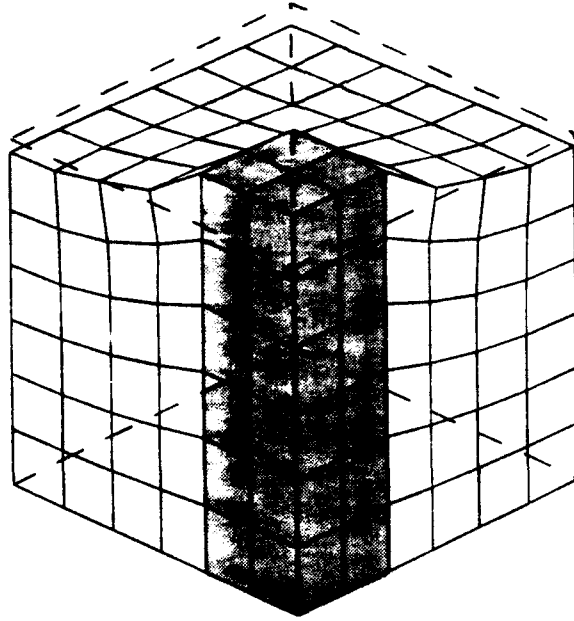

Figure 9.   Influence of a cap plate upon rod displacement in a composite with a
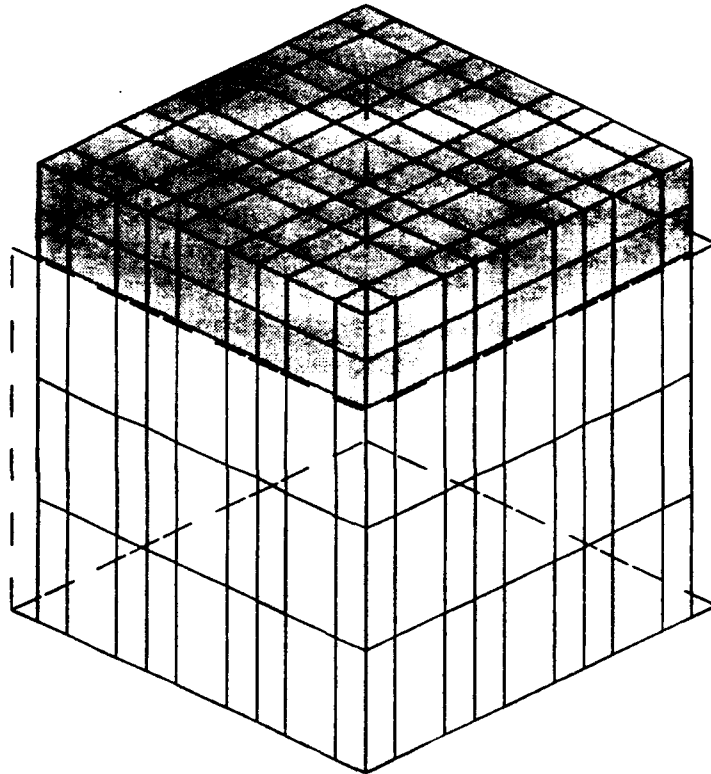polyurethane matrix.

Figure 10.   Deformation of the surface of a urethane composite: (a) No cap
subjected to a zero lateral displacement condition, and (b) With cap
depicting reduced rod displacements.

The effective compressibility is defined as the inverse of the bulk modulus B_e, i.e. as $K_e = 1/B_e$ where the effective bulk modulus is given by

$$B_e = \lambda_e + \frac{2\mu_e}{3} \tag{4}$$

The effective Poisson ratio is defined in terms of the effective Lame' constants as

$$\sigma_e = \frac{\lambda_e}{2(\lambda_e + \mu_e)} \tag{5}$$

The density of the voided polymer is given simply by

$$\rho_e = \rho(1-\phi) \tag{6}$$

The effective bulk modulus and Poisson ratio of a voided urethane[7] are presented in Figures 11 and 12. The inclusion of up to 50% voids decreases the bulk modulus by about a factor of three in the glassy regime to two orders of magnitude in the rubbery regime. In the transition region near 100 Hz the decrease is approximately an order of magnitude.

The addition of 50% voids decreases the Poisson ratio to approximately 0.36 in the rubbery regime and 0.31 - 0.32 in the glassy regime.

The effect of these decreased moduli on the performance of a 1-3 composite is illustrated in Table 2. Compared are the displacements generated by a 100 volt, 100 Hz potential applied to rods (12% volume fraction) embedded in an epoxy and a urethane matrix which may be covered with a GRP cap plate.

As illustrated previously in Figure 8 the motion of the rod in the epoxy matrix is approximately 45% of the motion predicted for the urethane matrix. Adding the cap plate reduces the displacement for the urethane to that predicted for the epoxy. However, voiding the urethane beneath the cap plate to a 50% volume fraction restores the displacement to that predicted for the free urethane surface.

The compressibility (or Poisson ratio) has reduced sufficiently with the addition of the voids to enable the cap plate to move without constraining the rod motion. The volume of the matrix, in this case the voided urethane, no longer must be conserved.
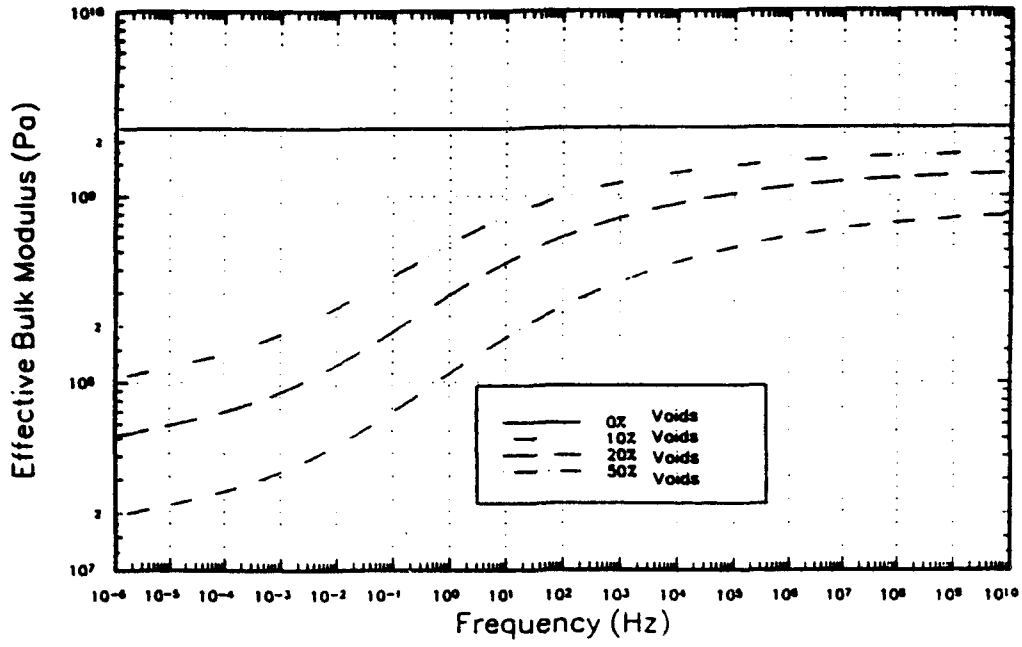
Figure 11. Effective bulk modulus of a voided urethane
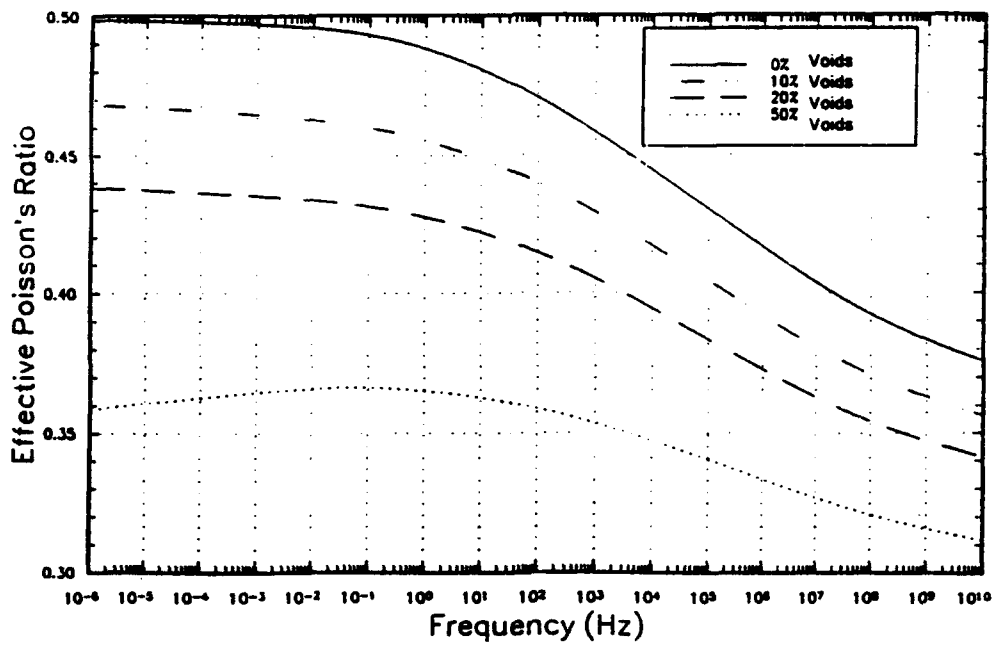
Figure 12. Effective Possion's ratio of a voided urethane

MAXIMUM ROD DISPLACEMENTS FOR VARIOUS TYPES OF MATRIX POLYMERS 12% VOLUME FRACTION 8.3 ASPECT RATIO, f = 100 Hz				
	FREE SURFACE (NO CAP PLATE)		W/ 1mm GRP CAP	
FREE PZT ROD ($\times 10^{-9}$m)	EPOXY MATRIX ($\times 10^{-9}$m)	SOLID URETHANE MATRIX ($\times 10^{-9}$m)	SOLID URETHANE MATRIX ($\times 10^{-9}$m)	VOIDED URETHANE MATRIX* ($\times 10^{-9}$m)
29.7	17.4	28.6	19.1	27.5

* CONTAINS 50% GAS VOIDS BY VOLUME

Table 2.   Rod displacements for various matrix polymers

CONCLUSIONS

The primary conclusions gleaned from the finite element analysis of 1-3 composites are twofold:

1. Traditional 1-3 composite designs which employ glassy polymers to force uniform surface motion may constrain axial displacement of the rods to 45 % of their free motion.

2. The use of voided polymers as the matrix encapsulant, if selected to be in their mid-transition to rubbery regimes, enables actuators to be designed which produce the maximum rod displacement even when attached to a lightweight structure.

ACKNOWLEDGEMENT

REFERENCES

1. Newnham, R.E., D.P. Skinner, and L.E. Cross, "Connectivity and Piezoelectric - Pyroelectric Composites," Materials Research Bulletin, vol. 13, pp. 525-536, 1978.

2. Jaffe, B., W.R. Cook, Jr. and H. Jaffe, "Piezoelectric Ceramics, Academic Press, New York, p. 10, 1971.

3. Smith, W.A. and B. Auld," Modeling 1-3 Composite Piezoelectrics - Thickness Mode Oscillations," IEEE Trans. on Ultrasonic Ferroelectric, and Frg. Control, vol 38, No. 1, pp. 40-47, Jan 1991.

4. Products Research & Chemical Corporation, 2820 Empire Avenue, Burbank, CA 91504 (818) 240-2060.

5. Sauter, D.F. and Reader, W.T. "1-3 Composites for use as Actuators", VRC Technical Report 01-93 prepared for Carderock Division, Naval Surface Warfare Center under Contract N00167-89-D-0012, Jan 1993.

REFERENCES (Continued)

6.   Chaban, I.A., "Calculation of the Effective Parameters of Microhomogeneous Media by the Self-consistent Field Method", Sov. Physics-Acoustics, vol 11, No. 1, pp. 81-86, July-Sept 1965.

7.   PR 1592 is produced by Products Research and Chemical Corporation, Aerospace/Defense Group, 21800 Burbank Boulevard, Wcodland Hills, CA 92367 (818) 702-8900. Fax: (818) 702-7499 Atten: Robert S. Giller, Market Manager.

DAMPING IN SMART MATERIALS AND STRUCTURES

Nisar Shaikh
ANALYTIC ENGINEERING COMPANY
Sunnyvale, CA 94087

Sam David Haddad
SANTA CLARA UNIVERSITY

ABSTRACT

In a class of smart materials being studied, piezoelectric constituent impart the desired sensing and actuating capabilities. These materials can be designed to exhibit novel vibration damping characteristics, that can be manipulated or controlled by microprocessor. In vibration of structures, there is a periodic exchange of kinetic and potential energy, which typically consist of strain energy. When piezoelectric constituents are present the kinetic energy is also transformed partly into electrical energy. The novel damping mechanism proposed dissipates the electrical energy before it could convert back into kinetic energy. Unlike viscous damping this damping would be independent of frequency. By use of switching circuits and filters/resonators this damping can be turned on or off as well as manipulated. The preliminary results of work in progress are demonstrated by varying vibration damping of a beam sample of a piezoelectric ceramics.

INTRODUCTION

Smart structural composites have been developed by synthesizing carbon filaments by coating thin films of piezoelectric zinc oxide [1-4]. The primary objective was to impart intrinsic features of sensing and actuation. The sensing capability enables monitoring vibration and detecting damage through strain sensing. The actuation capability would allow active vibration control. In the particular activity reported here, a novel damping is devised exploiting the presence of piezoelectric constituents. Unlike conventional materials, the damping can be increased or decreased under command. Different modes or frequency spectrum can be damped at the desired level, including negative damping where certain vibrations can be amplified if desired.

EXPERIMENTAL PREPARATION

Small test samples of cantilever beams, 5mm X 1mm, 3 to 5 cm in length were fabricated from ceramics, PZT-5H. Both sides of the ceramic were metalized to construct electrodes and were connected to a dissipating circuits shown in Figure 1. The vibration was excited by dropping small ball bearings on the beam and measured by the accelerometer mounted on the beam.

DISSIPATION CIRCUIT

A simple circuit using diodes is constructed to remove electrical energy from the vibrating beam. As the beam vibrates the charge is developed due to the presence of piezoelectric constituents. The charge is removed by transferring to the capacitor. In this simple arrangement the objective is to remove all the electrical energy and thus provide maximum damping indiscriminately. Future activity would device elaborate circuits including filters that would enable selective damping of certain frequency. It would also be possible to create a false signature by putting in electrical energy and enhance certain vibration modes.

EXPERIMENTAL RESULTS

The beams were excited by dropping ball bearing and the vibration was measured by accelerometer. The electrodes were also connected to oscilloscope to measure the electric field generated, Figure 2 shows the plot of both signals. The electrical switch is at off position and the case is termed 'damping off.' When the switch turned on the diode clips off the maximum charge developed, which is shown in Figure 3. The damping is measured by calculating logarithmic decrement as shown in Figure 4. The computation is shown below, with zero subscript referring to the case of electric damping turned off. The electrical damping, when turned on provides additional damping over materials natural damping.
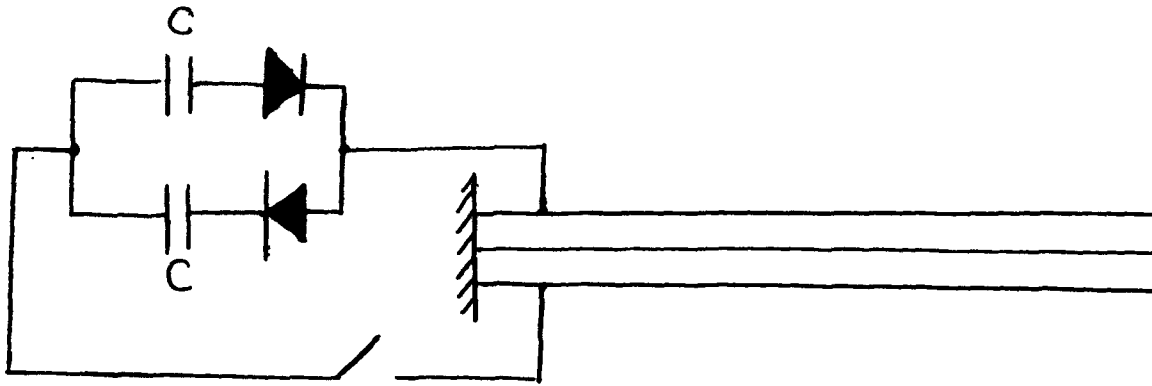
DAMPING ANALYSIS

In a vibrating system there is a continuous exchange between kinetic and potential energy. In structures, the potential energy is essentially strain energy. There is a continuous loss of the strain energy to heat due to damping in the material, which results in decay of vibration amplitude. In material with piezo-electric constituent an additional partition of kinetic energy in to electrical energy. The electro-mechanical coupling coefficient K^2 is defined as follows.

$$k^2 = \frac{\frac{1}{2}\epsilon^s_{zz}E_z^2}{\frac{1}{2}\sigma_x S_x - \frac{1}{2}\epsilon^s_{zz}E_z^2}$$

$$\frac{StrainEnergy}{StrainEnergy + ElectricalEnergy} = \frac{1}{1+k^2}$$

Following expressions relate logarithmic decrement η, through coupling coefficient to vibration amplitude. The additional damping achieved through electrical dissipation is shown in the table below. The calculated values are higher than experimentally achieved. This is due to limitation of a simple dissipation circuit use. There should be no problem in achieving the full value of theoretical predicted damping by a proper dissipation device.

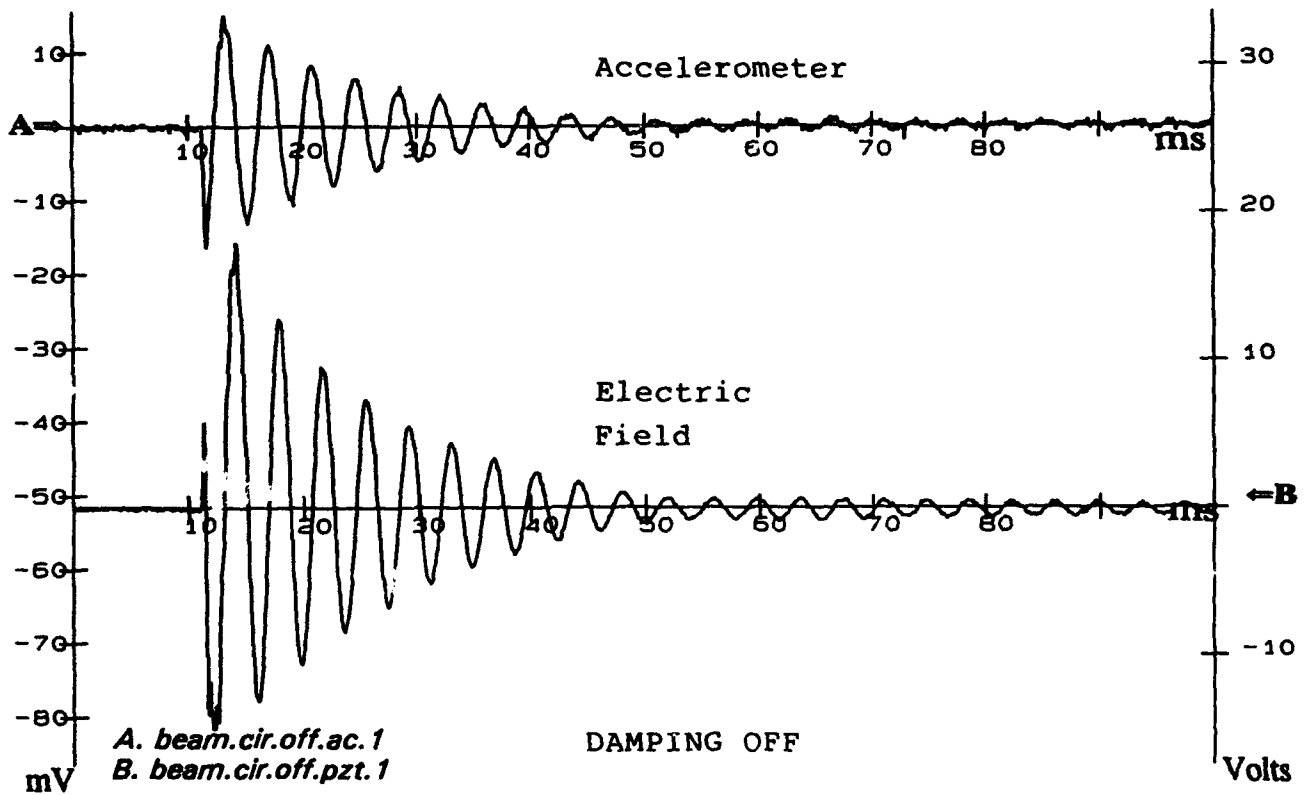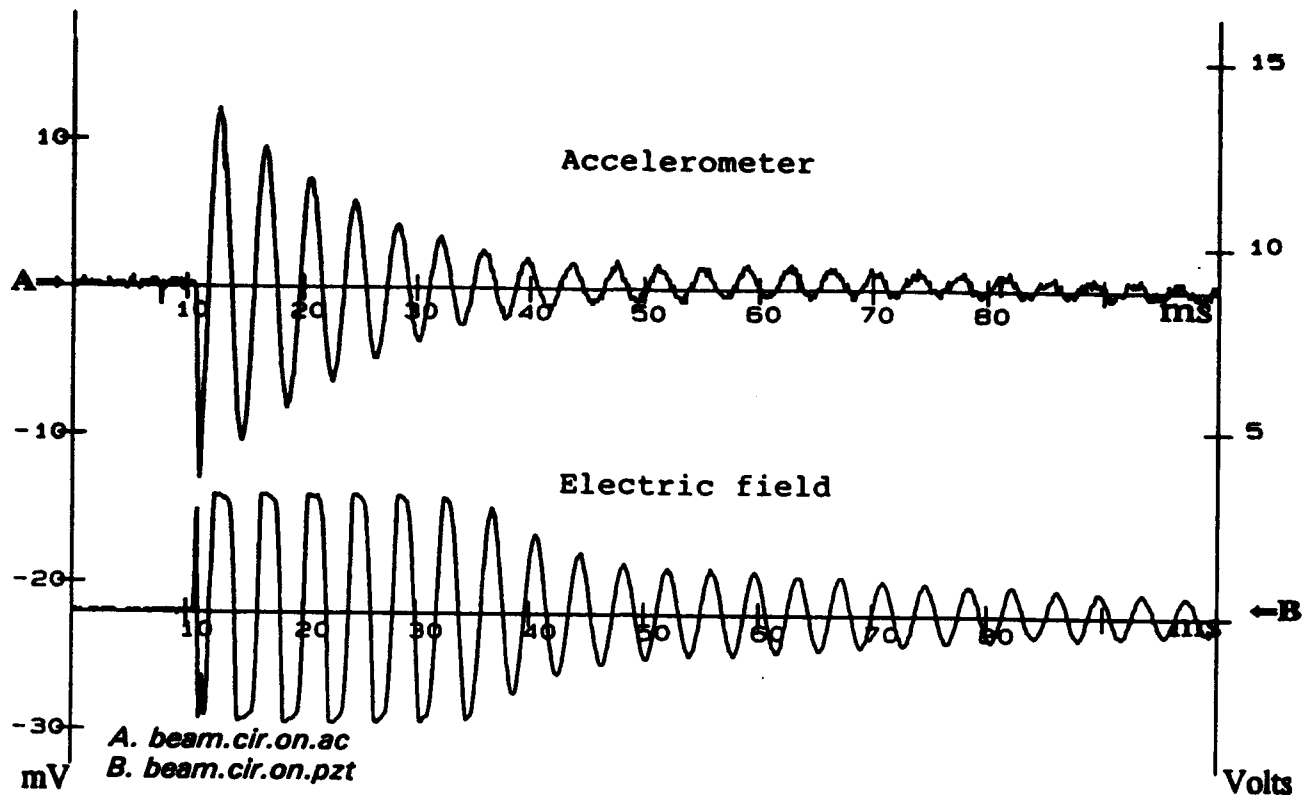SIMPLE DEVICE FOR EXTRACTING

CHARGE FROM BEAM

Figure 1

Accelerometer

Electric
Field

A. beam.cir.off.ac.1
B. beam.cir.off.pzt.1

DAMPING OFF

Figure 2

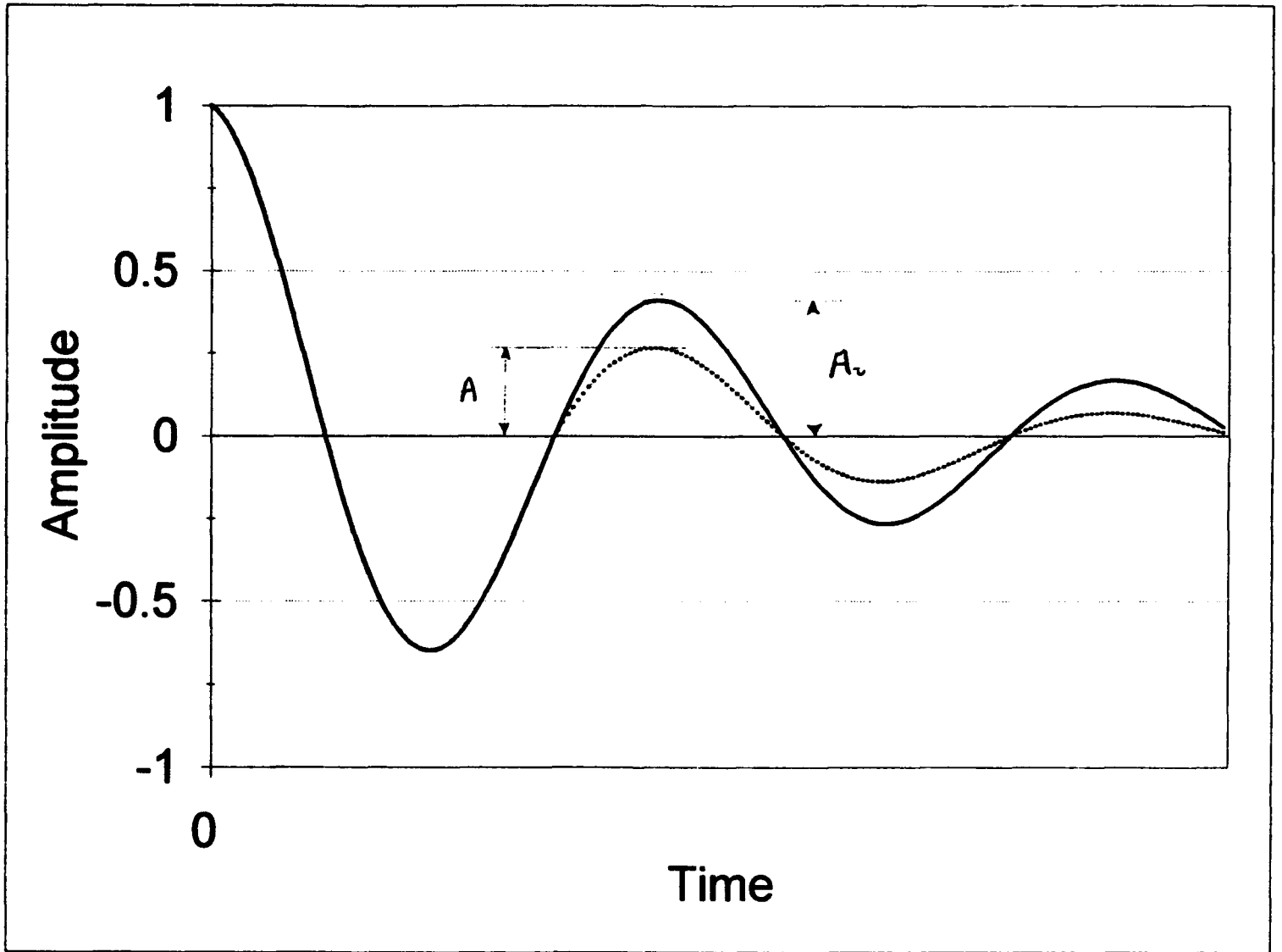DAMPING TURNED ON

Figure 3

Figure 4

$$\delta_o = \ln(1/A_o) \qquad \delta = \ln(1/A)$$

$$\delta - \delta_o = \ln(A_o/A)$$

$$\delta - \delta_o = \tfrac{1}{2}\ln(1+k^2)$$

$$\xi - \xi_o = \frac{1}{4\pi}\ln(1+k^2)$$

	Estimated	Measured
$\delta - \delta_o$	0.049	0.027
$\xi - \xi_o$	0.0078	0.0043

CONCLUSION

The damping mechanism proposed can be developed to provide additional damping in the smart material containing piezoelectric constituents. In the material and structure capable of active control, such a damping mechanism could be used in a passive mode, saving elaborate capability only for critical phases.

ACKNOWLEDGEMENT

The technical support from Yaojun Lu in preparation and conduction of test is acknowledged.

REFERENCES

1. 'Smart Structural Composites', N. Shaikh and R. Dillon, Proceedings of US/Japan Workshop on Smart/Intelligent Materials and Systems, held March 19-23, 1990, Honolulu, Hawaii
2. 'A Novel Sensor for Adaptive and Smart Structures', N. Shaikh, Proceedings of the Conference on Active Materials and Adaptive Structures, Alexandria, Virginia, Nov. 5-7 1991
3. 'Smart Structural Composites with Inherent Sensing Properties,' N. Shaikh, Proceedings of the Conf. on Active Materials and Adaptive Structures, Alexandria, Virginia, Nov. 5-7 1991
4. 'Characterization of Pulsed Laser Deposited Zinc Oxide,' Ianno, N.J., McConvile, L., and Shaikh, N., Smart Material Fabrication and Materials for Micro-Electro-Mechanical Systems, MRS Vol. 276, 1992

Actively Damped Piezoelectric Composite Wing

P.Santini, F.Betti, P.Gasbarri, A.Rossi

Dipartimento Aerospaziale, Università di Roma "La Sapienza"
Via Eudossiana 18 - 00184 Roma, Italia

Abstract

Aerospace structures require low weight and high performances. The interaction of these structures with their environment can be of different kinds. A very important one is the aeroelastic interaction between a wing and a subsonic or supersonic stream.

In this paper the aeroelastic interaction of a composite laminate swept wing in a supersonic stream will be analyzed and modeled by means of the so called 'Piston Theory'.

Due to aeroelastic effects, vibrations will be induced in the wing. These vibrations are, of course, highly undesidered. Much attention has been paid, during the last decade, to active vibration control for different kinds of structures.

In this case the vibration control will be achieved by means of direct velocity feedback. The actuators and sensors needed in order to augment the control will be piezoelectric elements. This kind of materials offers a number of advantages, such as, for example, the possibility of being easily shaped, the low weight and cost.

The structural dynamic problem (i.e. finding the modes of vibration and the natural frequencies of the structure) has been solved by using a modified finite element method. The equations of motion are then discretized using the same method. This method is particulary suitable for wing structures and differs from the classical one because it takes as unknowns chordwise global quantities instead of local ones such as flexural displacements, torsional rotations, mean-line curvature, etc.

Once the equations of motion for the controlled wing are found, they are solved by using the Runge-Kutta method. It will be shown how the control system contributes to give a more damped system.

1 Introduction

The problem of the aeroelastic behaviour of a wing is one of the major concerns in aeronautical design. The advent of composites has greatly amplified the domain of the relevant investigation.

Due to the high flexibility of their use, composite structure can prevent, or delay, undesired phenomena, such as divergence and changes in aerodynamics loads. In dynamic problems, however, simple use of composite structures may be not sufficient or viable.

Now, another tool which is to-day available to aeronautical designers is represented by active structures; in particular, by piezoelectric elements imbedded in the structure itself. As well known, a piezoelectric element (or 'piezo'), has the property that there is a coupling, in it, of elastic properties and quantities, with electric properties and quantities. This means in particular that a piezo, when subjected to elastic deformations, such as those arising on account on the aeroelastic actions on the wing, exhibits an electric field, that, for time varying phenomena, give rise to an electric current from the piezo; so it can act as a sensor. On the other hand, when properly polarized, piezos may have the role of actuators.

Special attention is here devoted to the so-called Direct Velocity Feedback Control (DVFB), where output signals from velocity sensors are electronically multiplied by gains and directly fed-back to co-located force actuators. Co-location is choosen because in this way the voltage applied to each active element can be related only to the velocity degree of freedom relevant to the element. The net effect is a closed loop augmented damping system.

When dealing with aeroelastic problems, adequate modeling for structural and aerodynamic behaviour must be provided. For the former, no special problems arise, since there is a large number of modeling techniques, starting from simple analytical solutions to sophisticated finite elements approaches. However, if one is wishing to obtain global predictions, then 'global' quantities and not 'local' quantities must be taken to describe the structural behaviour. For aerodynamics, as a principle, unsteady formulations should be used; quasi-unsteady approximations may give questionable results.

Thus, in the aeroelastic control loop three kinds of forces arise; from structure, aerodynamics, control. The purpose of this paper is that of showing the possibility of controlling the aeroelastic phenomena by means of intelligent (or 'smart') elements; therefore a sufficiently sophisticated structural model is used; for aerodynamics the simplified Piston Theory in supersonic flow is introduced. Control forces are, as said, those arising from DVFB control.

2 Constitutive Relationships of an Orthotropic Piezo-electric Lamina

The general form of the constitutive equations of a piezoelectric material can be written in the following form:

$$\epsilon_i = S_{ij}^E \sigma_j + d_{ih}^* E_h ; \qquad (i,j = 1,\ldots,6)$$
$$D_k = d_{kj}\sigma_j + \epsilon_{kh}^{\sigma} E_h ; \qquad (k,h = 1,2,3) \qquad (1)$$

where $d_{sr}^* = d_{rs}$. Superscripts indicate those fields which are kept constant; σ_i and ϵ_i represent stress and strain respectively, while S_{ij} is the flexibility matrix, ϵ_{kh} the dielectric matrix and d_{ki} is the piezoelectric strain/electric field matrix. Choosing the intrinsic coordinate axes according to the symmetry that exists in certain classes of piezoelectric materials, the piezoelectric strain/electric field matrix can be written, for a commonly available class, in the form:

$$d = \{d_{ki}\} = \begin{bmatrix} 0 & 0 & 0 & 0 & d_{15} & 0 \\ 0 & 0 & 0 & d_{24} & 0 & 0 \\ d_{31} & d_{32} & d_{33} & 0 & 0 & d_{36} \end{bmatrix} \qquad (2)$$

where the 3-axis is the poling axis. PZT (lead, zirconate, titanate) and PVDF (polivinylidene fluoride polymer), for example, belong to this class. Confining our attention to a piezoelectric lamina, due to its geometry, we assume that the hypothesis of plane stress state is applicabile, and that only E_3 and D_3 can be applied or detected.

Based on these assumption, Eqs. (1) can be rewritten as follows:

$$\begin{bmatrix} \epsilon_1 \\ \epsilon_2 \\ \gamma_{12} \end{bmatrix} = \begin{bmatrix} S_{11}^E & S_{12}^E & 0 \\ S_{12}^E & S_{22}^E & 0 \\ 0 & 0 & S_{66}^E \end{bmatrix} \begin{bmatrix} \sigma_1 \\ \sigma_2 \\ \tau_{12} \end{bmatrix} + \begin{bmatrix} d_{31} \\ d_{32} \\ d_{36} \end{bmatrix} E_3 \qquad (3)$$

$$D_3 = \begin{bmatrix} d_{31} & d_{32} & d_{36} \end{bmatrix} \begin{bmatrix} \sigma_1 \\ \sigma_2 \\ \tau_{12} \end{bmatrix} + \epsilon_{33}^{\sigma} E_3 \qquad (4)$$

For our purpose it is more useful to write Eq. (3) in the form:

$$\begin{bmatrix} \sigma_1 \\ \sigma_2 \\ \tau_{12} \end{bmatrix} = \begin{bmatrix} \bar{H}_{11} & \bar{H}_{12} & 0 \\ \bar{H}_{21} & \bar{H}_{22} & 0 \\ 0 & 0 & \bar{H}_{66} \end{bmatrix} \left\{ \begin{bmatrix} \epsilon_1 \\ \epsilon_2 \\ \gamma_{12} \end{bmatrix} - \begin{bmatrix} d_{31} \\ d_{32} \\ d_{36} \end{bmatrix} E_3 \right\} = \bar{H}(\epsilon - dE_3) \qquad (5)$$

where $\{\bar{H}_{ij}\} = \{S_{ij}\}^{-1}$ is the stiffness matrix. It should be noticed that Eq. (5) holds also for a non-piezoelectric orthotropic lamina when E_3 is set to zero.

A laminated piezoelectric wing plate is made of several piezoelectric as well as non-piezoelectric laminae. In general they can be oriented at an angle α with respect to the

global reference axes. Introducing the stress matrix transformation from the intrinsic axes of each lamina to the global reference axes of the wing :

$$\mathbf{T}(\alpha) = \begin{bmatrix} c^2 & s^2 & -2sc \\ s^2 & c^2 & 2sc \\ sc & -sc & c^2 - s^2 \end{bmatrix} \tag{6}$$

where $c = \cos\alpha$ and $s = \sin\alpha$, we can write:

$$\begin{bmatrix} \sigma_x \\ \sigma_y \\ \tau_{xy} \end{bmatrix} = \mathbf{T}(\alpha) \begin{bmatrix} \sigma_1 \\ \sigma_2 \\ \tau_{12} \end{bmatrix} ; \quad \begin{bmatrix} \epsilon_x \\ \epsilon_y \\ \gamma_{xy} \end{bmatrix} = \mathbf{T}_1(\alpha) \begin{bmatrix} \epsilon_1 \\ \epsilon_2 \\ \gamma_{12} \end{bmatrix} \tag{7}$$

with $\mathbf{T}_1 = \mathbf{N}^{-1}\mathbf{T}\mathbf{N}$ and $\mathbf{N} = \text{diag}\{1, 1, 1/2\}$.

In the wing frame of references, Eq.(5) can be written for each lamina in the form:

$$\begin{bmatrix} \sigma_x \\ \sigma_y \\ \tau_{xy} \end{bmatrix} = \begin{bmatrix} H_{11} & H_{12} & H_{13} \\ H_{12} & H_{22} & H_{23} \\ H_{13} & H_{23} & H_{33} \end{bmatrix} \begin{bmatrix} \epsilon_x \\ \epsilon_y \\ \gamma_{xy} \end{bmatrix} - \begin{bmatrix} r_1 \\ r_2 \\ r_3 \end{bmatrix} E_3 = \mathbf{H}\epsilon - \mathbf{r}E_3 \tag{8}$$

where:

$$\mathbf{H} = \mathbf{T}(\alpha)\bar{\mathbf{H}}\mathbf{T}_1(\alpha)^{-1} \tag{9}$$

and

$$\mathbf{r} = \mathbf{T}(\alpha)\bar{\mathbf{H}}\mathbf{d} \tag{10}$$

The classical thin laminate plate theory is used, and Kirchhoff's hypothesis are assumed for the displacements; so we have:

$$\begin{aligned} u(x,y,z;t) &= u_0(x,y;t) + z\theta_x(x,y;t) \\ v(x,y,z;t) &= v_0(x,y;t) + z\theta_y(x,y;t) \\ w(x,y,z;t) &= w_0(x,y;t) \end{aligned}$$

where u_0, v_0, w_0 represent the middle plane displacement in the x, y, z direction, and :

$$\theta_x = \frac{\partial w}{\partial x}; \qquad \theta_y = \frac{\partial w}{\partial y} \tag{11}$$

As a consequence the strains are given by:

$$\epsilon = \begin{bmatrix} \epsilon_x \\ \epsilon_y \\ \gamma_{xy} \end{bmatrix} = \begin{bmatrix} u_{0,x} \\ v_{0,y} \\ u_{0,y} + v_{0,x} \end{bmatrix} + z \begin{bmatrix} w_{,xx} \\ w_{,yy} \\ 2w_{,xy} \end{bmatrix} = \epsilon_0 + z\mathbf{k} \tag{12}$$

where ϵ_0 and $\mathbf{k}$ are middle plane deformation and the curvature vectors respectively.

Assuming that the lamination sequence is such that no coupling mechanical effect arises between in-plane quantities and out-of-plane quantities (i.e., the layers are symmetrically placed with respect to the middle plane), when the electric field is applied out of phase to each couple of symmetric piezoelectric laminae and no external in-plane forces exist, the middle plane does not stretch. With these assumptions only internal flexural moments exist in the wing and they are given by:

$$\begin{bmatrix} M_x \\ M_y \\ M_{xy} \end{bmatrix} = 2 \sum_{i=1}^{N} \int_{z_{i-1}}^{z_i} z \begin{bmatrix} \sigma_x \\ \sigma_y \\ \sigma_{xy} \end{bmatrix}_i dz = \mathbf{D}k(x,y;t) + \mathbf{p}^* \mathbf{V}(x,y;t) \qquad (13)$$

where $\mathbf{V}$ is the vector containing the voltages applied to each piezoelectric lamina, and $\mathbf{p}^*$ is the electromechanical coupling matrix. Using the simplified assumption that the same voltage is applied to each lamina in order to generate the electric field ($V = E_j h_j$), one can write for the vector $\mathbf{V}$:

$$\mathbf{V} = V\mathbf{Z}; \qquad \mathbf{Z}^T = [1; 1; \dots; 1]$$

So the following explicit expressions hold:

$$\mathbf{D} = 2 \sum_{i=1}^{N} \int_{z_{i-1}}^{z_i} z^2 \mathbf{H}_i dz = \frac{2}{3} \sum_{i=1}^{N} (z_i^3 - z_{i-1}^3) \mathbf{H}_i \qquad (14)$$

$$\mathbf{p} = \mathbf{p}^* \mathbf{Z} = -2 \sum_{j=1}^{N_p} \int_{z_{j-1}}^{z_j} z \mathbf{r}_j \frac{1}{h_j} dz = -2 \sum_{j=1}^{N_p} z_{0j} \mathbf{r}_j \qquad (15)$$

Eqs. (13), (14) and (15) hold for a wing made of $2N$ laminae, symmetric with respect to the middle plane, N_p of these laminae are piezoelectric. In Eq.(15), h_j and z_{0j} are respectively the thickness and the mean value of z for the $j.-th$ lamina. Eq.(13) is the same as that of the classical laminated plate except for the coupling electromechanical term $\mathbf{p}V$, $\mathbf{p}$ is a 3-elements vector depending on the properties and the lamination order of the piezoelectric laminae, and V is the voltage applied to each lamina. Independent commanded voltages in each lamina can be easily accounted for in the theory.

3   Strain Velocity Sensor Equation

In this work, piezoelectric laminae have also been used as velocity sensors.

The current generated across the thickness direction of every single lamina, caused by the displacements of the wing, can easily be measured through the surface electrode of each lamina by connecting it with a current amplifier.

Following the derivation proposed in [4], Eq.(4) will be used as a starting point to relate the current generated across the electrodes of the sensor to the strain velocity of the laminate.

For a piezo acting as a sensor, we have to consider the case $E_3 = 0$; so Eq.(5) reads, as combined with Eq.(7) and (12):

$$
\begin{bmatrix} \sigma_1 \\ \sigma_2 \\ \tau_{12} \end{bmatrix} = \mathbf{T}^{-1}(\alpha) \begin{bmatrix} \sigma_x \\ \sigma_y \\ \tau_{xy} \end{bmatrix} = \mathbf{T}^{-1}(\alpha)\mathbf{H}(\epsilon_0 + z\mathbf{k}) \tag{16}
$$

Substitution into Eq.(4) provides the equation:

$$
D_3 = [e_x \; e_y \; e_{xy}] \left\{ \epsilon_0 + z \begin{bmatrix} k_{xx} \\ k_{yy} \\ k_{xy} \end{bmatrix} \right\} + \epsilon_{33} E_3 \tag{17}
$$

where, using the fact that $[\mathbf{T}_1^{-1}(\alpha)]^T = \mathbf{T}(\alpha)$:

$$
\begin{bmatrix} e_x \\ e_y \\ e_{xy} \end{bmatrix} = \mathbf{T}(\alpha)\mathbf{\bar{H}} \begin{bmatrix} d_{31} \\ d_{32} \\ d_{36} \end{bmatrix} \tag{18}
$$

Gauss' law states that the electric charge enclosed by a surface S is given by the flux of the electric displacement vector $\mathbf{D}$ over the surface S. Now, since the charge is collected on the electrodes of the piezoelectric lamina and the electric displacement vector is parallel to the z axis, choosing S as the boundary surface of the lamina, application of the Gauss' law gives the charge on the electrode of the $k.-th$ sensor layer:

$$
q_k(t) = \int_{S_{e(z=z_k)}} D_3 dS + \int_{S_{e(z=z_{k-1})}} D_3 dS; \quad (k = 1, \ldots, N_s) \tag{19}
$$

where S_e is the surface of the electrodes (assuming that they cover the whole upper and lower surface of each lamina), and N_s is the number of sensor layers.

Furthermore since $i(t) = dq/dt$, Eq.(19) yields:

$$
i_k(t) = \int_{S_{e(z=z_k)}} \dot{D}_3 dS + \int_{S_{e(z=z_{k-1})}} \dot{D}_3 dS \tag{20}
$$

Finally by applying Eq.(17) to the $k.-th$ lamina and by using Eq.(20) we obtain the following sensor equation:

$$
i_k(t) = [e_x \; e_y \; e_{xy}]_k \left\{ \int_{S_e} \dot{\epsilon}_0 dS + z_{0k} \int_{S_e} \begin{bmatrix} \dot{k}_{xx} \\ \dot{k}_{yy} \\ \dot{k}_{xy} \end{bmatrix} dS \right\}; \quad (k = 1, \ldots, N_s) \tag{21}
$$

Since we are interested in relating the current signal to the mechanical deformation, E_3 has been dropped in Eq.(21), that means that the surface electrodes on both sides of the piezoelectric lamina are short-circuited.

4 Governing Equations

From Eq.(13) the following expressions holds respectively for the strain and kinetic energies:

$$\mathcal{U} = \frac{1}{2} \int_{\Sigma} \mathbf{k}^T \mathbf{D} \mathbf{k} d\Sigma + \int_{\Sigma} \mathbf{k}^T \mathbf{p} V d\Sigma \tag{22}$$

$$\mathcal{T} = \frac{1}{2} \int_{\Sigma} \mu \left(\frac{\partial w}{\partial t}\right)^2 d\Sigma \tag{23}$$

while the work done by external forces per unit area f can be expressed as:

$$\mathcal{P} = \int_{\Sigma} f w d\Sigma \tag{24}$$

From the stationariety of the functional:

$$\int_0^t \mathcal{E} dt = \int_0^t (\mathcal{U} - \mathcal{T} - \mathcal{P}) dt \tag{25}$$

the well known equation of motion is obtained:

$$\left[\frac{\partial^2}{\partial x^2}; \frac{\partial^2}{\partial y^2}; 2\frac{\partial^2}{\partial x \partial y} \right] \mathbf{D} \left[\begin{array}{c} w_{,xx} \\ w_{,yy} \\ 2w_{,xy} \end{array} \right] + f_p + \mu \frac{\partial^2 w}{\partial t^2} = f \tag{26}$$

where f_p is the load relevant to the piezo. To solve Eq. (26) we shall use a modified finite elements method, especially suitable for wing structures, proposed in [1]. This method takes as unknowns chordwise global quantities (such as displacement of center-line of the section, torsional rotation, centerline curvature of the section, etc.) instead of local ones. For spanwise quantities the classical finite element modelling is used.

Let us introduce now the non-dimensional coordinates:

$$\begin{array}{ll} \eta &= y/L \\ u &= (x - \theta y)/c \end{array} \tag{27}$$

with:

$$-0.5 \leq u \leq 0.5; \qquad 0 \leq \eta \leq 1 \tag{28}$$

where $\theta = \tan \Lambda$, L = semi-span, c = chord-length. In this paper we shall consider only the case $\Lambda(u) = cost$. For the non-dimensional elastic displacement, $W = w/L$, the following expression has been used:

$$W(u,\eta) = \sum_{k=0}^{N} (\beta u)^k W_k(\eta) \tag{29}$$

The term β^k has been introduced in order to give all the quantities $W_k(\eta)$ the same order of magnitude.
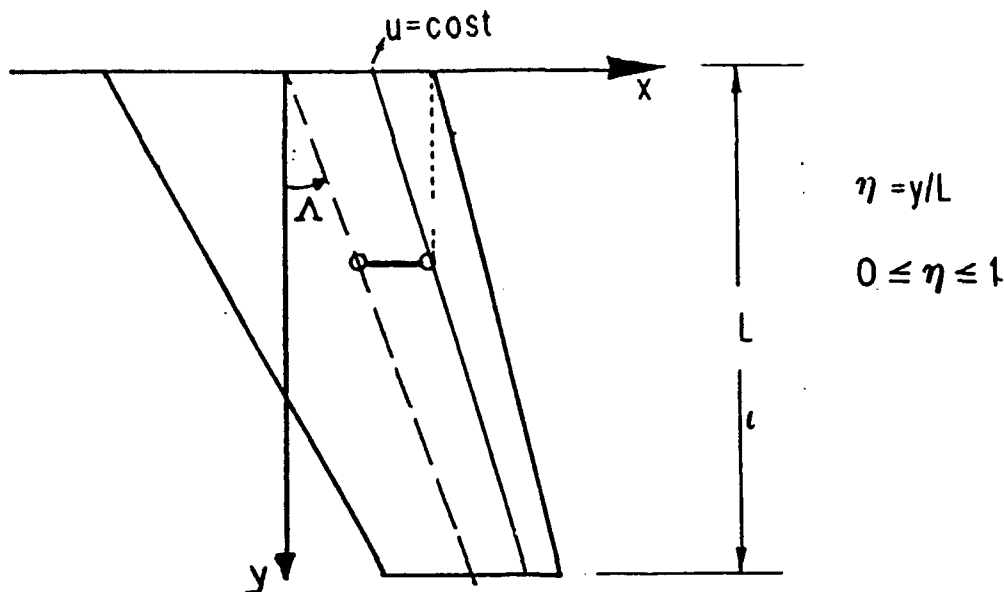
Figure 1: Coordinate transformations adopted for the wing planform

The explicit expressions for the shape functions, used for $W_k(\eta)$ in the finite element formulation, are given in App.[A]

We shall use Eq.(29) with $N = 2$, so that the $W_k(\eta)$ functions have a clear physical meaning: W_0 represents the vertical displacement of a generic section of the wing, W_1 is the torsional rotation, while W_2 is the chordwise curvature.

In order to write the strain and kinetic energy for the generic finite element, the following non-dimensional variables are introduced:

$$T^2 = \frac{ML^2}{D_{11}}; \quad \tilde{D} = \frac{D}{D_{11}}; \quad \tilde{\mu} = \frac{\mu L c}{M}; \tag{30}$$

$$\tilde{p} = \frac{p}{h_{p_{TOT}} Y_p d_{31}}; \quad \tilde{V} = \frac{V}{E_{max} h_p}; \quad \tilde{f} = \frac{fL^3}{D_{11}} \tag{31}$$

where:

- $\tau = t/T$: non-dimensional time;

- M : mass of half wing;

- D_{11} : first element of the $\mathbf{D}$ matrix;

- μ : density per unit area;

- $h_{p_{TOT}}$: total thickness of the piezoelectric laminae;

- h_p : $h_{p_{TOT}}/N_p$

- E_{max} : maximum electric field that can be applied to the piezoelectric lamina;

- Y_p : Young modulus of the piezoelectric material.

The non-dimensional curvature vector reads:

$$
\mathbf{C} = \begin{bmatrix} C_1 \\ C_2 \\ C_3 \end{bmatrix} = L \begin{bmatrix} k_{xx} \\ k_{yy} \\ k_{xy} \end{bmatrix} = \begin{bmatrix} (1/\beta^2)W_{,uu} \\ (\theta/\beta)^2 W_{,uu} - 2(\theta/\beta)W_{,u\eta} + W_{,\eta\eta} \\ 2(\theta/\beta^2)W_{,uu} + (2/\beta)W_{,u\eta} \end{bmatrix} \quad (32)
$$

where the explicit expression of these quantities are given in App.[A]. Using these non-dimensional variables the total energy of each element is given by:

$$
\mathcal{E}_e = D_{11} \left\{ \frac{1}{2} \int_{S_e} \bar{\mu} \dot{W} W dS - \frac{1}{2}\beta \left(\int_{S_e} \mathbf{C}^T \bar{\mathbf{D}} \mathbf{C} dS + 2\frac{\Gamma\lambda}{\beta} \int_{S_e} \mathbf{C}^T \bar{\mathbf{p}} \tilde{V} dS \right) - \beta \int_{S_e} \tilde{f} W dS \right\}
$$
$$(33)$$

where $\lambda = E_{max} d_{31}$ is the maximum value of the strain that can be induced in a not constrained piezoelectric lamina and

$$
\Gamma = \frac{Y_p h_p h_{pTOT} c}{D_{11}} \quad (34)
$$

These parameters are very useful in order to relate the strain energy directly transferred to the element by the piezoelectric lamina, with the strain energy stored in the element, as it is clear from Eq.(33). Thus the product $\Gamma\lambda$ gives an idea of the effectiveness of the piezoelectric laminae in actuating the system. Using Eqs.(29) and (32), Eq.(33) can be written in finite terms as:

$$
\mathcal{E}_j = \frac{1}{2} \dot{\mathbf{X}}_j^T \mathbf{M}_j \dot{\mathbf{X}}_j + \frac{1}{2} \mathbf{X}_j^T \mathbf{K}_j \mathbf{X}_j + \mathbf{X}_j^T \mathbf{P}_j \tilde{V}_j - \mathbf{X}_j^T \mathbf{F}_j; \quad (j = 1, n_e) \quad (35)
$$

where n_e is the number of elements, $\mathbf{X}_j$ is the vector of the degree of freedom of the j-th element, that in the present case is, as defined in App.[A]:

$$
\mathbf{X}_j^T = [(W_0 W_0' W_1 W_1' W_2 W_2')_0 \ (W_0 W_0' W_1 W_1' W_2 W_2')_1] \quad (36)
$$

and $\mathbf{P}_j$ is given by:

$$
\mathbf{P}_j = \mathbf{A}^T \bar{\mathbf{p}}_j \quad (37)
$$

$\mathbf{M}_j$ and $\mathbf{K}_j$ are respectively the mass and the stiffness of the element and $\mathbf{A}$ is given in App.[A]. According to the FEM methodology, assembling Eqs.(35) in order to write the total energy of the wing and differentiating with respect to the whole set of the degrees of freedom $\mathbf{X}$, we obtain, adding a viscous damping term, the general governing equation for the discretized system:

$$
\mathbf{M}\ddot{\mathbf{X}} + \Delta\dot{\mathbf{X}} + \mathbf{K}\mathbf{X} + \mathbf{F}_p = \mathbf{F} \quad (38)
$$

In Eq.(38) the vector $\mathbf{F}_p$ takes into account the actions exerted by the piezoelectric actuators. This vector can be explicitly written in terms of the control variables, that is the vector of the voltages applied to each element, in the form:

$$
\mathbf{F}_p = \mathbf{P}\tilde{\mathbf{V}} \quad (39)
$$

where P is a $(m \times n_e)$ matrix transforming the voltage applied to each element in nodal forces, and m and n_e are respectively the number of degrees of freedom and the number of elements of the finite element model. It can easily be seen that P is made of blocks of vectors P_j arranged as it is shown in Fig.(2).

Of course, it is assumed $V_j = 0$ for non-piezoelectric elements.

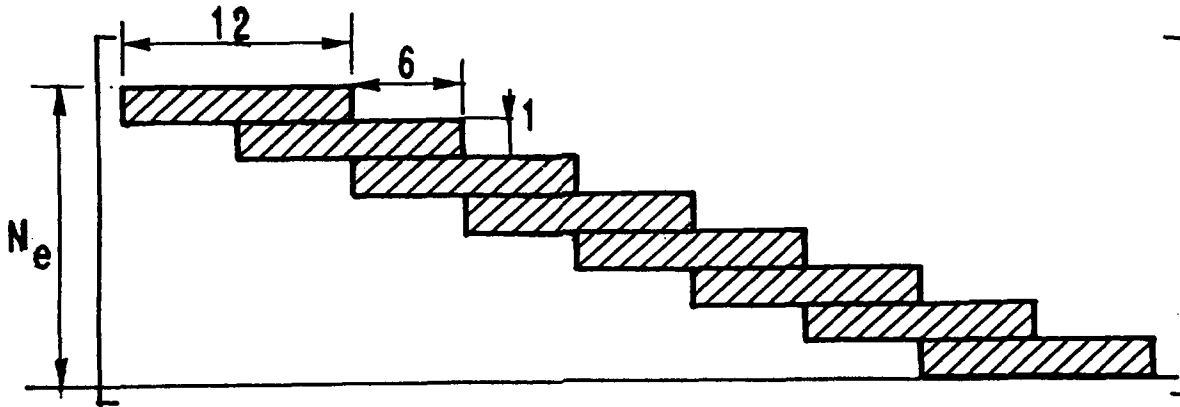Figure 2: Block structure of the transpose of the matrices P and B.

5 Direct Velocity Feedback Control

Direct velocity feedback (DVFB) [5] is a method for active damping augmentation in which the output signals from the velocity sensors are electronically multiplied by gains, and directly fed-back to co-located force actuators. Usually, this method is applied in conjunction with point-force actuators and point-sensors; in this paper it will be shown how it applies to piezoelectric actuators and sensors. Since actuators and sensors should be co-located, the voltage applied to each active element can be related only to the velocity degrees of freedom corresponding to that element. The expression for the voltage vector is:

$$\mathbf{V}(t) = \mathbf{G}\mathbf{B}^T\dot{\mathbf{X}}(t) \tag{40}$$

where G is a diagonal matrix $(n_e \times n_e)$ of gains; of course G_{jj} should be set equal to zero for non-active elements. B is a rectangular $(m \times n_e)$ matrix that, because of the colocation, is made of blocks of vectors B_j, of order equal to the number of the degrees of freedom of each element (12 in the present work), arranged in the same way as the matrix P as it shown in Fig.(2). Each vector B_j depends upon the sensor used for the element. The control forces exerted by the active elements can be written as:

$$\mathbf{F}_p(t) = \mathbf{Q}\dot{\mathbf{X}}(t) \tag{41}$$

with:

$$\mathbf{Q} = \mathbf{P}\mathbf{G}\mathbf{B}^T \tag{42}$$

Generally $\mathbf{Q}$ is not a symmetric matrix, however if its symmetric part is non-negative definite, the closed loop system with DVFB is energy dissipative. This means that the DVFB controller cannot destabilize any part of the system no matter what the choice of the feedback gains is. Also, the pole locations of the closed loop system will never be placed, in the complex plane, on the right side of their locations for the open loop system. The net effect is a closed loop damping augmented system. In order to apply this method it should be checked that for the particular choice of the actuators and sensors the matrix $\mathbf{Q}$ is non-negative definite.

In the following it will be shown how the non-negative definiteness of $\mathbf{Q}$ can be checked on largely reduced matrices relevant to single active elements.

Looking at the structure of the matrices $\mathbf{P}$ and $\mathbf{B}$, it can be noted that $\mathbf{Q}$ is a block diagonal matrix obtained by assembling element matrices:

$$\mathbf{Q}_j = \mathbf{P}_j G_{jj} \mathbf{B}_j^T, \quad (j = 1, \ldots, n_e) \tag{43}$$

where G_{jj} is the $j.-th$ element gain and $\mathbf{P}_j$ and $\mathbf{B}_j$ depend on the choce of actuators and sensors used for the element.

The quadratic form $\mathbf{X}^T sym\{\mathbf{Q}\}\mathbf{X}$ can be written:

$$\mathbf{X}^T sym\{\mathbf{Q}\}\mathbf{X} = \sum_{j=1}^{n_e} \mathbf{X}_j^T sym\{\mathbf{Q}_j\}\mathbf{X}_j \tag{44}$$

so that a sufficient condition for $sym\{\mathbf{Q}\}$ to be non-negative definite is that all the $sym\{\mathbf{Q}_j\}$ are non-negative definite.

From this point of view it is clear that, if the actuators and the sensors of each active element are choosen in such a way to satisfy that restriction, they are able to increase the damping of the system. Since piezoelectric elements have already been choosen as actuators, different choices of sensors can be used to make $sym\{\mathbf{Q}_j\}$ non-negative definite. This involves properly choosing the vector $\mathbf{B}_j$.

A mathematical derivation of the constraints that should be imposed on the vector $\mathbf{B}_j$ in order to check the aforementioned condition has not been carried out. The metodology followed in this work has been to use the piezoelectric materials, laminated in the active elements, as velocity sensors as described in Sec.3, and check that the resulting $\mathbf{Q}_j$ matrices satisfy the condition. The expression of the vector $\mathbf{B}_j$ can be obtained using the finite element method developed in App.A, in order to evaluate Eq.(21) for the $j.-th$ element.

Assuming that each couple of symmetric layers of sensor are connected out of phase, so that their output is independent of the middle plane deformation, we obtain for the output voltage of the sensor circuit of the $j.-th$ element:

$$\bar{V}_j(t) = \bar{\mathbf{b}}_j^T \mathbf{A}\dot{\mathbf{X}}_j = \mathbf{B}_j^T \dot{\mathbf{X}}_j \tag{45}$$

with:

$$\check{\mathbf{b}}_j = \left\{ 2 \sum_{k=1}^{N_s} \check{z}_{0k} \check{g}_k \left[\begin{array}{c} \check{e}_x \\ \check{e}_y \\ \check{e}_{xy} \end{array} \right]_k \right\}_j \qquad (46)$$

where N_s is the number of middle plane symmetric layers. In Eq.(46) the following non-dimensional quantities have been introduced:

$$\check{z}_{0k} = \frac{z_{0k}}{h_p}; \qquad \check{g}_{0k} = g_{0k} \Gamma \frac{D_{11} d_{31}}{E_{max} h_p T}; \qquad \check{e}_k = \frac{e_k}{h_p Y_p d_{31}}$$

where:

- z_{0k} : mean value of z for the k-th lamina of sensor;

- g_{0k} : gain for the current amplifier of the k-th lamina.

The $\mathbf{Q}_j$ matrix is:

$$\mathbf{Q}_j = \mathbf{P}_j G_{jj} \mathbf{B}_j^T = \Gamma \Lambda G_{jj} \mathbf{A}^T \check{\mathbf{p}}_j \check{\mathbf{b}}_j^T \mathbf{A} \qquad (47)$$

This matrix is very sparse and of a much smaller order than $\mathbf{Q}$ (in the present work is (12×12)), hence the non negative definiteness of it can be easily verified for any choice of the actuators and sensors laminae.

6 Wing Aeroelastic Equations

In order to study the dynamic behavior of the wing two kinds of aerodynamic forces will be considered: the first one, assiociated to the wing incidence, is given by the aerodynamic operator; the second ones, are the external loads, for example produced by a vertical gust.

The Piston Theory is used to build the aerodynamic operator [6]:

$$\mathcal{A} = -\frac{2q}{V_\infty \sqrt{M_\infty^2 - 1}} \left[V_\infty \frac{\partial}{\partial x} + \frac{M_\infty^2 - 2}{M_\infty^2 - 1} \frac{\partial}{\partial t} \right] (\frac{w}{V_\infty}) \qquad (48)$$

This theory represents an approximation of the aerodynamic theory in which the influence of three-dimensional aerodynamic effects are neglected. The aerodynamic force, including the effects of a vertical gust is given by:

$$f = \frac{2q}{\sqrt{M_\infty^2 - 1}} \left[\alpha_g - \left(\frac{\partial w}{\partial x} + \frac{M_\infty^2 - 2}{M_\infty^2 - 1} \frac{1}{V_\infty} \frac{\partial w}{\partial t} \right) \right] \qquad (49)$$

where:

$$\alpha_g = \frac{V_g}{V_\infty} \qquad (50)$$

represents the incidence due to a vertical gust of velocity V_g.

If the following non-dimensional quantities are used:

$$W = \frac{w}{L}; \qquad \tau = \frac{t}{T}; \qquad X = \frac{x}{L} \qquad (51)$$

a non-dimensional expression for the aerodinamic force is obtained:

$$\bar{f} = k\left[\alpha_g - \left(\frac{\partial W}{\partial X} + \gamma^2 \frac{\partial W}{\partial \tau}\right)\right] \qquad (52)$$

with

$$k = \frac{2q}{M^2 - 1} \frac{T^2}{\mu L}; \qquad \gamma^2 = \frac{M^2 - 1}{M^2 - 1} \frac{L}{TV_\infty} \qquad (53)$$

Substituting Eq. (49) in Eq. (26), the aeroelastic equations are found. These equations are then discretized following the procedure described in Sec.4. However, it has to be noted that the aeroelastic force is dependent from the vertical displacement and Eq. (29) has to be used.

7 Numerical Results

A considerable reduction of the degrees of freedom in Eq.(38) can be obtained by eliminating the inertial and elastic coupling. This is accomplished by expressing the vector X in terms of undamped natural vibration modes. From the equation:

$$\mathbf{M\ddot{X} + KX = 0} \qquad (54)$$

it is possible to find the eigenvectors matrix, which contains the natural mode shape vectors, Φ of order $(m \times m)$. By introducing the coordinate transformation $\mathbf{X = \Phi U}$ and premultipling for the matrix Φ^T, Eq.(38) becomes:

$$\mathbf{\Phi^T M \Phi \ddot{U} + \Phi^T \Delta \Phi \dot{U} + \Phi^T K \Phi + \Phi^T F_p = \Phi^T F} \qquad (55)$$

where $\mathbf{Q^T MQ, Q^T \Delta Q}$ and $\mathbf{Q^T KQ}$ are diagonal matrices.

In order to carry out the analysis it is possible to work with a reduced set of equations. Therefore, the number of equations retained in Eq.(55), in practical calculations, may be restricted to a lower number of degrees of freedom (natural modes), the most important of which are usually those with the lowest eigenvalues. So, by taking into account only the first n modes the matrix Φ is rectangular $(m \times n)$, and the Eq.(55) yields the reduced matrix equation:

$$\mathbf{\bar{M}\ddot{U} + \bar{\Delta}\dot{U} + \bar{K}U + \bar{F}_p = \bar{F}} \qquad (56)$$

where the diagonal matrices $\mathbf{\bar{M}}$, $\mathbf{\bar{\Delta}}$, and $\mathbf{\bar{K}}$ are of the order $(n \times n)$.
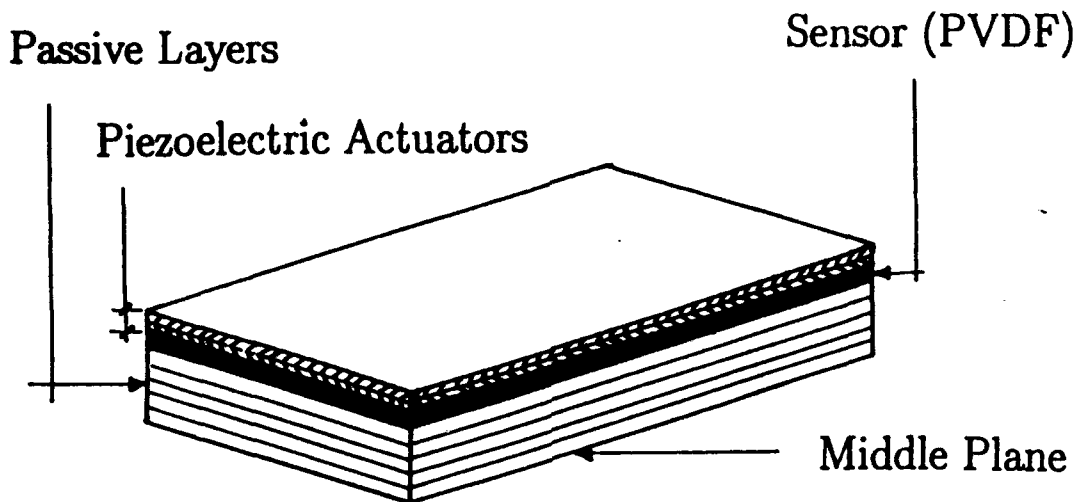
Figure 3: Wing piezoelectric finite element

This system is the one that has been directely integrated via Runge-Kutta method, with $n = 6$.

In order to apply the proposed method, a wing active element made of 20 layers has been used. The first three upper and lower layers are piezoelectric; the first two are used as actuators while the third one as a sensor, see Fig.(3). Because of the different mechanical properties of piezoelectric materials, PZT laminae has been chosen for the actuators, while PVDF for the sensors. The piezoelectric material properties are given in Tab.1. In the configuration adopted, the intrinsic axes of the piezoelectric laminae coincide with the global coordinate axes of the wing, so that for each of them $\alpha = 0$.

With this choice of actuators and sensors, the condition that $sym\{Q_j\}$ is non-negative definite is verified, so that we are sure that the active element acts as a damper on the system. Each of such active element is assumed to coincide with a finite element of the FEM discretization.

In the present work, a wing with a positive swept angle $\Lambda = 45°$ and aspect ratio of 10 has been considered; 15 spanwise elements are used to modelize the wing, three of which are piezoelectric. Starting numbering the element from the root of the wing, the elements number 1,2,3 are active. The parameter $\Gamma\lambda$ has been set equal to 0.01, moreover for all the elements the feedback gains G_{jj} has been set equal to 100.

The following examples has been considered:

(i) dynamic response to a unit impulse vertical force applied at the tip of the wing;

(ii) aeroelastic response to a vertical gust in a supersonic flow (Mach number: $M_\infty = 1.5$, dynamic pressure: $q = 5400 N/m^2$). Two classical laws are considered for the incidence due to the gust; they are the rectangular gust:

$$\alpha_g(\tau) = \begin{cases} 1; & 0 \leq \tau \leq T_g \\ 0; & \tau > T_g \end{cases}$$

	PZT	PVDF
Y_p	63 (GPa)	2 (GPa)
d_{31}	171 e-12 (m/V)	23 e-12 (m/V)
d_{32}	171 e-12 (m/V)	3 e-12 (m/V)
d_{36}	0	0
E_{max}	10 e+5 (V/m)	80 e+5 (V/m)

Table 1: Piezoelctric material properties

with T_g =20; and the 'one-minus-cosine' gust:

$$\alpha_g(\tau) = \begin{cases} 1 - \cos\left(\frac{2\pi}{T_g}\tau\right); & 0 \le \tau \le T_g \\ 0; & \tau > T_g \end{cases}$$

with T_g =5.

Figs.(4) and (5) represent the time histories of the vertical displacement and torsional rotation respectively, corresponding to example (i). The thick line is relative to the controlled system, while the thin line to the uncontrolled one. These figures clearly show how the damping of the system has been largely increased by the active piezoelectric elements in conjunction with DVFB control.

A physical limitation exists to the maximum voltage that can be applied to a piezoelectric lamina, due to the fact that the electric field should not exceed the depoling field E_{max}. With the adimensionalization adopted in this work (see Eq.(31)), this means that the non-dimensional voltage $\tilde{V}$, fed-back to each active element, should satisfy the limitation: $-1 \le \tilde{V} \le 1$.

This condition is satisfied in the present case as it can be seen in Fig.(6). The figure represents the non-dimensional voltage fed-back to the piezoelectric laminae of the active element placed at the root of the wing; this element is the one with the higher voltage applied to, because the root of the wing is a peak strain point for all the modes.

Figs. (7) and (8) represent respectively the tip displacement and the torsional rotation due to the rectangular gust of example (ii), while the same quantities relative to the 'one-minus-cosine' gust are represented in Figs.(10) and (11). In these examples, because the aerodynamic damping is larger than the structural viscous damping, a fairly smaller percentage damping augmentaion is obtained. However the controlled system still shows a satisfactory behaviour.

Figs. (9) and (12) give the voltage feed-back, in the controlled system, to the element placed at the wing root for the rectangular and the 'one-minus-cosine' gust respectively. As for the previous example the non-dimensional voltage is well inside the range [-1,1].

8 Conclusions

The dynamic aeroelastic behavior of an adaptative swept composite wing was examined.

A vibration control has been achieved by means of direct velocity feed-back. The actuators and sensors needed in order to augment the control system are piezoelectric laminae.

The numerical results show how the wing structural damping is increased using the aforementioned direct velocity feed-back. They also illustrate the potential role of piezoelectric actuators and sensors in the develpment of vibration control system.

Further investigation will be concentrated on the effects of the number of actuators, their orientation and position on the wing.

Appendix A

Using the variable transformation adopted for the wing planform Eq.(27), the differentiation rules for a generic function $F(x, y)$ are:

$$\frac{\partial F}{\partial y} = \frac{1}{L}[F_\eta - \frac{\theta}{\beta}F_u] \tag{57}$$

$$\frac{\partial F}{\partial x} = \frac{1}{c}\frac{\partial F}{\partial u} \tag{58}$$

where $\beta = c/L$ is the inverse of the wing aspect ratio.

Following this rule we obtain for the non-dimensional curvature vector C the expression written in Eq.(32) of the main text, where:

$$
\begin{aligned}
C_1(u, \eta; t) &= C_{10}(\eta; t) \\
C_2(u, \eta; t) &= C_{20}(\eta; t) + (\beta u)C_{21}(\eta; t) + (\beta u)^2 C_{22}(\eta; t) \\
C_3(u, \eta; t) &= C_{30}(\eta; t) + (\beta u)C_{31}(\eta; t)
\end{aligned} \tag{59}
$$

and:

$$
\begin{aligned}
C_{10}(\eta; t) &= 2W_2(\eta; t) \\
C_{20}(\eta; t) &= W_0''(\eta; t) - 2\theta W_1'(\eta; t) + 2\theta^2 W_2(\eta; t) \\
C_{21}(\eta; t) &= W_1''(\eta; t) - 4\theta W_2'(\eta; t) \\
C_{22}(\eta; t) &= W_2''(\eta; t) \\
C_{30}(\eta; t) &= 2W_1'(\eta; t) - 4\theta W_2(\eta; t) \\
C_{31}(\eta; t) &= 4W_2'(\eta; t)
\end{aligned}
$$

A local variable is then introduced for each element:

$$z = \frac{\eta - \eta_j}{\delta_j} \tag{60}$$

where δ_j is the non-dimensional length of the finite element, so that the functions $W_k(\eta)$ are expressed in the form:

$$W_k(z;t) = W_{k0}(t)\psi_1(z) + \delta_k W_{k0}'(t)\psi_2(z) + W_{k1}(t)\psi_3(z) + \delta_k W_{k1}'(t)\psi_4(z) \qquad (61)$$

where the ψ_j are the describing functions used in the classic FEM formulation for a beam:

$$\begin{aligned}
\psi_1(z) &= 1 - 3z^2 + 2z^3 \\
\psi_2(z) &= z(1 - 2z + z^2) \\
\psi_3(z) &= -3z^2 - 2z^3 \\
\psi_4(z) &= -z^2 + z^3
\end{aligned}$$

As a consequence the degree of freedom vector of the $j.-th$ finite element is:

$$\mathbf{X}_j^T = [(W_0 W_0' W_1 W_1' W_2 W_2')_0 \ (W_0 W_0' W_1 W_1' W_2 W_2')_1] \qquad (62)$$

Using Eqs.(59) and (61) the classical finite elements rules are used in order to build the mass and stiffness matrices, and the force vector that appear in Eq.(33) of the main text.

As far as the vector $\mathbf{P}_j$ is concerned, that appears in the piezoelectric elements, since properties of the piezoelectric laminae and the voltage applied are constant in the element, from Eqs.(33) and (35), we have:

$$\mathbf{P}_j = \Gamma\lambda \int_{S_e} \mathbf{C}^T dS \ \tilde{\mathbf{p}} \qquad (63)$$

Using, Eqs.(59) and (61), we can set:

$$\int_{S_e} \mathbf{C} dS = \mathbf{A}\mathbf{X}_j \qquad (64)$$

and finally:

$$\mathbf{P}_j = \Gamma\lambda \mathbf{A}^T \tilde{\mathbf{p}}_j$$

References

[1] P. SANTINI, M. A. SNEIDER, L. LEUZZI, "Structural dynamic of a cantiliver swept wing ", *L'Aerotecnica Missili e Spazio*, September 1986, pp. 141-149

[2] P. SANTINI, "Costruzioni Aeronautiche", 1986, E.S.A.

[3] P. SANTINI, P. GASBARRI, A. SERMONETA, "Dynamic Response of a Composite Swept Wing" *Sampe 92, 13-th International Conference and Exhibition European Chapter*, Hamburg, Germany, May 11-13, 1992

[4] C. K. LEE, "Theory of Laminated Piezoelectric Plates for the Design of Distributed Sensors/Actuators. Part I: Governing Equations and Reciprocal Relationships", *Journal of Acoustic Society of America* 87(3), March 1990.

[5] M. J. BALAS, "Direct Velocity Feed-back Control of Large Space Structures", *Journal of Guidance and Control*, 1978, Vol.2, No.3, pp.252-253.

[6] ASHLEY H. AND ZARTARIAN G., "Piston Theory, a New Aerodynamic Tool for the Aerolastician ", *Aero Sciences* , vol.23, n. 12, December 1956, pp. 1109-1118.

[7] BISPLINGHOFF R. L., ASHLEY H., " Principles of Aerolasticity", John Wiley New York, 1962.
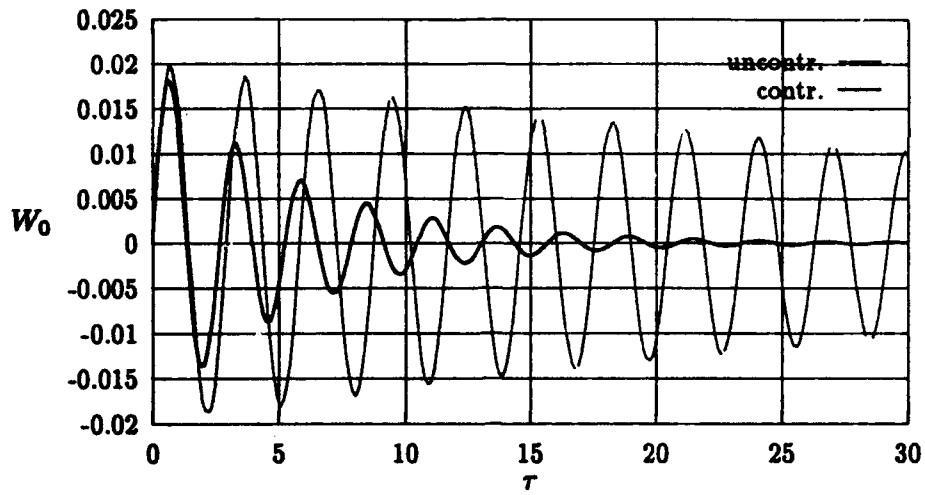
Figure 4: Tip displacement response to an impulse force with and without control.
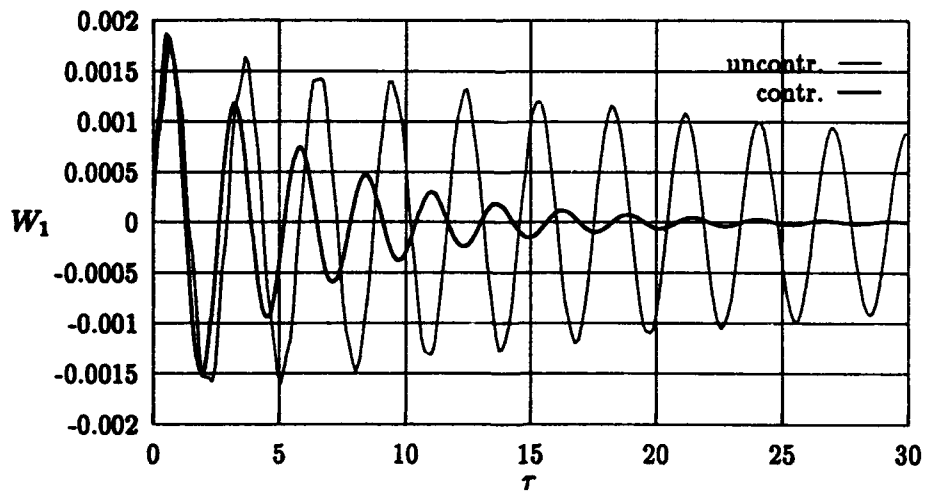
Figure 5: Tip torsional rotation response to an impulsive force with and without control.
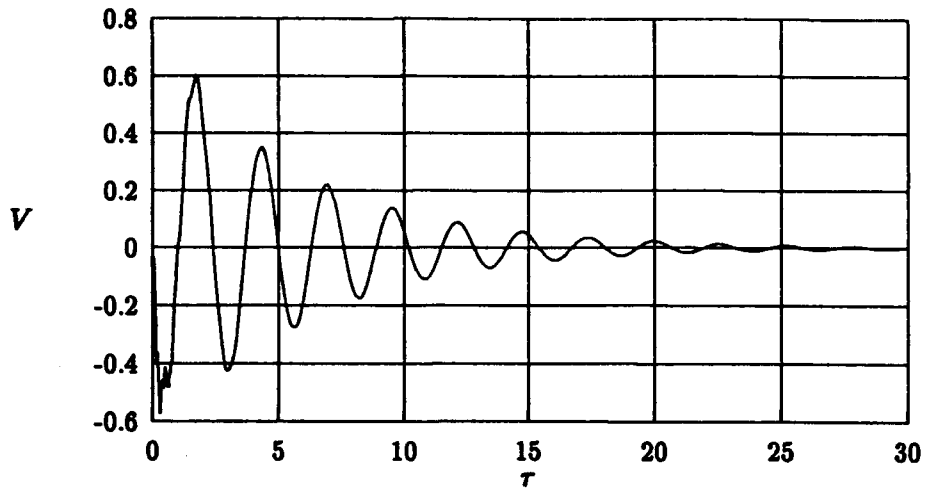
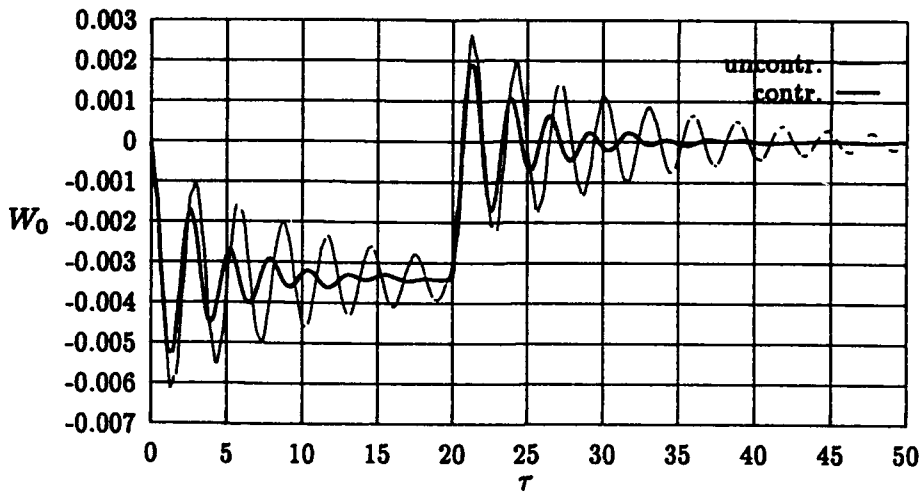Figure 6: Voltage applied to the piezo (impulse response).

Figure 7: Tip displacement response to a rectangular gust with and without control.
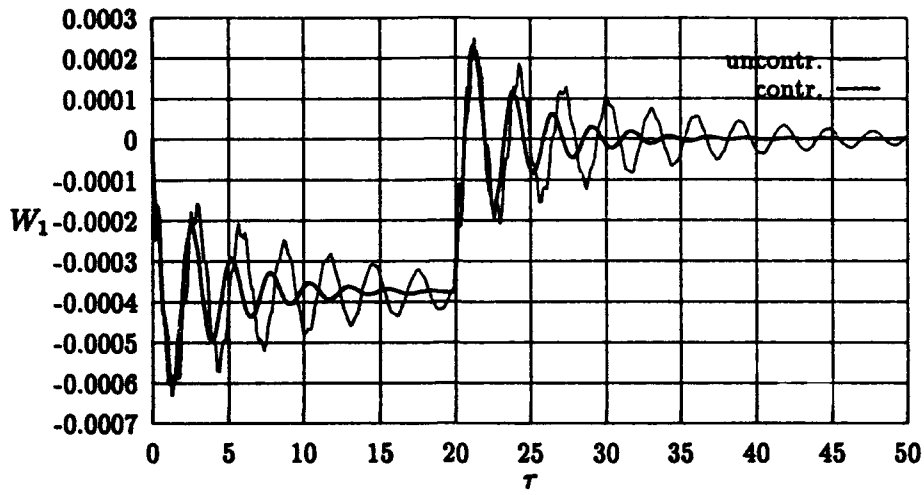
Figure 8: Tip torsional rotation response to a rectangular gust with and without control.
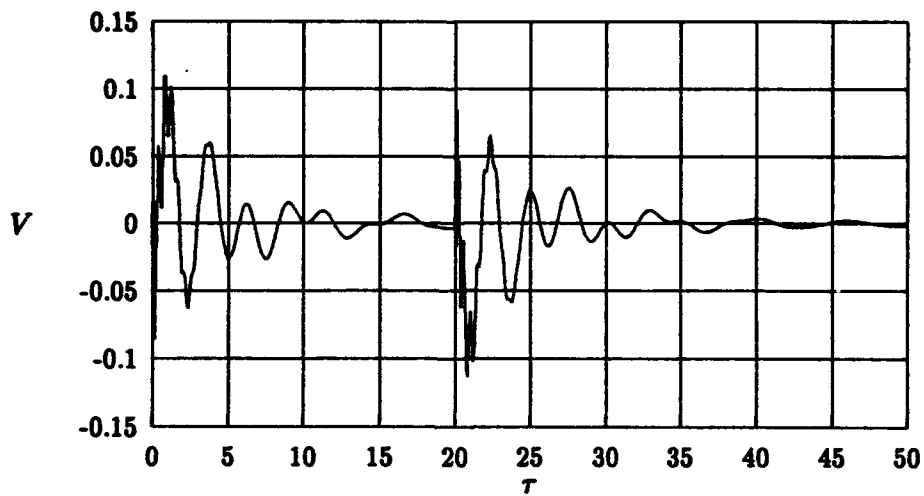

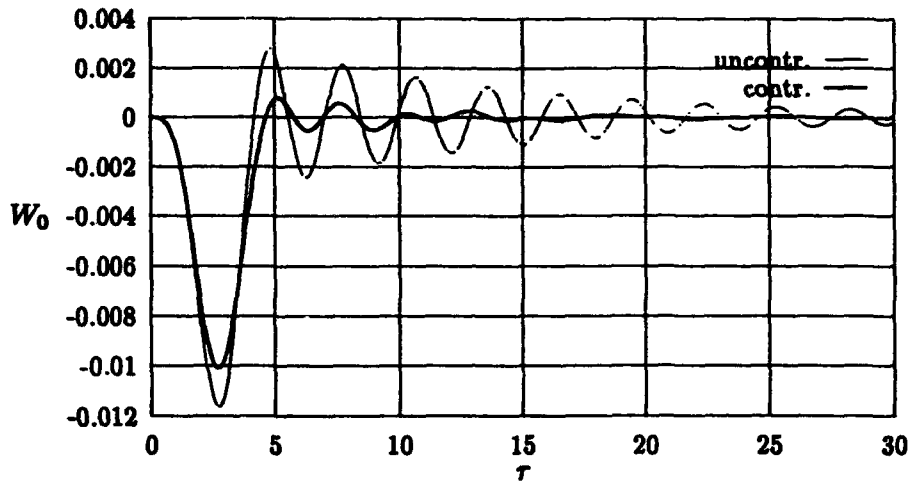Figure 9: Voltage applied to the piezo (rectangular gust response).

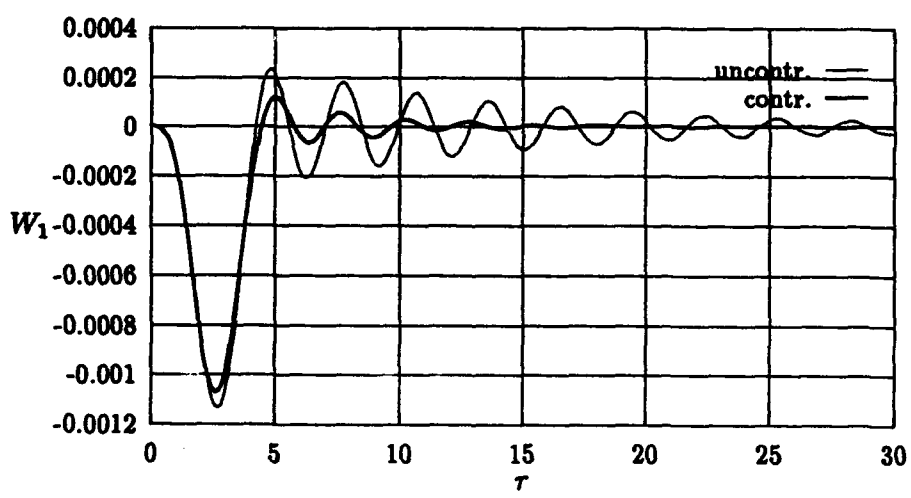Figure 10: Tip displacement response to the 'one-minus-cosine' gust with and without control.

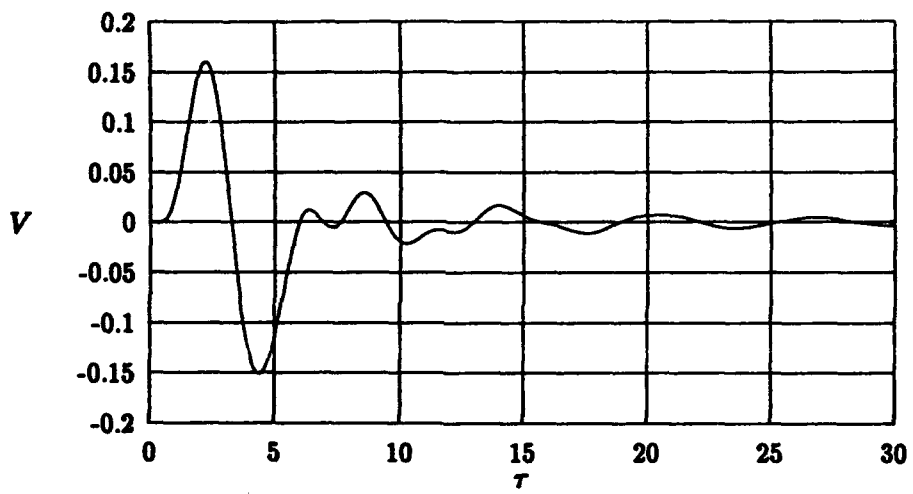Figure 11: Tip torsional rotation response to the 'one-minus-cosine' gust with and without control.

Figure 12: Voltage applied to the piezo ('one-minus-cosine' gust)